

Performance of T-shaped Reinforced Concrete Structural Walls  
under Multi-Directional Loading

A DISSERTATION  
SUBMITTED TO THE FACULTY OF THE GRADUATE SCHOOL  
OF THE UNIVERSITY OF MINNESOTA  
BY

Beth Louise Brueggen

IN PARTIAL FULFILLMENT OF THE REQUIREMENTS  
FOR THE DEGREE OF  
DOCTOR OF PHILOSOPHY

Catherine E. French

August 2009



## Acknowledgements

I would like to thank all of the people who helped to bring this effort to fruition. Several undergraduate research assistants, including Vanessa Storlie, Andy Atkins, Jake Turgeon, Danielle Berry, and Charlie Devore assisted with the construction of the test specimens. Additionally, Mingliang (Leon) Zhao and Hirokazu Onoe provided valuable assistance with construction. The cooperation and assistance of Jon Waugh, Sriram Aaletti, Ben Johnson, and Narina Jung, who were involved in the larger cooperative project are also appreciated. The staff of the MAST Laboratory, including Paul Bergson, Drew Daughtery, Chen Wan, Angela Kingsley, and Jon Messier, provided assistance with the instrumentation and testing of the walls. The advice and insight of my advisor, Cathy French, as well as the co-PIs on the project, Sri Sritharan and Susie Nakaki are greatly appreciated. Finally, I would like to thank all of my friends and family who supported me in this endeavor.

## Table of Contents

List of Figures .....	vi
List of Tables .....	xvi
Chapter 1 Introduction.....	1
1.1 Introduction.....	1
1.2 Scope of Research.....	7
1.3 Organization of Thesis .....	9
Chapter 2 Literature Review.....	13
2.1 Introduction.....	13
2.2 Reinforced Concrete Structural Wall Design.....	13
2.2.1 Boundary Elements .....	13
2.2.2 Shear Reinforcement.....	18
2.2.3 Shear Transfer across Web-to-Flange Interface.....	23
2.2.4 Shear Lag and Effective Flange Width.....	24
2.2.5 Distribution of Longitudinal Reinforcement .....	26
2.2.6 Lap Splices.....	27
2.2.7 Bar Anchorage and Strain Penetration Effects .....	29
2.2.8 Performance-Based Engineering: Prediction of Damage States.....	35
2.3 Selected Tools Available for Analysis of Structural Walls .....	38
2.3.1 Confined Concrete Material Models.....	38
2.3.2 Sectional Analysis Tools, Including BIAX (Wallace 1992).....	40
2.3.3 Empirical Models for Estimating Flexural Deformation Capacity .....	41
2.3.4 Simplified Model for Well-Confined Bridge Piers (Hines <i>Et Al.</i> 2004).....	45
2.3.5 Modified Multiple Vertical Line Element Model (Massone <i>Et Al.</i> 2006) ...	51
2.3.6 Modified Fiber-Based Model (Waugh <i>Et Al.</i> 2009) .....	52
2.4 Previous Tests of Non-rectangular Structural Walls.....	55
2.4.1 Oesterle <i>et al.</i> (1979).....	55
2.4.2 Sittipunt and Wood (1993).....	59
2.4.3 Thomsen and Wallace (1995) .....	62
2.4.4 Palermo and Vecchio (2002) .....	66
2.5 Effects of Applied Loading History on Wall Response.....	69
Chapter 3 Specimen Design and Description .....	72
3.1 Introduction.....	72
3.2 Prototype Building Design.....	72
3.2.1 General information .....	72
3.2.2 Uniaxial Bending Requirements and Distribution of Forces Among Walls.	77
3.2.3 Biaxial Bending Requirements .....	81
3.2.4 Shear Reinforcement.....	83
3.3 One-Half Scale Test Specimens.....	87
3.3.1 Scaling From Prototype Structure.....	87
3.3.2 Detailing of Specimens .....	89
3.3.3 Foundation and Top Blocks .....	97
3.3.4 Construction Sequence.....	98
3.3.5 Material Properties.....	102

3.3.6	Specimen Instrumentation .....	105
3.3.7	Testing Protocol .....	111
Chapter 4	Determination of Deformation Components and Comparison of Instrumentation Systems .....	125
4.1	Introduction.....	125
4.2	Experience of Previous Researchers .....	125
4.2.1	Massone and Wallace (2004).....	125
4.2.2	Sritharan <i>et al.</i> (1996) .....	128
4.2.3	Johnson (2007).....	131
4.3	Calculation of Components of Deformation.....	132
4.3.1	NTW1 .....	132
4.3.2	NTW2 .....	136
4.4	Comparison of Traditional and Optical Measurement Systems .....	137
4.5	Data Archival .....	140
Chapter 5	Specimen NTW1.....	141
5.1	Introduction.....	141
5.2	Observed Damage and Failure.....	141
5.2.1	Testing through Yielding .....	142
5.2.2	Post-Yielding through Failure.....	149
5.2.3	Post-Testing Autopsy of Specimen.....	160
5.3	Load versus Displacement Response .....	162
5.4	Components of Deformation.....	165
5.4.1	Flexure .....	167
5.4.2	Shear .....	170
5.4.3	Strain Penetration.....	172
5.4.4	Contribution of Components to Total Deformation.....	174
5.5	Effective Flange Width.....	183
Chapter 6	Specimen NTW2.....	186
6.1	Introduction.....	186
6.2	Observed Damage and Failure.....	186
6.2.1	Testing through Yielding .....	186
6.2.2	Post-Yielding Through Failure in Web Direction.....	191
6.2.3	Post-Web Failure through Failure in Flange-Direction Loading .....	197
6.2.4	Post-Testing Autopsy of Specimen.....	201
6.3	Load versus Displacement Response .....	203
6.4	Components of Deformation.....	206
6.4.1	Flexure .....	207
6.4.2	Shear .....	211
6.4.3	Strain Penetration.....	214
6.4.4	Splice Slip .....	216
6.4.5	Contribution of Components to Total Deformation.....	217
6.5	Effective Flange Width.....	224
Chapter 7	Comparison of NTW1 and NTW2.....	226
7.1	Introduction.....	226

7.2	Applied Load History and Deformed Shape.....	226
7.3	Load and Displacement Capacities and Relationships .....	230
7.4	Energy Dissipation.....	234
7.5	Crack Distribution.....	239
7.6	Flexural Deformation.....	247
7.7	Shear Lag Effects .....	251
7.8	Shear Deformation .....	253
7.9	Strain Penetration.....	257
7.10	Summary of Effects of Design Parameters on Wall Behavior.....	259
7.10.1	Effects of Lap Splices .....	259
7.10.2	Effects of Distributed Steel.....	261
7.10.3	Effects of Decreased Horizontal Steel Spacing .....	262
7.10.4	Effects of Increased Confinement Region .....	264
7.10.5	Specimen Size.....	265
7.11	Design Recommendations Based on Results of Testing Program.....	266
Chapter 8	Development of Simplified Modeling Procedure .....	268
8.1	Introduction.....	268
8.2	Simplified Modeling Procedure .....	269
8.2.1	Deformation due to Flexure .....	271
8.2.2	Deformation due to Shear .....	280
8.2.3	Deformation due to Strain Penetration .....	290
8.2.4	Modeling Lap Splices .....	299
8.2.5	Effects of Previous Damage: Flange Direction Loading .....	302
8.2.6	Skew Direction and Multidirectional Loading.....	308
8.3	Predicting Damage States for Performance-Based Engineering.....	310
Chapter 9	Application and Validation of F-S-SP Integration Model .....	316
9.1	Introduction.....	316
9.2	Validation of F-S-SP Integration Model.....	316
9.2.1	Comparison of F-S-SP Integration Model to Test Results .....	317
9.2.2	Rectangular Walls (Johnson 2007) .....	326
9.2.3	T-Shaped Wall TW2 (Thomsen and Wallace 1995).....	333
9.2.4	C-Shaped Wall CMS (Sittipunt and Wood 1993).....	335
9.2.5	Barbell and Hollow Box Bridge Piers (Hines 2002).....	337
9.3	Comparison to Other Simplified Models .....	339
9.3.1	FEMA 356 Model .....	340
9.3.2	Hines <i>et al.</i> (2004) model.....	344
9.3.3	Use of Nominal Material Properties and Effects of Material Property Variation on Model Results .....	349
Chapter 10	Conclusions and Recommendations .....	356
10.1	Design and detailing of non-rectangular structural walls .....	356
10.1.1	Applicability of current design provisions.....	356
10.1.2	Shear Lag Effects .....	361
10.1.3	Distribution of Longitudinal Reinforcement .....	363
10.1.4	Location of Lap Splices at the Base of the Second Story .....	365

10.2	Simplified Modeling of Reinforced Concrete Structural Walls.....	366
10.2.1	Validation of Model.....	369
10.2.2	Comparison to Other Simplified Models.....	370
10.3	Recommendations for Further Research.....	371
Chapter 11	References.....	373
Appendix A	Specimen As-Built Dimensions and Foundation/Top Block Design	
Appendix B	Instrumentation	
Appendix C	Telepresence System Information	
Appendix D	Post-testing Condition of Specimens	
Appendix E	Sample Calculations for F-S-SP Integration Method	

## List of Figures

Figure 2.1. Minimum boundary element dimensions given in ACI 318-02.....	16
Figure 2.2. Effect of shear lag on strain distribution in flange for a T-shaped cross section with the flange in tension. ....	26
Figure 2.3. Generalized force-deformation relations for concrete elements (from FEMA 356 2000).....	37
Figure 2.4. Effect of confinement on concrete stress vs. strain relationship. ....	39
Figure 2.5. Cross sections of specimens used by Hines <i>et al.</i> for model calibration. (from Hines <i>et al.</i> 2004).....	47
Figure 2.6. Schematic of nonlinear fiber-based OpenSees model of rectangular wall section (Waugh <i>et al.</i> 2009).....	54
Figure 2.7. Cross section of specimen F2 tested by Oesterle <i>et al.</i> (1979).....	58
Figure 2.8. Cross section of specimen CLS tested by Sittipunt and Wood (1993).....	61
Figure 2.9. Cross section of specimen CMS tested by Sittipunt and Wood (1993) .....	62
Figure 2.10. Cross section of TW1 tested by Thomsen and Wallace (1995) .....	63
Figure 2.11. Cross section of NTW2 tested by Thomsen and Wallace (1995) .....	64
Figure 2.12. Cross section of specimens tested by Palermo and Vecchio (2002) .....	68
Figure 2.13. Crack pattern in Specimen DP2 at failure (Palermo and Vecchio 2002)....	69
Figure 2.14. Reversed cyclic loading histories compared by Oesterle <i>et al.</i> (1979) .....	71
Figure 3.1. Typical story framing plan. ....	73
Figure 3.2. Prototype wall detailing – section view from first story. ....	75
Figure 3.3. Prototype wall detailing – elevation views.....	76
Figure 3.4. Effect of loading direction on neutral axis location and effective stiffness. .	78
Figure 3.5. Biaxial bending moment diagram for T-wall showing design moments for two interpretations of IBC 2003 Section 1620.3.2. ....	83
Figure 3.6. Section view of first story of NTW1 showing detailing.....	92
Figure 3.7. Section view of second through fourth stories of NTW1 showing detailing.	93
Figure 3.8. NTW1 detailing – elevation views.....	94
Figure 3.9. Section view of first story and lower portion of second story of NTW2 showing detailing.....	95
Figure 3.10. Section view of upper portion of second story of NTW2 showing detailing. ....	96
Figure 3.11. NTW2 detailing – elevation views.....	97
Figure 3.12. Moving of specimen NTW2 from staging area to strong floor.....	100
Figure 3.13. Strain gauges in stories 1 and 2 of web of NTW1.....	108
Figure 3.14. LVDTs and string pots on stories 1 and 2 of web of NTW1.....	109
Figure 3.15. Krypton LEDs first story of web of NTW1.....	111
Figure 3.16. Loading of prototype structure and specimens.....	113
Figure 3.17. Displacements applied to NTW1 in each ramp.....	115
Figure 3.18. Typical differences between first and later cycles to a given displacement. ....	116
Figure 3.19. Plan view of applied displacements compared to predicted failure surface: NTW1 at base of crosshead .....	116
Figure 3.20. Comparison of displacement histories at top of second story .....	117

Figure 4.1. Instrumentation used by Massone and Wallace (from Massone and Wallace, 2004).....	126
Figure 4.2. Flexural model accounting for vertical displacement (from Massone and Wallace, 2004).....	127
Figure 4.3. Decomposition of joint panel deformation into five independent modes (from Sritharan <i>et al.</i> 1996).....	129
Figure 4.4. Joint panel deformation (from Sritharan <i>et al.</i> 1996).....	131
Figure 4.5. Krypton LEDs used to determine components of deformation for NTW1 first story web.....	134
Figure 4.6. Calculation of flexural displacement from panel rotations.....	135
Figure 5.1. First story flange of NTW1 at end of elastic loading cycles.....	145
Figure 5.2. Second story flange of NTW1 at end of elastic loading cycles.....	145
Figure 5.3. Third story flange of NTW1 at end of elastic loading cycles (cracks not marked).....	146
Figure 5.4. Fourth story flange of NTW1 at end of elastic loading cycles (cracks not marked).....	146
Figure 5.5. First story web of NTW1 at end of elastic loading cycles.....	147
Figure 5.6. Second story web of NTW1 at end of elastic loading cycles.....	147
Figure 5.7. Third story web of NTW1 at end of elastic loading cycles (cracks not marked).....	148
Figure 5.8. Fourth story web of NTW1 at end of elastic loading cycles (cracks not marked).....	148
Figure 5.9. First story flange of NTW1 after web failure.....	151
Figure 5.10. Second story flange of NTW1 after web failure.....	151
Figure 5.11. Third story flange of NTW1 after web failure.....	152
Figure 5.12. Fourth story flange of NTW1 after web failure.....	152
Figure 5.13. First story web of NTW1 after web failure.....	153
Figure 5.14. Second story web of NTW1 after web failure.....	153
Figure 5.15. Third story web of NTW1 after web failure.....	154
Figure 5.16. Fourth story web of NTW1 after web failure.....	154
Figure 5.17. First story flange of NTW1 after flange failure.....	156
Figure 5.18. Second story flange of NTW1 after flange failure.....	156
Figure 5.19. Third story flange of NTW1 after flange failure.....	157
Figure 5.20. Fourth story flange of NTW1 after flange failure.....	157
Figure 5.21. First story web of NTW1 after flange failure.....	158
Figure 5.22. Second story web of NTW1 after flange failure.....	158
Figure 5.23. Third story web of NTW1 after flange failure.....	159
Figure 5.24. Fourth story web of NTW1 after flange failure.....	159
Figure 5.25. Damage to confining hoops near foundation block.....	160
Figure 5.26. Web tip after removal of loose concrete.....	161
Figure 5.27. North flange tip after removal of loose concrete.....	161
Figure 5.28. South flange tip after removal of loose concrete.....	162
Figure 5.29. Flange direction load versus displacement response of NTW1.....	164

Figure 5.30. Flange direction load versus displacement response of NTW1, early portion of test .....	164
Figure 5.31. Web direction load versus displacement response of NTW1 .....	165
Figure 5.32. Locations of measurement panels on NTW1 .....	166
Figure 5.33. Flange direction moment versus curvature relationships for NTW1 .....	168
Figure 5.34. Web direction moment versus curvature relationships for NTW1 .....	168
Figure 5.35. Flange direction shear force versus shear strain relationships for NTW1 .....	170
Figure 5.36. Web direction shear force versus shear strain relationships for NTW1 ....	171
Figure 5.37. Flange direction load versus rotation due to strain penetration relationship for NTW1 .....	173
Figure 5.38. Web direction load versus rotation due to strain penetration relationship for NTW1 .....	173
Figure 5.39. Flange direction relationship between curvature in lower portion of wall and rotation due to strain penetration for NTW1 .....	174
Figure 5.40. Web direction relationship between curvature in lower portion of wall and rotation due to strain penetration for NTW1 .....	174
Figure 5.41. Flange direction load versus component displacement, first story, NTW1 .....	176
Figure 5.42. Flange direction load versus component displacement, second story, NTW1 .....	176
Figure 5.43. Web direction load versus component displacement, first story, NTW1 ..	177
Figure 5.44. Web direction load versus component displacement, second story, NTW1 .....	177
Figure 5.45. Web direction load versus component displacement, third story, NTW1 ..	178
Figure 5.46. Web direction load versus component displacement, fourth story, NTW1 .....	178
Figure 5.47. Flange direction contribution of each component to total first story displacement versus total displacement, NTW1 .....	179
Figure 5.48. Flange direction contribution of each component to total second story displacement versus total displacement, NTW1 .....	179
Figure 5.49. Web direction contribution of each component to total first story displacement versus total displacement, NTW1 .....	180
Figure 5.50. Web direction contribution of each component to total second story displacement versus total displacement, NTW1 .....	180
Figure 5.51. Web direction contribution of each component to total third story displacement versus total displacement, NTW1 .....	181
Figure 5.52. Web direction contribution of each component to total fourth story displacement versus total displacement, NTW1 .....	181
Figure 5.53. Strain distribution across width of flange, 6 in. above foundation, NTW1	184
Figure 6.1. First story flange of NTW2 at end of elastic loading cycles .....	189
Figure 6.2. Second story flange of NTW2 at end of elastic loading cycles .....	190
Figure 6.3. First story web of NTW2 at end of elastic loading cycles .....	190
Figure 6.4. Second story web of NTW2 at end of elastic loading cycles .....	191
Figure 6.5. First story flange of NTW2 after web failure .....	195

Figure 6.6. Second story flange of NTW2 after web failure. ....	195
Figure 6.7. First story web of NTW2 after web failure. ....	196
Figure 6.8. Second story web of NTW2 after web failure. ....	196
Figure 6.9. First story flange of NTW2 after flange failure. ....	199
Figure 6.10. Second story flange of NTW2 after flange failure. ....	200
Figure 6.11. First story web of NTW2 after flange failure. ....	200
Figure 6.12. Second story web of NTW2 after flange failure. ....	201
Figure 6.13. Web tip after removal of loose concrete. ....	202
Figure 6.14. North flange tip after removal of loose concrete. ....	202
Figure 6.15. South flange tip after removal of loose concrete. ....	203
Figure 6.16. Flange direction load versus displacement response of NTW2 .....	204
Figure 6.17. Flange direction load versus displacement response of NTW2, early portion .....	205
Figure 6.18. Web direction load versus displacement response of NTW2. ....	205
Figure 6.19. Locations of measurement panels and splice region in NTW2 .....	207
Figure 6.20. Flange direction moment versus curvature relationships for NTW2 .....	208
Figure 6.21. Web direction moment versus curvature relationships for NTW2. ....	210
Figure 6.22. Flange direction shear force versus shear strain relationships for NTW2. 212	
Figure 6.23. Web direction shear force versus strain relationships for NTW2 .....	213
Figure 6.24. Flange direction load versus rotation due to strain penetration relationship for NTW2. ....	214
Figure 6.25. Web direction load versus rotation due to strain penetration relationship for NTW2 .....	215
Figure 6.26. Flange direction relationship between curvature in lower portion of wall and rotation due to strain penetration for NTW2 .....	215
Figure 6.27. Web direction relationship between curvature in lower portion of wall and rotation due to strain penetration for NTW2 .....	216
Figure 6.28. Flange direction load versus rotation due to splice slip relationship for NTW2 .....	217
Figure 6.29. Web direction load versus rotation due to splice slip relationship for NTW2 .....	217
Figure 6.30. Flange direction load versus component displacement, first story, NTW2 .....	218
Figure 6.31. Flange direction load versus component displacement, second story, NTW2 .....	219
Figure 6.32. Web direction load versus component displacement, first story, NTW2..	220
Figure 6.33. Web direction load versus component displacement, second story, NTW2 .....	220
Figure 6.34. Flange direction contribution of each component to total first story displacement versus total displacement, NTW2. ....	221
Figure 6.35. Flange direction contribution of each component to total second story displacement versus total displacement, NTW2. ....	221
Figure 6.36. Web direction contribution of each component to total first story displacement versus total displacement, NTW2. ....	222

Figure 6.37. Web direction contribution of each component to total second story displacement versus total displacement, NTW2.....	222
Figure 6.38. Strain distribution across width of flange, 6 in. above foundation, NTW2225	225
Figure 7.1. Comparison of overall deformed shapes .....	227
Figure 7.2. Relationships between measured first and second story displacements.....	228
Figure 7.3. Comparison of applied load histories.....	230
Figure 7.4. Web direction load versus displacement at top of second story of each specimen. ....	233
Figure 7.5. Flange direction load versus displacement at top of second story of each specimen. ....	234
Figure 7.6 Web direction component of total energy dissipated in each half cycle of loading. ....	235
Figure 7.7. Flange direction component of total energy dissipated in each half cycle of loading. ....	236
Figure 7.8. Dissipated fraction of web direction energy absorbed by each half cycle. .	237
Figure 7.9. Dissipated fraction of flange direction energy absorbed by each half cycle. ....	238
Figure 7.10. Crack patterns in first stories of flanges after initial web direction loading. ....	241
Figure 7.11. Crack patterns in first stories of flanges after initial skew- and flange-direction loading. ....	242
Figure 7.12. Crack patterns in first stories of flanges after completion of testing.....	243
Figure 7.13. Crack patterns in second stories of webs after web failure. ....	246
Figure 7.14. Web direction load versus interstory rotation in first story of specimens.	249
Figure 7.15. Web direction load versus interstory rotation in second story of specimens. ....	249
Figure 7.16. Flange direction load versus interstory rotation in first story of specimens. ....	250
Figure 7.17. Flange direction load versus interstory rotation in second story of specimens.....	250
Figure 7.18. Decrease in moment resistance at base of wall due to shear lag at various strain levels. ....	251
Figure 7.19. Measured strain distributions across flange. ....	253
Figure 7.20. Web direction load versus interstory shear deformation in first story of specimens.....	255
Figure 7.21. Web direction load versus interstory shear deformation in second story of specimens.....	255
Figure 7.22. Flange direction load versus interstory shear deformation in first story of specimens.....	256
Figure 7.23. Flange direction load versus interstory shear deformation in second story of specimens.....	257
Figure 7.24. Comparison of strain penetration component of deformation: web direction loading. ....	258

Figure 7.25. Comparison of strain penetration component of deformation: flange direction loading. ....	259
Figure 8.1. Measured and predicted moment versus curvature relationships, NTW1 web-direction loading. ....	273
Figure 8.2. Measured and predicted distributions of tensile strain and curvature, flange-in-tension loading direction, 1.1 percent drift .....	274
Figure 8.3. Measured and predicted distributions of tensile strain and curvature, flange-in-tension loading direction, 1.5 percent drift .....	275
Figure 8.4. Measured and predicted distributions of tensile strain and curvature, flange-in-tension loading direction, 2.1 percent drift .....	275
Figure 8.5. Measured and predicted load versus flexural deformation relationships, NTW1 web direction loading .....	277
Figure 8.6. Post-peak distribution of curvature over height of wall .....	279
Figure 8.7. Modification of moment versus curvature relationship to model post-peak response .....	280
Figure 8.8. Approximately bi-linear relationship observed between flexural and shear components of deformation, top of specimen NTW1. ....	282
Figure 8.9. Comparison of curvature and shear strain profiles, NTW1 web direction loading. ....	284
Figure 8.10. Verification of shear mode for specimen NTW11: comparison of measured shear deformations and prediction based on measured interstory rotations. ....	287
Figure 8.11. Relationship between diagonal crack inclination and axial load applied to shear panels. ....	289
Figure 8.12. Measured and predicted load versus shear deformation relationships, NTW1 web direction loading. ....	290
Figure 8.13. Terms required in strain penetration calculations. ....	291
Figure 8.14. Detailed and simplified models of strain distribution in anchorage region. ....	293
Figure 8.15. Comparison of simplified bar stress-slip model to Zhao and Sritharan (2007) model. ....	295
Figure 8.16. Measured and predicted load versus rotation due to strain penetration relationships, NTW1 web direction loading. ....	298
Figure 8.17. Measured and predicted load versus rotation due to strain penetration relationships, NTW1 web direction loading: comparison to Zhao and Sritharan (2007). ....	298
Figure 8.18. Measured curvature distribution near maximum applied moment, NTW2 web direction loading. ....	299
Figure 8.19. Measured and predicted curvature distributions near maximum applied moment, NTW2 web direction loading. ....	301
Figure 8.20. Measured and predicted load versus displacement due to flexure, NTW2 web direction loading. ....	302
Figure 8.21. Comparison of measured and predicted moment versus curvature relationships, NTW1 flange direction loading. ....	303
Figure 8.22. Stress-strain history for typical bar in flange tip. ....	305

Figure 8.23. Original and modified steel material models used, specimen NTW1 .....	305
Figure 8.24. Comparison of calculated monotonic flange direction envelope of NTW1 with measured response (from Waugh <i>et al.</i> 2009).....	307
Figure 8.25. Comparison of measured and calculated flange direction cyclic response of NTW1 (from Waugh <i>et al.</i> 2009).....	307
Figure 8.26. Comparison of measured and calculated 45° direction monotonic and cyclic response of NTW1 using tool from Waugh <i>et al.</i> 2009.....	309
Figure 8.27. Comparison of orthogonal load components for 45° skew direction loading predicted with F-S-SP Integration model and OpenSEES model. ....	310
Figure 9.1. Comparison of measured and predicted responses, NTW1 web direction loading, at top of specimen.....	322
Figure 9.2. Comparison of measured and predicted responses, NTW1 flange direction loading, at top of specimen.....	323
Figure 9.3. Comparison of measured and predicted responses, NTW2 web direction loading, at top of specimen.....	323
Figure 9.4. Comparison of measured and predicted responses, NTW2 flange direction loading, at top of specimen.....	324
Figure 9.5. Comparison of measured and predicted responses, NTW1 web direction loading, at top of first story.....	324
Figure 9.6. Comparison of measured and predicted responses, NTW1 flange direction loading, at top of first story.....	325
Figure 9.7. Comparison of measured and predicted responses, NTW2 web direction loading, at top of first story.....	325
Figure 9.8. Comparison of measured and predicted responses, NTW2 flange direction loading, at top of first story.....	326
Figure 9.9. Application of F-S-SP Integration model to specimen RWN (described in Johnson 2007).....	329
Figure 9.10. Measured and predicted flexural envelope of RWN (described in Johnson 2007).....	330
Figure 9.11. Measured and predicted shear envelope of RWN (described in Johnson 2007).....	330
Figure 9.12. Measured and predicted strain penetration envelope of RWN (described in Johnson 2007).....	331
Figure 9.13. Application of F-S-SP Integration model to specimen RWS (described in Johnson 2007).....	332
Figure 9.14. Curvature distribution accounting for splice in application of proposed model to RWS (described in Johnson 2007).....	333
Figure 9.15. Application of F-S-SP Integration model to specimen TW2 tested by Thomsen and Wallace (1995).....	335
Figure 9.16. Application of F-S-SP Integration model to specimen CMS tested by Sittipunt and Wood (1995).....	336
Figure 9.17. Application of F-S-SP Integration model to specimen 3A tested by Hines (2002).....	338

Figure 9.18. Application of F-S-SP Integration model to specimen LMS tested by Hines (2002).....	339
Figure 9.19. Comparison of F-S-SP Integration model and FEMA 356 simplified model: NTW1 web direction loading. ....	341
Figure 9.20. Comparison of F-S-SP Integration model and FEMA 356 simplified model: NTW2 web direction loading. ....	342
Figure 9.21. Comparison of F-S-SP model to Hines <i>et al.</i> (2004) model: NTW1 .....	346
Figure 9.22. Comparison of F-S-SP model to Hines <i>et al.</i> (2004) model: NTW1 flexural deformation.....	347
Figure 9.23. Comparison of F-S-SP model to Hines <i>et al.</i> (2004) model: NTW1 shear deformation.....	348
Figure 9.24. Comparison of F-S-SP model to Hines <i>et al.</i> (2004) model: NTW1 strain penetration .....	348
Figure 9.25. Predicted moment versus curvature relationships with varying material properties, NTW1 web direction. ....	353
Figure 9.26. Effect of material strengths on curvature at failure. ....	354
Figure 9.27. Comparison of measured web-direction response of Specimen NTW1 and response predicted using measured and nominal material properties. ....	355

## List of Tables

Table 2.1. Modeling parameters and performance levels for walls with boundary elements controlled by flexure (from FEMA 356 2000).....	36
Table 2.2 Damage levels and local EDPs (from Berry <i>et al.</i> 2008).....	38
Table 3.1 Assumptions used in analysis methods to determine $M_{pr}$ .....	86
Table 3.2 Shear requirements for prototype walls calculated with various analysis methods.....	87
Table 3.3. Detailing differences between specimens NTW1 and NTW2.....	91
Table 3.4. Nominal concrete mix used in specimens NTW1 and NTW2.....	101
Table 3.5. Modified gypsum cement grout proportions .....	102
Table 3.6. Measured hardened concrete properties at testing: NTW1.....	103
Table 3.7. Measured hardened concrete properties at testing: NTW2.....	104
Table 3.8. Reinforcement properties: NTW1 .....	105
Table 3.9. Reinforcement properties: NTW2 .....	105
Table 3.10. Load history applied to NTW1 .....	119
Table 3.11. Load history applied to NTW2 .....	122
Table 5.1. Average contribution of each component of deformation to total, NTW1...	182
Table 5.2. Effects of shear lag on flange-in-tension moment resistance, NTW1 .....	185
Table 6.1. Average contribution of each component of deformation to total, NTW2...	223
Table 6.2. Effects of shear lag on flange-in-tension moment resistance, NTW2 .....	225
Table 7.1. Measured loads, displacements and stiffnesses at first yielding.....	232
Table 7.2. Measured loads and displacements at wall failure.....	232
Table 7.3. Energy dissipated over entire load history (k-in).....	236
Table 8.1. Material property parameters used to represent measured properties of specimen NTW1 .....	271
Table 8.2. Material property parameters used to represent damaged properties of reinforcement in specimen NTW1.....	306
Table 8.3. Recommended threshold values for EDPs.....	312
Table 9.1. Comparison between measured and predicted loads, displacements and stiffnesses at first yielding. ....	317
Table 9.2. Comparison between measured and predicted wall capacities.....	318
Table 9.3. Cases considered to estimate effects of material strength variations on analysis .....	351

## Chapter 1 Introduction

### 1.1 Introduction

Engineers often use structural walls in buildings to serve as the primary lateral load resisting elements because of their large in-plane stiffness and strength, which enables them to carry large lateral loads due to wind and earthquakes while also minimizing lateral displacements. Architects often prefer the walls to be concentrated around hallways or elevator cores to minimize their effect on the floor plan and to maximize available window space. Therefore, linear rectangular walls are often combined to form I-, C-, T- and L-shapes. These configurations lead to complicated interactions between the wall segments, such that it is no longer reasonable to assume that the linear segments of the walls resist lateral loads in each direction independently. In both symmetric and non-symmetric configurations, the “out-of-plane” wall segments act as flanges. This increases the stiffness and capacity of the wall relative to that of the individual segments, and it leads to interaction between the loading directions, with the capacity in each direction dependent upon the demand in the orthogonal direction.

Previous tests of nonrectangular walls (i.e., Oesterle *et al.* 1979, Sittipunt and Wood 1995, Thomsen and Wallace 1995) have been restricted to unidirectional loading due to limitations in testing capabilities. Application of more complicated loading procedures (i.e., multidirectional testing) can provide information regarding the behavior of these systems under more realistic loading schemes. As an example, multidirectional testing can provide information on the effects of damage accumulated in one direction on the performance of the system in other directions.

Field experience (Wallace 1996) and past research on the unidirectional loading of walls (Thomsen and Wallace 1995) led to the development of the displacement-based approach to the detailing of the confinement regions of wall systems that is currently incorporated in the American Concrete Institute structural building code (ACI 318-08). The displacement-based approach was first introduced into the model building codes with the 1994 edition of the Uniform Building Code (UBC) and was adopted into ACI 318 in 1999. In comparing the performance of their unidirectionally loaded rectangular and T-shaped wall systems, Thomsen and Wallace (1995) concluded that the detailing of the confined region in T-shaped walls loaded uniaxially along the direction of the stem of the T could be designed using methods similar to those developed for rectangular wall systems.

The effects of multidirectional loading on the response of these systems had not been investigated prior to the beginning of this research. Preliminary analyses of the nonrectangular wall systems subjected to skew loading (Brueggen *et al.* 2006) indicated that the depth of the compression region in the section may be significantly increased in the skew loading direction, which may necessitate enlargement of the required confinement region. Additionally, testing of walls under multidirectional loading histories was undertaken to verify predictions of their response under non-orthogonal loading directions, which are expected in “real-world” applications.

In addition to addressing potential issues with the detailing of nonrectangular walls, better understanding and quantification of wall performance are needed to facilitate the use of performance-based engineering (PBE) for seismic regions, a design

methodology being developed to help building owners and engineers quantify the economic costs and benefits of various design options in order to meet the uncertain seismic demands that may be placed on buildings during their service life as economically as possible (Stanford 2008).

The current codified seismic design approach in the United States, contained in the International Building Code (IBC 2000) uses a force-based approach to ensure life-safety during a design-level earthquake. While more sophisticated analysis is allowed, a static equivalent force procedure is provided. The goal of this design approach is to ensure that the building occupants are not trapped in a collapsed building after a design-level earthquake, represented by an acceleration response spectrum with a 2 percent probability of exceedance in 50 years. The design forces calculated with this approach are less than the forces expected in a moderate to large earthquake, because design considers the structural ductility and the redistribution of forces in redundant systems (Naeim 2001). Within this procedure, a design base shear is determined according to the building location, site characteristics, and mass. This base shear is then modified according to the type of lateral force resisting system used and the expected use of the building. Each type of lateral force resisting system (e.g., bearing wall systems with special reinforced concrete shear walls or building frame systems with special steel concentrically braced frames) has an associated response modification coefficient ( $R$ ) that is used to reduce the design base shear and accounts for typical ductility levels of the various lateral force resisting systems. In order to address the desire for certain structures to sustain less damage than others, buildings are divided into three seismic use groups

according to their intended use (i.e., importance), and the design base shear is amplified by 25 percent or 50 percent for more “important” structures in Seismic Use Groups II and III, respectively. The purpose of these amplifications is to ensure that facilities with “substantial public hazard due to occupancy or use,” such as high-occupancy buildings and non-essential utilities in Seismic Use Group II sustain more limited damage, and that facilities required for post-earthquake response and recovery, such as hospitals and fire stations, in Seismic Use Group III, remain operational.

There are two primary shortcomings of this approach. First, the use of importance factors to ensure reliable performance of critical facilities does not provide a consistent level of response for all structures of these types (Naeim 2001). Second, it does not provide for a desire of many building owners, regardless of the building type, to consider mitigating the damage resulting from earthquakes of all magnitudes, including more frequently expected, smaller events, in order to reduce building downtime and repair costs. This second shortcoming became apparent after the 1994 Northridge earthquake and the 1995 Great Hanshin-Awaji earthquake. The total economic losses associated with these earthquakes have been estimated at \$40 billion (USGS 1996) and \$200 billion (Schiff 1999), respectively. A substantial portion ( $\frac{1}{3}$  to  $\frac{1}{2}$ , USGS 1996, Schiff 1999) of these losses was due to the loss of use of buildings requiring repair or replacement, as opposed to the direct repair or replacement costs. As a result, attention has been turned towards developing design procedures that allow for the consideration of the repair costs and indirect economic effects of frequent, moderate, and severe

earthquakes on buildings and for these costs to be considered in the selection and detailing of the building structure in addition to the initial construction costs.

This new design approach is known as performance-based engineering. Performance-based engineering has been used by the automotive and aerospace industries for many years (Naeim 2001). However, in these applications, extensive prototype testing for each design is acceptable because of the large number of identical products produced. Because building structures are generally unique, tools are needed to accurately predict the response of structures, including the expected degree of damage, to earthquakes of various magnitudes without doing extensive prototype testing for each structure.

A series of documents has been produced outlining framework for performance-based engineering of building structures. The earliest of these documents (ATC-40 1996, FEMA 273 and 274 1997) focused on retrofit of existing buildings, but more recent documents (ATC 58-2 2004, FEMA 445 2006) are focused on expanding the efforts to new construction. While there are minor variations in the frameworks proposed in the various documents, all of them seek to establish target minimum performance levels for buildings subjected to selected demand levels based on the importance of the building. While some groups recommend using more than four performance levels, all recommend a minimum of four: Functional, Immediate Occupancy, Life Safety, and Collapse Prevention. Generally, four earthquake hazard levels are considered. These have probabilities of exceedance of 50 percent in 50 years (frequent earthquakes), 20 percent in 50 years (moderate earthquakes), 10 percent in 50 years (rare earthquakes), and 2

percent in 50 years (very rare earthquakes). The minimum acceptable performance levels for ordinary (Seismic Use Group I) buildings are life safety during the 10 percent in 50 year event and collapse prevention during the 2 percent in 50 year event. This is analogous to the current prescriptive design requirement. However, the expanded framework of performance-based engineering allows owners to specify enhanced behavior, such as designing for immediate occupancy after frequent or moderate earthquakes, potentially reducing costs over the life of the building.

In order to successfully meet these enhanced performance goals and to quantify the expected economic benefits of using them, adequate tools are necessary to predict both the likely demands on the structure, including both frequent and rare events, and the expected performance of the structure during each of these events. With regard to predicting the performance of structures, research is needed to more accurately predict the force-displacement response of the building and to predict the amount of damage associated with the various demand levels. In addition to the highly detailed models being developed for use by researchers or for engineers working on landmark buildings, it is also important that simplified tools are available for practicing engineers to use in routine design practice. There is a highly simplified modeling approach recommended in FEMA 273 (1997). However, this approach is limited in that it considers only the flexural component of deformation, neglecting the contributions of shear and strain penetration, and it considers only a very limited number of parameters (e.g., resistance at first yielding and axial load ratio) in determining the capacity of the wall and the expected degree of damage. Because of these simplifications, it is often considered

excessively conservative, yet its reliability has not been investigated, discouraging engineers from using it (Hamburger 1997). As a result, a tool that is more sophisticated, yet still sufficiently simplified for use in routine design work, is needed.

## **1.2 Scope of Research**

The study described in this thesis was a key component of a larger, collaborative project involving researchers from the University of Minnesota (Narina Jung, Ben Johnson), Iowa State University (Sri Sritharan, Jon Waugh, Sriram Aaleti), University of Puerto Rico at Mayagüez (Ricardo Lopez) and a practitioner from the State of California (Suzanne Dow Nakaki). This research effort was funded through the National Science Foundation (NSF) George E. Brown, Jr., Network for Earthquake Engineering Simulation (NEES), and was the first research project conducted within the University of Minnesota Multi-Axial Subassemblage Testing (MAST) facility.

Other contributions associated with this effort include the unidirectional testing of three planar reinforced concrete structural wall systems described by Johnson (2007) to investigate the effects of bar anchorage and splicing; Jung (2007), which describes the preliminary design considerations of the wall specimens and the preliminary instrumentation plan; and Waugh *et al.* (2009), which describes the development of a fiber-based finite element model for use with reinforced concrete structural walls. Additionally, the researchers associated with this project evaluated, enhanced and expanded the information technology (IT) tools for collaboration within the National Science Foundation (NSF) George E. Brown, Jr., Network for Earthquake Engineering Simulation (NEES) described in Waugh *et al.* (2009)

The primary focus of the portion of the project described in this thesis was the finalization of the design and the instrumentation, construction, experimental testing, and data interpretation of the two T-shaped reinforced concrete structural walls subjected to multidirectional, cyclic loading. In addition, a simplified modeling approach was developed to predict the load-deformation response of structural walls in order to facilitate the adoption of performance-based engineering for structural systems incorporating walls. This approach is intended for use by structural engineers. In addition to determining the load-displacement response of walls, the simplified modeling procedure also associates predicted strain levels with expected degrees of damage. This is one of the key areas associated with performance-based engineering that is currently lacking for many types of structural systems. The predicted load-displacement response is separated into the components of deformation due to flexure, shear, and strain penetration to give further indication of the types of damage that are expected, such as flexural cracks or web shear cracks.

Both of the nonrectangular walls tested in this project represented half-scale subassemblages of the wall system in a six-story prototype building. The first structure, NTW1, represented a four-story subassemblage for which the top of the subassemblage was located near the resultant lateral force associated with an assumed inverted triangular lateral load distribution on the prototype structure. NTW2, the second nonrectangular wall tested, represented a two-story subassemblage. This test specimen enabled the investigation of the effects of reducing the subassemblage size and locating the very stiff top block nearer to the plastic hinge region on the response of the subassemblage. In

addition, modifications to the wall detailing were studied including the horizontal distribution of the longitudinal reinforcement and the effect of lap-splicing the longitudinal reinforcement away from the potential plastic hinge region.

The simplified model, termed the F-S-SP Integration model, developed to quantify the force-deformation response of the nonrectangular wall systems and to estimate the damage level associated with various demand levels was investigated with respect to the force-deformation envelope in the orthogonal and skew loading directions of the tested specimens. In addition, to investigate the robustness of this model relative to the prediction of the force-deformation response of wall systems, the model was compared to the response of several specimens tested by other researchers. These included two rectangular walls tested by Johnson (2007), a C-shaped wall tested by Sittipunt and Wood (1993), a T-shaped wall tested by Thomsen and Wallace (1993), and barbell-shaped and hollow box bridge piers tested by Hines (2002). Existing simplified models, including the model developed by Hines *et al.* (2004) and the highly simplified FEMA 356 (2000) model were also applied to the two nonrectangular wall systems tested in this research program and their results compared. The strengths and weaknesses of the various models were identified.

### **1.3 Organization of Thesis**

This section provides a brief description of the topics covered in each of the chapters and appendices.

Chapter 2 presents a summary of the literature search. Topics covered within this section include background on the design of reinforced concrete structural wall systems,

performance-based engineering and the prediction of damage states, existing modeling tools and approaches, and a summary of the previous tests of nonrectangular reinforced concrete wall systems.

Chapter 3 describes the design of the prototype building and the two nonrectangular wall specimens, including the process of scaling the prototype building to create the one-half-scale specimens. This chapter includes discussion of the detailing of the specimens and the determination of the applied loading histories. It also presents a summary of the instrumentation used during the tests.

Chapter 4 discusses the use of subassemblage testing and the investigation of appropriate specimen sizes and boundary conditions to reduce testing costs without compromising the representation of the prototype structure. It also compares the relative merits of an optical measuring system to those of more traditional LVDTs and string potentiometers. This chapter discusses the required density of these instruments to adequately measure deformations in the plastic hinge region and to facilitate separation of the total deformation into its components of flexure, shear, and strain penetration. Better understanding of the contributions of each deformation mechanism to the wall behavior facilitates the development of more robust numerical modeling tools.

Chapter 5 discusses the results of specimen NTW1, and Chapter 6 discusses the results of specimen NTW2. Each of these chapters describes the progression of damage including the development of cracks throughout the applied testing protocol and the observed failure modes. These chapters also present the derived components of deformation at each story level and discuss the effects of shear lag on the flange

contribution to the flexural response. These results are compared in Chapter 7 and the effects of each of the design differences between the specimens are discussed.

Chapters 8 and 9 discuss the F-S-SP Integration model, the simplified modeling procedure developed to aid engineers in the application of performance-based engineering. Chapter 8 includes a discussion of the development of the method used to predict each of the components of deformation (flexure, shear, strain penetration, and splice slip) and the development of recommended threshold strain values to associate with significant damage levels in order to predict the degree of damage associated with various levels of deformation. In Chapter 9, the model is validated using the results of several wall tests, including the two T-shaped walls described in this thesis and walls tested by other researchers. In addition, it is compared to predictions made with existing simplified modeling procedures.

Chapter 10 presents the conclusions from this research, including both the experimental and modeling portions. It also makes recommendations for future research.

The appendices include additional information about the testing program and the simplified model developed in this research. Appendix A includes drawings of the specimens and the as-built dimensions. Appendix B includes detailed locations of instrumentation (nominal and as-built) on each of the specimens. Appendix C includes documentation related to the use of the MAST telepresence system during testing including camera tower locations. Appendix D includes information from the post-testing investigation of the specimens, which documented the degree of damage to the

confined concrete core. Appendix E includes sample calculations showing the implementation of the proposed simplified model for specimen NTW1.

## **Chapter 2 Literature Review**

### **2.1 Introduction**

This chapter consists of three major sections. Section 2.2 presents a review of the design of special reinforced concrete structural walls, as defined in the American Concrete Institute *Building Code Requirements for Structural Concrete*, ACI 318-02, which was used in the original design of the wall specimens, and the literature supporting these design provisions. Section 2.3 reviews some of the existing tools available to aid in the design and analysis of structural walls. Section 2.4 reviews previous tests of nonrectangular structural walls subjected to reversed cyclic loading, including both experimental and numerical investigations.

### **2.2 Reinforced Concrete Structural Wall Design**

This section presents a summary of the design of special reinforced concrete structural walls, with attention given to issues that did not have clear design guidance in ACI 318-02 or that were particular to the design of non-rectangular walls. Section 21.7 of ACI 318-02, “Special reinforced concrete structural walls and coupling beams,” contains design guidance particular to these elements. In addition, Section 21.2 contains general provisions for all special reinforced concrete elements.

#### **2.2.1 Boundary Elements**

Prior to the development of displacement-based design provisions by Wallace and Moehle (1992), which were further developed by the Structural Engineers Association of California (SEAOC) and incorporated into the 1994 UBC and subsequently incorporated, with modification, into ACI 318-99 (Wallace and Orakcal 2002), the requirement for

including special boundary elements was determined by the expected compressive stress at the extreme fiber. These requirements are included in Section 21.7.6.3 of ACI 318-02 as an alternate provision to the newer requirements. According to these specifications, special boundary elements are required when the maximum extreme fiber compressive stress due to factored forces including earthquake effect is larger than  $0.2f'_c$ . The confinement must be extended over the height until the extreme fiber stress is less than  $0.15f'_c$ . These stresses are to be calculated for the factored forces based on a linear elastic model and gross section properties. Additionally, the older provisions required that the special boundary elements should resist all axial loads and overturning moments without considering the contributions of the wall web reinforcement.

Wallace and Moehle (1992) found that these stress-based requirements were overly conservative and led to a need for special boundary elements in nearly all walls. They proposed an alternate, displacement-based approach to determine the need for special boundary elements and the associated dimensions where required. With this approach, the need for boundary elements is determined in accordance with the building configuration. Specifically, they found that the need for boundary elements is related to four issues: (1) the ratio of wall cross-sectional area to total floor-plan area, where boundary elements are generally not needed when this ratio exceeds approximately 1 percent; (2) the wall aspect ratio and configuration; (3) the wall axial load; and (4) the wall reinforcement ratio (Thomsen and Wallace 1995).

The implementation of Wallace and Moehle's recommendations led to Section 21.7.6.2 of ACI 318-02, which requires confined boundary elements when

$$c \geq \frac{l_w}{600(\delta_u / h_w)} \quad (2.1)$$

where  $c$  is the neutral axis depth,  $l_w$  is the wall length,  $\delta_u$  is the roof displacement expected under the design earthquake, and  $h_w$  is the total wall height. ACI 318-02 states that the drift ratio  $\delta_u/h_w$  cannot be taken less than 0.007 for the determination of boundary element requirements. Additionally, IBC 2003 limits the interstory drift ratio of buildings in Seismic Use Group I (i.e., ordinary structures that would not pose a public hazard if they were to fail and do not house essential facilities for post-earthquake recovery) to 0.02 under factored loads, so this value can be used as an upper limit when determining whether confined boundary elements are required. When a more precise estimate of the drift ratio is desired in early stages of design, rather than assuming the upper bound value, Thomsen and Wallace (1995) derived an estimate of the drift demand for a particular building and wall configuration as

$$\frac{\delta_u}{h_w} = 0.00023 \frac{h_w}{l_w} \sqrt{\frac{1}{p}} \quad (2.2)$$

where  $p$  is the ratio of wall area to floor-plan area. Where confined boundary elements are required, Section 21.7.6.2 goes on to state that they must extend vertically from the critical section a distance not less than the larger of  $l_w$  or  $M_u/(4V_u)$ , where  $M_u$  and  $V_u$  are the design moment and shear, respectively.

Section 21.7.6.4 of ACI 318-02 gives the requirements for the horizontal dimension of confined boundary elements, extension of the special confining reinforcement into the foundation, and the required transverse reinforcement of the

elements, regardless of whether the displacement-based or older strength-based requirements are used. The horizontal dimension of the confined boundary element must be at least the larger of  $c-0.1(l_w)$  or  $c/2$ . In flanged sections, if confinement is required when the loading places the entire flange in compression, the boundary element must include the entire effective flange width and extend at least 12 in. into the web, as discussed below. At a wall base, the transverse reinforcement must extend into the support at least the development length of the largest reinforcement in the element, or at least 12 in. into a footing or mat foundation. Figure 2.1 shows the application of these minimum boundary element dimensions for a typical structural wall.

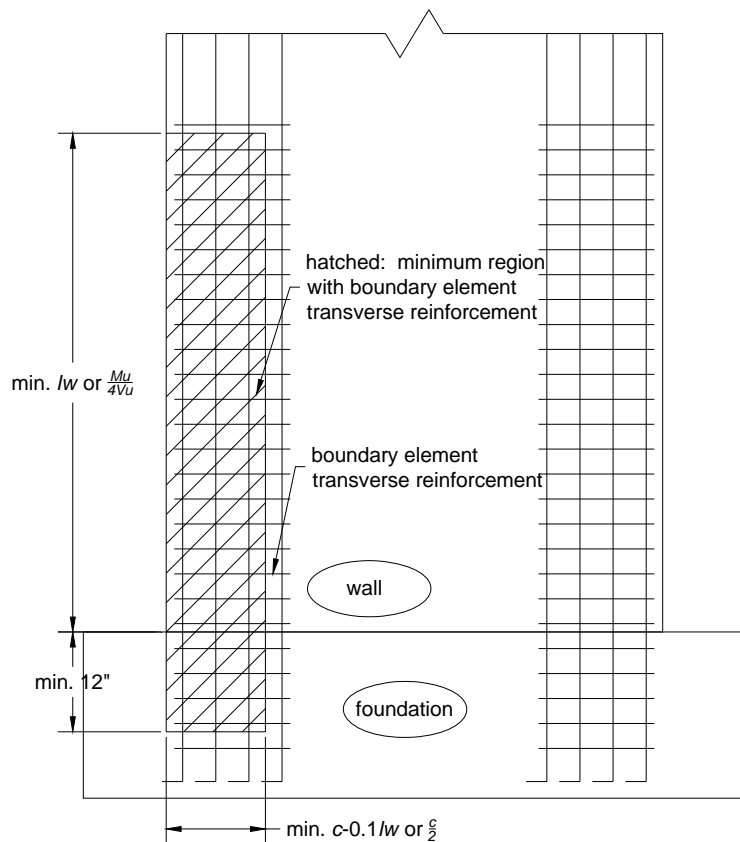


Figure 2.1. Minimum boundary element dimensions given in ACI 318-02.

Section 21.7.6.4 of ACI 318-02 refers to the transverse confining reinforcement requirements for columns, in Sections 21.4.4.1 through 21.4.4.3. These requirements are that the minimum cross-sectional area of rectangular hoop reinforcement,  $A_{sh}$ , must be at least  $A_{sh}=0.09sh_c f'_c/f_{yh}$ , where  $s$  is the hoop spacing,  $h_c$  is the cross-sectional dimension of the column core measured center-to-center of the confining reinforcement,  $f'_c$  is the nominal compressive strength of the concrete, and  $f_{yh}$  is the nominal yield strength of the transverse reinforcement. The maximum spacing of the transverse reinforcement is limited to the smaller of (a) one-quarter of the minimum member dimension, (b) six times the diameter of the longitudinal reinforcement, and (c)  $s_x$ , where

$$s_x = 4 + \frac{14 - h_x}{3} \quad (2.3)$$

The maximum spacing of legs of overlapping hoops or crossties perpendicular to the longitudinal axis of the member is limited to 14 in.

For the purposes of determining confinement requirements, boundary elements of reinforced concrete walls behave similarly to columns, so applying the requirements for boundary element confinement in columns to boundary elements in structural walls is a reasonable approach for estimating the special confinement requirements. For this purpose, the primary differences between boundary elements in walls and columns are aspect ratio and minimum dimension. The boundary elements in the prototype walls had aspect ratios of approximately five. According to Section 1908.1.1 of IBC 2003, the maximum aspect ratio of a column section is 2.5; an aspect ratio of five can never arise in column confinement design. Additionally, concrete walls are generally much narrower than columns. As a result, the requirement that the minimum transverse reinforcement

spacing be less than one-quarter of the minimum member dimension may not be rational, and testing by Thomsen and Wallace (1995) indicated that walls with transverse reinforcement at a larger spacing can achieve adequate performance, but this requirement remains in the most recent revision of the code, ACI 318-08.

### 2.2.2 Shear Reinforcement

The general procedure for shear design of reinforced concrete members, summing the contributions to the shear strength from the concrete and the steel, is applicable to special reinforced concrete structural walls. However, there are some special provisions in Section 21.7.4 of ACI 318-02. These include limiting the total nominal shear strength  $V_n$  to

$$V_n = A_{cv}(\alpha_c \sqrt{f'_c} + \rho_n f_y) \quad (2.4)$$

where  $A_{cv}$  is the gross area of the cross section assumed effective in shear (e.g., the area defined by the web thickness and length of section in the direction of shear force considered),  $\alpha_c$  varies from 2 to 3 according to the aspect ratio of the wall,  $\rho_n$  is the longitudinal reinforcement ratio of the wall, and  $f_y$  is the nominal yield strength of the longitudinal reinforcement. Additionally, in order to minimize the amount of shear force redistribution, the nominal shear resistance,  $V_n$ , of a group of walls or wall piers sharing a common lateral load, such as all of the walls in a given story, is limited to

$V_n = 8A_{cv} \sqrt{f'_c}$ , and  $V_n$  of a single wall or wall pier within a group is limited to

$$V_n = 10A_{cv} \sqrt{f'_c}.$$

Section 21.7.2 contains limitations on the area and spacing of web reinforcement in both perpendicular directions, including shear reinforcement, to control the width of inclined cracks. Unless the design shear force is very small ( $< A_{cv} \sqrt{f'_c}$ ), the minimum required web reinforcement ratio is 0.0025. The maximum spacing of the reinforcement is 18 in., and if the in-plane factored shear force assigned to the wall exceeds  $2A_{cv} \sqrt{f'_c}$ , at least two curtains of reinforcement are required, regardless of the wall thickness. Section 21.7.6.4 includes provisions for the anchorage of shear reinforcement in addition to the provisions for boundary elements discussed previously. Shear reinforcement must be fully anchored within any boundary elements to ensure it is able to develop its specified yield strength,  $f_y$ , or, where no boundary elements are required, the horizontal shear reinforcement terminating at the edge of the walls must have standard hooks that engage the edge reinforcement. An alternative to the latter requirement is that the edge reinforcement must be enclosed in U-stirrups spliced to the horizontal reinforcement using the same bar size and spacing.

Section 9.3.4(a) of ACI 318-02 states that a shear-controlled failure is allowed in special reinforced concrete walls as long as a more severe strength reduction factor,  $\phi$ , of 0.6 is used. The commentary to this section states that this provision is included for "members such as low-rise walls, portions of walls between openings, or diaphragms that are impractical to reinforce to raise their nominal shear strength above the nominal flexural strength for the pertinent loading conditions." The reduced  $\phi$  is intended to ensure that the wall will remain in the elastic range, with minimal damage, during a design-level seismic event.

Because special reinforced concrete structural walls are intended to be designed to withstand large inelastic flexural deformations and dissipate energy in a seismic event, such a wall should not be designed to remain elastic. To ensure ductile behavior and good energy dissipating characteristics of flexurally-controlled special reinforced concrete structural walls, the shear reinforcement should be designed to achieve the maximum probable flexural strength,  $M_{pr}$ , of the wall before the nominal shear capacity,  $V_n$ , is exceeded. When the lateral force resisting system of a building consists of orthogonal rectangular walls, the provided strength in each orthogonal direction is independent of the other. As a result, it is possible to design the walls so that  $M_{pr}$  is not much higher than the required moment ( $M_u/\phi$ ). However, when nonrectangular walls are used, the orthogonal moment capacities are coupled, and it is more likely that a significant overstrength in one direction may occur. An example of this situation was encountered in the design of the prototype building considered in this study. This is addressed in Section 3.2.4 of this thesis. In this case, increasing the flexural capacity by adding more wall reinforcement in one direction had a significant impact on the strength of the wall in the other direction. The resulting flexural overstrength caused a large discrepancy between the required shear strength ( $V_u/\phi$ ) based on the lateral force demands and the shear strength required to ensure flexural failure.

ACI 318-02 does not specifically require the designer to ensure development of the flexural capacity of the walls; it only requires consideration of the design for the factored shear forces. It is noted in the commentary to ACI 318-02 Section 21.7.3 “However, the designer should consider the possibility of yielding in components of such

structures, as in the portion of a wall between two window openings, in which case the actual shear may be in excess of the shear indicated by lateral load analysis based on factored design forces.”

If the designer chooses to promote flexural failure of the wall, ACI 318-02 does not provide guidance. However, more extensive guidance is provided for special moment frames, and this design philosophy was adopted for the design of the wall specimen in this study. Section 21.5.4 states that the design shear force  $V_e$  should be used in the design of special moment frames, where  $V_e$  is the shear force required to generate the maximum probable moment strength,  $M_{pr}$ , of the member. The maximum probable moment strength,  $M_{pr}$ , is defined in Section 21.0 as the "probable flexural strength of members determined using the properties of the member at the joint faces assuming a yield strength in the longitudinal bars of at least  $1.25f_y$  and a flexural strength reduction factor  $\phi$  of 1.0." In this calculation,  $f_y$  is the specified minimum yield strength of the steel. Additionally, Section 9.3.4(c) allows an increased strength reduction factor  $\phi$  of 0.85 to be used for shear in joints and diagonally-reinforced coupling beams.

SEAOC (1999) “strongly recommends” that engineers design walls to be flexurally controlled. They recommend a minimum shear strength,  $\phi V_n$ , of  $\phi(M_n/M_u)(\omega_v)V_u$ , where  $\phi$  is taken as 0.85 and the term  $\omega_v$  is an amplification factor accounting for inelastic dynamic effects and higher-mode deformations. Recommended values of  $\omega_v$  are  $(0.9+n/10)$  for buildings up to six stories and  $(1.3+n/30)$  for buildings over six stories, where  $n$  is the number of stories in the building, with a maximum value of 1.8, corresponding to a 15-story building. These provisions are based on the *New*

*Zealand Standard Code of Practice for the Design of Concrete Structures*, NZS 3101 (Paulay and Priestley 1992). SEAOC (1999) also recommends using  $M_{pr}$  instead of  $M_n$  in the determination of minimum design shear strength as a more conservative practice, and recommends calculating  $M_{pr}$  by assuming a tensile stress in the flexural reinforcement of  $1.25f_y$ .

Paulay and Priestley (1992) suggest that large inelastic shear deformations are primarily the result of insufficient horizontal reinforcement yielding and allowing wide diagonal cracks to form, and that this yielding should be prevented. However, Oesterle *et al.* (1979) and Sittipunt and Wood (1995) compared the effects of adding additional horizontal and vertical web reinforcement to structural walls beyond that required to ensure a flexurally-controlled wall. They found that the width of shear cracks is primarily a function of the flexural behavior of the wall and that using additional horizontal reinforcement does not affect either the width of shear cracks or the performance of the wall.

Oesterle *et al.* (1979) found that designing horizontal reinforcement to remain elastic at a shear corresponding to the maximum calculated moment capacity of the wall had only small effects on the measured shear deformation and the energy dissipation capacity of a specimen compared to a similar specimen with horizontal reinforcement designed only to promote flexural failure. There was little difference in the observed shear deformation responses of these specimens, even though in one case the horizontal reinforcement remained elastic throughout the test, whereas, in the other case, the horizontal reinforcement yielded soon after the flexural reinforcement as intended.

Sittipunt and Wood (1995) conducted a parametric study using the finite element method to investigate the effects of adding additional web reinforcement to structural walls beyond that required to ensure a flexurally-controlled wall and control crack widths. They found that doubling the amount of horizontal shear reinforcement or vertical web reinforcement did not significantly affect the displacement capacity, energy dissipation, or failure mode of the walls because neither of these modifications was able to limit diagonal crack widths as determined from the model used. However, they did find that adding diagonal reinforcement allowed the steel to carry shear forces in direct tension and reduced the amount of shear distortion in the walls.

### **2.2.3 Shear Transfer across Web-to-Flange Interface**

Localized damage in the web-to-flange interface region causing separation of the wall elements could lead to a nonrectangular wall acting as individual, planar walls. Section 21.7.6.4 b) of ACI 318-02 states that “in flanged sections, the boundary element shall include the effective flange width in compression and shall extend at least 12 in. into the web.” The commentary to this section indicates that this provision is included to prevent local crushing in the web-to-flange interface in cases where the expected flange compression strains are large enough to require a special boundary element. This consideration is for loading parallel to the web, placing the entire flange in compression. As shown previously, the expected neutral axis depth for this loading direction is generally very small for T-shaped or other flanged walls, and the compression region does not include material outside the flange. This provision would not apply for the case

of loading parallel to the flange, because the compression strains are concentrated toward the flange tips and tensile strains are expected at the web-to-flange interface.

Previous tests of T-shaped walls by Thomsen and Wallace (1995) included a boundary element at the web-to-flange interface. This was done primarily to examine the results of combining two independent planar walls into a single T-shaped wall without considering the interaction between the elements in the design process. Tests of flanged walls by Palermo and Vecchio (2002) did not include boundary elements at the web-to-flange interface. Oesterle *et al.* (1979) tested one flanged wall specimen with boundary elements at the web-to-flange interfaces, and one without boundary elements. None of these testing programs reported localized damage around the web-to-flange interface.

#### **2.2.4 Shear Lag and Effective Flange Width**

Accurately estimating the portion of the flange that participates when a wall is loaded parallel to the web is necessary for predicting the behavior of a flanged wall section. For the case of the flange in tension, the tension must be carried across the width of the flange through shear from the intersection with the web toward the flange tips. This causes deformations that lead to reinforcement further away from the web being less heavily loaded than reinforcement near the web. This shear lag reduces the tension force in the reinforcement further from the web interface, and causes a reduction in the flexural capacity of the section compared to an assumption of a fully effective flange. Figure 2.2 shows a schematic of strain distributions in the wall with and without shear lag effects. The degree that shear lag reduces the tension force and effectiveness of the flange likely depends on the width of the flange and the distribution of steel within the

flange. Variation in the effectiveness of the flange can lead to a large variation in the expected strength and cracked stiffness of the wall. Overestimating the participation of the flange leads to an unconservative estimate of the flexural capacity of the wall and potentially poor performance in a seismic event. However, as noted by Wallace (1996), underestimating the participation of the flange may also lead to an unconservative design if the wall does not have sufficient shear capacity to reach its flexural strength and instead fails in a brittle manner. The consequences of shear-controlled failure are further discussed in Section 2.2.2. Variation in the effectiveness of the flange also has a large effect on the neutral axis depth in the web and, consequently, the requirements for confinement.

UBC 1994 required that the assumed effective flange width not exceed one-tenth of the wall height. Based on tests of two T-shaped wall specimens, Wallace (1996) recommended that this limit be increased to one-quarter of the wall height to represent the observed behavior more accurately and to reduce the likelihood of shear failures. This recommendation was adopted in ACI 318-99. Section 21.7.5.2 of ACI 318-02 limits the effective overhanging flange width of walls to the smaller of one-half the distance to an adjacent wall web or one-quarter of the total wall height, where the effective flange width is measured from the face of the web. Hassan and El-Tawil (2003) conducted a parametric study of coupled flanged wall systems using finite element models to examine these provisions. They found that increasing the axial compression applied to a wall tended to decrease the effective flange width and that increasing the applied drift tended to increase the effective flange width. Additionally, they found that the effective flange

width was correlated more strongly to wall length than to wall height, and the correlation to wall height was dependent on wall length being proportional to wall height. They recommended using varying maximum values of effective width based on the design drift level. For walls in axial compression: for 0.5 percent drift, use an overhanging effective width of  $0.6d$ ; for 1 percent drift, use  $0.95d$ ; and for 2 percent drift use  $1.15d$ . Research on T-beams has found similar correlations with drift level and beam width as opposed to span, where beam width is analogous to wall length, and beam span is analogous to wall height (Pantazopoulou and French 2002, Pantazopoulou and Moehle 1992).

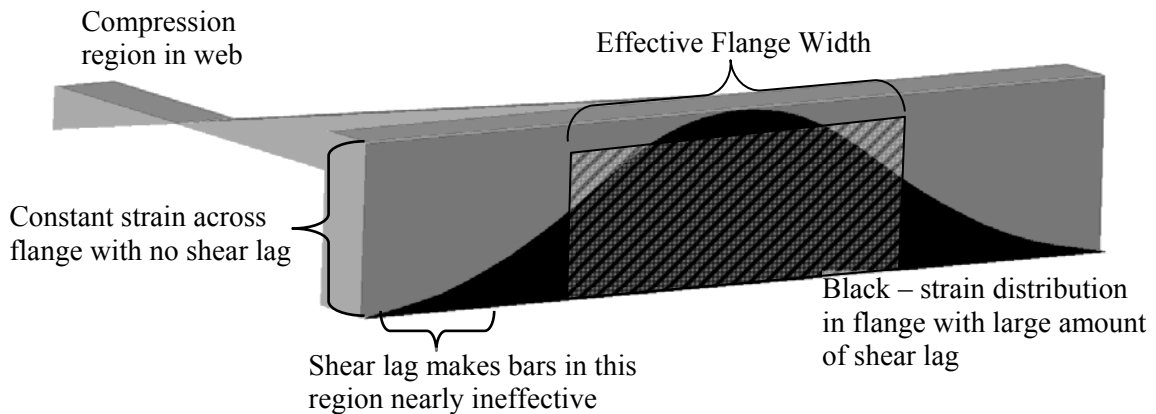


Figure 2.2. Effect of shear lag on strain distribution in flange for a T-shaped cross section with the flange in tension.

### 2.2.5 Distribution of Longitudinal Reinforcement

Concentrating longitudinal reinforcement in the boundary elements of a wall element (i.e., a rectangular wall or a web or flange in a non-rectangular wall), rather than uniformly distributing it across section, leads to a small increase in the moment capacity of the section and a more substantial increase in the ductility of the section because it allows for a shallower neutral axis depth due to an increased area of steel in compression.

However, this shallower neutral axis depth can lead to an increased susceptibility to sliding shear failures (Paulay and Priestley 1992). Additionally, tests have shown that using more closely spaced, smaller bars in the web of a wall improves its hysteretic response and energy dissipation capacity by minimizing the width of shear cracks (Paulay and Priestley 1992). SEAOC (1999) also recommends uniform distribution of reinforcement to facilitate the design and construction of boundary elements and lap splices.

### **2.2.6 Lap Splices**

Limited research has been done on the performance of walls with lap splices. As a result, research on columns has been applied to walls. Two issues must be considered when locating lap splices in walls. The first is ensuring that the splice will not fail under the load and ductility demands to be placed on it. Section 21.3.2.3 of ACI 318-02 prohibits the use of lap splices in regions of columns where plastic hinging is expected because ductility demands cannot be met reliably. While ACI 318-02 does not apply this provision to walls, SEAOC (1999) does recommend that this restriction be applied to walls for the same reasons it is applied to columns. The second is the effect of the splice on the performance of the specimen when the splice itself does not fail. SEAOC (1999) states that an additional problem with splices in plastic hinge regions of columns or walls that do not slip is their tendency to concentrate yielding and large strains over a short length of reinforcement at one or both ends of the lap, reducing the rotation and ductility capacities of the plastic hinge region. Additionally, SEAOC (1999) recommends that splices outside plastic hinge regions be staggered to avoid the creation of weak sections.

Sittipunt and Wood (1993) used finite element analysis to investigate the utility of several detailing schemes to decrease inelastic shear deformations and increase the energy dissipation capability of barbell-shaped walls. One of the options studied was the addition of extra longitudinal web reinforcement in the lower portion of the wall. This reinforcement was not anchored in the foundation, so it had a similar effect as a lap splice at the base of the wall causing an abrupt change in the amount of steel and a concentration of steel yielding over a limited region. The analysis indicated that this detailing would produce a wall with superior behavior compared to a wall without the additional reinforcement. By concentrating the damage in a localized region at the wall-to-foundation interface, the extra web reinforcement would help to reduce the width of web cracks, increasing the shear stiffness and reducing pinching of the load versus displacement relationship. This study did not identify premature failure as a possible result of this concentration of damage.

Johnson (2007) describes the testing of three rectangular walls comparing continuous longitudinal reinforcement, lap splices located at the wall-to-foundation interface, and mechanical couplers under reversed cyclic loading. While the specimens with continuous reinforcement and mechanical couplers had similar behavior, the specimen with lap splices did not perform as well. Damage was localized at the wall-to-foundation interface that led to slip of the splices and premature buckling and fracture of the reinforcement embedded in the foundation. Both the displacement capacity and the energy dissipation capacity of this specimen were reduced compared to the specimens with continuous or mechanically-coupled reinforcement.

### 2.2.7 Bar Anchorage and Strain Penetration Effects

The development of stresses in reinforcing bars causes some relative movement between the bars and the foundation in which they are anchored. This slip occurs even when bars are sufficiently anchored, and it is distinct from the much larger slip that is observed when bars are insufficiently anchored. Because of this slip, a rigid body rotation is observed in addition to the deformations from flexure and shear of the wall. Historically, rotations due to strain penetration have generally not been separated from those due to flexural plastic hinging. While neglecting the effects of strain penetration in analysis often leads to satisfactory predictions of the overall force versus displacement response of a structure, it often overestimates the curvature demands on the plastic hinge region (Zhao and Sritharan 2007). Because correct prediction of local damage levels is critical to performance-based engineering, strain penetration effects cannot be ignored in the modeling of walls.

Researchers have used three general types of tests to investigate bond strengths and bond stress-slip relationships between reinforcing bars and concrete. These are pullout tests of bars with very short embedment lengths, where the bond fails and the bar pulls out of the concrete prior to yielding (e.g., Eligehausen *et al.* 1983), pullout tests of bars with sufficient embedment lengths to yield prior to bond failure (e.g., Viwathanatepa *et al.* 1979), and tests of subassemblages with instrumentation to measure bar slip due to strain penetration (e.g., Sritharan *et al.* 1998). Pullout tests with short embedment lengths constitute the majority of the tests in the literature because it can be assumed in these tests that the bond stress-slip relationship is constant over the entire bar length,

simplifying the instrumentation required for testing (Eligehausen *et al.* 1983). While tests with short anchorage lengths are useful for establishing the maximum local bond strength and local bond stress-slip relationships, applying the results to determine the pullout force-slip relationship for a longer bar requires the assumption of a bond stress distribution over the anchorage length (ACI 408.2R-92). A particular difficulty with this approach is its application to fully anchored bars at large inelastic strains, where bond is degraded by Poisson effects on the cross section of the reinforcement (Zhao and Sritharan 2007). Pullout tests of longer, sufficiently anchored bars eliminate this issue but require the attachment of many strain gauges along the bar length in order to determine the bar stress distribution over the embedment length. Zhao and Sritharan (2007) found only 16 tests reported in the literature of bars with sufficient anchorage length to ensure yielding before pullout failure. Finally, measuring and isolating strain penetration effects within subassembly tests ensures that important detailing and three-dimensional stress states are included that may not be present in simple pullout tests, but providing instrumentation to isolate and measure the strain penetration effects is challenging. This difficulty has discouraged researchers from this type of investigation (Lowe and Altoontash 2003).

Several approaches have been proposed to predict strain penetration effects in reinforced concrete structures (ACI 408.2R-92). Because the current state of the art represents an incomplete understanding of bond and pullout, the reliability of all of these methods is limited. Despite this incomplete understanding, there is consensus that bond and strain penetration behavior are primarily determined by concrete compressive strength, concrete transverse reinforcement and confinement, size and grade of bars being

developed, cover, and bar spacing (ACI 408.2R-92). The existing methods include highly detailed three-dimensional solid finite element models including the surface ribs of the bar or fiber-based models with zero-length interface elements representing the effects of strain penetration. Empirically-based macroscopic-level models are also available, such as those incorporating rotational springs explicitly representing strain penetration effects and plastic hinge models using increased plastic hinge lengths to account for strain penetration effects in addition to flexural hinging. These empirical models are computationally inexpensive but may be applicable to a limited range of geometries and detailing (Zhao and Sritharan 2007, Park and Paulay 1975). The remainder of this discussion will describe two existing macroscopic models, because more computationally-expensive modeling was not considered to be warranted in the development of the simplified modeling procedure developed herein.

Lowes and Altoontash (2003) developed a simplified bar stress-slip relationship based on the local stress-slip model developed by Eligehausen *et al.* (1983). Simplifying assumptions of this model included 1) bond stress assumed to be piecewise uniform over the anchorage length, with values determined for the elastic and inelastic portions of the anchorage length, 2) slip assumed to be a function of the strain distribution along the bar, and 3) slip assumed to be zero where the bar stress is zero. The average bond stresses for each of the elastic and inelastic portions of the anchorage length were determined assuming maximum bond stresses reported by previous researchers and the bond stress distribution proposed by Eligehausen *et al.* (1983). These average bond stresses are  $\tau_E = 21\sqrt{f'_c}$  (psi) ( $\tau_E = 0.685\sqrt{f'_c}$  (ksi),  $\tau_E = 1.8\sqrt{f'_c}$  (MPa)) defined for the portion of

reinforcement that remains elastic and a reduced bond stress  $\tau_Y=0.6$  to  $4.8\sqrt{f'_c}$  (psi) ( $\tau_Y=0.05$  to  $0.4\sqrt{f'_c}$  (MPa)) for any portion that has yielded, where  $f'_c$  is the compressive stress of the concrete. It should be noted that these stresses did not consider the case of highly confined concrete or concrete under significant transverse compression. Both of these prevent splitting failure of the concrete and increase the friction resistance between the bar and concrete, increasing the effective bond stress. For example, Sritharan, *et al.* (1998) reported average bond stresses in excess of  $30\sqrt{f'_c}$  (psi) ( $2.5\sqrt{f'_c}$  (MPa)) in tests of highly confined cap beams. Based on the assumptions above and a bilinear model for the reinforcing steel, the bar strains over the anchorage length can be integrated to produce the bar stress-slip relationships

$$slip = 2 \frac{\tau_E}{E} \frac{l_{fs}^2}{d_b} \text{ for } \tilde{f}_s < f_y \quad (2.5)$$

$$slip = 2 \frac{\tau_E}{E} \frac{l_e^2}{d_b} + \frac{f_y}{E} l_y + 2 \frac{\tau_Y}{E_h} \frac{l_y^2}{d_b} \text{ for } \tilde{f}_s \geq f_y \quad (2.6)$$

$$\text{where } l_{fs} = \frac{\tilde{f}_s}{\tau_E} \frac{A_b}{\pi d_b}, l_e = \frac{f_y}{\tau_E} \frac{A_b}{\pi d_b}, l_y = \frac{\tilde{f}_s - f_y}{\tau_Y} \frac{A_b}{\pi d_b} \quad (2.7)$$

and  $l_{fs}$  is the development length when the bar is stressed in the elastic range,  $l_e$  and  $l_y$  are the portions of the development length where the bar stress is less than and greater than the yield stress, respectively,  $\tilde{f}_s$  is the bar stress at the joint face,  $f_y$  is the yield stress of the steel,  $E$  is the elastic modulus of the steel,  $E_h$  is the strain hardening modulus of the steel,  $A_b$  is the nominal bar area, and  $d_b$  is the nominal bar diameter.

Zhao and Sritharan (2007) developed a bar stress-slip relationship based on an empirical fit to the results of sixteen tests in the literature. These tests were selected on the basis of having an anchorage length ( $l_a$ ) sufficient to ensure yielding of the bar prior to pullout failure, based on an assumed average bond stress of  $20.4\sqrt{f'_c}$  (psi) ( $0.667\sqrt{f'_c}$  (ksi),  $1.75\sqrt{f'_c}$  (MPa)) recommended by Eligehausen *et al.* (1983). These are the same stresses used by Lowes and Altoontash (2003), except that one more significant digit was retained. Using this bond stress, the resulting minimum anchorage length for inclusion in Zhao and Sritharan's (2007) data set was then

$$l_a = \frac{3}{8} \frac{f_y}{\sqrt{f'_c}} d_b \quad (f_y \text{ and } f'_c \text{ in ksi}) \quad \text{or} \quad l_a = \frac{1}{7} \frac{f_y}{\sqrt{f'_c}} d_b \quad (f_y \text{ and } f'_c \text{ in MPa}) \quad (2.8)$$

The concrete compressive stresses in these tests ranged from 2800 to 5450 psi, the steel yield strengths ranged from 51 to 119 ksi, and the bar diameters ranged from 0.40 to 1.0 in., with both U.S. and Metric bar sizes included. In their model, a relationship to determine the slip at yielding was obtained using an empirical fit to the selected data.

The slip at yielding is calculated as

$$s_y = \frac{1}{10} \left( \frac{d_b (\text{in.})}{126.5} \frac{f_y (\text{ksi})}{\sqrt{f'_c} (\text{ksi})} (2\alpha + 1) \right)^{1/\alpha} + 0.0134 \quad (2.9)$$

where  $d_b$  is the bar diameter,  $f_y$  is the yield stress of the reinforcement,  $f'_c$  is the compressive strength of the concrete, and  $\alpha$  is a parameter describing the shape of the bond stress distribution over the anchorage length and is taken as 0.4. Prior to yielding, the stress-slip relationship is assumed to be linear, and the post-yielding portion is represented by the relationship

$$\tilde{\sigma} = \frac{\frac{\tilde{s}}{\mu - \tilde{s}}}{\left[ \left( \frac{1}{\mu * b} \right)^{R_e} + \left( \frac{\tilde{s}}{\mu - \tilde{s}} \right)^{R_e} \right]^{1/R_e}} \quad (2.10)$$

$$\text{where } \tilde{\sigma} = \frac{\sigma - f_y}{f_u - f_y}, \tilde{s} = \frac{s - s_y}{s_y}, \mu = \frac{s_u - s_y}{s_y} \quad (2.11)$$

and  $\sigma$  is the stress being developed,  $f_y$  is the yield stress of the reinforcement,  $s_y$  is the slip when the stress equals  $f_y$ , defined in Equation 2.9,  $f_u$  is the ultimate stress of the reinforcement,  $s_u$  is the slip when the stress equals  $f_u$ ,  $\mu$  is assumed to be between 30 and 40,  $b$  is the stiffness reduction factor and is assumed to be between 0.3 and 0.5, and  $R_e$  is taken as 1.01.

Both Lowes and Altoontash (2003) and Zhao and Sritharan (2007) evaluated their respective models using a comparison to a pullout test reported by Viwathanatepa *et al.* (1979). Post-yielding, both models predicted the test results reasonably well. Prior to yielding, Lowes and Altoontash (2003) underpredicted the measured slip, while Zhao and Sritharan (2007) predicted it with good accuracy. One reason for the underprediction by Lowes and Altoontash (2003) was that the maximum average bond stress reported by Viwathanatepa *et al.* (1979) was only  $17\sqrt{f'_c}$  (psi), which was 20 percent less than the value assumed by Lowes and Altoontash (2003). Substituting this value into the Lowes and Altoontash relationship greatly improves the prediction. The utility of the Zhao and Sritharan (2007) model in predicting the bond in relatively high-strength or highly-confined concrete is unclear. Especially concerning is the constant 0.0134 in. term in the

yield slip, which dominates the calculated yield slip relation in cases with relatively high concrete strengths and small bars. For instance, this term represents over 80 percent of the predicted yield slip for Gr. 60 No. 4 bars with any concrete compressive strength and for No. 6 bars with concrete compressive strength greater than 6000 psi. With No. 8 bars, this term does not represent more than 75 percent of the predicted slip for any concrete compressive strength less than 10000 psi. As a result, this model is likely to give better predictions for full-scale structures than for reduced-scale test specimens.

### **2.2.8 Performance-Based Engineering: Prediction of Damage States**

Performance-based engineering for seismic regions is being developed to provide engineers and owner-users with the tools required to make rational design decisions incorporating the costs of potential repairs and downtime into the costs of distinct design options that meet or exceed current life-safety provisions. In order to accomplish this objective, performance-based engineering requires the linking of defined performance levels, damage states, and likely repair requirements to engineering demand parameters (EDPs) that can be determined from structural analysis.

Previous work (FEMA 356 2000, ATC-58 2004, Berry *et al.* 2008) has considered the use of both macro level, deformation- or drift-based EDPs, such as drift or displacement ductility, and local EDPs, such as strain. While both approaches have been found to be reliable, the use of local EDPs is commonly understood to provide a better understanding of the expected damage level (Berry *et al.* 2008).

The selection of appropriate EDPs and damage measures for various performance levels is ongoing. FEMA 356 (2000) represents an early effort in defining limits for the

performance levels of immediate occupancy (IO), life safety (LS), and collapse prevention (CP). The simplified modeling procedure recommend in FEMA 356 considers only flexural deformations and the axial load and shear demands on the member. Figure 2.3 and Table 2.1 summarize the modeling procedure and definition of performance levels in FEMA 356. In Table 2.1,  $A_s$  is the area of longitudinal reinforcement in tension,  $A'_s$  is the area of longitudinal reinforcement in compression,  $t_w$  is the thickness of the web,  $l_w$  is the length of the web,  $f_y$  is the yield strength of the reinforcement,  $f'_c$  is the compressive strength of the concrete,  $P$  is the applied axial compression load,  $a$  and  $b$  are plastic hinge rotations indicated in Figure 2.3, and  $c$  is the residual fraction of the strength after the collapse prevention limit is reached, as indicated in Figure 2.3. In Figure 2.3,  $Q/Q_y$  is the ratio of the resistance of the member at a particular rotation ( $\theta$ ) or displacement ( $\Delta$ ) to the value at yielding. This resistance may be a shear force or a bending moment, depending on the particular analysis.

Table 2.1. Modeling parameters and performance levels for walls with boundary elements controlled by flexure (from FEMA 356 2000)

Conditions		Plastic Hinge Rotation (rad)		Residual Strength Ratio	Acceptable Plastic Hinge Rotation (rad)		
$\frac{(A_s f_y - A'_s f_y + P)}{t_w l_w f'_c}$	$\frac{Shear}{t_w l_w \sqrt{f'_c}}$	a	b	c	Performance Level		
					IO	LS	CP
$\leq 0.1$	$\leq 3$	0.015	0.020	0.75	0.005	0.010	0.015
$\leq 0.1$	$\geq 6$	0.010	0.015	0.40	0.004	0.008	0.010
$\geq 0.25$	$\leq 3$	0.009	0.012	0.60	0.003	0.006	0.009
$\geq 0.25$	$\geq 6$	0.005	0.010	0.30	0.0015	0.003	0.005

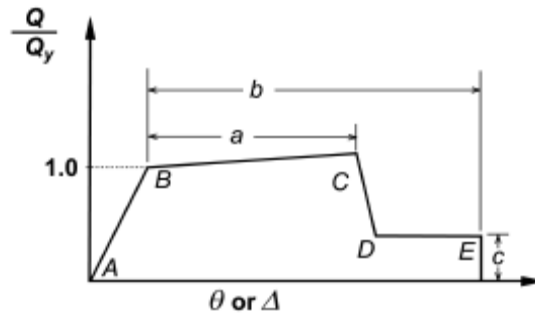


Figure 2.3. Generalized force-deformation relations for concrete elements (from FEMA 356 2000)

More recent efforts have refined the definitions of performance levels and have correlated more specific damage measures with the general performance levels, and many of these efforts have expanded the number of performance and damage levels defined. For instance, Pagni and Lowes (2006) recommend 12 discrete damage levels for reinforced concrete beam-column joints. These damage levels range from initial hairline cracking requiring the replacement of finishes to crushing of the concrete core and reinforcement failure due to buckling, pullout, or fracture requiring replacement of the entire section. Berry *et al.* (2008) determined that these damage levels are appropriate for describing the damaged condition of reinforced concrete structural elements in general and selected four of these damage levels as the most important for predicting repair costs and downtime for performance-based engineering of reinforced concrete columns. They then correlated these four damage levels with local EDPs, as shown in Table 2.2, although they do not recommend critical values for the proposed local EDP's. A minimum residual crack width of 0.024 in. was chosen as the threshold for requiring repair by epoxy injection. Cracks as small as 0.005 in. can be successfully repaired with this method (ACI 503.7-07), but a larger value was chosen to reflect the service-load

crack width limits that are implied by ACI 318-02 for the prevention of corrosion and based on typical practice following recent earthquakes (Pagni and Lowes 2006).

Table 2.2 Damage levels and local EDPs (from Berry *et al.* 2008)

Damage and Performance Levels	Method(s) of Repair	Damage Measure	Local EDP
Negligible	None	Max. residual crack width <0.024 in.	Reinforcing steel tensile strain
Minimum (Immediate Occupancy)	Epoxy injection of cracks	Max. residual crack width >0.024 in.	Reinforcing steel tensile strain
Minimal	Patching of concrete cover and epoxy injection of cracks	Spalling of cover concrete	Cover concrete compressive strain
Moderate (Life Safety)	Replacement of concrete cover and epoxy injection of cracks	Significant spalling of cover concrete that exposes column reinforcement	Core concrete compressive strain
Significant	Replacement of section	Buckling or fracture of longitudinal steel, extensive damage to core concrete	Maximum tensile strain reduced for cyclic demand

Additional work is needed to define meaningful limits for the local EDPs recommended by Berry *et al.* (2008). Some of these limits may be found to apply to all reinforced concrete structural elements, while other limits may depend on the type of element under consideration (e.g., walls, columns, and beam-column joints).

## 2.3 Selected Tools Available for Analysis of Structural Walls

### 2.3.1 Confined Concrete Material Models

When concrete is loaded in uniaxial compression, Poisson effects cause tensile strains to develop in the directions perpendicular to the applied load. These strains eventually lead to cracks and crushing of the concrete. Richart, *et al.* (1928) studied the use of active hydraulic pressure to confine concrete cylinders, and found that the lateral confinement delayed the crushing of the concrete, leading to an increase in the

compressive strength,  $f'_c$ , and the ductility of the specimens. Figure 2.4 shows typical stress vs. strain relationships for unconfined and confined concrete, as represented by the Modified Kent and Park model. Appropriate consideration of the confined concrete properties is crucial in the modeling of reinforced concrete elements that include confinement. The tools described in Sections 2.3.2 through 2.3.6 all require the consideration of confined concrete material properties, whether this is explicitly defined in the model or not.

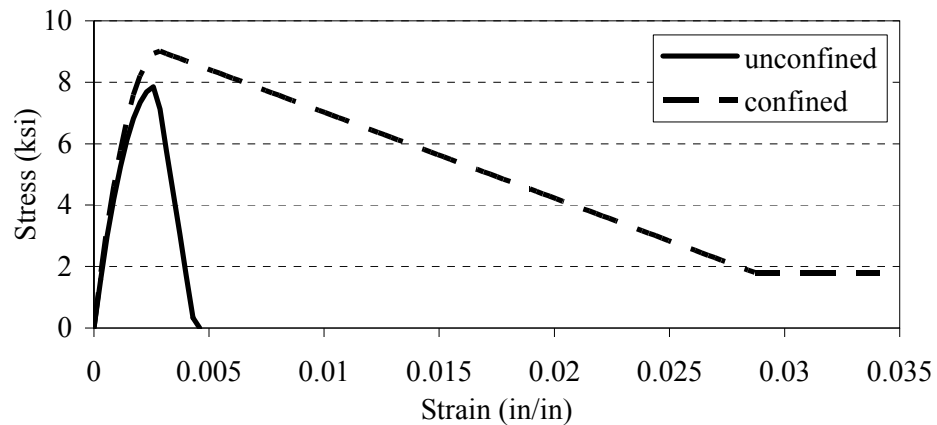


Figure 2.4. Effect of confinement on concrete stress vs. strain relationship.

The success of Richart's work motivated several researchers to study confinement of concrete further. Applying active confining pressure to reinforced concrete structural members is not feasible, but transverse reinforcement can be used to create passive confinement in reinforced concrete members. This passive confinement is not effective at low load levels. It develops as internal microcracks develop in the concrete and cause increased lateral expansion and an apparent increase in Poisson's ratio of the concrete. The confining steel then begins to restrain the expansion of the concrete and confine it effectively. Because the confining transverse steel is inside the cover concrete on a

member, the cover concrete will spall off, but the confined core will remain and continue to resist additional load.

Most of the experimental research regarding confinement of rectangular concrete members has been done on square sections or rectangular members with low aspect ratios (Sheikh 1982, Mander, *et al.* 1988a). Mander, *et al.* (1988a) tested 14 sections with an aspect ratio of 4.7, and the results of these tests have been used in the calibrations of stress-strain models of confined concrete by Mander, *et al.* (1988b) and Saatcioglu and Razvi (1992).

In reinforced concrete shear walls, a compression block is formed as part of the couple resisting the bending moments in the wall. The deformation capacity of a wall is greatly increased when special confined regions are created in the portions of the wall that are expected to undergo large compression strains.

### **2.3.2 Sectional Analysis Tools, Including BIAX (Wallace 1992)**

Several software tools have been developed to perform flexural section analysis of reinforced concrete, including BIAX (Wallace 1992). Any of these tools can be used to calculate the moment-curvature response of a reinforced concrete section based on the input geometry and material properties. For this study, BIAX was chosen because of its ready availability, its ability to consider the response of a section bending about any axis, and its ability to incorporate strain hardening of reinforcement and confined concrete section properties into the model. In general, this class of tools discretizes a section into several elements and uses a strain compatibility approach to determine the stresses and

strains in a particular element. In this approach, it is assumed that plane sections remain plane (i.e., deep beam effects are not considered).

### **2.3.3 Empirical Models for Estimating Flexural Deformation Capacity**

Several empirical models have been proposed to predict the flexural deformation capacity of reinforced concrete members by estimating the rotation capacity of plastic hinges. These models are intended for hand calculation, and limit the number of parameters included accordingly. They allow the calculation of a bilinear load-displacement relationship using values calculated at first yielding and at ultimate. These models separate the elastic portion of the deformation from the inelastic portion, lumping the inelastic portion of deformation into a plastic hinge at the critical section. Additionally, they assume that shear deformations are negligible and consider only the effects of flexure and possibly strain penetration.

Each of these models estimates both the effective plastic hinge length and the inelastic curvature at failure. The total rotation of the plastic hinge is equal to the product of these two values. Each of the models has been calibrated to optimize the prediction of the plastic hinge rotation rather than the individual values of plastic hinge length and ultimate curvature. As a result, mixing the models (e.g., calculating the plastic hinge length using one model and the plastic curvature using another) is not recommended (Park and Paulay 1975).

The simplest of these models estimates the plastic hinge rotation by idealizing the moment-curvature relationship, assuming it to be bilinear. However, this approach generally underestimates the plastic hinge rotation because it neglects the contributions of

strain penetration, discussed in Section 2.2.7, and tension shift. Tension shift is the result of diagonal cracking within the section causing yielding of the flexural reinforcement to occur further along the member span than would be expected from the external moment diagram. This effect may be understood by a review of a free-body diagram of the member that is cut along a diagonal shear crack. As a result, the reinforcement yields over a larger portion of the element (wall, column, or beam) than would be expected from a section taken orthogonal to the longitudinal axis of the member (Park and Paulay 1975).

Park and Paulay (1975) summarized three of these models. For members with tension over part of the sections, Baker (1964) recommended a plastic hinge length

$$l_p = 0.8k_1k_3\left(\frac{z}{d}\right)c \quad (2.12)$$

and an ultimate curvature calculated assuming that the ultimate compression strain in the confined concrete

$$\varepsilon_c = 0.0015\left[1 + 150\rho_s + (0.7 - 10\rho_s)\frac{d}{c}\right] \leq 0.01 \quad (2.13)$$

and that the maximum concrete compressive stress be taken as

$$f_c'' = \left(0.8 + 0.1\frac{d}{c}\right)f_c' \leq f_c' \quad (2.14)$$

In these equations,  $k_1=0.7$  for mild steel reinforcement,  $k_3=0.6$  when  $f_c'=5100$  psi,  $z$  is the shear span,  $c$  is the neutral axis depth at the ultimate moment,  $\rho_s$  is the ratio of the volume of the transverse confining reinforcement to the volume of the concrete core,  $d$  is the effective depth of the member, and all lengths are in inches.

Based on tests of simply supported beams, Corley (1966) recommended a plastic hinge length

$$l_p = 0.5d + 0.2\sqrt{d}\left(\frac{z}{d}\right) \quad (2.15)$$

and a maximum concrete compression strain

$$\varepsilon_c = 0.003 + 0.02\frac{b}{z} + \left(\frac{\rho_s f_y}{20}\right)^2 \quad (2.16)$$

where  $b$  is the width of the beam,  $f_y$  is the yield strength of the confining steel, and the other terms are the same as described above for Baker's model, with length terms in inches. Mattock (1967) recommended a simplification of Corley's model, using  $l_p=0.5d+0.05z$  and

$$\varepsilon_c = 0.003 + 0.02\frac{b}{z} + 0.2\rho_s \quad (2.17)$$

Sasani and Der Kiureghian (2001) have recalibrated Corley's and Mattock's models using the results of eight previous tests of rectangular and barbell-shaped walls, rather than the simply-supported beams used in the initial development of these models, finding optimal expressions of

$$l_p = 0.52d + 0.295\sqrt{d}\left(\frac{z}{d}\right) \quad (2.18)$$

for Corley's model and  $l_p=0.56d+0.051z$  for Mattock's simplification.

Finally, Sawyer (1964) recommended using a plastic hinge length  $l_p=0.25d+0.075z$  along with a rational estimation of the curvature capacity of the section. This estimation is based on assumptions that the yield moment,  $M_y$ , is 85 percent of the

ultimate moment  $M_u$  and that the zone of yielding spreads a distance  $d/4$  beyond the region where it is expected to account for tension shifting.

More recently, Paulay and Priestley (1992) recommend a plastic hinge length  $l_p=0.08l+0.15d_b f_y$  (ksi) and an ultimate curvature based on rational analysis, where the first term represents plastic rotations due to tension shift and the second term represents rotations due to strain penetration. In this expression,  $l$  is the shear span,  $d_b$  is the diameter of the longitudinal reinforcing bars, and  $f_y$  is the yield stress of the longitudinal reinforcing bars. Additionally, based on the same eight tests of rectangular and barbell-shaped walls used to recalibrate Corley's and Mattock's models, Sasani and Der Kiureghian (2001), recommend a change in the form of the relationship from that used by Corley and a plastic hinge length of

$$l_p = 0.427d + 19.0 \left( \frac{\sqrt{z}}{d} \right) \quad (2.19)$$

where  $d$  is the effective member depth and  $z$  is the shear span, and all of the length terms are in inches. They recommend using this plastic hinge length with a maximum concrete compressive strain

$$\varepsilon_c = 0.00355 + 0.822 \frac{f_{yh} \rho_{sh}}{f_{ys}} \quad (2.20)$$

where  $f_{yh}$  is the yield stress of the confining hoops,  $\rho_{sh}$  is the volumetric ratio of the confining steel hoops, and  $f_{ys}$  is taken as 60 ksi or 413 MPa.

#### **2.3.4 Simplified Model for Well-Confined Bridge Piers (Hines *Et Al.* 2004)**

Hines *et al.* (2004) developed a simplified, semi-empirical model for determining the force-displacement relationship for rectangular and hollow box-shaped bridge piers with confined corner elements. This model extends the empirical models developed to estimate plastic hinge length and rotation in reinforced concrete members, discussed in Section 2.3.3, by adding terms explicitly describing the deformations due to shear and strain penetration to those describing flexural deformations.

Hines *et al.* (2004) recommend this model for use with both shear-dominant or “squat” and flexure-dominant or “slender” piers. Both cases were used in the calibration of the model, although piers with aspect ratios greater than four were not considered in the model calibration. Axial load ratios were limited to  $P/(f'_c A_g) \leq 0.20$ . The model was intended to be applicable for all levels of curvature ductility, from first yielding through the ultimate capacity of the pier. The model was developed and calibrated using measured loads, strains, curvatures, and displacements from specimen testing, but all of the necessary input values can be determined from a flexural analysis in order to apply the model to design problems.

This model has four primary shortcomings when applied to building structures. First, the model is limited to structures loaded with a single point load and cannot be easily applied to structures with variable shear demand. Second, it can only be used to determine deflections at inflection points of members and cannot be used to determine interstory displacements or the overall deformed shape of a member as a result of some assumed loading pattern. In its intended application to bridge piers, these first two issues

are of minimal importance, but the ability to apply distributed lateral loads or multiple point loads and to estimate interstory drifts is of great importance for building structures. Third, its applicability is limited to prismatic sections and cannot accommodate changes to the cross section of the member, including lap splices or bar cutoffs. Finally, the output terminates when the ultimate moment capacity of the section is reached and does not include provisions to estimate post-peak behavior.

Hines *et al.* (2004) developed and calibrated the model based on the results of testing two circular, eight barbell-shaped and two hollow-box bridge piers, all of which had circular boundary elements. Figure 2.5 shows the cross sections of these specimens, which were one-quarter scale models of prototype bridge structures. All of the circular and barbell-shaped specimens were tested as cantilevers with axial load applied in addition to the lateral load. The hollow box sections were tested using fixed-free boundary conditions in the direction transverse to the longitudinal direction of the bridge and fixed-fixed in the longitudinal direction of the bridge. The applied axial load ratios ( $P/(A_g f'_c)$ ) were approximately 6.5 to 7.5 percent in each of the specimens. The specimen aspect ratios varied between 2.0 and 4.0.

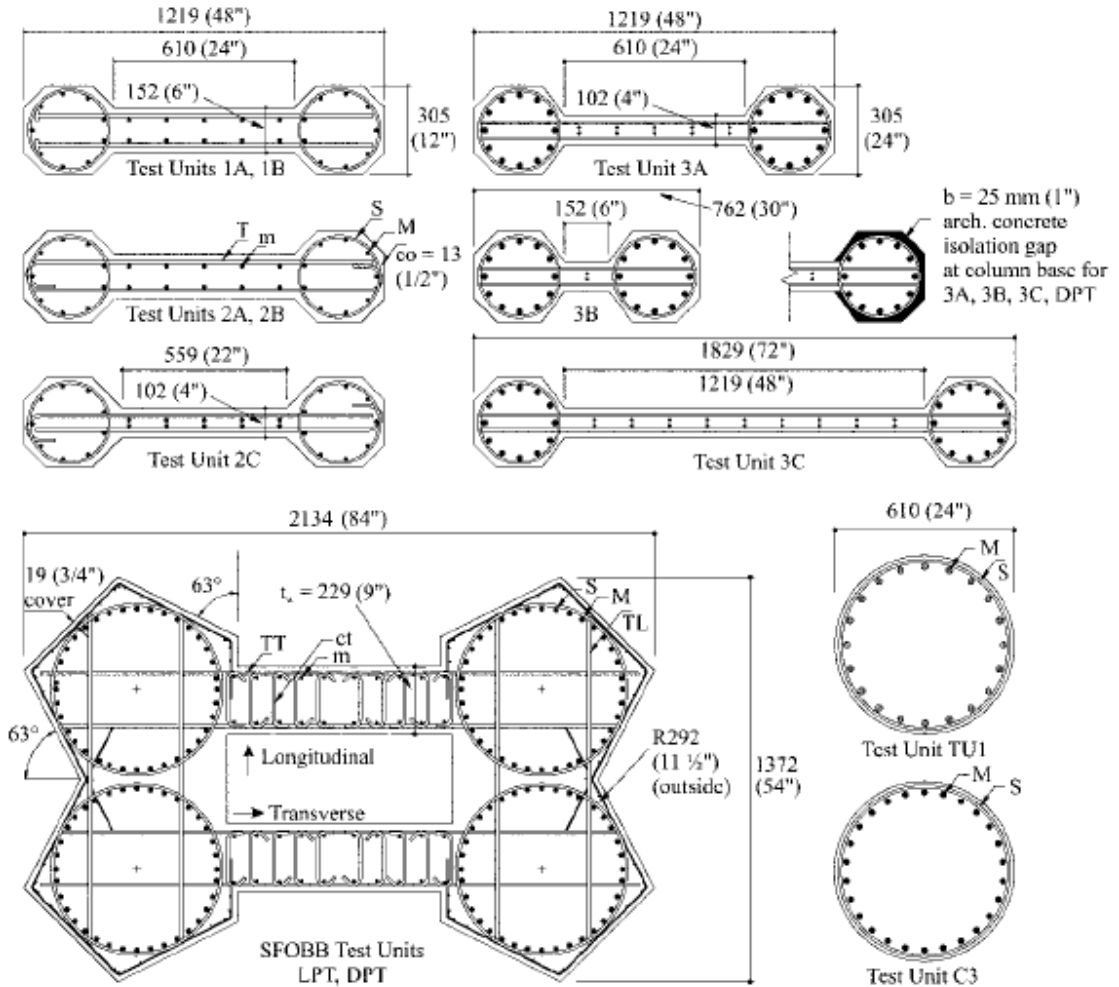


Figure 2.5. Cross sections of specimens used by Hines *et al.* for model calibration. (from Hines *et al.* 2004)

While the specimens were intended as bridge piers, they were similar to structural walls in many ways, and the application of the modeling tool to structural walls is not unreasonable. The specimens were tested at one-quarter scale, and the scaled dimensions of the cross sections (web thickness and depth) were of similar magnitude to many existing structural wall tests conducted at one-third and one-half scale, and similar-sized reinforcing bars were used. The bridge pier specimens did have larger axial loads applied than many structural walls (e.g., axial load ratios of 6.5 percent to 7.5 percent), and they

had lower aspect ratios than many structural walls, with both shear-dominant (aspect ratio <2.5) and flexure-dominant (aspect ratio >3.5) specimens considered, but none with aspect ratios greater than 4.0.

In the model proposed by Hines *et al.* (2004), the total displacement,  $\Delta$ , at the inflection point of a cantilever member with a given base moment  $M$  is given as

$$\Delta = \Delta'_y \frac{M}{M'_y} + \left( \phi - \phi'_y \frac{M}{M'_y} \right) L_p L \left( 1 + \frac{\Delta_s}{\Delta_f} \right) \quad (2.21)$$

In this expression, values of  $\phi$ , the base curvature associated with the base moment  $M$ ,  $M'_y$  and  $\phi'_y$ , the moment and curvature associated with the first reinforcing bar in the section reaching yield strain, can be determined from a sectional analysis.  $L$  is the shear span of the member. In this equation, it is assumed that the plastic hinge rotation occurs at the base of the pier, not the centroid of the assumed plastic hinge region. The remaining terms are calculated according to equations 2.22 through 2.26.

In this model,  $\Delta'_y$  is the displacement at the inflection point associated with first yielding. If only flexural deformations are considered, this value is equal to  $\phi'_y L^2/3$ .

Hines *et al.* (2004) incorporated additional terms so that the effects of strain penetration and shear are included, resulting in

$$\Delta'_y = \phi'_y L \left( \frac{L}{3} + L_{spp} \right) \left( 1 + \frac{\Delta_s}{\Delta_f} \right) \quad (2.22)$$

where  $L_{spp}$  is the additional plastic hinge length incorporated to account for strain penetration effects at first yielding and can be estimated as  $L_{spp}=0.30d_b f_y$ , where  $d_b$  is the reinforcing bar diameter and  $f_y$  is the reinforcing bar yield strength in ksi.

$L_p$  is the equivalent plastic hinge length, assuming a constant inelastic curvature over the equivalent hinge length, and it incorporates the effects of both tension shifting and strain penetration. It is calculated as

$$L_p = \frac{L_{pr} + L_{spy}}{2} \quad (2.23)$$

where  $L_{pr}$  and  $L_{spy}$  represent the contributions of plastic hinging within the pier itself and additional rotations due to strain penetration, respectively, and both of these values are calculated assuming a triangular distribution of plastic curvature over the hinge length.

$$L_{pr} = (T - T_{yav}) \frac{jd}{V} + \frac{V}{2 \left( \frac{A_v f_{yv}}{s} + 1.4 t_{cr} t_w \right)} \geq 0 \quad (2.24)$$

In this expression,  $T$  is the sum of the tensile forces in the reinforcement at the base moment being considered and  $T_{yav}$  is the average of the sums of tensile forces when the first reinforcing bar reaches its yield strain and when the first reinforcing bar reaches a strain of 0.015. The length  $jd$  is the distance between the flexural tension and compression centroids, which can be calculated as  $d-a/2$  using the results of the sectional analysis, where  $d$  is the distance from the extreme compression fiber to the centroid of the reinforcement in tension and  $a/2$  is the distance from the extreme compression fiber to the centroid of the compression block.  $V$  is the shear force associated with the moment, and the absolute value of  $V$  must be used when non-symmetric sections are considered and one loading direction is assigned negative values for shear, moment, curvature, and displacement. The term  $A_v$  represents the area of horizontal (shear) reinforcement over

some uniform spacing  $s$ , and  $f_{yv}$  is the yield strength of this reinforcement. The term  $t_{cr}$  represents the tensile strength of the concrete, and  $t_w$  is the thickness of the web.

Hines *et al.* (2004) observed a linear relationship between shear and flexural displacements measured at the tips of cantilever specimens over the entire range of displacement capacity when only the peak displacements from each loading ramp were considered. Based on this observation, an assumption that the majority of the shear displacements occurs in the plastic hinge region, and an assumption of a fanning crack pattern, Hines *et al.* derived and calibrated the following expression relating shear deformations,  $\Delta_s$ , to flexural deformations with strain penetration effects included,  $\Delta_f$ .

$$\frac{\Delta_s}{\Delta_f} = 0.35\alpha(1.6 - 0.20\theta_m)\frac{D}{L} \quad (2.25)$$

In this expression,  $\theta_m$  is the angle of the diagonal cracks measured from the vertical in degrees, and  $D$  is the total member depth. The term  $\alpha$  is an empirical multiplier intended to account for the very large shear deformations observed in walls intended to fail in shear, and is calculated as

$$1 \leq \alpha = \left( \frac{V}{V_n} + \frac{V}{V_{wc}} \right) \leq 2 \quad (2.26)$$

Where  $V_n$  is the shear capacity of the member under diagonal tension and  $V_{wc}$  is the shear capacity of the member under diagonal compression. For flexurally-controlled walls,  $\alpha$  can be assumed equal to 1.

In the specimens tested by Hines (2002), which had large confined regions and very slender webs, inelastic web crushing was found to control. Hines (2002)

recommended limiting the capacity found using the method described above to the inelastic web crushing capacity.

### **2.3.5 Modified Multiple Vertical Line Element Model (Massone *Et Al.* 2006)**

Massone *et al.* (2006) combined a multiple vertical line element representing the axial and flexural behavior of the wall with a shear spring in order to create a finite element that incorporates membrane behavior and shear-flexure interaction with a reduced computational demand relative to three-dimensional finite element modeling. A multiple vertical line element is a simplified fiber-based element where the curvature is assumed to be constant over the element length rather than linearly interpolated between element nodes. A rotating angle softened truss model was used to represent the panel behavior. In this model, a biaxial constitutive model for the concrete is used, and the principle stress directions are assumed to coincide with the principle strain directions.

Additional assumptions include plane sections remaining plane and constant shear strain over the width of the wall. Cyclic behavior is included in the models for both the concrete and the reinforcing steel. The Menegotto-Pinto model is used for the steel. The constitutive model used for the concrete assumes that one of the principle strains will be tensile and the other compressive. In order to include the effects of shear-flexure interaction, the compressive behavior of the concrete includes biaxial compression softening, with the compressive stress reduced based on the tensile strains in the orthogonal direction. The compression softening parameter proposed by Vecchio and Collins (1993) is used. The tensile behavior of the concrete includes effects of tension stiffening, that is the apparent increase in post-peak concrete tensile capacity as a result

of bond between the concrete and reinforcement and averaging the response over the entire element. This is done using the model proposed by Belarbi and Hsu (1994).

The model was calibrated using the results of five previous wall tests, with one slender (shear span ratio of 3.0) and four squat (shear span ratios of 1.0, 0.69, 0.56, and 0.35) rectangular walls. The results were considered acceptable for the slender wall, although the flexural deformation was overpredicted and the shear deformation underpredicted. Errors were larger in the squat walls and increased as the shear span decreased, and it was recommended that additional refinement of the model would be required for its use with squat walls.

### **2.3.6 Modified Fiber-Based Model (Waugh *et al.* 2009)**

In a companion study based on the testing program described in this thesis, Waugh *et al.* (2009) describes the development of new section definitions and material models so that fiber-based finite element analysis could be adapted for use with structural walls. The primary intended application of this model is for research, rather than design, and using this model is substantially more time-consuming than the simplified model described in Chapter 8 of this thesis. The fiber-based approach represents the section with a group of uniaxial fibers with only uniaxial material properties defined, and it is significantly less computationally expensive than traditional finite element analysis using three-dimensional elements and material properties.

The fiber-based concept has previously been applied to beam-column elements with success, but three limitations have prevented its application to wall sections. First, an inherent assumption in the fiber-based model formulation is that plane sections remain

plane and perpendicular. When this assumption is incorrect, strains and curvatures may not be calculated correctly at the critical sections. An additional limitation of this assumption is that the fiber-based model neglects shear deformations. Previous testing, such as that by Thomsen and Wallace (1995), discussed in Section 2.4.3, indicates that even for “slender” structural walls (e.g., those with aspect ratios greater than 2.5) shear deformations can contribute more than 10 percent of the total deformation of the wall. Finally, fiber-based analyses typically assume perfect bond between the concrete and the reinforcement, neglecting the contributions of strain penetration to the total deformation of the wall. These last two limitations of the fiber-based formulation lead to an artificially stiff model and inaccurate force-displacement responses for structural walls under lateral loads.

Waugh *et al.* (2009) used the open source finite element program OpenSees (Mazzoni *et al.* 2006) because it was capable of using fiber-based elements in conjunction with beam-column elements and because it allowed for access to the source code. Access to the source code was necessary in order to create and incorporate new section definitions and material models addressing the limitations described above.

Waugh *et al.* (2009) modeled a wall using a combination of a zero-length fiber based element modeling strain penetration and force-based fiber-based beam-column elements representing the flexural response of the wall, with a force-based shear model overlaid on these elements. Figure 2.6 shows a schematic of this model applied to a rectangular wall section.

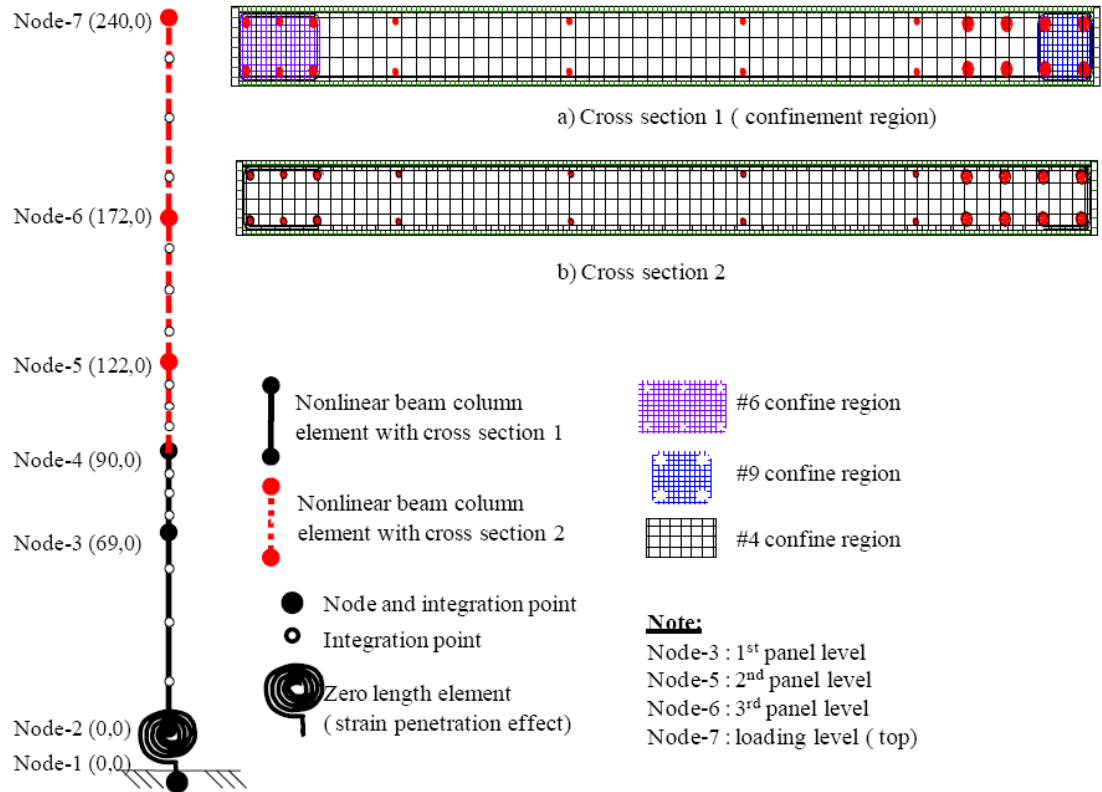


Figure 2.6. Schematic of nonlinear fiber-based OpenSees model of rectangular wall section (Vaughan *et al.* 2009)

The flexural portion response of the wall was modeled with the fiber-based beam-column elements. The concrete in these elements was modeled with an adaptation of the uniaxial, cyclic material model for concrete developed by Chang and Mander (1994) for implementation into OpenSees, with modifications to improve numerical stability and computational efficiency. This modified material model was submitted to the OpenSees community and is identified as Concrete07 in version 1.7.4 of OpenSees. Strain hardening effects were included in the material model for the steel reinforcement, and unloading and reloading, including Bauschinger effects, was modeled using the Menegotto-Pinto rules, which were already incorporated into OpenSees as Steel02.

The portion of the response due to shear deformations was modeled by aggregating a uniaxial material behavior over the flexural response of the beam-column elements. A new material model, identified as Pinching4 in OpenSees, was created by fitting four points to the envelope of a previous laboratory test and fitting parameters so that the modeled behavior matched the results of the test reasonably well. The selection of parameters for the application of this model to new sections is unclear. Additionally, this model does not account for the effects of flexure-shear interaction or shear degradation under cyclic loading.

Strain penetration effects at the interface between the wall and foundation were modeled with zero length interface elements with stress-slip properties as determined by Zhao and Sritharan (2007).

In general, the model developed by Waugh *et al.* (2009) was found to be successful for modeling rectangular wall tests described by Johnson (2007) and the T-shaped walls described in Chapters 3 through 7 of this thesis under cyclic loads. Its primary shortcoming is that shear deformations are determined by a purely empirical process, and no guidance is available for the application of the shear model to other sections. With the exception of shear degradation under cyclic loading, the model accounts for the accumulation of damage in the specimens very well.

## **2.4 Previous Tests of Non-rectangular Structural Walls**

### **2.4.1 Oesterle *et al.* (1979)**

Oesterle *et al.* (1979) tested two flanged walls along with several rectangular and barbell-shaped walls. The researchers determined the flexural and shear strengths,

ductilities, and energy dissipation capacities of walls with a variety of configurations under reversed cyclic loading with the objective of developing appropriate design procedures for reinforced concrete structural walls resisting earthquake loading. The flanged specimens were included in this study to investigate the effectiveness of flanges resisting shear deformations in dowel action as compared to the boundary elements of a barbell section.

Figure 2.7 shows a cross section of specimen F2. Both of the flanged wall sections had 36 in. wide flanges connected by a 72 in. long web. The specimens were 14 ft. 8 in. tall and 4 in. thick. Specimen F1 did not include any confined boundary elements, and it had horizontal reinforcement designed using a shear force corresponding to the calculated design moment. This specimen was tested under reversed cyclic lateral loading with no axial load applied. Specimen F2 included confined boundary elements at the intersections between the web and flanges. It also had more longitudinal reinforcement in the flanges ( $\rho_f = 4.35$  percent vs. 3.89 percent) than specimen F1, but a reduced amount of horizontal shear reinforcement ( $\rho_h = 0.63$  percent vs. 0.71 percent), which was chosen to match a barbell-shaped specimen tested in the same program. While the then-current ACI 318-71 provisions required boundary elements to extend the full height of the wall, the boundary elements in specimen F2, as well as in all specimens in this testing program, were included only in the lower 6 ft. of the specimen. This specimen was tested under reversed cyclic loading with an applied axial compressive stress of 480 psi maintained throughout the test.

Cracks in specimen F2 were small and closely spaced in the confined boundary elements, and larger and more widely spaced in the unconfined portions of the specimen. Cracks in the flanges were primarily horizontal flexural cracks, and cracks in the web were primarily diagonal shear cracks. A horizontal crack formed in the web 5 in. above the foundation block during the cycle in which the maximum load was resisted. Some shear sliding occurred along this crack, leading to reverse curvature of the flanges in the lower 1 ft. of the specimen, but the ability of the specimen to resist lateral load was not compromised at this drift level of 2.3 percent. The specimen resisted 80 percent or more of the maximum applied load through nine inelastic cycles. When the applied drift was increased to 2.8 percent, a large portion of the web crushed and the compression flange sheared along the horizontal failure plane. This caused a sudden decrease in the load resistance to 20 percent of the maximum load.

Shear deformation was concentrated in the lower 3 ft. of the specimen. Approximately 15 percent of the shear deformation in this region of the specimen was concentrated at the construction joint between the wall and foundation block. Apparent shear “yielding” of this portion of the specimen occurred in the same cycle as flexural yielding in this specimen as well as all others tested in this program. The relative contributions of shear and flexural deformations to the total specimen deformation were approximately constant throughout the testing, with flexural deformations contributing approximately 70 percent of the total displacement at the top of the specimen and shear deformations contributing approximately 30 percent. Two-thirds of this shear

deformation, or 20 percent of the total deformation of the specimen, was concentrated in the lower 3 ft. of the specimen.

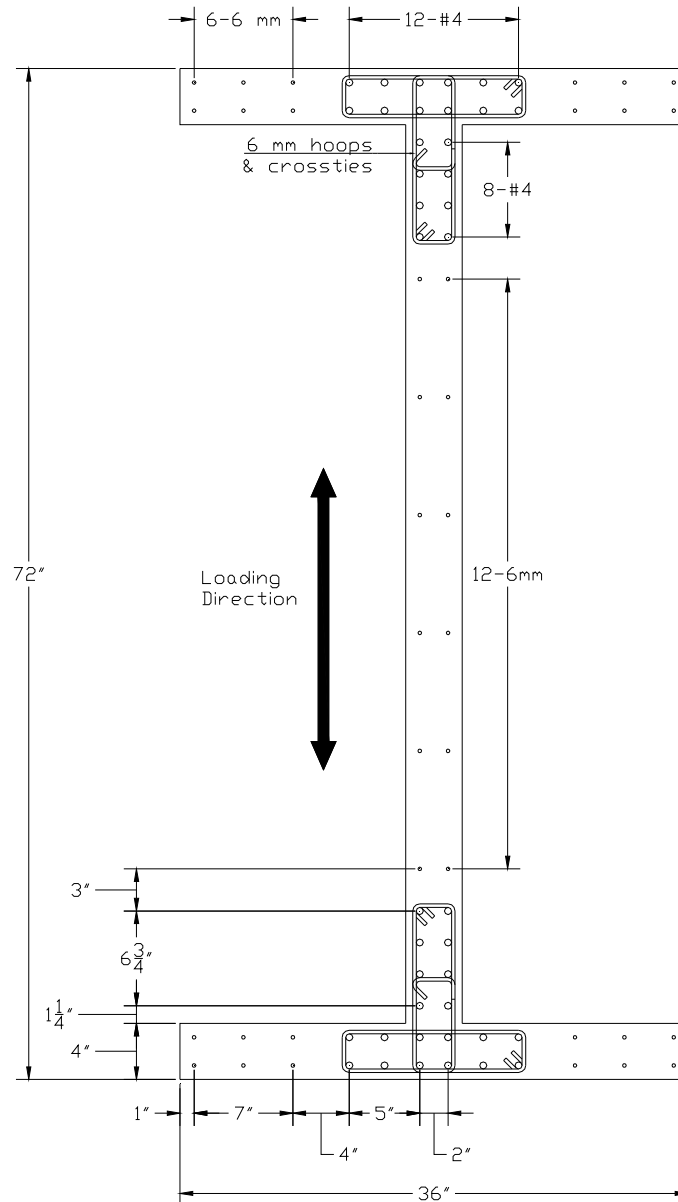


Figure 2.7. Cross section of specimen F2 tested by Oesterle *et al.* (1979)

#### **2.4.2 Sittipunt and Wood (1993)**

Sittipunt and Wood (1993) tested two C-shaped reinforced concrete walls. The objectives of their study were to investigate the cyclic response characteristics of nonrectangular walls, to determine the effective stiffness of nonrectangular walls at various displacement levels, to determine the influence of the amount of web reinforcement on the behavior of nonrectangular walls, and to verify the results from finite element models of nonrectangular walls.

Figure 2.8 and Figure 2.9 show cross sections of the specimens. Each specimen had two 36 in. wide webs connected by a 60 in. long flange. The specimens were 9 ft. tall and 3 in. thick. The flange was designed to be wider than the effective width given in ACI 318-89. The flexural reinforcement and boundary elements in each specimen were identical, with a group of six No. 3 bars in each of the web tips, and a group of four No. 3 bars in the intersection between the webs and the flange. Each of these groups was confined by rectangular spirals fabricated with No. 10 wire. This confinement was approximately two-thirds of that required by ACI 318-89, the then-current requirements. Specimen CLS had the minimum web reinforcement ratio allowed by ACI 318-89 of 0.0025, and specimen CLM had twice this web reinforcement. In both specimens, all of the web reinforcement was in one curtain. Shear reinforcement was provided so that the nominal shear capacity was greater than the nominal flexural capacity. The specimens were tested under quasi-static, unidirectional reversed cyclic loading. A constant applied axial compressive stress of 265 psi was maintained throughout the tests.

The two specimens failed similarly. At approximately 1.5 percent lateral drift with the flange in tension, all cover concrete spalled off the web tip boundary elements and slight buckling of the longitudinal steel was observed. Specimen CLS failed when several bars buckled, causing fracture of the spiral reinforcement in one boundary element. Specimen CMS also failed due to buckling of the longitudinal reinforcement, but the spiral reinforcement did not fracture. Continued loading of the specimens after the boundary elements of each specimen failed caused crushing of the entire web. In both specimens, the flange was found to be fully effective.

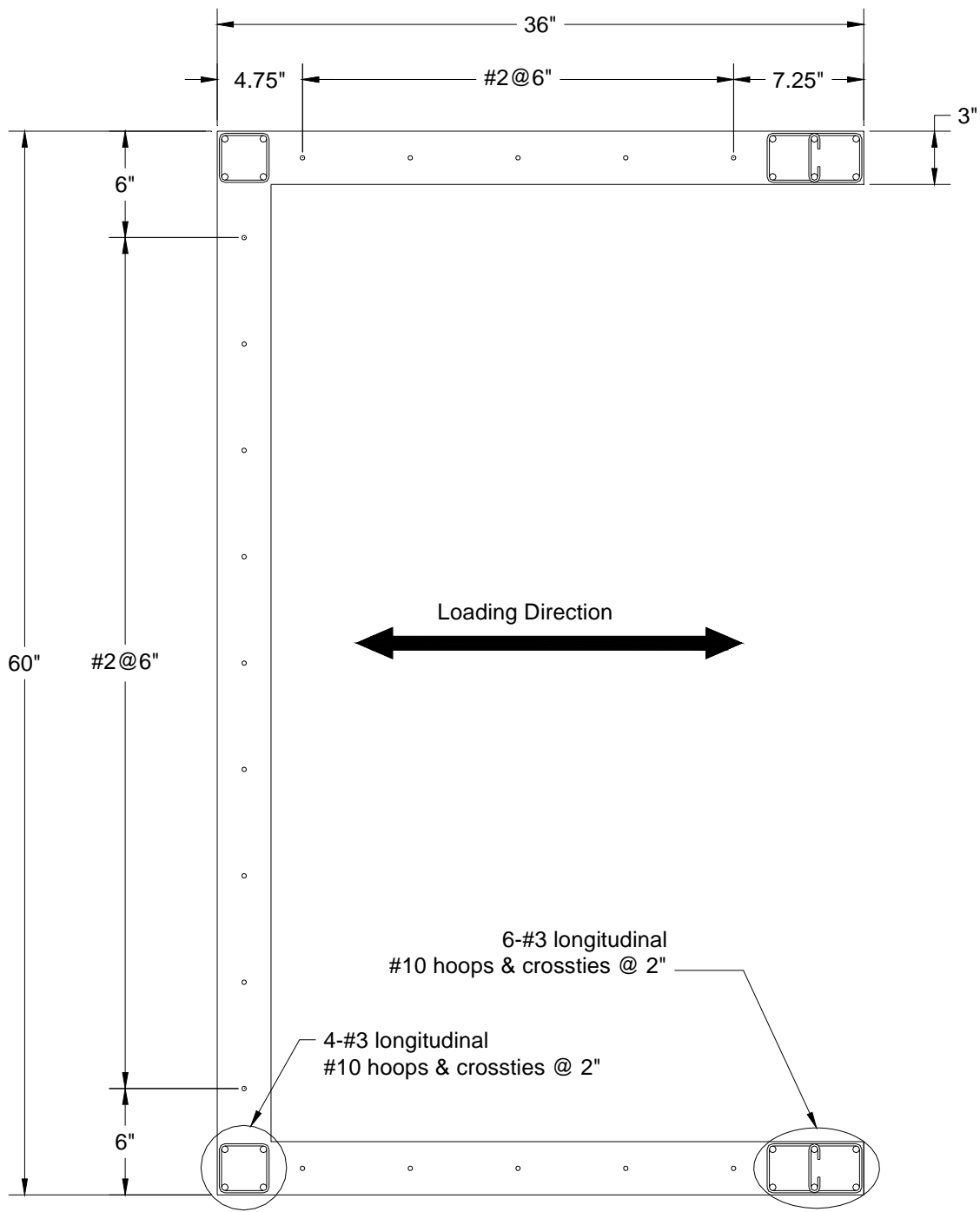


Figure 2.8. Cross section of specimen CLS tested by Sittipunt and Wood (1993)

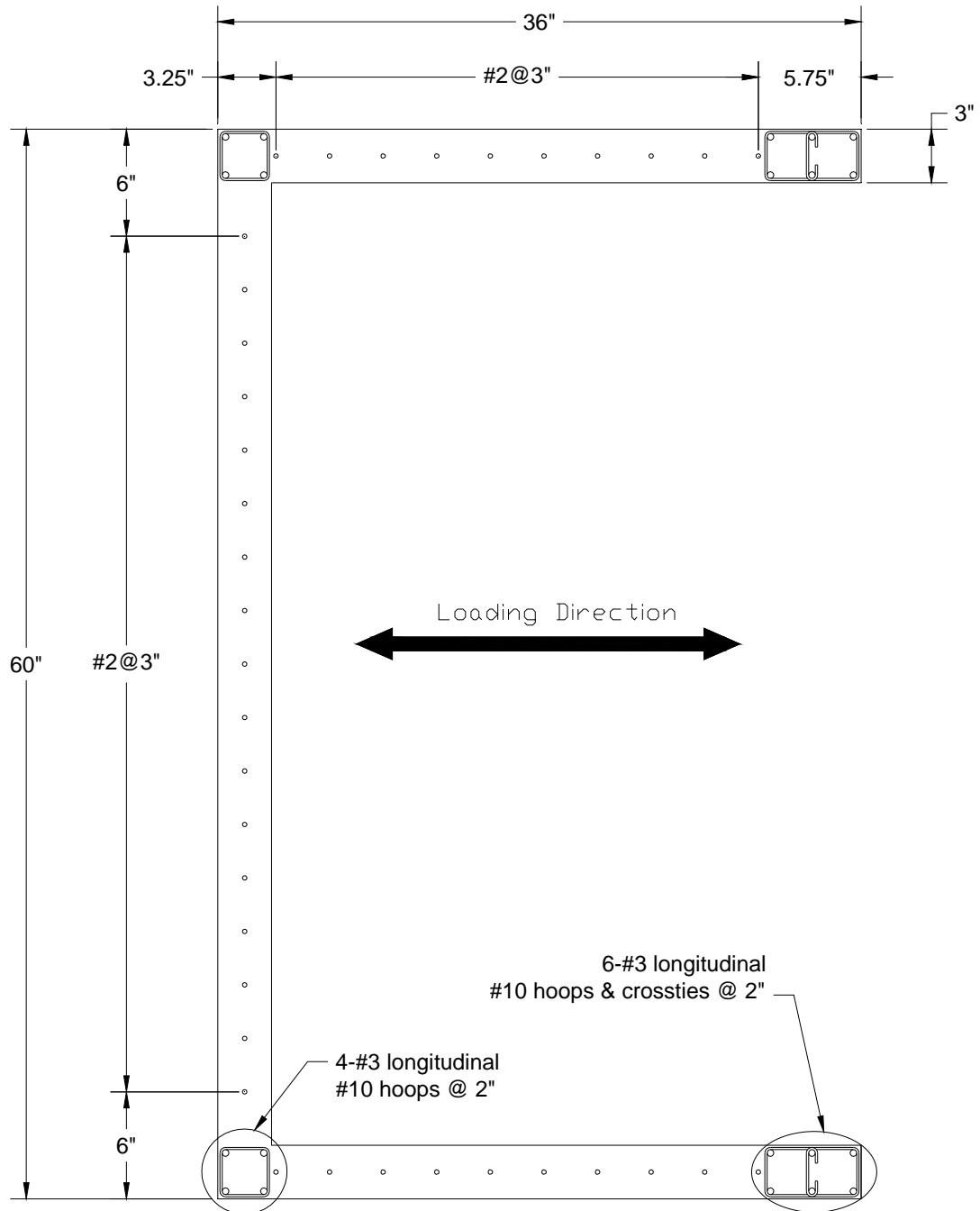


Figure 2.9. Cross section of specimen CMS tested by Sittipunt and Wood (1993)

### 2.4.3 Thomsen and Wallace (1995)

Thomsen and Wallace (1995) tested two rectangular and two T-shaped reinforced concrete structural walls at one-quarter scale. These tests were done to validate the

displacement-based design and detailing requirements initially developed by Moehle and Wallace (1992) that were subsequently incorporated into the UBC (1994) and ACI 318 (1999) building codes.

Figure 2.10 and Figure 2.11 show cross sections of each specimen. The specimens were 1/4-scale models of prototype walls, representing the lower four stories of a six-story building, with a point load applied at the top of each specimen. Overall specimen dimensions were 4 ft. long, 4 ft. wide, and 12 ft. tall. Confining reinforcement in the boundary elements was designed for a target drift level of 1.5 percent. The specimens were tested under quasi-static, unidirectional reversed cyclic loading. A constant applied axial load of  $0.10A_g f'_c$  was maintained throughout the tests.

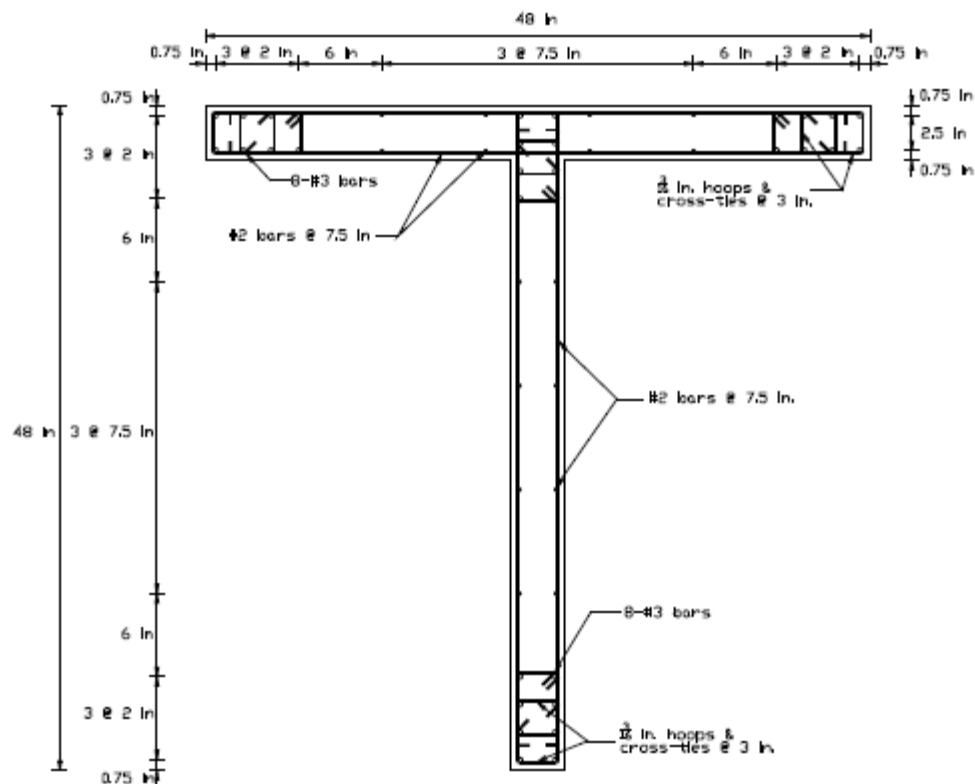


Figure 2.10. Cross section of TW1 tested by Thomsen and Wallace (1995)

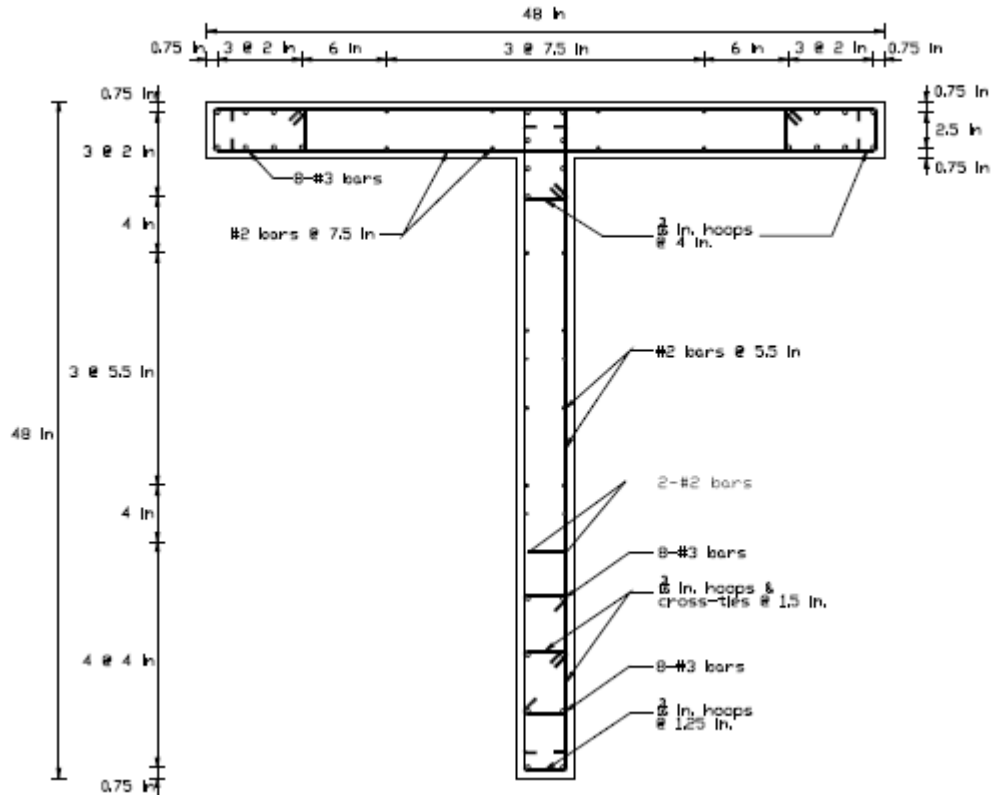


Figure 2.11. Cross section of NTW2 tested by Thomsen and Wallace (1995)

Specimen TW1 was detailed to mimic two independent rectangular walls that were joined without modification to the longitudinal reinforcement or boundary elements. There was a large amount of reinforcement in the flange (equivalent to three times the area of reinforcement in the web tip), and this was expected to increase the compression demand on the web tip beyond the capacity of the boundary element, causing the specimen to not meet the requirements in Section 10.3.4 of ACI 318-02 for tension controlled members. Additionally, the contribution of the flange to the moment capacity was intentionally neglected in the design of the shear reinforcement in the wall web. As a result of these two effects, brittle failure was expected in this specimen. Specimen TW2 was detailed to acknowledge the effects of joining the walls on the strain demands

and mitigate these problems. The horizontal dimension of the web tip boundary element was increased relative to TW1, and the hoop spacing was decreased. Additionally, the horizontal shear reinforcement spacing was decreased to avoid a shear-controlled failure.

The two specimens had similar behavior when the flange was in compression. The expected differences did arise when the loading was reversed and the flange was in tension. Specimen TW1 had a brittle failure due to buckling of all of the longitudinal reinforcement in the web tip boundary element at a drift of 1.25 percent. Specimen TW2 was not severely damaged until the web tip buckled out-of-plane at a drift of 2.5 percent.

Strain gauges were used in both specimens to measure strains in the longitudinal reinforcement. The measured strain distribution was in good agreement with the predicted distribution when the flange was in compression, indicating that the assumption of the entire flange width being effective was reasonable for this loading direction. However, when the flange was in tension, the predicted strains were larger than the measured strains for drifts of 1.0 percent and 1.5 percent. This indicates that the flange was not fully effective, as assumed in the analysis, at lower drifts. When the drift was increased to 2.5 percent, all of the longitudinal steel in the flange was yielded, and there was closer agreement between the observed results and the predicted behavior.

The tests indicated that the displacement-based design provisions used to determine detailing requirements in the wall boundaries could produce structural walls with adequate ductility. However, they noted that it is important to make an accurate estimate of the effective flange width of the wall when determining the web-direction capacity and detailing requirements of the wall. Additionally, it was determined that the

detailing requirements of the web tip were much more critical than those at the web-flange intersection. The flange serves to reduce the neutral axis depth and compression strains when the wall is loaded with the flange in compression such that the tensile limit of the web tip reinforcement is reached prior to concrete crushing in the flange.

In these tests, load was applied unidirectionally in the web direction. The effects of multidirectional loading increasing the strain demands on portions of the boundary elements were not considered. Additionally, the effects of loading in one direction causing damage to the specimen and reducing capacity in the orthogonal direction were not studied. In these tests, a limited number of instruments were used to measure the contributions of flexural and shear deformations of the specimens as well as rigid body rotations of the entire test setup. It was found that the distribution of instrumentation at the base of the wall could have been further refined to provide better detail in this region, where deformations and inelastic coupling between deformation modes are greatest, and where the amount of deformation is expected to have the largest gradient. In addition, the effects of strain penetration causing rigid-body rotation of the wall were not adequately captured.

#### **2.4.4 Palermo and Vecchio (2002)**

Palermo and Vecchio (2002) tested two squat flanged walls under reversed cyclic loading. These tests were done to aid in the development of improved analytical models of squat, shear-dominated walls and to provide additional documentation regarding the behavior of walls with complex geometries. The specimens were identical to two

specimens tested under dynamic loading by the Nuclear Power Engineering Corporation of Japan (NUPEC).

Figure 2.12 shows a cross section of the specimens. Each specimen had two 120 in. (3045 mm) wide, 3.74 in. (95 mm) thick flanges connected by a 114 in. (2885 mm) wide, 2.95 in. (75 mm) thick web and was 79.5 in. (2020 mm) tall. Special boundary elements were not included in these specimens. Specimen DP1 had a constant axial stress of  $0.054f'_c$  applied throughout the test, and specimen DP2 had no axial load applied. Similar unidirectional lateral loading histories were applied to the two specimens, with specimen DP2 failing and having the test terminated at a lower drift level than specimen DP1.

In both specimens, cracks in the flanges were U-shaped, as shown in Figure 2.13, and vertical cracks formed at the web-to-flange interfaces. Specimen DP1 (with axial load applied) was stiffer than specimen DP2 (without axial load applied), and it had a higher drift capacity. A small amount of concrete crushed at the base of each specimen near the web-to-flange interfaces, but this was not the cause of failure. Specimen DP1 failed when six vertical failure planes formed in the web. The flanges provided restraint to the web, preventing diagonal cracks from opening, which led to the formation of the vertical failure planes. Specimen DP2 failed when a horizontal sliding shear plane formed in the web near the top of the specimen, leading to a punching failure near the top of the flanges. This failure can be seen in Figure 2.13. This appears to be the result of the concrete being weaker near the top of the specimen.

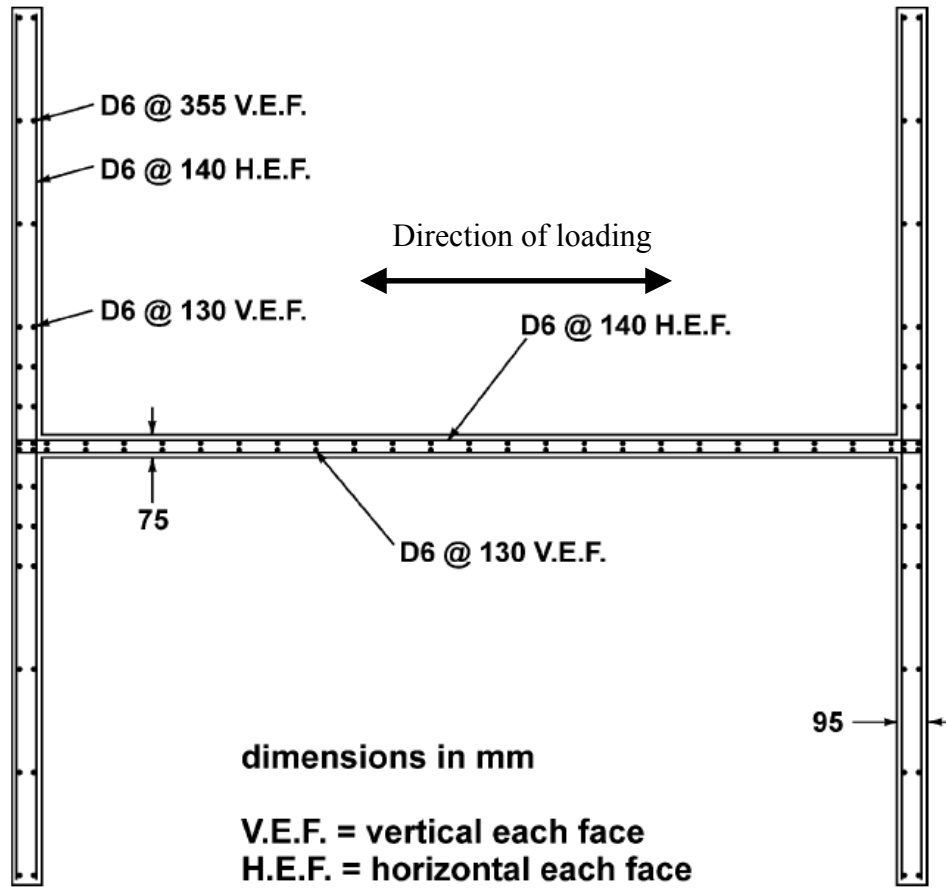


Figure 2.12. Cross section of specimens tested by Palermo and Vecchio (2002)

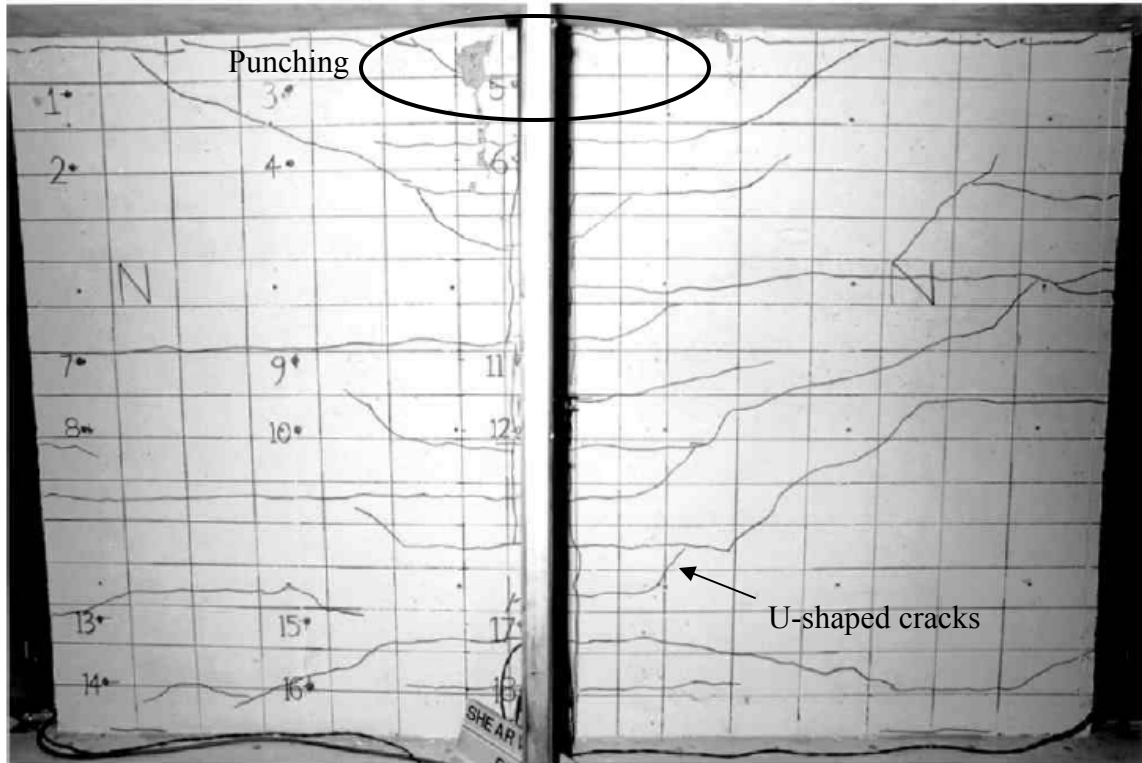


Figure 2.13. Crack pattern in Specimen DP2 at failure (Palermo and Vecchio 2002)

## 2.5 Effects of Applied Loading History on Wall Response

Oosterle *et al.* (1979) compared the responses of barbell-shaped walls under two reversed cyclic load histories, an incrementally increasing history and a modified history alternating cycles of small and large magnitude. Figure 2.14 shows these histories. Specimens loaded with the incrementally increasing history were subjected to three cycles at a given maximum load or displacement before the load was increased to the next level. This type of load history is commonly used by researchers, and it allows them to document specimen behavior at many levels of loading and to confirm that a specimen has a stable response at each loading level before the test proceeds. Additionally, because the magnitude of loading increases throughout the test, having an accurate estimate of the specimen's ultimate displacement capacity prior to testing is not required.

The modified reversed cyclic loading history used by Oesterle *et al.* (1979) addressed concerns that repeated loading cycles approaching the specimen capacity may soften it and lead to an underestimation of its load capacity or an overestimation of its displacement capacity. Additionally, Oesterle *et al.* (1979) indicated that using a load history with a large initial cycle would be more representative of the actual response of a building in an earthquake. In this history, an initial cycle was used to crack the specimen in both loading directions. The second cycle was a large inelastic cycle, followed by cycles to large ductility levels alternated with cycles to a ductility of 1.1 until failure was observed.

One difficulty with applying the modified reversed cyclic loading history is that the ultimate ductility of the specimen must be estimated prior to testing in order to apply appropriate displacements because the specimen is cycled several times to the large deformations early in the testing sequence. Such knowledge of the ultimate ductility of the specimen is not critical in the incrementally increasing load history. In that case, the magnitude of loading increases throughout the test, without requiring displacements to large ductilities early in the history.

Comparison of companion specimens loaded with these two histories indicated that wall behavior was dependent on the previous maximum level of deformation rather than the entire previous load history. The loss of stiffness resulting from one large cycle at a rotational ductility of 5 was equivalent to that from three reversals each at ductilities of 1, 2, 3, 4, and 5. This testing indicated that the modified loading history was as severe

as the increasing history, but it did not indicate that one history was more severe than the other.

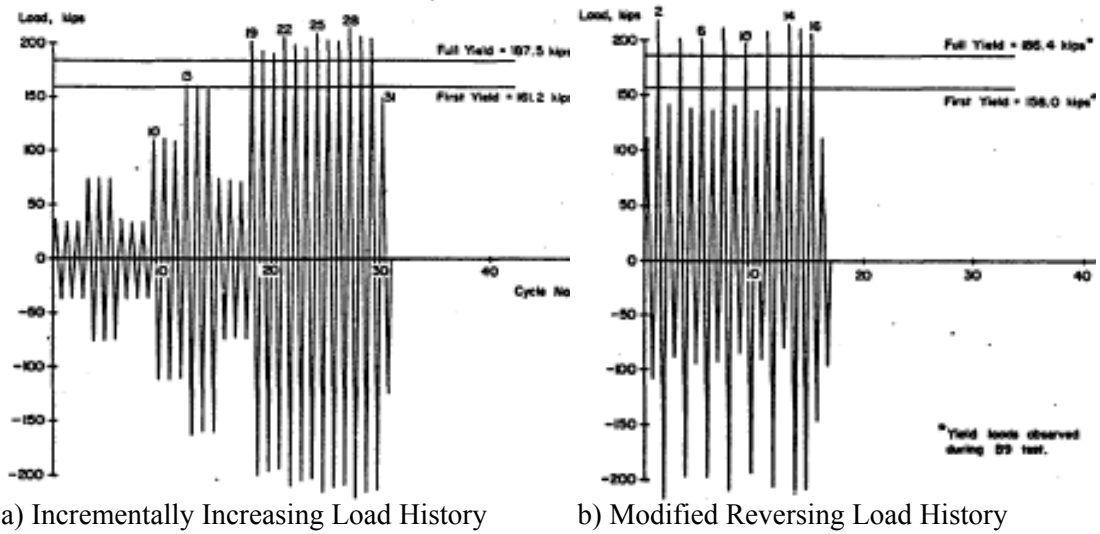


Figure 2.14. Reversed cyclic loading histories compared by Oesterle *et al.* (1979)

Prior to the study described herein, previous research had not specifically addressed the effects of multidirectional load histories on nonrectangular walls.

## **Chapter 3 Specimen Design and Description**

### **3.1 Introduction**

The behavior of two half-scale T-shaped structural walls subjected to multidirectional loading were the focus of this study. To maximize the applicability of this research to current practice, the specimens were based on a prototype building designed according to the appropriate design specifications (ACI 318-02 and IBC 2003) and accepted best practices. This chapter describes the prototype building and the design process used to develop it, as well as the scaling of the prototype and final detailing of the test specimens.

### **3.2 Prototype Building Design**

The prototype building used to determine the design forces on the T-shaped walls considered in this study was a six-story office building assigned to Seismic Design Category D. The Nakaki-Bashaw Group, Inc. provided the preliminary design of the prototype. This section discusses issues encountered in the design that may not arise in the design of structures with only rectangular walls. Additional details regarding the design can be found in Jung (2007).

#### **3.2.1 General information**

The structural system used in this building was a building frame system with special reinforced concrete structural walls. In the analysis of the structure, it was assumed that the structural walls resisted all lateral forces applied to the building, and no interaction between the walls and frames was considered. Figure 3.1 shows the framing plan of a typical story of the prototype building. The building had a 22,500 ft.<sup>2</sup> floor plan

with story heights of 12 ft. for all stories. The floor system consisted of a 7 in. thick cast-in-place concrete slab spanning between precast or cast-in-place concrete beams. This floor system was assumed to act as a rigid diaphragm. The beams were supported by columns and, in some locations, the web tip of a T-shaped wall, on an approximately 20 ft. x 45 ft. grid. The total seismic weight of the building was 180 psf, or 4,050 kips per floor.

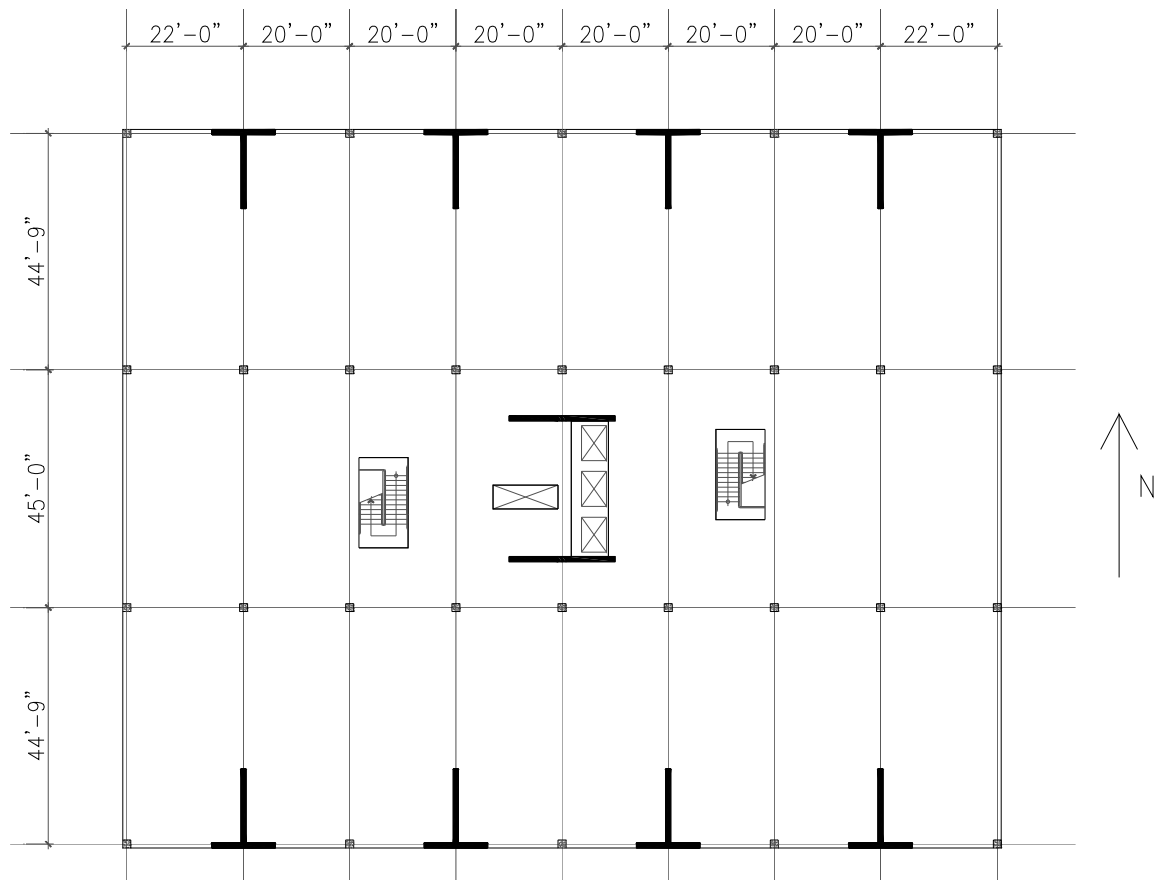


Figure 3.1. Typical story framing plan.

A combination of four pairs of T-shaped walls and two rectangular cast-in-place concrete walls was used to resist all of the lateral loads. Two rectangular walls were added to increase the lateral force capacity of the building in the E-W direction in order

to improve the efficiency of the building design, as discussed in Section 3.2.2. Each T-shaped wall had a 15 ft. long web and 12 ft. wide flange. The thickness of each wall was 12 in. Figure 3.2 and Figure 3.3 show the reinforcement details of the prototype walls in plan and elevation views. The T-shaped walls were assumed to resist all of the lateral forces in the N-S direction of the building. The flanges of the T-shaped walls and the two additional rectangular walls were assumed to resist all of the lateral forces in the E-W direction of the building.

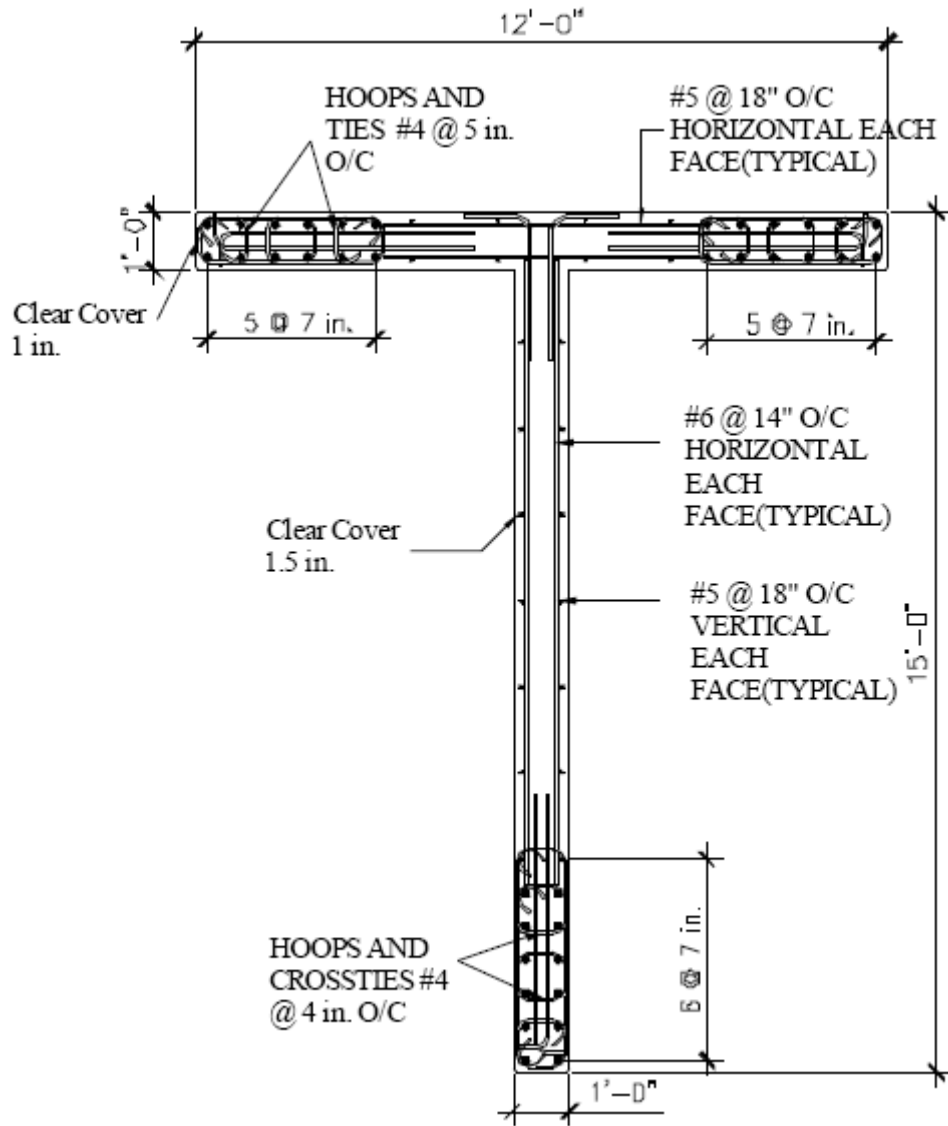


Figure 3.2. Prototype wall detailing – section view from first story.

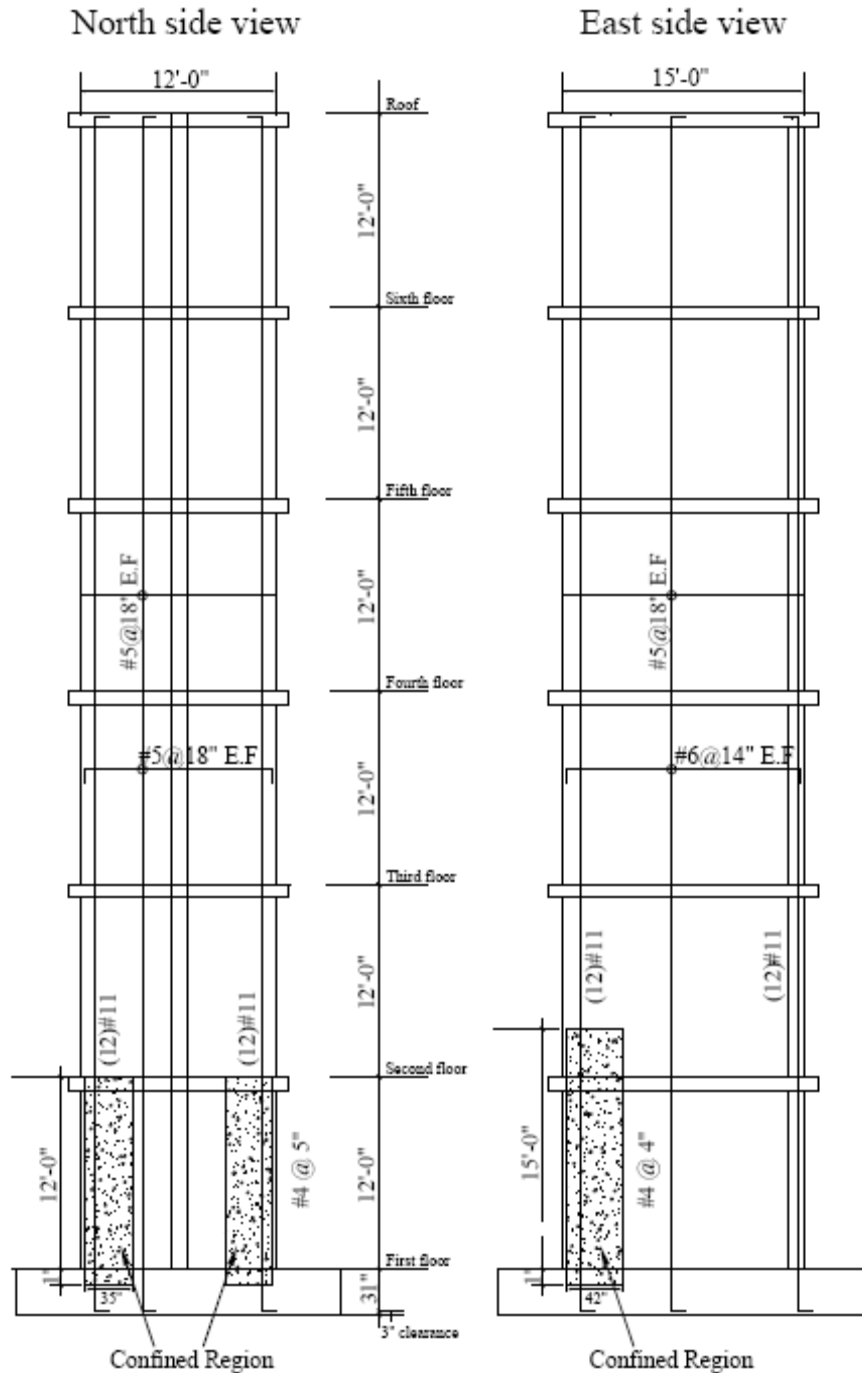


Figure 3.3. Prototype wall detailing – elevation views.

Design lateral loads for the building were determined using IBC 2003. The seismic coefficients for this building were taken as Site Class: C (Very dense soil and soft

rock);  $S_S$  (short-period spectral response acceleration): 1.50 g;  $S_I$  (1-second period spectral response acceleration): 0.60 g;  $I_E$  (importance factor): 1.0;  $F_a$  (site coefficient for short periods): 1.0; and  $F_v$  (site coefficient for 1-second period): 1.3. The lateral system was considered to be a “Building Frame System with Special Reinforced Concrete Structural Walls.” This system has an  $R$  (response modification coefficient) equal to 6.0,  $\Omega_0$  (system overstrength factor) equal to 2, and  $C_d$  (deflection amplification factor) equal to 5. The resulting design forces were a base shear of 3510 kips and a base overturning moment of 184,000 k-ft in each orthogonal direction. Nominal material strengths for the design were a concrete compressive strength  $f'_c=5000$  psi and a steel yield stress  $f_y=60$  ksi.

### **3.2.2 Uniaxial Bending Requirements and Distribution of Forces Among Walls**

Lateral forces were distributed among the structural walls based on relative stiffness. This approach assumed that the floor slabs acted as rigid diaphragms in-plane, but were still able to deform out-of-plane. When lateral loads were applied parallel to the wall flanges (i.e., in the E-W direction in Figure 3.1) although the nonrectangular walls were not individually symmetric about the direction of loading, the pairs of walls maintained symmetry assuming that the floor diaphragm was rigid and prevented twisting of the individual walls. Consequently, the lateral forces assigned to the T-walls in the E-W direction were assumed to be divided equally among the walls. When lateral loads were applied parallel to the wall webs (i.e., the N-S direction in Figure 3.1) the direction of loading had a significant influence on the stiffness of the individual walls. As shown in Figure 3.4, for the flange-in-tension case, the large amount of reinforcement within the

tension flange caused a large depth of the web to be in compression to maintain equilibrium. However, in the flange-in-compression case, the large width of the flange in compression and smaller amount of reinforcement in tension resulted in a very shallow neutral axis depth.

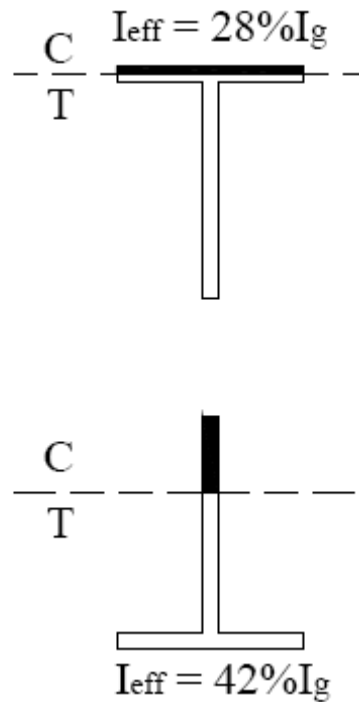


Figure 3.4. Effect of loading direction on neutral axis location and effective stiffness.

Because of this difference in stiffness based on loading direction, proportioning load between pairs of walls loaded parallel to the web required assumed relative wall stiffnesses. Section 10.11.1 of ACI 318-02 recommends assuming an effective cracked flexural stiffness of  $0.35EI_g$  for all for wall sections. Paulay and Priestley (1992) recommend an effective flexural stiffness of

$$\left( \frac{14.5}{f_y} + \frac{P_u}{f'_c A_g} \right) I_g \quad (3.1)$$

for all sections. Because the total story shear is defined in IBC 2003 independently of member stiffness, the relative stiffnesses of the wall segments resisting the load are important rather than the actual stiffnesses. The constant effective flexural stiffness assumption for all sections does not account for the asymmetry of a T-shaped wall depending on the direction of the load relative to the wall orientation. To investigate the effect of wall reinforcement on the secant wall stiffness relative to the loading direction, a parametric study was conducted that compared the secant wall stiffness at the yield moment in each direction for varying amounts of reinforcement while the overall wall dimensions were held constant. For these comparisons, the secant stiffness  $EI$  was determined by dividing the moment at yielding of the first reinforcement by the associated curvature, as determined with sectional analysis. As the area of steel in each of the three boundary elements was increased from  $6.24 \text{ in}^2$  to  $18.72 \text{ in}^2$ , the ratio of secant stiffness of flange-in-tension to flange-in-compression increased from 0.87 to 1.52. For the cases with lightly reinforced sections, the wall was stiffer when the flange was in compression than when the flange was in tension. Conversely, for the cases with heavily reinforced sections, the wall was stiffer when the flange was in tension than when the flange was in compression. This indicates that proportioning of web direction loads between T-shaped walls may require an iterative approach.

For the final T-shaped wall section considered in this study, the effective stiffness was  $0.28EI_g$  for the flange in compression case and  $0.42EI_g$  for the flange-in-tension case, or a stiffness ratio of 1.56. Wallace (2002) reported cracked stiffness values of  $0.27EI_g$  and  $0.30EI_g$  for a particular T-shaped wall geometry loaded with the flange in

compression and flange in tension, respectively, or a ratio of 1.11. Assuming that a T-shaped wall has the same cracked stiffness when the flange is in tension and when the flange is in compression may lead to an inefficient design or premature degradation of the wall. It may overestimate the load carried by a wall in one direction, resulting in an increase in the amount of steel provided, and underestimate the load carried by a wall in the other direction, resulting in inadequate capacity.

A second design challenge associated with the distribution of loads between T-shaped walls was creating a section with appropriate strength in both orthogonal directions. For the prototype building, designing the wall flanges to resist 100 percent of the lateral load in the E-W direction would have required a longer wall flange width or substantially more flange reinforcement than was used in the final prototype design. An increased flange width was not considered architecturally acceptable, and initial analysis indicated that the chosen wall geometry was adequate for resisting the lateral load in the N-S direction. The most effective design option was to add two rectangular walls to the core of the building in the E-W direction. Based on relative stiffnesses, the two additional walls were designed to resist 45 percent of the load in the E-W direction with the remaining demand on the wall flanges being 55 percent of the total load, or 1930 kips base shear. The reinforcement chosen for the flanges of the T-wall for the E-W loading case resulted in a 125 percent flexural overstrength for the flange-in-tension case for loading in the N-S direction.

Avoiding the use of the rectangular walls would have led to significantly further increased moment capacity in the flange-in-tension direction (N-S loading) due to the

increased steel required to resist the lateral load in the flange direction (E-W loading). The potential increase in the moment capacity in the N-S direction would have led to an increase in shear demand associated with designing a flexurally-controlled wall. The total required length of structural walls was substantially larger in the E-W direction than in the N-S direction. This was due to the increased strength (and thus efficiency) provided by the T-shaped walls in the N-S direction (i.e., web direction) relative to a rectangular wall.

### **3.2.3 Biaxial Bending Requirements**

There is not a need to investigate critical biaxial bending combinations for each wall when rectangular walls are used in structural systems. The out-of-plane stiffness of a rectangular wall is a small fraction of the in-plane stiffness, so it is reasonable to assume that rectangular walls carry only in-plane loads. When non-rectangular walls are used, however, biaxial bending effects on individual walls must be considered. The choice of the appropriate loading direction and combination can be interpreted in different ways in many documents (i.e., IBC 2003, FEMA 450, ASCE 7). These documents state that for all buildings with T-shaped walls in seismic category C (IBC 2003) or D (FEMA 450) and higher, the design orthogonal loading combination is equal to "100 percent of the forces for one direction plus 30 percent of the forces for the perpendicular direction. The combination requiring the maximum component strength shall be used," (IBC 2003 1620.3.2; FEMA 450 4.4.2.2). Several practicing engineers were polled regarding their interpretation of this requirement, and it was found that it is generally interpreted in two very different ways. The first interpretation is that members

should be designed for uniaxial bending moments of  $M_x^L + 0.3M_x^T$  and  $M_y^T + 0.3M_y^L$  independently, where L represents longitudinal direction loading, T represents transverse direction loading, and x and y coincide with the L and T directions, respectively. With this interpretation, biaxial loading effects need only be considered for asymmetrical buildings in which loading in the direction transverse to an element causes resistance in the element in the orthogonal direction. For symmetrical buildings, transverse moments (i.e.,  $M_x^T$  and  $M_y^L$ ) are not generated, so the demands resulting from this interpretation are the same as the uniaxial bending requirement; therefore an increase in capacity is not required. The second interpretation is that members should be designed for the simultaneous occurrence of biaxial bending in the combinations of  $M_x^L + 0.3M_y^T$  and  $M_y^T + 0.3M_x^L$ . For symmetrical buildings, this interpretation represents a significantly larger demand on the members than the first, and it affects the design of symmetrical and asymmetrical members alike.

The design points for both of these interpretations are superimposed onto the biaxial bending moment diagram for the T-shaped walls in the prototype building in Figure 3.5. For the prototype building considered in this study, the four pairs of T-shaped walls and two rectangular walls provided would not be adequate if the second interpretation were followed; the lateral load capacity would have to be increased by increasing the capacity of the T-shaped walls or adding additional structural wall area to the building. Designing for biaxial bending significantly amplifies the demands on the T-shaped walls, and potentially leads to a requirement for an "overdesigned" wall relative to

the uniaxial bending requirements. As discussed in Section 3.2.4, increasing the flexural capacity may result in a brittle shear failure. Design of asymmetrical buildings requires more careful handling of biaxial bending requirements, as well as torsion on the building.

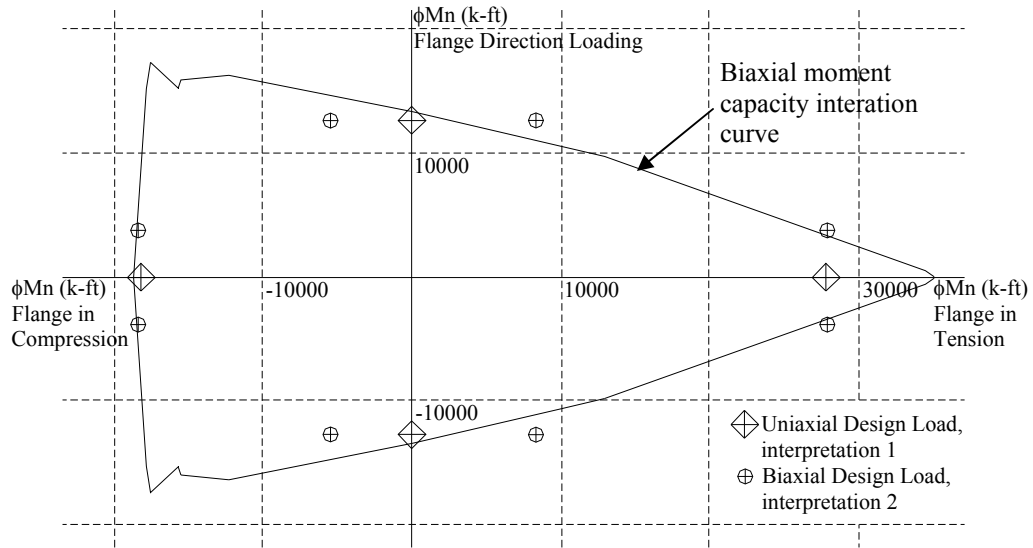


Figure 3.5. Biaxial bending moment diagram for T-wall showing design moments for two interpretations of IBC 2003 Section 1620.3.2.

### 3.2.4 Shear Reinforcement

Because there is an increased likelihood of having substantial flexural overstrength in one direction in a nonrectangular wall, extra consideration must be taken if shear-controlled failures are to be avoided. Due to flexural overstrength, it is likely that the amount of shear reinforcement required to carry the design shear force may be insufficient to ensure a flexural failure prior to shear failure in the wall. As discussed in Section 2.2.2, shear-controlled walls are permitted by ACI 318-02, but designing to ensure a flexurally-controlled failure is considered more prudent and consistent with the intent of the code.

Because there is no guidance provided in ACI 318-02 regarding the appropriate calculation of  $M_{pr}$ , the maximum probable moment capacity of a member, or choice of  $\phi$ -factors to use for determination of the shear reinforcement in walls to promote a flexural failure, the method given for design of special moment frames, assuming a tensile strength of  $1.25f_y$  was adapted for the design of the prototype structure. This approach is consistent with the recommendations of SEAOC (1999). Because there are multiple layers of reinforcement in walls, the yield strength of the reinforcement was amplified to  $1.25f_y$  and an elastic-perfectly plastic material model was used for the reinforcement in tension and in compression. This assumption enabled the application of strain compatibility to determine the stresses in the reinforcement layers that had not yielded. For comparison, a more refined analysis was conducted using BIAX (Wallace 1992) to perform a sectional analysis based on a strain compatibility approach. In this analysis, the measured material properties, including the effects of strain hardening, were used. Table 3.1 summarizes the material properties and assumptions used in the determination of  $M_{pr}$  with both of these methods [i.e., sectional analysis using BIAX (1992) and Whitney Stress Block (WSB) assuming a yield strength of  $1.25f_y$ ]. In addition, Table 3.1 includes the assumptions used in the determination of  $M_n$  (i.e., WSB and nominal yield strength assumption for  $f_y$ ).

The maximum probable moment ( $M_{pr}$ ) and associated base shear ( $V_e$ ) calculated for the prototype specimen using both methods (i.e., BIAX and WSB) are given in Table 3.2. The expected shear,  $V_e$ , associated with the development of  $M_{pr}$  was determined assuming the centroid of an inverted triangular lateral load distribution was located at 52

ft. above the foundation. The nominal moment, factored base moment, and factored base shear ( $M_n$ ,  $M_u$ , and  $V_u$ ) are also included in this table for reference and comparison. Note that  $V_u=M_u/52$ ft.

For the six-story walls considered in this study, the required reinforcement for flexure due to loading in the flange direction controlled the amount of reinforcement in each tip of the flange, and the provided nominal moment capacity  $M_n$  was 3 percent greater than the required value ( $M_u/\phi$ ). In the flange-in-compression loading direction, the addition of extra compression steel had little effect on the moment capacity and  $M_n$  was only 1 percent greater than the required value ( $M_u/\phi$ ). In the flange-in-tension loading direction, the addition of extra flange steel significantly affected the capacity; the provided  $M_n$  was 25 percent greater than  $M_u/\phi$ .

The nominal required shear was determined by dividing the base shear values calculated as described above by an appropriate  $\phi$ -factor. For the shear demands associated with developing the maximum probable moment and nominal moment, a  $\phi$ -factor of 0.85 was used, consistent with the design requirements for beam-column joints in ACI 318-02. For the flange-in-tension loading case, this resulted in required shear capacities ranging from 870 to 1100 k. The current minimum code requirement for shear capacity is determined from the factored loads and a  $\phi$ -factor of 0.75. For the flange-in-tension loading case, this resulted in a required shear capacity of only 710 k, much lower than the expected shears to develop if the flexural capacity of the walls were realized. The ACI 318-02 code requires a more conservative  $\phi$ -factor of 0.65 to be used in cases where the wall is not expected to achieve its flexural capacity. With this assumption, a

shear demand of 880 k was obtained. In the design of special reinforced concrete structural walls, this latter design approach seems in direct conflict with the spirit of the code.

In order to ensure flexural failure of the test specimens, the value of  $M_{pr}$  calculated with BIAx was used to determine the required amount of shear reinforcement for the prototype walls because it was felt that this gave a more reasonable estimate of the potential shear demand.

Table 3.1 Assumptions used in analysis methods to determine  $M_{pr}$ .

Model	BIAx		Whitney Stress Block	
Moment capacity calculated	$M_{pr}$	$M_{pr}$	$M_{pr}$	$M_n$
$f_y$ (ksi)	68	75	75	60
$f_y$ source	coupon tests	1.25*specified $f_y$	1.25*specified $f_y$	specified $f_y$
Strain hardening included	yes	no	no	no
$f'_c$ (psi)	5000	5000	5000	5000
$f'_c$ source	specified minimum			
Concrete model	Modified Kent-Park	$\epsilon_c=0.003$		
Confinement included	yes	no		

Table 3.2 Shear requirements for prototype walls calculated with various analysis methods.

<b>Web Loading Direction: Flange in Tension</b>					
	BIAX $M_{pr}$	*WSB $M_{pr}$	WSB $M_n$	$V_u$	$V_u$
$M$ (k-ft)	48580	45190	38430	---	---
$M/M_{req}$	1.57	1.46	1.25	---	---
$V_e$ (k)= $M/52$ ft.	930	870	740	530	530
$\phi$	0.85	0.85	0.85	0.75	0.6
$V_{n-req}$ (k)= $V_e/\phi$	1100	1020	870	710	880
$M_{req} = M_u/\phi = 30850$ k-ft, $\phi=0.90$					
<b>Web Loading Direction: Flange in Compression</b>					
	BIAX $M_{pr}$	WSB $M_{pr}$	WSB $M_n$	$V_u$	$V_u$
$M$ (k-ft)	34620	24440	20420	---	---
$M/M_u$	1.71	1.21	1.01	---	---
$V_e$ (k)= $M/52$ ft.	670	470	390	350	350
$\phi$	0.85	0.85	0.85	0.75	0.6
$V_{n-req}$ (k)= $V_e/\phi$	780	550	460	470	580
$M_{req} = M_u/\phi = 20230$ k-ft, $\phi=0.90$					
<b>Flange Loading Direction</b>					
	BIAX $M_{pr}$	WSB $M_{pr}$	WSB $M_n$	$V_u$	$V_u$
$M$ (k-ft)	20610	17220	14480	---	---
$M/M_u$	1.47	1.23	1.03	---	---
$V_e$ (k)= $M/52$ ft.	400	330	280	240	240
$\phi$	0.85	0.85	0.85	0.75	0.6
$V_{n-req}$ (k)= $V_e/\phi$	470	390	330	320	400
$M_{req} = M_u/\phi = 14050$ k-ft, $\phi=0.90$					

\*WSB = Whitney Stress Block

### 3.3 One-Half Scale Test Specimens

#### 3.3.1 Scaling From Prototype Structure

As much as possible, the dimensions and reinforcement sizes of the specimens were scaled linearly from the prototype structure. However, because the required reinforcing bar size was not available in all cases, adjustments to the reinforcement had to be made. In these cases, a mixture of bar sizes was selected so that the reinforcement

ratio,  $\rho$ , was maintained as closely as possible to that of the prototype structure. For instance, in the prototype structure, twelve No. 11 bars on 7 in. spacing were used for longitudinal reinforcement in each of the three boundary elements, with a reinforcement ratio  $\rho=3.96$  percent. In the test specimens, groups of eight No. 6 and four No. 5 bars on 3.5 in. spacing were used in the boundary elements, which resulted in  $\rho=4.02$  percent. Additionally, because the smallest standard reinforcing bar is a No. 3, size D5 (0.25 in. diameter) deformed wire was used for confining hoops in the scaled specimens.

The scaled specimen design was checked to ensure that all of the applicable minimum and maximum dimension and spacing requirements of ACI 318-02, with the exception of clear cover and confinement hoop spacing, were met by the scaled design. Specifically, the maximum horizontal and vertical reinforcement spacing (21.7.2.1), confined region dimensions (21.7.6.2 and 21.7.6.4), and confinement hoop spacing (21.4.4.1 through 21.4.4.3, except eq. 21-3 and 21.4.4.2a as discussed below) were checked, as well as confirming that the provided shear reinforcement was adequate to promote flexural failure of the wall, as discussed in Section 3.2.4.

In general, boundary elements of reinforced concrete walls behave similarly to columns, so modeling a boundary element as a column is a reasonable approach for estimating the special confinement requirements. The primary differences between boundary elements in walls and columns are aspect ratio and minimum dimension. The boundary elements in the prototype walls had aspect ratios of approximately five. According to Section 1908.1.1 of IBC 2003, the maximum aspect ratio of a column section is 2.5; an aspect ratio of five can never arise in column confinement design.

Additionally, concrete walls are generally much narrower than columns. Section 21.4.4.2 a) of ACI 318-02 requires that the minimum transverse reinforcement spacing in a confined element be less than one-quarter of the minimum member dimension. Because walls tend to be narrower than columns, this provision leads to very tight spacing of hoops and a high level of congestion. Part (c) of this same requirement states a minimum spacing of  $s_x$ , which need not be less than 4 in., which is reduced to 2 in. by scaling. For this study, it was decided to investigate the behavior of the walls ignoring the requirement of part (a) because it was felt that the 1.5 in. spacing it required for the transverse reinforcement was unreasonably tight considering constructability.

### **3.3.2 Detailing of Specimens**

Figure 3.6 through Figure 3.11 show the final detailing of the two specimens tested, NTW1 and NTW2. Specimen NTW1 was based entirely on the prototype structure. Specimen NTW2 was modified slightly from NTW1 and the prototype structure based on the results of testing NTW1 and a desire to investigate the effects of certain parameters on wall behavior. The differences between the specimens are summarized in Table 3.3.

The distributed flange reinforcement in NTW2 resulted in a total area of steel of  $A_s=9.32 \text{ in.}^2$ . This was similar to the area of steel concentrated in the flange tips of NTW1 (i.e.,  $A_s=9.52 \text{ in.}^2$ ); however, it neglected the additional contribution of the distributed reinforcement across the flange of NTW1, which increased the total area of steel in the flange of NTW1 to  $10.2 \text{ in.}^2$ . The measured yield strength of the reinforcement in NTW2 was slightly higher than that of NTW1 (i.e., 71-73ksi in NTW2

versus 62-63ksi in NTW1) which more than compensated for this difference when determining the flange-in-tension capacity for the web direction loading. It was understood that the distribution of the reinforcement across the flange width would decrease the flange-direction moment capacity of NTW2. The effects of these differences are discussed further in Chapter 7, which provides a comparison of the results of the tests of NTW1 and NTW2.

Table 3.3. Detailing differences between specimens NTW1 and NTW2

	NTW1	NTW2
Longitudinal reinforcement splice configuration and location	Continuous reinforcement from foundation to top of specimen (no splice)	Lap splice located at second story base to minimize the effect of the splice on the plastic hinge region
Distribution of longitudinal reinforcement across the flange	Concentrated in boundary elements $\rho=2.51\%$ overall $\rho=3.78\%$ in boundary elements $\rho=0.59\%$ between boundary elements*	Distributed uniformly across the flange $\rho=2.16\%$ overall
Horizontal dimension of web tip boundary element	Element met requirements of 21.7.6.4 dimension = 22.5 in	Element exceeded requirements of 21.7.6.4 dimension = 26 in
Spacing of No. 3 horizontal (shear) reinforcement in flange	$s=14$ in. $\rho_v=0.26\%$ Met requirement for flexurally-controlled failure and unscaled maximum spacing of 21.7.2.1 (i.e., 18 in.)	$s=9$ in. $\rho_v=0.41\%$ Met requirement for flexurally-controlled failure and scaled requirement of 21.7.2.1 (i.e., 18 in. * scale factor of one-half)
Number of stories included in specimen (applied axial load = 186.5 k, base moment to shear ratio = 312 in. **)	Four of six stories Lateral load and small superimposed moment were applied to top of specimen near centroid of assumed inverted triangular load distribution	Two of six stories Lateral load and larger superimposed moment were applied to top of specimen to achieve desired moment to shear ratio at base
* This is greater than the minimum because bars were added to anchor the horizontal web reinforcement into the flange ** Determined from centroid of assumed inverted triangular load distribution		

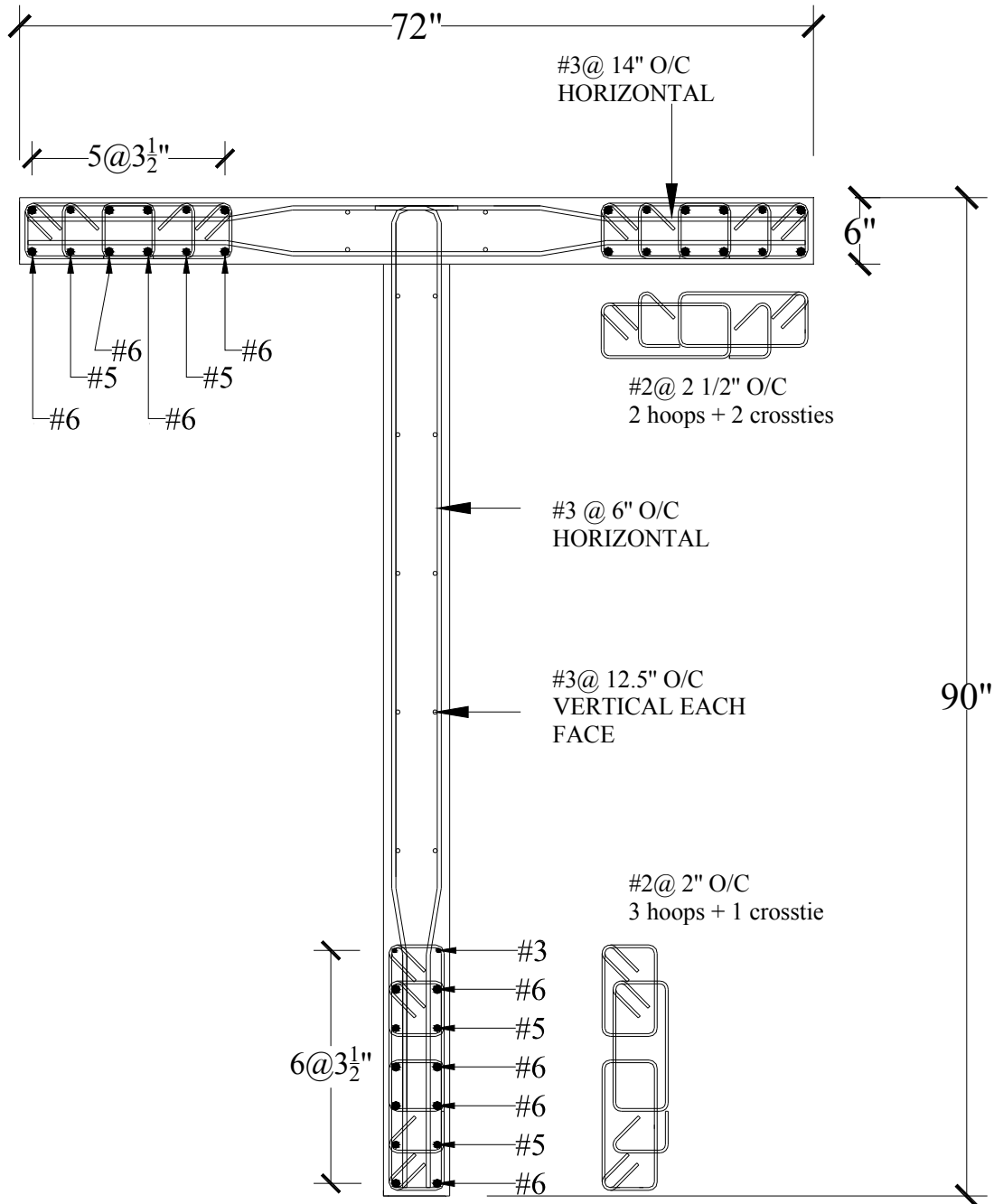


Figure 3.6. Section view of first story of NTW1 showing detailing.

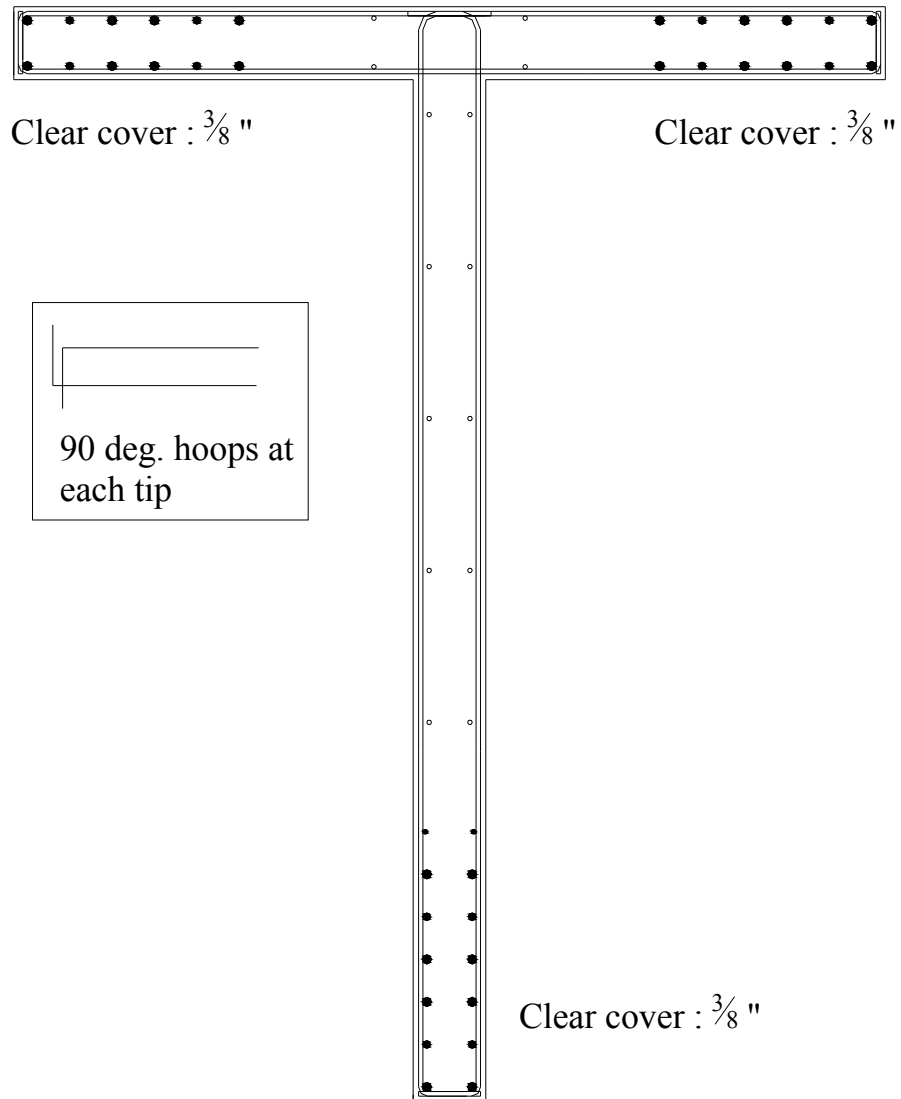


Figure 3.7. Section view of second through fourth stories of NTW1 showing detailing.

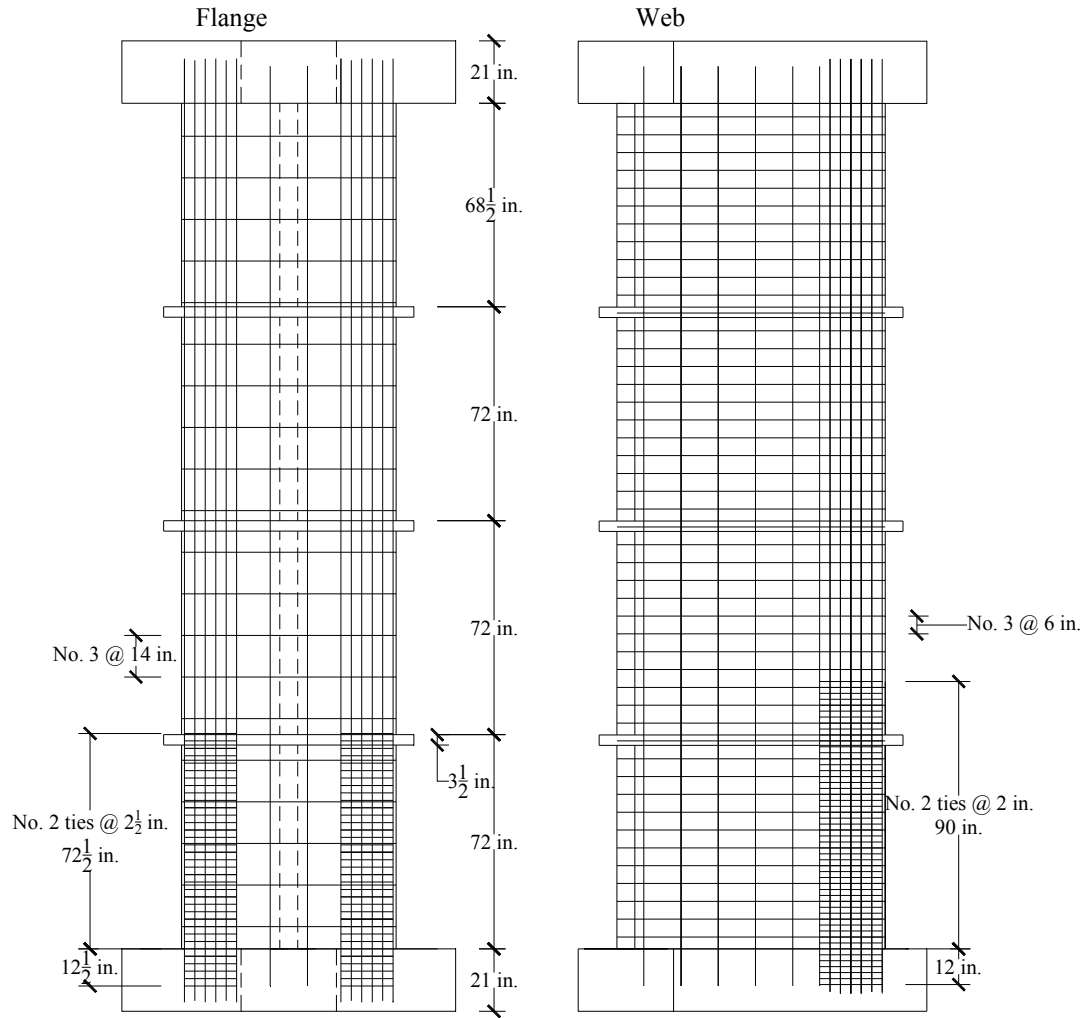


Figure 3.8. NTW1 detailing – elevation views.

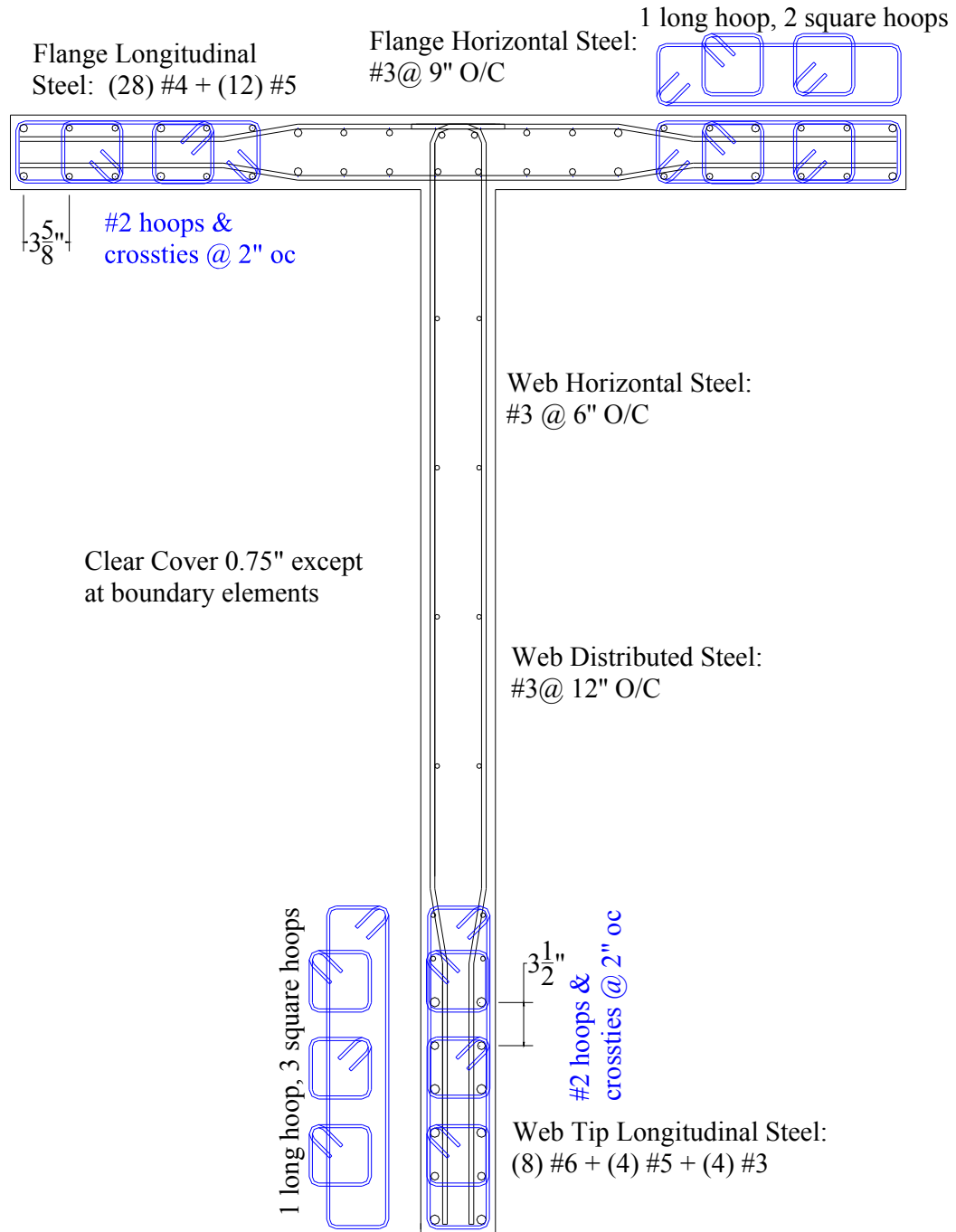


Figure 3.9. Section view of first story and lower portion of second story of NTW2 showing detailing.

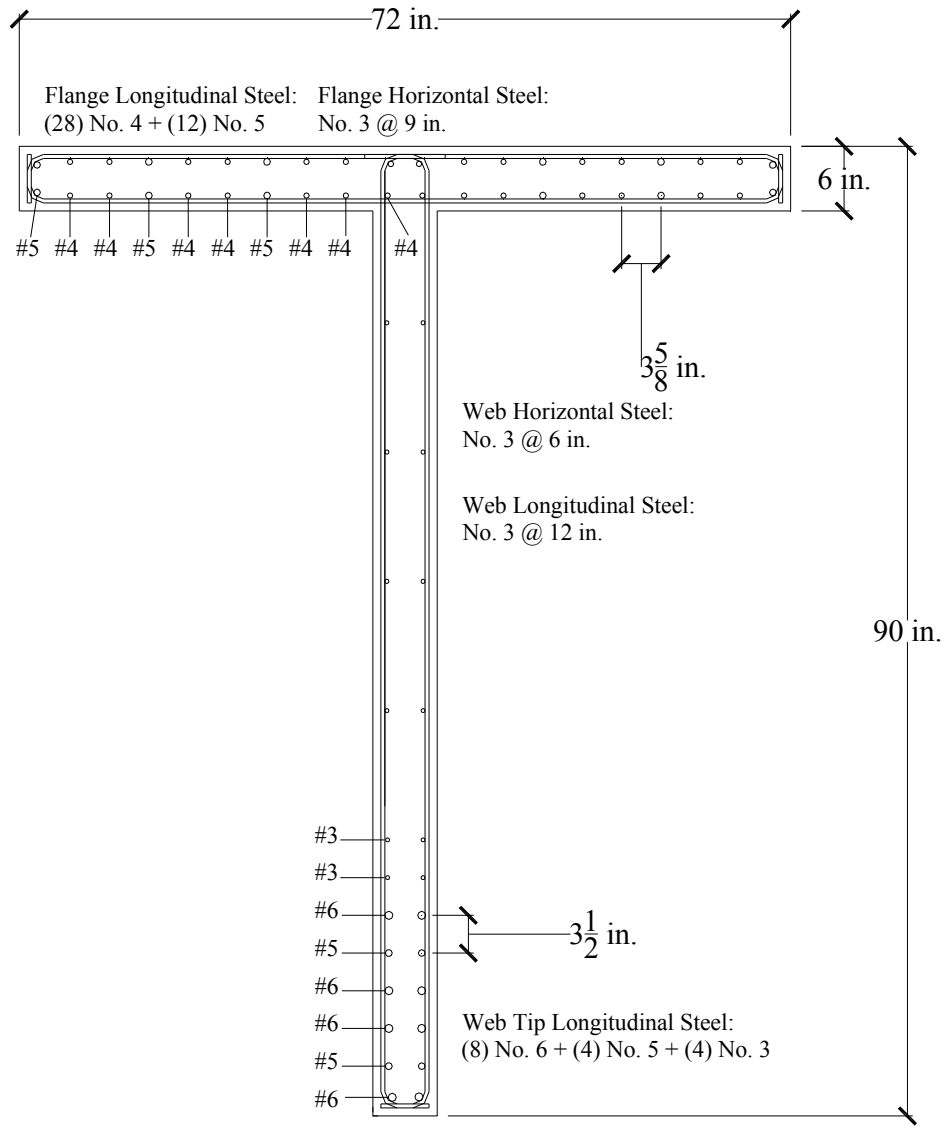


Figure 3.10. Section view of upper portion of second story of NTW2 showing detailing.

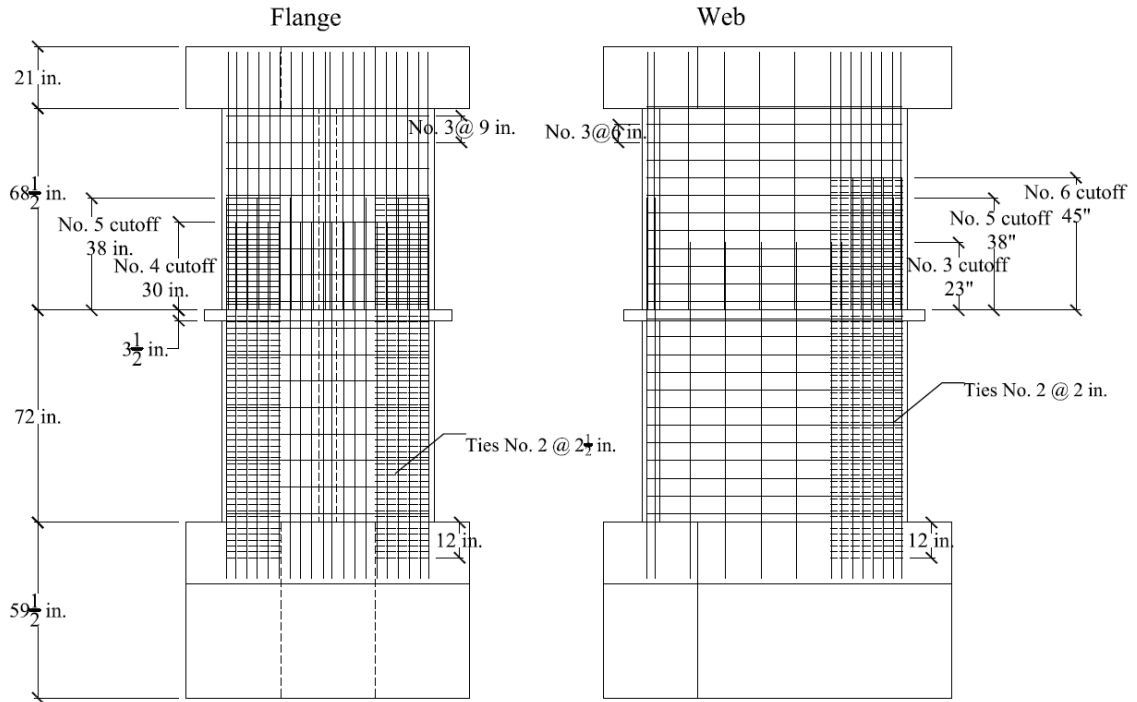


Figure 3.11. NTW2 detailing – elevation views.

### 3.3.3 Foundation and Top Blocks

Each specimen included 21 in. deep foundation and top blocks to anchor the longitudinal reinforcement of the wall and to attach the wall to the strong floor and crosshead of the MAST facility. This depth was selected in order to accommodate 19 in. anchorage lengths for the largest bars used in the specimens. In order to make specimen NTW2 tall enough to reach the MAST crosshead, an additional, lightly reinforced, spacer block was placed under the foundation block. The connections between the base blocks and the strong floor and between the top block and the crosshead were made with 1 1/2 in. diameter Grade B7 post-tensioned rods passing through ducts in the blocks. In the base block of NTW2, the connecting rods were continuous through the base block and spacer block into the strong floor. The blocks were designed to remain elastic throughout the

test. The reinforcement in the blocks was detailed using the strut and tie method in two orthogonal planes, projecting the non-orthogonal forces onto each orthogonal plane. In order to avoid cracking, large load factors were used to determine the design forces. In the base blocks, each bar was assumed to reach its ultimate strength of 90 ksi, and a load factor of two was applied to this value to determine the design loads. In the top blocks, the applied loads were reduced somewhat because of the reduced moments expected in this region. Design calculations and reinforcing details for the blocks are included in Appendix A. The layout of the post-tensioning rods is also included in Appendix A.

#### **3.3.4 Construction Sequence**

The general construction sequence followed for both specimens NTW1 and NTW2 was to construct the foundation block in its final location on the strong floor, then to construct the wall and floor slab for each story in separate pours, working from the base of the wall to the top, and to finish with the top block. Using this sequence, all of the construction joints were horizontal. In general, the wall portion of each story was constructed in a single lift. However, there was a form blowout in the flange of the second story of specimen NTW1. As a result, the pour was terminated approximately one foot from the top of the story, and the story was completed with a second pour.

Specimen NTW1 was constructed entirely in its final position on the strong floor. Both the lower, “spacer” block and the upper, “foundation” block for specimen NTW2 were constructed in place on the strong floor, then they were removed to the adjacent staging area using a system of 2 in.x 4 in. aluminum rails and Hillman rollers. During this process, large steel angle brackets were post-tensioned to the sides of the base block

so that the specimen could ride on the rollers with minimal lifting of the specimen. The maximum clearance between the base of the specimen and the floor was less than one inch. The first and second story wall segments and the slab between them were then constructed in the staging area. The specimen was returned to the strong floor using the same roller system. The top block was then cast with the specimen located in its final location for testing. Figure 3.12 shows the specimen being moved back into position. During this moving operation, strain gauges in each of the flange tips and the web tip were monitored using a switch and balance unit to insure that tensile strains that would cause cracking of the concrete were not being induced into the wall.



Figure 3.12. Moving of specimen NTW2 from staging area to strong floor.

For consistency, all of the concrete in the specimens, including the base blocks and top blocks, was provided by a local ready-mix company. The same mix proportions were used for all lifts, and all of the concrete was placed using a pump and 2 in. hose. The nominal mix proportions are shown in Table 3.4. A maximum coarse aggregate dimension of  $3/8$  in. was selected based on the specimen scale factor of one-half and to prevent difficulties with consolidation of the concrete in the congested boundary regions. Provided slumps ranged from  $7 \frac{1}{2}$  in. to  $9 \frac{3}{4}$  in.

Table 3.4. Nominal concrete mix used in specimens NTW1 and NTW2.

Component	Amount/cubic yard
Sand	1647 lb.
Gravel (max. dimension 3/8 in.)	1334 lb.
Portland cement (Type I)	595 lb.
Fly ash	105 lb.
High-range water reducer (MB7500)	17.5 oz.
Mid-range water reducer (MBPOL1020)	35.0 oz.
Water	37.8 gal.

Each of the construction joints in the specimens was roughened using a steel rake with ½ in. diameter teeth prior to setting of the concrete. The grooves made with the rake were parallel to the short dimension of the wall element. Any loose material was removed using a hammer and chisel after the concrete hardened. In order to further reduce the likelihood of failure in the construction joint, a proprietary bonding agent rich in acrylic (Weldcrete) was applied to the hardened surface according to the manufacturer’s directions prior to the pouring of the subsequent lift.

In order to ensure uniform contact between the base block of Specimen NTW2 and the strong floor and between the top blocks of both specimens and the MAST crosshead, a nominal ½ in. gap was created and filled with a modified gypsum cement grout. Grouting was not necessary under the base block of Specimen NTW1 because the specimen was cast against the floor and was not moved from its original position prior to testing. The grout was modified in order to delay its set time and allow for the complete filling of the gap prior to the initial setting of the leading edge of the grout, which would create a dam and prevent the filling of the remaining space. The water:gypsum cement ratio and mixing time were based on the manufacturer’s recommendations. Admixtures were then added to retard the setting time, to increase the flowability, and to prevent

separation or segregation of the mixture resulting from the delayed setting and increased flowability. Discussion of the use of sodium citrate to retard the setting of gypsum cements can be found in Hewlett (1998). Table 3.5 shows the quantities of each component used in the grout. The amounts shown in this table produce approximately 1/4 cubic feet of grout; this batch size is appropriate for mixing in a 5-gallon bucket. Mixing of each batch of grout was done using an electric drill and 4 in. diameter paint mixing paddle for 3 minutes.

Table 3.5. Modified gypsum cement grout proportions

Component	Purpose	Quantity/batch
USG Hydrostone	Gypsum cement	25 lb.
Sodium Citrate	Set retarder	10 g
MB Melflux 2651	Superplasticizer	0.9 g
MB Starvis 4320F	Viscosity modifier	1.5 g
Water		8 lb.

After the grout was set, the post-tensioning rods were tensioned. Square steel bearing plates, 8 3/4 in. x 8 3/4 in. x 1 1/2 in., were placed under the nuts in order to distribute the post-tensioning forces over a sufficient area of concrete to prevent localized crushing. Gypsum cement was used between the concrete and steel plates to ensure uniform bearing on the concrete. A calibrated wrench was used to determine when sufficient post-tensioning had been achieved in each rod.

### 3.3.5 Material Properties

As discussed in Section 3.3.4, all of the concrete was nominally the same throughout both specimens. Table 3.6 and Table 3.7 list the measured properties of the concrete in each of the specimens. Except where noted, the reported values for compressive strength, elastic modulus, and split cylinder tensile strength are the average

of a minimum of three tests, and the reported values for MOR tensile strength are the average of two tests; this test was not conducted for all pours. Compressive strengths, elastic moduli, and split cylinder tensile strength were determined using 4 in. x 8 in. cylinders. Modulus of rupture (MOR) tensile strength was determined using 6 in. x 6 in. x 24 in. prisms. All of these specimens were created and tested following the applicable ASTM standards. Elastic modulus is not reported for Specimen NTW1 because the measured values were an order of magnitude larger than expected. As a result, they were discarded as erroneous. It should be noted that the measured compressive strengths consistently exceeded the specified minimum of 5000 psi by more than 1000 psi.

Table 3.6. Measured hardened concrete properties at testing: NTW1

Segment	Compressive strength (psi)	Tensile strength (split cyl.) (psi)	Tensile strength (MOR) (psi)
Foundation Block	8980	960	900
Wall 1	7260	850	820
Slab 1	7870 <sup>1</sup>	860	na
Wall 2 – lower	6880	620 <sup>1</sup>	920
Wall 2 – upper	6600	540	na
Slab 2	6340	720	na
Wall 3	7700	960	na
Slab 3	8050 <sup>1</sup>	690 <sup>1</sup>	920 <sup>2</sup>
Wall 4	6850	770	890
Top Block	8230	860	na

na Test was not conducted

<sup>1</sup>Average of two tests

<sup>2</sup>Single test

Table 3.7. Measured hardened concrete properties at testing: NTW2

Segment	Compressive strength (psi)	Elastic modulus (ksi)	Tensile strength (split cyl.) (psi)	Tensile strength (MOR) (psi)
Foundation Block - lower	6910	3440 <sup>1</sup>	1020 <sup>2</sup>	na
Foundation Block - upper	6100	3290	880	na
Wall 1	6570	3750	730	800
Slab 1	6440	3350	760 <sup>1</sup>	na
Wall 2	6230	2960 <sup>1</sup>	790	700
Top Block	6140	3110	730	na

na Test was not conducted

<sup>1</sup>Average of two tests

<sup>2</sup>Single test

In both specimens, the No. 3 and larger reinforcement met the requirements of ASTM A615 Gr. 60. Because of the difficulty in obtaining deformed hot-rolled No. 2 reinforcement, the confining hoops were made from cold-rolled AD5 deformed wire meeting the requirements of ASTM A496. Within each specimen, all of the reinforcement of a given size was of the same manufacturing heat. Table 3.8 and Table 3.9 summarize the properties of the reinforcement. The values in these tables include both values measured from coupons taken from the delivered material and values reported by the manufacturer in certified mill test reports; the sources of the various values are included in the tables. Where coupon tests were conducted on the delivered material, the procedures prescribed by ASTM E8 were followed.

Table 3.8. Reinforcement properties: NTW1

Bar size	Yield (ksi) <sup>1</sup>	Elastic modulus (ksi) <sup>1</sup>	Ultimate (ksi) <sup>1</sup>	Strain at strain hardening <sup>1</sup>	Elongation (%) <sup>2</sup>
D5 <sup>2</sup>	79.4	na	96.3	na	na
No. 3 <sup>3</sup>	72.9	29000	105.5	<sup>3</sup>	14.0
No. 5	63.0	28000	91.5	0.0046	15.0
No. 6 <sup>3</sup>	63.6	28700	92.3	<sup>3</sup>	15.0
No. 7 <sup>4</sup>	69.9	na	104	na	16.3
No. 8 <sup>4</sup>	70.2	na	103	na	13.8

na Not measured or reported

<sup>1</sup> Measured from coupons taken from delivered material

<sup>2</sup> Reported by mill

<sup>3</sup> No yield plateau; 0.2% offset method used to determine yielding

<sup>4</sup> Used only in foundation block and top block, all values reported by mill

Table 3.9. Reinforcement properties: NTW2

Bar size	Yield (ksi) <sup>1</sup>	Elastic modulus (ksi) <sup>1</sup>	Ultimate (ksi) <sup>1</sup>	Strain at strain hardening <sup>1</sup>	Elongation (%) <sup>2</sup>
D5 <sup>3</sup>	96.5	29800	104.4	<sup>3</sup>	4.0 <sup>1</sup>
No. 3 <sup>2</sup>	73.2	na	104.9	na	14.1
No. 4 <sup>2</sup>	74.5	na	105.5	na	14.2
No. 5	66.2	27700	102.5	0.0069	13.6
No. 6 <sup>3</sup>	66.8	29600	100.8	<sup>3</sup>	14.5

na Not measured or reported

<sup>1</sup> Measured from coupons taken from delivered material

<sup>2</sup> Reported by mill

<sup>3</sup> No yield plateau; 0.2% offset method used to determine yielding

### 3.3.6 Specimen Instrumentation

Extensive instrumentation was used to document the response of the specimen to the applied loading. This instrumentation included strain gauges bonded to reinforcing steel, strain gauges embedded in the concrete, string potentiometers (string pots), linear variable displacement transducers (LVDTs), and an optical measuring system (Krypton) utilizing LEDs and an infrared camera. The instrumentation was arranged so that the

contributions of flexural deformations, shear deformations, and strain penetration to the total deformation of the wall in each orthogonal direction could be determined.

Additionally, these instruments were installed so that redundant information would be obtained. This redundancy provided a means to compare the information obtained by different types of instruments and evaluate the effectiveness of each for various uses.

String pots and LVDTs measure changes in the distance between two points, while the Krypton system measures the location of target LEDs in three-dimensional space. The ability to generate a three-dimensional displacement field is especially advantageous when applied to specimens, such as these, that are loaded in multiple directions. In addition to duplicating the in-plane measurements of the string pots and LVDTs, the data recorded by the Krypton system could be used to evaluate out-of-plane deformations, such as warping or twisting.

Traditional instrumentation (i.e., LVDTs and string pots) does have some benefits over the Krypton system, however. One significant limitation of the Krypton system is the need for all target LEDs to be in the limited measurement volume of the camera, and to maintain an open line of sight between the LEDs and the camera. The dimensions of this specimen were such that the Krypton system could view only a single story of the specimen. The bottom story was selected because the largest deformations were expected to occur near the base of the wall.

Figure 3.13 shows the arrangement of strain gauges in the web of specimen NTW1. Similar arrangements of strain gauges were used in the flange of NTW1 and in NTW2. Additional details about strain gauges, including measured (as-built) gauge

locations are included in Appendix B. Rows of strain gauges on the longitudinal bars were used to measure the curvature of the section and the neutral axis depth, the distribution of the axial load in the specimen, and the degree of shear lag in the flange at various points over the specimen height. Series of strain gauges were also bonded to the anchorage length of selected longitudinal bars to measure the development of strain in the bar and the effects of strain penetration. Multiple gauges were bonded to certain horizontal bars in order to measure the variation in strains along the length of the shear reinforcement. Additionally, embedded concrete gauges were installed in the web at 45° angles in order to measure the strains in the compression struts that were expected to develop for resisting shear in the section. At selected locations, groups of strain gauges were placed on the confining steel to examine the demand on the confinement at different heights. Embedded concrete gauges were used near the base of the wall to measure both the vertical and horizontal strains that developed in the compression block.

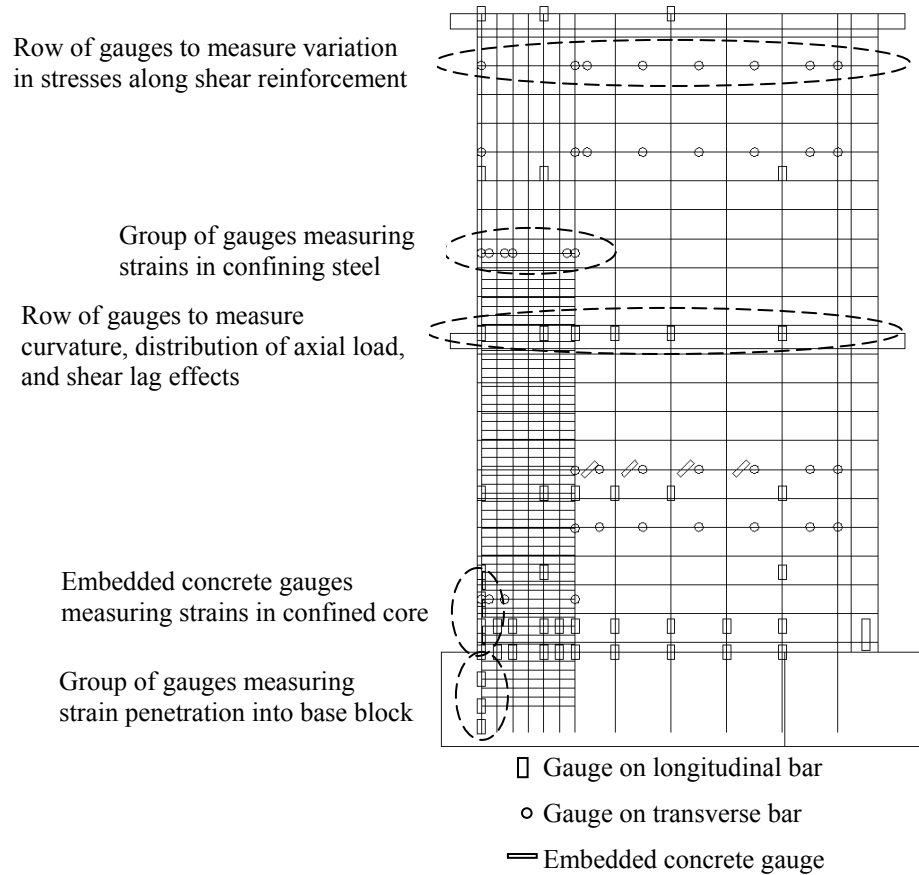


Figure 3.13. Strain gauges in stories 1 and 2 of web of NTW1.

Figure 3.14 shows the arrangement of string pots and LVDTs on the web of NTW1. Similar arrangements were used on the flange of NTW1 and on NTW2. Additional details about these instruments, including measured (as-built) gauge locations are included in Appendix B. Instruments were arranged in “boxed-X” configurations to identify flexural and shear deformations in the wall. The bottom story of the wall was subdivided into four smaller panels to increase the resolution of the measurements where deformations were expected to have the most variation. Rows of LVDTs were used to measure the rotation of the wall relative to the foundation block at three elevations near the base. These instruments provided additional information about both flexural

deformations near the wall base and rigid body rotation of the wall due to strain penetration. Additional string pots were used to measure the deflection of the wall relative to a fixed external reference frame. The information from these instruments was useful in determining the deformed shape of the wall, and it provided a comparison to the derived data obtained from the instruments used to measure the internal deformations of the wall.

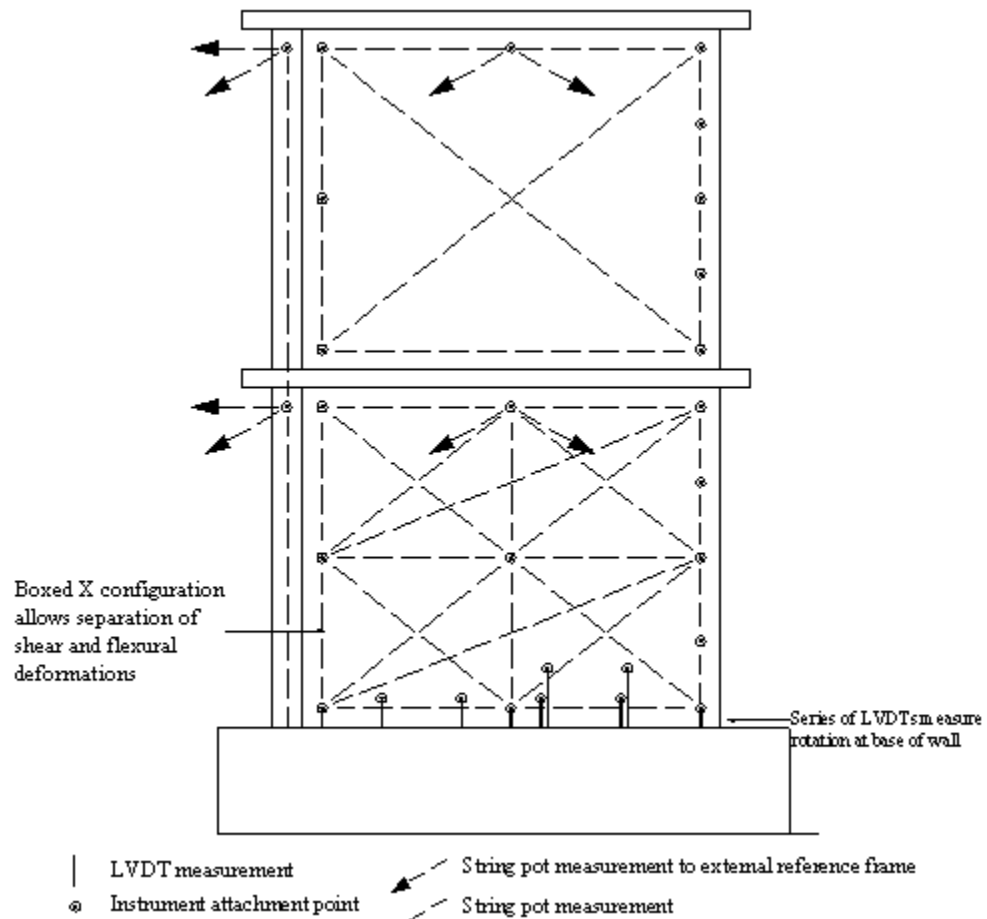


Figure 3.14. LVDTs and string pots on stories 1 and 2 of web of NTW1.

In addition to the LVDTs and string potentiometers, an optical system was used to measure deformations of the specimen in three-dimensional space. This system, termed Krypton by the manufacturer, is a coordinate measuring machine (CMM) that enables the

capture of positions in three-dimensional space using three linear charge-coupled device (CCD) cameras and triangulation to determine the position of re-usable LEDs mounted on the test structure. In locations with studs for mounting LVDTs or string pots, the LEDs were attached to the end of the stud. In Specimen NTW1, the remaining LEDs were glued directly to the concrete surface. In Specimen NTW2, the remaining LEDs were attached to small (3/16 inch diameter) threaded rods embedded in the wall. Figure 3.15 shows the arrangement of Krypton LEDs on the web of NTW1. Additional LEDs were attached to short posts attached to the strong floor and to the base block to verify that movement of the camera or rocking of the base block were not occurring. Because of the limitations of the Krypton system measurement space, targets were applied only to the first story. A single Krypton unit was used to measure deformations of both the web and one-half of the flange of NTW1. Two Krypton units were used with NTW2: one measured deformations of the web and one-half of the flange, similar to NTW1, and the second measured the full width of the flange. Complete Krypton target locations and measured, final locations of all targets are included in Appendix B. The data collected from these targets were used in similar ways to the data collected from the string pots and LVDTs. Additionally, the displacement field generated from these instruments was useful in examining the out-of-plane response of the specimen.

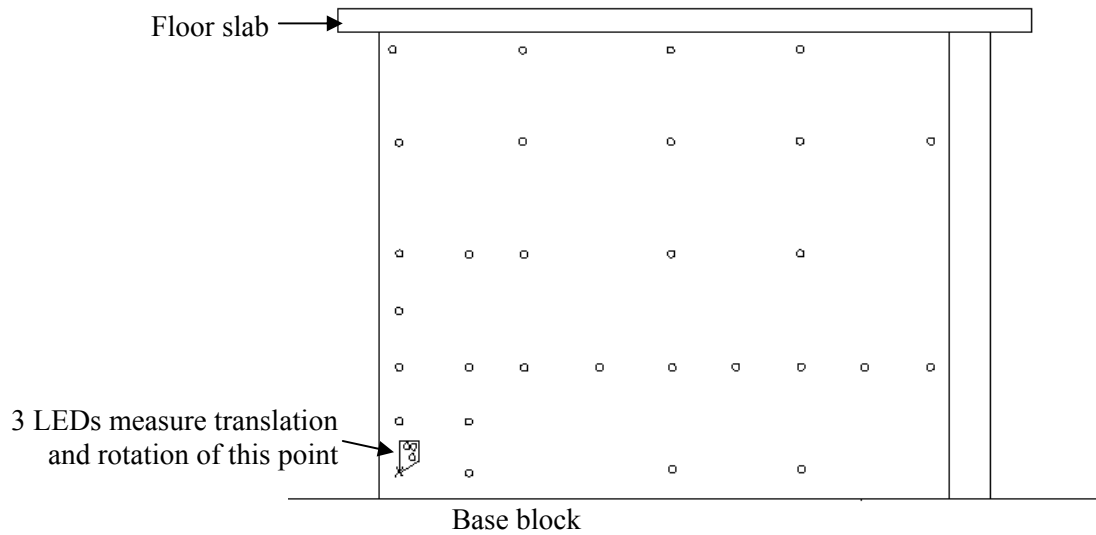


Figure 3.15. Krypton LEDs first story of web of NTW1.

LVDTs were used to measure slip at the extreme bars in the web and flange tips relative to the top of the foundation block so that rotations due to strain penetration could be determined. Each of these LVDTs had one end attached to a small, No.10, stud welded to the rebar using a capacitor discharge welder. This welding process allowed the attachment of a small stud to the rebar with minimal damage or effect on the bar strength, which was verified with tensile testing of samples. Foam was used to block out around these studs before placing concrete so that the stud was exposed to the outside of the specimen.

### 3.3.7 Testing Protocol

#### Applied Load History

The mixed-mode controls of the MAST system allowed for the specimen height to be varied without leading to difficulty in maintaining the desired moment to shear ratio in the specimen. Throughout both tests, the effects of a triangular load distribution over the height of the prototype wall were simulated. Figure 3.16 compares the design loads

on the prototype structure to the loads and moments applied to the test specimens. Displacement control was used to apply the lateral loads to the specimen in each of the horizontal directions, and moments were applied about the horizontal axes as linear functions of the measured shear forces. Additionally, a constant axial compression force, termed “P (external)” in Figure 3.16, equal to the design gravity load on the wall was maintained throughout the testing. In specimen NTW1, an axial load of 186.5 k was maintained, representing the scaled design gravity load resulting from floor live and dead loads. In specimen NTW2, an axial load of 186.5 k was maintained through three cycles at 75 percent of the nominal yield displacement. The axial load was then increased to 201.2 k for the remainder of the test to account for the self-weight of the third and fourth stories of the wall specimen that were excluded from specimen NTW2.

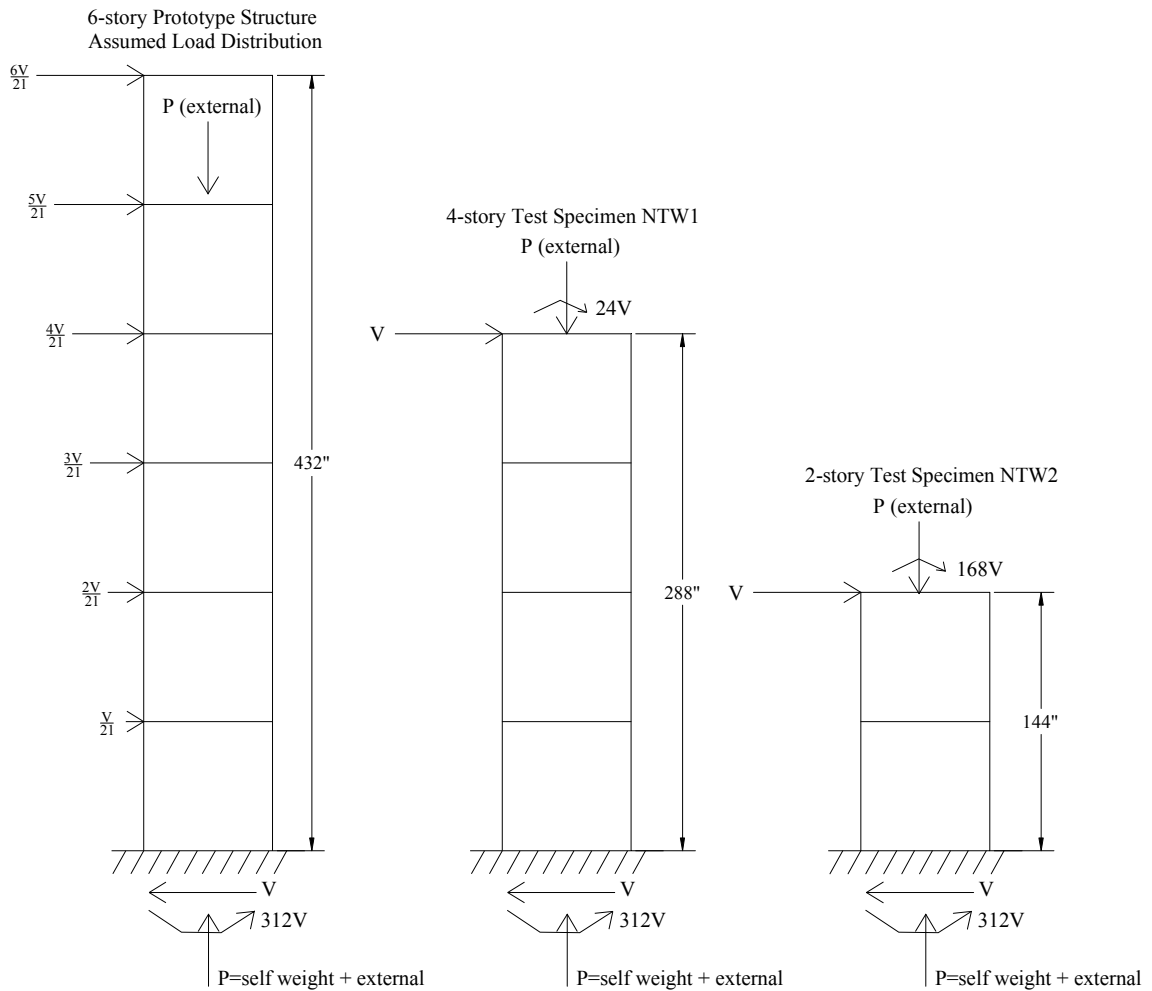


Figure 3.16. Loading of prototype structure and specimens.

The load history applied to each specimen included loading in each orthogonal direction, loading in various skew directions starting at zero deformation, and loading paths mimicking the shape of the yield envelope. The orthogonal direction loading ramps were applied to provide information about the unidirectional behavior of the specimens and to allow for comparison to previous research using only orthogonal loading (e.g., Thomsen and Wallace 1995). The skew directions included in the load history were displacement at a  $45^\circ$  angle to the orthogonal directions and displacements using the

100%+30% combination recommended in IBC 2003 for determining the design biaxial bending combinations. In addition to skew direction ramps passing through the origin, loop and figure-eight patterns were included that did not pass through the origin with each ramp. These were included to allow for the evaluation of the effect of load history on the response of the wall and to allow for the validation of the modeling tool described in Waugh *et al.* (2009). As the testing progressed, the magnitudes of the displacements were increased from the initial cycles in the elastic range to the final cycles at failure.

A preliminary version of the predictive model described in Waugh *et al.* (2009) was used to determine two biaxial bending response surfaces, one corresponding to yielding, which was defined as the point where the first bar in the cross section reached its yield strain, and the other corresponding to ultimate failure, which was defined by the strain in the confined concrete reaching its compressive strain capacity, defined as 130 percent of the value determined using the model proposed by Mander *et al.* (1988), or the tensile strains in the critical reinforcing bar reaching 0.006, a reduced value chosen to account for low cycle fatigue. These surfaces were then used to determine target displacements and loads for the loading ramps. Additional information about this process and the selection of the loading history can be found in Waugh *et al.* (2009).

Figure 3.17 shows the sequence of orthogonal displacement components that were applied to specimen NTW1. With limited exceptions, each displacement level was repeated three times in order to confirm that the wall response at the given displacement was stable before progressing to an increased displacement or loading the specimen in another direction. Exceptions to this were the initial cycle to 10 percent of yielding in the

flange-in-tension and flange-in-compression loading directions, the initial cycle to 25 percent of yielding in the flange direction, and all of the non-orthogonal direction cycles, which were only applied once. Typically, a slightly larger force is required to take a test specimen to a given displacement level the first time than the second and subsequent times, as shown in Figure 3.18. The first loading causes some damage to the specimen, such as cracking of concrete, which reduces its stiffness for future loadings. In general, unless the specimen is very near to failure, these future loadings should not cause significant additional damage to the specimen.

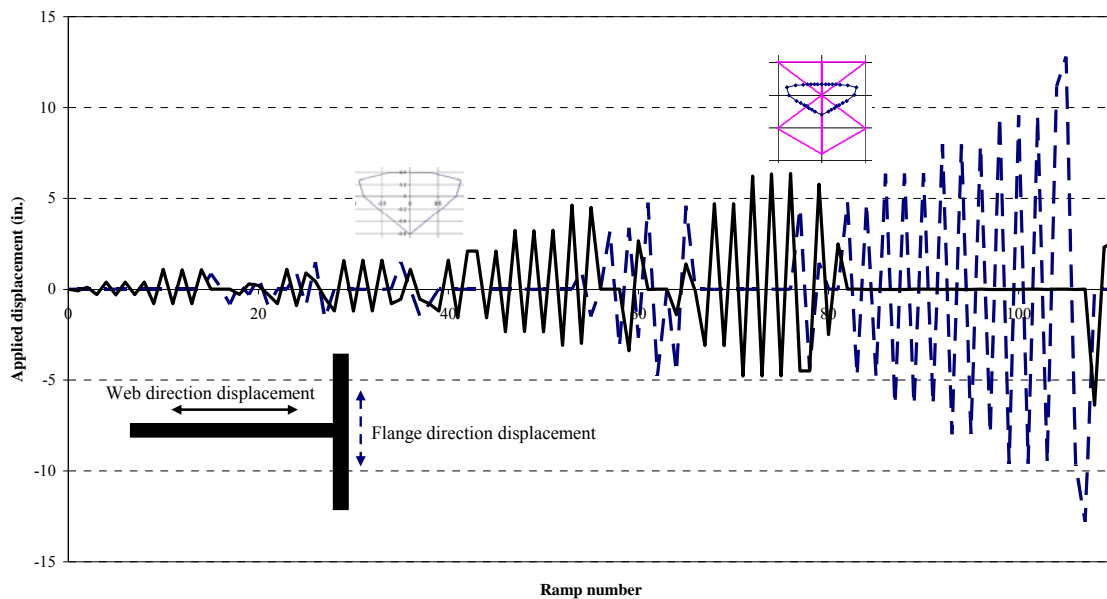


Figure 3.17. Displacements applied to NTW1 in each ramp.

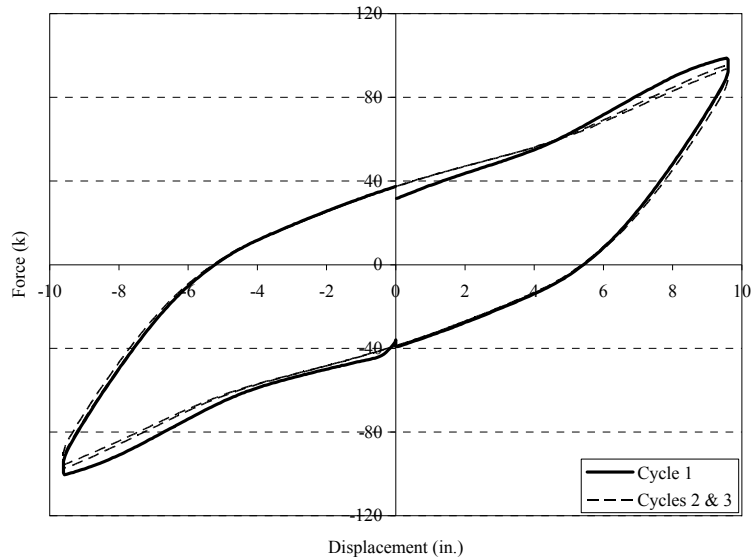


Figure 3.18. Typical differences between first and later cycles to a given displacement.

Figure 3.19 plots all of the displacement paths that were applied to specimen NTW1, as well as the failure surface predicted by the OpenSEES model. This figure includes the observed failures, with the sequence of these failures indicated.

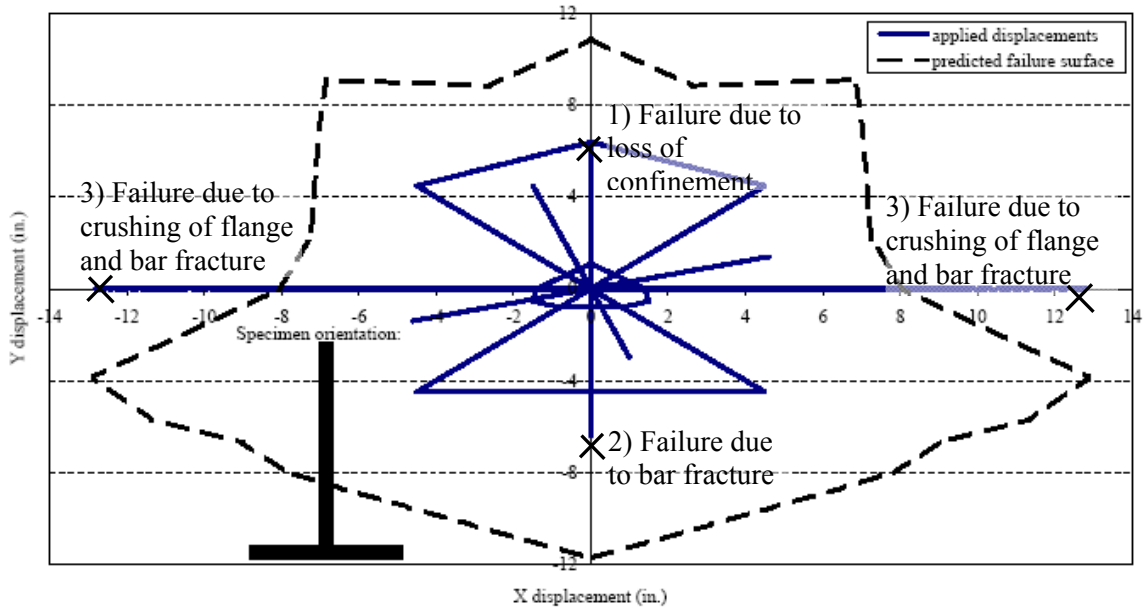


Figure 3.19. Plan view of applied displacements compared to predicted failure surface: NTW1 at base of crosshead

The displacement targets for NTW2 were selected with the goal of applying similar demands to both specimens, as measured by the displacement at the top of the second story. However, the presence of lap splices in the second level of NTW2 affected the stiffness of this portion of the specimen, and, consequently, the deformed shape. This is discussed further in Chapter 6. Figure 3.20 compares the displacement history applied to each of the specimens at the second story.

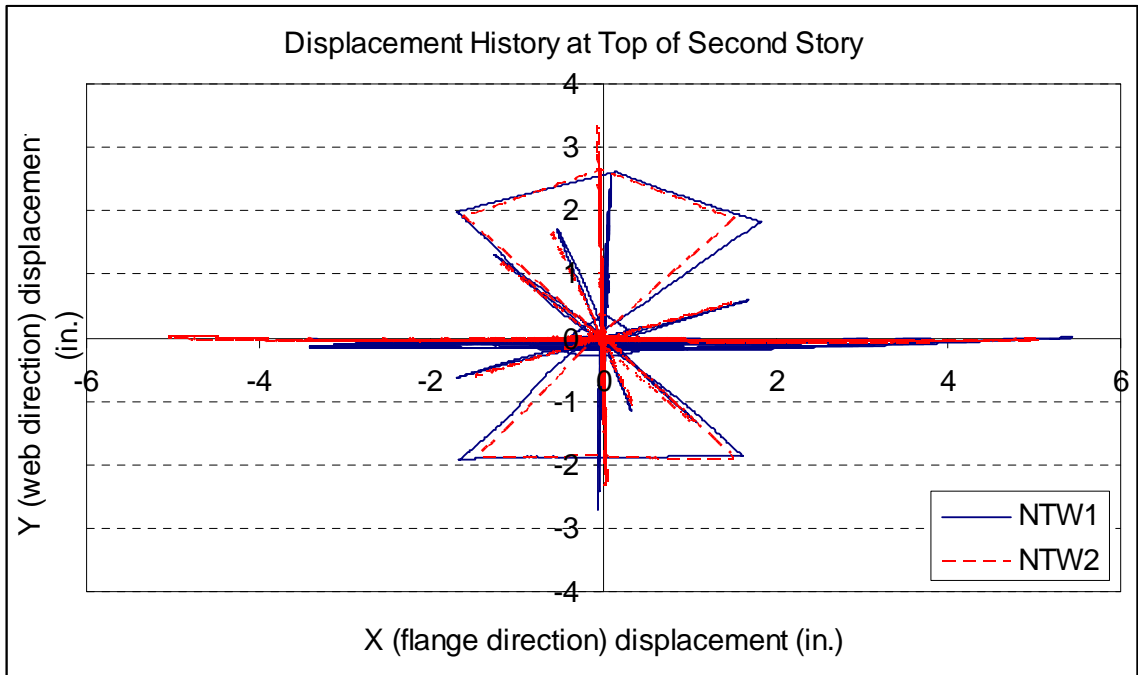


Figure 3.20. Comparison of displacement histories at top of second story

Table 3.10 and Table 3.11 summarize the load histories applied to specimens NTW1 and NTW2, respectively. These tables include both the targeted displacements (and loads, for ramps prior to yielding) and the measured values at the end of each ramp. In these tables, ramps are grouped by displacement level and loading direction, and the nominal displacement level (i.e., 25 percent of predicted yielding, 1.5 percent drift) is indicated for each group. These detailed tables are provided here to be used for reference

with the descriptions of test results, which are given in Chapters 5 and 6, for NTW1 and NTW2, respectively. These tables indicate that the RX and RY degrees of freedom are slaved to other degrees of freedom. Moments were applied by the crosshead proportional to the applied shear and axial forces in order to maintain the desired moment to shear ratio at the base of the specimen and to account for the centroid of the applied axial load not coinciding with the centroid of the section.

Table 3.10. Load history applied to NTW1

cycle	Ramp #	Control Target Value							Time to peak (s)	Actual Value			
		X (in.)	X (k)	Y (in.)	Y (k)	Z (k)	MX & MY (k-in)	RZ (rad)		X (in.)	X (k)	Y (in.)	Y (k)
0 10% yield	1	0	0	0	0	-186.5	slaved*	0	360	0	-0.4	0	0.15
	2	0	0	-0.08	-24.5	-186.5	slaved	0	300	0	-0.4	-0.08	19
	3	0	0	0.12	36.4	-186.5	slaved	0	600	0	-0.28	0.12	29.4
1 25% yield	4	0	0	-0.19	-50.1	-186.5	slaved	0	600	0	-0.6	-0.3	-37.5
	5	0	0	0.3	88.2	-186.5	slaved	0	600	0	-0.52	0.4	67.8
	6	0	0	-0.19	-50.1	-186.5	slaved	0	360	0	-0.7	-0.3	-37.5
	7	0	0	0.3	88.2	-186.5	slaved	0	360	0		0.4	65
	8	0	0	-0.19	-50.1	-186.5	slaved	0	360	0		-0.3	-36.2
3 50% yield	9	0	0	0.3	88.2	-186.5	slaved	0	360	0		0.4	103.8
	10	0	0	-0.39	-72.1	-186.5	slaved	0	360	0	-0.8	-0.8	-62.3
	11	0	0	0.6	125.8	-186.5	slaved	0	360	0	0	1.1	116.7
	12	0	0	-0.39	-72.1	-186.5	slaved	0	360	0	-0.8	-0.8	-63.5
	13	0	0	0.6	125.8	-186.5	slaved	0	360	0	0	1.1	112.3
	14	0	0	-0.39	-72.1	-186.5	slaved	0	360	0	-0.8	-0.8	-62.7
	15	0	0	0.6	125.8	-186.5	slaved	0	360	0	-0.14	1.1	111.5
7 flange direction	16	0	n/a	0	n/a	-186.5	slaved	0	180	0	-0.4	0	-5.16
	17	0.4	37.81	0	n/a	-186.5	slaved	0	300	0.4	15	0	-7.6
	17.5									0.86	30.1	0	-11.9
8 45 degree	18	-0.4	-37.81	0	n/a	-186.5	slaved	0	600	-0.82	-30	0	-10.9
	19	0	n/a	0	n/a	-186.5	slaved	0	300	0	-0.4	0	-5.6
	20	0.3	12.8	-0.3	-55.6	-186.5	slaved	0	300	0.29	12.8	-0.29	-24.8
9 25% yield	21	-0.3	-16.84	0.3	49.8	-186.5	slaved	0	600	-0.3	-7.1	0.3	26.1
	22	0	0	0.2	0	-186.5	slaved	0	300	0	0	0	-3.9
10 100+30	23	0.66	23.19	0.2	25.9	-186.5	slaved	0	300	0.66	19.5	0.2	9
	24	-0.88	-36.5	-0.27	-45	-186.5	slaved	0	600	-0.88	-35	-0.27	-29.5
11 25% yield	25	0	n/a	0	n/a	-186.5	slaved	0	300	0	1.1	0	0.9
	26	0	0	-0.8	-72.1	-186.5	slaved	0	180	0	-0.3	-0.8	-60.9
	27	0	0	1.1	125.8	-186.5	slaved	0	360	0	-0.2	1.1	110
12 duplicate of 4	28	0	n/a	0	n/a	-186.5	slaved	0	180	0	-0.7	0	-5.3
	29	0.9	42.93	-0.9	-82.7	-186.5	slaved	0	300	0.9	40.2	-0.9	-70
	30	-0.9	-15.18	0.9	118.8	-186.5	slaved	0	600	-0.71	-15.2	0.71	67
13 75% yield										-0.9	-17.2	0.9	85.2
	31	0	n/a	0	n/a	-186.5	slaved	0	300	0	0.6	0	-4.5
	32	2	42.15	0.6	27.5	-186.5	slaved	0	300	2	42.2	0.6	20
14 100+30	33	-2.7	-71.09	-0.8	-76.9	-186.5	slaved	0	600	-2.7	-60	-0.8	-50
	34	0	n/a	0	n/a	-186.5	slaved	0	300	0	1.8	0	1.9
15 75% yield	35	0	0	-1.2	-82.9	-186.5	slaved	0	300	0	0.6	-1.2	-80
	36	0	0	1.7	151.9	-186.5	slaved	0	600	0	-0.1	1.7	143.5
	37	0	0	-1.2	-82.9	-186.5	slaved	0	360	0	-0.5	-1.2	-80
	38	0	0	1.7	151.9	-186.5	slaved	0	360	0	-0.1	1.7	140.7
	39	0	0	-1.2	-82.9	-186.5	slaved	0	360	0	-0.5	-1.2	-79.5
	40	0	0	1.7	151.9	-186.5	slaved	0	360	0	-0.2	1.7	139.9
	41	0	0	-0.8	-72.1	-186.5	slaved	0	600	0	-0.6	-0.8	-52.8
16	42	0.8	31.02	-0.8	-71.87	-186.5	slaved	0	300	0.8	33	-0.8	56.2
	43	1.8	55.67	-0.55	-65.63	-186.5	slaved	0	300	1.5	52	-0.55	-46
	44	1.7	51.13	0	-20.85	-186.5	slaved	0	300	1.4	39.6	0	-9.5
	45	0	0	1.2	127.4	-186.5	slaved	0	300	0	-1.5	1.1	90
	46	-1.7	-51.15	0	-20.85	-186.5	slaved	0	300	-1.4	-43	0	-16.5
	47	-1.8	-55.67	-0.55	-65.63	-186.5	slaved	0	300	-1.5	-51.5	-0.55	-50
	48	-0.8	-31.02	-0.8	-71.87	-186.5	slaved	0	300	-0.8	-26.7	-0.8	-49.3
	49	0	0	-0.8	-72.1	-186.5	slaved	0	300	0	3.1	-0.8	-49.3
	50	0	n/a	0	n/a	-186.5	slaved	0	300	0	-0.1	0	3.9
	51	0	0	-1.2	-82.9	-186.5	slaved	0	180	0	0.6	-1.2	-78
17	52	0	0	1.7	151.9	-186.5	slaved	0	360	0	-0.1	1.6	139
	53	0	n/a	0	n/a	-186.5	slaved	0	300	0	-0.5	0	-6.7
18 Yield	53.1	0	0	-1.6	-95.2	-186.5	slaved	0	300	0	-0.9	-1.56	-95.2
	54	0	0	2.1	181	-186.5	slaved	0	600	0	-0.3	2.1	173
	55	0	0	-1.6	-95.2	-186.5	slaved	0	360	0	-1.1	-1.56	-93
	56	0	0	2.1	181	-186.5	slaved	0	360	0	-0.2	2.1	169
	57	0	0	-1.6	-95.2	-186.5	slaved	0	360	0	-1.2	-1.56	-92
	58	0	0	2.1	181	-186.5	slaved	0	360	0	-0.1	2.1	168
19 0.5 & 0.66%	58.5	0	n/a	0	n/a	-186.5	slaved	0	300	0	-0.8	0	-8.4
	59	0	n/a	-2.35	n/a	-186.5	slaved	0	300	0	-0.9	-2.35	-108.5
	60	0	n/a	3.25	n/a	-186.5	slaved	0	600	0	-0.2	3.25	208
	61	0	n/a	-2.35	n/a	-186.5	slaved	0	360	0	-1.2	-2.35	-103
	62	0	n/a	3.25	n/a	-186.5	slaved	0	360	0	-0.1	3.25	203
	63	0	n/a	-2.35	n/a	-186.5	slaved	0	360	0	-1.2	-2.35	-105
	64	0	n/a	3.25	n/a	-186.5	slaved	0	360	0	-0.1	3.25	203

Table 3.10. Load history applied to NTW1, cont.

cycle	Ramp #	Control Target Value							Time to peak (s)	Actual Value			
		X (in.)	X (k)	Y (in.)	Y (k)	Z (k)	MX & MY (k-in)	RZ (rad)		X (in.)	X (k)	Y (in.)	Y (k)
24	65	0	n/a	-3.1	n/a	-186.5	slaved	0	600	0	-1.1	-3.1	-112
2 yield	66	0	n/a	4.7	n/a	-186.5	slaved	0	600	0	-0.2	4.7	224.3
1 & 1.5%	67	0	n/a	0	n/a	-186.5	slaved	0	300	0	-1.2	0	-46.3
25	68	1	n/a	-3	n/a	-186.5	slaved	0	300	1	13.2	-3	-112
30+100	69	-1.5	n/a	4.5	n/a	-186.5	slaved	0	600	-1.5	-9	4.5	196
1 & 1.5%	70	0	n/a	0	n/a	-186.5	slaved	0	300	0	6	0	-45.4
26	71	3.2	n/a	0	n/a	-186.5	slaved	0	300	3.2	55.1	0	-41
1%	72	-3.2	n/a	0	n/a	-186.5	slaved	0	600	-3.2	-61.8	0	-37
flange dire	73	0	n/a	0	n/a	-186.5	slaved	0	300	0	10	0	-18.3
27	74	3.4	n/a	-3.4	n/a	-186.5	slaved	0	300	3.4	82.5	-3.4	-115
45 degree	75	-3.4	n/a	3.4	n/a	-186.5	slaved	0	600	-3.4	-28	3.4	142
1.50%	76	0	n/a	0	n/a	-186.5	slaved	0	300	0	14.1	0	-28.3
28	77	4.8	n/a	0	n/a	-186.5	slaved	0	300	4.8	81.2	0	-39.5
flange dire	78	-4.8	n/a	0	n/a	-186.5	slaved	0	600	-4.8	-81.8	0	-41
1.50%	79	0	n/a	0	n/a	-186.5	slaved	0	300	0	17.2	0	-12
29	80	4.6	n/a	1.4	n/a	-186.5	slaved	0	300	-4.6	-86.5	-1.4	-86
1.5%	81	-4.6	n/a	-1.4	n/a	-186.5	slaved	0	600	4.6	60.4	1.4	30
100+30	82	0	n/a	0	n/a	-186.5	slaved	0	300	0	-15	0	-10
30	83	0	n/a	-3.1	n/a	-186.5	slaved	0	180	0	-9.5	-3.1	-105.5
1% & 1.5%	84	0	n/a	4.7	n/a	-186.5	slaved	0	360	0	0	4.7	213.4
31	85	0	n/a	-3.1	n/a	-186.5	slaved	0	360	0	-1.9	-3.1	-106
	86	0	n/a	4.7	n/a	-186.5	slaved	0	360	0	0	4.7	208
32	87	0	n/a	-4.8	n/a	-186.5	slaved	0	600	0	-1.5	-4.8	-118.5
1.5 & 2%	88	0	n/a	6.4	n/a	-186.5	slaved	0	600	0	0.1	6.4	225
33	89	0	n/a	-4.8	n/a	-186.5	slaved	0	600	0	-1.3	-4.8	-117
	90	0	n/a	6.4	n/a	-186.5	slaved	0	600	0	-0.2	6.4	217
	90.5	0	n/a	0	n/a	-186.5	slaved	0	360	0	-1.5	0	-63
34	91	0	n/a	-4.8	n/a	-186.5	slaved	0	300	0	-1.3	-4.8	-120.1
	92	0	n/a	6.4	n/a	-186.5	slaved	0	600	0	0	6.4	208
	93	0	n/a	0	n/a	-186.5	slaved	0	300	0	-1.4	0	-64
35	94	4.5	n/a	-4.5	n/a	-186.5	slaved	0	360	4.5	60	-4.5	-120
2.00%	95	-4.5	n/a	-4.5	n/a	-186.5	slaved	0	720	-4.5	-88	-4.5	-103
	96	4.5	n/a	4.5	n/a	-186.5	slaved	0	720	4.5	28	4.5	135
	97	0	n/a	6.4	n/a	-186.5	slaved	0	360	0	-13.5	6.4	160
	98	-4.5	n/a	4.5	n/a	-186.5	slaved	0	360	-4.5	-49.5	4.6	42.5
	99	0	n/a	0	n/a	-186.5	slaved	0	360	0	5.2	0	-60
back to ze	100	0	n/a	-2.5	n/a	-186.5	slaved	0	180	0	1	-2.5	-100.2
	101	0	n/a	2.5	n/a	-186.5	slaved	0	360	0	0.4	2.5	43.8
	102	0	n/a	0	n/a	-186.5	slaved	0	180	0	0.2	0	-28.9
	103	0	n/a	-0.75	n/a	-186.5	slaved	0	90	0	0.15	-0.75	-50
	104	0	n/a	0	n/a	-186.5	slaved	0	60	0	0	0	-19
	105	0	n/a	0.1	n/a	-186.5	slaved	0	60	0	0	0.1	-16
	106	0	n/a	0.1	n/a	-40	slaved	0	300	0	0	0.1	-14
	107	0	n/a	0.1	n/a	-186.5	slaved	0	300	0	-0.1	0.1	-17
	108	0	n/a	0	n/a	-186.5	slaved	0	120	0	-0.1	0	-21
36	109	4.8	n/a	0	n/a	-186.5	slaved	0	300	4.8	55.2	0	-21
1.50%	110	-4.8	n/a	0	n/a	-186.5	slaved	0	600	-4.8	-65.2	0	-18
	111	4.8	n/a	0	n/a	-186.5	slaved	0	600	4.8	64.7	0	-17
	112	-4.8	n/a	0	n/a	-186.5	slaved	0	600	-4.8	-65.3	0	-18
37	113	6.4	n/a	0	n/a	-186.5	slaved	0	720	6.4	81	0	-31
2%	114	-6.4	n/a	0	n/a	-186.5	slaved	0	720	-6.4	-82	0	-32
38	115	6.4	n/a	0	n/a	-186.5	slaved	0	720	6.4	81.4	0	-30
	116	-6.4	n/a	0	n/a	-186.5	slaved	0	720	-6.4	-82.6	0	-31
39	117	6.4	n/a	0	n/a	-186.5	slaved	0	720	6.4	81.3	0	-30
	118	-6.4	n/a	0	n/a	-186.5	slaved	0	720	-6.4	-82.3	0	-31
	119	0	n/a	0	n/a	-186.5	slaved	0	360	0	23	0	-6.4
40	120	8	n/a	0	n/a	-186.5	slaved	0	480	8	93.3	0	-45
2.50%	121	-8	n/a	0	n/a	-186.5	slaved	0	960	-8	-94.7	0	-46
41	122	8	n/a	0	n/a	-186.5	slaved	0	960	8	91.3	0	-43
	123	-8	n/a	0	n/a	-186.5	slaved	0	960	-8	-92	0	-44
42	124	8	n/a	0	n/a	-186.5	slaved	0	960	8	90.3	0	-42
	125	-8	n/a	0	n/a	-186.5	slaved	0	960	-8	-91.2	0	-43

Table 3.10. Load history applied to NTW1, cont.

cycle	Ramp #	Control Target Value							Time to peak (s)	Actual Value			
		X (in.)	X (k)	Y (in.)	Y (k)	Z (k)	MX & MY (k-in)	RZ (rad)		X (in.)	X (k)	Y (in.)	Y (k)
43 3.00%	126	9.6	n/a	0	n/a	-186.5	slaved	0	1050	9.6	98.8	0	-55
	127	0	n/a	0	n/a	-186.5	slaved	0	600	0	-37	0	-10
	127.1	-9.6	n/a	0	n/a	-186.5	slaved	0	600	-9.6	-100	0	-56
44	128	9.6	n/a	0	n/a	-186.5	slaved	0	1200	9.6	95.7	0	-51
	129	-9.6	n/a	0	n/a	-186.5	slaved	0	1200	-9.6	-97.3	0	-53
45	130	9.6	n/a	0	n/a	-186.5	slaved	0	1200	9.6	93.8	0	-50
	131	-9.6	n/a	0	n/a	-186.5	slaved	0	1200	-9.6	-94	0	-52
46 4%	132	12.8	n/a	0	n/a	-186.5	slaved	0	1350	12.8	58	0	-26
	133	-12.8	n/a	0	n/a	-186.5	slaved	0	1530	-12.8	-38	0	-15
	134	n/a	0	0	n/a	-186.5	slaved	0	1530	-10.4	0	0	-3.7
	134.1	0	n/a	0	n/a	-186.5	slaved	0	1530	0	24	0	19
	134.2	2.5	n/a	0	n/a	-186.5	slaved	0	1530	2.5	26	0	22
	135	0	n/a	0	n/a	-186.5	slaved	0	1530	0	1.8	0	19
47	136	0	n/a	-6.4	n/a	-186.5	slaved	0	780	0	-1.7	-6.4	-90
	137	0	n/a	6.4	n/a	-186.5	slaved	0	360	0	9	2.8	58

\*MX=376.6-0.25VY (k-ft)

MY=0.25VX (k-ft)

Table 3.11. Load history applied to NTW2

cycle	Ramp #	Control Target Value							Time to peak (min)	Actual Value				
		X (in.)	X (k)	Y (in.)	Y (k)	Z (k)	MX & MY (k-in)	RZ (rad)		X (in.)	X (k)	Y (in.)	Y (k)	
0	0	0		0		-186.5	slaved*	0	6	0	0	0	0	0.25
1	1	0.000		-0.062	-11.0	-186.5	slaved	0	5	0	0	-0.062	-30	
25% yield	2	0.000		0.073	18.7	-186.5	slaved	0	10	0	0	0.073	44	
	3	0.000		-0.062		-186.5	slaved	0	6	0	0	-0.062	-30	
	4	0.000		0.073		-186.5	slaved	0	6	0	0	0.073	43	
	5	0.000		-0.062		-186.5	slaved	0	6	0	0	-0.062	-30	
	6	0.000		0.073		-186.5	slaved	0	6	0	0	0.073	43	
	7	0.000		-0.127	-54.8	-186.5	slaved	0	10	0	0	-0.127	-42	
50% yield	8	0.000		0.168	93.6	-186.5	slaved	0	10	0	0	0.168	75	
	9	0.000		-0.127	-54.8	-186.5	slaved	0	6	0	0	-0.127	-42	
	10	0.000		0.168	93.6	-186.5	slaved	0	6	0	0	0.168	72	
		0.000			0.0	-186.5	slaved	0	3	0	0	0.01	0	
	11	0.000		-0.127	-54.8	-186.5	slaved	0	3	0	0	-0.127	-41	
	12	0.000		0.168	93.6	-186.5	slaved	0	6	0	0	0.168	72	
	13	0.000		0.000		-186.5	slaved	0	3	0	0	0	-3.8	
	14	0.170	20.1	0.000		-186.5	slaved	0	5	0.16	20.1	0	-6.6	
25% yield	15	-0.170	-20.1	0.000		-186.5	slaved	0	10	-0.155	-20.1	0	-5.5	
FD	16	0.000		0.000		-186.5	slaved	0	3	0	1.4	0	-0.8	
	17	0.044	5.1	-0.046	-27.3	-186.5	slaved	0	5	0.044	7	-0.046	-15	
25% yield	18	0.040	-13.9	0.061	35.1	-186.5	slaved	0	10	-0.04		0.061	24	
45 degree	19	0.000		0.000		-186.5	slaved	0	3	0	0.2	0	-2.2	
	20	0.118	13.2	0.031	13.2	-186.5	slaved	0	5	0.118	13.1	0.03	7	
25% yield	21	-0.159	-22.1	-0.056	-25.9	-186.5	slaved	0	10	-0.159	-21.4	-0.06	-21	
100+30	22	0.000		0.000		-186.5	slaved	0	3	0	1	0	1	
	23	0.000		-0.127	-54.8	-186.5	slaved	0	3	0	0.7	-0.127	39	
50% yield	24	0.000		0.168	93.6	-186.5	slaved	0	6	0	-0.2	0.168	-70	
duplicate	25	0.000		0.000		-186.5	slaved	0	3	0	0	0	-3	
	26	0.269	41.6	-0.296	-81.9	-186.5	slaved	0	5	0.269	38	-0.296	-68	
75% yield	27	-0.245	-15.2	0.263	105.2	-186.5	slaved	0	10	-0.245	-10	0.263	90	
45 degree	28	0.000		0.000		-186.5	slaved	0	3	0	2	0	-4	
	29	0.440	33.9	0.125	49.5	-186.5	slaved	0	5	0.435	33.9	0.124	20	
75% yield	30	-0.592	-66.2	-0.225	-77.6	-186.5	slaved	0	10	-0.592	-59	-0.225	-6.2	
100+30	31	0.000		0.000		-186.5	slaved	0	3	0	2.7	0	4.1	
	32	0.000		-0.310	-82.2	-186.5	slaved	0	5	0	3	-0.31	-63	
				-0.400	-82.2	-186.5	slaved	0	1	0	3	-0.4	-80	
75% yield	33	0.000		0.510	140.4	-186.5	slaved	0	10	0	0	0.51	140	
	34	0.000		-0.400	-82.2	-186.5	slaved	0	6	0	-1	-0.4	-80	
	35	0.000		0.510	140.4	-186.5	slaved	0	6	0	0	0.51	135	
			0.0	0.0	0.0	-186.5	slaved	0	3	0	0	0.04	0	
	36	0.000		-0.400	-82.2	-186.5	slaved	0	3	0	-2	-0.4	-79	
	37	0.000		0.510	140.4	-186.5	slaved	0	6	0	0	0.51	135	
	38		0.0	0.0	0.0	-186.5	slaved	0	3	0	0	0.04	0	
	39					-201.2	slaved	0	3	0	0	0.04	0	
	40	0.000		-0.400	-82.2	-201.2	slaved	0	3	0	2	-0.4	-79	
	41	0.000		0.510	140.4	-201.2	slaved	0	6	0	0	0.51	132.2	
	42	0.000		-0.127	-54.8	-201.2	slaved	0	6	0	1	-0.127	-28	
50% yield	43	0.116	14.0	-0.127	-54.6	-201.2	slaved	0	6	0.116	14.3	-0.127	-28	
surface	44	0.417	40.1	0.000		-201.2	slaved	0	6	0.417	35	0	-13	
	45	0.000		0.168	93.6	-201.2	slaved	0	6	0	-1	0.168	41	
	46	-0.417	-40.1	0.000		-201.2	slaved	0	3	-0.417	-34	0	-14	
	47	-0.116	-14.0	-0.127	-54.6	-201.2	slaved	0	5	-0.116	-9	-0.127	-28	
	48	0.000		-0.127	-54.8	-201.2	slaved	0	3	0	3	-0.127	-26	
		0.000		0.000		-201.2	slaved	0	3	0	0.5	0.000	2	
	49	0.000		-0.400	-82.2	-201.2	slaved	0	3	0	2	-0.4	-78	
75% yield	50	0.000		0.510	140.4	-201.2	slaved	0	6	0	0	0.51	131	
	51	0.000		-0.616	-109.6	-201.2	slaved	0	10	0	2	-0.616	-107	
yield	52	0.000		0.733	187.2	-201.2	slaved	0	10	0	0	0.733	178	
	53	0.000		-0.616	-109.6	-201.2	slaved	0	6	0	2	-0.616	-105	
	54	0.000		0.733	187.2	-201.2	slaved	0	6	0	0	0.733	172	
	55	0.000		-0.616	-109.6	-201.2	slaved	0	6	0	2	-0.616	-103	
	56	0.000		0.733	187.2	-201.2	slaved	0	6	0	0	0.733	172	
		0.000			0.0	-201.2	slaved	0	5	0	0	0.06	0	
	57	0.000		-0.924		-201.2	slaved	0	10	0	1	-0.924	-120	
150% yield	58	0.000		1.100		-201.2	slaved	0	10	0	0	1.100	220	
	59	0.000		-0.924		-201.2	slaved	0	6	0	1	-0.924	-118	
	60	0.000		1.100		-201.2	slaved	0	6	0	0	1.100	210	
	61	0.000		-0.924		-201.2	slaved	0	6	0	1	-0.924	-116	
	62	0.000		1.100		-201.2	slaved	0	6	0	0	1.100	207	

Table 3.11. Load history applied to NTW2, cont.

cycle	Ramp #	Control Target Value							Time to peak (min)	Actual Value			
		X (in.)	X (k)	Y (in.)	Y (k)	Z (k)	MX & MY (k-in)	RZ (rad)		X (in.)	X (k)	Y (in.)	Y (k)
25	63	0.000		-1.616		-201.2	slaved	0	10	0	1	-1.616	-130
1% & 1.5%	64	0.000		2.403		-201.2	slaved	0	10	0	-1	2.403	241
	65	0.000		-1.616		-201.2	slaved	0	6	0	0	-1.616	-124
26	66	0.000		2.403		-201.2	slaved	0	6	0	-1	2.403	228
	67	0.000		-1.616		-201.2	slaved	0	6	0	0	-1.616	-126
	68	0.000		2.403		-201.2	slaved	0	6	0	-1	2.403	225
	69	0.000		0.000		-201.2	slaved	0	3	0	0	0.000	-62
28	70	0.430		-1.330		-201.2	slaved	0	5	0.43	6	-1.330	-117
30+100	71	-0.680		2.010		-201.2	slaved	0	10	-0.68	-10	2.010	182
1 & 1.5%	72	0.000		0.000		-201.2	slaved	0	3	0	3	0.000	-54
	73	1.250		0.000		-201.2	slaved	0	5	1.25	31	0	-42
1%	74	-1.250		0.000		-201.2	slaved	0	10	-1.25	-38	0	-36
FD	75	0.000		0.000		-201.2	slaved	0	3	0	8	0	-28
	76	1.300		-1.560		-201.2	slaved	0	5	1.3	63	-1.56	-126
45 degree	77	-1.450		1.530		-201.2	slaved	0	10	-1.45	-21	1.53	135
1.50%	78	0.000		0.000		-201.2	slaved	0	3	0	10	0	-36
	79	1.910		0.000		-201.2	slaved	0	5	1.91	62	0	-41
1.50%	80	-1.910		0.000		-201.2	slaved	0	10	-1.91	-64	0	-40
FD	81	0.000		0.000		-201.2	slaved	0	3	0	13	0	-19
	82	-1.810		-0.700		-201.2	slaved	0	5	-1.81	-70	-0.7	-93
100+30	83	1.850		0.690		-201.2	slaved	0	10	1.85	44	0.69	33
1.50%	84	0.000		0.000		-201.2	slaved	0	3	0	-12	0	-13
	85	0.000		-1.616		-201.2	slaved	0	3	0	-5	-1.616	-118
1% & 1.5%	86	0.000		2.403		-201.2	slaved	0	6	0	0	2.403	222
	87	0.000		-1.616		-201.2	slaved	0	6	0	0	-1.616	-121
	88	0.000		2.403		-201.2	slaved	0	6	0	0	2.403	278
	89	0.000		-2.460		-201.2	slaved	0	10	0	0	-2.46	-133
1.5 & 2%	90	0.000		3.150		-201.2	slaved	0	10	0	-1	3.15	235
	91	0.000		-2.460		-201.2	slaved	0	6	0	0	-2.46	-134
	92	0.000		3.150		-201.2	slaved	0	6	0	0	3.15	229
	93	0.000		-2.460		-201.2	slaved	0	6	0	0	-2.46	-133
	94	0.000		3.150		-201.2	slaved	0	6	0	0	3.15	220
	95	0.000		0.000		-201.2	slaved	0	3	0	0	0	-72
	96	1.810		-2.205		-201.2	slaved	0	3	1.81	40	-2.21	-130
	97	-1.810		-2.205		-201.2	slaved	0	6	-1.81	-69	-2.21	-110
	98	0.000		0.000		-201.2	slaved	0	3	0.00	11	0	47
2.00%	99	1.900		2.260		-201.2	slaved	0	3	1.90	15	2.26	162
figure 8	100	0.000		3.150		-201.2	slaved	0	3	0.00	-6	3.15	210
	101	-1.900		2.260		-201.2	slaved	0	3	-1.90	-32	2.26	55
	102	0.000		0.000		-201.2	slaved	0	3	0.00	4	0.00	-67
	103	0.000		-2.777		-201.2	slaved	0	10	0.00	0	-2.78	-134
2 & 2.5%	104	0.000		3.889		-201.2	slaved	0	10	0.00	-1	3.89	210
	105	0.000		-2.777		-201.2	slaved	0	7	0.00	0	-2.78	-105
	106	0.000		3.889		-201.2	slaved	0	7	0.00	0	2.81	87
return to Δy=0						-5	not slaved	0	3	0.00	0	2.81	80
						-5	not slaved	0		0.00	0	1.82	0
						-5	slaved	0		0.00	0	-0.71	-50
						-5	slaved	0		0.00	0	0	-7
						-201.2	slaved	0	12	0.00	0	0	-13
39	107	1.910		0.000		-201.2	slaved	0	5	1.91	33	0	-10
1.5% FD	108	-1.910		0.000		-201.2	slaved	0	10	-1.91	-37	0	-7
	109	2.690		0.000		-201.2	slaved	0	10	2.69	52	0	-13
2% FD	110	-2.690		0.000		-201.2	slaved	0	10	-2.69	-52	0	-11
	111	2.690		0.000		-201.2	slaved	0	6	2.69	53	0	-13
	112	-2.690		0.000		-201.2	slaved	0	6	-2.69	-53	0	-11
	113	2.690		0.000		-201.2	slaved	0	6	2.69	54	0	-13
	114	-2.690		0.000		-201.2	slaved	0	6	-2.69	-53	0	-12
	115	3.410		0.000		-201.2	slaved	0	10	3.41	68	0	-21
2.5% FD	116	-3.410		0.000		-201.2	slaved	0	10	-3.41	-68	0	-20
	117	3.410		0.000		-201.2	slaved	0	7.5	-1.90	0	0	-7
										3.41	68	0	-20
	118	-3.410		0.000		-201.2	slaved	0	7.5	-3.41	-67	0	-19
	119	3.410		0.000		-201.2	slaved	0	9	3.41	68	0	-20
47	120	-3.410		0.000		-201.2	slaved	0	9	-3.41	-67	0	-19

Table 3.11. Load history applied to NTW2, cont.

cycle	Ramp #	Control Target Value							Time to peak (min)	Actual Value			
		X (in.)	X (k)	Y (in.)	Y (k)	Z (k)	MX & MY (k-in)	RZ (rad)		X (in.)	X (k)	Y (in.)	Y (k)
48	121	4.150		0.000		-201.2	slaved	0	11	4.15	80	0	-29
3% FD	122	-4.150		0.000		-201.2	slaved	0	11	-4.15	-79	0	-28
	49	123	4.150		0.000	-201.2	slaved	0	11	4.15	77	0	-28
50	124	-4.150		0.000		-201.2	slaved	0	11	-4.15	-77	0	-27
	125	4.150		0.000		-201.2	slaved	0	11	4.15	77	0	-27
51	126	-4.150		0.000		-201.2	slaved	0	11	-4.15	-76	0	-27
	127	5.950		0.000		-201.2	slaved	0	14	5.95	75	0	-35
4% FD	128	-5.950		0.000		-201.2	slaved	0	14	-5.95	-63	0	-28
	52	129	5.950		0.000	-201.2	slaved	0	14	5.95	41	0	-9
	130	-5.950		0.000		-201.2	slaved	0	14	-5.95	-16	0	12

\*MX=376.6-12.25VY (k-ft)

MY=12.25VX (k-ft)

### Documentation of Specimen Damage during Testing

Specimen damage was documented during construction using digital photography and the marking and measuring of cracks. The primary photographic record during testing was obtained using the MAST telepresence system. Photographs of both the flange and web were taken at each story level using the tower-mounted cameras after the first and last ramps to each displacement level. To document particular points of interest and significant damage, additional photographs were taken with a hand-held camera. Cracks were marked on all faces of the first and second stories of each specimen at the same times photographs were taken until damage to the specimen was such that marking cracks was considered unsafe. The crack patterns and widths were recorded on a scaled drawing. Appendix C includes additional information about the photography, including the locations of the camera towers. All photographs taken of the specimens can be found in the NEES Repository, currently located at <https://central.nees.org/?projid=22&action=DisplayProjectMain>. Additional information about crack marking for each specimen can be found in Chapters 5 and 6.

## **Chapter 4    Determination of Deformation Components and Comparison of Instrumentation Systems**

### **4.1 Introduction**

This chapter presents a discussion of some of the issues related to the instrumentation of subassemblages and the derivation of deformation components from the data collected. The first section describes the experience of previous researchers in instrumenting structural walls and beam-column connections and the methods they used to separate the contributions of shear and flexural deformations to the total deformations. The second section describes the instrumentation methods used in this research to separate the contributions of shear, flexure, strain penetration, and splice slip. The chapter concludes with a comparison of the two measurement systems used in this research, a combination of string pots and LVDTs and an optical measurement system.

### **4.2 Experience of Previous Researchers**

#### **4.2.1 Massone and Wallace (2004)**

Several researchers, including Massone and Wallace (2004) have instrumented walls using groups of horizontal, vertical, and diagonal LVDTs or string potentiometers (string pots) to measure the deformations of “panels” within the specimen, as shown in Figure 4.1. In their research, each panel used only a single pair of vertical instruments to measure flexural deformations. The result of this was that large curvature gradients, expected to occur near the base of the specimen, could not be captured, and subdivision into smaller segments was recommended for future researchers.

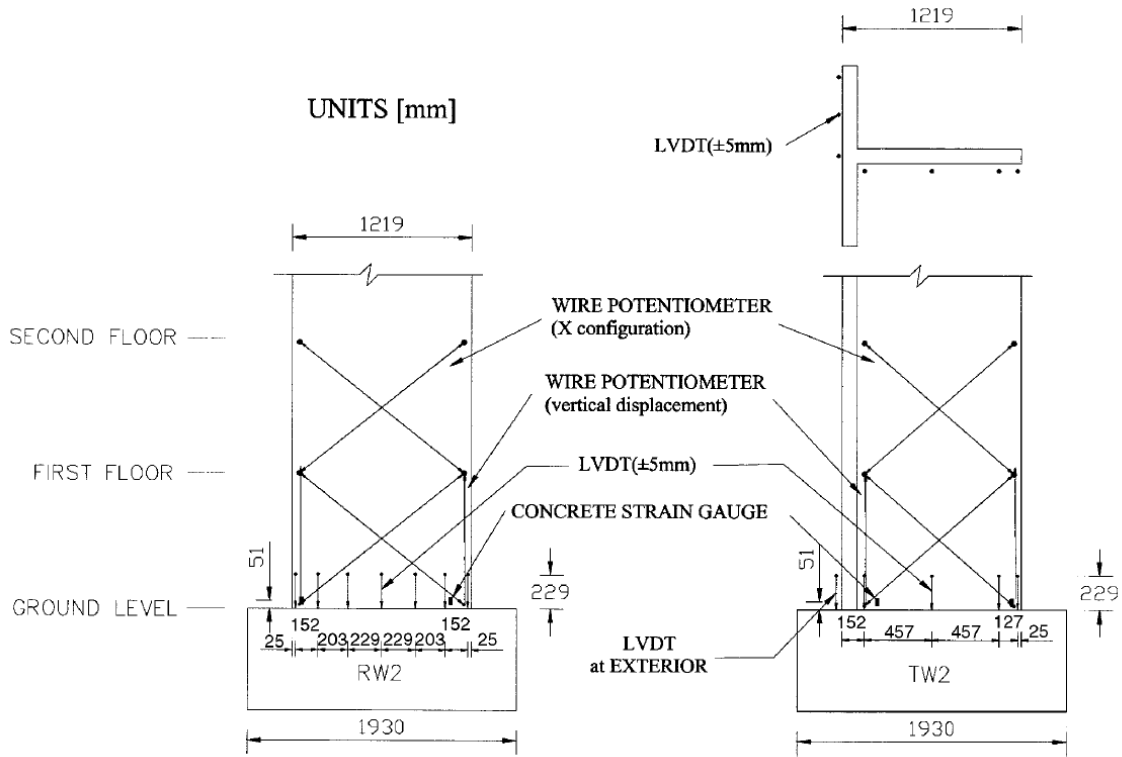


Figure 4.1. Instrumentation used by Massone and Wallace (from Massone and Wallace, 2004)

Most researchers have used the expression

$$U_{s, Xoriginal} = \frac{\sqrt{D_{1, meas}^2 - h^2} - \sqrt{D_{2, meas}^2 - h^2}}{2} \quad (4.1)$$

to calculate the contribution of shear to the total deformation. In this expression,  $U_{s, Xoriginal}$  is the uncorrected shear deformation within the panel being considered,  $D_{1, meas}$  and  $D_{2, meas}$  are the deformed dimensions of the diagonals of the panel, and  $h$  is the height of the panel, as shown in Figure 4.2. In this expression, the center of rotation of the panel is assumed to be at its mid height. Massone and Wallace (2004) added a correction to this to allow for a curvature gradient in the panel moving the center of rotation, resulting in the expression

$$U_{s,corrected} = \frac{\sqrt{D_{1,meas}^2 - (h + V_2)^2} - \sqrt{D_{2,meas}^2 - (h + V_1)^2}}{2} - U_f \quad (4.2)$$

Where  $U_{s,corrected}$  is the corrected shear deformation,  $V_1$  and  $V_2$  are the changes in height of the sides of the panel, and  $U_f$  is the lateral deformation due to flexure, derived as

$$U_f = \alpha \frac{V_1 - V_2}{l} h \quad (4.3)$$

where  $\alpha$  is the assumed distance from the top of the story to the centroid of the curvature distribution, which varies from 0.5 for a rectangular distribution to 0.67 for a triangular distribution.

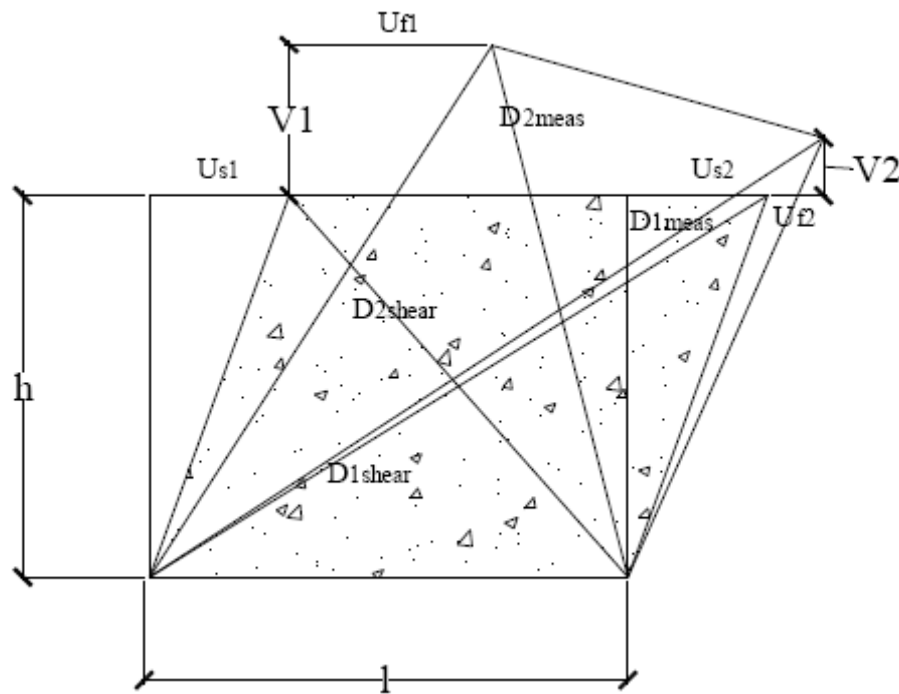


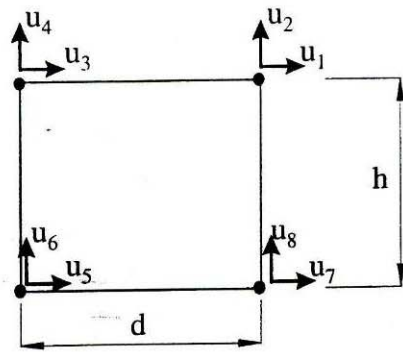
Figure 4.2. Flexural model accounting for vertical displacement (from Massone and Wallace, 2004)

#### 4.2.2 Sritharan *et al.* (1996)

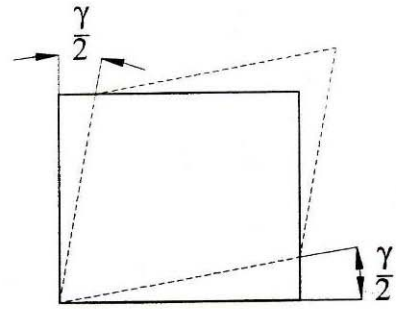
Sritharan *et al.* (1996) used a different formulation to determine the contribution of each of five independent modes of deformation (pure shear  $\gamma$ , extension in x and y directions  $\Delta_x$  and  $\Delta_y$ , and flexure about x and y axes  $\Delta\theta_x$  and  $\Delta\theta_y$ ) to the total deformation of a panel. These deformation modes are shown in Figure 4.3. Treating a panel as an isoparametric element, the contribution of each deformation mode can be expressed as

$$\begin{Bmatrix} \gamma \\ \Delta\theta_x \\ \Delta\theta_y \\ \Delta_x \\ \Delta_y \end{Bmatrix} = \begin{bmatrix} \frac{1}{2h} & \frac{1}{2d} & \frac{1}{2h} & -\frac{1}{2d} & -\frac{1}{2h} & -\frac{1}{2d} & -\frac{1}{2h} & \frac{1}{2d} \\ -\frac{1}{h} & 0 & \frac{1}{h} & 0 & -\frac{1}{h} & 0 & \frac{1}{h} & 0 \\ 0 & \frac{1}{d} & 0 & -\frac{1}{d} & 0 & \frac{1}{d} & 0 & -\frac{1}{d} \\ \frac{1}{2} & 0 & -\frac{1}{2} & 0 & -\frac{1}{2} & 0 & \frac{1}{2} & 0 \\ 0 & \frac{1}{2} & 0 & \frac{1}{2} & 0 & -\frac{1}{2} & 0 & -\frac{1}{2} \end{bmatrix} \begin{Bmatrix} u_1 \\ u_2 \\ u_3 \\ u_4 \\ u_5 \\ u_6 \\ u_7 \\ u_8 \end{Bmatrix} \quad (4.4)$$

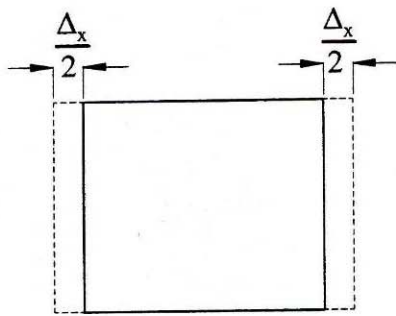
Figure 4.3 shows the naming convention for the nodal displacements  $u_1$  through  $u_8$ .



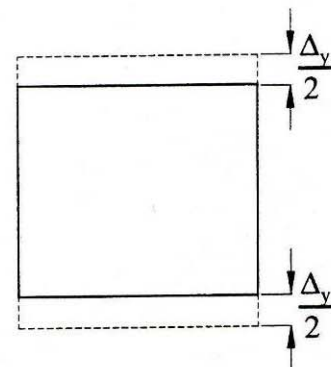
(a) Joint panel nodal displacements



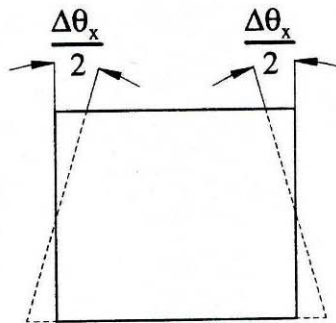
(b) Mode 1 - pure shear



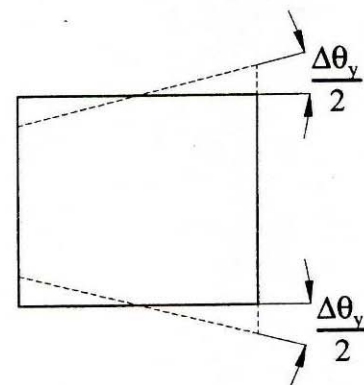
(c) Mode 2 - extension in x direction



(d) Mode 3 - extension in y direction



(e) Mode 4 - curvature about x axis



(f) Mode 5 - curvature about y axis

Figure 4.3. Decomposition of joint panel deformation into five independent modes (from Sritharan *et al.* 1996)

Each panel was instrumented with five linear potentiometers, as shown in Figure 4.4, where B, T, N, S, and D represent the deformed lengths of each potentiometer. The deformed nodal coordinates can be calculated from these deformed lengths using the expressions in Equations 4.5 through 4.14.

$$\theta_1 = \cos^{-1}\left(\frac{B^2 + S^2 - D^2}{2BS}\right) \quad (4.5)$$

$$\theta_2 = \cos^{-1}\left(\frac{B^2 + D^2 - S^2}{2BD}\right) \quad (4.6)$$

$$\theta_3 = \cos^{-1}\left(\frac{N^2 + D^2 - T^2}{2ND}\right) \quad (4.7)$$

$$\theta_7 = \pi - \theta_1 \quad (4.8)$$

$$u_1 = S \cos \theta_7 \quad (4.9)$$

$$u_2 = S \sin \theta_7 - h \quad (4.10)$$

$$u_3 = N \cos(\theta_2 + \theta_3) \quad (4.11)$$

$$u_4 = N \sin(\theta_2 + \theta_3) \quad (4.12)$$

$$u_7 = B - d \quad (4.13)$$

$$u_5 = u_6 = u_8 = 0 \quad (4.14)$$

Because the change in flexural rotations,  $\Delta\theta_x$  and  $\Delta\theta_y$ , over the panel are calculated, rather than the total rotation including rigid body rotations of the panel, setting  $u_5$ ,  $u_6$ , and  $u_8$  equal to zero is acceptable. The rigid body translations and rotations of the panel are measured with other instrumentation and can be added back as needed.

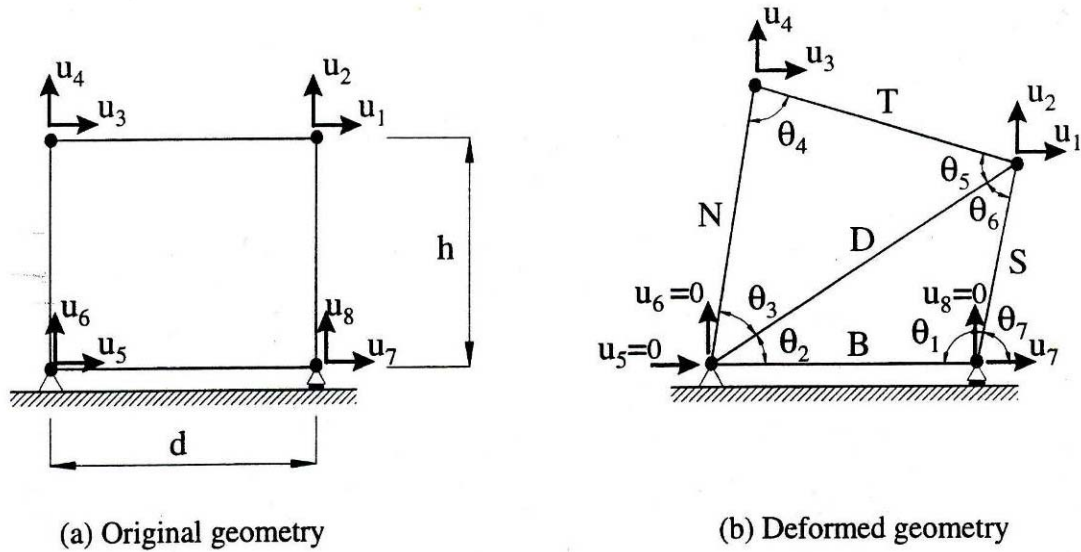


Figure 4.4. Joint panel deformation (from Sritharan *et al.* 1996)

#### 4.2.3 Johnson (2007)

As part of the larger study of which this research is a component, three rectangular walls were tested to failure. Instrumentation of these walls was very similar to the T-shaped walls discussed in this thesis. In particular, the specimen was subdivided into smaller portions for instrumentation, as recommended by Massone and Wallace (2004), both traditional instrumentation (LVDTs and string pots) and an optical measurement system (Krypton) were used to instrument the wall, and instrumentation was included to measure the contribution of strain penetration to the total wall deformation.

Johnson (2007) did an extensive comparison of the results provided by the various types of instrumentation, confirming the accuracy and utility of each. He found that longitudinal strains across the width of the wall were nonlinear, with a larger gradient in the half of the section including the compression block and a small gradient in the half of the section entirely in tension. Similar results were also found by Oesterle *et al.* (1979).

Paulay and Priestley (1992) suggest that this observation is common in walls developing large shear cracks, but that flexural strength calculations assuming plane sections remain plane are still reasonable. Johnson (2007) found that accurate calculation of the section curvature and the flexural deformation of the wall required using the axial strains at both ends of the section. Using only strains from the compression half or tension half of the wall resulted in large over- or under-estimates of the flexural deformation, respectively.

### **4.3 Calculation of Components of Deformation**

#### **4.3.1 NTW1**

The first story of the structure was instrumented with two types of devices to measure the flexural and shear components of lateral deformation. Traditional length measuring devices (string pots and LVDTs) were used on both the web and flange, and in addition, on the web and one half of the flange, an optical measuring system (Krypton) was also used to provide a means of comparison. The Krypton system was not used on the second, third, and fourth stories because of limitations in its measurement volume. The deformation components of shear and flexure for the first story were derived using both measurement systems, and the results were compared. For web direction deformations, the Krypton was selected as the more accurate system and used for the values reported in this thesis, because it was not sensitive to accidental bumping or plucking of the strings, nor was there concern about extension wires slipping during the test and introducing error into the results. For flange direction deformations, the string pots and LVDTs were preferred over the Krypton system. Some slip in the string pot strings over the course of the testing was apparent in the data. However, the individual

components of deformations calculated by the Krypton did not sum to the directly measured displacement. This was the result of the Krypton system being used only on one half of the flange and the nonlinearity of the strain distribution across the flange.

The method used by Sritharan *et al.* (1996) was used to calculate the contributions of shear and flexural deformations using both types of instrumentation. Equation 4.3 was used directly with the Krypton system, and Equations 4.4 to 4.13 were used to calculate the nodal displacements from the LVDT and string pot measurements to use with Equation 4.3. Only two of the five quantities calculated,  $\gamma$  and  $\Delta\theta_y$  were required for this study. This method was preferred over the method used by Massone and Wallace (2004) and other researchers because it uses trigonometric functions instead of first or second degree approximations, making it more accurate at large deformation levels. Because this method requires only a single diagonal measurement, the components of deformation for each panel of string pots were calculated twice, once using each diagonal instrument, and the results were averaged. In all cases, the two calculations gave very similar results, and doing only a single calculation would have been acceptable.

The provided instrumentation subdivided the first story of the specimens both horizontally and vertically. Johnson (2007) found that neglecting the horizontal subdivision, effectively assuming that plane sections remain plane, resulted in better correlation between the derived components of deformation and the directly measured total deformation. For the purposes of this investigation, the horizontal subdivision was neglected for the determination of the components of deformation using both measurement systems. Figure 4.5 highlights the Krypton LEDs and indicates the four

“panels” that were used to determine the components of deformation parallel to the web for the first story of NTW1. Similar procedures were followed to determine the deformation components in the other stories and in NTW2.

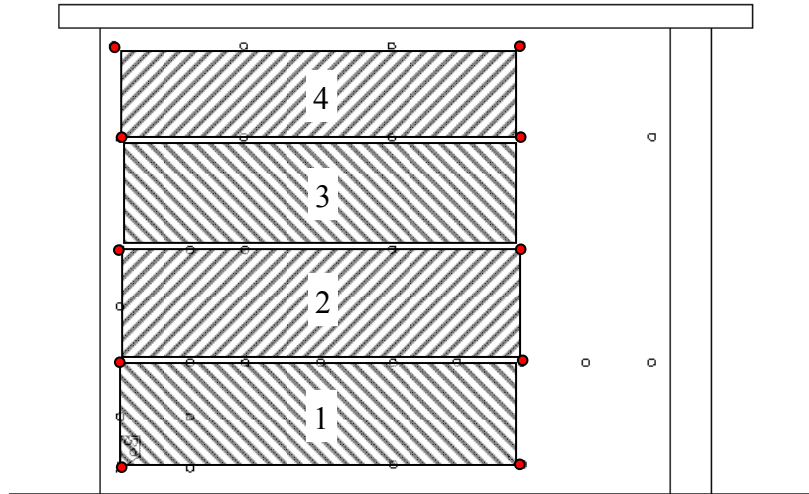


Figure 4.5. Krypton LEDs used to determine components of deformation for NTW1 first story web

While the total shear deformation below a particular point on the specimens could be calculated directly by summing the shear deformation in all panels below the point in question, numerical integration was required to calculate displacement due to flexural deformation from the change in rotation in each panel. For this calculation, it was assumed that rotation varied linearly between the known points, as shown in

Figure 4.6. Because instruments were not installed to measure deformations through the slab thickness and approximately 3 inches immediately above and below the slab, it was assumed that the curvature through each slab was equal to the average of the curvatures in the panels immediate above and below the slab.

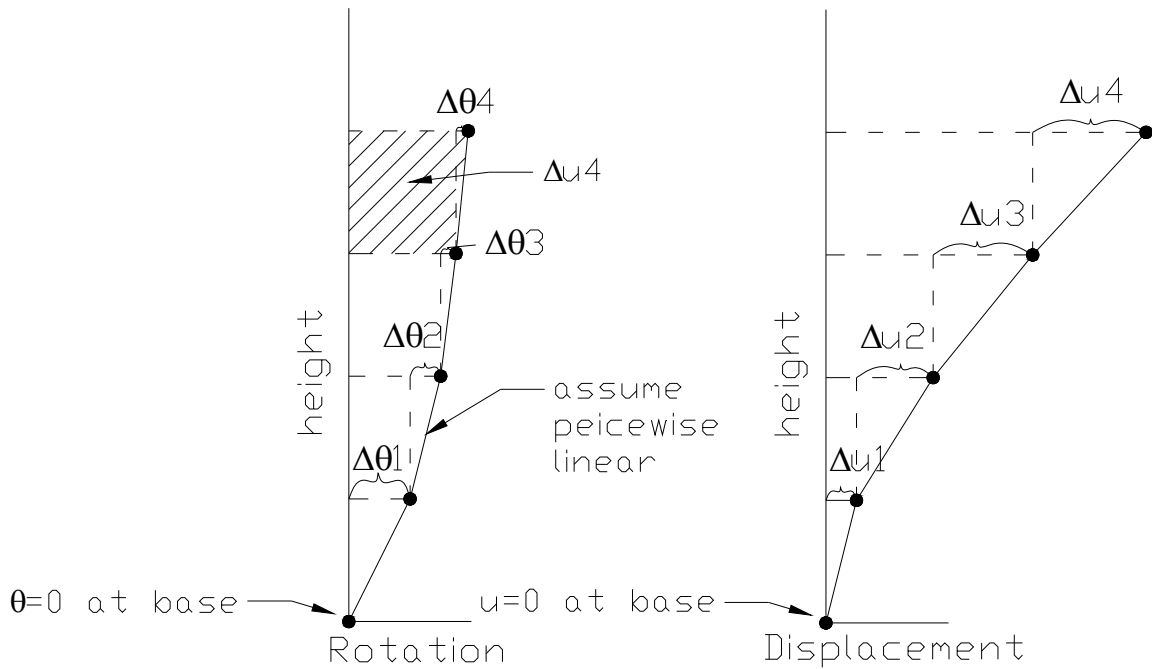


Figure 4.6. Calculation of flexural displacement from panel rotations

Rotations due to strain penetration were calculated from the LVDTs used to measure slip at the extreme bars in the web and flange tips relative to the top of the foundation block. The stud for mounting the LVDT in the south flange tip was damaged during construction of the specimen, so only the north flange tip and the web tip were instrumented for NTW1. In the flange direction, the rotation due to strain penetration was calculated by assuming that the profile of axial displacement due to strain penetration was anti-symmetric over the width of the flange, and that the bars in the center of the flange had zero displacement due to strain penetration. This assumption would tend to overestimate rotations due to strain penetration when the instrumented flange tip was in tension, and to underestimate rotations when the instrumented tip was in compression. The LVDT measuring displacement due to strain penetration in the north

flange tip was assumed to be representative of the entire flange for calculation of strain penetration effects in the web direction. Due to the effects of shear lag, this may have led to an underestimation of the rotation in the web direction. Additionally, strain penetration across the flange was not constant for skew direction loading, so this calculation may not have been meaningful for this portion of the testing.

#### **4.3.2 NTW2**

In most cases, the components of deformation in NTW2 were calculated in the same way, and using the same instrumentation, as in NTW1 described above. Exceptions to this are described in the following paragraphs.

Two Krypton systems were used to measure deformations of the first story of this specimen. One was used to measure deformations of the web, and the other was used to measure deformations over the entire flange width. As a result, the data collected with the Krypton system could be used to calculate the components of deflection in both the flange and web directions for the first story.

LVDTs were attached to two bars at both of the flange tips and at the web tip to measure the effects of strain penetration. An additional stud was attached to a bar in the center of the flange to provide a more accurate measurement of strain penetration in the web direction, but this stud was damaged during construction of the specimen and could not be used. The LVDTs at each flange tip were used to calculate rotation due to strain penetration in the flange direction. Because the stud intended to measure strain penetration displacement in the center of the flange was damaged, the displacements of the LVDTs at the flange tips were averaged to estimate the strain penetration

displacement at the web-to-flange intersection when calculating the rotation in the web direction. Due to the effects of shear lag, this may have led to an underestimation of the rotation in the web direction, but it did help to resolve the difficulties associated with skew direction loading.

Rotations due to splice slip were measured by the difference in LVDTs measuring displacement of the two lapped bars. Four studs were attached to the reinforcement at each location of interest: one on each of the bars at the top and bottom of the lap region. The remaining end of each LVDT was secured to the top of the slab, so that the motion of the bars relative to the slab was measured. However, one of the four studs was inadvertently damaged in each grouping. As a result, only one meaningful difference was available for each group to measure the relative slip of the bars: the difference between the LVDTs attached either at the top of the splice or at the bottom. Mixing between the top and bottom was not done because this measurement would have been affected by strains in the bars over the lap length and would not have been a true representation of the slip between the bars. Comparing the slips measured at the top of the lap in one flange tip to the slips measured at the bottom of the lap in the other indicated that the location of measurement did not make a significant difference in the measured slip.

#### **4.4 Comparison of Traditional and Optical Measurement Systems**

Experience in testing the T-shaped walls described in this report and in testing the rectangular walls described by Johnson (2007), with redundant instrumentation, demonstrated that each of the measurement systems was capable of providing researchers

with useful data, but the systems each had strengths and weaknesses that should be considered in the choice of measurement system to be used.

The Krypton system has three major advantages over traditional instrumentation with string pots and LVDTs. First, instead of reporting only the change in distance between two points, the Krypton system reports the position of each target in three-dimensional space. This additional information can simplify the derivation of components of deformation, and it provides a check that these components are being calculated correctly because the total of the components of deformation can be compared to the displacement of an individual Krypton LED in three-dimensional space. Second, the instrumentation is more compact and less obtrusive to the surface of the specimen. Targets can be placed more densely than traditional measuring devices because of their very small size and the lack of a need for large mounting brackets. Attaching string pots to the specimen in the desired X pattern was challenging because the size of the string pots and their brackets often caused interference between individual instruments. Additionally, during the testing, particular care had to be taken to avoid bumping the many string pot wires crossing the specimen while marking cracks. These issues did not exist with the Krypton system. Third, while individual Krypton targets can be accidentally detached from the specimen, there is no concern about strings being bumped or slipping, or of brackets becoming loose, and introducing errors into the data. In NTW1, the Krypton targets that coincided with the studs used to mount the string pots and LVDTs were attached to the studs, and the remaining targets were attached to the concrete surface. As large amounts of damage accumulated and cover concrete began to

spall, some of these targets came off. In NTW2, this difficulty was addressed by embedding 3/16 in. diameter studs in the wall for mounting the Krypton targets that did not coincide with string pots or LVDTs. As a result, the targets were not affected by the development of surface damage on the concrete.

Traditional instrumentation has two major advantages over the Krypton system. First, instruments can be placed in any location on the specimen, without concern for remaining inside the limited measurement volume of the Krypton camera or being in a shadow behind other instrumentation. Instrumentation on only the first story of each specimen filled the Krypton measurement volume, both horizontally and vertically. Had the specimens been larger, viewing an entire face with a single camera would have been difficult or impossible. Second, the observed noise level associated with string pots and LVDTs was much less than that of the Krypton during these initial applications of the system at the University of Minnesota MAST laboratory.

Concerning reliability, traditional instrumentation generally functions on an instrument-by-instrument basis, or problems occur with small groups of instruments. Single instruments may fail to read, but once initial debugging is complete, complete system failure is unlikely and known immediately through real-time monitoring of the system. The Krypton system acts as a whole. Failures occur system-wide, and may not be apparent to the researchers until after a portion of testing is complete. For instance, in both tests there were groups of several ramps where the recorded data was clearly erroneous and offsets of tens of inches were observed for all targets, while the imposed displacements were less than an inch. Additionally, data were lost in both tests due to

software issues and the inability to download a data set. These risks were minimized by frequently downloading the data so that the volume of data potentially lost was reduced.

#### **4.5 Data Archival**

All of the collected raw data, as well as corrected data for all instruments and the components of deformation derived from the various instruments have been archived in the NEES repository. This repository can currently be accessed at <https://central.nees.org/?projid=22&action=DisplayProjectMain>.

## **Chapter 5 Specimen NTW1**

### **5.1 Introduction**

This chapter presents a summary of the test results of specimen NTW1. The chapter begins with a description of the overall observed damage and failure of the specimen, followed by a summary of the load versus deformation response. The components of the deformation (i.e., flexure, shear, strain penetration, and splice slip) were determined from the external instrumentation. The effective flange width for the case of the flange-in-tension in the web loading direction was determined from the measured strain distribution.

### **5.2 Observed Damage and Failure**

This specimen had cracks marked and corresponding crack widths measured on the first and second stories of the structure and photographs taken of the entire specimen. This documentation was done after the first and third cycles in groups of three cycles to the same displacement level, and in all cycles that were not repeated. In the following discussion, observed cracking patterns and crack widths in the first and second stories are described. Additional photographs taken with the MAST telepresence system and with handheld cameras throughout the testing have been archived with the sensor data in the NEES repository. Selected photographs showing representative behavior are included herein. The archived photographs have higher resolution than the reproductions and may be used to further investigate the damage state of the wall at a more detailed level.

### 5.2.1 Testing through Yielding

The initial loading to the specimen was a single cycle to 10 percent of the expected yield displacement in the flange-in-tension and flange-in-compression loading directions. No cracking was observed after these ramps. Initial shear cracking was observed in the web at 25 percent of the expected yield displacement in both the flange-in-tension and flange-in-compression loading directions. Initial flexural cracking in the web tip was also observed at this loading level. At this loading level, cracks were observed in both the first and second stories of the structure. At 50 percent of the expected yield displacement, both flexural and shear cracking extended over the first two stories of the specimen for both loading directions. This cracking included flexural cracks in the flange crossing into the web and transitioning into shear cracks. The cracking pattern in the flange consisted of horizontal cracks over the confined region in the flange tips that extended into diagonal (shear) cracks in the central portion of the wall, resulting in a “V” pattern around the web-to-flange intersection. All cracks in the confined region were hairline width ( $<0.005$  in.), but shear cracks in the first story were as wide as 0.020 in. for flange-in-tension loading and 0.016 in. wide for flange-in-compression loading. Shear cracks in the second story were open up to 0.016 in. wide in flange-in-tension loading and 0.010 in. wide in flange-in-compression loading.

Loading to 25 percent of the yield displacement in the flange direction did not cause new cracks to form. The largest cracks opened to 0.007 in. wide. Loading to 25 percent of yield displacement in the  $45^\circ$  direction with the web tip in tension caused flexural cracks in the web tip to open to hairline width. Shear cracks in the web opened

up to 0.010 in. Loading in the 45° direction caused shear cracks in the web to open 0.009 in. In both loading directions, cracks in the confined regions opened 0.005 in. or less. Loading in both 100% + 30% directions to 25 percent of the predicted yield displacement did not cause any new cracks to form. Shear cracks in the web opened up to 0.013 in. when the web tip was in tension and to 0.005 in. when the web tip was in compression. Repeating loading to 50 percent yield in the web direction after loading in other directions caused small extensions of existing cracks. The largest cracks in the flange were 0.025 in. wide.

Loading in the 45° directions to 75 percent of the expected yield displacement caused small extensions to the existing cracks. The widest flexural cracks, near the base of the specimen, were <0.005 in. wide. Shear cracks in the web were more widely spaced than flexural cracks and opened up to 0.020 in. wide. Loading in the 100%+30% direction caused several new cracks to form in the second story of the specimen. The shear cracks in the web opened up to 0.013 in., and the shear cracks in the flange opened up to 0.020 in. Loading in the web direction to 75 percent of the yield displacement caused additional large shear cracks to form. Loading with the flange in compression caused a maximum shear crack width of 0.030 in. and a maximum flexural crack width of 0.007 in. Loading with the flange-in-tension caused a maximum shear crack width of 0.025 in. in both the first and second stories.

Loading to the predicted yield displacement with the flange in compression caused a few new cracks and extensions to existing cracks. The largest web shear cracks opened up to 0.025 in. wide in both the first and second stories. Flexural cracks in the

web tip opened up to 0.010 in. wide, and the crack at the wall-to-foundation block interface opened to 0.009 in. wide. This particular crack was not documented prior to this point in the loading history; identifying very fine cracks near the wall-to-foundation interface was difficult because of the surface roughness in this region. Loading with the flange in tension caused shear cracks to open up to 0.035 in. wide in the first story and 0.026 in. wide in the second story. Flexural cracks in the flange opened up to 0.007 in. wide in the confined region of the first story, 0.035 in. wide in the center portion of the first story, 0.005 in. wide in the confined region of the second story, and 0.025 in. wide in the center portion of the second story.

At this point in the test, the overall crack pattern included approximately uniformly spaced, horizontal flexural cracks in the boundary elements in the web and flange, with more widely spaced diagonal shear cracks in the more lightly reinforced portions of the web and flange. The cracks in the boundary elements were spaced approximately 3 in. apart, and there was a distinct transition in the crack pattern from the confined region, with closely spaced, flexural cracks, to the unconfined region, with much more widely spaced cracks that opened up to three times wider than the flexural cracks in the confined regions. In both the web and the flange, the crack widths decreased with wall height. Figure 5.1 through Figure 5.8 show the specimen at this point in the testing. These photos were taken at the final peak load in this group of cycles, prior to unloading.

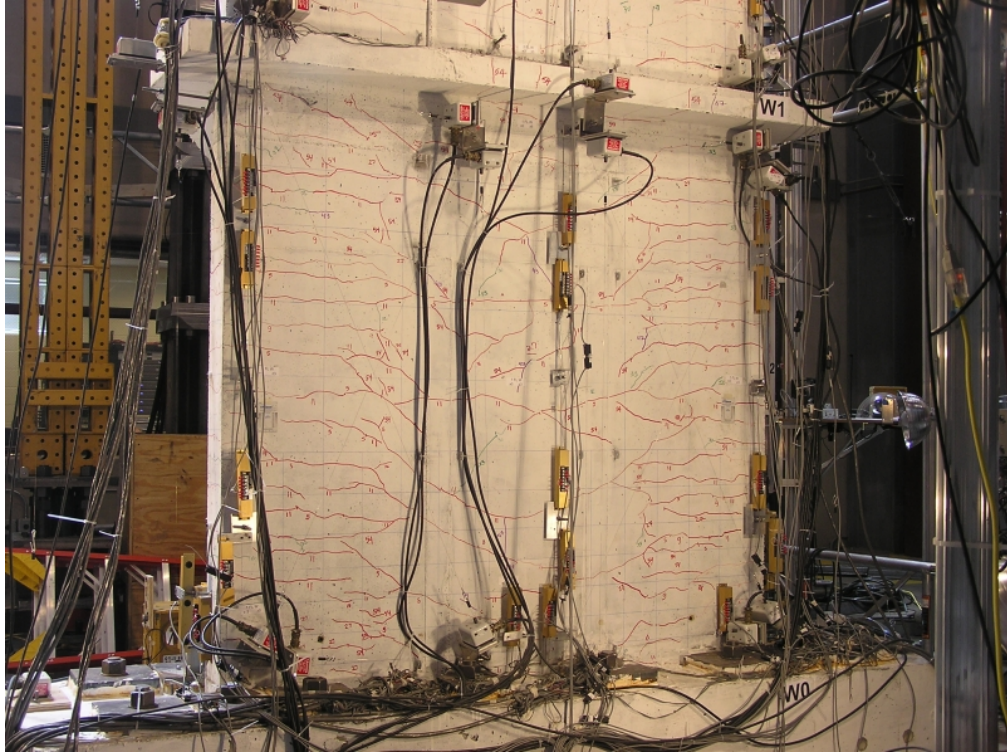


Figure 5.1. First story flange of NTW1 at end of elastic loading cycles.

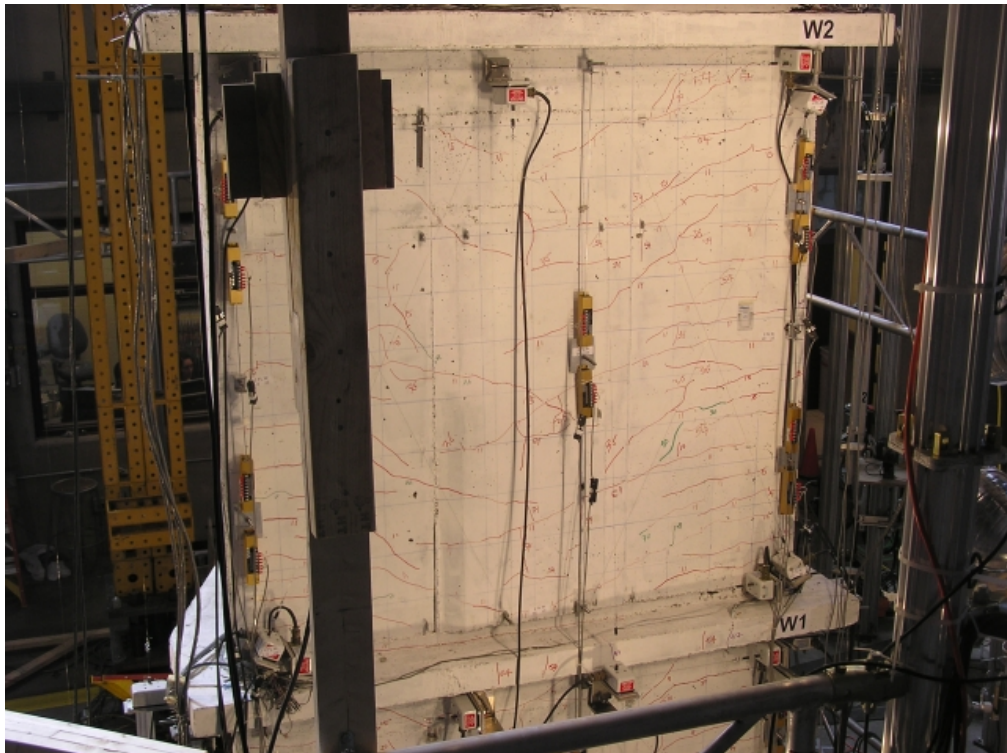


Figure 5.2. Second story flange of NTW1 at end of elastic loading cycles.

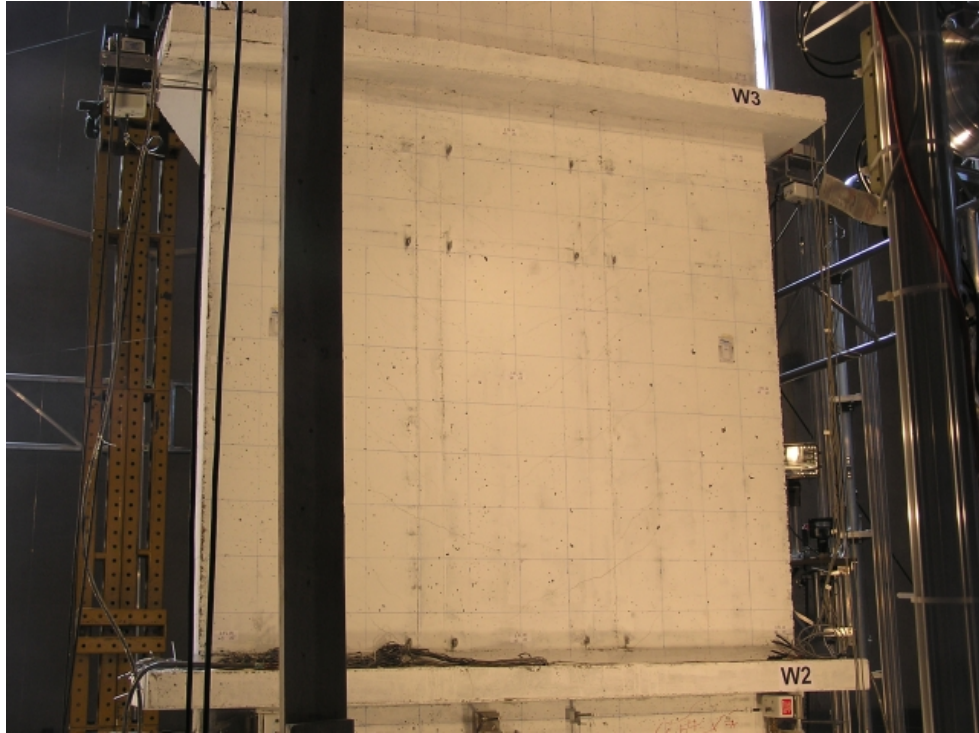


Figure 5.3. Third story flange of NTW1 at end of elastic loading cycles (cracks not marked).



Figure 5.4. Fourth story flange of NTW1 at end of elastic loading cycles (cracks not marked).

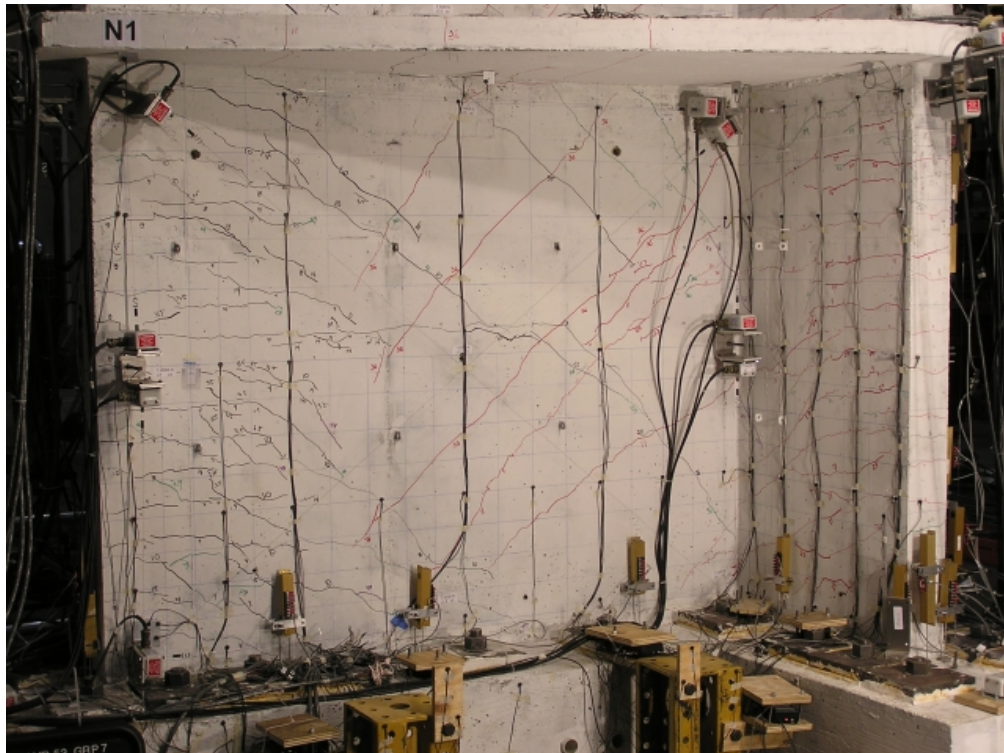


Figure 5.5. First story web of NTW1 at end of elastic loading cycles.

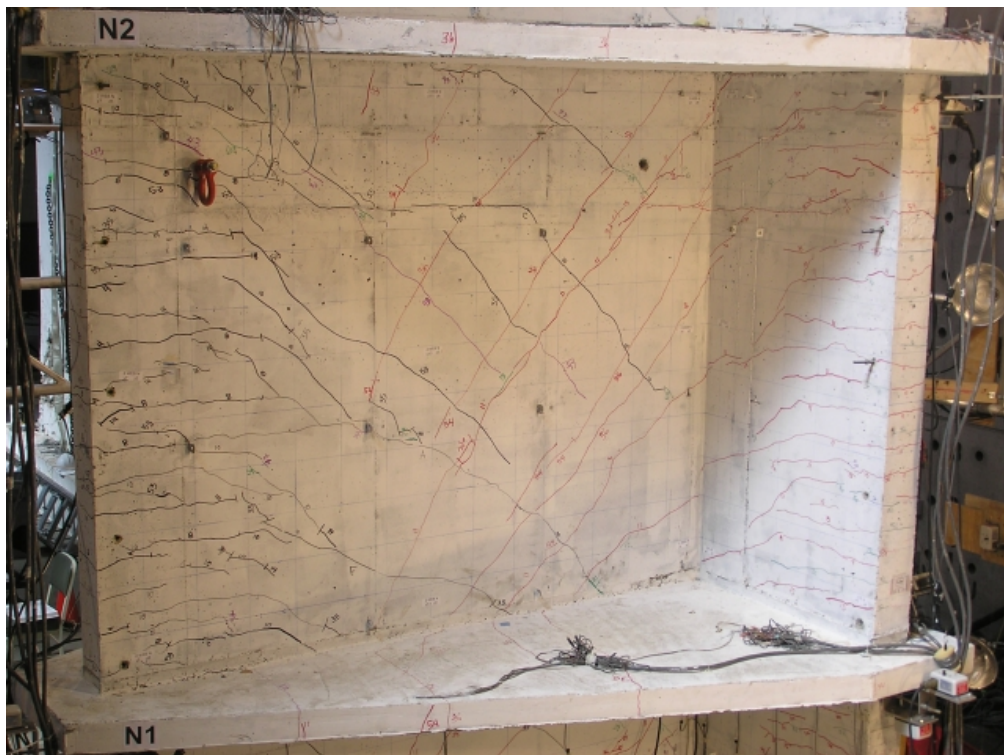


Figure 5.6. Second story web of NTW1 at end of elastic loading cycles.

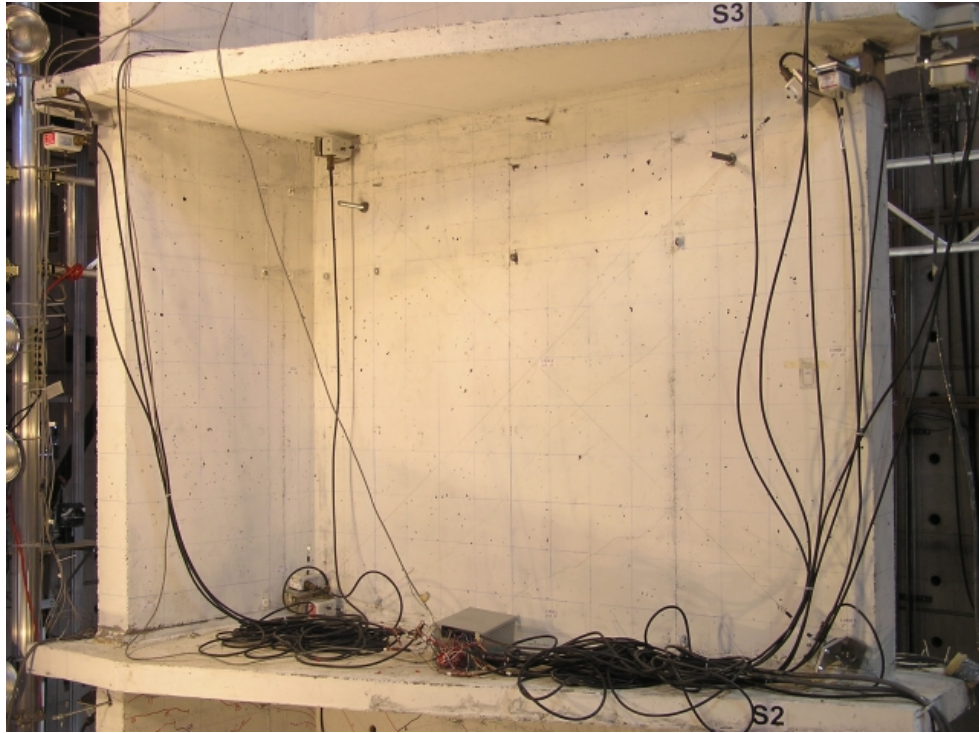


Figure 5.7. Third story web of NTW1 at end of elastic loading cycles (cracks not marked).

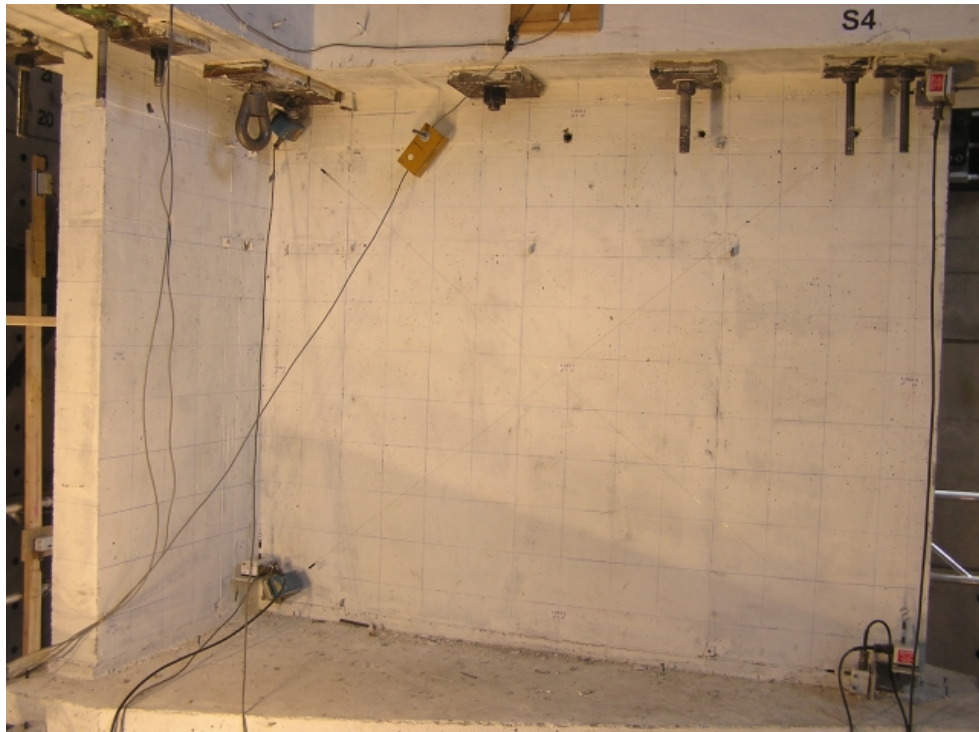


Figure 5.8. Fourth story web of NTW1 at end of elastic loading cycles (cracks not marked).

### 5.2.2 Post-Yielding through Failure

Loading in the web direction to 150 percent of the yield displacement caused one new shear crack to form in each of the first two stories and extensions to existing cracks. Flexural cracks in the web tip were up to 0.025 in. wide in the lower two-thirds of the bottom story and 0.010 in. wide in the top third. In the second story, flexural cracks were 0.005 in. wide. Flexural cracks in the flange were up to 0.013 in. wide in the confined portion of the bottom story and 0.007 in. wide in the confined region of the second story. In the central portion of the flange, cracks were open up to 0.035 in. wide. Web shear cracks opened up to 0.050 in. wide in the bottom story when the flange was in compression and up to 0.060 in. wide when the flange was in tension. In the second story, web shear cracks opened up to 0.035 in. wide in both flange-in-tension and flange-in-compression loading directions.

Loading in the flange-in-compression direction to 1 percent drift caused flexural cracks to open to 0.030 in. in the lower portion of the first story and 0.020 in. in the upper portion. The crack at the wall-to-foundation interface opened to 0.060 in. In the second story, flexural cracks were 0.007 in. wide. Web shear cracks were up to 0.060 in. wide in the first story and 0.030 in. wide in the second story.

Loading in the flange-in-tension direction to 1.5 percent drift caused spalling of the cover concrete over an approximately 12 in. x 12 in. area at the base of the web tip. Several cracks in the center 24 in. of the flange were approximately 1/8 in. wide. Cracks in the confined region in the flange were 0.02 in. wide. The crack at the wall-to-foundation interface was 3/16 in. wide in the center of the flange and 1/8 in. wide at the

tips. Cracks were 0.060 in. wide in the center portion of the second story. The largest web shear cracks opened more than 0.060 in. wide in the bottom story and up to 0.050 in. wide in the second story in both flange-in-tension and flange-in-compression loading directions. Loading in the 100%+30% directions at this drift level did not cause new cracking and existing cracks did not open as wide as previously observed.

Beyond this point in the test, cracks were marked and widths recorded, but this information was lost. Loading with the flange in tension to 1.5 percent drift caused shear sliding across cracks in the first story of the web. Loading with the flange in tension to 2.0 percent drift caused additional spalling in the web tip, and the 135° hooks closing the confinement hoops near the base of the specimen were partially straightened, making them appear to be 90° hooks. Visible crushing of the core was noted after the third cycle to this drift level. Subsequent loading in the hourglass pattern caused buckling of bars in the web tip. Two bars buckled in the first ramp of the hourglass that involved tension in the flange, loading to 2 percent drift in the 45° direction with one flange tip in compression. The subsequent orthogonal load step, once again loading to 2 percent drift in the flange-in-tension direction, caused two more bars in the web tip to buckle. Testing of the specimen in the web direction was discontinued. Figure 5.9 through Figure 5.16 show the specimen at this point in the testing, at the maximum displacement, prior to unloading, similar to the other photographs in this chapter.

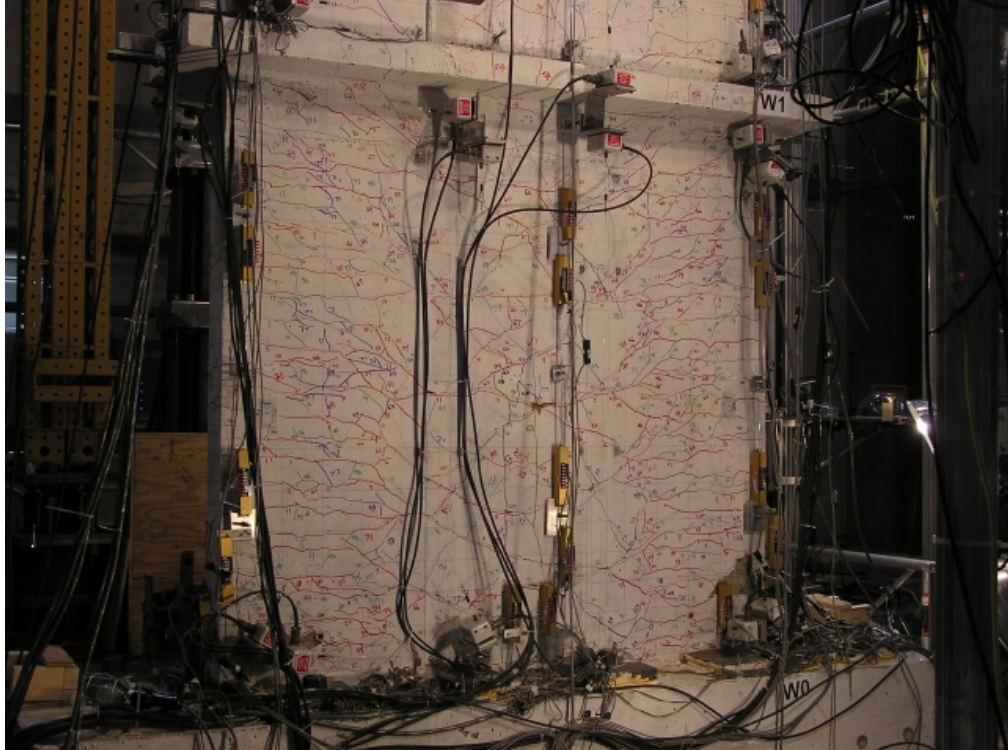


Figure 5.9. First story flange of NTW1 after web failure.

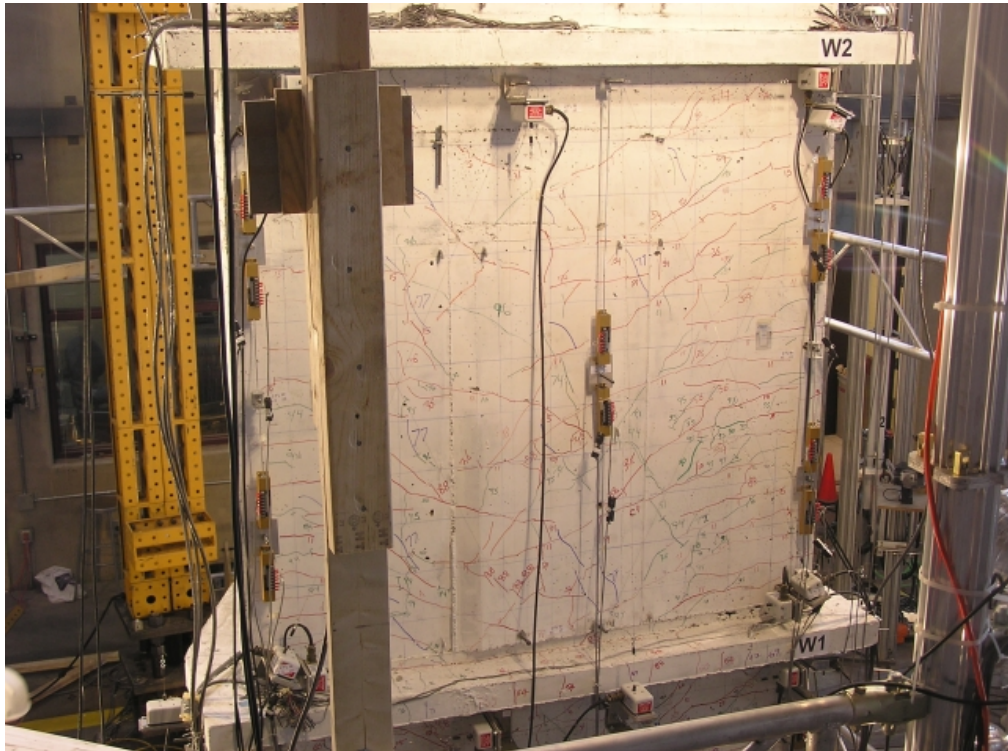


Figure 5.10. Second story flange of NTW1 after web failure.



Figure 5.11. Third story flange of NTW1 after web failure.



Figure 5.12. Fourth story flange of NTW1 after web failure.

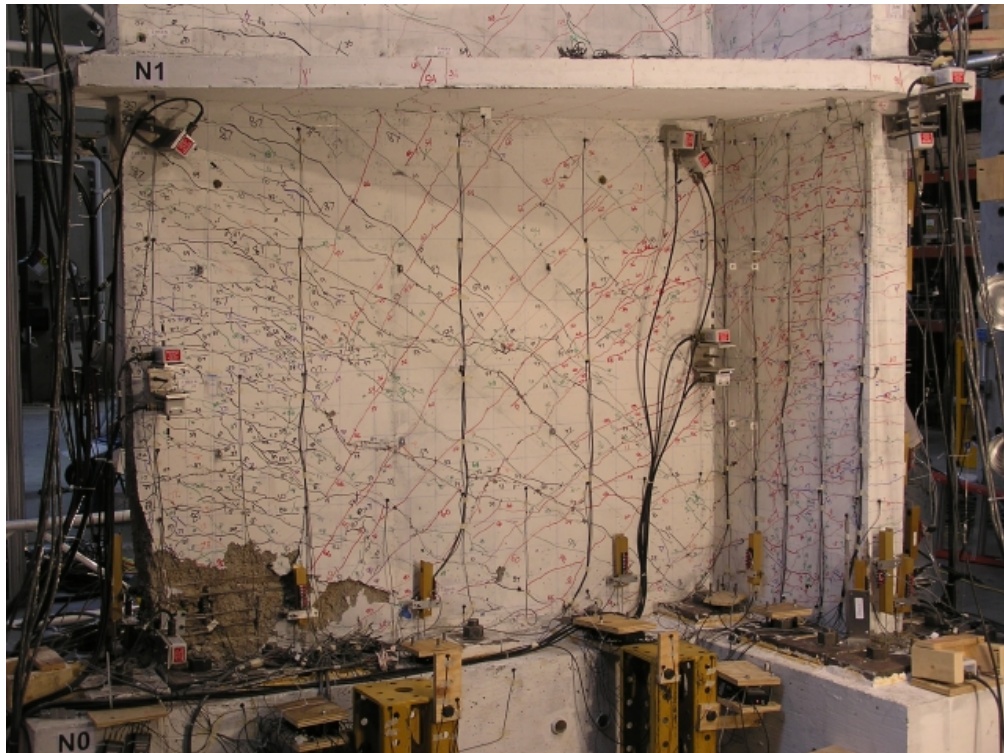


Figure 5.13. First story web of NTW1 after web failure.

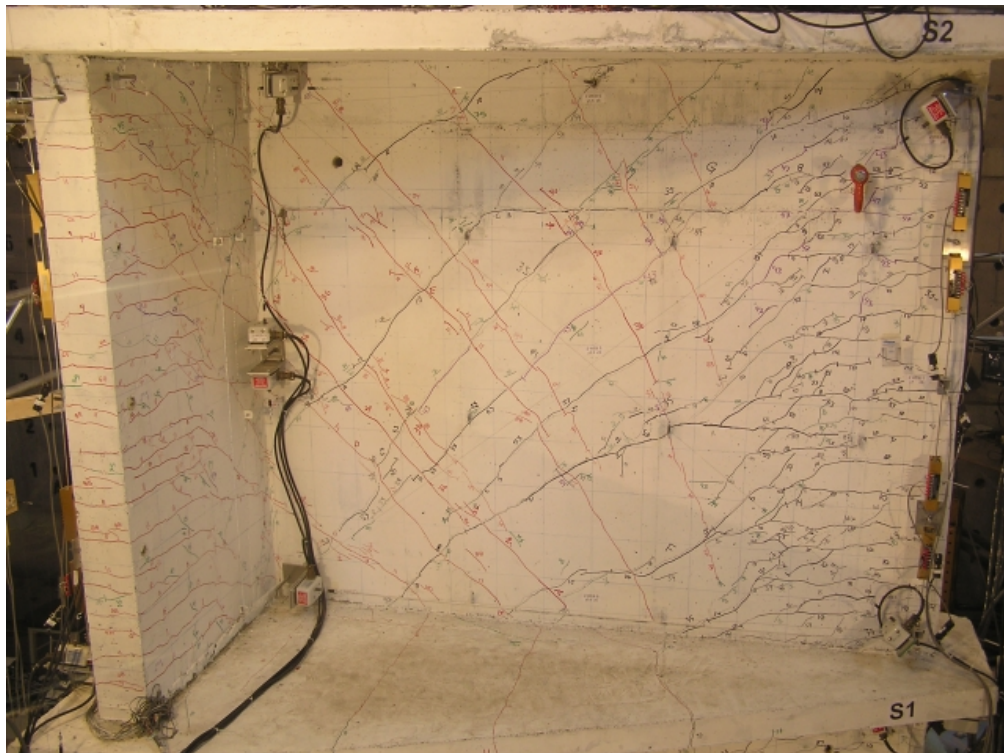


Figure 5.14. Second story web of NTW1 after web failure.

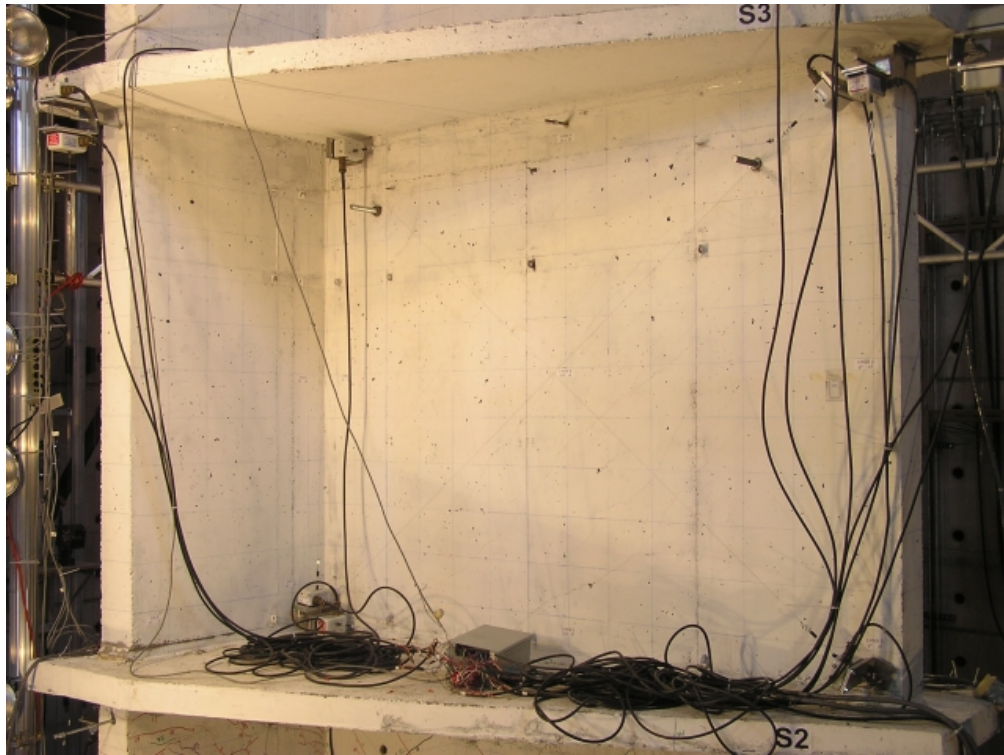


Figure 5.15. Third story web of NTW1 after web failure.

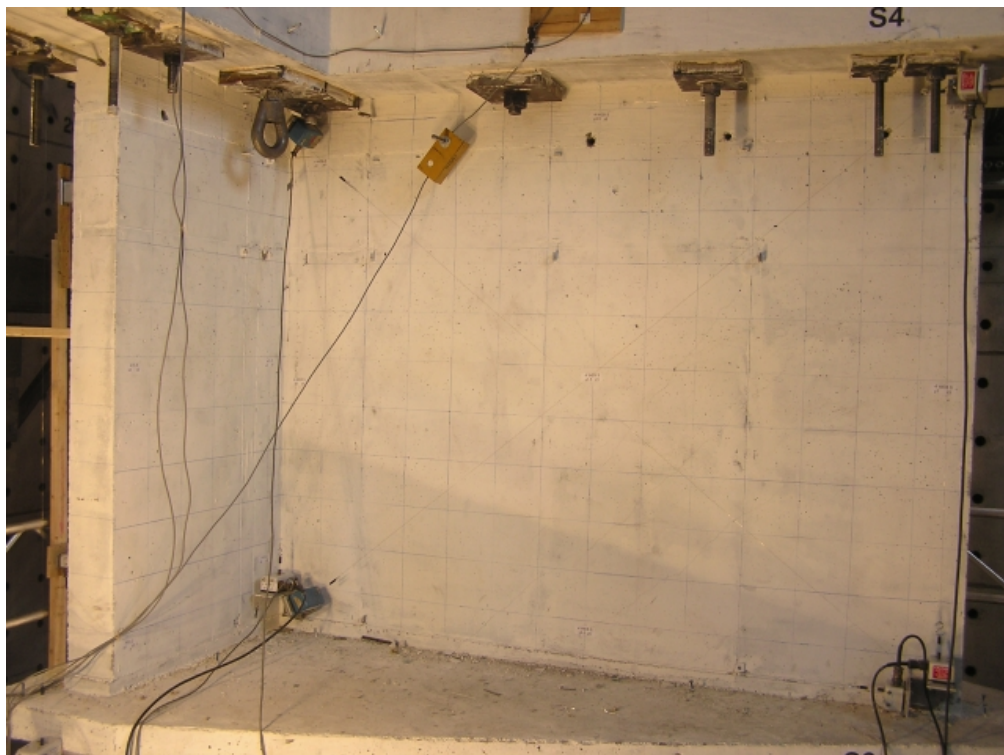


Figure 5.16. Fourth story web of NTW1 after web failure.

Load was applied in the flange direction to 1.5 percent, 2.0 percent, and 2.5 percent drift levels without severe damage observed. Spalling from the flange tips was observed in the second cycle to 3 percent drift, but the loads reached in the second and third cycles did not decrease substantially from the first cycle. Crushing of the flange tips occurred in the first ramp to 4 percent drift, causing a substantial loss of capacity. Unloading and reloading in the opposite direction caused three bars in tension to fracture, in addition to causing buckling of bars in compression. The specimen was still able to resist gravity load, so the specimen was tested to failure in the web direction. Loading to 2 percent drift in the flange-in-compression direction caused four previously buckled bars in the web tip to fracture. Attempting to load to 2 percent drift in the flange-in-tension direction caused crushing of the web, including spalling in the unconfined region. The web was damaged from the tip to approximately 36 in. towards the flange, and from the base block up approximately 30 in. The specimen was no longer able to resist the applied gravity load, and the test was ended. Figure 5.17 through Figure 5.24 show the specimen at the end of testing.

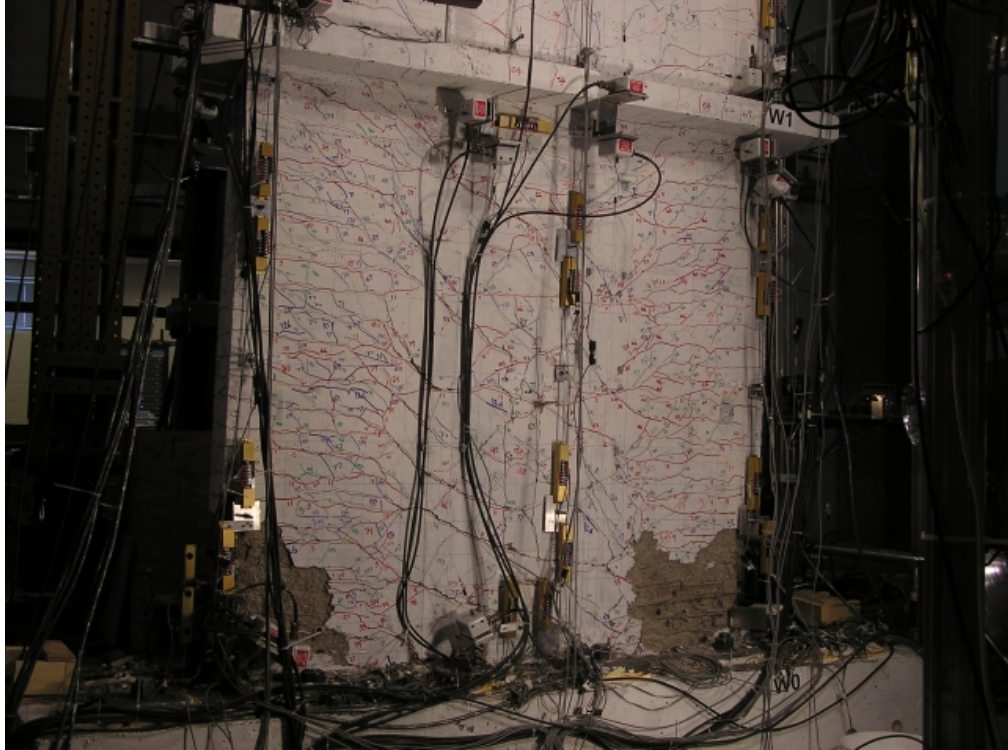


Figure 5.17. First story flange of NTW1 after flange failure.

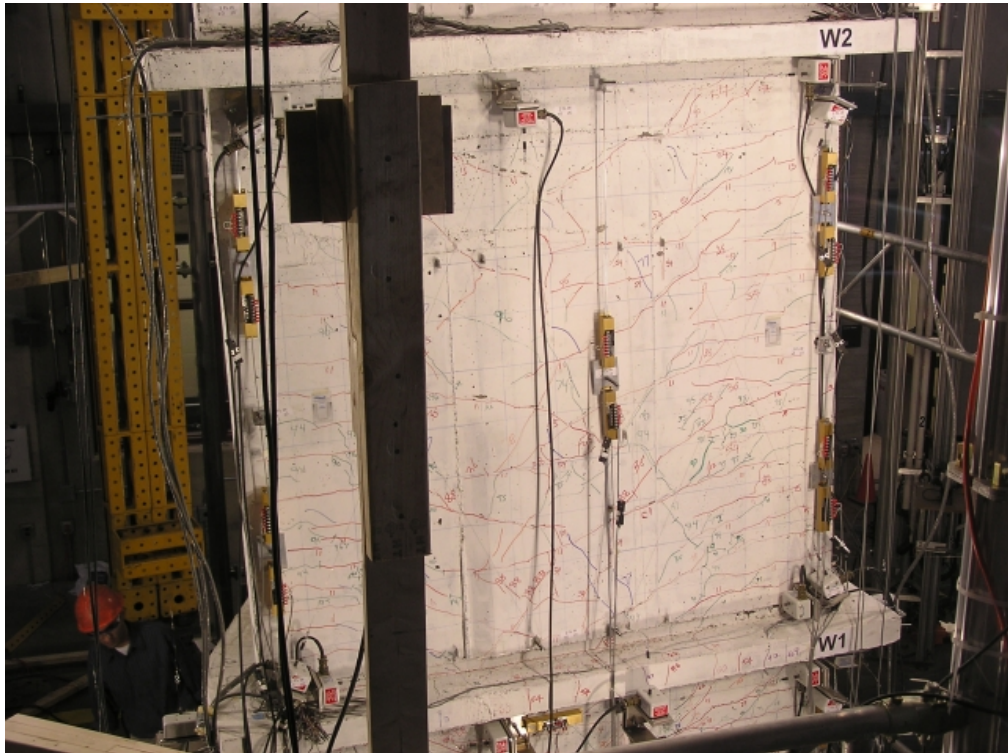


Figure 5.18. Second story flange of NTW1 after flange failure.

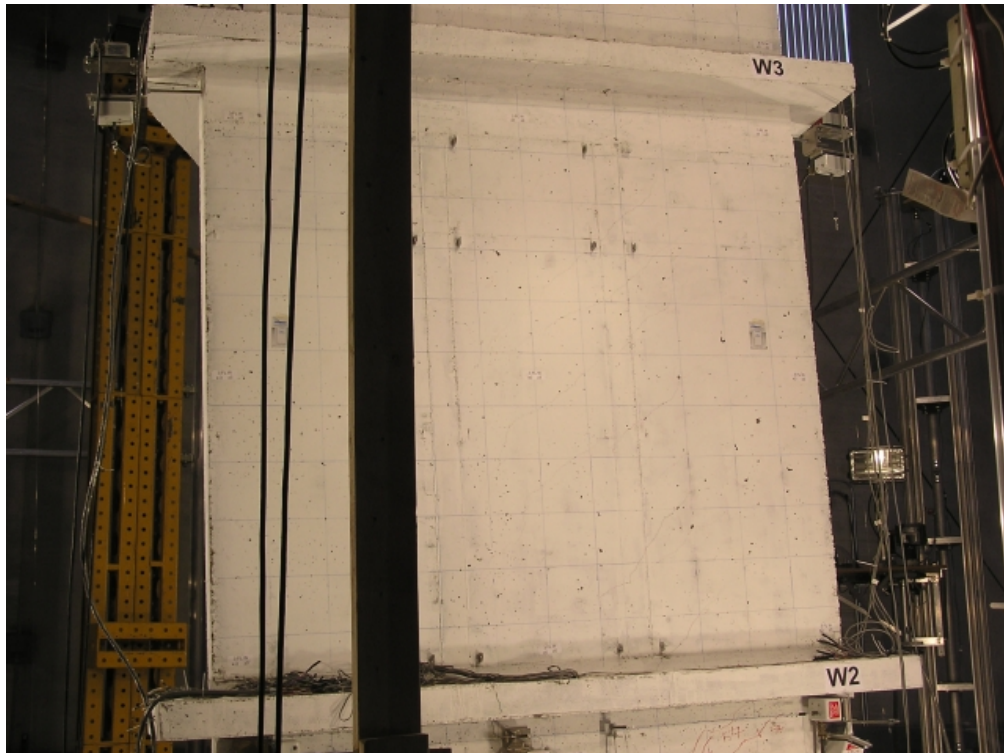


Figure 5.19. Third story flange of NTW1 after flange failure.



Figure 5.20. Fourth story flange of NTW1 after flange failure.

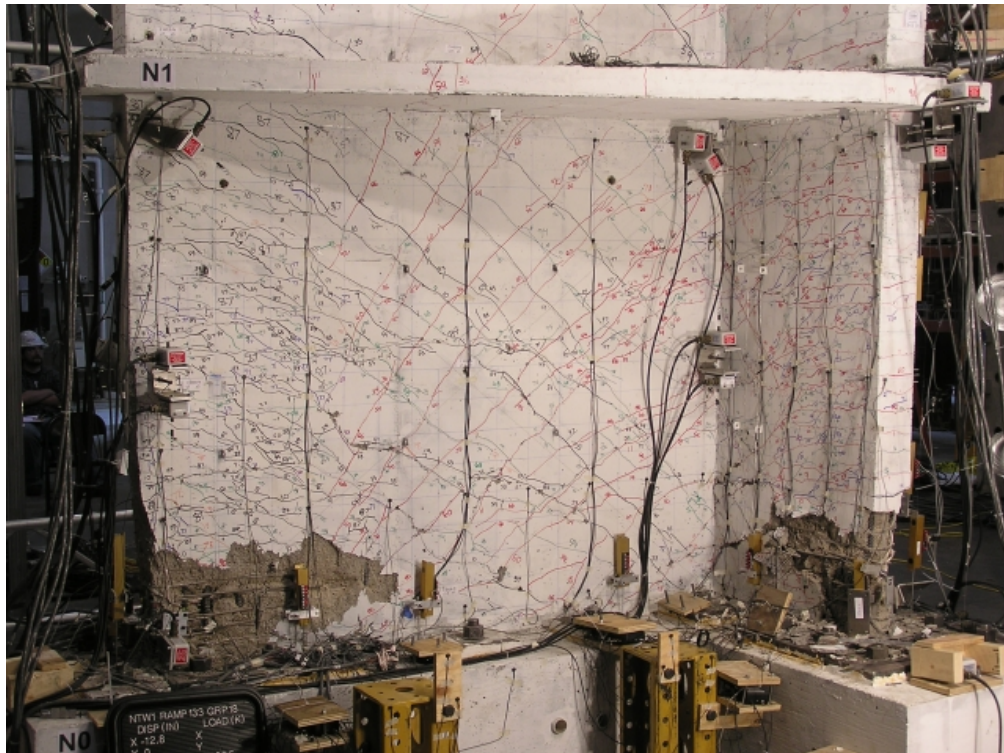


Figure 5.21. First story web of NTW1 after flange failure.

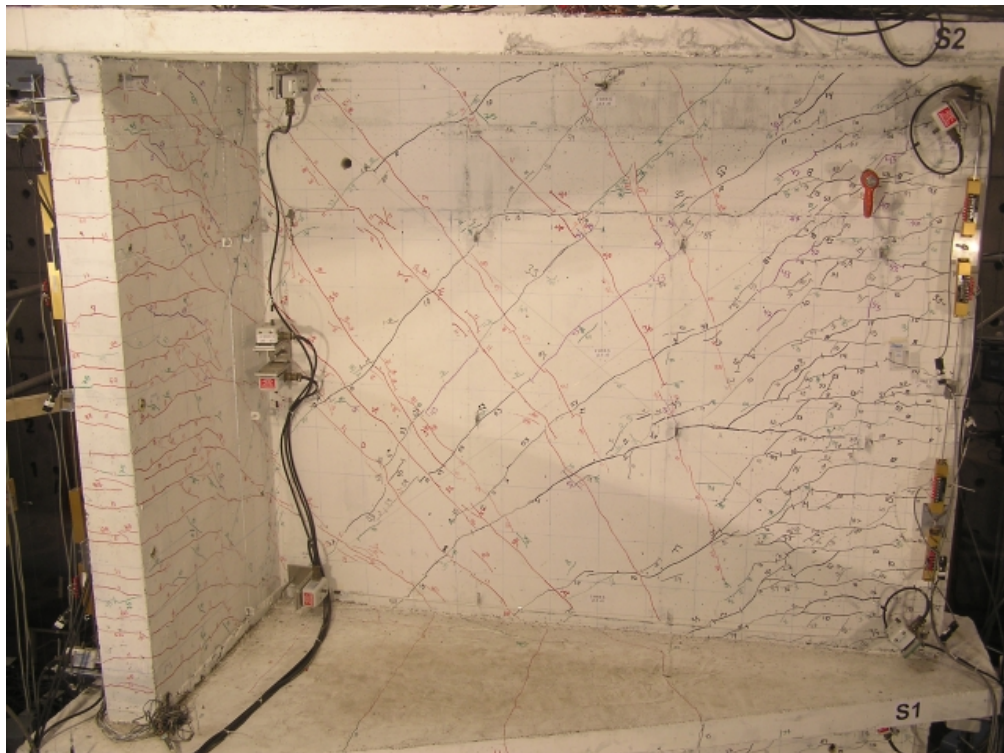


Figure 5.22. Second story web of NTW1 after flange failure.

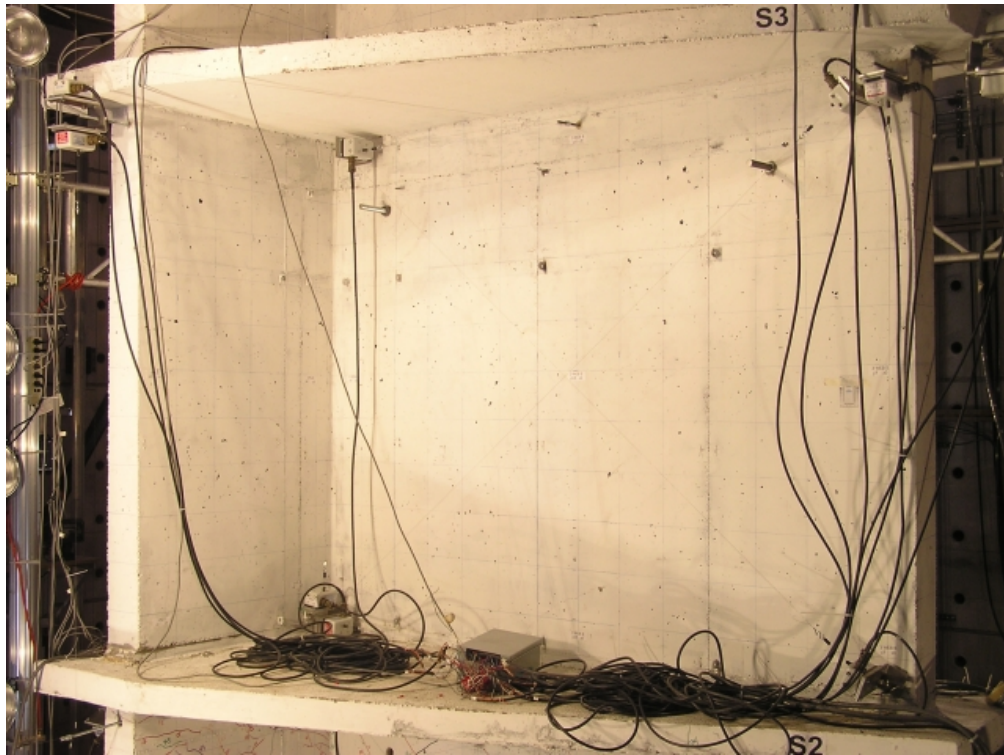


Figure 5.23. Third story web of NTW1 after flange failure.

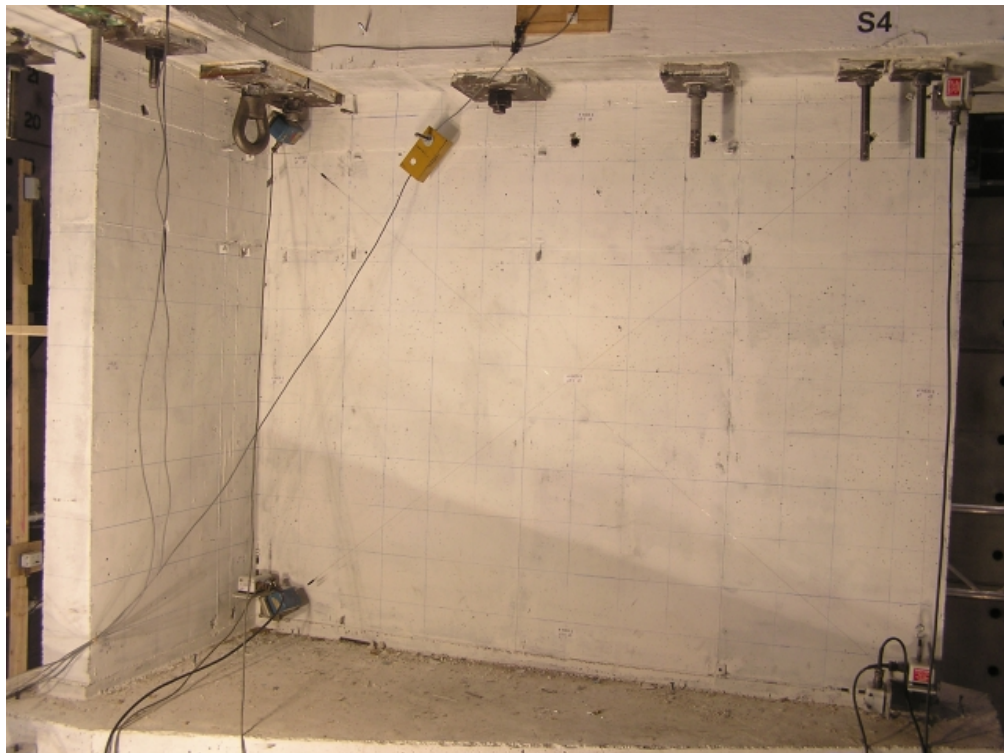


Figure 5.24. Fourth story web of NTW1 after flange failure.

### 5.2.3 Post-Testing Autopsy of Specimen

After testing was complete, the specimen was cut off at approximately mid-height of the first story and a small jackhammer was used to carefully remove the concrete from this portion, where the damage was concentrated, to examine the condition of the longitudinal and confining reinforcement. While it was obvious prior to the autopsy that the section was severely damaged and 135° hooks on hoops in the web had “unwound” (i.e., opened) to approximately 90°, as shown in Figure 5.25, much of the damage to the confining hoops was not apparent until the concrete was removed. It was found that several confining hoops between 2 and 10 in. above the foundation in each of the boundary elements were either severely deformed or fractured. The bottom 2 to 4 in. closest to the foundation block was not damaged as severely; the cover had spalled, but the core was intact. This was likely the result of the foundation providing some extra restraint to this portion of the wall. Figure 5.26 through Figure 5.28 show the three boundary elements after the loose concrete was removed to expose the confining steel. Additional photographs from this investigation are included in Appendix D.

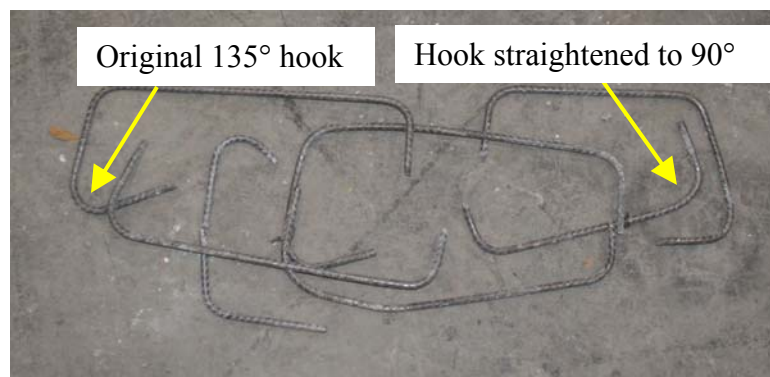


Figure 5.25. Damage to confining hoops near foundation block.

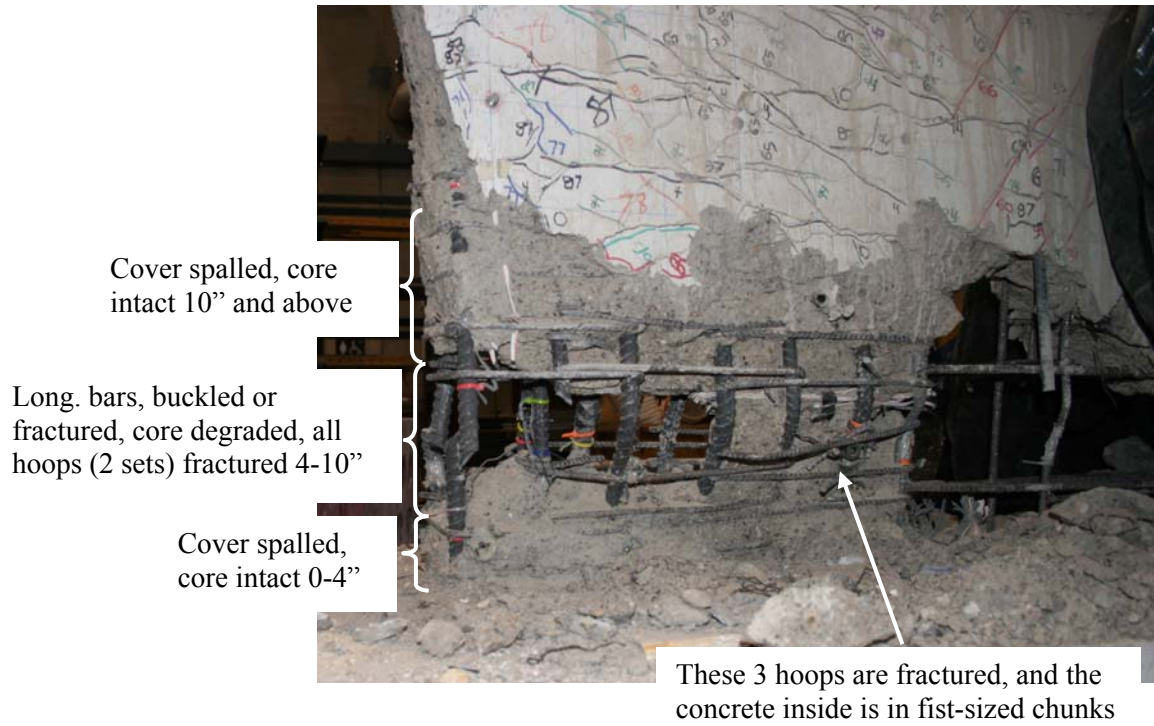


Figure 5.26. Web tip after removal of loose concrete.

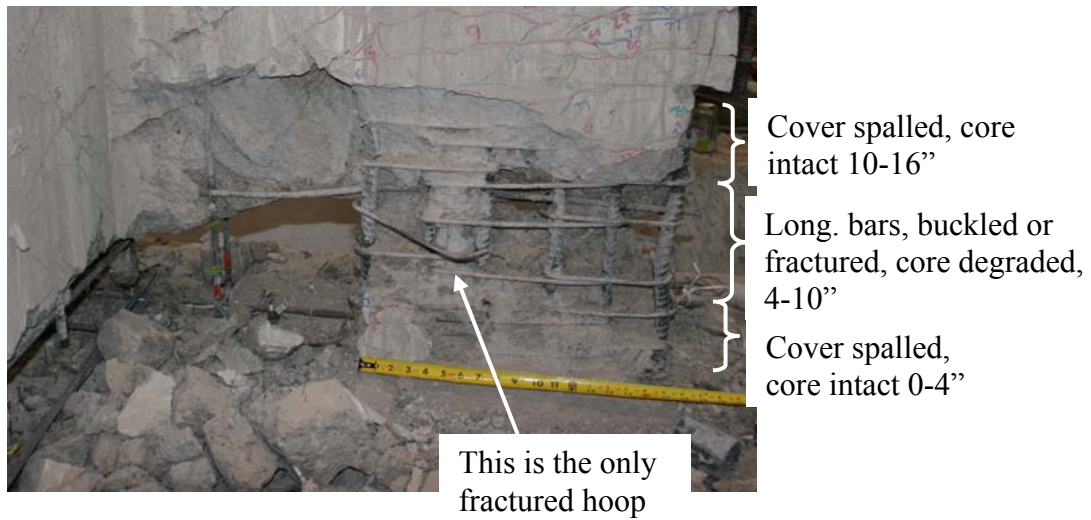


Figure 5.27. North flange tip after removal of loose concrete.

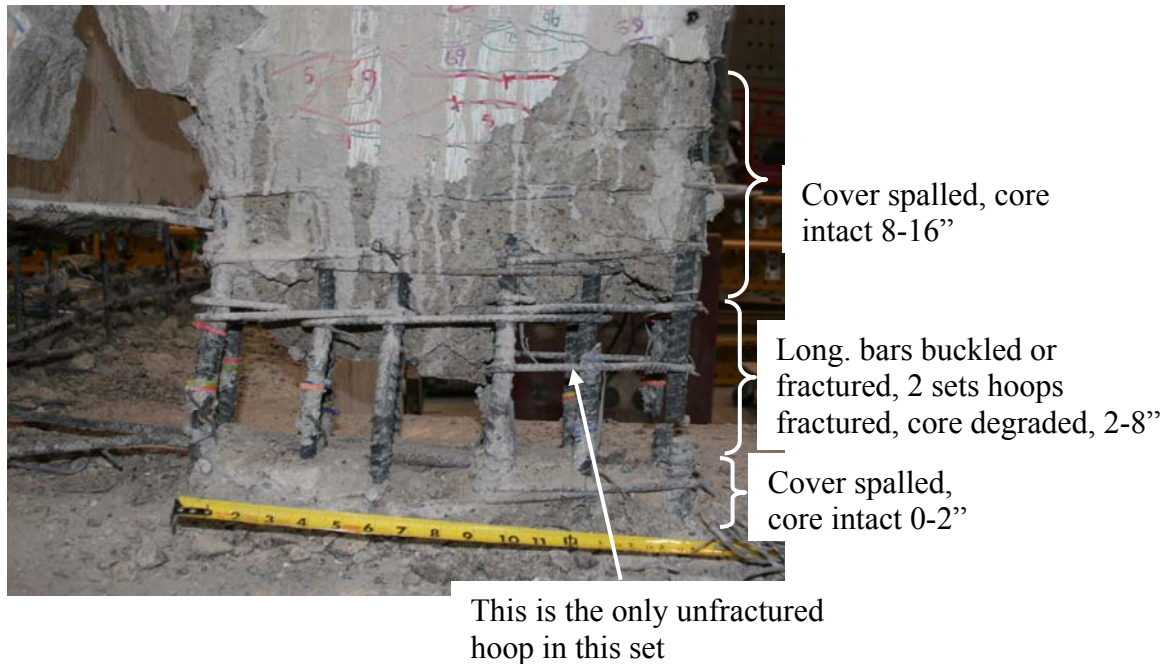


Figure 5.28. South flange tip after removal of loose concrete.

### 5.3 Load versus Displacement Response

Figure 5.29 through Figure 5.31 show the orthogonal components of the measured load versus displacement response of the specimen. Figure 5.29 shows the flange-direction response over the entire load history, Figure 5.30 shows the flange-direction response in the early part of the test, and Figure 5.31 shows the web-direction response over the entire load history. The orthogonal components of the skew direction loading ramps are distinguished from orthogonal flange-direction and web-direction loads in these plots by the use of dashed lines. When the skew direction loading ramps were decomposed into their orthogonal components, the elastic stiffnesses in each orthogonal direction were found to be similar to the stiffness associated with orthogonal loading. After yielding, the flange direction component of the response under skew direction

loading varied from the orthogonal loading, while the web direction component of the response did not. This is likely due to the skew direction loading itself, as opposed to being the result of the order of the load history and damage accumulating in the specimen over the course of the test. As mentioned above, Figure 5.30 shows the same data as Figure 5.29, but only the first portion of the testing is shown, for clarity. In this figure, the stiffer skew direction loading cycle, marked “2,” was conducted between the two orthogonal directional loading cycles, marked “1” and “3”. Multidirectional loading effects are discussed further in Chapter 7.

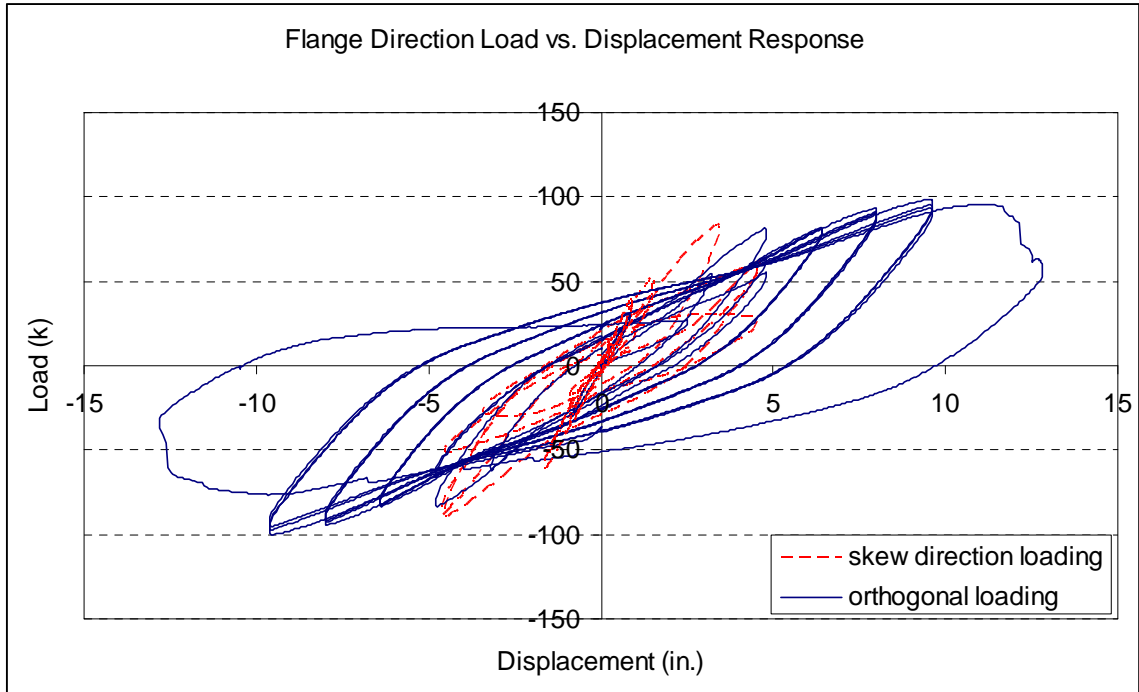


Figure 5.29. Flange direction load versus displacement response of NTW1

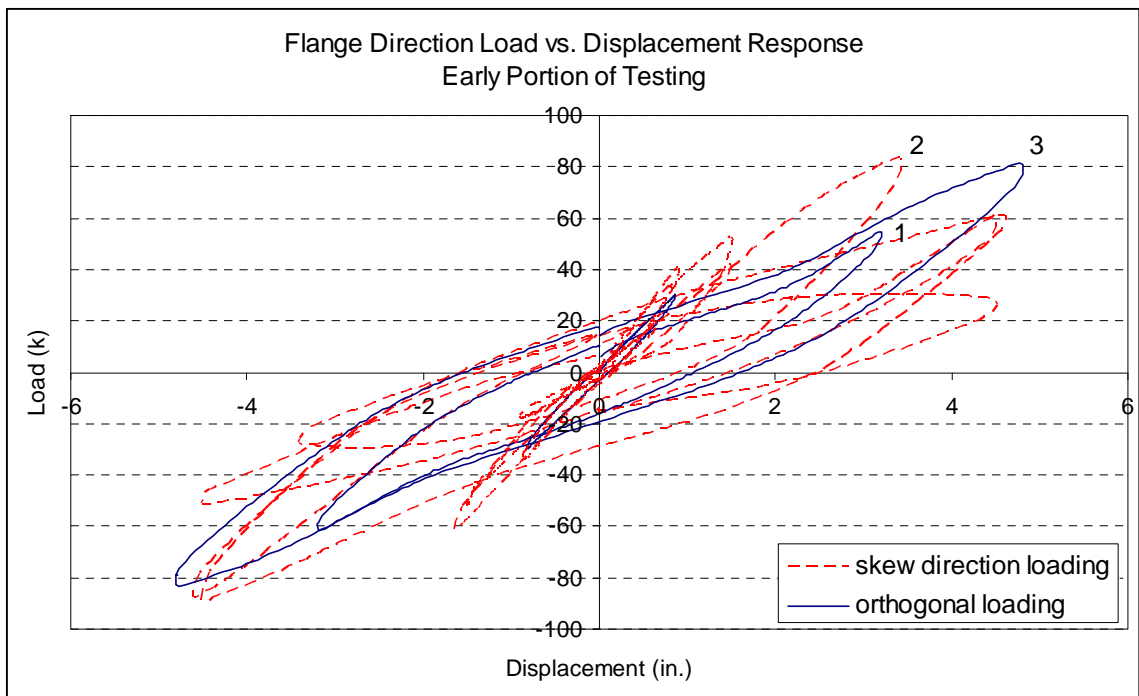


Figure 5.30. Flange direction load versus displacement response of NTW1, early portion of test

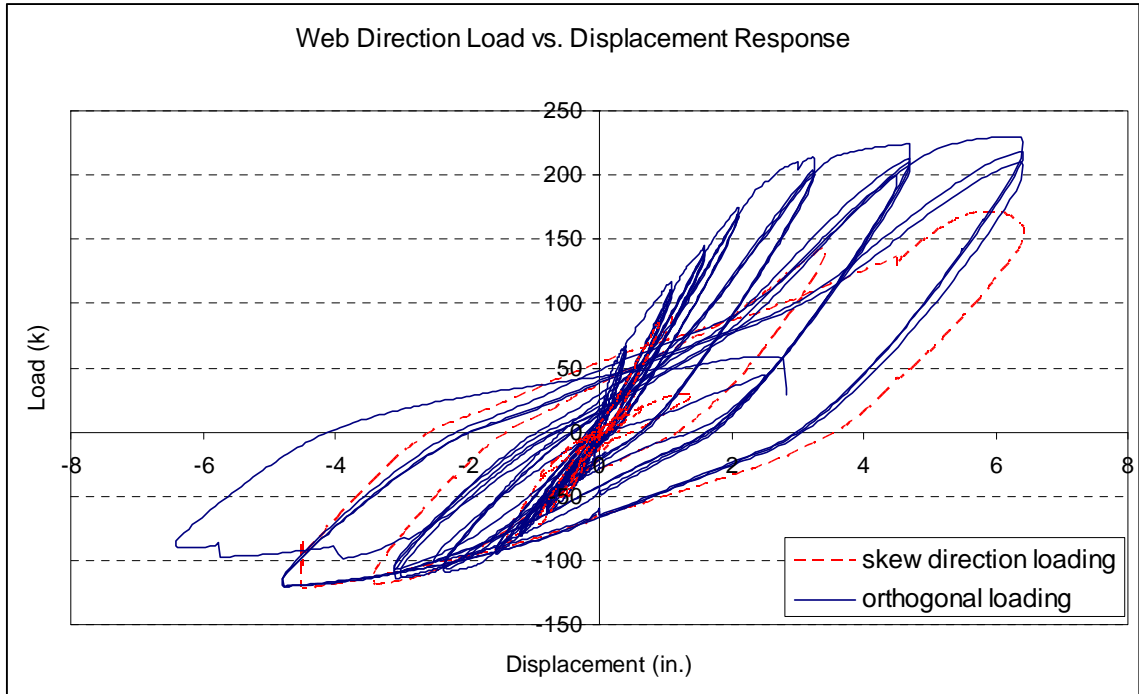


Figure 5.31. Web direction load versus displacement response of NTW1

#### 5.4 Components of Deformation

The contributions of each component of deformation, flexure, shear, strain penetration, and splice slip, were calculated using the external instrumentation attached to the wall. Data collected with the Krypton measuring system were used to determine the contributions of shear and flexure to the deformation of the first story. Data collected with LVDTs and string pots were used to determine the contributions of shear and flexure in the second story, as well as strain penetration at the foundation. Chapter 4 further describes these calculations and the choice of instruments. Near the end of the applied loading history, the lower tier of instruments was removed. The concrete near the instruments was extensively spalled, and there was some concern that leaving the instruments would subject them to damage. Additionally, many of the embedded studs

used to support the instruments were becoming loose in the concrete, rendering those measurements unreliable.

Several plots in the following sections refer to various heights on the specimen. Figure 5.32 shows the positions of representative heights and instrumentation panels on the specimen for reference. Only the first and second stories of the flange were instrumented to separate shear and flexural deformations, so components of deformation are not reported for the third and fourth stories in the flange loading direction.

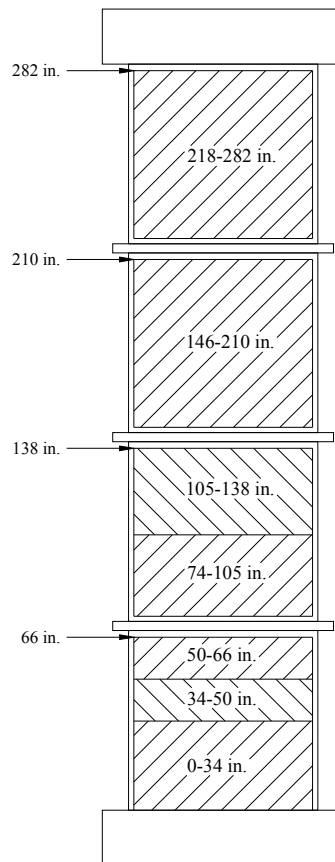


Figure 5.32. Locations of measurement panels on NTW1.

#### **5.4.1 Flexure**

Figure 5.33 and Figure 5.34 show the measured moment versus curvature relationships over the height of the specimen for the flange and web loading directions, respectively. In the flange direction, nonlinear flexural deformations were present over the entire first story of the structure and into the lower half of the second story. Strain gauge data indicated that bars in the flange tip were yielded over the entire height of the first and second stories, and into the third story. In the web direction, the moment versus curvature plots suggest that the plastic hinge length was shorter, with nonlinearity restricted to the first story. However, the data recorded with the strain gauges indicated that the longitudinal reinforcement in the web had yielded over the entire height of the first and second stories, in both the flange-in-tension and flange-in-compression directions.

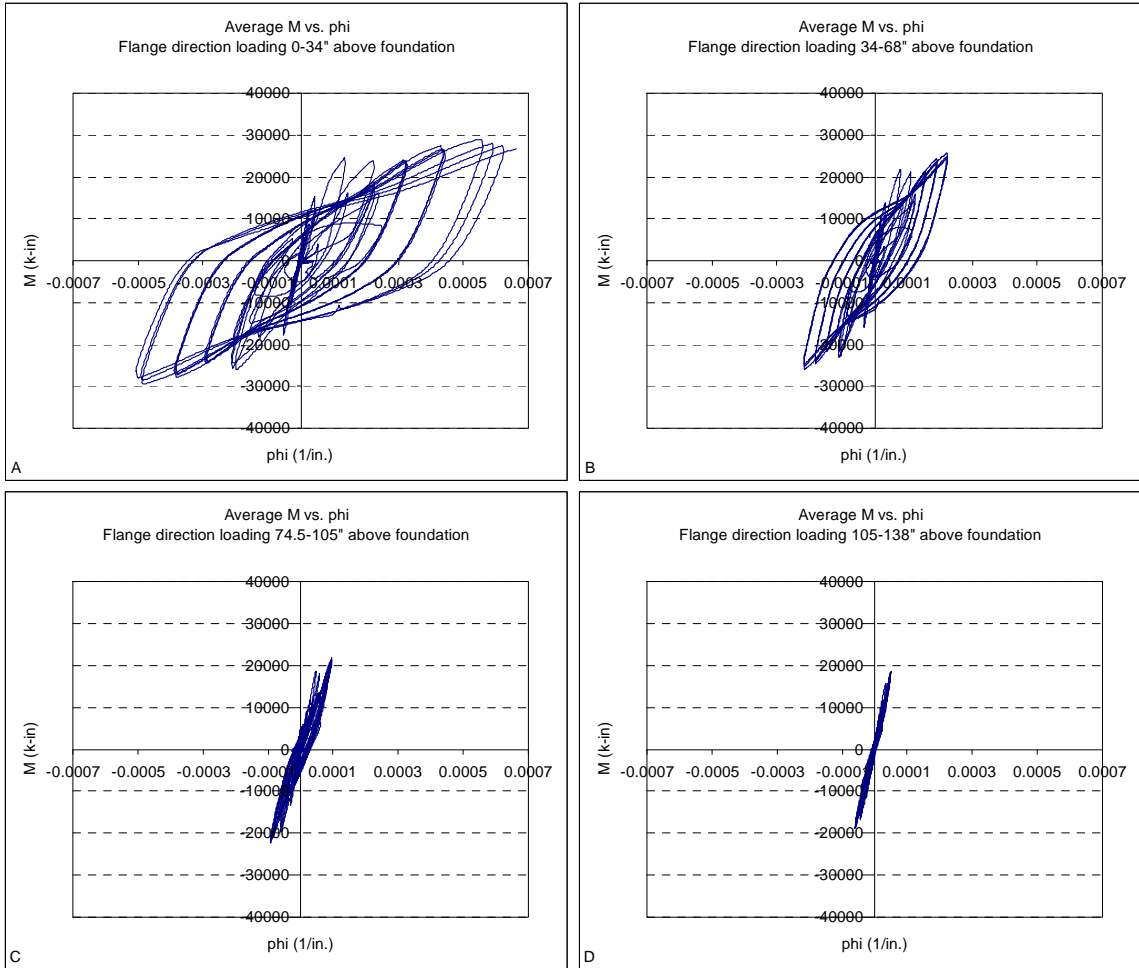


Figure 5.33. Flange direction moment versus curvature relationships for NTW1

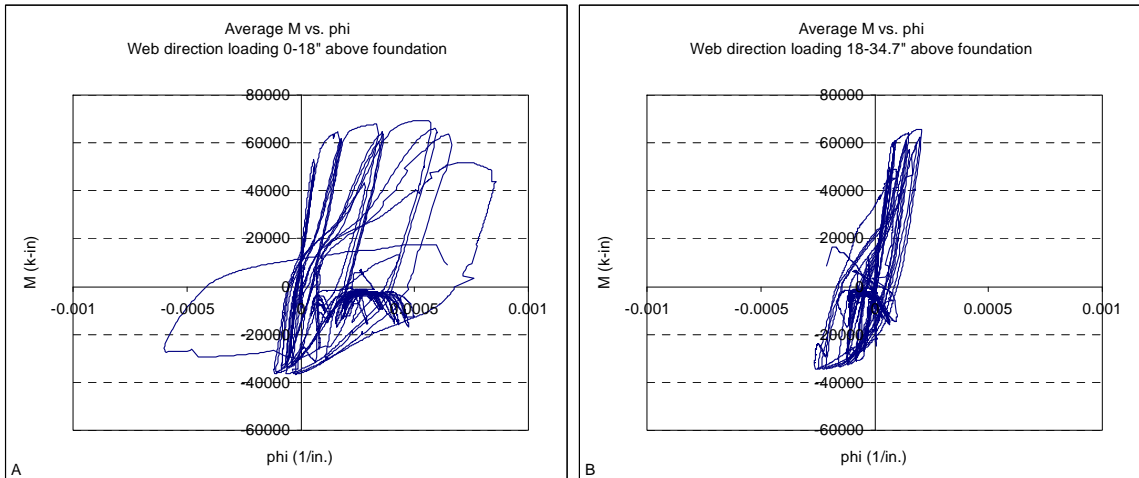


Figure 5.34. Web direction moment versus curvature relationships for NTW1

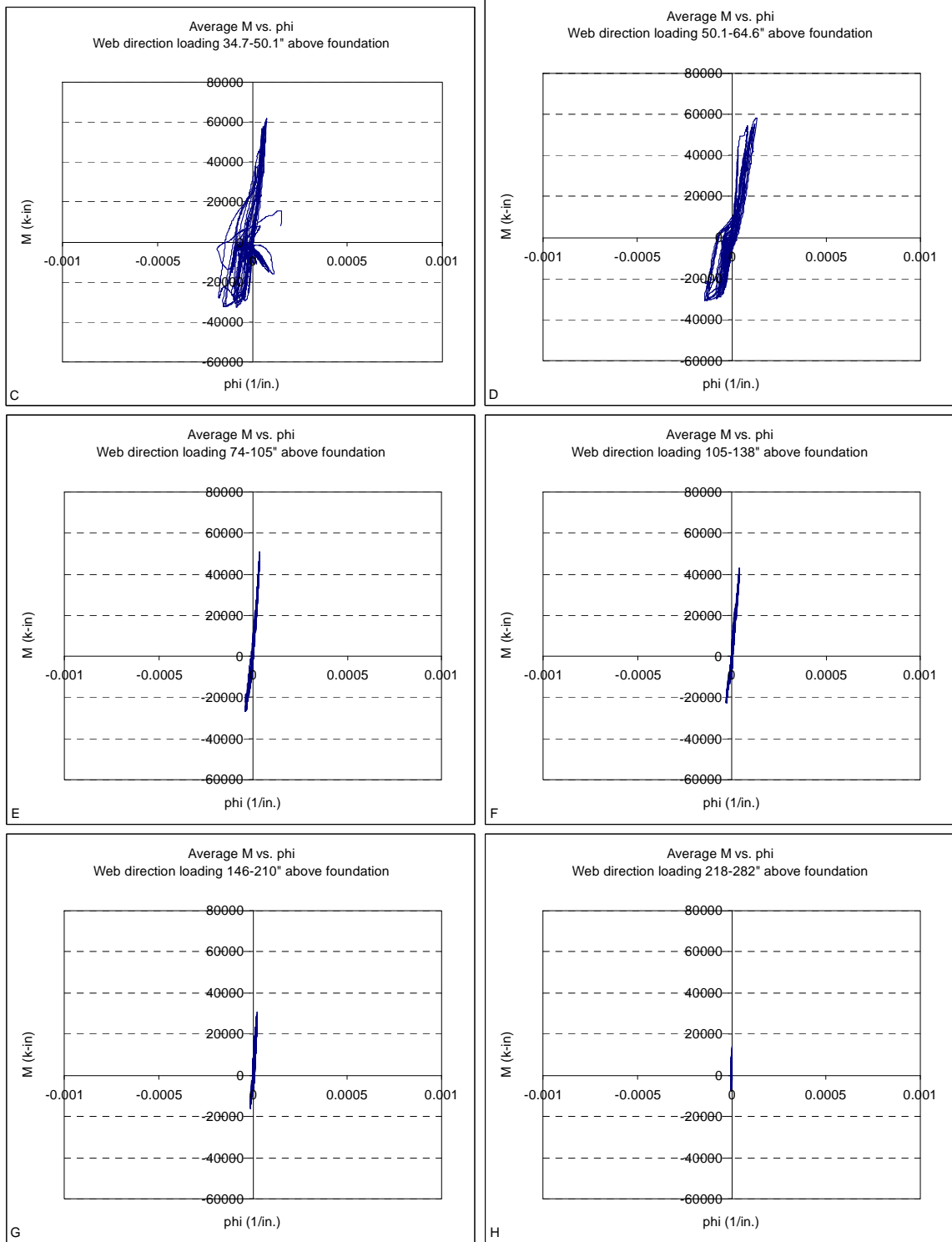


Figure 5.34. Web direction moment versus curvature relationships for NTW1, cont.

## 5.4.2 Shear

Figure 5.35 and Figure 5.36 show the average shear force versus shear strain over the height of each panel for the flange and web loading directions, respectively. The measured shear strains in the first story of the flange were approximately three times larger than those in the second story. In the web, the shear strains decreased with height in the first story, with strains in the bottom quarter approximately three times greater than those in the top quarter. Strains continued to decrease over the second and third stories, with similar magnitudes in the third and fourth stories, although the fourth story had a shift. Because the shear force applied to the specimen was constant over its height, the larger shear deformations toward the base provide an indication of the effect that plastic hinging and flexural damage have on shear deformations and reducing shear stiffness.

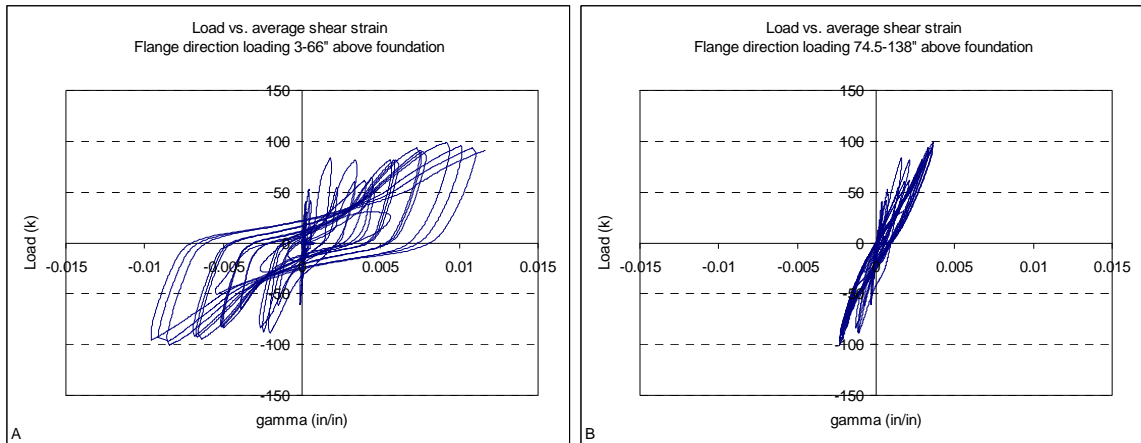


Figure 5.35. Flange direction shear force versus shear strain relationships for NTW1

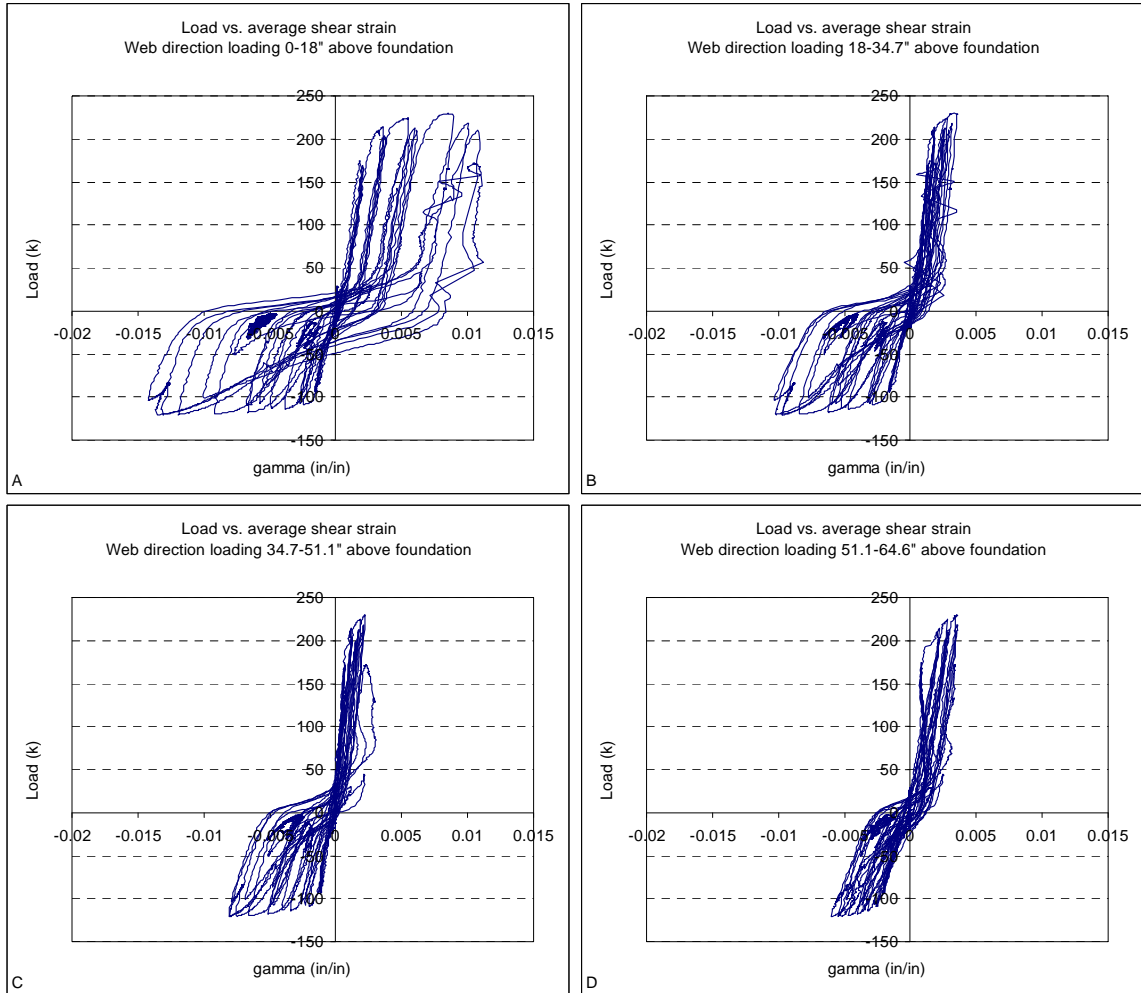


Figure 5.36. Web direction shear force versus shear strain relationships for NTW1

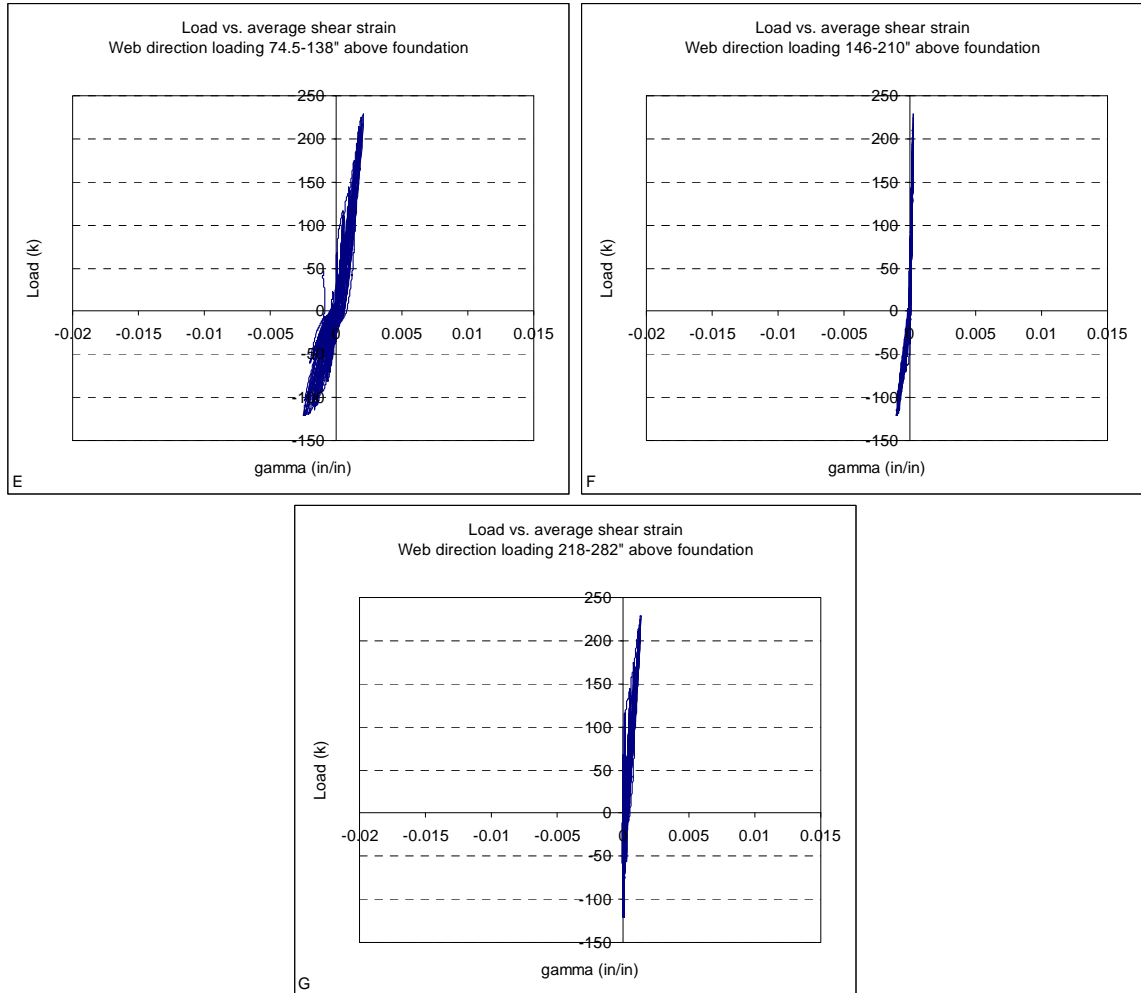


Figure 5.36. Web direction shear force versus shear strain relationships for NTW1, cont.

### 5.4.3 Strain Penetration

Figure 5.37 and Figure 5.38 show the relationship between applied load and rotation at the base of the wall due to strain penetration. Figure 5.39 and Figure 5.40 show the relationship between rotation due to strain penetration and average curvature in the lower portion of the specimen. A strong relationship between these two values was expected because both depend on the strains in the longitudinal reinforcement. There was some linear correlation between the two values in the flange direction, and the rotation due to strain penetration is approximately equal to the rotation expected from an

additional 7.3 in. of wall height (into the foundation). The correlation between the two values was weaker in the web direction, and included a tendency for the rotation due to strain penetration to become more negative, or for the top of the specimen to rotate towards the flange, as the test progressed.

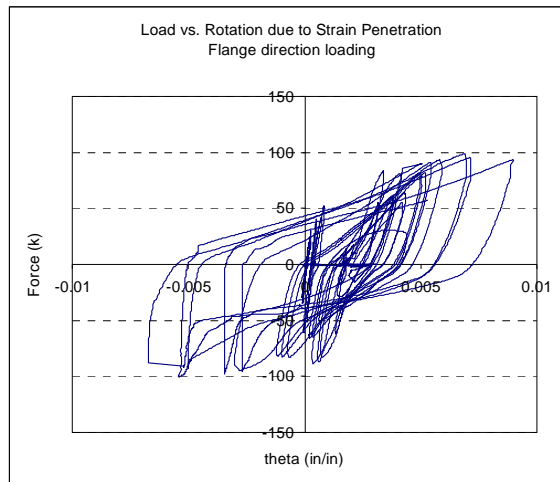


Figure 5.37. Flange direction load versus rotation due to strain penetration relationship for NTW1

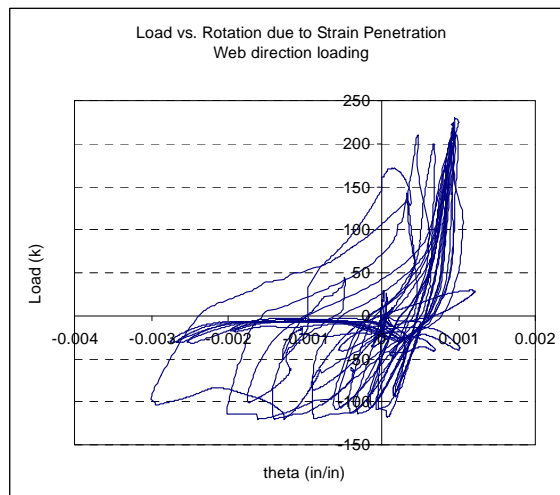


Figure 5.38. Web direction load versus rotation due to strain penetration relationship for NTW1

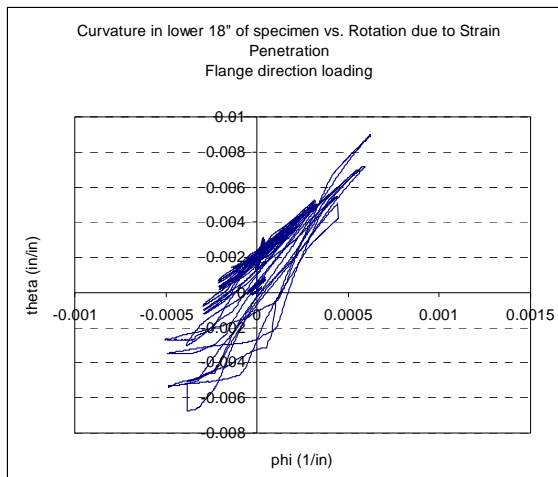


Figure 5.39. Flange direction relationship between curvature in lower portion of wall and rotation due to strain penetration for NTW1

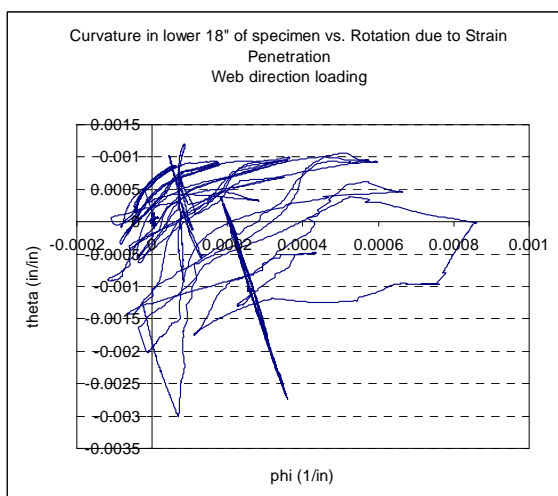


Figure 5.40. Web direction relationship between curvature in lower portion of wall and rotation due to strain penetration for NTW1

#### 5.4.4 Contribution of Components to Total Deformation

Figure 5.41 through Figure 5.46 show the deformation associated with each component of the total deformation along with the total of these components and the deformation measured directly by an external string pot at the top of each instrumented story and for each loading direction. Figure 5.47 through Figure 5.52 plot the fractional contribution of each component to the total deformation at the top of each story for each

peak in the applied loading history relative to the lateral displacement. In each of these tables, the ratio of the total of the components to the directly measured displacement, plotted as the y-axis, should equal one (i.e., the components should sum to the measured displacement). The “total” deformation value plotted in these figures is the sum of the three components of deformation: flexure, shear, and strain penetration. In web-direction loading, the sum of the individual displacement components matches the directly measured value well when the displacement is at least 50 percent of the yield displacement, but the proportional error is larger in the early ramps to 25 percent of the yield displacement. In the flange direction loading, there was significant error in determining the deformation components throughout the test attributed to difficulties with the flange instrumentation. The majority of the error appears to be in the isolation of the flexural component of deformation in the first story of the structure, where the string pots and LVDTs used to measure deformations were subject to inadvertent bumping during the measurement of crack widths. The derived flexural response is not symmetric as expected; it is larger in the positive direction than in the negative direction, suggesting the possibility of error here. These difficulties are discussed further in Sections 4.3 and 4.4. Table 5.1 summarizes the contribution of each component to the total displacement. These values were found by averaging the contribution at each peak in the applied history.

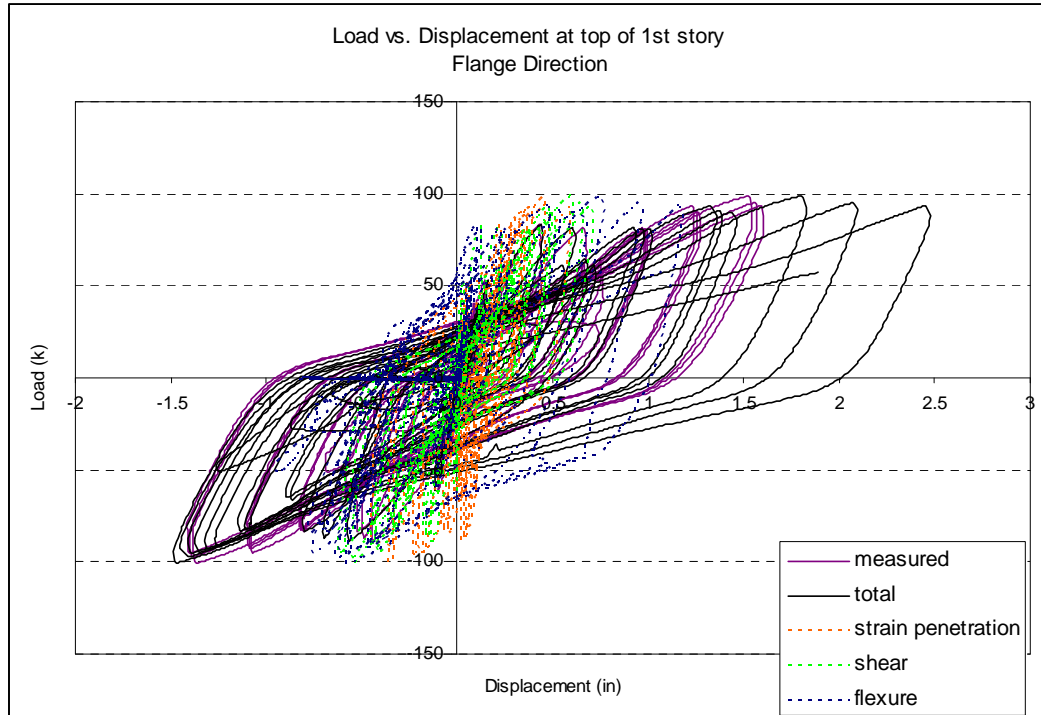


Figure 5.41. Flange direction load versus component displacement, first story, NTW1

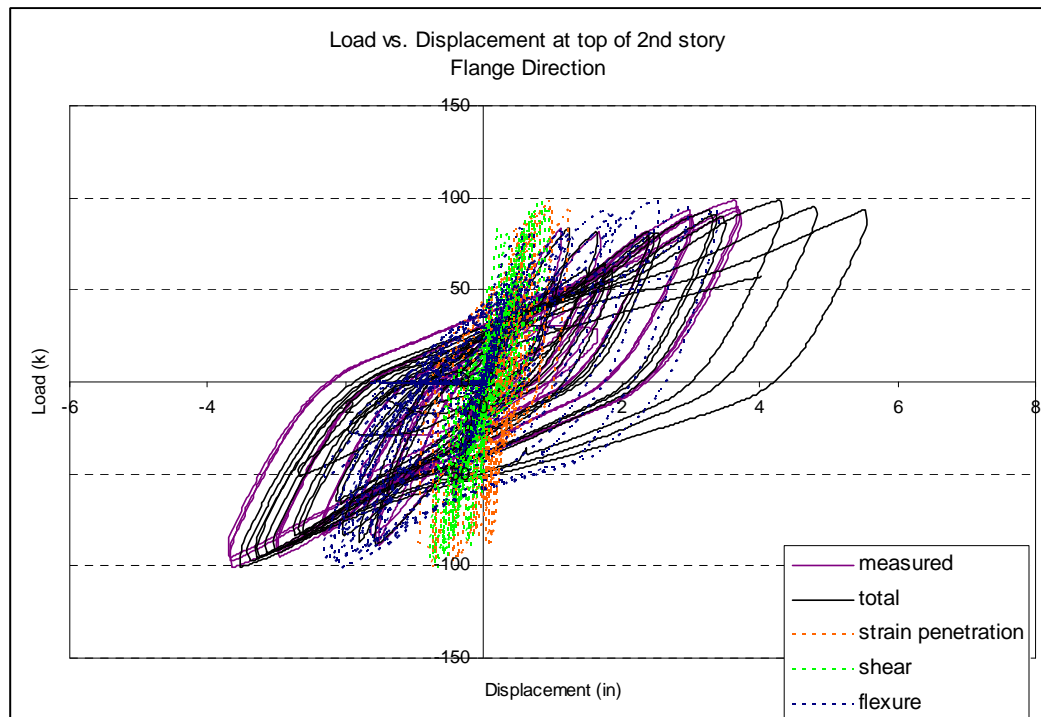


Figure 5.42. Flange direction load versus component displacement, second story, NTW1

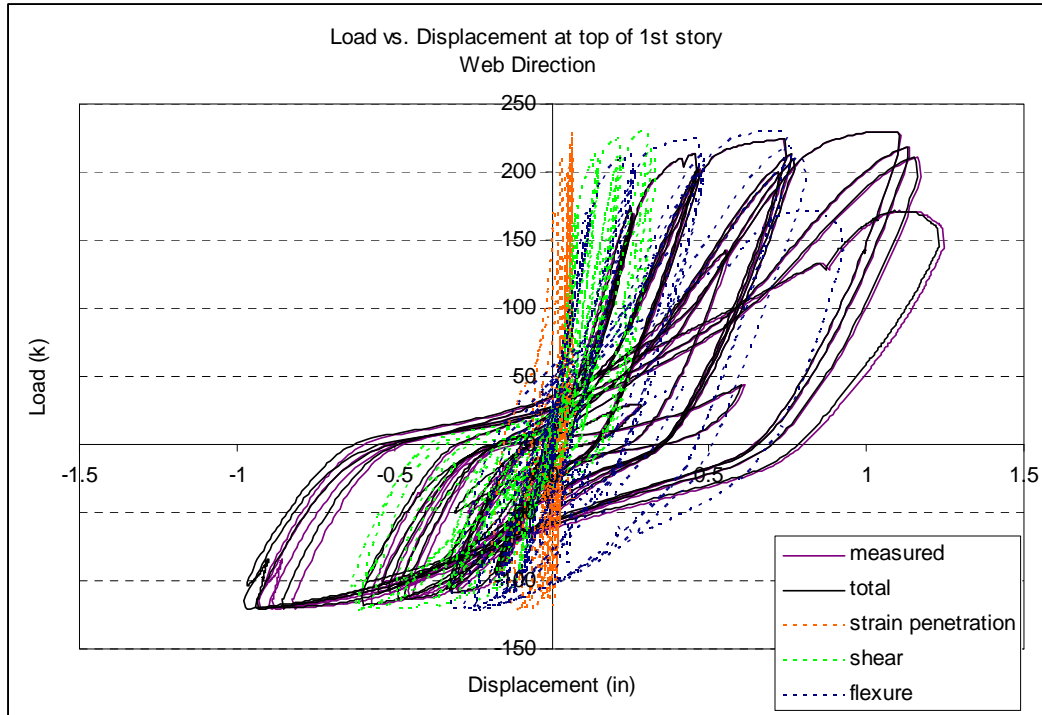


Figure 5.43. Web direction load versus component displacement, first story, NTW1

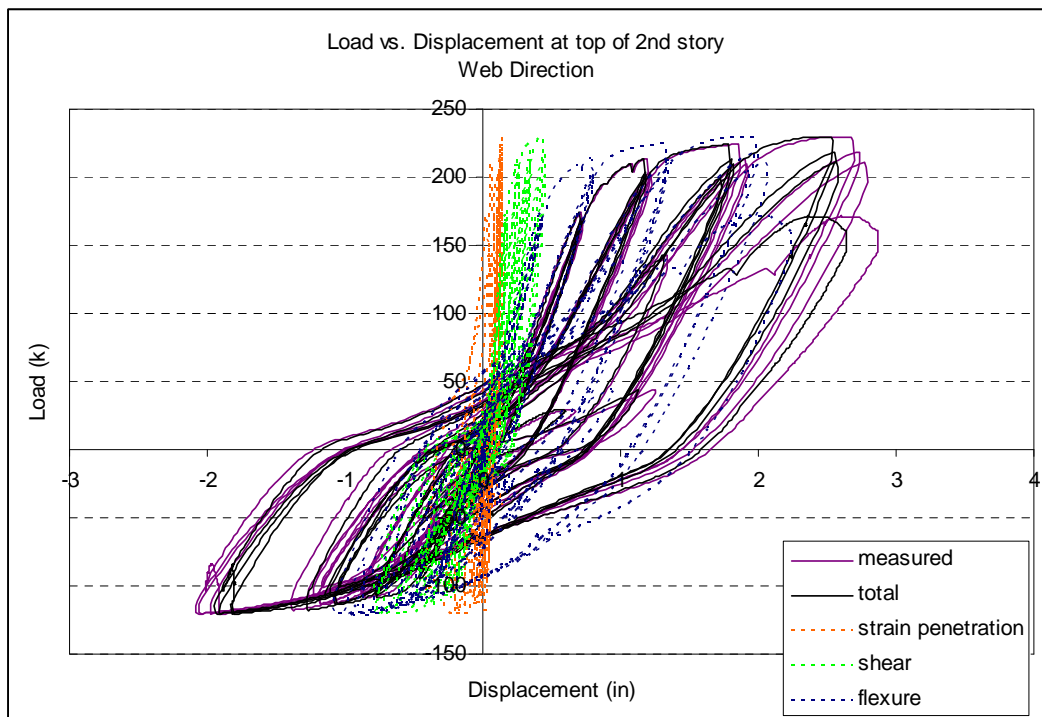


Figure 5.44. Web direction load versus component displacement, second story, NTW1

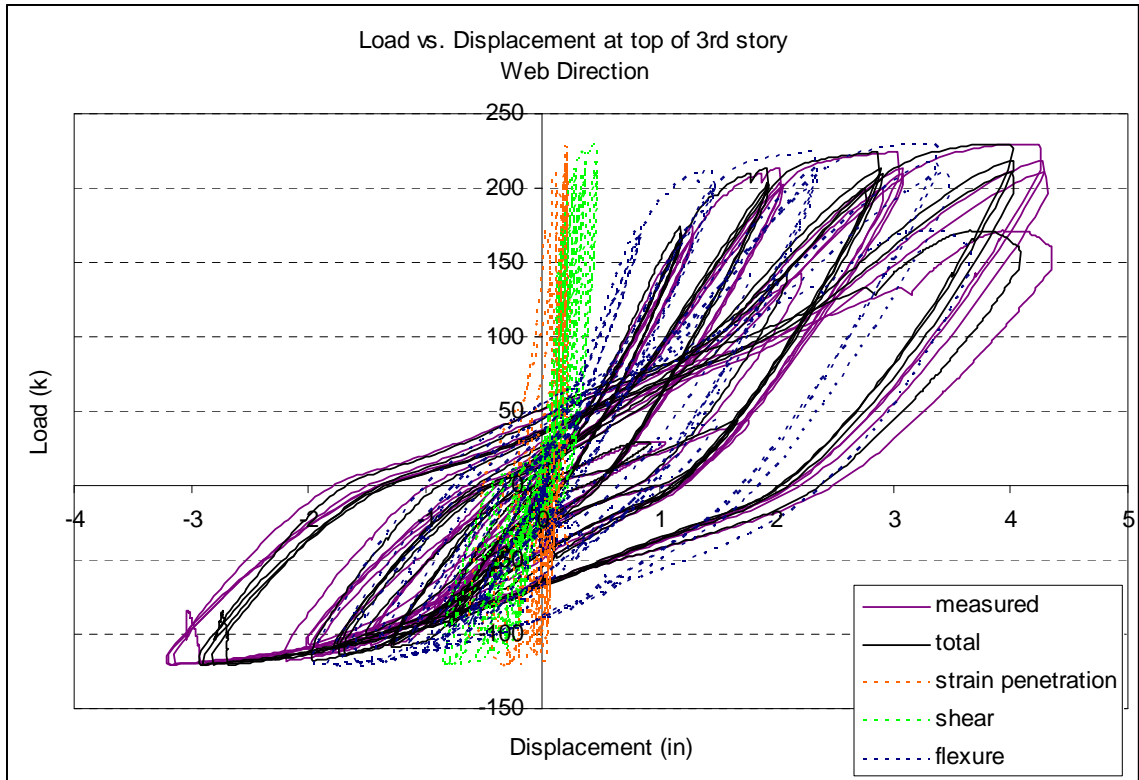


Figure 5.45. Web direction load versus component displacement, third story, NTW1

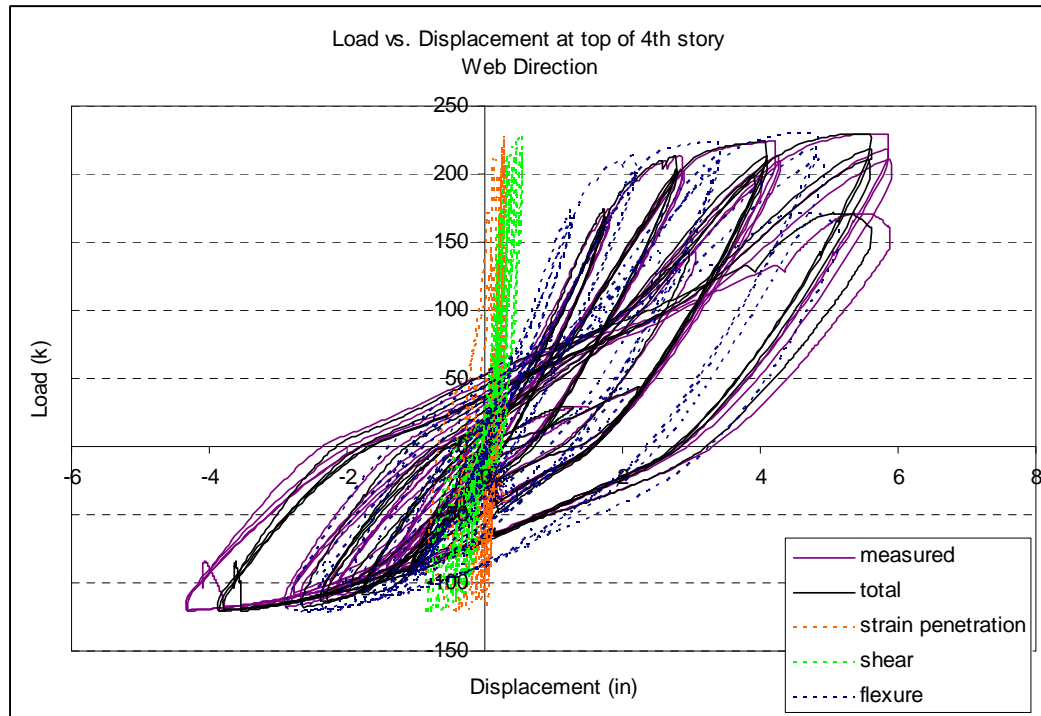


Figure 5.46. Web direction load versus component displacement, fourth story, NTW1

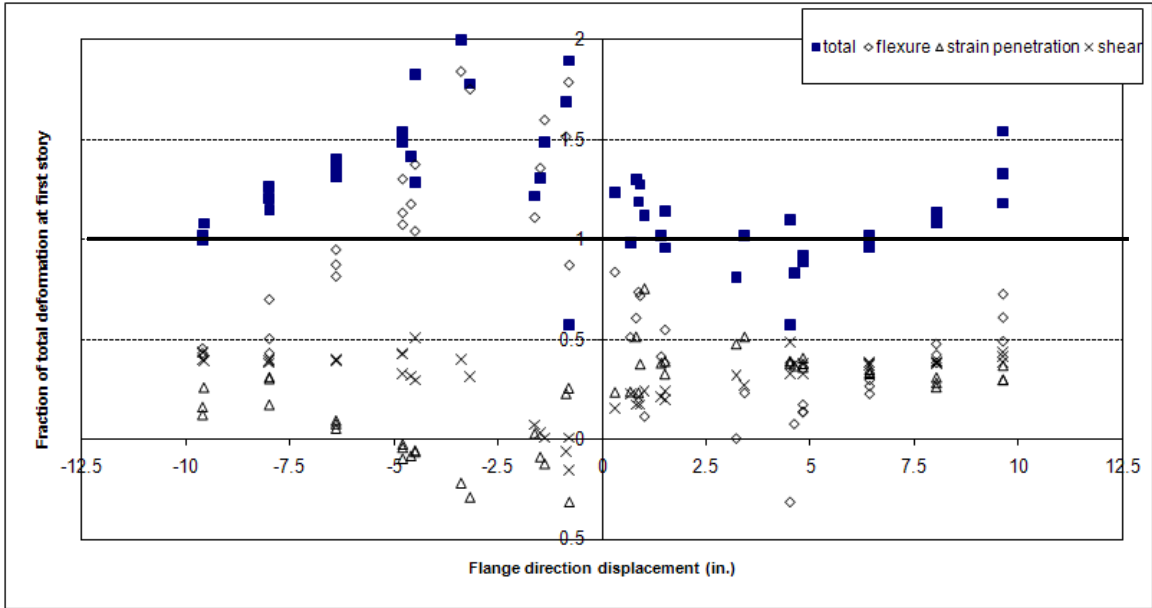


Figure 5.47. Flange direction contribution of each component to total first story displacement versus total displacement, NTW1

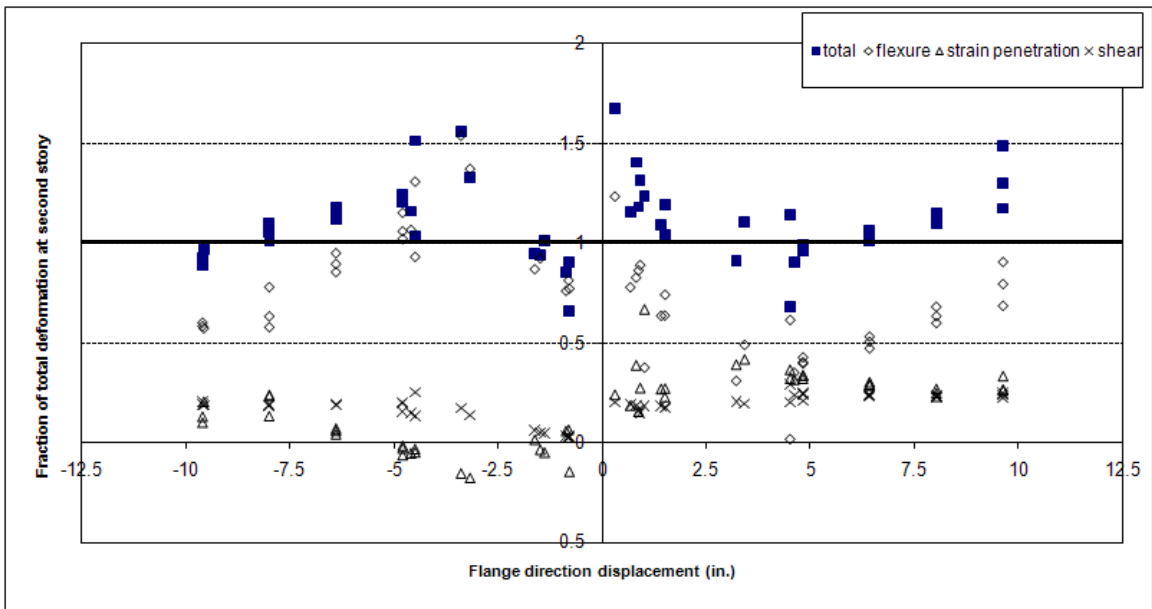


Figure 5.48. Flange direction contribution of each component to total second story displacement versus total displacement, NTW1

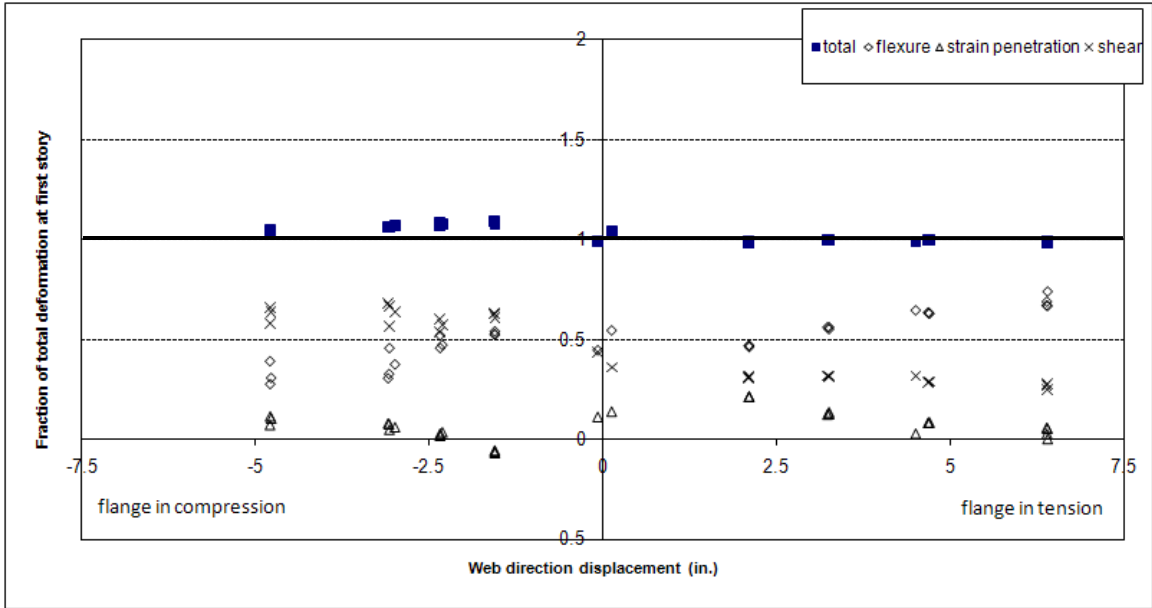


Figure 5.49. Web direction contribution of each component to total first story displacement versus total displacement, NTW1

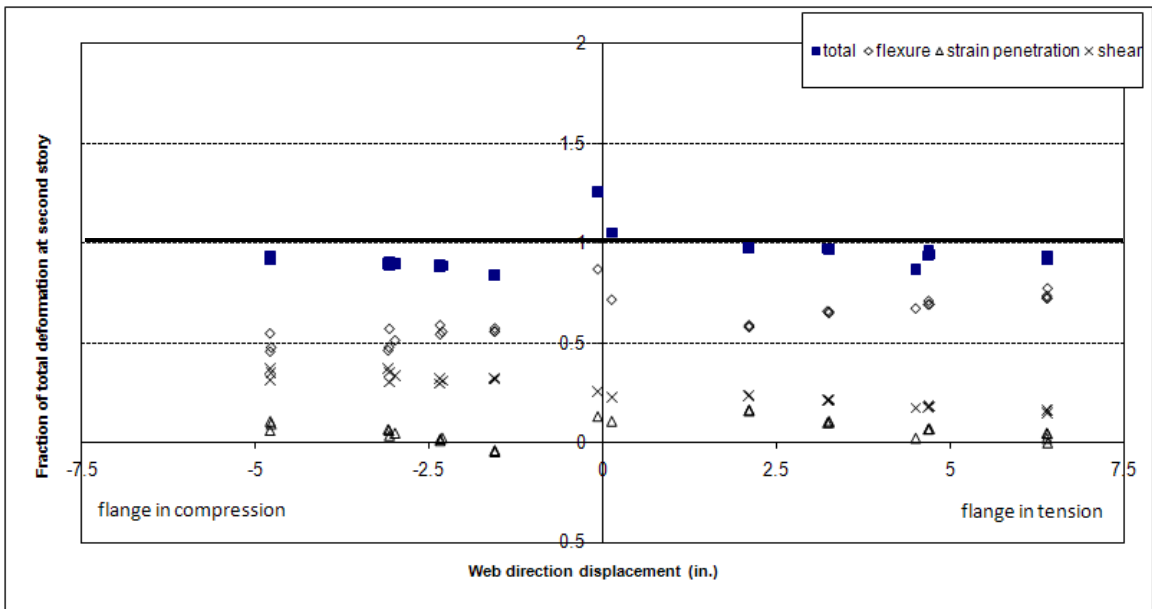


Figure 5.50. Web direction contribution of each component to total second story displacement versus total displacement, NTW1

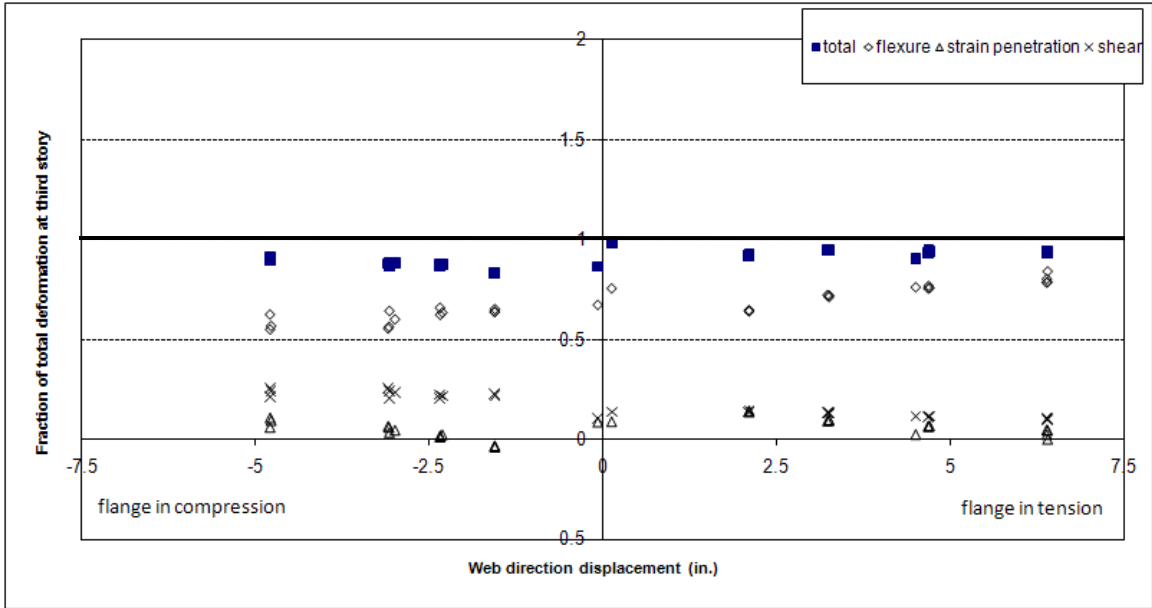


Figure 5.51. Web direction contribution of each component to total third story displacement versus total displacement, NTW1

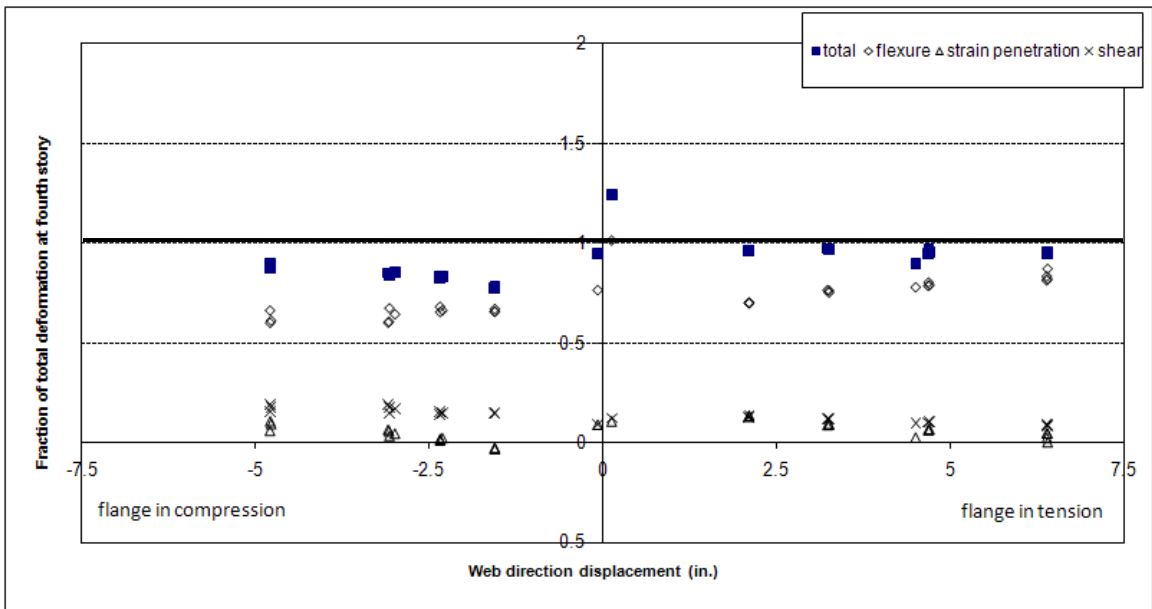


Figure 5.52. Web direction contribution of each component to total fourth story displacement versus total displacement, NTW1

Table 5.1. Contribution of each component of deformation to total, NTW1

		Story	Flexure	Shear	Strain Pen.	Total	
Flange Direction	Pre-yielding	1	126%	3%	25%	154%	
		2	84%	10%	11%	104%	
	1% drift	1	88%	32%	10%	129%	
		2	84%	17%	11%	112%	
	1.5% drift	1	66%	38%	17%	121%	
		2	74%	21%	15%	110%	
	2.0% drift	1	57%	39%	21%	117%	
		2	70%	22%	18%	109%	
	2.5% drift	1	49%	39%	28%	116%	
		2	65%	21%	23%	109%	
	3.0% drift	1	52%	41%	25%	119%	
		2	69%	22%	22%	112%	
	Flange in Tension	100% predicted yield	1	47%	31%	21%	99%
			2	64%	23%	16%	103%
3			69%	14%	14%	96%	
4			75%	13%	13%	100%	
150% predicted yield		1	55%	32%	13%	100%	
		2	71%	21%	11%	103%	
		3	76%	13%	10%	99%	
		4	80%	12%	9%	101%	
1.5% drift		1	63%	29%	8%	100%	
		2	77%	18%	7%	102%	
		3	82%	12%	6%	100%	
		4	85%	10%	6%	102%	
2.0% drift		1	67%	27%	6%	100%	
		2	79%	16%	5%	100%	
		3	84%	11%	5%	99%	
		4	87%	9%	5%	101%	
Flange in Compression	100% predicted yield	1	54%	61%	-7%	108%	
		2	63%	31%	-4%	90%	
		3	70%	22%	-4%	88%	
		4	71%	15%	-3%	82%	
	150% predicted yield	1	52%	54%	2%	107%	
		2	64%	29%	1%	95%	
		3	70%	21%	1%	92%	
		4	72%	14%	1%	88%	
	1.0% drift	1	46%	57%	5%	107%	
		2	62%	30%	4%	96%	
		3	68%	21%	3%	93%	
		4	72%	15%	3%	89%	
	1.5% drift	1	39%	58%	7%	104%	
		2	59%	31%	6%	97%	
		3	66%	22%	6%	94%	
		4	70%	16%	6%	92%	

## 5.5 Effective Flange Width

Figure 5.53 shows the measured distribution of strain across the width of the flange near the base block associated with flange-in-tension loading at the peaks of several ramps during the testing. Strains associated with flange-in-tension loading were selected for analysis because shear lag effects tend to be larger for flanges in tension than for flanges in compression.

The overhanging flange width of 33 in. was less than the limits suggested in current code provisions (ACI 318-02) of 25 percent of total wall height (resulting in a limit of 108 in. for a half-scale model of a six-story prototype), previous code provisions (UBC 1994) of 10 percent of total wall height (43.2 in.), or the value recommended by Hassan and El-Tawil (2003) of  $0.6*d$  for low drift levels (48.6 in.), all suggesting that the flange should be expected to be fully effective in tension. However, from the plot of measured strain, it is apparent that there was some shear lag effect. It should be noted that at 50 percent of the expected yield displacement, the strain gauges indicated that the few bars near the center of the flange had yielded. At the expected yield displacement, nearly all of the bars were yielded, and the bars near the center were at approximately twice the yield strain.

Table 5.2 compares the applied base moment at several loading levels with the moment calculated using the sectional analysis tool BIAX to reach the measured strain at the center of the web. Measured material properties, including the effects of strain hardening on the reinforcement were used in this analysis. When strains in the center of the flange were in the range of 1500 to 2500  $\mu\epsilon$ , the measured load was more than 30

percent less than the expected load as a result of shear lag causing decreased strains in the boundary element reinforcement. As the drift level increased beyond this region, the effects of shear lag on the load capacity of the specimen decreased as additional steel reached the yielding point. When the strain in the center of the section reached  $5000 \mu\epsilon$ , shear lag caused a decrease in load relative to the expected load of less than 2 percent. Because the stress in the steel remained relatively constant after yielding, large differences in strain beyond yielding did not cause large differences in the moment resisted by the section. This indicates that the flange can be assumed to be fully effective as long as the entire section has yielded, but using a reduced effective flange width is appropriate for analysis prior to yielding.

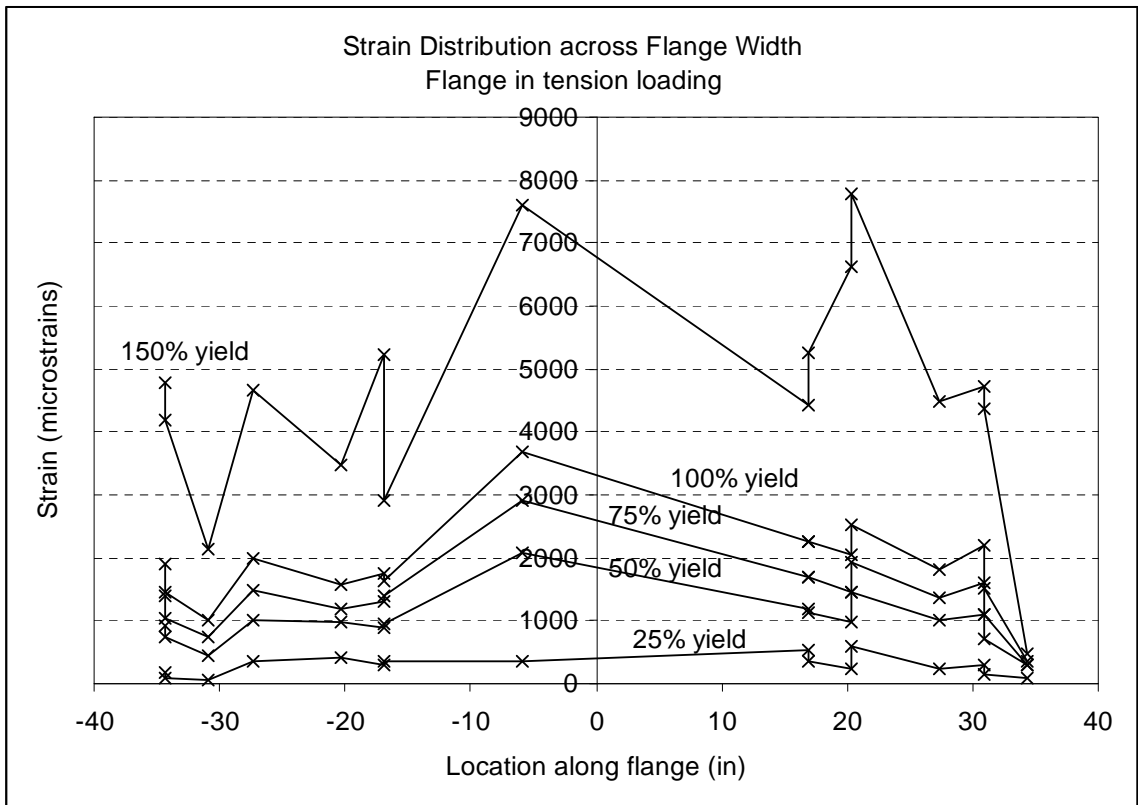


Figure 5.53. Strain distribution across width of flange, 6 in. above foundation, NTW1

Table 5.2. Effects of shear lag on flange-in-tension moment resistance, NTW1

Maximum flange reinforcement strain ( $\mu\epsilon$ )	Measured base moment (k-in)	Expected base moment for measured strain (k-in)	Difference
500	25200	23200	-8.8%
1000	28800	32100	10%
1500	30000	43200	30%
2000	35900	54300	34%
2500	35900	60600	34%
3000	46000	60700	24%
4000	55900	62500	11%
5000	62800	63900	1.7%
6000	65300	65200	-0.3%
7000	66300	66200	-0.2%

## Chapter 6 Specimen NTW2

### 6.1 Introduction

This chapter discusses the testing of specimen NTW2 and the results of this testing.

### 6.2 Observed Damage and Failure

This specimen had cracks marked and widths measured on the first and second stories and photographs taken of the entire two-story specimen. This documentation was done after the first and third cycles in groups of three cycles to the same displacement level, and in all cycles that were not repeated.

#### 6.2.1 Testing through Yielding

Prior to the start of testing, no cracks were observed in the specimen. Initial flexural cracking in the web tip was observed at 25 percent of the expected yield displacement in the flange-in-compression loading direction. Initial shear cracking was observed in the web at 25 percent of the expected yield displacement in both the flange-in-tension and flange-in-compression loading directions. At 50 percent of the expected yield displacement, both flexural and shear cracking extended over the entire first story of the specimen for both loading directions, but no cracks were observed in the second story. All cracks were hairline width ( $<0.005$  in.), but some very long cracks were observed, including flexural cracks in the flange crossing into the web and transitioning into shear cracks.

Loading to 25 percent of the expected yield displacement in the flange direction caused additional flexural cracks to form in the flange, but did not cause cracks to open

wider than the previously observed hairline level resulting from flange-in-tension and flange-in-compression loading. Loading to 25 percent of the expected yield displacement in the 45° direction with the web tip in tension caused new flexural cracks to form in the web tip, including the first observed cracks in the second story. Loading in the 45° direction with the web tip in compression did not cause new cracks to form. Loading in both 100% + 30% directions to 25 percent of the predicted yield displacement did not cause any new cracks to form. Repeating loading to 50 percent yield in the web direction after loading in other directions did not cause any existing cracks to extend or new cracks to form, as expected.

Loading in the 45° directions to 75 percent of the expected yield displacement caused extensive new cracking. Flexural cracks extended over the entire height of the specimen, and were spaced approximately 3 in. apart in the first story and 6 in. apart in the second story. The widest flexural cracks, near the base of the specimen, were <0.005 in. wide. Shear cracks in the web were more widely spaced than flexural cracks and opened up to 0.016 in. wide. Unlike the multidirectional loading to 25 percent of the expected yield displacement, some additional cracking was observed after loading in the 100%+30% direction to 75 percent of the expected yield displacement. Additionally, the shear cracks in the web opened slightly wider, up to 0.020 in. Loading in the web direction to 75 percent of the expected yield displacement caused some additional cracking. Loading with the flange in compression caused a maximum shear crack width of 0.013 in. and a maximum flexural crack width of 0.005 in. Loading with the flange in

tension caused a maximum shear crack width of 0.025 in. in the first story and 0.013 in. in the second story.

Loading to the predicted yield displacement with the flange in compression caused a few new cracks and extensions to existing cracks. The largest web shear cracks opened up to 0.025 in. wide in the first story and 0.020 in. wide in the second story. Flexural cracks in the web tip opened up to 0.010 in. wide. Loading with the flange in tension caused shear cracks to open up to 0.030 in. wide in the first story and 0.016 in. wide in the second story. Flexural cracks in the flange opened up to 0.013 in. wide in the first story and 0.010 in. wide in the second story above the splice cutoff. Cracks within the splice region were 0.005 in. wide or less.

At this point in the test, the overall crack pattern included approximately uniformly spaced, horizontal cracks across the entire flange width and distinct flexural and shear cracks in the web. The cracks in the flange were spaced approximately 3 in. apart, and the crack widths were consistent across the entire flange width at any height on the wall. There were a few short vertical cracks in the flange, but no diagonal cracks. Flexural cracks in the web were spaced similarly to those across the flange and had similar or slightly narrower widths. However, there was a distinct transition in the crack pattern from the confined region, with closely spaced, flexural cracks, to the unconfined region, with much more widely spaced cracks that opened up to three times wider than the flexural cracks. In both the web and the flange, crack widths decreased with wall height, from the foundation to the slab. Flexural cracks were much narrower in the lower portion of the second story, where reinforcement was lapped, then increased in width

above the bar cutoff. Shear crack widths were relatively unaffected by the bar splice region. Figure 6.1 through Figure 6.4 show the specimen at this point in the testing.

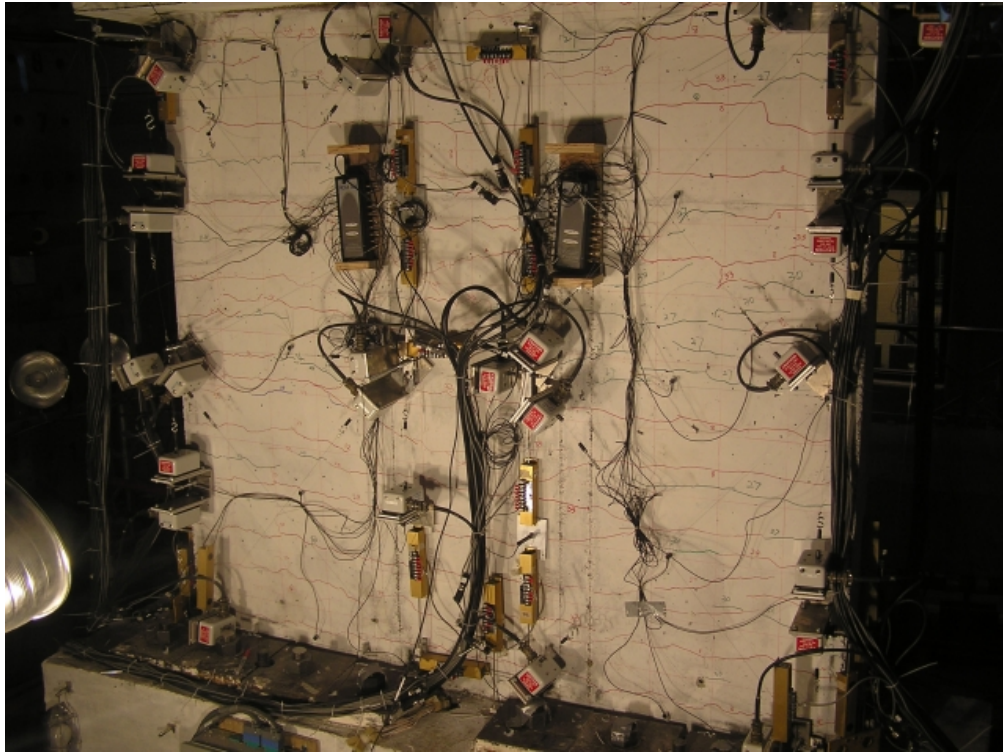


Figure 6.1. First story flange of NTW2 at end of elastic loading cycles.

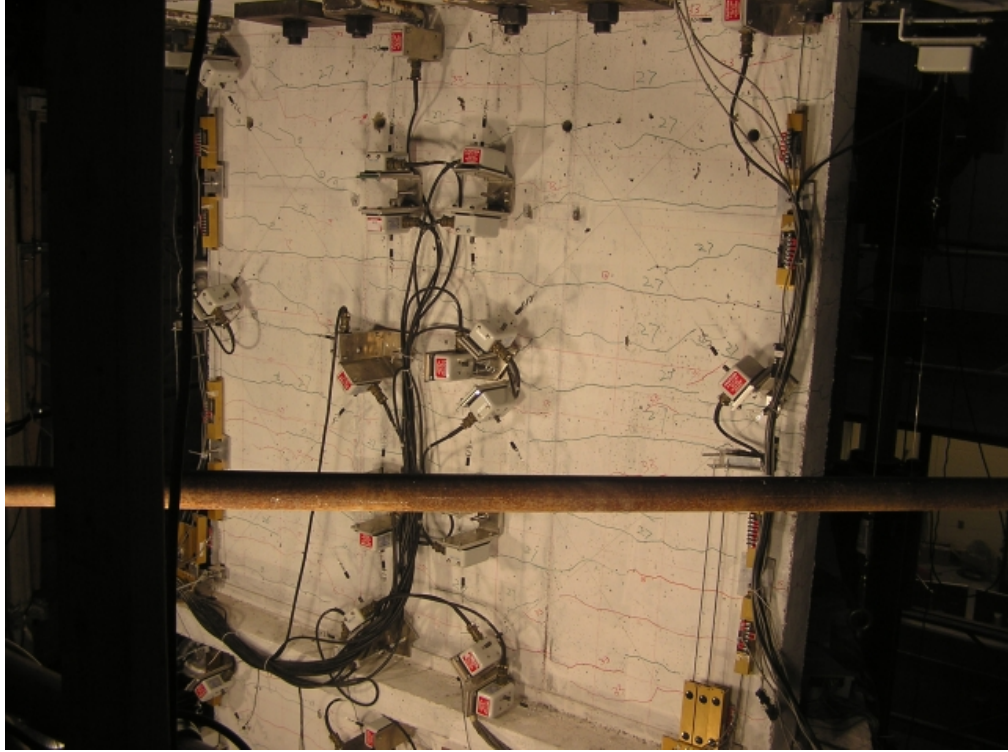


Figure 6.2. Second story flange of NTW2 at end of elastic loading cycles.



Figure 6.3. First story web of NTW2 at end of elastic loading cycles.

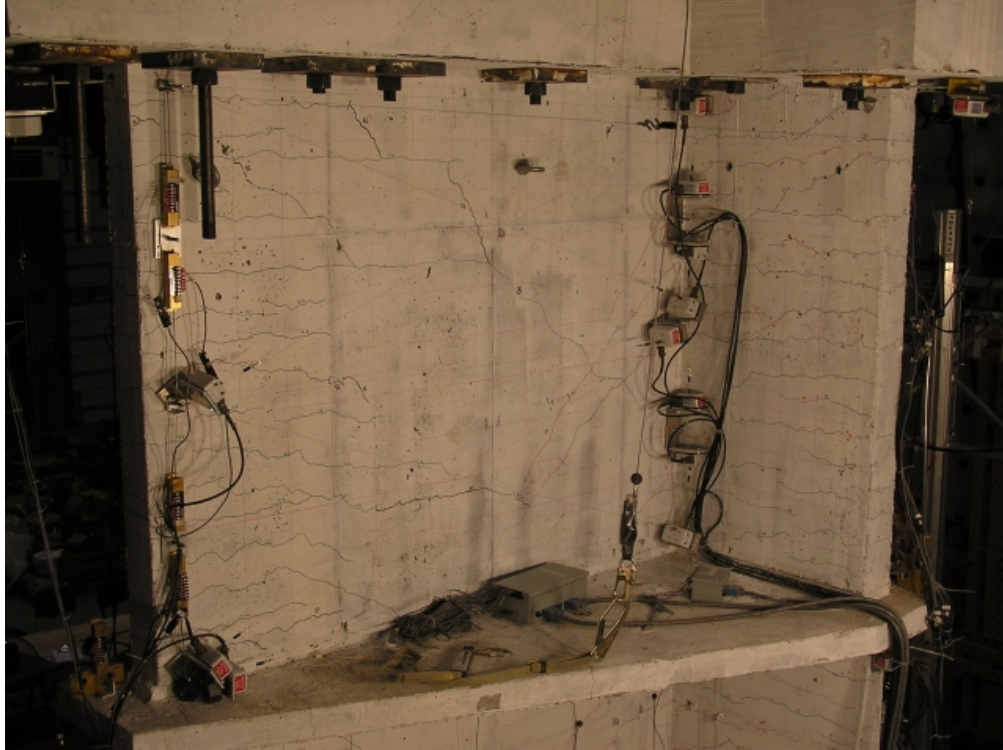


Figure 6.4. Second story web of NTW2 at end of elastic loading cycles.

### 6.2.2 Post-Yielding Through Failure in Web Direction

Loading in the web direction to 150 percent of the expected yield displacement caused a few new cracks and extensions to existing cracks. Flexural cracks in the web tip were 0.016-0.020 in. wide in the lower third of the bottom story, 0.007 in. wide in the middle third, and 0.013 in. wide in the top third. In the second story, flexural cracks were 0.005 in. wide in the splice region and 0.007 in. wide above the splice cutoff. Flexural cracks in the flange were 0.016 in. wide in the lower portion of the bottom story, 0.009 in. wide in the top portion of the bottom story, 0.005 in. wide in the splice region of the second story, and 0.007 in. wide above the splice cutoff. Web shear cracks opened up to 0.030 in. wide in the bottom story and 0.020 in. wide in the second story in both the flange-in-tension and flange-in-compression loading directions.

Loading in the flange-in-compression direction to 1 percent drift caused flexural cracks to open to 0.035 in. in the lower portion of the first story and 0.016 in. in the upper portion. In the second story, flexural cracks were 0.005 in. wide in the splice region and 0.007 in. wide above the splice cutoff. Web shear cracks were up to 0.040 in. wide in the first story and 0.030 in. wide in the second story. Loading in the flange-in-tension direction to 1.5 percent drift caused spalling of the cover concrete over an approximately 12 in. x 12 in. area at the base of the web tip. Most flexural cracks in the flange were no more than 0.016 in. wide in the bottom story. One crack at approximately mid-height was 0.040 in. wide. Cracks were 0.005 in. wide in the splice region of the second story, and 0.007 in. wide above the splice cutoff. Web shear cracks opened up to 0.060 in. wide in the bottom story and 0.025 in. wide in the second story in both flange-in-tension and flange-in-compression loading directions. Loading in the 100%+30% directions at this drift level did not cause new cracking and existing cracks did not open as wide as previously observed.

Loading in the flange direction to 1 percent drift caused flexural cracks in the flange to open up to 0.030 in. near the base of the specimen. Typical flexural cracks in the upper portion of the first story were 0.010 in. wide. Cracks were 0.005 in. wide in the splice region of the second story, and 0.010 in. wide above the splice cutoff. Small diagonal (shear) cracks formed near the center of the flange, but no crack extended more than 6 in.

Loading in the 45° directions to 1.5 percent drift did not cause cracks to open as wide as previously observed. The widest web shear cracks were 0.035 in. wide, and the

widest flexural cracks were 0.013 in. wide. Loading in the flange direction to 1.5 percent drift caused flexural cracks in the flange to open up to 0.035 in. near the base of the specimen. The crack at the interface between the wall and foundation block opened up to 0.040 in. wide. Typical flexural cracks in the upper portion of the first story were 0.010 in. wide. Cracks were 0.005 in. wide in the splice region of the second story, and 0.016 in. wide above the splice cutoff. Loading in the 100% + 30% directions to 1.5 percent drift did not cause cracks to open as wide as previously observed. The widest web shear cracks were 0.035 in. wide, and the widest flexural cracks were 0.040 in. wide. However, horizontal sliding was measured across a horizontal crack along the web. A displacement of 0.05 in. was measured across this crack when one flange tip and the web tip were in tension. A displacement of 0.01 in. was measured in the opposite loading direction, when the other flange tip was in tension. Repeating the previous web direction loading to 1 percent drift with the flange in compression and 1.5 percent drift with the flange in tension did not cause additional cracking, but the horizontal sliding that was observed in the skew direction loading continued. Displacements of 0.05 in. with the flange in compression and 0.06 in. with the flange in tension were observed.

Loading in the flange-in-compression direction to 1.5 percent drift caused typical flexural cracks to open to 0.035 in. in the lower portion of the first story and 0.025 in. in the upper portion. The crack at the wall-to-foundation interface opened to between  $\frac{1}{8}$  and  $\frac{1}{4}$  in. wide. In the second story, flexural cracks were 0.005 in. wide in the splice region and 0.010 in. wide above the splice cutoff. Web shear cracks were up to 0.10 in. wide in the first story and 0.030 in. wide in the second story. Shear sliding in the first

story was 1/8 in. across a single horizontal crack. Additional spalling of cover concrete in the web tip was observed, extending horizontally an additional 3 in. In addition, some localized spalling was observed along shear cracks. Typical flexural cracks in the first story flange were 0.06 in. wide in the lower third, 0.05 in. wide in the middle third, and 0.016 in. wide in the top third. The crack along the top of the slab, at the base of the second story, which corresponded to the bottom of the splice region, was 0.016 in. wide. Cracks were 0.005 in. wide in the splice region of the second story, and 0.0076 in. wide above the splice cutoff. Web shear cracks opened up to 1/8 in. wide in the bottom story and 0.025 in. wide in the second story. Shear sliding in the first story was 1/8 in. Loading in the figure-8 pattern to 2 percent drift did not cause substantial new cracking, but loading with the flange in compression combined with flange direction loading placing additional compression on one flange tip did cause some vertical cracks to form in the flange tips.

Loading with the flange in compression to 2.0 percent drift caused flexural cracks in the web tip to open 0.06 in. near the base of the first story, just above the spalled region. Shear cracks were open up to 1/8 in., and shear sliding displacement across the horizontal crack in the web was approximately 1/8 in. Loading with the flange in tension to 2.5 percent drift caused failure of the web tip. Confinement hoops 8 in. above the foundation were fractured, and the endmost four bars in the web tip buckled. Cycling at this drift level caused the buckled bars to fracture and the remaining bars in the web tip to buckle. Figure 6.5 through Figure 6.8 show the specimen at this point in the testing.



Figure 6.5. First story flange of NTW2 after web failure.

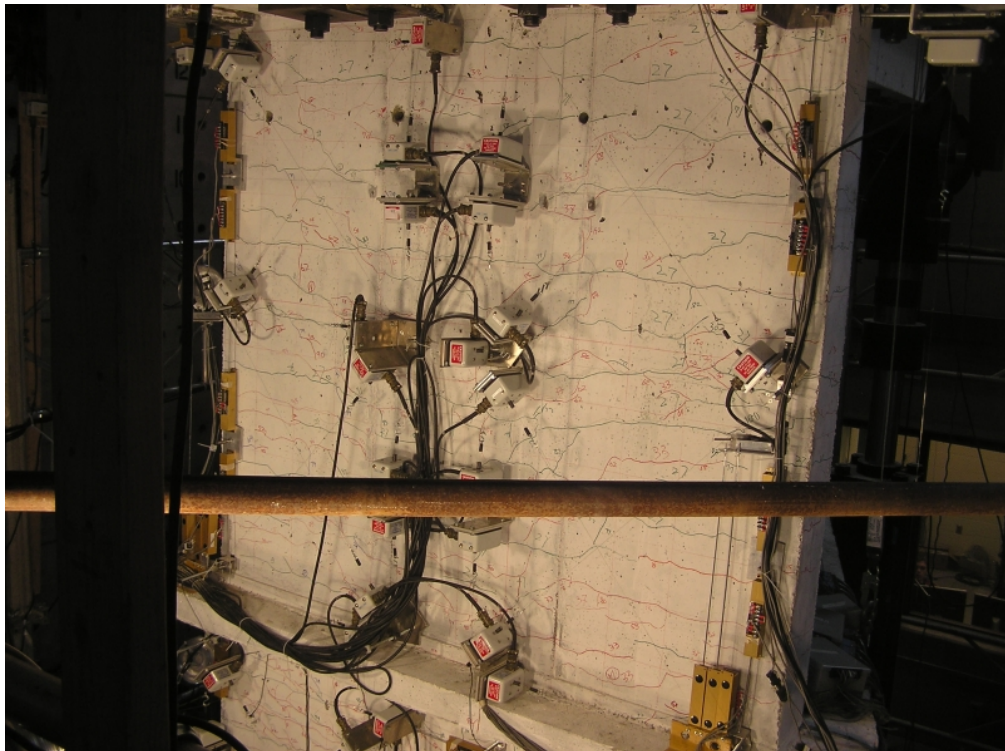


Figure 6.6. Second story flange of NTW2 after web failure.

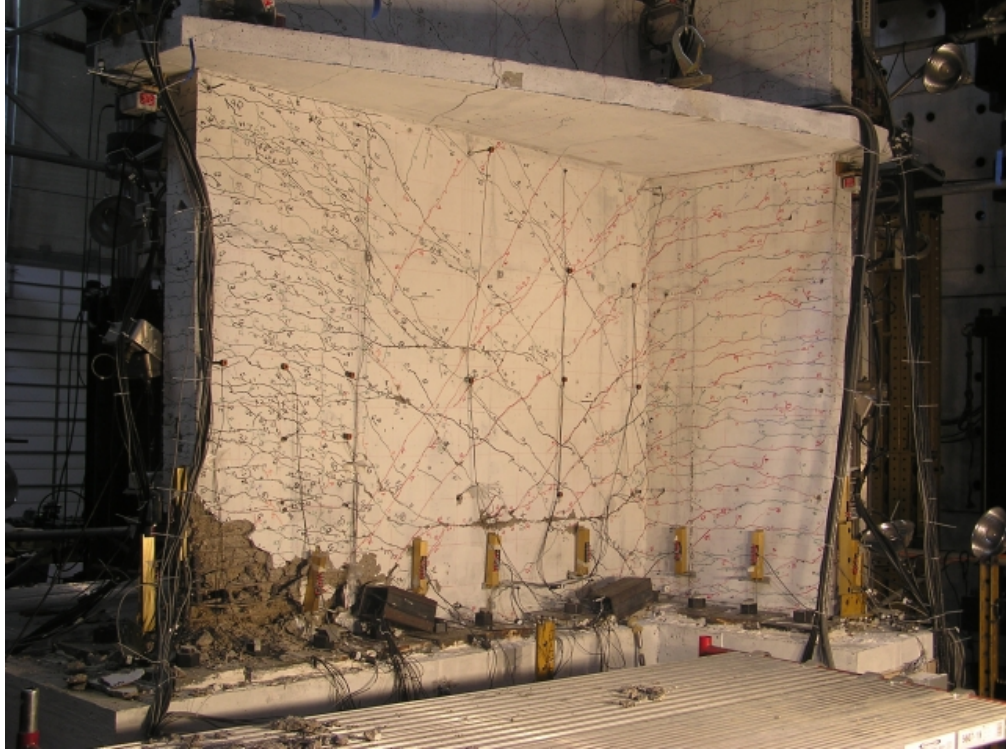


Figure 6.7. First story web of NTW2 after web failure.



Figure 6.8. Second story web of NTW2 after web failure.

### **6.2.3 Post-Web Failure through Failure in Flange-Direction Loading**

After failure of the web tip, the test was completed with flange-direction loading of increasing magnitude until the flange failed. Repeating the previous loading to 1.5 percent drift in the flange direction caused flexural cracks in the flange to open up to 0.040 in. near the base of the specimen. Typical flexural cracks in the upper portion of the first story were 0.016-0.020 in. wide. A small amount of spalling occurred around the vertical cracks that formed during the hourglass loading. The crack at the interface between the slab and the base of the second story was open to 0.025 in. Cracks were 0.005 in. wide in the splice region of the second story, and 0.013 in. wide above the splice cutoff.

Loading to 2.0 percent drift in the flange direction caused flexural cracks in the flange to open up to 0.060 in. near the base of the specimen. Typical flexural cracks in the upper portion of the first story were 0.020-0.030 in. wide. A small amount of spalling occurred around the vertical cracks that formed during the hourglass loading. The crack at the interface between the slab and the base of the second story, at the base of the lap splice was open to 0.025 in. Cracks were 0.005 in. wide in the splice region of the second story, and 0.013 in. wide above the splice cutoff.

Loading to 2.5 percent drift in the flange direction caused typical flexural cracks in the flange to open up to 0.10 in. near the base of the specimen. A single crack approximately 10 in. above the foundation opened more than  $\frac{1}{4}$  in. Typical flexural cracks in the upper portion of the first story were 0.040 in. wide. The concrete cover over the ends of the flange was loose and beginning to spall in the lower 6 in. of the specimen.

A small amount of shear sliding, 0.02 in., along a horizontal crack approximately 4 ft. from the foundation was measured in the final ramp of the set of three cycles. The crack at the interface between the slab and the base of the second story was open to 0.030 in. Cracks were 0.005 in. wide in the splice region of the second story, and 0.020 in. wide above the splice cutoff.

Loading to 3.0 percent drift in the flange direction caused typical flexural cracks in the flange to open up to 0.10 in. near the base of the specimen. A single crack approximately 10 in. above the foundation again opened more than  $\frac{1}{4}$  in. Typical flexural cracks in the upper portion of the first story were 0.040 in. wide. The concrete cover over the ends of the flange spalled over the entire bottom half of the first story. The crack at the interface between the slab and the base of the second story was open to 0.030 in. Cracks were 0.005 in. wide in the splice region of the second story, and 0.030 in. wide above the splice cutoff.

Loading to 4.0 percent drift in the flange direction caused typical flexural cracks in the flange to open up to 0.10 in. near the base of the specimen. Typical flexural cracks in the upper portion of the first story were 0.040 in. wide. The concrete cover over the ends of the flange spalled over the entire bottom half of the first story. The crack at the interface between the slab and the base of the second story was open to 0.025 in. Cracks were 0.005 in. wide in the splice region of the second story, and 0.035 in. wide above the splice cutoff. A large amount of cover concrete on the south flange tip spalled in the first ramp of this series, but no bars were visibly buckled. Unloading and loading in the opposite direction (towards the north) caused one bar in the south flange tip to fracture

and two bars in the north flange tip to buckle. Repeating this cycle caused buckling and fracture of additional bars and reduced the ability to resist the applied gravity load.

Visual evidence of the lap splices slipping was not apparent at any point in the testing. In particular, the crack that formed at the interface between the slab and the second story of the specimen was no larger than the typical cracks observed in the first story, and very large cracks concentrating damage in a small area, such as observed by Johnson (2007), were not observed. Figure 6.9 through Figure 6.12 show the specimen at the end of testing.



Figure 6.9. First story flange of NTW2 after flange failure.

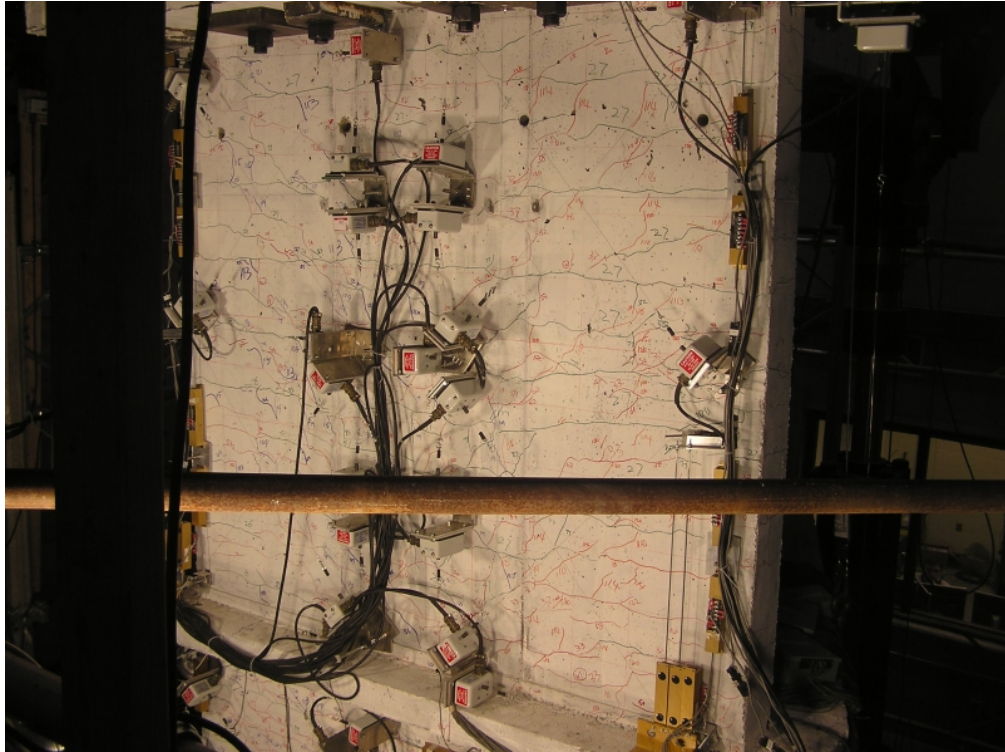


Figure 6.10. Second story flange of NTW2 after flange failure.

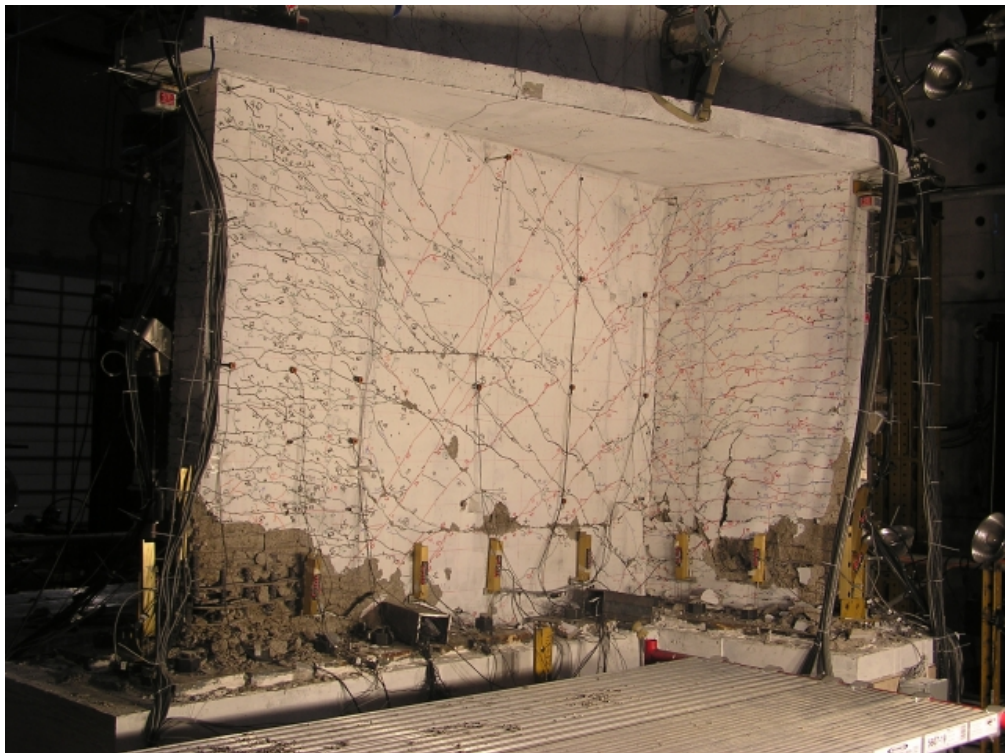


Figure 6.11. First story web of NTW2 after flange failure.

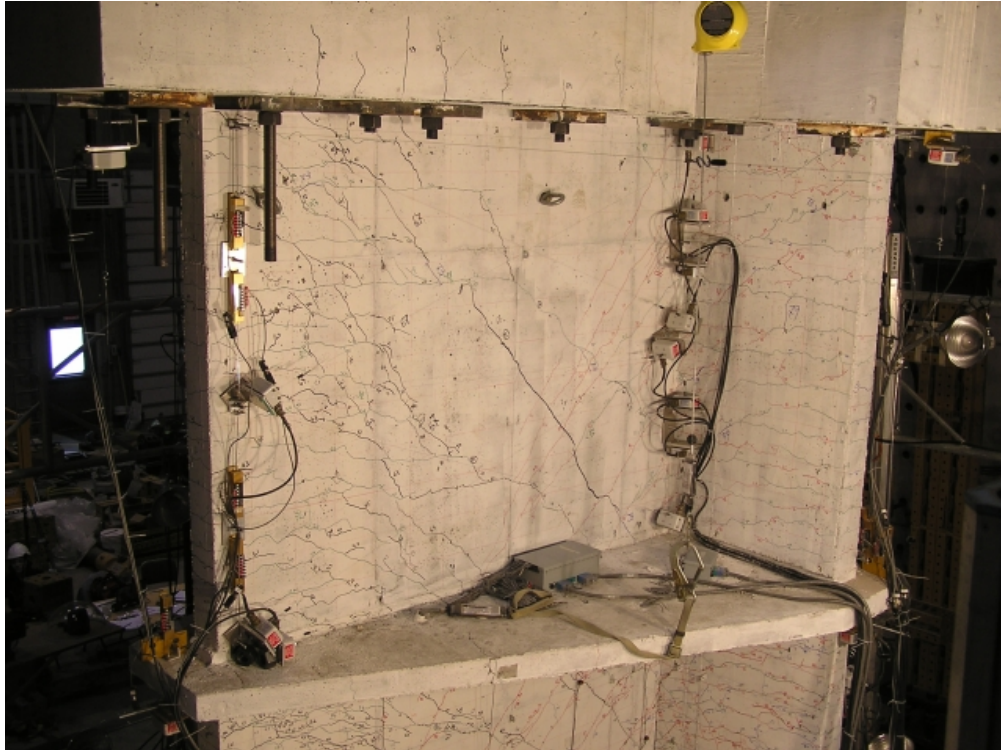


Figure 6.12. Second story web of NTW2 after flange failure.

#### **6.2.4 Post-Testing Autopsy of Specimen**

After testing was complete, the specimen was cut off at approximately mid-height of the first story and a small jackhammer was used to carefully remove the concrete from this portion, where the damage was concentrated, and examine the condition of the longitudinal and confining reinforcement. It was found that several confining hoops between 3 and 11 in. above the foundation in each of the boundary elements were either severely deformed or fractured, and, while it was obvious that the section was severely damaged, much of the damage to the confining hoops was not apparent until the concrete was removed. The bottom 3 in. closest to the foundation block was not damaged as severely; the cover had spalled, but the core was intact. This is likely the result of the foundation providing some extra restraint to this portion of the wall. Figure 6.13 through

Figure 6.15 show the three boundary elements after the loose concrete was removed to expose the confining steel. Additional photographs from this investigation are included in Appendix D.

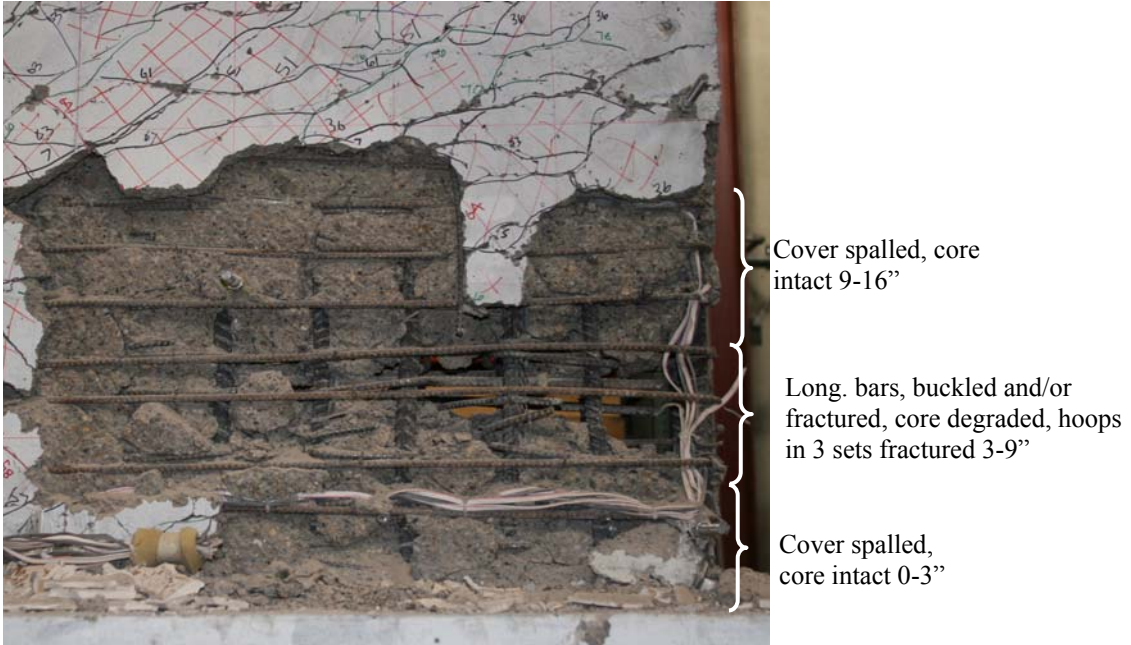


Figure 6.13. Web tip after removal of loose concrete.

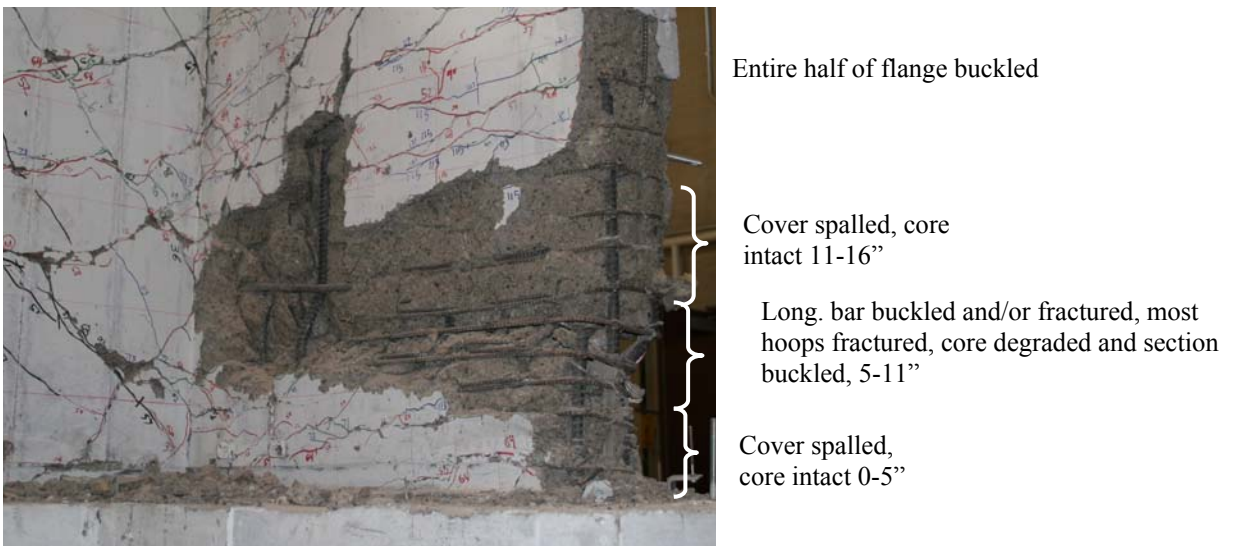


Figure 6.14. North flange tip after removal of loose concrete.

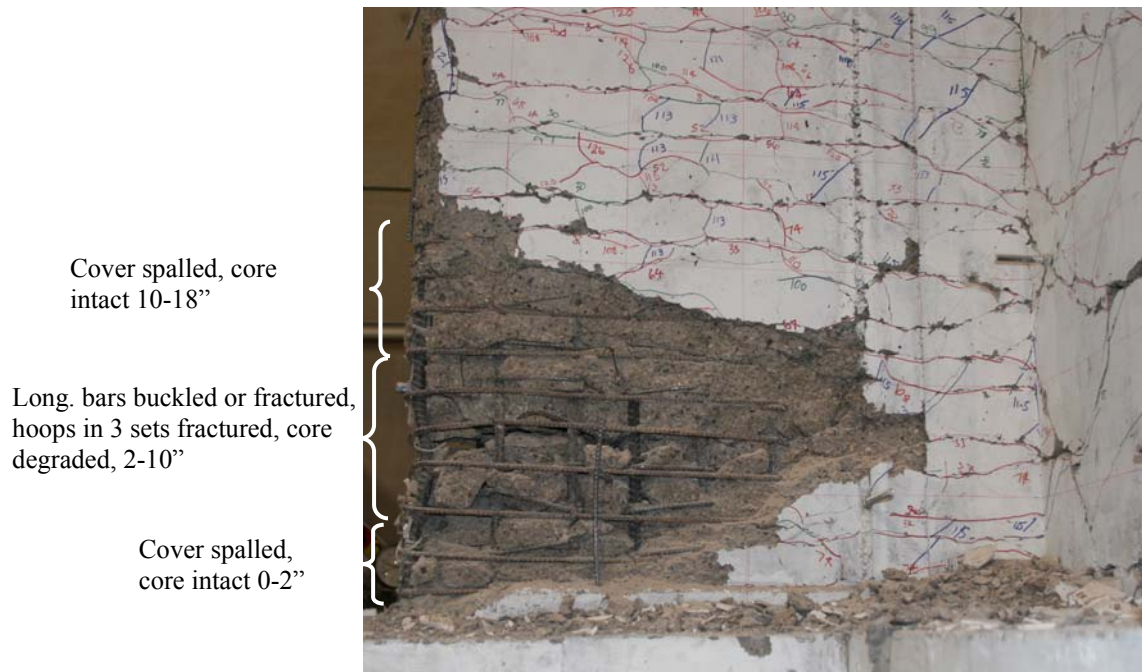


Figure 6.15. South flange tip after removal of loose concrete.

### 6.3 Load versus Displacement Response

Figure 6.16 through Figure 6.18 show the orthogonal components of the measured load versus displacement response of the specimen. Figure 6.16 shows the flange-direction response over the entire load history, Figure 6.17 shows the flange-direction response in the early part of the test, and Figure 6.18 shows the web-direction response over the entire load history. The orthogonal components of the skew direction loading ramps are distinguished from orthogonal flange-direction and web-direction loads in these plots by the use of dashed lines. When the skew direction loading ramps were decomposed into their orthogonal components, the elastic stiffnesses in each orthogonal direction were found to be similar to the stiffness associated with orthogonal loading. After yielding, the flange direction component of the response under skew direction loading varied from the orthogonal loading, while the web direction component of the

response did not. This is likely due to the skew direction loading itself, as opposed to being the result of the order of the load history and damage accumulating in the specimen over the course of the test. As mentioned above, Figure 5.30 shows the same data as Figure 5.29, but only the first portion of the testing is shown, for clarity. In this figure, the stiffer skew direction loading cycle, marked “2,” was conducted between the two orthogonal directional loading cycles, marked “1” and “3”. Multidirectional loading effects are discussed further in Chapter 7.

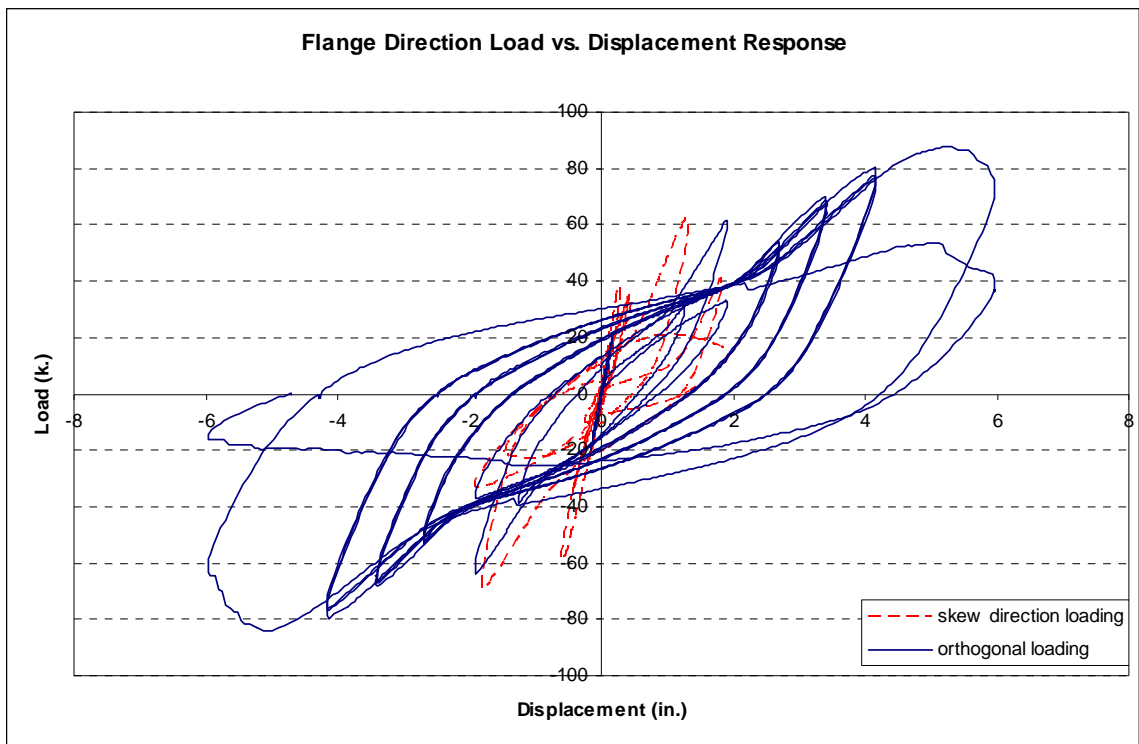


Figure 6.16. Flange direction load versus displacement response of NTW2

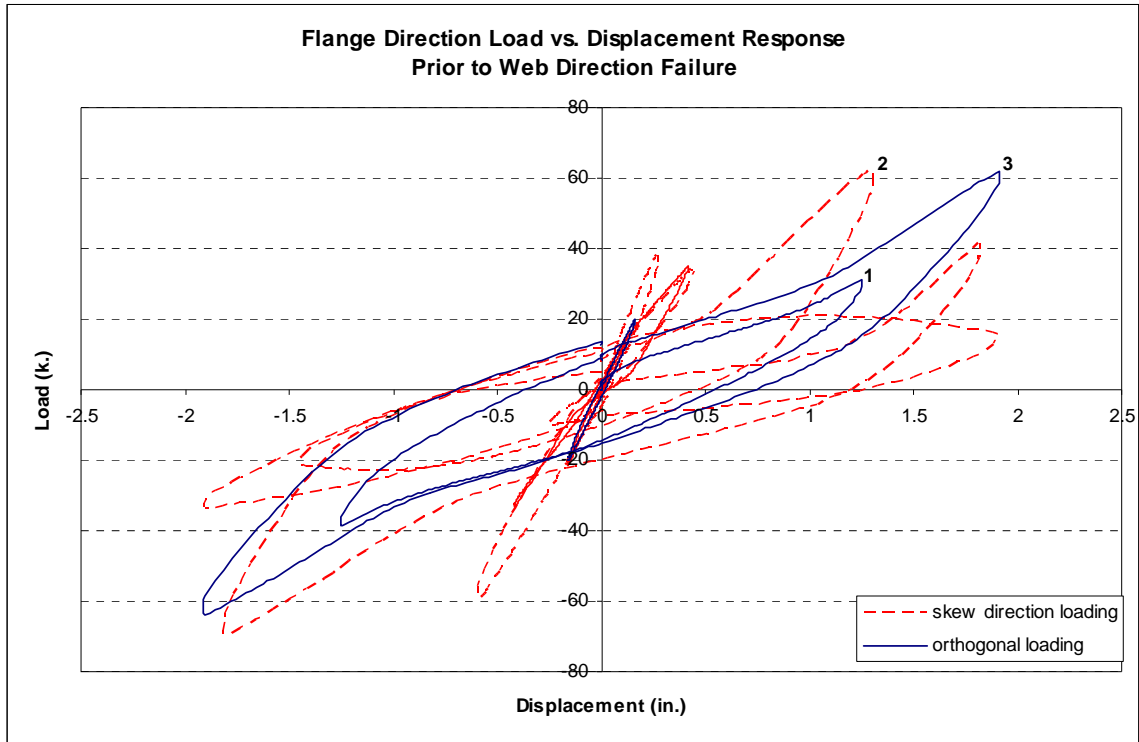


Figure 6.17. Flange direction load versus displacement response of NTW2, early portion

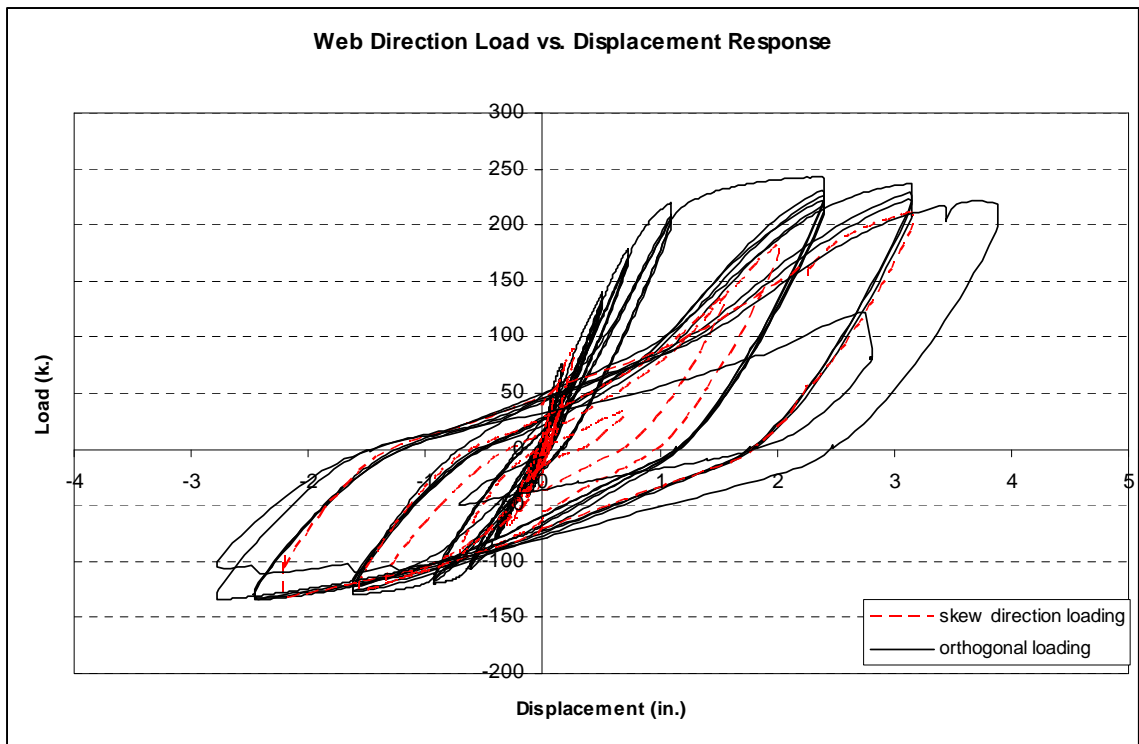


Figure 6.18. Web direction load versus displacement response of NTW2

## 6.4 Components of Deformation

The contributions of each component of deformation, flexure, shear, strain penetration, and splice slip, were calculated using the external instrumentation attached to the wall. As described in Sections 4.3 and 4.4, redundant systems (i.e., LVDTs and string pots and the Krypton system) were used to instrument the first story of this specimen. Data from both systems were reduced and are available in the NEES repository. Data collected with the Krypton measuring system were considered more accurate and were used to determine the contributions of shear and flexure to the deformation of the first story reported here, despite the large amounts of noise that were observed in this data. Data collected with LVDTs and string pots were used to determine the contributions of shear and flexure in the second story, as well as strain penetration and splice slip. Chapter 4 describes these calculations and the choice of instruments further. Near the end of the applied loading history, the lower tier of instruments was removed. The concrete near the instruments was extensively spalled, and there was some concern that leaving the instruments would subject them to damage. Additionally, many of the embedded studs used to support the instruments were becoming loose in the concrete, rendering those measurements unreliable.

Several plots in the following sections refer to various heights on the specimen. Figure 6.19 shows the positions of representative heights and instrumentation panels on the specimen for reference.

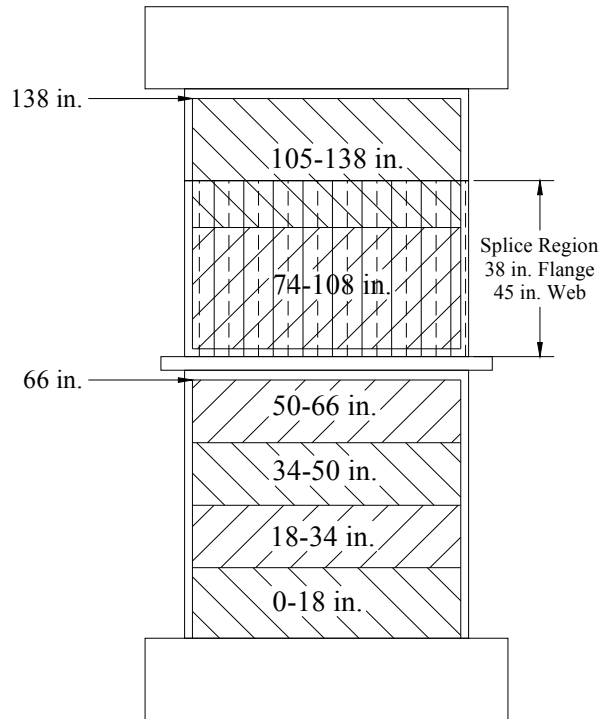


Figure 6.19. Locations of measurement panels and splice region in NTW2

#### 6.4.1 Flexure

Figure 6.20 and Figure 6.21 show the measured moment versus curvature relationships over the height of the specimen for the flange and web directions, respectively. In the flange direction, nonlinear flexural deformations were present over the entire first story of the structure. In the web direction, the moment versus curvature plots suggest that the plastic hinge length was shorter, with a reduced amount of nonlinearity in the top half of the first story. However, the data recorded with the strain gauges indicated that the longitudinal reinforcement in the web tip did yield over the entire first story. In both loading directions, the splice region in the second story remained elastic as a result of the increased reinforcement. However, the strain gauges attached to the longitudinal reinforcement indicated that yielding did occur above the

splice cutoff in the second story, but not within the splice region. This observation was corroborated by the observed crack widths, where there was a distinct reduction in the crack width in the splice region.

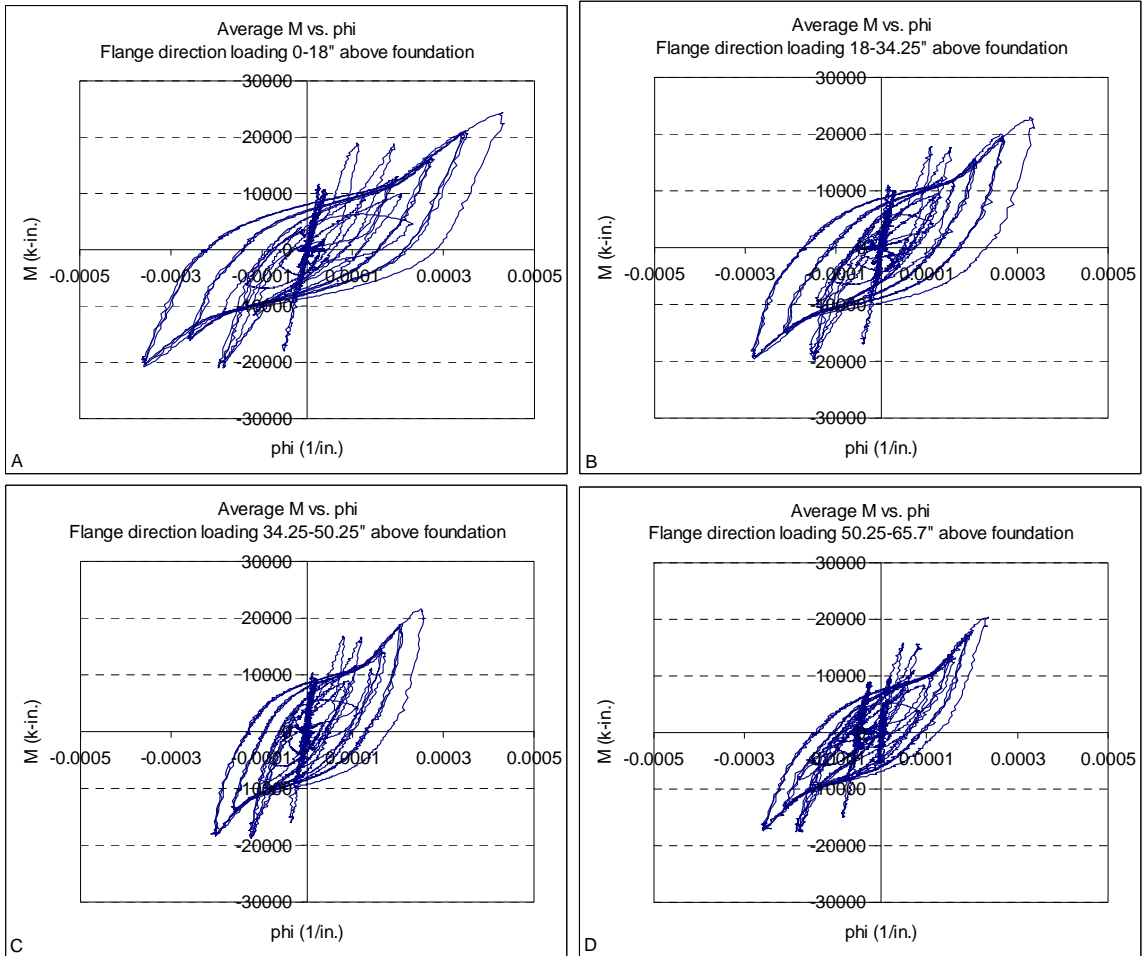


Figure 6.20. Flange direction moment versus curvature relationships for NTW2

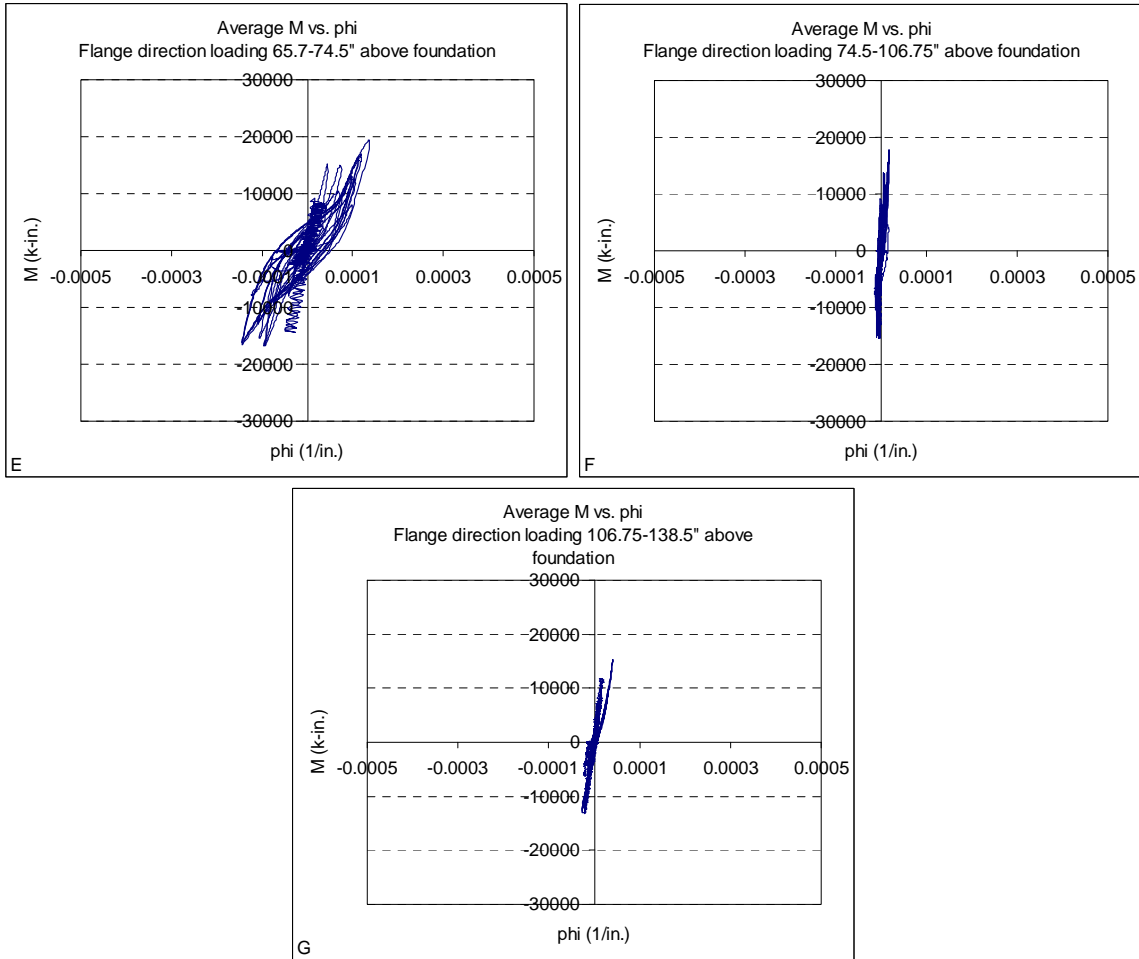


Figure 6.20. Flange direction moment versus curvature relationships for NTW2, cont.

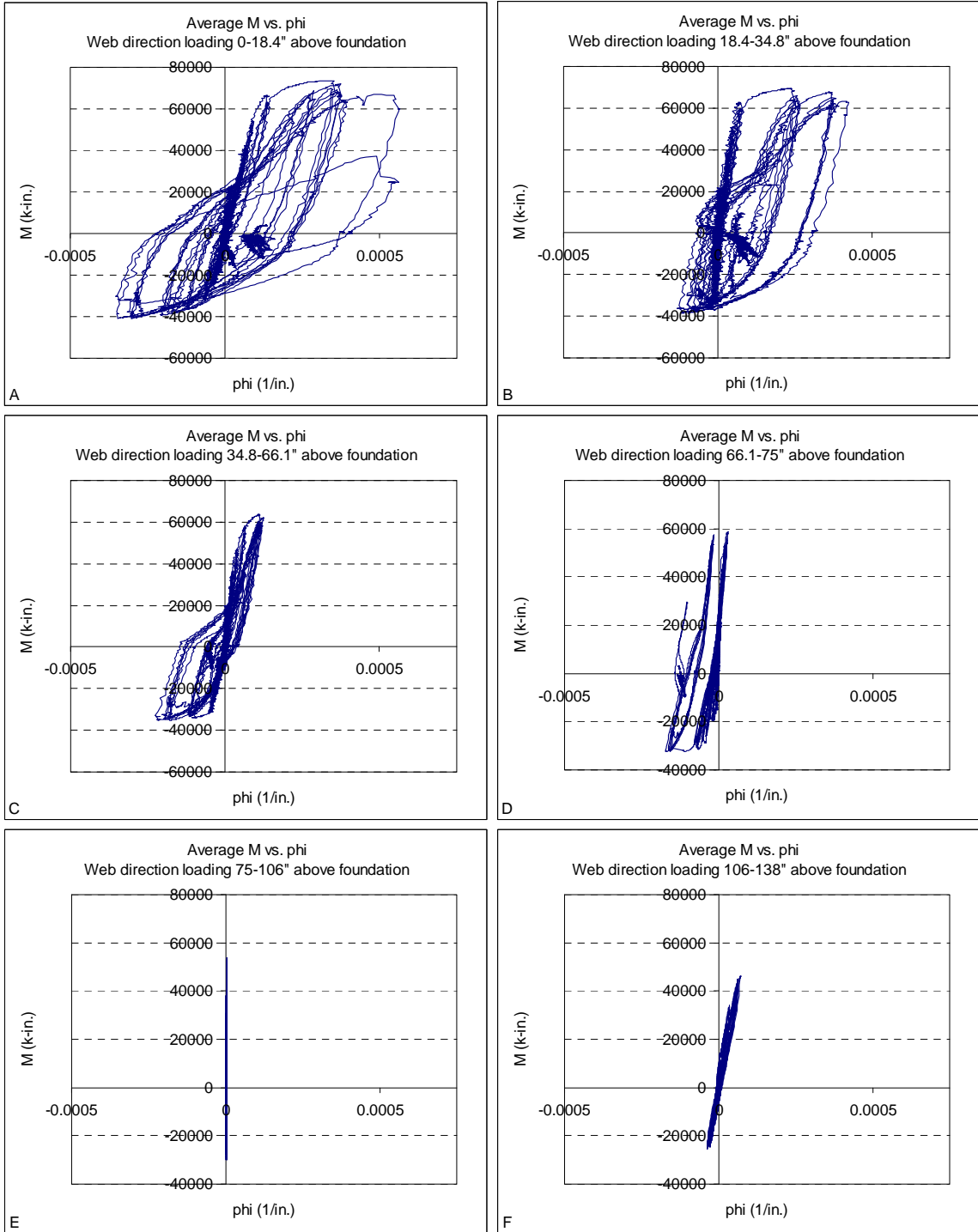


Figure 6.21. Web direction moment versus curvature relationships for NTW2

#### **6.4.2 Shear**

Figure 6.22 and Figure 6.23 show the average shear force versus shear strain for flange and web loading directions, respectively. In these figures, the subdivisions of the specimen over its height are the same as used in the moment versus curvature plots above, except that shear strains were not measured across the slab. The measured shear strains in the first story of the flange were approximately three times larger than those in the second story, and in the web, they were approximately ten times larger in the first story than in the second. Because the shear force applied to the specimen was constant over its height, this is an indication of the effect that plastic hinging and flexural damage have on reducing shear stiffness and increasing shear deformations.

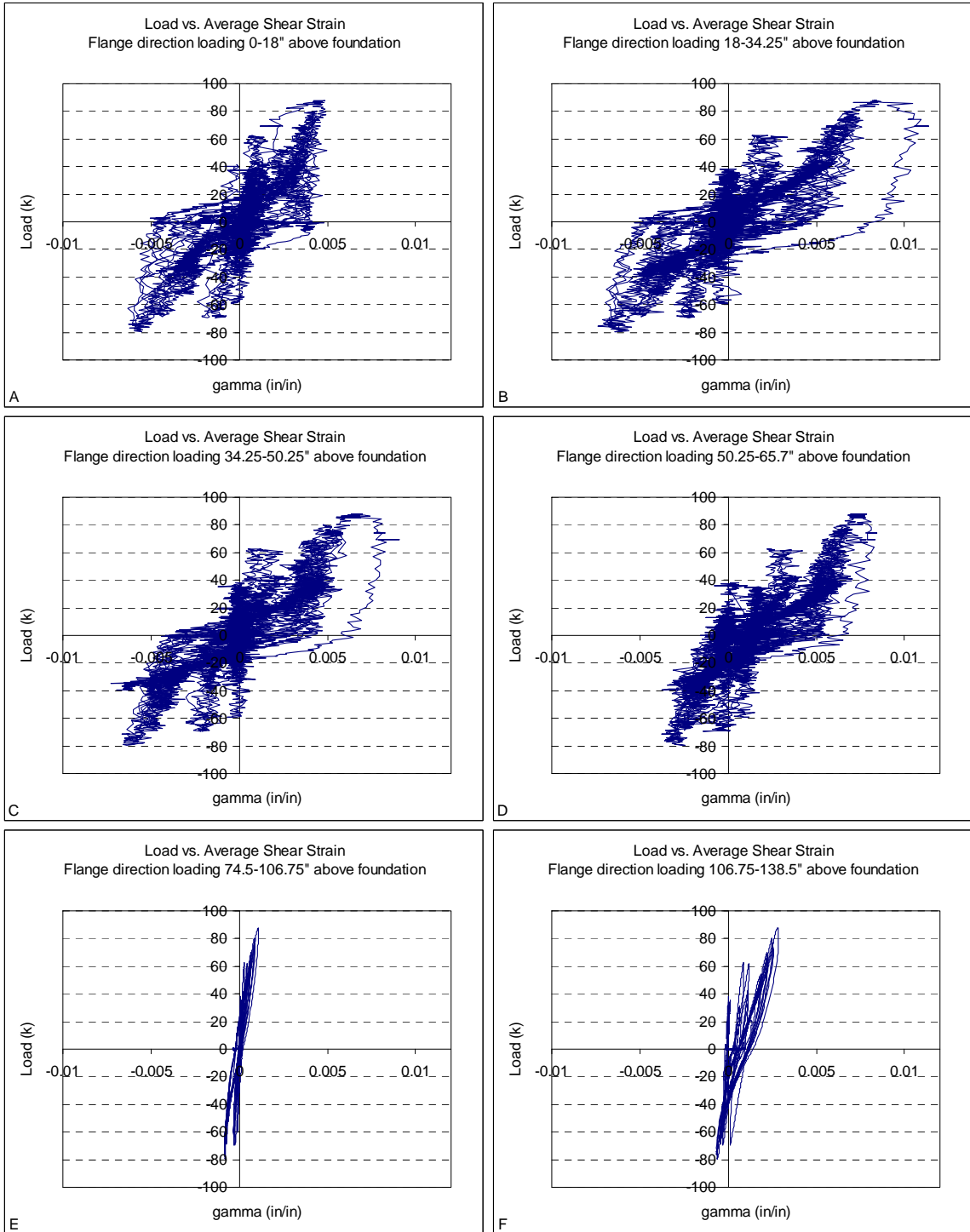


Figure 6.22. Flange direction shear force versus shear strain relationships for NTW2

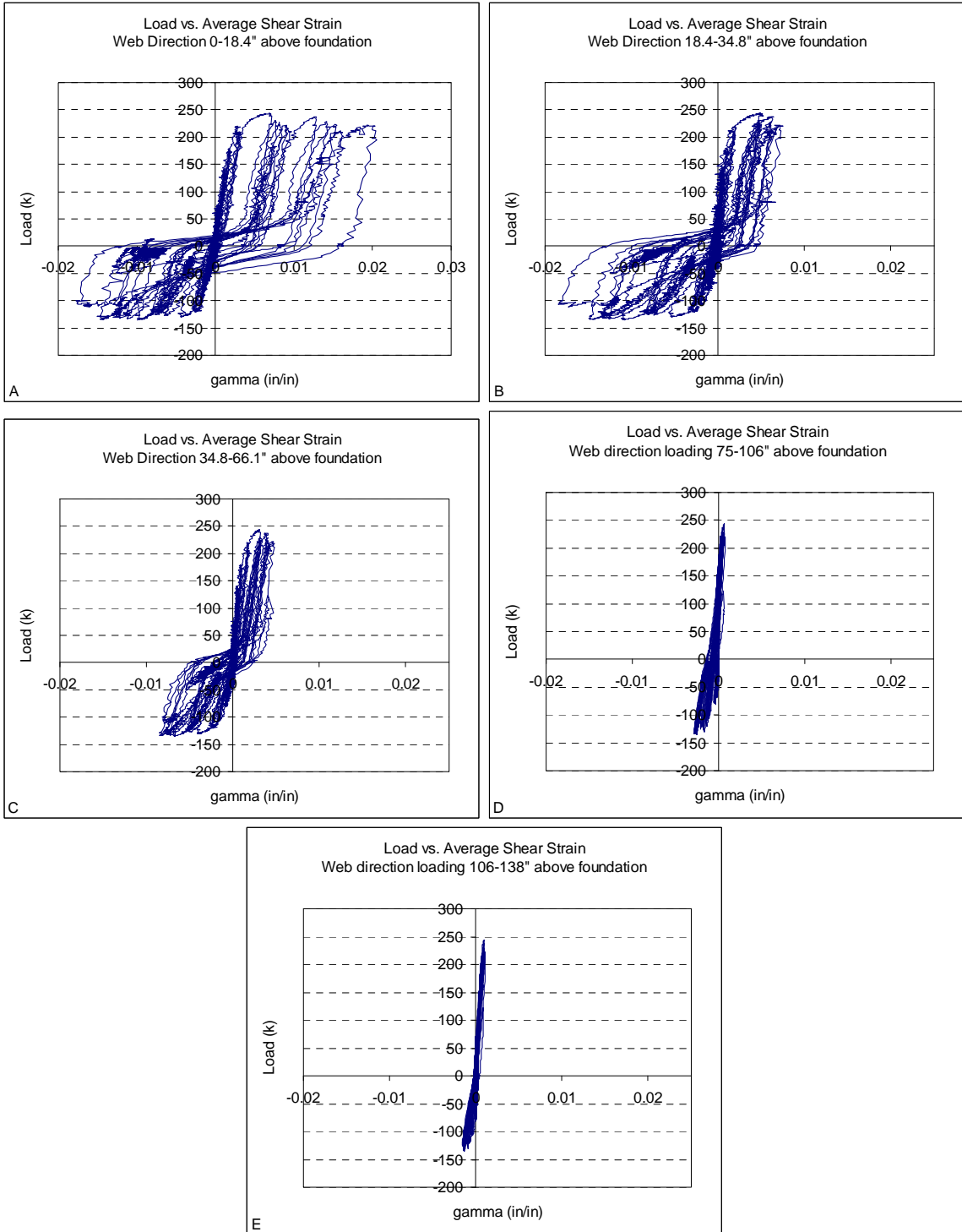


Figure 6.23. Web direction shear force versus strain relationships for NTW2

### 6.4.3 Strain Penetration

Figure 6.24 and Figure 6.25 show the relationship between applied load and rotation at the base of the wall due to strain penetration, and Figure 6.26 and Figure 6.27 show the relationship between rotation due to strain penetration and average curvature in the lower portion of the first story of the specimen. A strong relationship between these two values was expected because both depend on the strains in the longitudinal reinforcement. There was a strong linear correlation between the two values in the flange direction, and the rotation due to strain penetration was approximately equal to the rotation expected from an additional 6.3 in. of wall height. The correlation between the two values was weaker in the web direction, and included a tendency for the rotation due to strain penetration to become more negative, or for the top of the specimen to rotate towards the flange, as the test progressed.

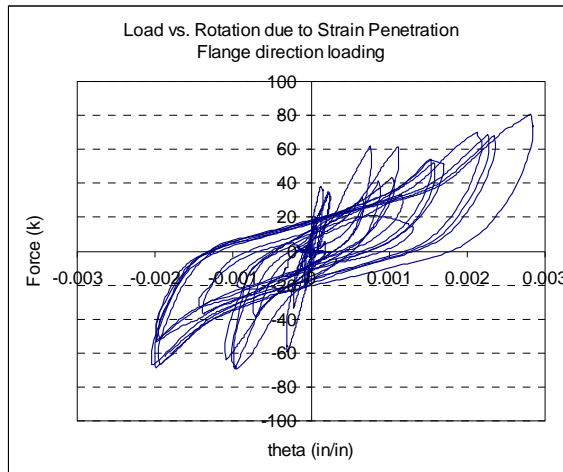


Figure 6.24. Flange direction load versus rotation due to strain penetration relationship for NTW2

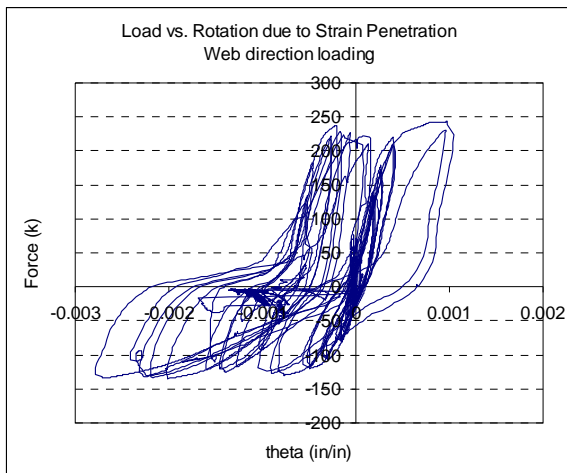


Figure 6.25. Web direction load versus rotation due to strain penetration relationship for NTW2

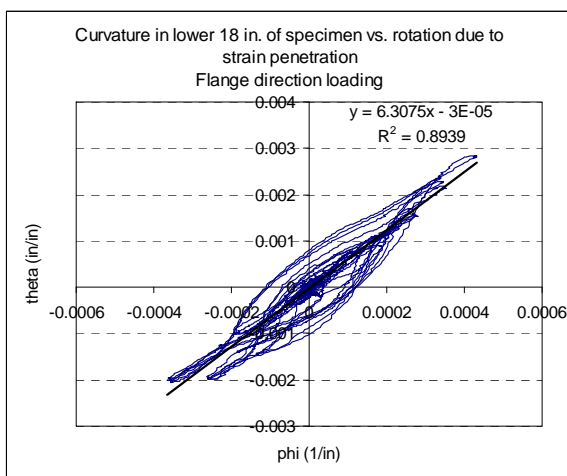


Figure 6.26. Flange direction relationship between curvature in lower portion of wall and rotation due to strain penetration for NTW2

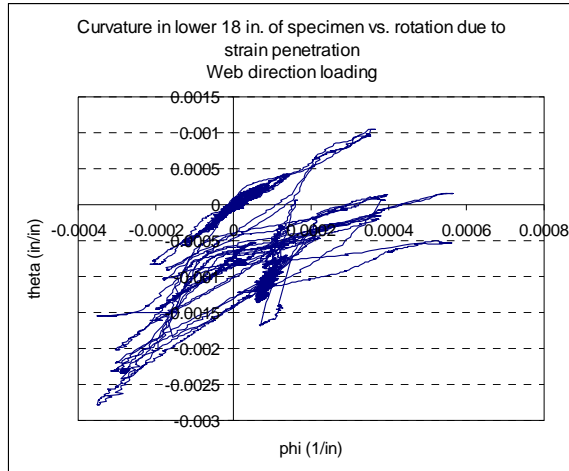


Figure 6.27. Web direction relationship between curvature in lower portion of wall and rotation due to strain penetration for NTW2

#### 6.4.4 Splice Slip

Figure 6.28 and Figure 6.29 show the relationships between rotation in the second story of the wall due to slip of the lapped longitudinal reinforcing bars and the applied load. Very little slip was measured, providing evidence in addition to the observed behavior and lack of damage in this region that placing the splice in the second story of the specimen reduced the demand on the splice enough to prevent failure. In Figure 6.28, it is apparent that one of the instruments used to derive the rotation of the flange was not working properly in the early portion of the test, producing a very noisy signal. This spontaneously resolved during the testing, before the majority of the flange-direction loading ramps were applied. Figure 6.29 includes some jumps in values that occurred at ramp peaks. It is expected that these jumps were the result of the instruments being bumped during the crack-marking process. However, because the jumps represent splice slips of  $<0.003$  in., the jumps were not removed in data processing because of the possibility that they may have represented real relative movement of the bars.

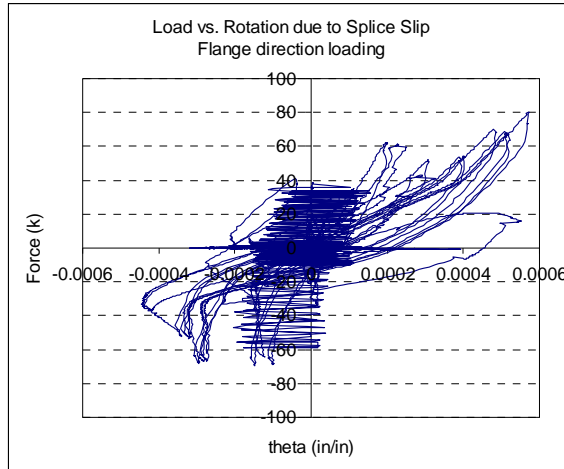


Figure 6.28. Flange direction load versus rotation due to splice slip relationship for NTW2

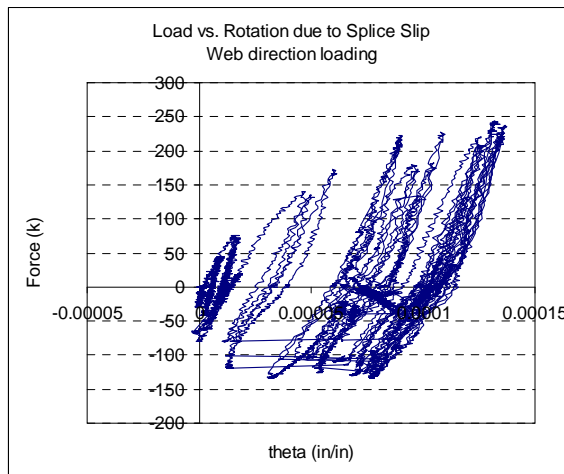


Figure 6.29. Web direction load versus rotation due to splice slip relationship for NTW2

#### 6.4.5 Contribution of Components to Total Deformation

Figure 6.30 through Figure 6.33 show the deformation associated with each component of the total deformation along with the total of these components and the deformation measured directly by an external string pot at the top of each story and for each loading direction. Figure 6.34 through Figure 6.37 plot the fractional contribution of each component to the total deformation at the top of each story for each peak in the applied loading history versus the lateral displacement. The sum of the individual

displacement components matches the directly measured value well when the displacement is at least 75 percent of the yield displacement, but the proportional error is larger in the early ramps to 25 percent and 50 percent of the yield displacement. Table 6.1 summarizes the contribution of each component to the total, externally measured displacement.

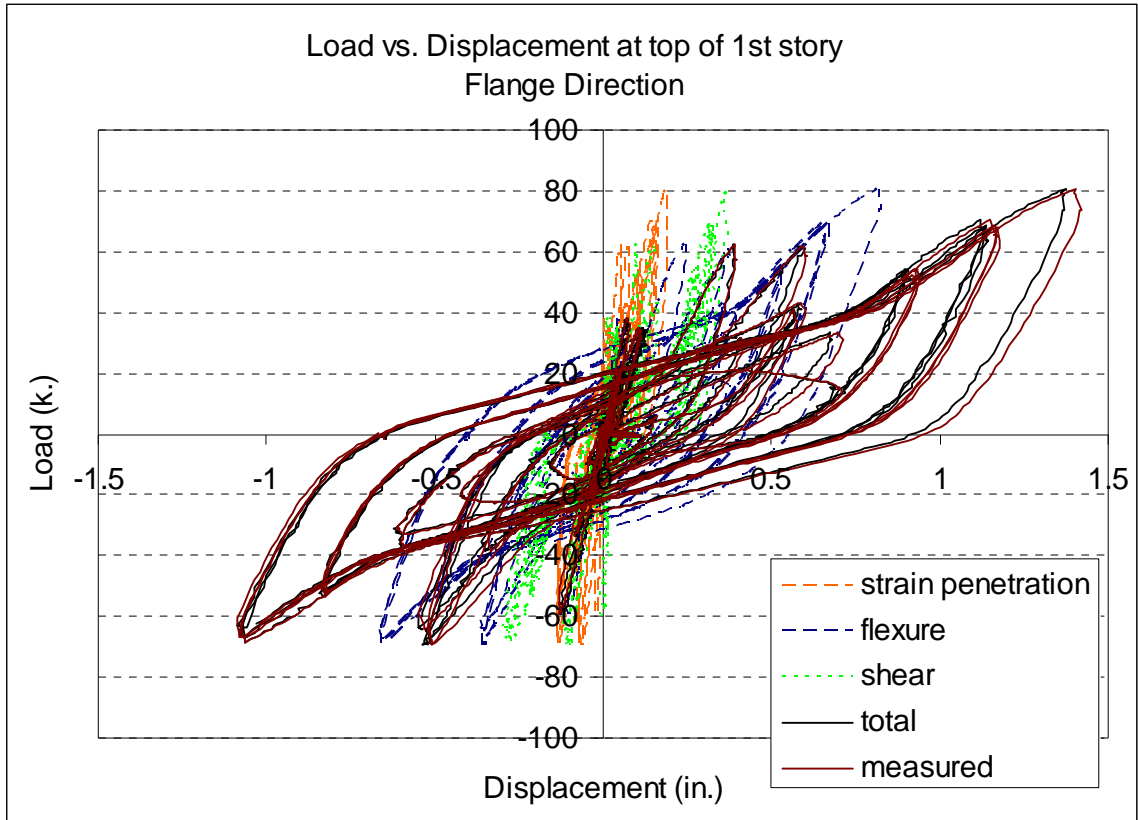


Figure 6.30. Flange direction load versus component displacement, first story, NTW2

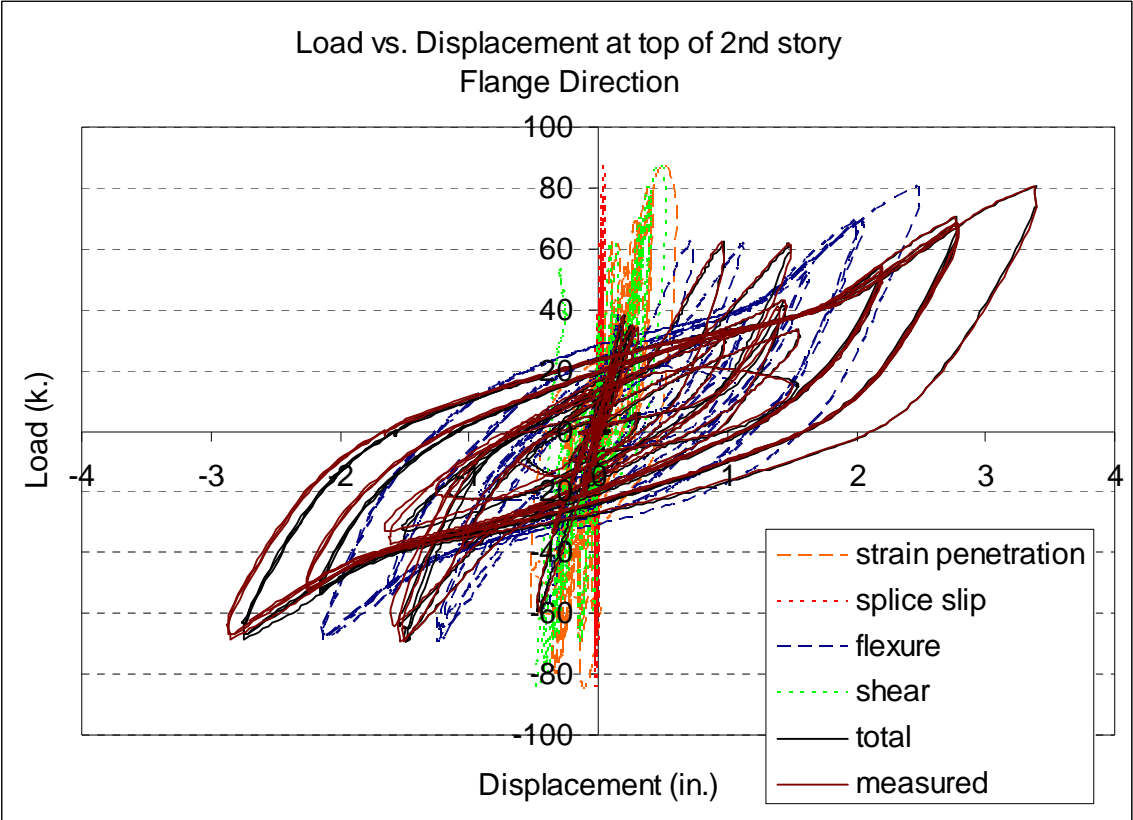


Figure 6.31. Flange direction load versus component displacement, second story, NTW2

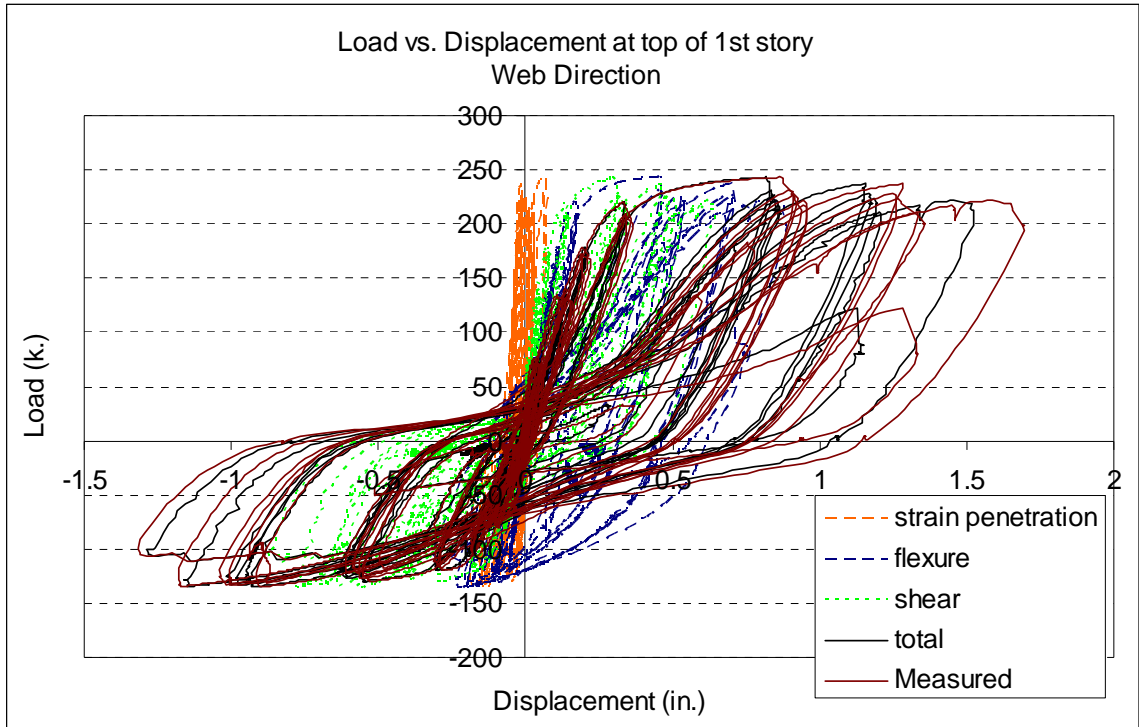


Figure 6.32. Web direction load versus component displacement, first story, NTW2

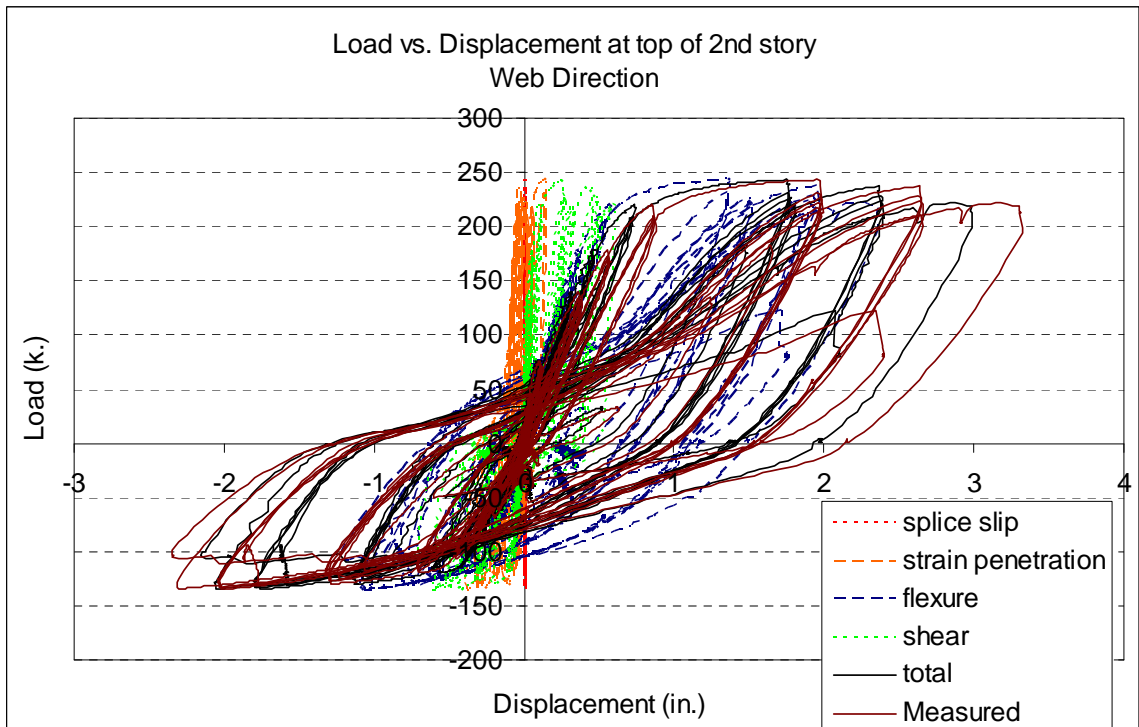


Figure 6.33. Web direction load versus component displacement, second story, NTW2

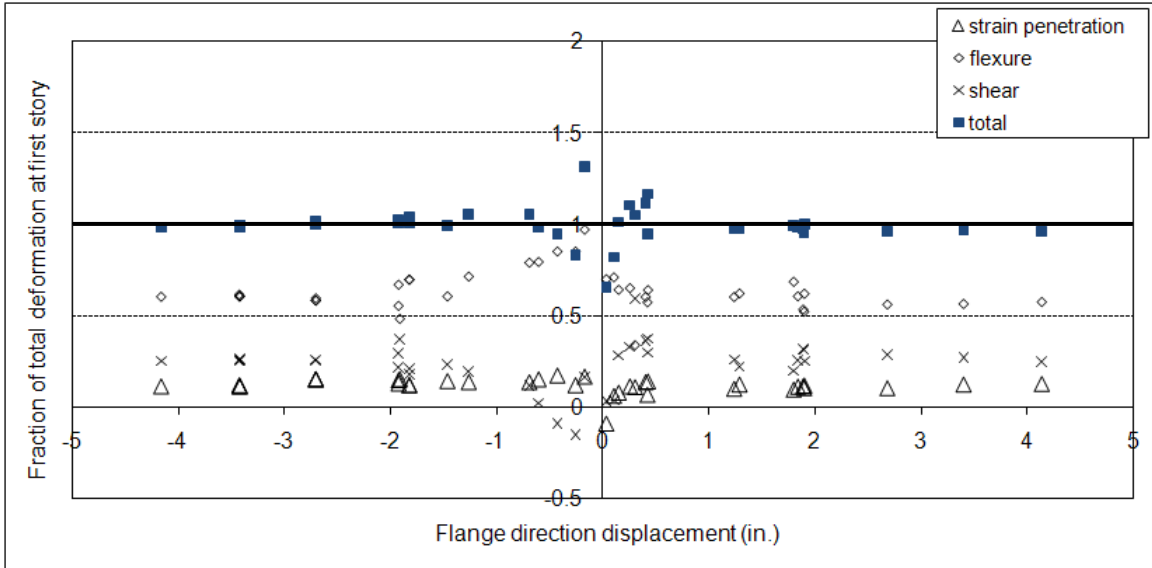


Figure 6.34. Flange direction contribution of each component to total first story displacement versus total displacement, NTW2

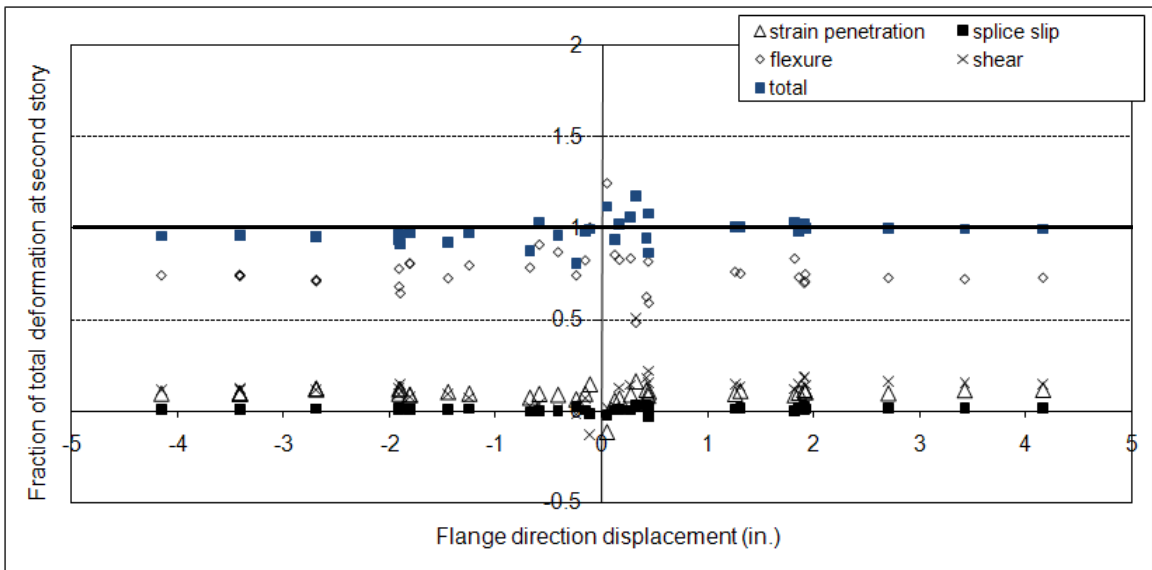


Figure 6.35. Flange direction contribution of each component to total second story displacement versus total displacement, NTW2

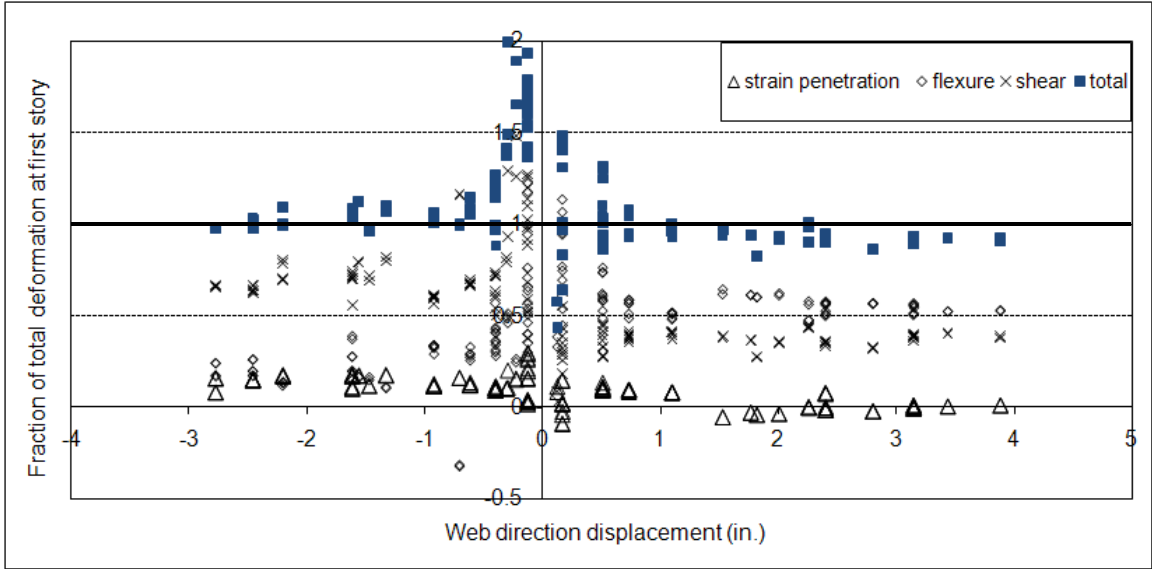


Figure 6.36. Web direction contribution of each component to total first story displacement versus total displacement, NTW2

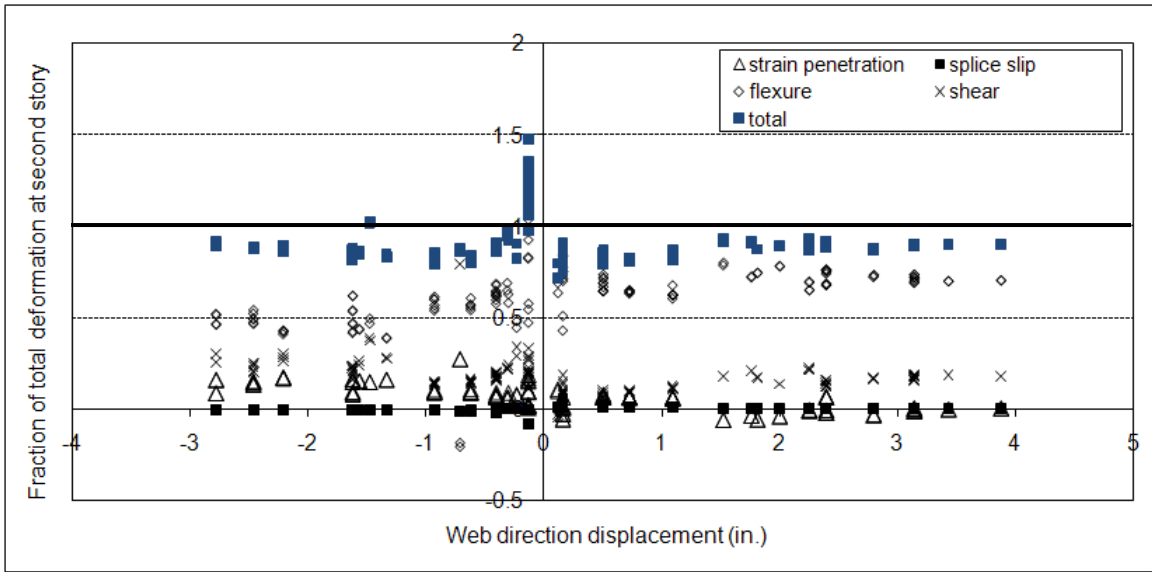


Figure 6.37. Web direction contribution of each component to total second story displacement versus total displacement, NTW2

Table 6.1. Contribution of each component of deformation to total, NTW2

		Story	Flexure	Shear	Strain Pen.	Splice Slip	Total	
Flange Direction	Pre-yielding	1	64%	29%	9%	NA	102%	
		2	83%	12%	7%	0%	102%	
	1% drift	1	66%	23%	13%	NA	102%	
		2	78%	11%	9%	1%	99%	
	1.5% drift	1	59%	27%	13%	NA	100%	
		2	73%	13%	11%	1%	98%	
	2.0% drift	1	58%	27%	15%	NA	100%	
		2	72%	12%	12%	1%	97%	
	2.5% drift	1	60%	26%	12%	NA	99%	
		2	74%	12%	10%	1%	97%	
	3.0% drift	1	59%	26%	13%	NA	97%	
		2	74%	13%	11%	1%	98%	
	Flange in Tension	Pre-yielding	1	72%	36%	5%	NA	113%
			2	70%	9%	4%	2%	84%
100% pred. yield		1	55%	38%	9%	NA	102%	
		2	65%	10%	7%	1%	82%	
150% pred. yield		1	50%	40%	8%	NA	98%	
		2	63%	12%	6%	1%	83%	
1.5% drift		1	54%	35%	2%	NA	91%	
		2	73%	15%	2%	0%	90%	
2.0% drift		1	53%	38%	0%	NA	91%	
		2	72%	18%	0%	0%	90%	
2.5% drift		1	52%	39%	0%	NA	92%	
		2	71%	19%	0%	0%	90%	
Flange in Compression		Pre-yielding	1	52%	80%	12%	NA	144%
			2	81%	20%	8%	-3%	107%
	100% pred. yield	1	28%	68%	12%	NA	109%	
		2	57%	16%	10%	-1%	82%	
	150% pred. yield	1	32%	60%	11%	NA	103%	
		2	58%	15%	10%	-1%	83%	
	1.0% drift	1	23%	68%	13%	NA	104%	
		2	51%	25%	13%	0%	89%	
	1.5% drift	1	21%	64%	15%	NA	99%	
		2	50%	23%	15%	0%	88%	
	2.0 % drift	1	20%	66%	12%	NA	98%	
		2	49%	28%	13%	0%	90%	

## 6.5 Effective Flange Width

Figure 6.38 shows the measured distribution of strain across the width of the flange associated with flange-in-tension loading at several displacement levels through the expected yield displacement. Loading to larger displacement is not included because all bars were yielded and can be assumed to have similar stress levels regardless of strain. These strains were measured with the strain gauges attached to the longitudinal reinforcement 6 in. above the foundation block.

The overhanging flange width of 33 in. was less than the limits suggested in ACI 318-02 of 25 percent of total wall height (108 in.), previous code provisions (UBC 1994) of 10 percent of total wall height (43.2 in.), or the literature ( $0.6*d$  for low drift levels = 48.6 in.), suggesting that the flange should be expected to be fully effective in tension. However, from the plot of measured strain, it is apparent that there was some shear lag effect. Table 6.2 compares the measured base moment at several loading levels with the moment calculated using BIAX to reach the measured strain at the center of the web. When strains in the center of the flange were in the range of 1000 to 2500  $\mu\epsilon$ , the measured load was approximately 20 percent less than the expected load as a result of shear lag causing decreased strains in the boundary element reinforcement. As the drift level increased beyond this region, the effects of shear lag on the load capacity of the specimen decreased as additional steel reached the yielding point. When the strain in the center of the section reached 5000  $\mu\epsilon$ , shear lag caused a decrease in load of less than 1 percent. Because the stress in the steel remains relatively constant after yielding, large differences in strain do not cause large differences in the moment resisted by the section.

This indicates that the flange can be assumed to be fully effective as long as the entire section has yielded, but using a reduced effective flange width is appropriate for analysis prior to yielding.

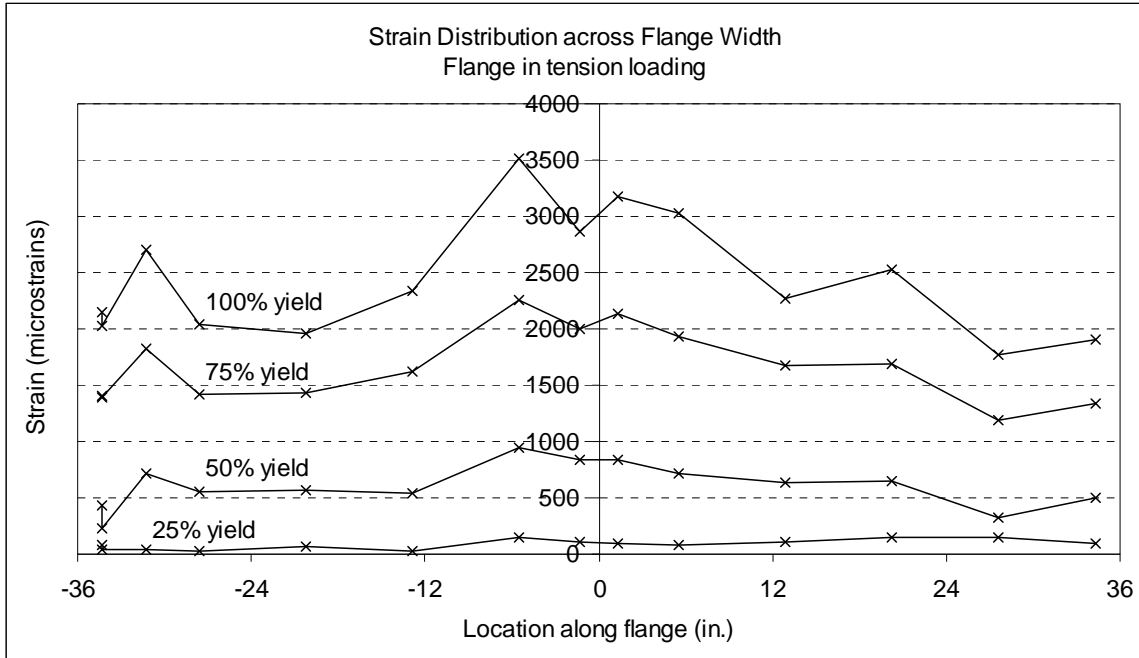


Figure 6.38. Strain distribution across width of flange, 6 in. above foundation, NTW2

Table 6.2. Effects of shear lag on flange-in-tension moment resistance, NTW2

Maximum Flange Reinforcement Strain ( $\mu\epsilon$ )	Measured base moment (k-in)	Expected base moment for measured strain (k-in)	difference
500	20200	20100	-0.3%
1000	23900	30000	20.0%
1500	31500	40200	22.0%
2000	40100	50300	19.0%
2500	48400	59700	19.0%
3000	53900	62000	13.0%
4000	60200	63800	6.0%
5000	64600	65300	1.0%
6000	67000	66500	-1.0%
7000	68100	67400	-1.0%

## **Chapter 7 Comparison of NTW1 and NTW2**

### **7.1 Introduction**

This chapter compares the observed behavior of the two T-shaped wall specimens, NTW1 and NTW2. It then attributes the observed differences between the specimens to the associated differences in the design and detailing of the specimens. It should be recalled that although specimen NTW2 included a smaller portion of the prototype structure than specimen NTW1, additional moment was superimposed at the top of specimen NTW2 using the MAST crosshead so that both specimens NTW1 and NTW2 had moment-to-shear ratios of 312 in. at the base.

### **7.2 Applied Load History and Deformed Shape**

To facilitate comparison of the observed responses of specimens NTW1 and NTW2 and avoid load-history-dependent effects, the load histories applied to the specimens were matched as closely as possible. However, because of the differences in detailing and sub-assembly size, there were small differences in the applied histories. During the initial elastic portion of testing specimen NTW1, peak displacements for each cycle were increased from the initially planned values so that the measured loads would more closely match the loads predicted by the preliminary model. The result of this was that strains were increased, and fewer cycles than desired were completed prior to yielding of the reinforcement. The elastic portion of the load history was modified for specimen NTW2 so that the applied displacement measured at the top of the second story was approximately 30 percent of that of specimen NTW1. The same number of cycles was imposed prior to reaching 1 percent drift, but the early cycles were re-scaled to keep

NTW2 in the elastic range for the first 18 cycles as originally intended for NTW1, rather than the three cycles for which NTW1 was observed to remain elastic.

Post-yielding, the loading history applied was intended to place similar displacement demands on specimen NTW2 as NTW1. The six-degree-of-freedom (6DOF), mixed-mode capabilities of the MAST system allowed for moments to be applied to the top of the specimen so that a consistent shear-to-moment ratio was applied to both specimens, despite the difference in specimen heights. The global displacements measured at the top of the second story of NTW1 were used to determine the displacements to be applied to NTW2, with measured rotations at the top of the second story of NTW1 used to account for the presence of the top block between the second story of NTW2 and the MAST crosshead. However, the differences in the specimens, particularly the inclusion of lap splices in the second story of NTW2 caused a small change in the deformed shape of the specimen, especially after yielding, as shown in Figure 7.1.

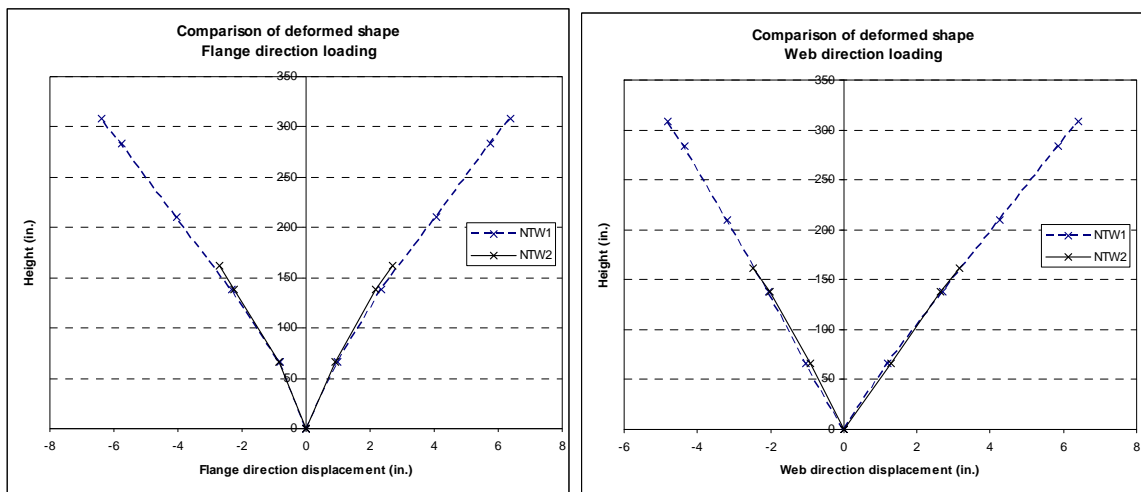


Figure 7.1. Comparison of overall deformed shapes

Figure 7.2 compares the relationships between the measured first and second story displacements at each displacement level applied during the testing. In the web loading direction, the first story displacement of specimen NTW1 was an average of 44 percent of the second story displacement, while the first story displacement of specimen NTW2 was an average of 45 percent of the second story displacement. In the flange loading direction, the first story displacement of specimen NTW1 was an average of 39 percent of the second story displacement, while the first story displacement of specimen NTW2 was an average of 40 percent of the second story displacement. As a result of these small differences in the deformed shapes of the specimens and the presence of the top block between the top of the second story, where similar displacements were desired, and the MAST crosshead, where the displacements were controlled, predicting the target displacements for the MAST crosshead, was not perfect, and the measured displacements at the top of the second story did not match perfectly.

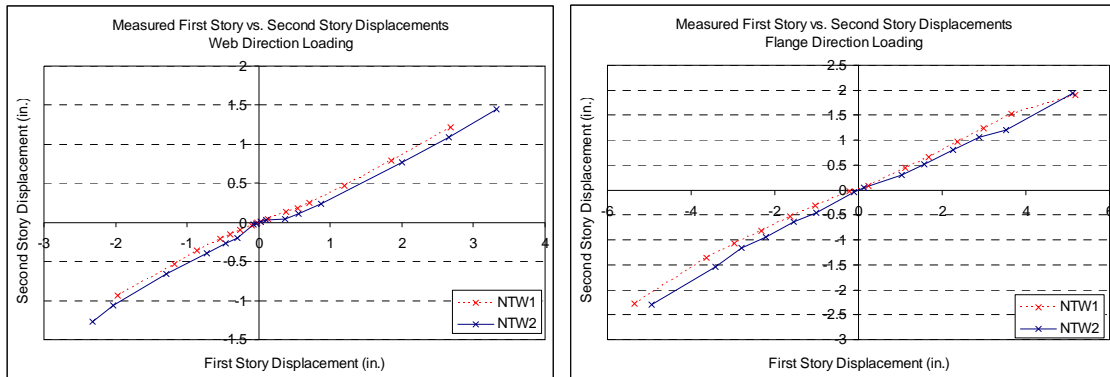


Figure 7.2. Relationships between measured first and second story displacements.

After yielding, the flange direction displacements measured at the top of the second story of specimen NTW1 were 5 to 15 percent larger than those measured in specimen NTW2. Web direction displacements measured at the top of the second story

of specimen NTW1 were 15 to 25 percent larger than those measured in NTW2 at yielding and ranged from 8 percent smaller to 4 percent larger after yielding. In addition to these variations in the displacement applied at the second story level, there was some concern that because of the potential changes to the deformed shape, the applied loading history would not place the same demands on NTW2 as NTW1, which was desired to facilitate comparison of the specimen behaviors. In particular, there was concern that the relatively rigid splice region in the second story would concentrate deformations and damage in the first story of the specimen at a given displacement measured at the top of the second story of either specimen. Because of this, an increased amount of damage was expected in the first story of NTW2 for a given displacement level. These concerns were not realized during the testing. Figure 7.3 compares the displacements of the two specimens at the top of the second story throughout the tests.

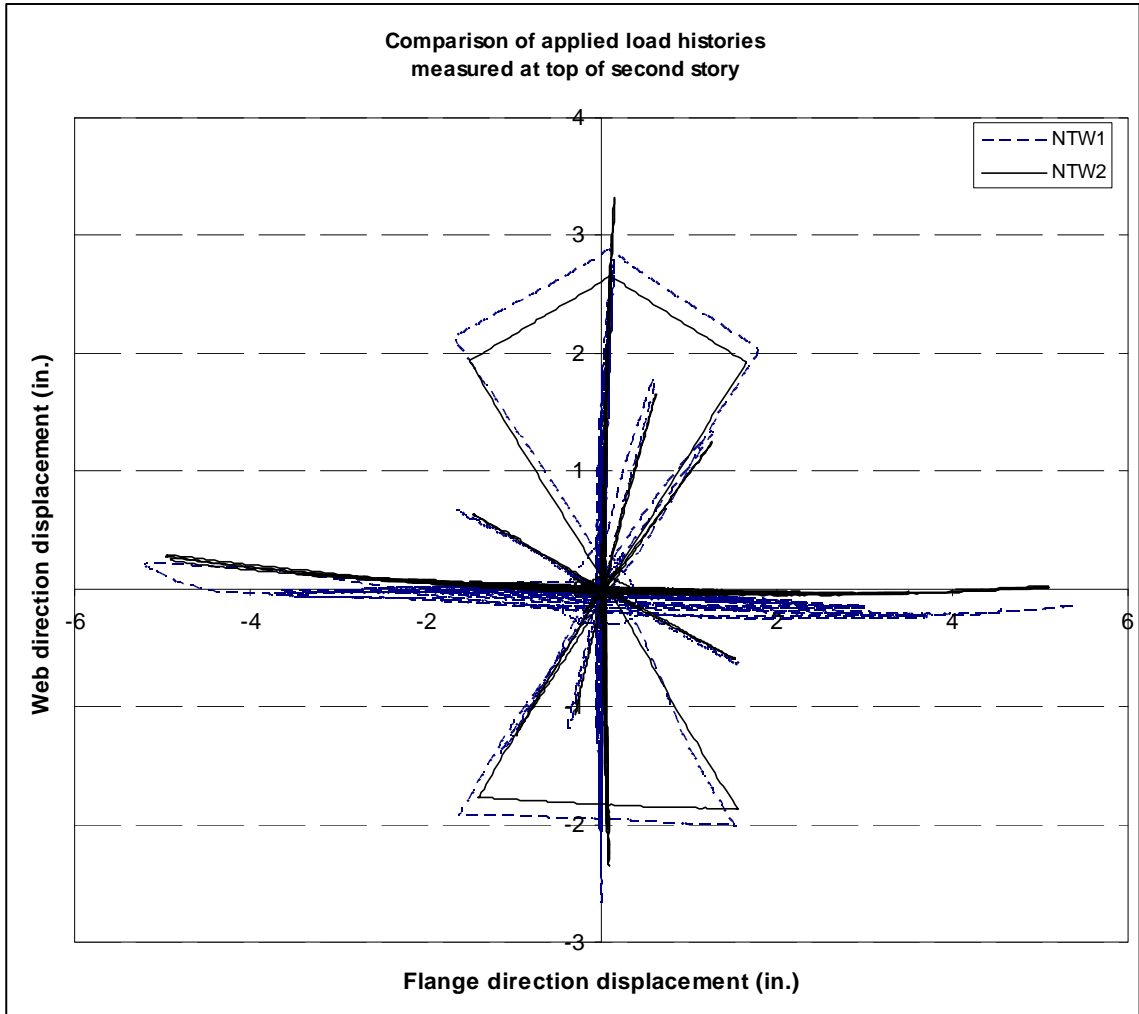


Figure 7.3. Comparison of applied load histories.

### 7.3 Load and Displacement Capacities and Relationships

Table 7.1 and Table 7.2 compare the loads and displacements associated with first yielding, maximum moment resistance, and failure for the two specimens in each of the orthogonal loading directions. Figure 7.4 and Figure 7.5 compare the load versus second story displacement relationships for the two specimens in each of the orthogonal loading directions. For this discussion, “failure” of the wall is defined at the displacement associated with a decrease in moment resistance to 90% of the maximum measured value.

As mentioned previously, there was some variation between the displacement histories applied to the specimens. It can be seen from the tables and figures that specimen NTW2 was initially stiffer than specimen NTW1 and had a larger load capacity when loaded parallel to the web. Specimen NTW1 consistently required larger forces than specimen NTW2 to reach displacement targets when loaded parallel to the flange. These differences may be the result of differences in the reinforcing steel used in the specimens.

Regardless of bar size, the reinforcement in specimen NTW1 had a yield stress  $f_y$  in the range of 62 to 63 ksi, while the reinforcement in specimen NTW2 had a yield stress in the range of 66 to 75 ksi. In addition, the reinforcement was uniformly distributed across the flange of specimen NTW2, while a similar area of steel (total area of steel  $A_s$  of 10.2 in.<sup>2</sup> versus 9.32 in.<sup>2</sup>) was primarily concentrated in the flange tips of specimen NTW1, which had only minimum reinforcement between the flange tips. Combining the area of steel and yield stress result in a total tensile stress at yielding  $A_s f_y$  of 631k for NTW1 and 661k for NTW2. Although specimen NTW2 had 10 percent less reinforcement in the flange, as discussed in Section 3.3.1, the greater shear lag effects associated with concentrating the reinforcement in the flange tips of specimen NTW1 likely contributed to the difference in stiffness prior to first yielding when loaded parallel to the web, while the increased reinforcement strength in specimen NTW2 increased the capacity of the specimen.

When loading parallel to the flange, concentrating the reinforcement in the flange tips of specimen NTW1 tended to cause an increase in the stiffness and load capacity of

this specimen relative to specimen NTW2, while the difference in reinforcement properties had an opposite, but smaller, effect, leading to specimen NTW1 having the greater load capacity.

Table 7.1. Measured loads, displacements and stiffnesses at first yielding.

	Loading Direction	Story	V (k)	$\Delta$ (in.)	V/ $\Delta$ (k/in.)
NTW1	Flange in Tension	2	115	0.5	250
		4		0.9	130
	Flange in Compression	2	81	0.4	188
		4		1.1	73
NTW2	Flange in Tension	2	132	0.4	350
	Flange in Compression	2	84	0.3	270

Table 7.2. Measured loads and displacements at wall failure.

	Loading Direction	Story	V <sub>max</sub> (k)	$\Delta$ @ V <sub>max</sub> (in.)	$\Delta$ @ 90%V <sub>max</sub> (in.)
NTW1	Flange Direction	2	100	3.6	4.7
		4		8.7	10.6
	Flange in Tension	2	229	2.7	2.8
		4		5.6	5.9
	Flange in Compression	2	121	2.1	2.1
		4		3.8	3.8
NTW2	Flange Direction	2	87	4.4	4.9
	Flange in Tension	2	240	2.0	3.3
	Flange in Compression	2	132	2.3	2.3

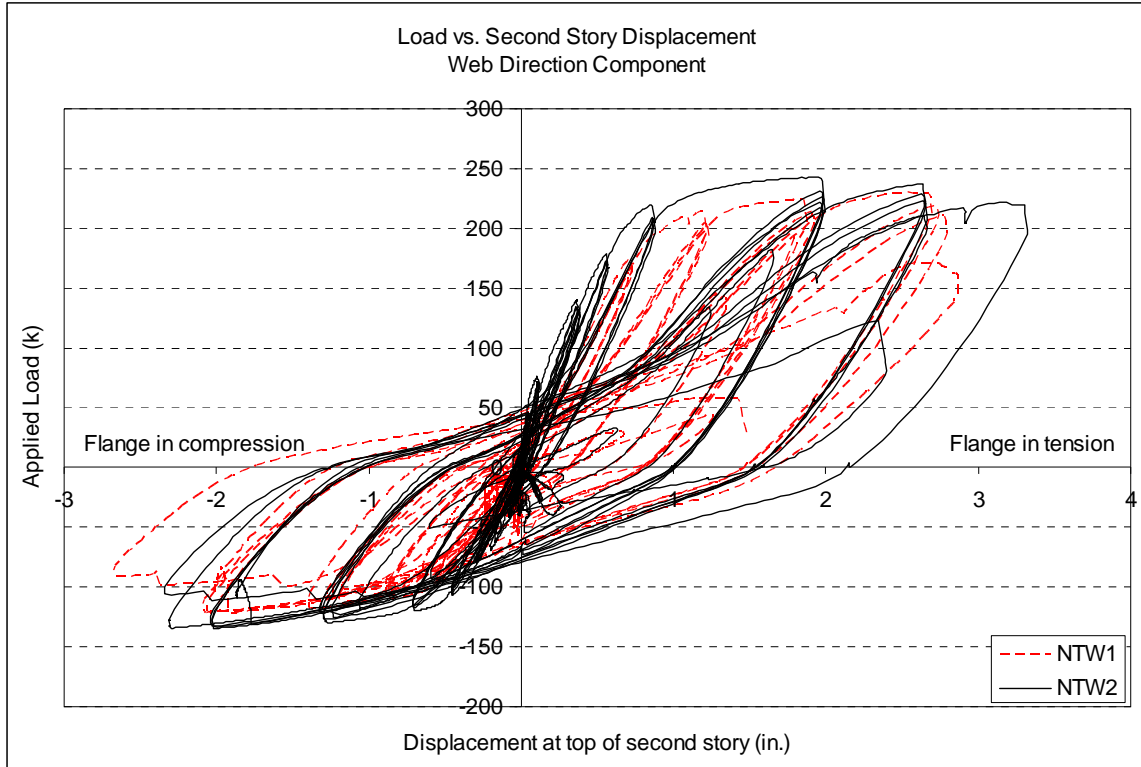


Figure 7.4. Web direction load versus displacement at top of second story of each specimen.

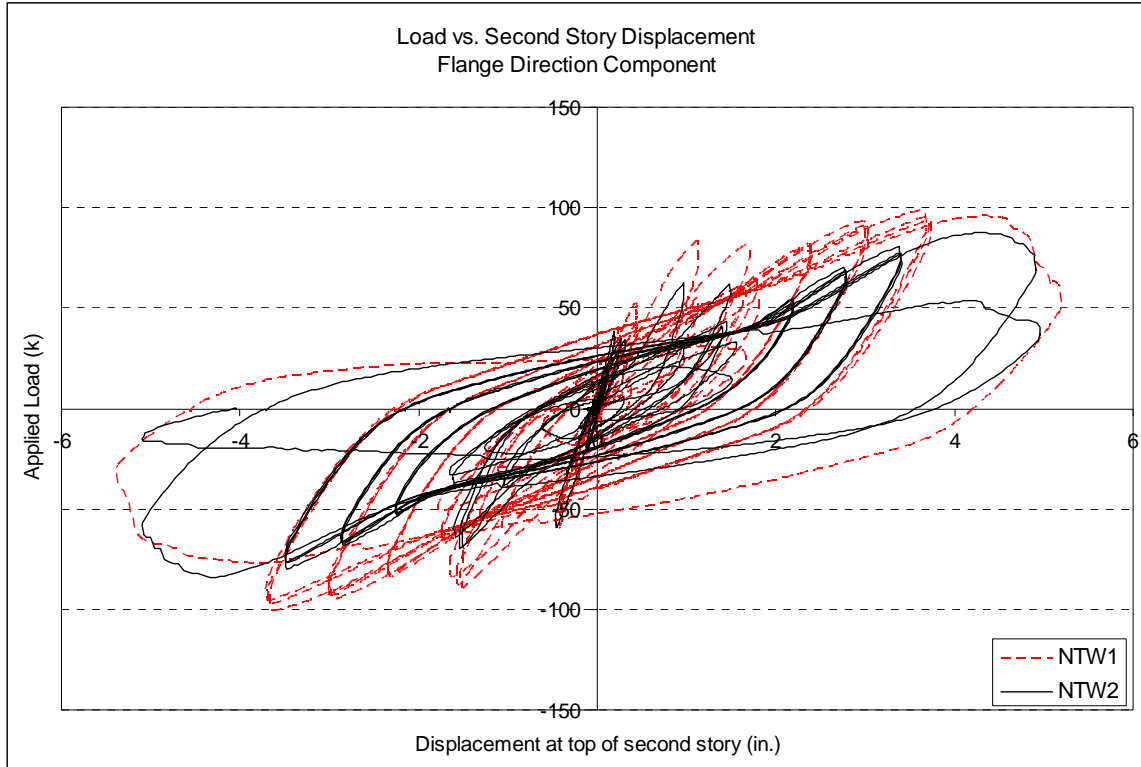


Figure 7.5. Flange direction load versus displacement at top of second story of each specimen.

#### 7.4 Energy Dissipation

The total energy absorbed by the specimen in each half cycle, from zero load to the peak, and the total energy dissipated in each half cycle, from zero load to zero load, were calculated for both specimens in each of the orthogonal loading directions. Skew direction ramps are included by using the orthogonal components of load and displacement. Figure 7.6 and Figure 7.7 show the total energy dissipated by each of the specimens during each half cycle of the loading history in each of the orthogonal loading directions. The total energy dissipated by the specimens over the entire applied load history is summarized in Table 7.3.

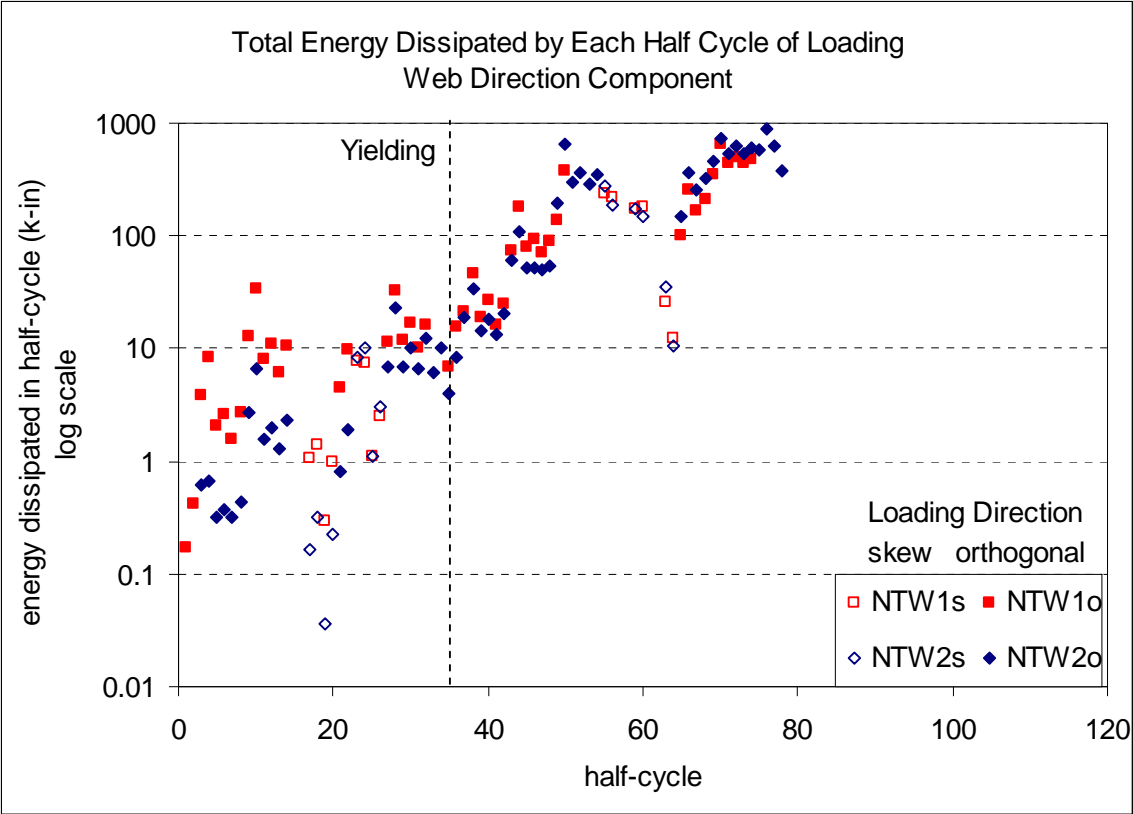


Figure 7.6 Web direction component of total energy dissipated in each half cycle of loading.

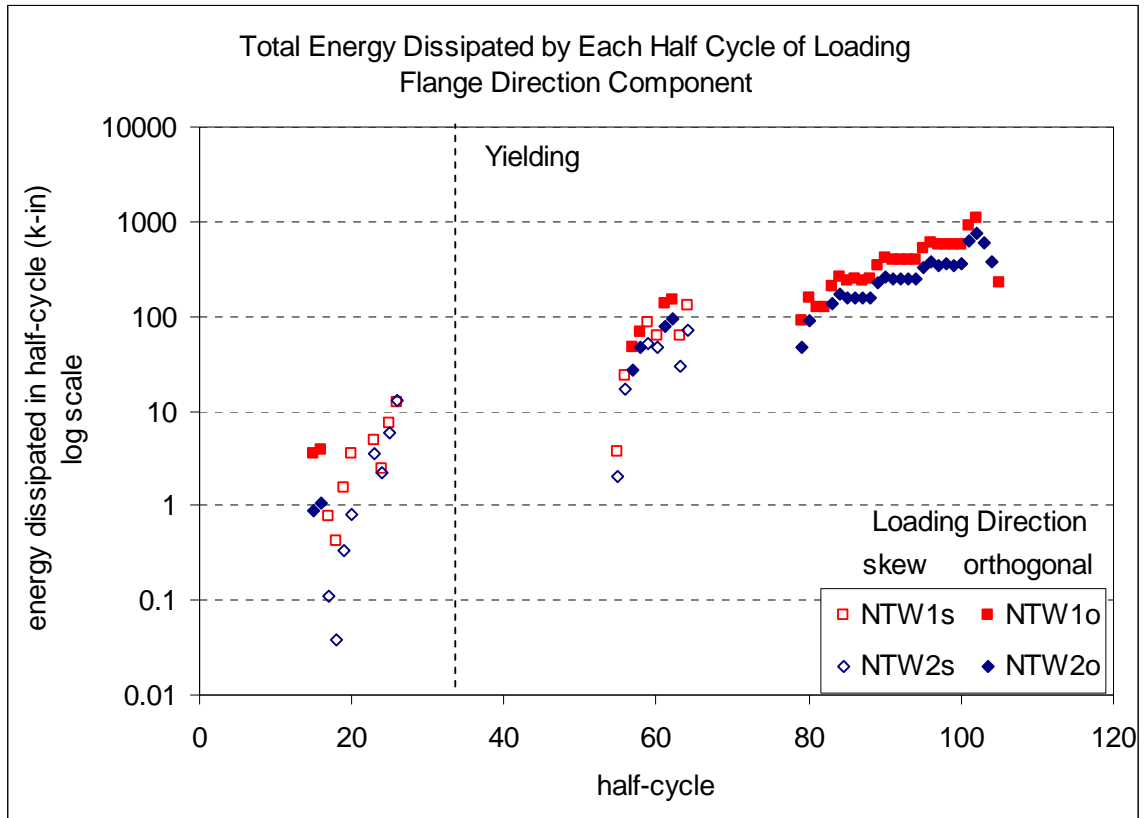


Figure 7.7. Flange direction component of total energy dissipated in each half cycle of loading.

Table 7.3. Energy dissipated over entire load history (k-in)

Component of Loading	NTW1	NTW2
Flange Direction	11200	7850
Web Direction	7720	11900

In the web direction, specimen NTW1 dissipated 50 percent more energy than specimen NTW2 in each half cycle with applied displacements in the range from 75 percent to 150 percent of expected yielding. This is largely the result of larger displacements being imposed on NTW1 in this portion of the testing, as discussed in Section 7.2. In each of these cycles, the energy dissipated was less than 10 k-in., while the energy dissipated over the course of the test was three orders of magnitude greater. Following this portion of the testing, when similar displacements were applied to the

specimens, specimen NTW2 dissipated 35 percent more energy than specimen NTW1 in each half cycle in the web direction. In the flange direction, specimen NTW1 dissipated 60 percent more energy than specimen NTW2 in each half cycle after yielding. These trends were applicable to both orthogonal-direction loading and to the orthogonal components of skew-direction loading. The large differences in the total energy dissipated by each specimen were primarily the result of the differences in stiffness and capacity noted above. In order to make a more meaningful comparison of the energy dissipation capacity of each specimen, the fraction of the total absorbed energy that was dissipated by each cycle was calculated. These values are compared in Figure 7.8 and Figure 7.9.

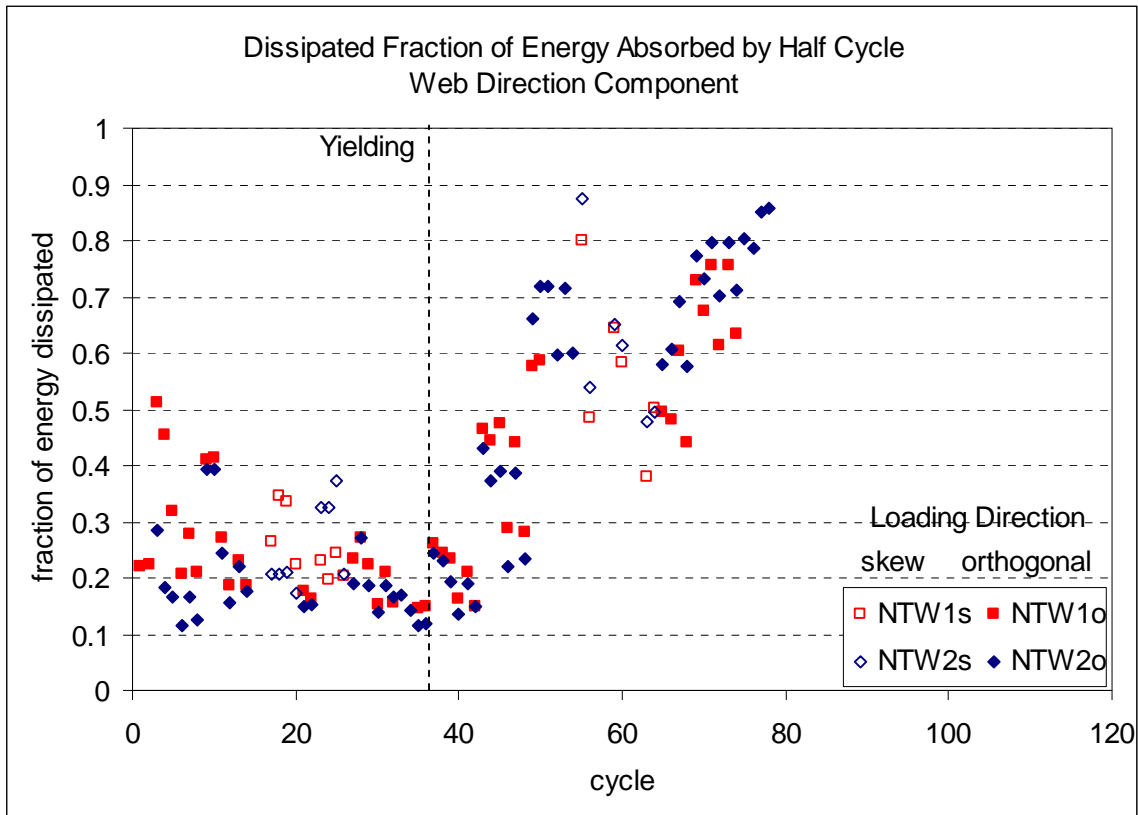


Figure 7.8. Dissipated fraction of web direction energy absorbed by each half cycle.

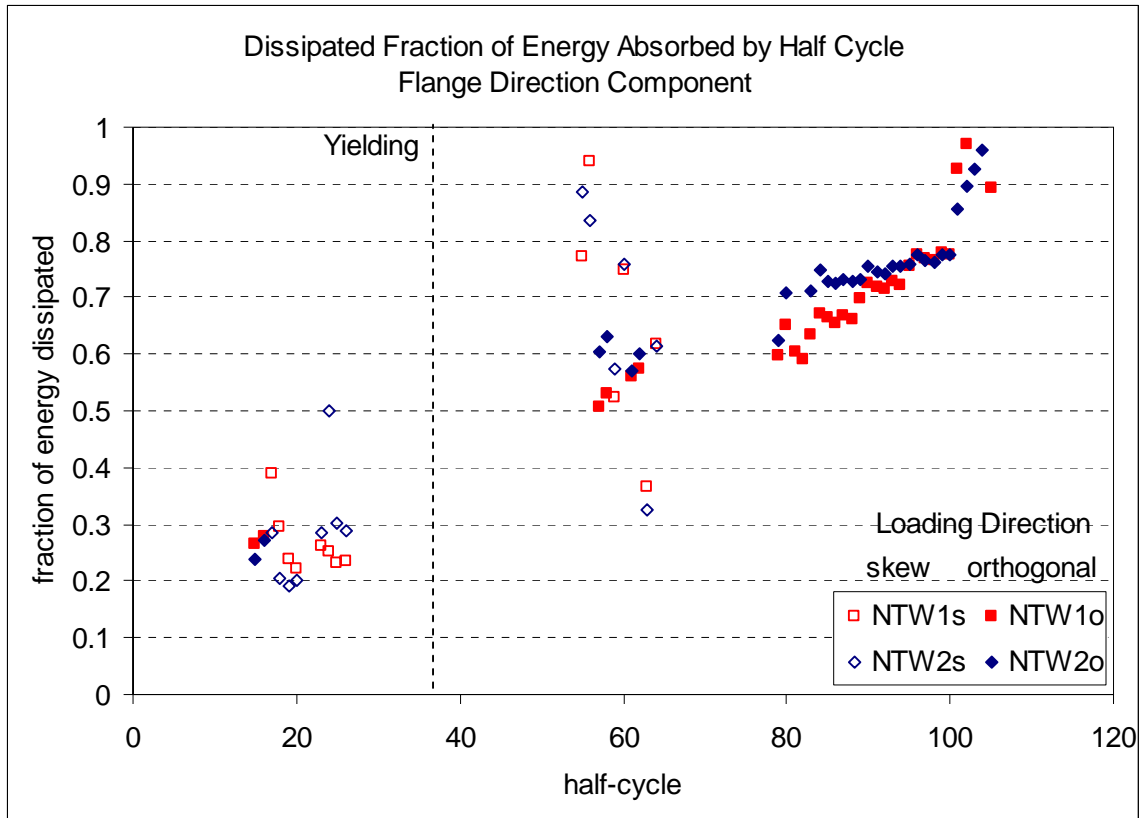


Figure 7.9. Dissipated fraction of flange direction energy absorbed by each half cycle.

In both loading directions, a larger fraction of energy was absorbed by specimen NTW1 prior to yielding. This was a result of larger displacements being imposed on specimen NTW1 in the early portion of the test. These larger displacements caused more extensive cracking and some yielding occurring in specimen NTW1. However, differences in energy dissipated at this point in the testing were two orders of magnitude smaller than those encountered at large ductilities. After yielding, the fraction of energy dissipated increased as well as the magnitude because of yielding and damage accumulation. In the web direction, specimen NTW2 dissipated a larger fraction of the absorbed energy than specimen NTW1 throughout the post-yielding portion of the testing. In the flange direction, specimen NTW2 dissipated a larger fraction of the

absorbed energy at drift levels up to 2.5 percent. At 3 percent drift, there was no significant difference between the two specimens, and at 4 percent drift, specimen NTW1 dissipated a larger fraction of energy in the first cycle to this drift level. This large energy dissipation was associated with failure of the specimen, and similar dissipation fractions occurred in specimen NTW2 in the second cycle to this drift level, where failure occurred.

### **7.5 Crack Distribution**

The modifications made to the detailing of specimen NTW2 (i.e., uniform distribution of flange reinforcement, incorporation of lap splices, increased confined region dimensions, and decreased spacing of shear reinforcement) led to three notable differences in the pattern and size of cracks that developed. First, the orientation and spacing of the cracks in the flanges of the specimens differed. In specimen NTW1, closely spaced horizontal cracks developed in the flange-tip boundary elements, while more widely-spaced, inclined cracks formed in the lightly reinforced center of the flange, forming a V shape. In specimen NTW2, uniformly spaced horizontal cracks formed over the entire flange width. In both specimens, these crack patterns were established in the first cycles of the applied load history, when only orthogonal loading placing the flange in tension and flange in compression was applied. Figure 7.10 compares the crack patterns in the two specimens at this point in the load history. Because these patterns developed prior to any skew- or flange-direction loading, it is an indication that they are associated with a reduction in shear lag effects in specimen NTW2, with uniformly distributed flange reinforcement, relative to NTW1, with reinforcement concentrated in

the boundary elements. Subsequent cracking in both specimens tended to follow the initially established patterns. This can be seen in Figure 7.11, which shows the crack patterns after the initial skew- and flange-direction cycles were applied, and Figure 7.12, which shows the crack patterns after testing was completed. In the photographs in Figure 7.11, cracks that formed during skew-direction loading are highlighted in green, and those that formed during flange-direction loading are highlighted in purple. As a result of this tendency, while several distinct inclined shear cracks developed in the flange of specimen NTW1 during flange direction loading, none were observed in the flange of specimen NTW2.

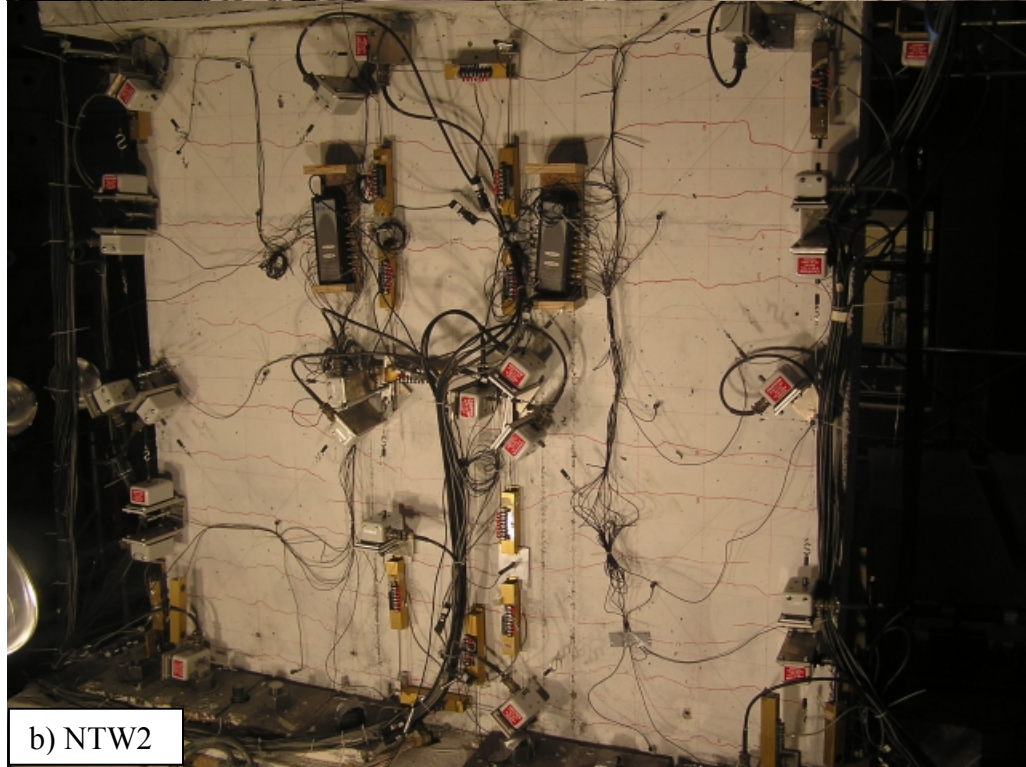
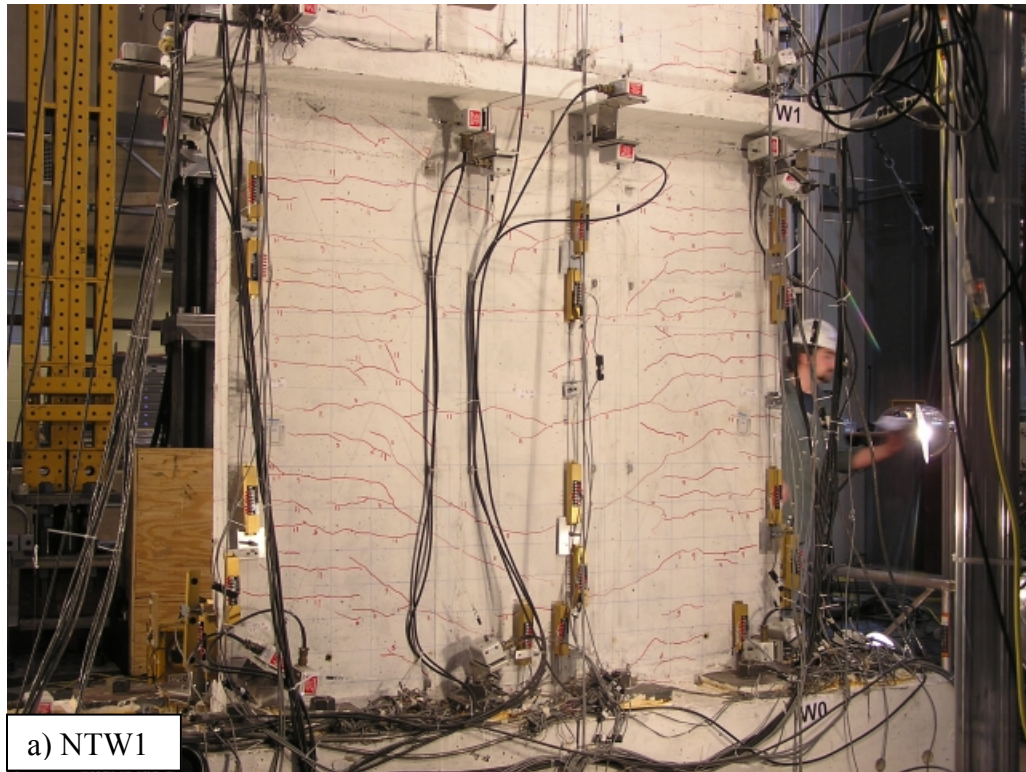


Figure 7.10. Crack patterns in first stories of flanges after initial web direction loading.

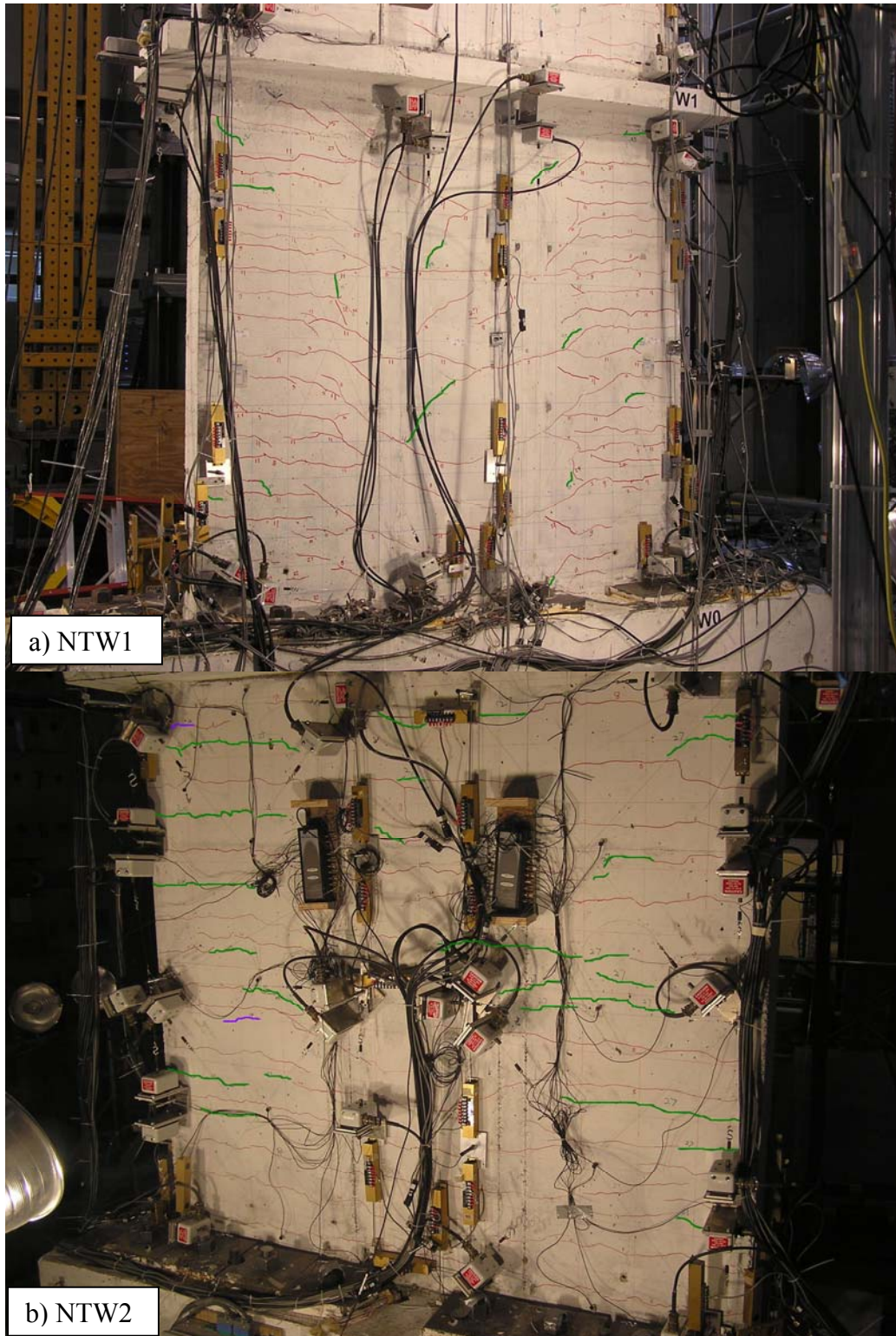


Figure 7.11. Crack patterns in first stories of flanges after initial skew- and flange- direction loading.



a) NTW1

b) NTW2

Figure 7.12. Crack patterns in first stories of flanges after completion of testing.

The second difference between the crack patterns observed in the two specimens was that both horizontal and inclined cracks in the splice region of specimen NTW2 were limited to a width of 0.007 in. or less. Cracks in specimen NTW1 were widest near the base of the specimen and consistently decreased as the flexural demand decreased with height, while this pattern of decreasing crack width was interrupted in specimen NTW2. While crack spacing was not affected, the lap splices in the lower portion of the second story of specimen NTW2 prevented yielding of the reinforcement. Above and below the lap region, crack widths in the two specimens were similar, but the reduced strains in the lap region of the specimen prevented cracks from becoming wider than hairline or 0.007 in.

The third difference in the observed crack patterns was that fewer shear cracks were observed in the web of the second story of specimen NTW2 than in specimen NTW1. As shown in Figure 7.13, shear cracks were approximately uniformly spaced over the lightly reinforced portion of the web of specimen NTW1, with several of the cracks intersecting the slab above, between the second and third stories. However, there were fewer shear cracks in the web of specimen NTW2 and none of the cracks intersected the top block above the wall. Because the upper portion of the wall segment was affected more than the lower, it is unlikely that this was a result of the lap splices in specimen NTW2 preventing yielding of the reinforcement. A much more likely source of this behavior was the restraining effect of the top block, which was heavily reinforced and designed to remain elastic throughout the testing. This behavior was not observed in

the flange, but, as discussed previously, the flange of specimen NTW2 was dominated by horizontal cracks and inclined shear cracks were not observed in specimen NTW2.

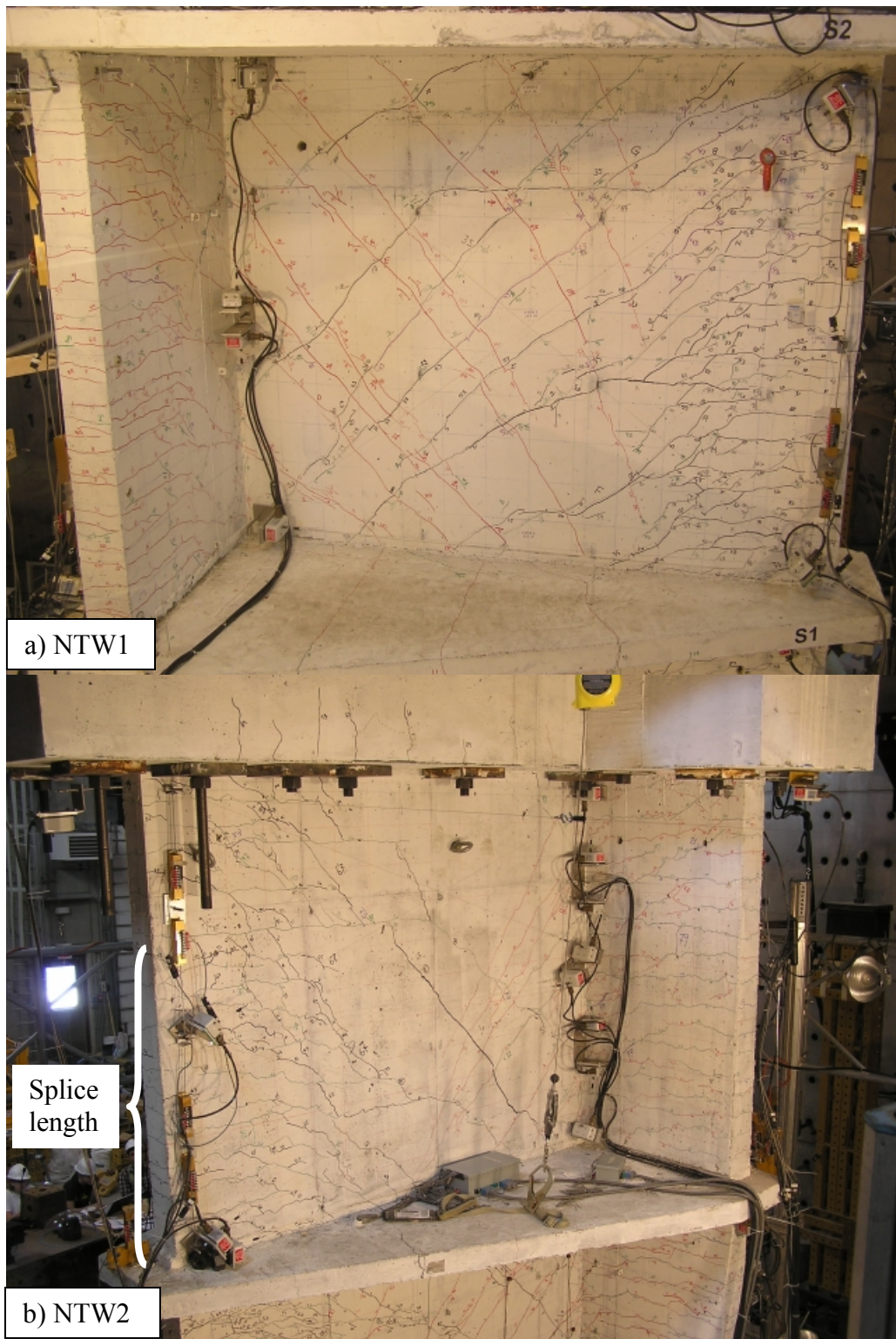


Figure 7.13. Crack patterns in second stories of webs after web failure.

## 7.6 Flexural Deformation

Figure 7.14 through Figure 7.17 compare the interstory rotations (i.e., the integration of curvature within the story over the story height) measured in the lower two stories of each specimen. In the web loading direction, the initial flexural stiffnesses of the first stories of the two specimens were very similar in the web direction, and the backbone curves were similar, although larger rotations were measured in specimen NTW2 when loading with the flange in compression. The small differences between the first story flexural responses were the result of several factors discussed previously.

These include

- 1) the lap splices decreasing the deformation of the second story of NTW2 and therefore increasing the deformation of the first story in order for the total displacement at the top of the second story to remain constant between NTW1 and NTW2;
- 2) the distribution of the flange reinforcement decreasing the flange direction flexural stiffness and capacity of NTW2 while slightly increasing the web direction stiffness by reducing the effects of shear lag; and
- 3) differences in the yield stress of the reinforcement between the specimens.

In the second story, neither specimen developed large hysteresis loops. Because the yielding was limited in the second story of both specimens, the following comparisons between the behavior of the two specimens were consistent throughout the testing. Specimen NTW2 was 10 percent stiffer than specimen NTW1 in the flange-in-tension loading direction and twice as stiff in the flange-in-compression loading direction. In the flange loading direction, the magnitudes of the rotation in the first

stories of each specimen were similar for each cycle, but specimen NTW1 required larger loads to reach these deformations. In the second story, specimen NTW2 was approximately 2.4 times stiffer than specimen NTW1.

The differences between the second story stiffnesses were primarily the result of the lap splices increasing the initial stiffness and preventing yielding in the lower portion of the second story of specimen NTW2. Additionally, there was some change in stiffness due to the reduced magnitude of shear lag in the flange of specimen NTW2 relative to specimen NTW1. The smaller difference in the flange-in-tension loading direction compared to the flange-in-compression or flange loading directions was likely the result of less yielding occurring in specimen NTW1 in the flange-in-tension loading direction, although yielding was measured in the reinforcement over the entire height of the first two stories of the structure. Particularly in specimen NTW1, the measured yielding may have been exaggerated by the process of grinding a flat spot on the bar for the application of the strain gauge, causing a reduced cross-sectional area and localized premature yielding at the gauge location.

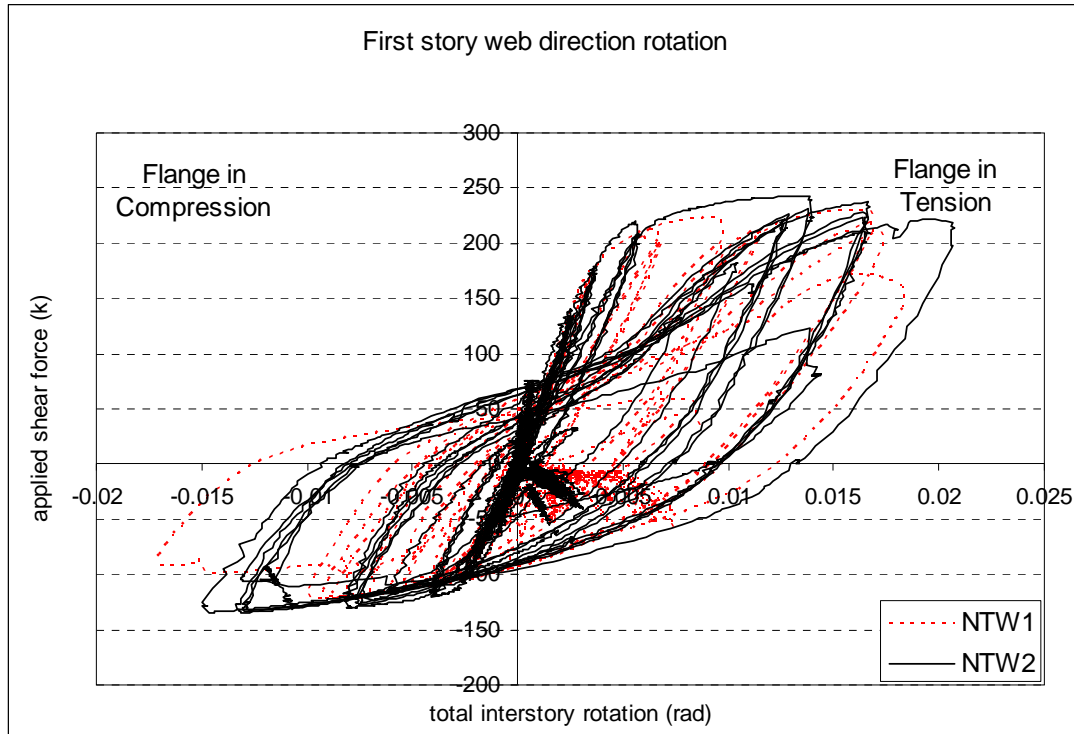


Figure 7.14. Web direction load versus interstory rotation in first story of specimens.

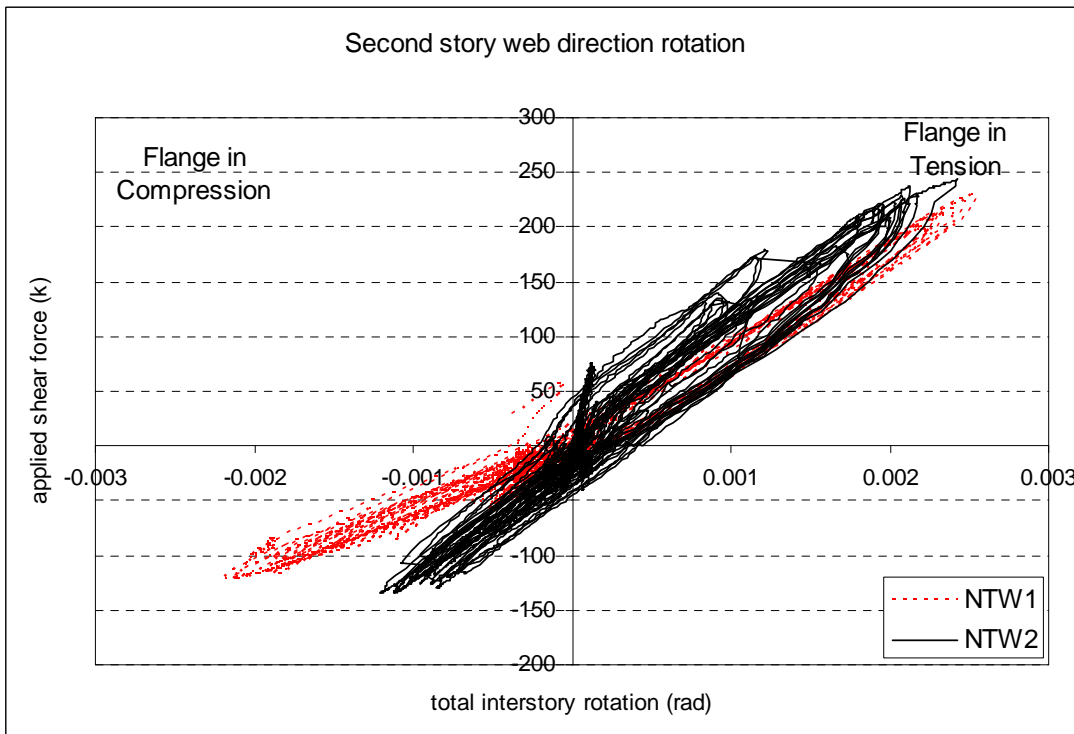


Figure 7.15. Web direction load versus interstory rotation in second story of specimens.

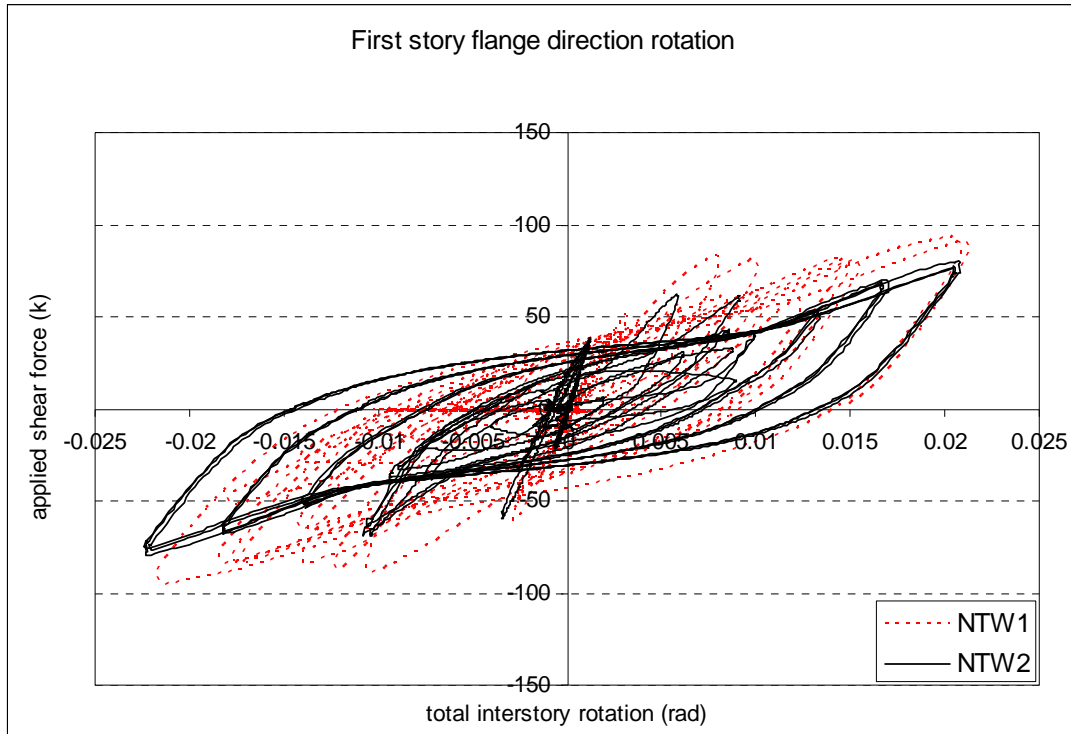


Figure 7.16. Flange direction load versus interstory rotation in first story of specimens.

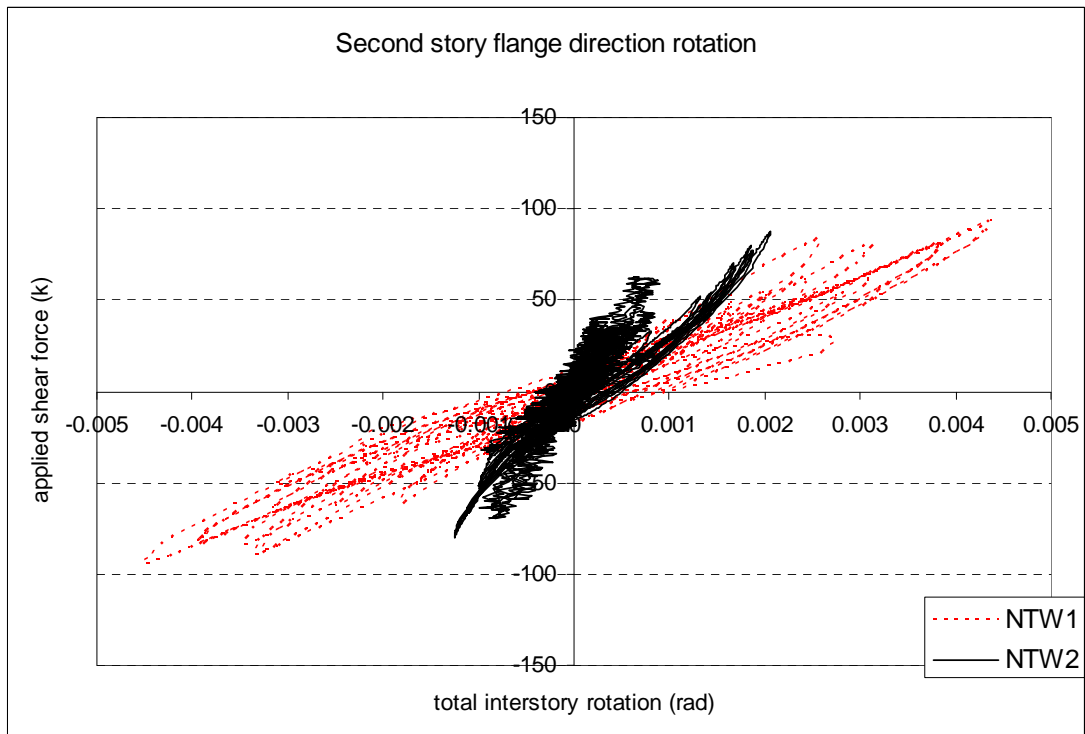


Figure 7.17. Flange direction load versus interstory rotation in second story of specimens.

## 7.7 Shear Lag Effects

Figure 7.18 compares the decrease in moment resistance in the flange-in-tension loading direction relative to the value predicted when shear lag is neglected at several strain levels. In both specimens NTW1 and NTW2, shear lag effects were minimal at 25 percent of yielding strain. This may be because very few cracks had formed in the concrete at this point in the loading, minimizing the effects of shear lag. The effects of shear lag became significant at approximately 50 percent of yielding, and a plateau was reached that extended through 125 percent of yielding, after which shear lag effects decreased until they became negligible at approximately 250 percent of the yielding strain, when reinforcement over the entire flange width had yielded. However, the effects of shear lag in specimen NTW1, with the reinforcement concentrated in the boundary elements, caused larger reductions in measured moments (as much as 60 percent larger) in specimen NTW1 than in NTW2.

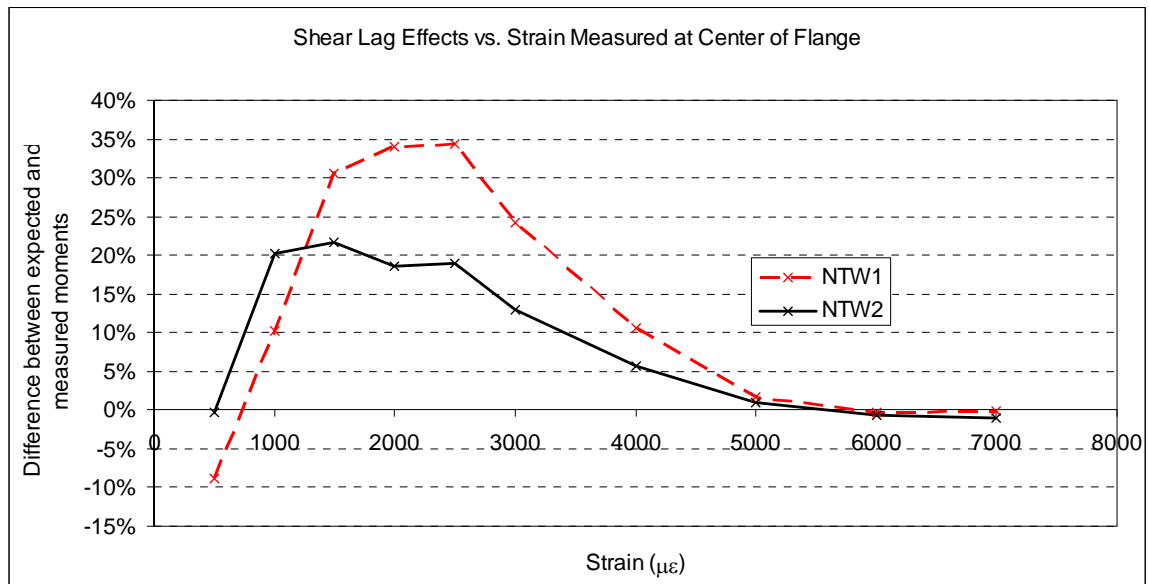


Figure 7.18. Decrease in moment resistance at base of wall due to shear lag at various strain levels.

Two mechanisms contributed to the increased shear lag effects in NTW1 (with reinforcement concentrated in boundary elements) relative to NTW2 (with reinforcement uniformly distributed across flange width). First, because there was less reinforcement in the center of the flange of specimen NTW1, the strain gradient caused by shear lag was larger. This can be seen in Figure 7.19, which compares the measured strain distributions across the flanges of the specimens near first yielding. In specimen NTW1, the average strain measured in the four extreme bars was  $650 \mu\epsilon$  when the strain measured in the center bars was  $2000 \mu\epsilon$ . In specimen NTW2, the average strain measured in the four extreme bars was  $1290 \mu\epsilon$  when the strain measured in the center bars was  $2000 \mu\epsilon$ .

Second, because a larger proportion of the reinforcement in specimen NTW1 was located in the boundary elements, even similar strain profiles over the flange width will cause a larger reduction in the generated tensile force than in specimen NTW2. For instance, if a bilinear strain profile is assumed, with the strain at the extreme fibers equal to  $1000 \mu\epsilon$  and the strain in the center equal to  $2000 \mu\epsilon$ , the effective tensile force in specimen NTW1 is reduced by 34 percent, while the effective tensile force in specimen NTW2 is reduced by 25 percent.

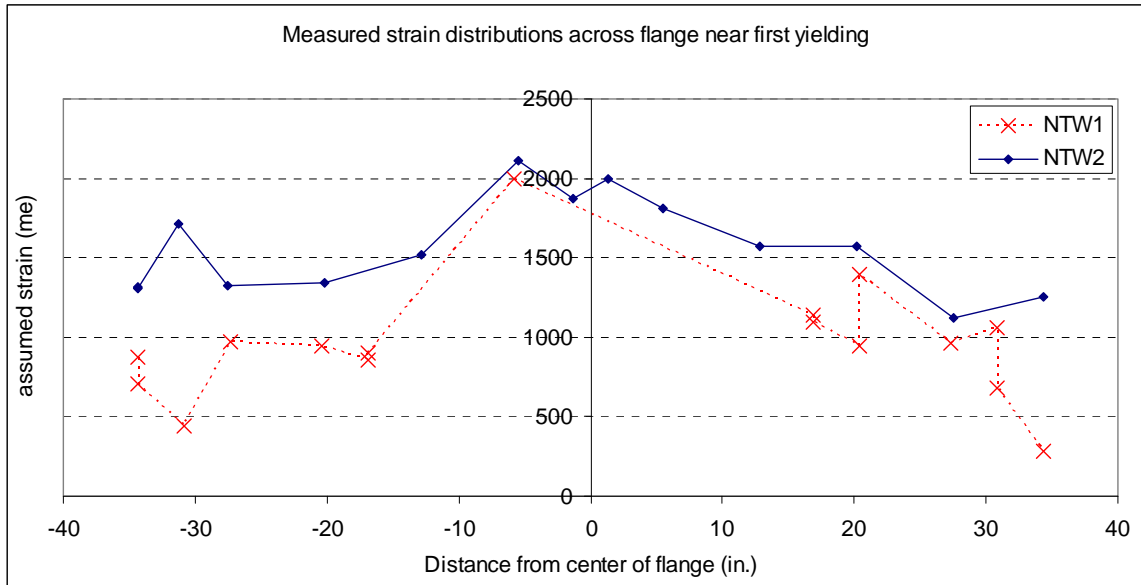


Figure 7.19. Measured strain distributions across flange.

## 7.8 Shear Deformation

Figure 7.20 through Figure 7.23 show the shear force versus shear deformation relationships for each story of each specimen in the two orthogonal directions. In the first story, the hysteresis loops included a large amount of pinching, as expected due to the large amount of flexural damage that occurred in this region. In the web loading direction, specimen NTW2 had larger shear deformations than specimen NTW1. This was partially the result of slightly larger forces being applied to specimen NTW2 than specimen NTW1, but it was also related to the larger flexural demand on this portion of this specimen as a result of the splice stiffening the upper portion of the specimen. In the flange loading direction, the magnitudes of shear deformation were similar, despite the longitudinal reinforcement in specimen NTW2 being distributed over the width of the flange and the horizontal reinforcement being more closely spaced, as discussed in Section 3.3.1. The observed behavior was consistent with the results of the finite element

study completed by Sittipunt and Wood (1995) that indicated that the addition of extra web reinforcement in either the horizontal or longitudinal direction did not reduce shear deformations or pinching after the longitudinal reinforcement yielded. As a result, the loss of shear stiffness at large displacement levels is difficult to mitigate. Additionally, the change in the crack pattern between the specimens, with diagonal shear cracks forming in specimen NTW1 and horizontal cracks forming across the entire flange width in specimen NTW2 did not appear affect the shear deformation of the specimens. In the second stories of the specimens, the shear deformation was generally linear, unlike the first stories, because the flexural demand and damage were reduced substantially. However, in both loading directions, specimen NTW2 had much smaller shear deformations in the second story as a result of the longitudinal reinforcement remaining elastic in the lap splice region and the top block restraining the development of diagonal cracks.

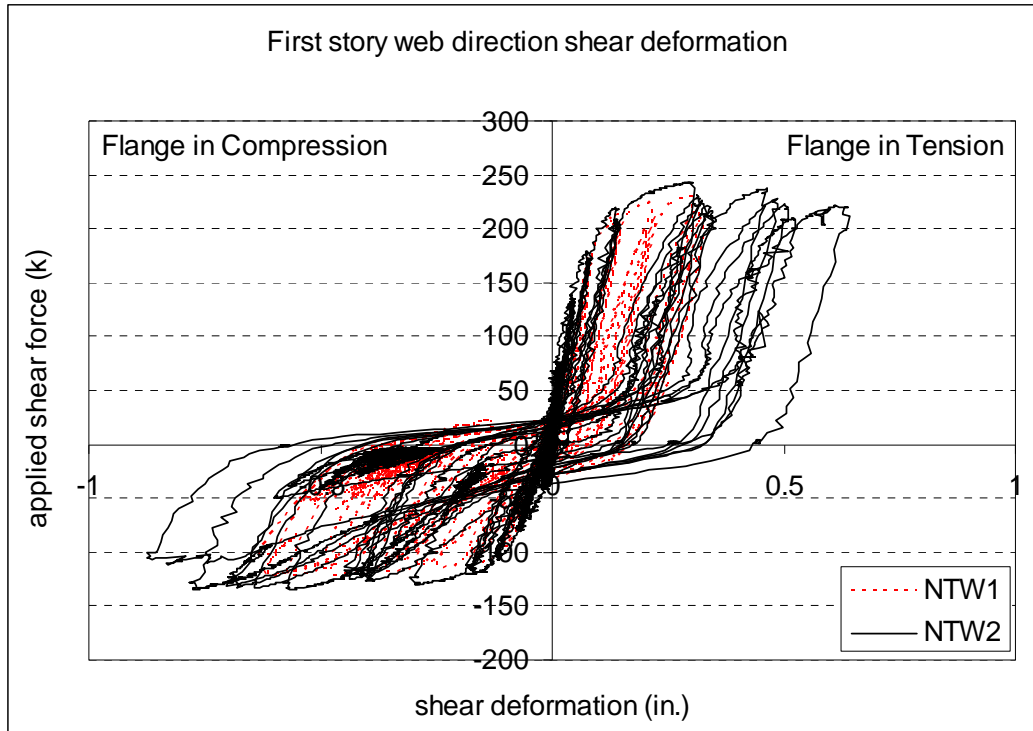


Figure 7.20. Web direction load versus interstory shear deformation in first story of specimens.

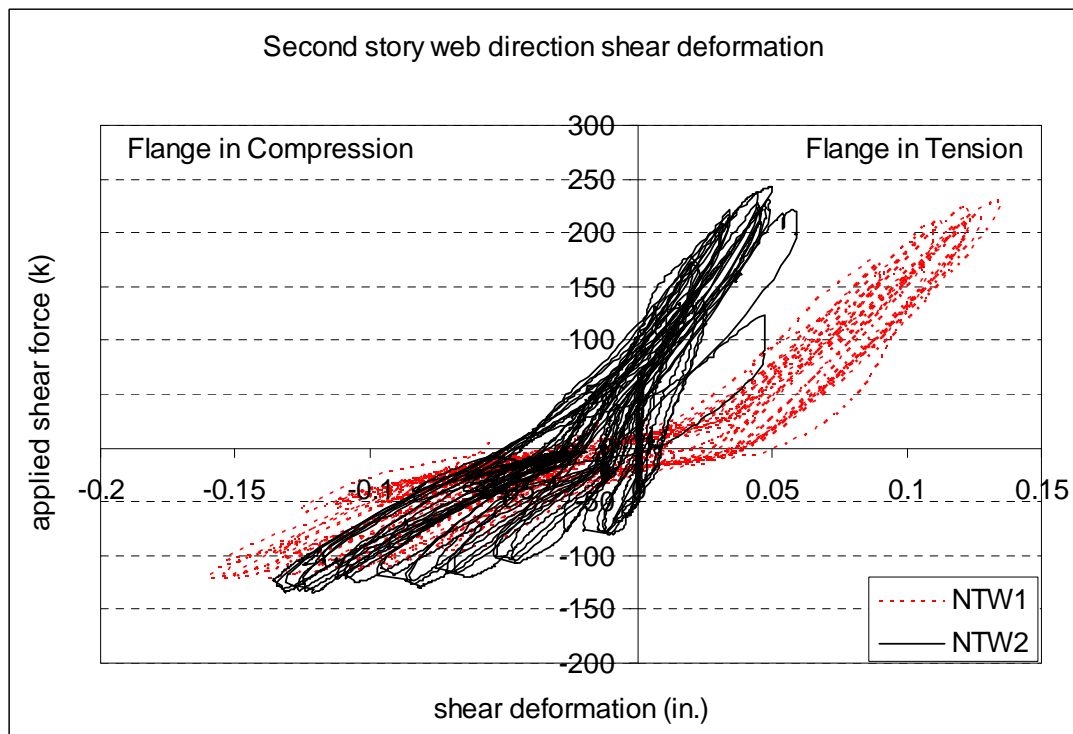


Figure 7.21. Web direction load versus interstory shear deformation in second story of specimens.

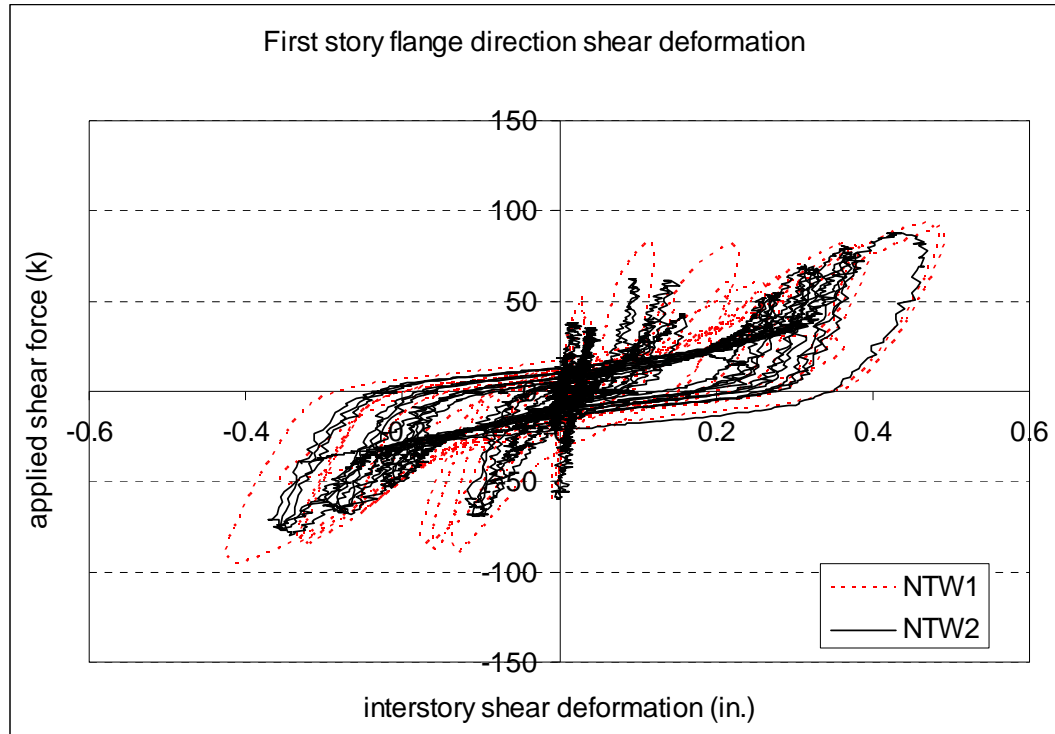


Figure 7.22. Flange direction load versus interstory shear deformation in first story of specimens.

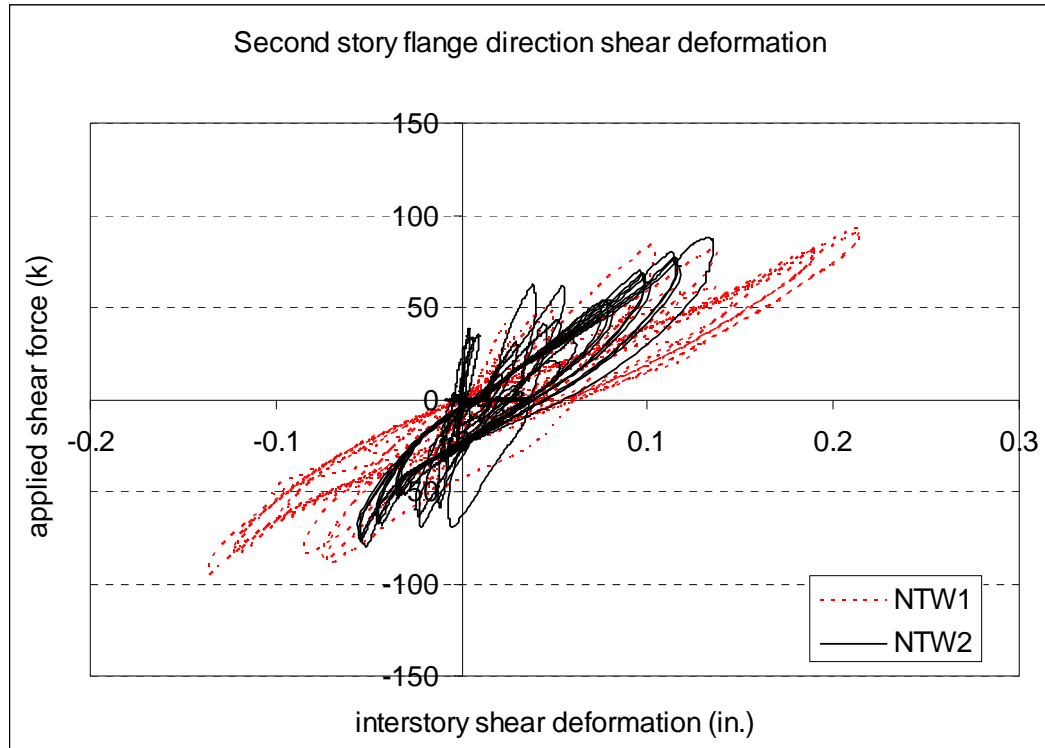


Figure 7.23. Flange direction load versus interstory shear deformation in second story of specimens.

## 7.9 Strain Penetration

Comparison of the contributions of strain penetration to the deformation of each of the specimens is complicated by difficulties with the instrumentation of the flange of specimen NTW1, as discussed in Section 4.3.1. These contributions are compared in Figure 7.24 and Figure 7.25. In the web loading direction, the overall magnitude of measured rotations due to strain penetration was similar in the two specimens. Because differences in the web longitudinal reinforcement between the two specimens are minor and the bar anchorage in the foundation block is similar, this consistency is not surprising. In the flange loading direction, the measured rotations are approximately one-half as large in specimen NTW2 as in NTW1. The measured rotations in NTW1 in this

loading direction are suspect due to the use of a single LVDT to determine rotations, but it is expected that the rotations in specimen NTW2 would be slightly smaller due to the use of smaller bars (No. 4 and No. 5 compared No. 5 and No. 6) with decreased development lengths and the distribution of reinforcement across the entire flange width, reducing the area of steel being developed at the flange tip.

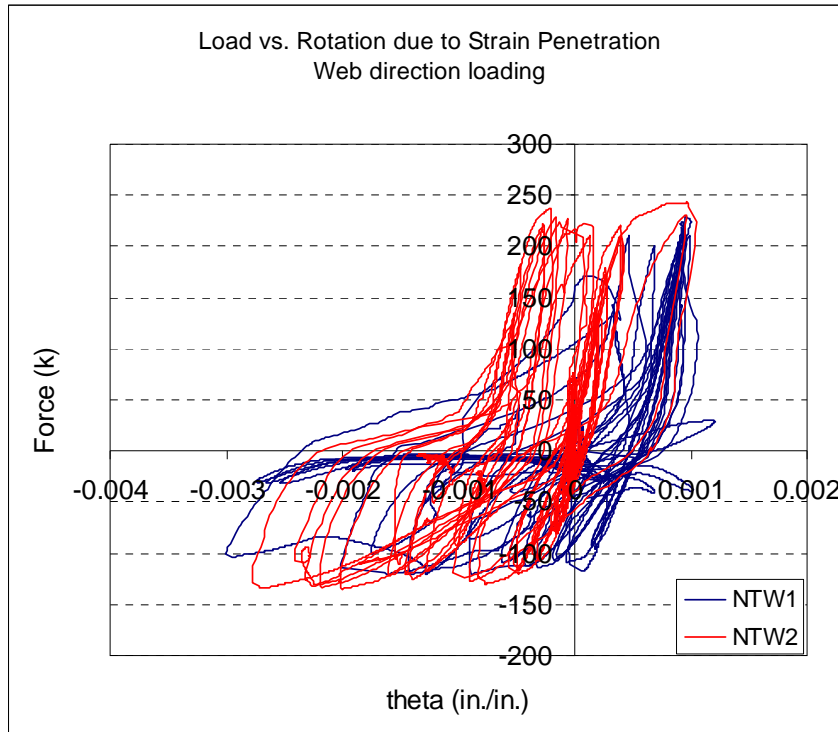


Figure 7.24. Comparison of strain penetration component of deformation: web direction loading.

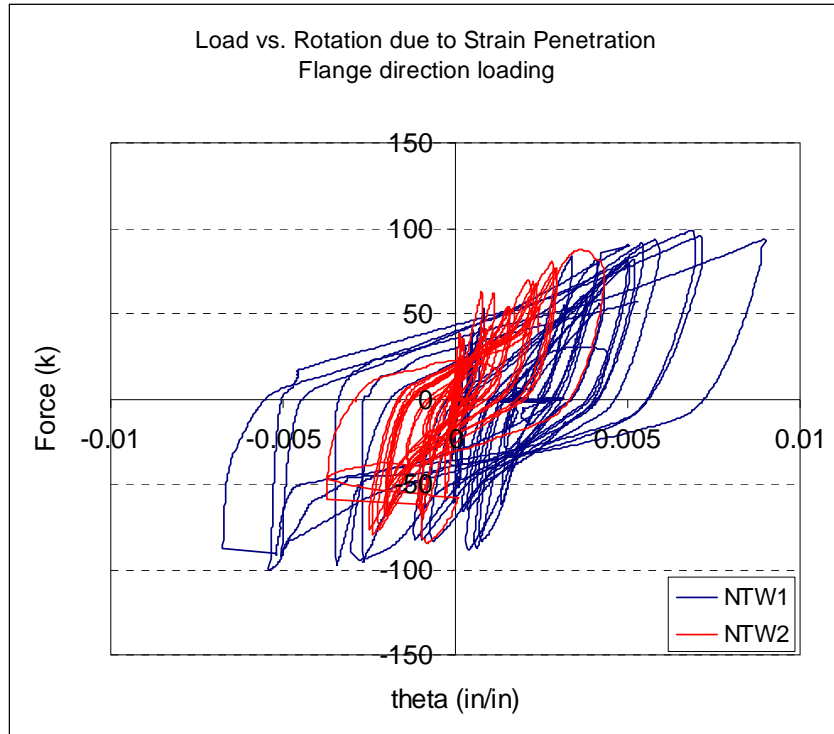


Figure 7.25. Comparison of strain penetration component of deformation: flange direction loading.

## 7.10 Summary of Effects of Design Parameters on Wall Behavior

### 7.10.1 Effects of Lap Splices

The lap splices in the lower portion of the second story prevented the plastic hinge from extending into the second story as it would have if the lap splice were not present. This affected the wall performance in several ways. Primarily, it decreased both the flexural and shear deformations of this portion of the specimen, changing both the deformed shape and the stiffness of the specimen slightly. The flexural deformation was reduced directly because the larger amount of reinforcement present in the region was not able to yield, limiting the deformations to the elastic range. The shear deformation was reduced indirectly, as a result of the unyielded reinforcement preventing cracks from becoming wider than hairline or 0.007 in. The result of this change in the deformed

shape of specimen NTW2 relative to NTW1 was that slightly larger first story deformations, and therefore, larger forces, were required for NTW2 to reach the same second story displacement as NTW1.

Unlike the rectangular wall specimens described in Johnson (2007) with the lap splice located at the base of the specimen, locating the lap splice at the base of the second story did not lead to a splice failure or other undesirable specimen behavior. While the portion of the wall where yielding of the longitudinal reinforcement was reduced from the entire first two stories of specimen NTW1 to the first story and the top half of the second story of specimen NTW2, this reduction in plastic hinge length did not appear to put an excessive, concentrated, demand on the lower portion of specimen NTW2. Post-yielding, specimen NTW2 did tend to dissipate a larger fraction of the energy it absorbed in each loading ramp than specimen NTW1, indicating that more damage may have occurred in specimen NTW2. However, other indicators of behavior do not suggest that this was a problem. For example, specimen NTW2 had a slightly larger drift capacity than specimen NTW1 in the web loading direction and a similar drift capacity in the flange loading direction, and the failure mode was similar in both specimens. In addition, the strains measured in the longitudinal steel near the base in both specimens were large, exceeding the capabilities of the gauges, and particularly large cracks associated with buckling and fracture of the reinforcement just below the splice, such as observed by Johnson (2007), were not observed in specimen NTW2. As a result of these observations, it is concluded that locating a lap splice at the base of the second story had a small effect on the deformed shape of the specimen, but it did not impair the

performance of the specimen. Therefore, it is recommended that locating lap splices outside the nominal plastic hinge region is sufficient to avoid premature, brittle failure, despite the splice limiting yielding from expanding further outside the expected plastic hinge region.

### **7.10.2 Effects of Distributed Steel**

Concentrating the longitudinal reinforcement in the boundary elements of the flange of specimen NTW1 and uniformly distributing the reinforcement in the flange of specimen NTW2 led to several differences in the responses of the specimens. As a result of concentrating the reinforcement in the boundary elements, specimen NTW1 had significantly increased shear lag effects when loaded with the flange in tension at displacements up to 2.5 times the yield displacement. This increased shear lag will likely lead to a decreased stiffness compared to predicted values and increased cosmetic damage during frequently occurring seismic events. In the flange direction, the concentration of reinforcement in the boundary elements of NTW1 resulted in a measured maximum moment capacity that was 14.5 percent larger than the maximum moment capacity of NTW2; however, there was little change in the displacement capacity.

Additionally, the distribution of reinforcement caused a different crack pattern to develop in the flange of specimen NTW2 than was observed in the flange of specimen NTW1 or the webs of both specimens. In the flange of specimen NTW1 and the webs of both specimens, relatively narrow, closely spaced flexural cracks formed in the confined region, while much wider and widely spaced inclined shear cracks formed in the lightly

reinforced portion of the web or flange. In the flange of specimen NTW2, closely spaced, narrow horizontal cracks formed across the entire flange width. This change in crack pattern did not cause a change in the measured shear response of specimen NTW2 relative to specimen NTW1.

There are relative advantages to both concentrating reinforcement in boundary elements and uniformly distributing it across a wall element, and the goals of a particular design will determine which approach is preferred. Concentrating the reinforcement in boundary elements leads to an increased in-plane moment capacity. This is advantageous for the prototype building considered in this study because maximizing the flange-direction capacity helps to minimize the development of flexural overstrength in the flange-in-tension loading direction, as discussed in Section 3.2.4. Uniform distribution of the reinforcement across the flange width helps to reduce crack widths in the center portion of the web, potentially reducing or eliminating the need for repair of the cracks after a small- to moderate-level seismic event.

### **7.10.3 Effects of Decreased Horizontal Steel Spacing**

Decreasing the spacing of the horizontal reinforcement in the flange of specimen NTW2 so that a scaled maximum spacing requirement was met, as discussed in Section 3.3.2, did not have a significant effect on the observed behavior of the specimen. Both specimens used No. 3 bars for horizontal reinforcement, leading to an increased horizontal reinforcement ratio  $\rho_v$  of 0.41 percent in specimen NTW2 compared to 0.26 percent in specimen NTW1. The differences in the observed crack patterns across the flange in the two specimens (i.e., as described in 7.10.2) were attributed to reduced shear

lag effects that occurred in NTW2 due to the uniformly distributed longitudinal flange reinforcement rather than a change in the shear resistance mechanism due to the differences in horizontal shear reinforcement. This was concluded because the two different crack patterns associated with the two specimens, developed during the initial flange-in-tension direction loading, prior to loading either specimen in the flange direction. The orientation of the initial cracks did not change significantly with the loading direction; it is not clear whether loading in the flange direction first might have altered the observed crack pattern. It is likely that the crack orientation will be load-path dependent. Increasing the amount of horizontal reinforcement did not lead to improved shear behavior in the specimen. In particular, it did not increase the post-yielding shear stiffness or reduce pinching of the hysteresis loops and therefore did not increase the energy dissipation capacity of the specimen.

Reduced crack widths were observed in the center of the flange of specimen NTW2 compared to NTW1, as discussed above. However, it was expected that this difference was primarily the result of the distribution of the longitudinal reinforcement rather than the decreased spacing of horizontal reinforcement. This expectation was based on the observed crack pattern in the web outside the boundary element under flange-in-compression loading, where minimum longitudinal reinforcement was included and the provided shear reinforcement was spaced at 6 in. ( $\rho_v = 0.61$  percent) in order to provide sufficient shear resistance in the flange-in-tension loading direction.

The maximum applied shear stresses in the flange-in-compression loading direction were  $2.5\sqrt{f'_c}$  and  $2.7\sqrt{f'_c}$  in specimens NTW1 and NTW2, respectively, similar

to the maximum flange-direction shear stresses of  $2.6\sqrt{f'_c}$  and  $2.2\sqrt{f'_c}$  in the two specimens, using the measured values of  $f'_c$ . In both specimens, the cracking pattern in the web was similar to the cracking pattern observed in the flange of specimen NTW1: there were fewer diagonal (shear) cracks than flexural cracks, and the diagonal cracks were much wider than the flexural cracks. As a result, the spacing and width of shear cracks seemed more related to the provided spacing of longitudinal reinforcement than the provided spacing of horizontal reinforcement, and it was concluded that decreasing the spacing of the horizontal reinforcement or increasing the provided area of horizontal reinforcement beyond the amount required to ensure a flexure-controlled failure did not improve the response of the wall and was not necessary. However, providing less horizontal reinforcement than required to ensure a flexure-controlled failure is not recommended, because of the potential for a brittle failure mode to develop.

#### **7.10.4 Effects of Increased Confinement Region**

In order to increase the drift capacity of the specimen in the flange-in-tension loading direction, the horizontal dimension of the web tip boundary element in specimen NTW2 was increased from 21 in. to 24.5 in, as discussed in Section 3.3.2. This increased dimension was selected so that the confined core remaining after the buckling of the extreme layer of longitudinal reinforcement would meet the required minimum horizontal dimension of the boundary element. In addition, because the 135° hooks closing the confining hoops were observed to unwind in specimen NTW1 prior to hoop fracture, care was taken in the construction of specimen NTW2 to ensure that all confining hoops were oriented so that the hooks were located away from the extreme fiber.

Web crushing failure was observed in specimen NTW1 during the “figure eight” pattern loading to 2 percent drift after successful orthogonal loading to 2 percent drift with the flange in tension. Web crushing failure was observed in specimen NTW2 during orthogonal loading to 2.5 percent drift with the flange in tension following successful loading in the “figure eight” pattern. This difference in drift capacity was attributed to the orientation of the confining hoops preventing premature failure of the boundary element rather than to the enlargement of the boundary element. In both specimens, once the confined core began to crush, buckling of the reinforcement and progression of the failure from the extreme fiber into the unconfined web followed as additional displacement was imposed on the specimen. Expanding the confined core beyond the dimensions required by ACI 318-02 did not appear to increase the displacement capacity of the specimen. Decreasing the spacing of the confining hoops to provide additional confinement may have increased the stress and strain capacity of the concrete, increasing the drift capacity in this loading direction. However, practical limitations on congestion of the cage and constructability limit the utility of this approach.

#### **7.10.5 Specimen Size**

Reducing the number of stories in the specimen from four to two had small effects on the behavior of specimen NTW2. The very stiff top block did provide restraint to the top portion of the second story. This restraint appeared to prevent the formation of diagonal shear cracks in the top portion of the web in this story, which increased the effective shear stiffness of this portion of the specimen. Because this shear deformation

was not expected to be large, the effects of the top block on the behavior of the specimen were believed to be minimal.

### **7.11 Design Recommendations Based on Results of Testing Program**

Based on the observed behavior of specimens NTW1 and NTW2, “best practices” can be recommended for the detailing of nonrectangular walls to ensure that these walls have good seismic load-resisting behavior.

Bar splices will be required in the construction of most walls. Based on the results of testing specimen NTW2 and the test of specimen RWS by Johnson (2007), it is recommended that lap splices be allowed in these walls with certain precautions. To avoid a splice failure, the splice should be located outside the nominal plastic hinge region. For the purpose of determining acceptable lap splice locations, the plastic hinge length can be determined using any of the several empirical expressions available (e.g., Paulay and Priestley 1992). When a splice is required within the plastic hinge region, mechanical couplers can be used successfully (Johnson 2007).

Distributing longitudinal reinforcement over the entire width of a wall element, rather than concentrating it in the boundary elements, is beneficial because it decreases the width of diagonal (shear) cracks. As a result, the need for crack repair, such as by epoxy injection, may be avoided for certain small- to moderate-level seismic events. The disadvantage of uniformly distributed longitudinal reinforcement is that it reduces the in-plane moment resistance. The designer must choose between these options based on the design objectives of the wall under consideration.

Two of the detailing modifications for specimen NTW2 had negligible effect on the wall response and thus are not recommended as “best practices.” These are the provision of additional horizontal (shear) reinforcement beyond the amount required to ensure that the wall is flexurally-controlled (although the inclusion of sufficient horizontal reinforcement to ensure flexural failure should be required), and the horizontal expansion of boundary elements beyond the dimension required by ACI 318-02.

For future research, it is recommended that including only two stories of a six-story prototype is an acceptable compromise between minimizing subassembly size (and cost) and minimizing extraneous constraints on the specimen that may lead to an artificially strengthened/stiffened specimen. A further reduction of the subassembly is not recommended. When walls of other proportions are considered, a minimum specimen height of approximately two to three times the nominal plastic hinge length is recommended.

## Chapter 8 Development of Simplified Modeling Procedure

### 8.1 Introduction

This chapter describes a simplified modeling procedure developed based on the results of the T-shaped wall tests described in this thesis. This modeling procedure is termed the F-S-SP Integration model, because it includes distinct terms for each of the flexural, shear, and strain penetration components of deformation. This chapter describes the development of the model, including a discussion of each component of deformation in Section 8.2. Section 8.3 describes the selection and calibration of local engineering demand parameters (EDPs) to predict damage levels for use in performance-based engineering. Chapter 9 provides validation of the F-S-SP Integration model using the results of several wall tests reported in the literature and includes discussion of the application of the model in design.

The purpose of this model was to provide practicing engineers with a simplified modeling tool appropriate for routine design work, including preliminary design, yet more accurate than the procedure described in FEMA 356, and with the capability of predicting displacements at any location over the height of the wall, which is not possible with either the procedure described in FEMA 356 or the procedure proposed by Hines *et al.* (2004). Also unique to the F-S-SP Integration model is that it can be applied to walls with any applied load configuration (i.e., one or more point loads, uniform or triangular distributed loads) and to nonprismatic walls and walls with changes in reinforcement, such as those due to lap splices or bar cutoff. The model can be used to generate monotonic pushover curves, explicitly accounting for each of the components of

deformation (flexure, shear, and strain penetration). The F-S-SP Integration model is intended to be applicable to cast-in-place flexural walls (i.e., walls with aspect ratios greater than 2.5) of any geometry, including both rectangular and flanged sections in any loading direction, and is not limited to particular wall detailing, such as reinforcement ratio, reinforcement distribution, confined regions, or bar splices. In order to achieve this utility, purely empirical relationships were avoided as much as practical. This could not be readily avoided in the determination of shear deformations because of the complicated interaction between flexural damage and shear deformations, so a semi-empirical approach was developed to account for this component. Until additional research provides a more rigorous method of handling shear lag in flanges of sections, it is recommended that only the effective flange width, as determined by ACI 318 or some other rational analysis method, be included when modeling flanged sections.

## **8.2 Simplified Modeling Procedure**

The F-S-SP Integration model is based on a flexural section analysis, which can be generated using readily available software, such as BIAX (Wallace 1992). The flexural behavior of the wall is used as the basis for the entire model because flexure is the most well-understood, and most predictable component of the total deformation, besides being the dominant component of deformation for flexural walls. Consequently, correct determination of the flexural properties of the section is essential to the accuracy of the model.

For simplicity and illustration of the model, Sections 8.2.1 through 8.2.3 consider specimen NTW1 in the flange-in-tension and flange-in-compression loading directions.

Section 8.2.4 uses specimen NTW2 to describe the application of the model to walls with lap splices, and Sections 8.2.5 and 8.2.6 consider issues that arose in modeling directions other than flange-in-tension and flange-in-compression using specimen NTW1 for illustration.

Measured material properties were used in the analyses described in this discussion of the model, and the Modified Kent and Park model was used to determine the confined concrete material properties from the measured unconfined concrete strength and the provided confinement. The parameters used to define the material properties in the flexural model are summarized in Table 8.1. Some modification was required for flange- and skew-direction loads in order to mimic the effects of previous damage on the wall. This is discussed in Sections 8.2.5 and 8.2.6.

The chapter concludes with initial recommendations for the prediction of damage associated with various performance levels (i.e., immediate occupancy, life safety, and collapse prevention) based on the monotonic pushover curve defined using the F-S-SP Integration model.

Table 8.1. Material property parameters used to represent measured properties of specimen NTW1

Material	Parameter	Value
Unconfined Concrete	$f'_c$ (peak compressive stress)	7.26 ksi
	$\epsilon_{c0}$ (strain at $f'_c$ )	0.0025
	$\epsilon_{50u}$ (strain at 50% stress decrease)	0.0035
	$f_t$ (peak tensile stress)	0.90 ksi
Confined Concrete <sup>1</sup>	$kf'_c$ (peak compressive stress)	8.31 ksi
	$\epsilon_{c0}$ (strain at $f'_c$ )	0.0029
	$\epsilon_{50u} + \epsilon_{50h}$ (strain at 50% stress decrease)	0.019
	$f_t$ (peak tensile stress)	0.90 ksi
	$f_m$ (compressive stress at high strain)	1.66 ksi
Steel	$f_y$ (yield stress)	62.0 ksi
	$f_u$ (maximum stress)	92.0 ksi
	$f_f$ (stress at failure)	85.0 ksi
	$\epsilon_1$ (strain at onset of strain hardening)	0.002137
	$\epsilon_2$ (strain at $f_u$ )	0.08
	$\epsilon_3$ (strain at $f_f$ )	0.17
	$E$ (elastic modulus)	29000 ksi
	$E_T$ (initial modulus of strain hardening region)	1000 ksi

<sup>1</sup>Using Modified Kent and Park model

### 8.2.1 Deformation due to Flexure

The flexural component of deformation is calculated directly from the moment-curvature relationship determined from a sectional analysis. For a given applied load, the moment distribution over the height of the wall is calculated. The moment-curvature relationship is then used to determine the distribution of curvature over the height of the wall. The curvature is integrated over the height of the wall twice, assuming that the rotation and displacement at the foundation are zero for cantilever walls, to determine the flexural rotations and displacements over the height of the wall. This approach neglects the effects of diagonal cracking and tension shifting, discussed in Section 2.3.3, which can increase the effective plastic hinge length. As a result, there is a tendency to underestimate flexural deformations in the inelastic range with this approach.

Figure 8.1 compares the calculated moment versus curvature relationship for specimen NTW1 in the web direction with the measured values from the top and bottom quarters of the first story. The calculated moment versus curvature relationship represents the observed behavior very well, including predicting the observed failure in the flange-in-tension loading direction. At the point marked “A” in the figure, the loss of capacity in the laboratory coincided with extensive crushing of the confined boundary element in the web tip and buckling of the reinforcement in the same region. The decrease in capacity in the model was associated with the majority of the concrete in compression exceeding the strain associated with maximum strength, which represents a crushing failure. In the flange-in-compression loading direction, failure in the laboratory was due to fracture of the longitudinal steel in the web tip after it had buckled in the opposite loading direction. The model considers only monotonic loading and does not identify buckling and subsequent fracture of reinforcement, so the model predicts a much larger curvature capacity than measured, with failure not occurring until the reinforcement ruptures at a very large curvature level.

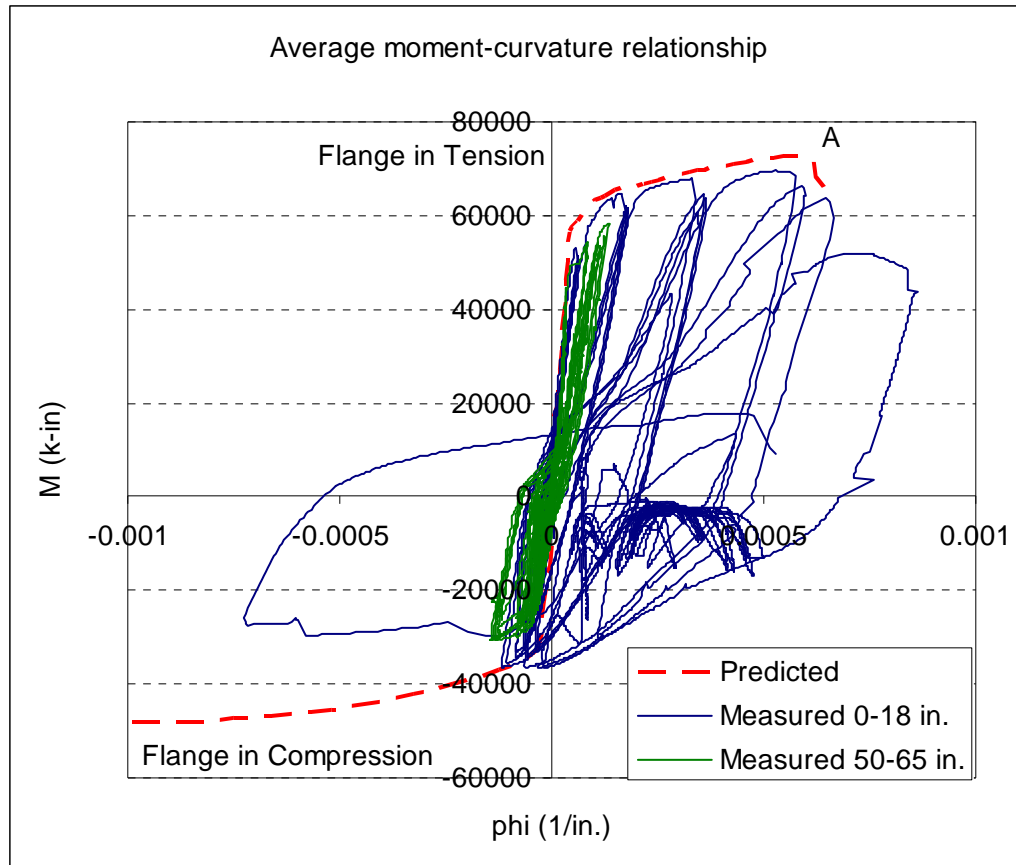


Figure 8.1. Measured and predicted moment versus curvature relationships, NTW1 web-direction loading.

It can be seen in Figure 8.1 that in the upper portion of the first story, yielding was observed at a reduced load in both flange-in-tension and flange-in-compression directions. This reduced moment resistance and spread of yielding over a larger portion of the wall than expected from the moment-curvature analysis was observed in the upper half of the first story of both specimens NTW1 and NTW2. This behavior was the result of diagonal cracking and tension shifting, described in Section 2.3.3, which increases the tensile demand on the reinforcement and causes a spread in the observed plastic hinging region. Figure 8.2 through Figure 8.4 compare the measured distributions of strain and curvature over the height of specimen NTW1 to predicted values, based only on applied

moment and neglecting tension shifting effects. Each of these three plots considers a different point in the loading history, each one at a ramp peak: 1.1 percent drift, 1.5 percent drift, and 2.1 percent drift, which is also associated with the maximum load resistance. Because there can be significant variation in measured strains from one gauge to another, each plot includes strains measured along two reinforcing bars; each of the measured strain lines includes strain gauges distributed over the height of a single bar in the flange, with the locations of the gauges marked on the lines.

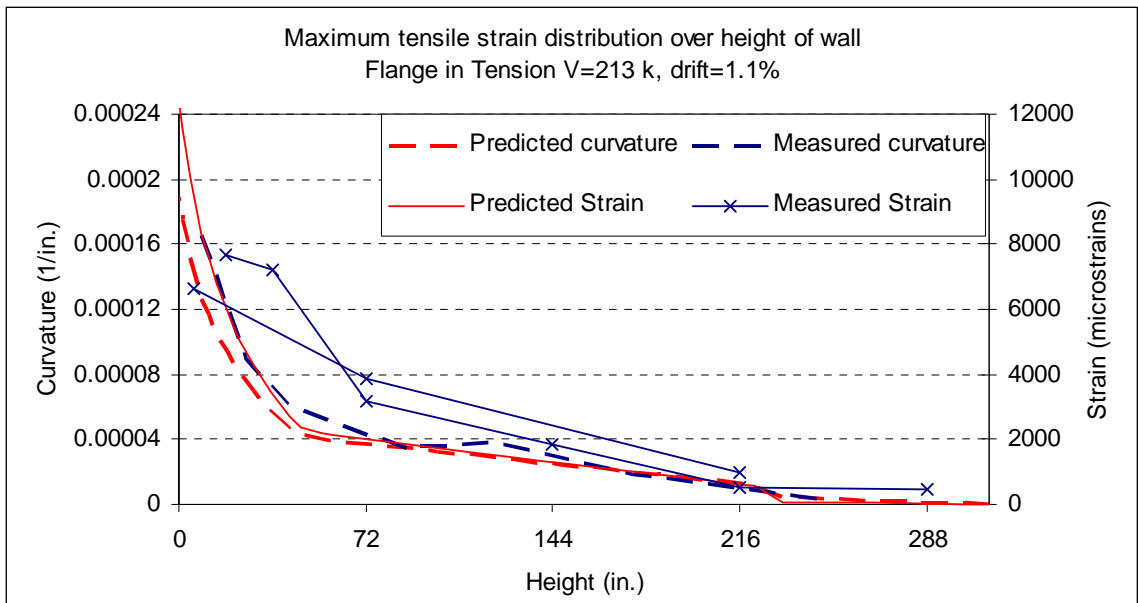


Figure 8.2. Measured and predicted distributions of tensile strain and curvature, flange-in-tension loading direction, 1.1 percent drift

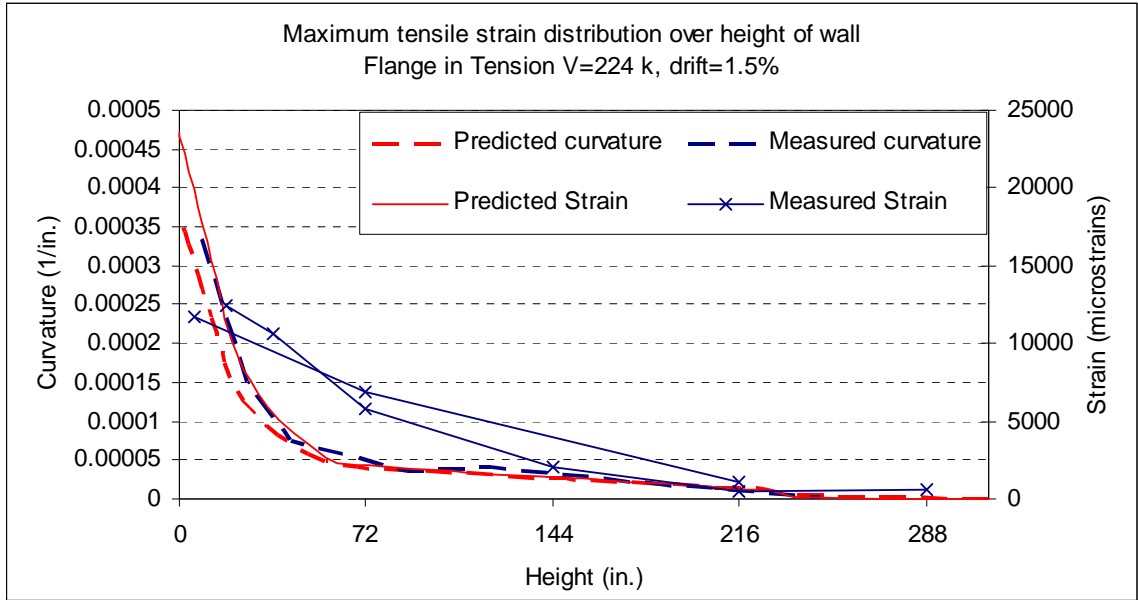


Figure 8.3. Measured and predicted distributions of tensile strain and curvature, flange-in-tension loading direction, 1.5 percent drift

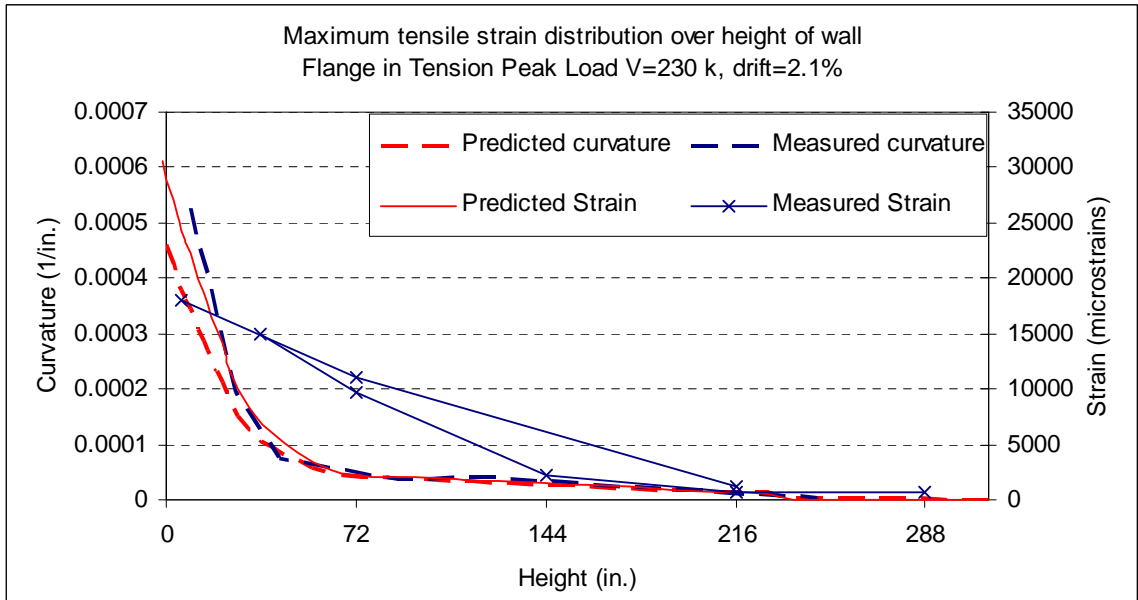


Figure 8.4. Measured and predicted distributions of tensile strain and curvature, flange-in-tension loading direction, 2.1 percent drift

In each of these comparisons, the measured curvature distribution is approximately parallel to the predicted distribution, with a shift of approximately 6 to 8 inches up the wall. Qualitatively, this is the expected behavior as a result of tension

shifting. The comparison of the measured to predicted tensile strains does not match the expected behavior as well. The strain gauges indicate a much larger spread of yielding over the height of the wall than the curvatures derived from measurements taken with the Krypton system and string pots. Because the measured strains were much larger than expected in the majority of the gauges, it is likely that some systematic error is involved. One possible cause of this was that the preparation of a flat spot on the reinforcing bars for the application of the strain gauges to the bars for specimen NTW1 reduced the cross-sectional area sufficiently to cause localized yielding of the gauge length, while the uninstrumented portion of the bars did not yield.

While modifying the calculated distribution of curvature over the height of the wall to account for tension shifting effects could improve the accuracy of the F-S-SP Integration model, it was chosen not to add this complexity. This decision was made for several reasons. First, the error associated with neglecting this effect is to underestimate the deformation capacity of the wall under consideration, which can generally be considered conservative. The yielding moment and pre-yielding stiffness are not affected by neglecting tension shifting (Park and Paulay 1975), so this does not introduce difficulties for performance-based engineering in predicting deformations and non-structural damage at low drift levels. Second, one of the goals in the development of the F-S-SP Integration method was to minimize both the complexity of the model and the use of empirical factors, so that it could be applied to a wide variety of wall configurations. Adding a term representing the additional plastic hinge rotation attributed to tension shifting would reduce the transparency of the model, making its appropriate application

to unusual wall systems more difficult. Finally, many existing models, including some that are more complex than the F-S-SP Integration method do not include tension shifting effects and these are considered sufficiently detailed. In particular, tension shifting is not currently considered in any of the models incorporating fiber-based elements (i.e., Waugh *et al.* 2009, Massone *et al.* 2006).

Figure 8.5 compares the measured and predicted relationship between load and displacement due to flexural deformation for specimen NTW1 in the web direction. As a result of tension shifting being neglected, the measured inelastic flexural deformation, or plastic hinge rotation, at failure is somewhat larger than the predicted value. However, the load capacity is predicted within 1 percent of the measured value. It should be noted that the tendency to underestimate deformation capacity is conservative.

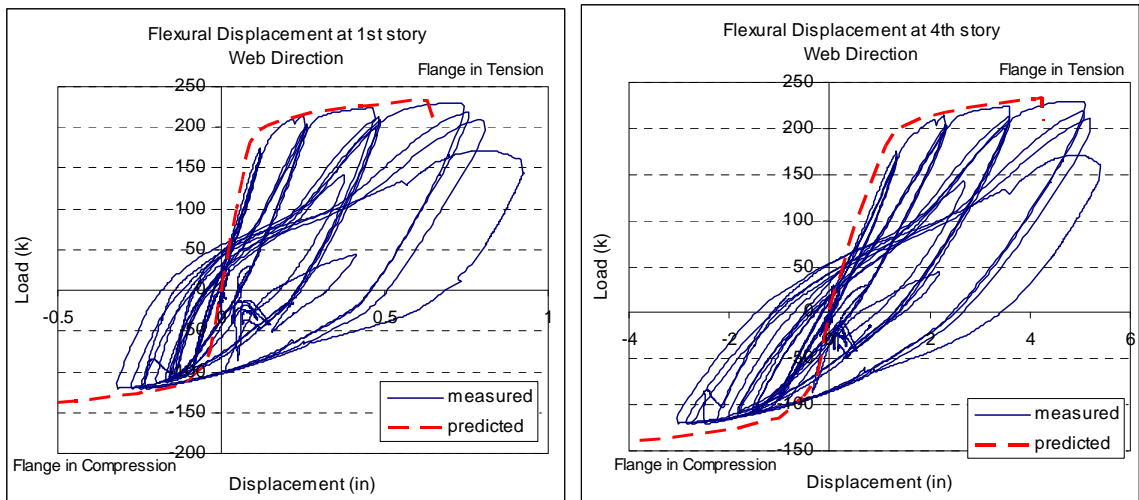


Figure 8.5. Measured and predicted load versus flexural loading relationships, NTW1 web direction loading

The load-deformation response shown in Figure 8.5 is plotted to “failure,” which is defined herein as the displacement associated with a post-peak moment reduction to 90 percent of the maximum moment. Integrating the curvature over the height of a wall to

find rotations and displacements is a straightforward procedure up to the maximum moment capacity, but additional consideration is required to determine the post-peak response. Figure 8.6 and Figure 8.7 illustrate the procedure used to determine the post-peak distribution of curvature over the height of a wall that was incorporated in the results plotted in Figure 8.5.

Simply applying the moment versus curvature relationship determined for the initial loading of the wall and substituting the calculated curvature at the base of the wall would greatly underestimate the deformations, to the extent of predicting a decrease in the total displacement from the peak moment. The cause of this decrease is apparent in Figure 8.6, where the curvature over the majority of the lower 70 in. of the wall is decreased substantially from that at the peak moment. As additional displacement is applied beyond the displacement causing the maximum resistance, the portion of the wall that is not severely damaged (i.e., where the concrete core is not crushed) unloads not along the original loading path, but along a path with a slope similar to the pre-yielding stiffness. These paths are compared in Figure 8.7, where the original and modified moment-curvature relationships are compared.

Figure 8.6 includes the curvature distribution over the height of the wall generated with the procedure illustrated in Figure 8.7. In this case, it was assumed that crushing of the concrete occurred over the lower 12 in. of the wall, based on observations of the laboratory specimen, and that there would be some reduction in the curvature above this point. Determining a reasonable length for crushing a priori is somewhat difficult, especially for walls that differ substantially from those that have been tested.

Fortunately, the results of the double integration to determine displacements are not very sensitive to the choice of this dimension. For this case, modifying the dimension from 1 in. to 18 in. caused a change of less than  $\frac{1}{2}$  in., or 7 percent, in the calculated deflection at the top of the fourth story of the wall.

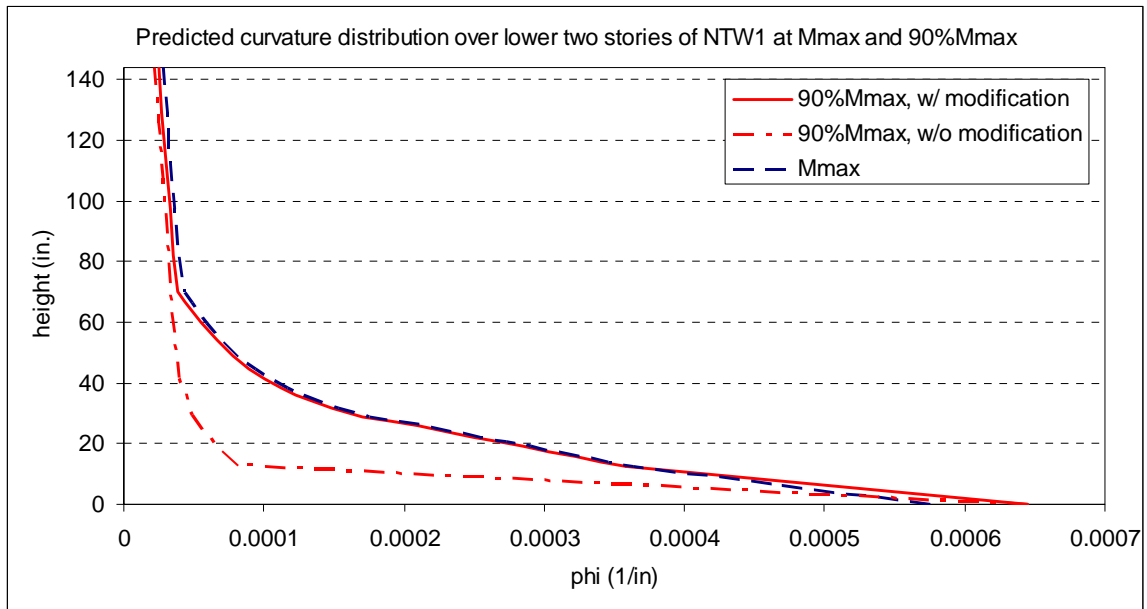


Figure 8.6. Post-peak distribution of curvature over height of wall

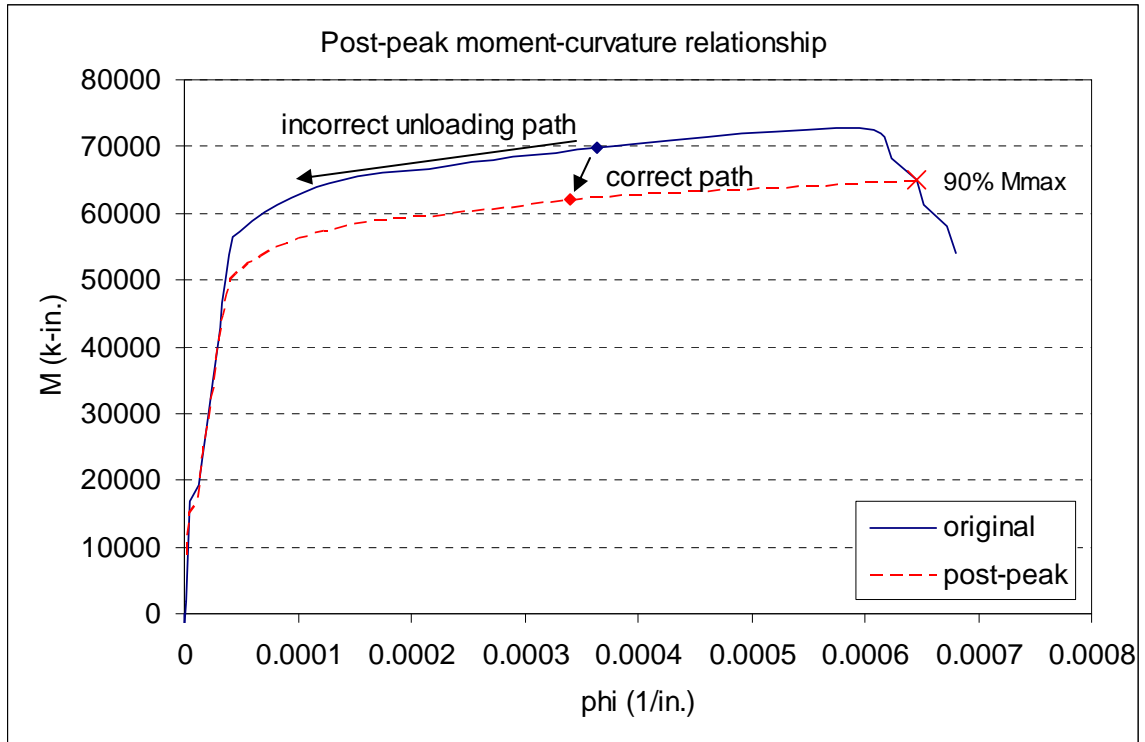


Figure 8.7. Modification of moment versus curvature relationship to model post-peak response

### 8.2.2 Deformation due to Shear

Prediction of shear deformations was much less straightforward than the prediction of flexural deformations because of the complicated interaction between flexural damage and increased shear deformations. The primary shortcoming of the method proposed by Hines, *et al.* (2004) for the prediction of shear deformations as a constant fraction of flexural deformations is that it is not capable of predicting interstory deformations; displacements can only be calculated at the top of the specimen. While flexural deformations at any point along the height of a wall can be estimated using the calculated elastic stiffness and plastic hinge length, the profile of displacements due to shear over the height of the wall is not similar to the profile of displacement due to flexure. As a result, applying the multiplier for shear displacement at the top of a wall at

any other location will not lead to reasonable results. In particular, it will underestimate the shear deformations in the plastic hinge region, and overestimate the shear deformations in the elastic region.

As a result of the inability of this method to predict interstory shear deformations, an alternate formulation was sought for use with structural walls in buildings. In developing a method to relate the shear deformations to the flexural deformations, an approximately bi-linear relationship was observed between the measured shear and flexural components of displacement at the top of specimens NTW1 and NTW2, with the flange-in-tension and flange-in-compression cases of web-direction loading having different slopes. Figure 8.8 shows this relationship for specimen NTW1. Hines (2002) noted a similar response for his specimens when only ramp peaks were considered. He also reported that this relationship has been observed by previous researchers for piers with a variety of cross-sectional shapes (round, rectangular, barbell, and hollow box) and aspect ratios ranging from 2.5 to 6.0. Therefore, this relationship appears to be valid for a variety of wall and pier geometries. This broad observation led to the investigation of a more robust approach that would allow for the determination of interstory drift levels but still include the proportional linking of flexural deformations and shear deformations.

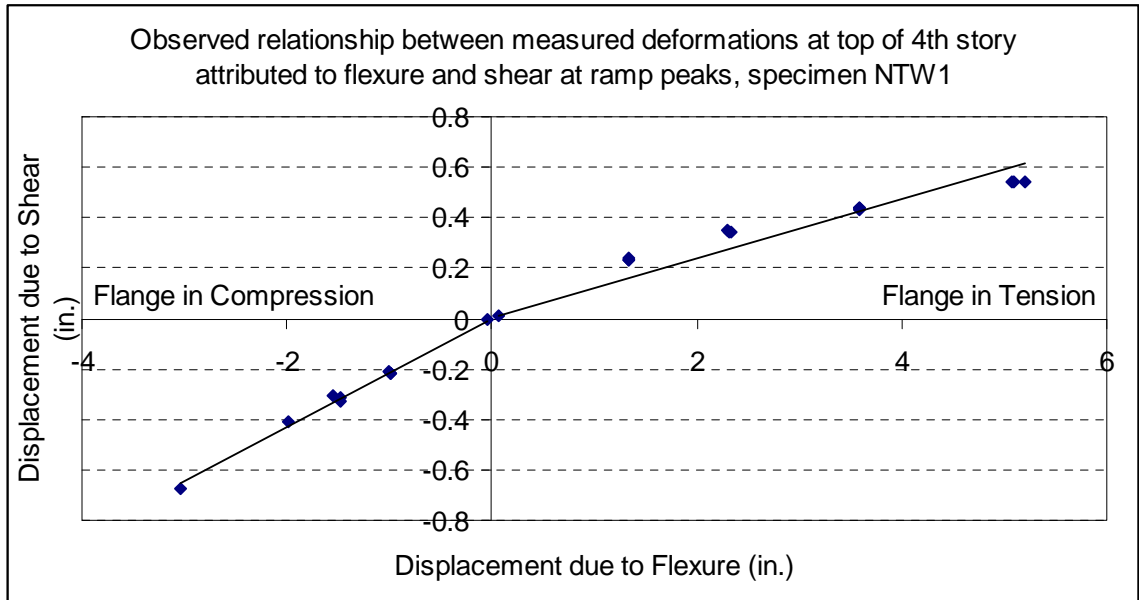


Figure 8.8. Approximately bi-linear relationship observed between flexural and shear components of deformation, top of specimen NTW1.

At all ductility levels, flexural displacements increase with rotations due to flexure. At large ductility levels, the total flexural deformation of a wall or pier is dominated by the plastic hinge rotation, and there is an approximately linear relationship between flexural rotations within the plastic hinge region and deformations at the top of the wall. Additionally, the interaction between flexural damage and shear deformations leads to a concentration of shear deformation in the plastic hinge region despite a constant shear demand over the height of each specimen. As a result, the gross shape of the distribution of curvature over the height of the wall has some similarity to the gross shape of the distribution of shear strains over the height of the wall, with the largest values observed near the base and the smallest near the top.

Figure 8.9 compares the shear strain and curvature profiles of specimen NTW1 at a selected point in the applied loading history, the first excursion to 150 percent of the

nominal yield displacement in the flange-in-compression loading direction. Similar relationships can be observed throughout the applied loading history. In this plot, the curvature is scaled so that the value nearest the base is the same as the shear strain nearest the base. As a result, the relationship between shear strains and curvatures (and consequently, shear deformations and flexural rotations), rather than displacements, was investigated throughout the applied loading history, including both the elastic and inelastic portions. The proportional relationship between the two values can be expressed as

$$\gamma = C * \phi \quad (8.1)$$

where  $\gamma$  is the shear strain,  $C$  is the proportionality constant with units of length, and  $\phi$  is the curvature. Integration of both sides of Equation 8.1 over the height of the wall leads to the distributions of shear deformation and flexural rotation, and the relationship

$$\Delta_{\text{shear}} = C * \theta_f \quad (8.2)$$

where  $\Delta_{\text{shear}}$  is the cumulative shear deformation,  $C$  is the proportionality constant used in Equation 8.1 with units of length, and  $\theta_f$  is the rotation due to flexure.

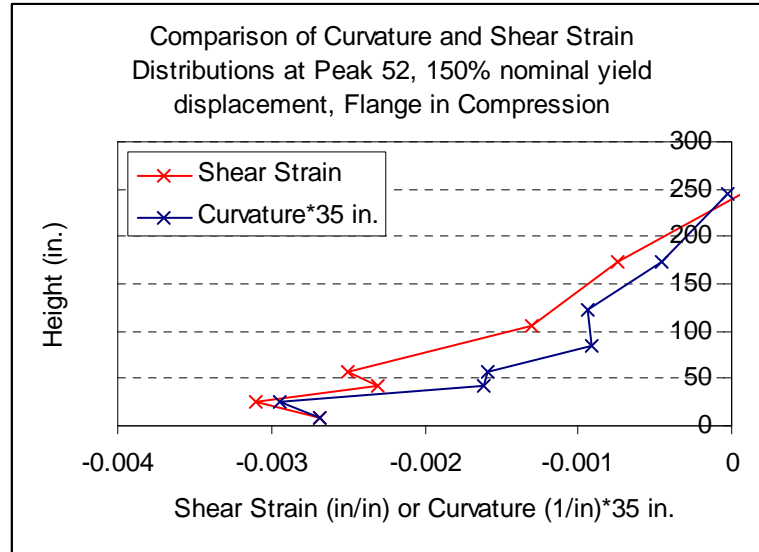


Figure 8.9. Comparison of curvature and shear strain profiles, NTW1 web direction loading.

Because the proportional relationship between shear strain and curvature is assumed to be constant over the entire range of loading, including the elastic range, predictions of the shear and flexural stiffness at first yielding can be used in order to determine a rational value of  $C$ . The flexural section analysis can predict the flexural stiffness at yielding well. Using a truss model and neglecting shear-flexure interaction, Park and Paulay (1975) calculated the theoretical cracked shear stiffness  $K_v$  of a reinforced concrete member with cracks inclined at an arbitrary angle  $\alpha$  from the longitudinal reinforcement and with shear reinforcement inclined at an arbitrary angle  $\beta$  from the longitudinal reinforcement as

$$K_v = \frac{\rho_v \sin^4 \alpha \sin^4 \beta (\cot \alpha + \cot \beta)^2}{\sin^4 \alpha + n \rho_v \sin^4 \beta} E_s b_w d \quad (8.3)$$

where  $\rho_v$  is the ratio of shear reinforcement area to the gross area of concrete perpendicular to that reinforcement,  $n$  is the ratio of the elastic modulus of steel to the

elastic modulus of concrete,  $E_s$  is the elastic modulus of steel,  $b_w$  is the width of the concrete web, and  $d$  is the depth from the extreme compression fiber to the centroid of the longitudinal tension reinforcement. Assuming that the shear cracks form at  $45^\circ$  angles and that the shear reinforcement is horizontal (i.e., perpendicular to the longitudinal reinforcement) this expression simplifies to

$$K_{v,45} = \frac{\rho_v}{1 + 4n\rho_v} E_s b_w d \quad (8.4)$$

where the terms are the same as in Equation 8.3.

Taking the ratio of the flexural stiffness at yielding to the cracked shear stiffness leads to a constant with units of length squared, while the desired constant has units of length. Multiplying the shear stiffness by the shear span corrects this and leads to the following value of  $C$  for use in the proposed simplified model:

$$C = \frac{M_y / \phi_y}{K_v * z} \quad (8.5)$$

In this expression,  $M_y$  and  $\phi_y$  are the moment and curvature at first yielding, as predicted by the flexural model,  $K_v$  is the cracked shear stiffness, as defined in Equation 8.4, and  $z$  is the shear span. The shear span was initially chosen in an arbitrary manner to give the constant  $C$  appropriate units. It was chosen as a reasonable value because it is a representative length relating shears and moments, and was found to give reasonable results for specimens NTW1 and NTW2 described in this thesis. Validation of the model using experimental data from other researchers, described in Section 9.2, provided further confirmation of the appropriateness of this assumption. For non-symmetric walls, such

as the T-shaped walls considered in this study, different values of  $C$  will be calculated for each loading direction (i.e., flange in tension, flange in compression, and flange direction) as a result of each loading direction having a different flexural stiffness at first yielding.

In order to verify the applicability of this relationship between shear strains and curvatures over the entire applied loading history and at each story level, the measured interstory shear deformation history was compared to the results of multiplying the measured flexural rotations occurring within each story by the calculated factor  $C$ . This was done so that all errors would be the result of the assumed relationship between rotations and shear deformations and the comparison would not be complicated by the variation of the predicted flexural response from the measured response. Figure 8.10 shows these comparisons for specimen NTW1 in the flange-in-tension and flange-in-compression loading directions. In order to minimize clutter, the entire measured shear response is shown, but only the envelope of the response calculated from the flexural rotations is included.

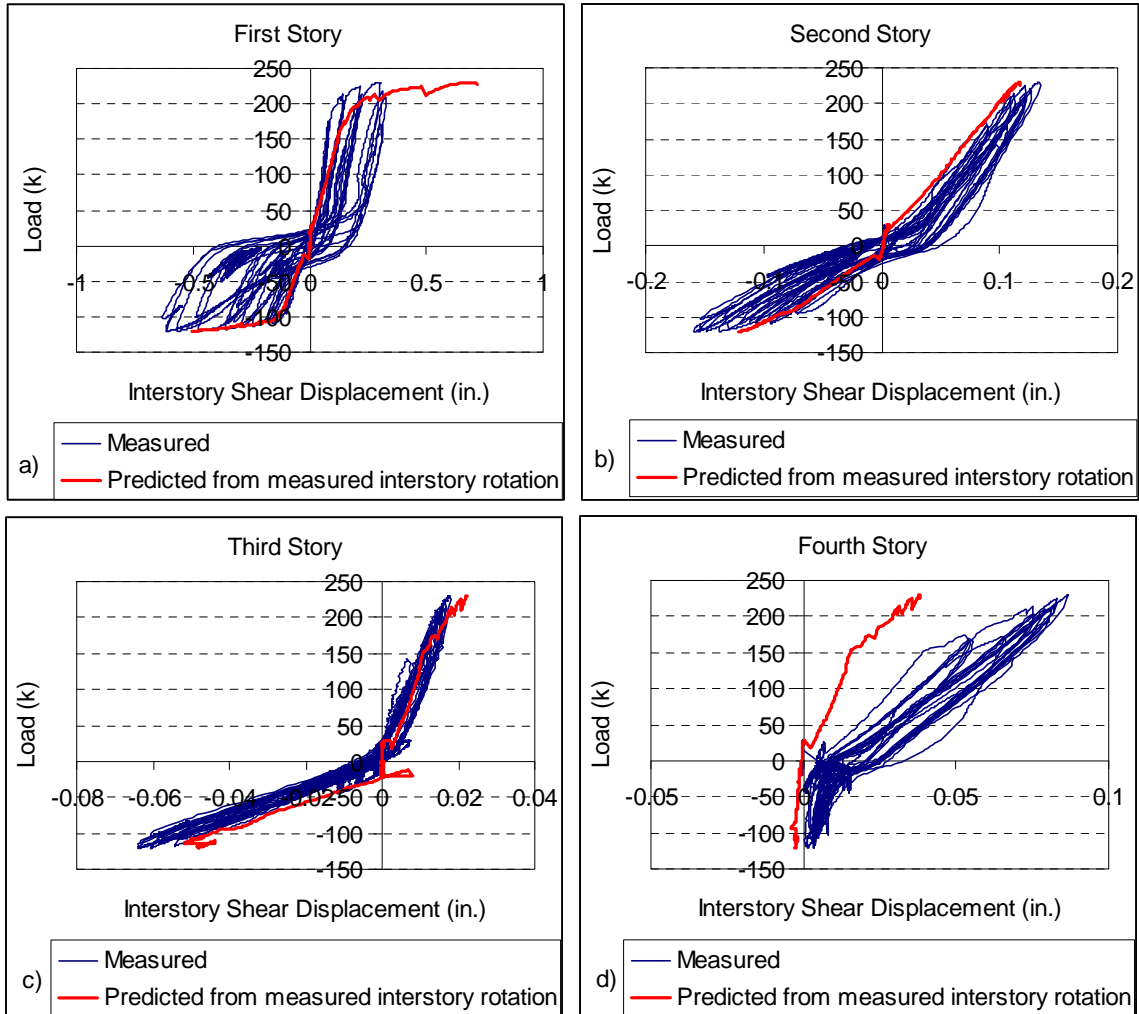


Figure 8.10. Verification of shear mode for specimen NTW11: comparison of measured shear deformations and prediction based on measured interstory rotations.

These figures indicate that the model overpredicted the shear deformations in the first story in the flange-in-tension loading direction, but predicted them with good accuracy in the flange-in-compression loading direction and in the second and third stories. The fourth story interstory shear deformations were underpredicted, but it should be remembered that the instrumentation of the fourth story led to some suspect measurements, because the measured deformations were very small compared to the accuracy of the instruments used. Additionally, because the shear deformations

occurring within the fourth story were much smaller than those elsewhere in the structure, this error is not as problematic.

In these comparisons, the diagonal cracks were assumed to have formed at  $45^\circ$  angles. In the first story in the flange-in-tension loading direction, the majority of the diagonal cracks formed at approximately  $30^\circ$  to  $40^\circ$  from the vertical. Using an angle of  $35^\circ$  in Equation 8.1 to calculate the cracked shear stiffness  $K_v$  to be used in the shear constant  $C$  greatly improved the fit of the model in the first story. The angle at which diagonal cracks form is a function of both the applied axial load and the amount and spacing of shear (horizontal) reinforcement (Collins and Mitchell 1991).

Because the crack angle varies between the flange-in-tension and flange-in-compression loading directions, it is expected that the deviation of the diagonal cracks from  $45^\circ$  in the flange-in-tension loading direction is related to the size of the compression block that must develop in order to resist the large tensile force developed in this loading direction. Collins and Mitchell (1991) show a qualitative relationship between superimposed axial loads and the angle of inclination for shear cracks, as shown in Figure 8.11. This relationship can be verified by using Mohr's circle to determine the angle associated with the principle tensile stresses. However, current methods of predicting the angle of diagonal cracks (e.g., Collins and Mitchell 1991, Kim and Mander 2007) include only terms accounting for the shear (horizontal) reinforcement and do not include terms accounting for imposed axial load or the amount of compressive force generated in the moment couple. Therefore, until such a tool is available, designers are limited to assuming a  $45^\circ$  crack angle for design purposes.

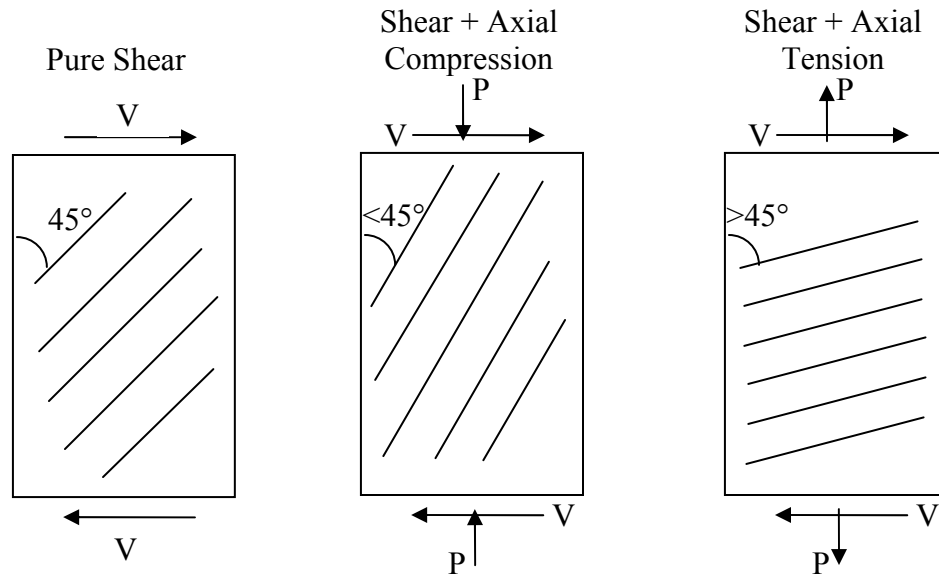


Figure 8.11. Relationship between diagonal crack inclination and axial load applied to shear panels.

Figure 8.12 compares the measured web direction shear deformations in specimen NTW1 to the predicted values of shear deformation calculated using the rotations obtained from sectional analysis for the first story and the entire structure. For this particular case, the prediction based on the measured rotations tended to overestimate the shear deformations, especially in the flange-in-tension direction, while the prediction based on a flexural section analysis provided a better estimate of the measured shear deformations because the sectional analysis tended to underestimate the flexural deformations. However, this effect of errors countering one another may not apply in all situations.

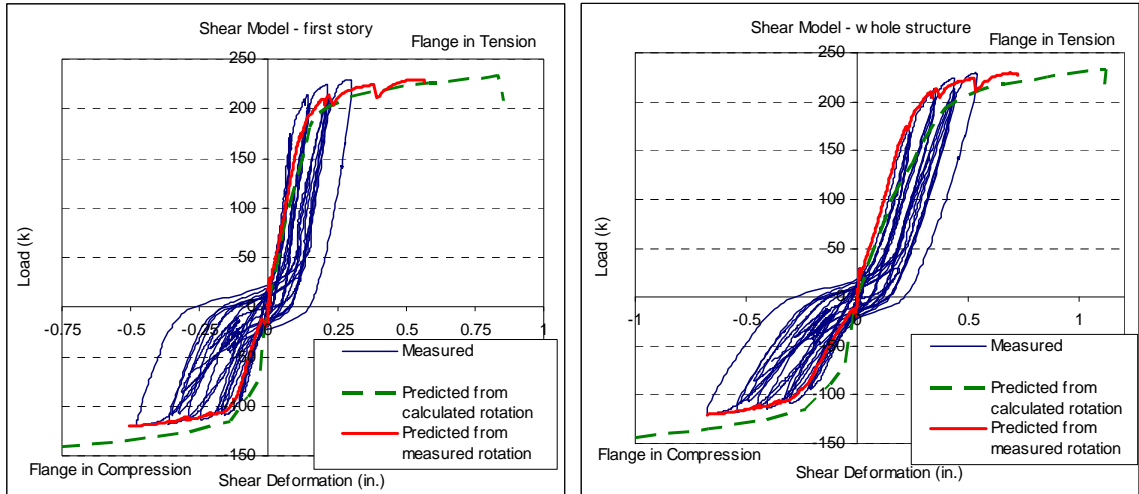


Figure 8.12. Measured and predicted load versus shear deformation relationships, NTW1 web direction loading.

### 8.2.3 Deformation due to Strain Penetration

The approximation of deformations due to strain penetration in the F-S-SP Integration model begins with assuming that plane sections remain plane, so that the rigid body rotation of a wall due to strain penetration can be calculated based on the slip of the extreme tensile bars and the neutral axis location. This assumption leads to the expression

$$\theta_{sp} = \delta_{slip} / (d - c) \quad (8.6)$$

where  $\theta_{sp}$  is the rotation due to strain penetration,  $\delta_{slip}$  is the slip of the extreme tensile bars in the anchorage zone,  $d$  is the distance from the extreme compression fiber to the extreme tensile bars, and  $c$  is the neutral axis location, as shown in Figure 8.13.

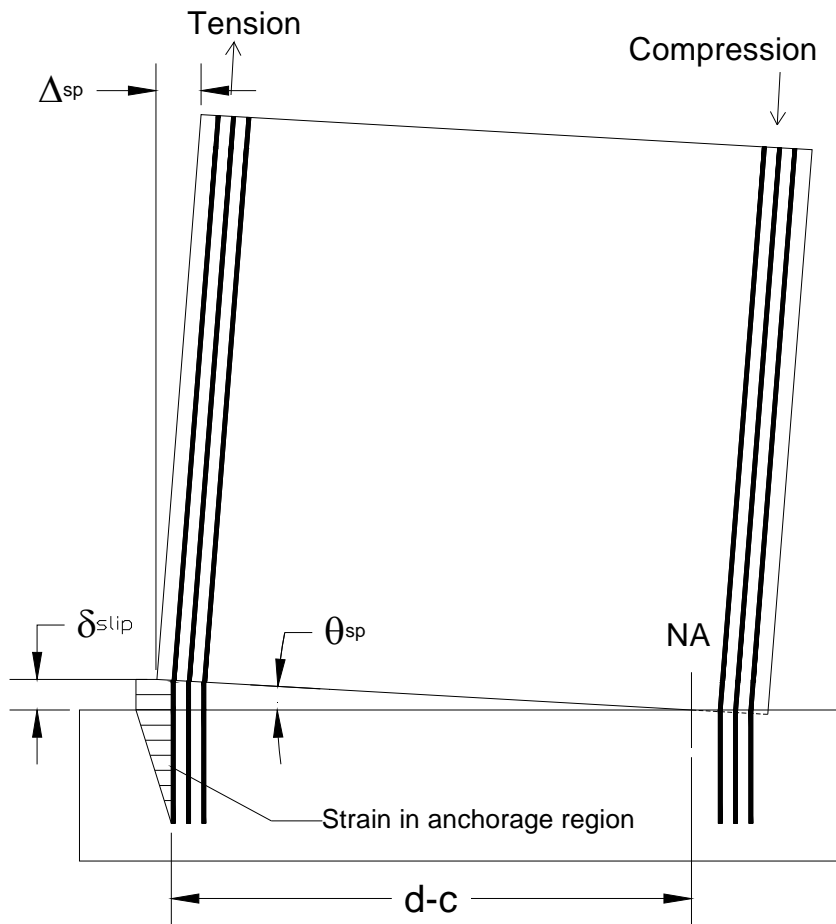


Figure 8.13. Terms required in strain penetration calculations.

The neutral axis location is readily determined from the flexural section analysis, and the slip of the extreme tension bar(s) can be determined using any desired method, such as Lowes and Altoontash (2003) or Zhao and Sritharan (2007) described in Section 2.2.7.

The slip model developed for incorporation into the F-S-SP Integration model represented a further simplification of the Lowes and Altoontash (2003) method. This approach was taken with the goals of simplicity, applicability to walls of all scales, and

sufficient transparency such that modifications to the model can be made by the structural engineer (e.g., modification of the average bond stress at yielding to account for confining effects) if the engineer feels this is warranted.

The strain penetration model used in the F-S-SP Integration method was developed by introducing two additional simplifying assumptions into the model proposed by Lowes and Altoontash (2003): 1) the anchorage length,  $l_a$ , over which the bar stress was assumed to be distributed, was calculated at the yield stress and assumed to be constant regardless of the applied bar stress, rather than increasing as the applied stress increased, and 2) the strain gradient was assumed to be constant over the anchorage length for a particular applied stress, rather than becoming nonlinear in any portions of the reinforcement that have yielded. The second assumption neglects both the decreased modulus of the reinforcement and the decreased bond stress that is observed in any portions of the reinforcement that have yielded. The effects of these assumptions are shown in Figure 8.14, with the strain distribution assumed by Lowes and Altoontash (2003) shown in Figure 8.14a and the simplified strain distribution assumed in the F-S-SP Integration model shown in Figure 8.14b. Applying these assumptions results in a model that overestimates the effects of strain penetration prior to yielding and underestimates these effects after yielding, particularly at very large inelastic strains. Because the majority of walls fail due to concrete crushing prior to fracture of the steel, these difficulties with prediction of strain penetration at very large inelastic strains will not be encountered in practice.

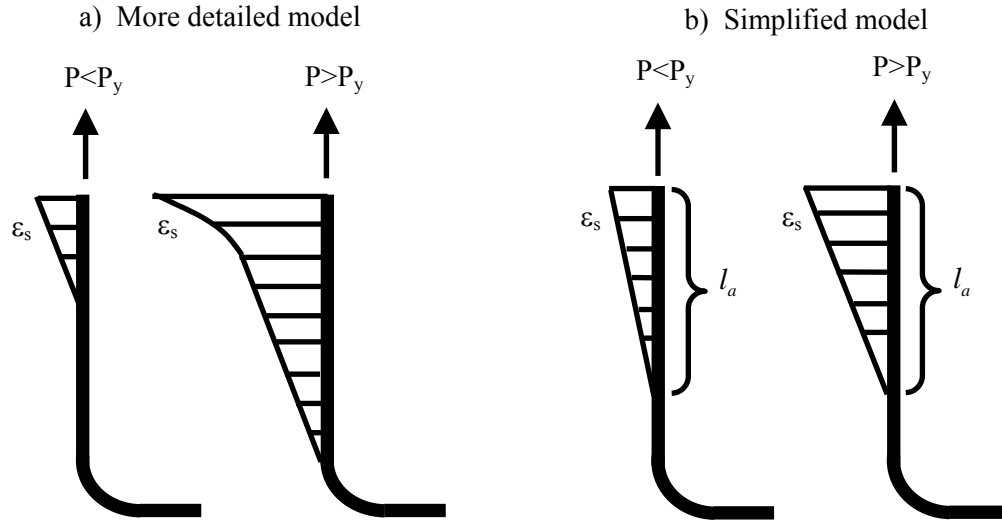


Figure 8.14. Detailed and simplified models of strain distribution in anchorage region.

Assuming a constant bond stress of  $\tau_{avg}=0.67\sqrt{f'_c}$  (ksi) or  $1.75\sqrt{f'_c}$  (MPa) as recommended by Eligehausen *et al.* (1983), the anchorage length  $l_a$  at yielding can be calculated as

$$l_a = \frac{3}{8} \frac{f_y \text{ (ksi)}}{\sqrt{f'_c} \text{ (ksi)}} d_b \text{ (ksi)} = \frac{1}{7} \frac{f_y \text{ (MPa)}}{\sqrt{f'_c} \text{ (MPa)}} d_b \approx 8-10d_b \quad (8.7)$$

Using this anchorage length for all applied stresses and assuming a triangular strain distribution leads to an approximation of  $\delta_{slip}=0.5*\epsilon_{wall\ base}*l_a$ , where  $\epsilon_{wall\ base}$  is the strain in the extreme tensile steel at the base of the specimen for a given loading, which can be obtained from the flexural section analysis. Substituting this expression into the expression for rotation due to strain penetration given previously leads to the final approximation

$$\theta_{sp} = \frac{\epsilon_{wall\ base} l_a}{2(d-c)} \quad (8.8)$$

Figure 8.15 compares the calculated relationships between bar stress and slip due to strain penetration for a No. 6 (3/4 in. diameter) bar using measured material properties of specimen NTW1. Three relationships are plotted: the simplified method used in the F-S-SP Integration model and the methods presented by Lowes and Altoontash (2003) and Zhao and Sritharan (2007). The measured stress-strain relationship for the reinforcing bars was used for the F-S-SP model. Lowes and Altoontash's model assumes a bilinear model for the steel; for this case, a strain hardening modulus of 1000 ksi was assumed, which was approximately equal to the measured tangent modulus immediately after yielding (the measured stress-strain curve for the bars in specimen NTW1 did not include a plateau between yielding and the onset of strain hardening). Zhao and Sritharan's model is based on stresses and is independent of the stress-strain relationship of the reinforcement.

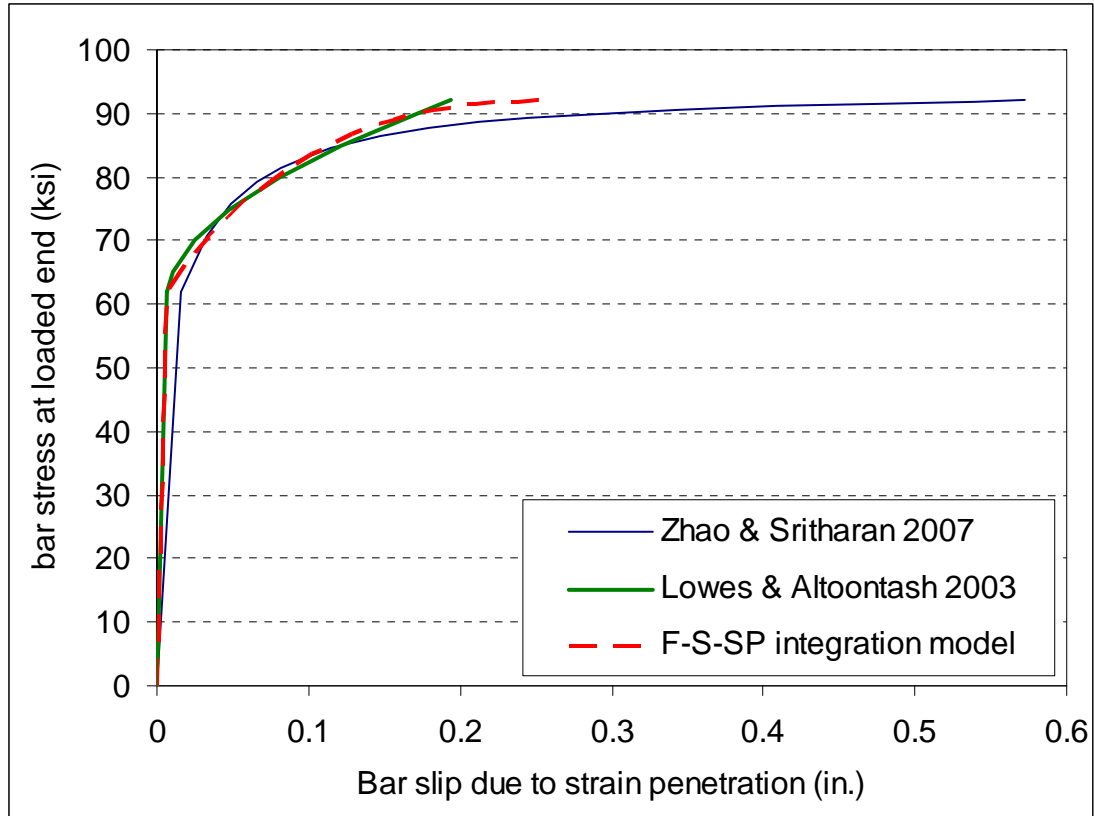


Figure 8.15. Comparison of simplified bar stress-slip model to Zhao and Sritharan (2007) model.

The F-S-SP model and Lowes and Altoontash's (2003) model predicted very similar values of slip at yielding. The small difference between these two models was due to the assumed average bond stress of  $0.67\sqrt{f'_c}$  in the F-S-SP model and  $0.685\sqrt{f'_c}$  in the Lowes and Altoontash model. Both of these numbers were based on the same data set (Eligehausen *et al.* (1983)), and the small differences between them are due to rounding. The Zhao and Sritharan (2007) model predicted a larger slip at yielding, based on fitting their model to empirical data. The results of all three of the models varied less than 10 percent for stresses in the range of 71 to 87 ksi. At larger stress levels, the simplified relationship in the F-S-SP model predicted a smaller slip than Zhao and Sritharan (2007) because of the simplifying assumptions used in the F-S-SP model, as

discussed above. Lowes and Altoontash (2003) predicted a smaller slip than the other two models as a result of the assumed bilinear material model. In this model, the assumed slip at large stresses, approaching the ultimate strength, is much less than the values reported in the literature from testing, which reduces the predicted amount of slip at these stress levels. Decreasing the strain hardening modulus in the Lowes and Altoontash (2003) model to achieve a best-fit of the entire stress-strain response would increase the predicted slip value for all post-yielding stresses, increasing the accuracy of the prediction near ultimate and decreasing the accuracy immediately post-yielding.

Many walls will fail due to concrete crushing before the steel ruptures. As a result, accurately predicting the slip and associated rotations due to strain penetration at very high stress or strain levels is less critical than accurately predicting them at smaller stress or strain levels, particularly for the case of performance-based engineering where it may be desirable to predict deformations due to low or moderate level events. The results of all three models were similar at these levels, so the use of the simplified expression proposed above was deemed appropriate for the purposes of the F-S-SP Integration method.

Figure 8.16 compares the measured rotations due to strain penetration in specimen NTW1 under web direction loading to the rotations predicted using the F-S-SP model. Contrary to the expected tendencies of the simplified strain penetration model, the strain penetration predicted after yielding in the flange-in-tension loading direction was overpredicted rather than underpredicted. At the peak moment in the flange-in-tension loading direction, the predicted rotation was twice the measured rotation. One possible

source of this discrepancy was the location of the stud used to measure bar slip in the flange: this stud was located in the flange tip, rather than at the center of the flange. Shear lag effects reduced the strain in this bar relative to the strain at the center of the flange, reducing the apparent bar slip in this loading direction. However, because the derived components of deformation sum to within 1 percent of the directly measured deformation in this loading direction, this is an unlikely explanation. Doubling the measured deformations due to strain penetration would cause the sum of deformation components at the top of the structure at the maximum moment to be approximately 5 percent larger than the directly measured value. Figure 8.17 superimposes the rotations due to strain penetration predicted using the model proposed by Zhao and Sritharan (2007) onto the information plotted in Figure 8.16. After yielding, both of these models lead to similar results, with near identical results at failure of the wall.

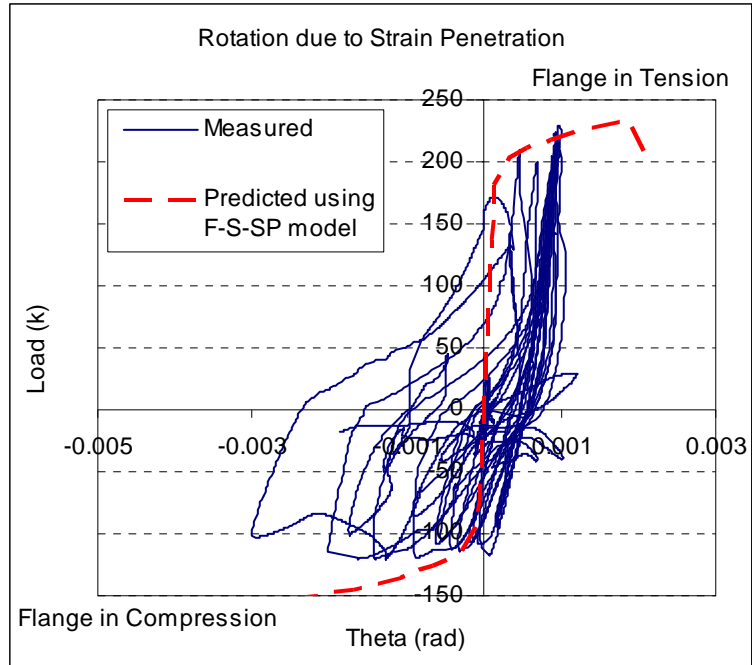


Figure 8.16. Measured and predicted load versus rotation due to strain penetration relationships, NTW1 web direction loading.

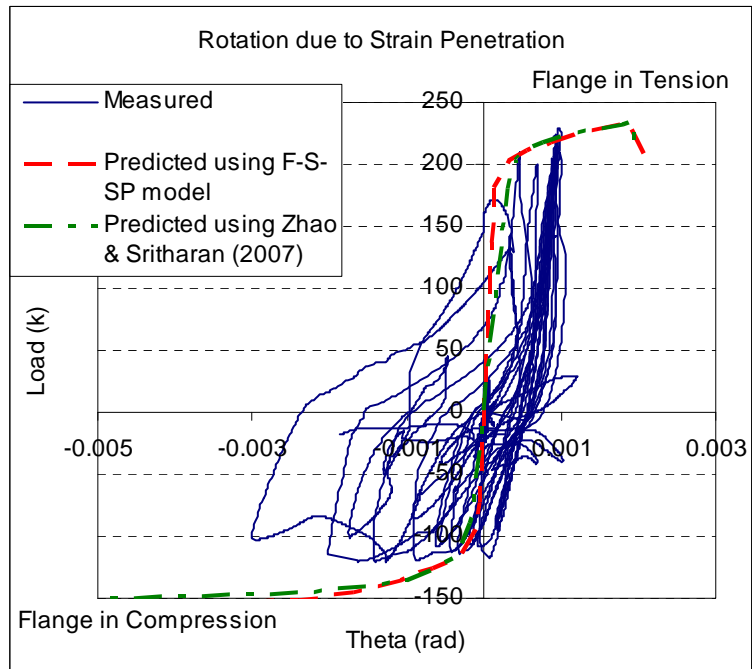


Figure 8.17. Measured and predicted load versus rotation due to strain penetration relationships, NTW1 web direction loading: comparison to Zhao and Sriitharan (2007).

### 8.2.4 Modeling Lap Splices

Lap splices locally increase the stiffness of a section due to the presence of an increased area of reinforcement. Figure 8.18 shows the effect of the lap splices in specimen NTW2 on the distribution of curvature over the height of the specimen near failure. The values of curvature shown in this plot are average values over the length of each instrument, resulting in a stair-step pattern. As discussed in Section 7.10.1, the lap splices prevented yielding from occurring in the region of the splice, while yielding was observed directly above and below the splice.

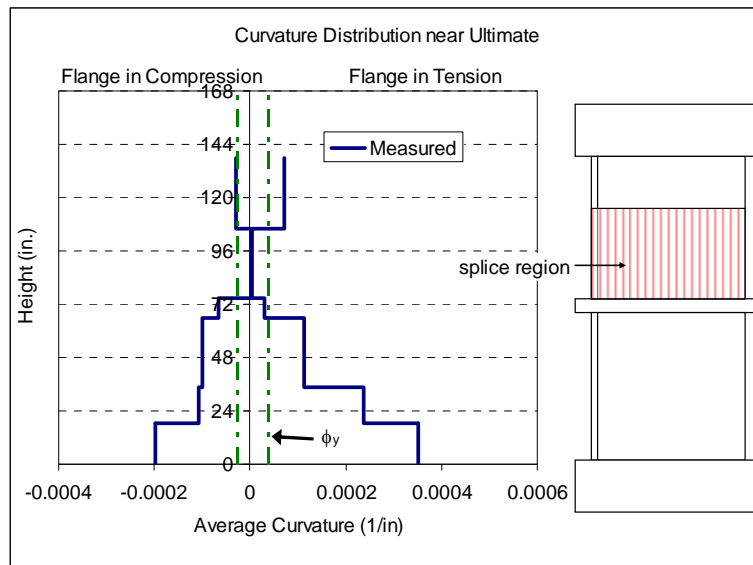


Figure 8.18. Measured curvature distribution near maximum applied moment, NTW2 web direction loading.

Two approaches may be taken when modeling a wall with lap splices outside the nominal plastic hinge region. As discussed in Section 7.10.1, the effects of the lap splice on the overall deformed shape and gross behavior of the specimen were small in this specimen, with lap splices located outside the nominal plastic hinge region. As a result, the designer may choose to neglect the effect of the splice when modeling, particularly in

the preliminary stages of design. When a more detailed examination of a wall is desired, the portion of the wall with the lap may be modeled using a second sectional analysis that considers the increased area of reinforcing steel in the lapped region. Because shear strains are assumed to be proportional to curvatures in the F-S-SP Integration model, this approach will locally decrease deformations resulting from both flexure and shear, which is consistent with the observations from specimen NTW2. The predicted distributions of curvature over the height of NTW2 considering the increased area of reinforcement in the splice region (i.e., doubling the area of reinforcement) are compared to the measured values in Figure 8.19, indicating the local decrease in predicted curvatures that results from the splice. Compared to the measured values, the model indicates a lesser effect from the splices. However, because the measured values indicate near zero curvature in the splice, there may have been some difficulty with instrumentation of the second story. The two instruments measuring vertical deformations of the lower and upper portions of the story were mounted to the wall using a common stud at mid-height. It is possible that movement of this stud could have added part of the deformation from the lower half of the second story to the upper half, exaggerating the effects of the splice on the curvature distribution.

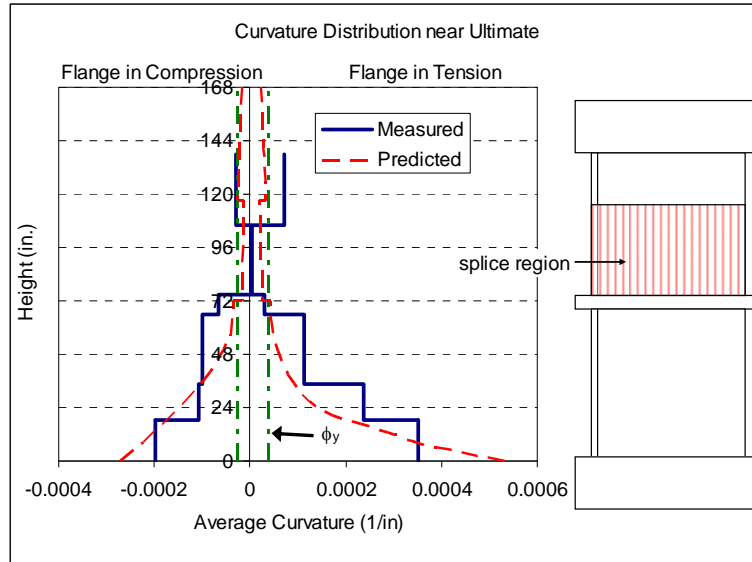


Figure 8.19. Measured and predicted curvature distributions near maximum applied moment, NTW2 web direction loading.

The measured load versus flexural displacement relationship for specimen NTW2 in the flange-in-tension and flange-in-compression loading directions is compared to predictions made both including and neglecting the splice in Figure 8.20. Because the splice is away from the plastic hinge region and near the top of the specimen, the effects of including or neglecting the splice in this case are small, with maximum effects in the elastic region: in both loading directions, the deflection at yielding is increased by 9 percent when the splice is neglected, and the deflection at failure is increased by 3 percent. If four stories of the structure are considered (i.e., a specimen similar to NTW1), the effects are only slightly larger, with 10 percent and 4 percent increases in the predicted deflections at yielding and failure, respectively. These differences may or may not be significant, depending on the goals of the analysis. However, engineers should be aware that the local effects of the splice are much larger. Neglecting the splice in the flange in tension direction increases the predicted local deformations (curvatures and

shear strains) by 65 to 70 percent in the flange-in-tension loading direction and by up to 100 percent in the flange-in-compression loading direction.

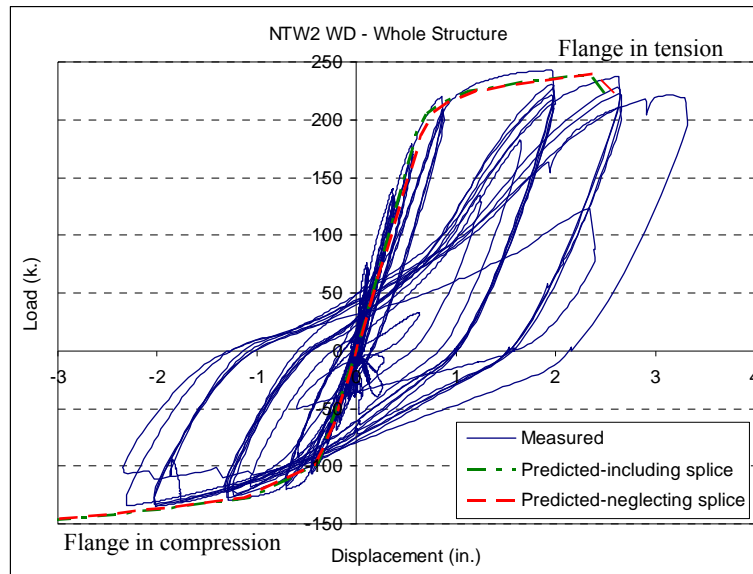


Figure 8.20. Measured and predicted load versus displacement due to flexure, NTW2 web direction loading.

### 8.2.5 Effects of Previous Damage: Flange Direction Loading

The loading history applied to the two specimens included only six flange direction ramps prior to failure of the web, and these cycles did not increase the longitudinal strain demands beyond those previously applied in the web direction loading. As a result of the damage due to web direction loading, particularly the previous yielding of the reinforcement, the measured moment resistance of the specimens was smaller than predicted. This is shown in the plot of the moment versus curvature relationship for specimen NTW1 in Figure 8.21, where the predicted moment-curvature relationship is shown with the dashed line. The pre-yielding flange direction cycles show that the initial flexural stiffness was calculated correctly in the flexural section analysis, but the post-yielding cycles had much smaller moment resistance than predicted, with

substantial softening occurring between the single group of three cycles prior to failure of the web tip and the several groups of cycles after failure of the web tip. This softening was largely the result of the reinforcement being yielded previously, and was also influenced by the damage state of the concrete in the specimen. Because the F-S-SP Integration model is based on flexural section analysis, the inability to predict the moment-curvature response correctly due to previous damage leads to an inability to predict the load-displacement response considering all components of deformation.

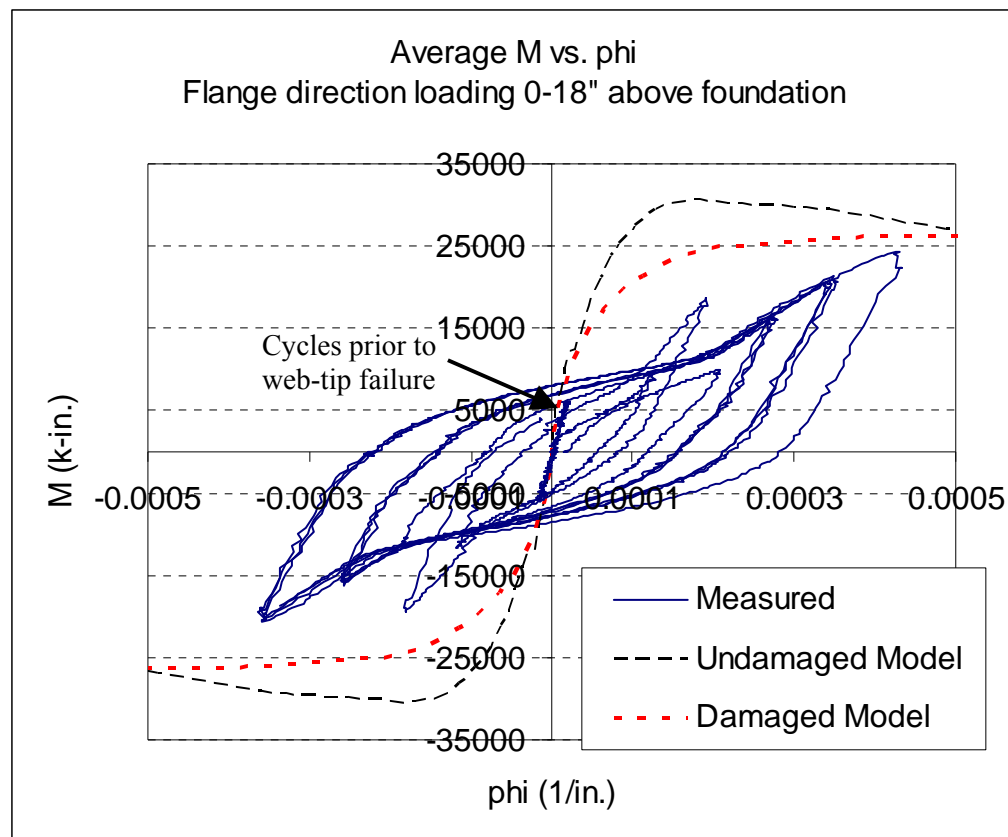


Figure 8.21. Comparison of measured and predicted moment versus curvature relationships, NTW1 flange direction loading.

Using the measured strain history of the reinforcement and the Menegotto-Pinto model for hysteretic behavior of steel, a modified stress-strain relationship was calculated

to model the behavior of the previously yielded reinforcement. The calculated stress-strain history for a typical bar in the flange tip is shown in Figure 8.22. A modified material model was created by offsetting the strain of a typical increasing segment so that a strain of zero was associated with zero stress. Because the loops have very similar shapes after the initial yielding cycle, the complete applied load history prior to the portion of interest is not critical to this modification. The original and modified material models are shown in Figure 8.23, and the original and modified input parameter values are given in Table 8.2. The effects of this modification on the moment-curvature relationship are shown in Figure 8.21. As expected, softening the steel model led to a softening of the calculated flexural response of the wall. However, the modeled moment-curvature response was still stiffer than the measured response, with good correlation for only the final cycles. This approach clearly does not account for all of the damage to the specimen prior to the flange direction loading cycles that ended the load history. Additionally, removing the failed concrete and reinforcement in the web tip from the modeled wall had limited effect on the flange direction response. This is because the web is generally not far from the neutral axis in flange direction loading, and has only limited effect on the wall response in this loading direction.

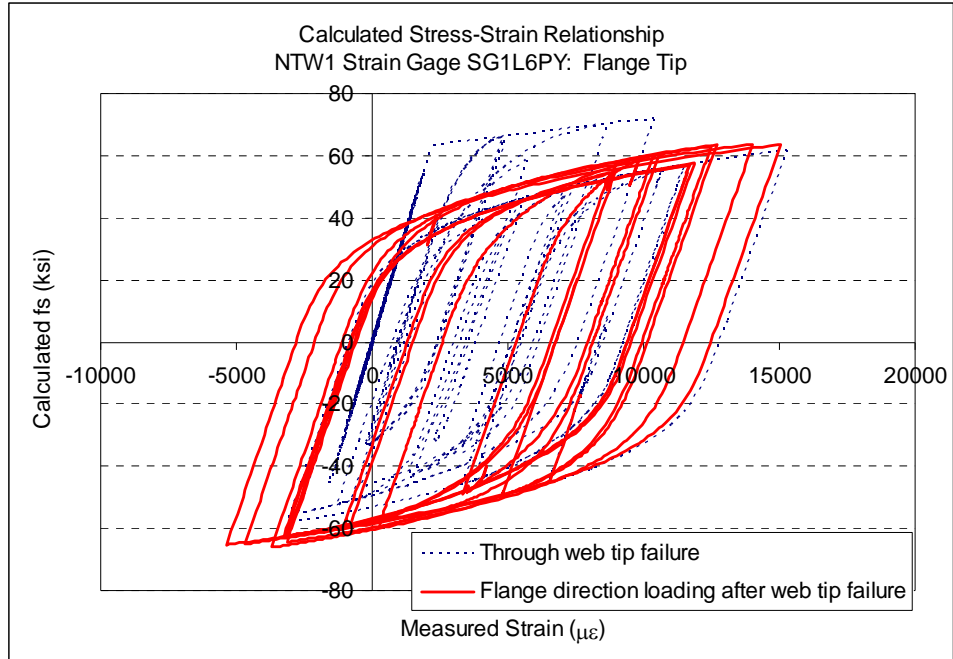


Figure 8.22. Stress-strain history for typical bar in flange tip.

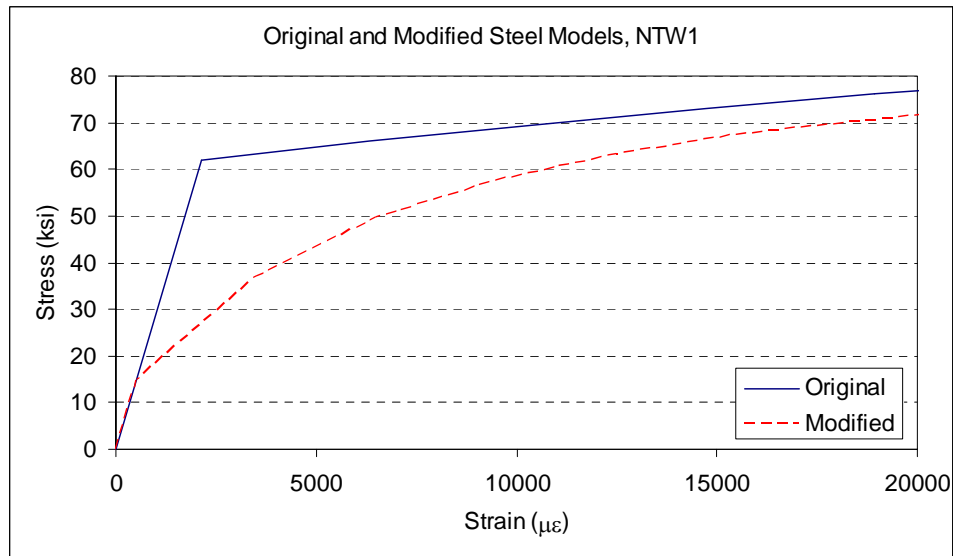


Figure 8.23. Original and modified steel material models used, specimen NTW1.

Table 8.2. Material property parameters used to represent damaged properties of reinforcement in specimen NTW1.

Material	Parameter	Original Value	Modified Value
Steel	$f_y$ (yield stress)	62.0 ksi	15.0 ksi
	$f_u$ (maximum stress)	92.0 ksi	82.0 ksi
	$f_f$ (stress at failure)	85.0 ksi	81.9 ksi
	$\epsilon_1$ (strain at onset of strain hardening)	0.002137	0.000517
	$\epsilon_2$ (strain at $f_u$ )	0.08	0.09
	$\epsilon_3$ (strain at $f_f$ )	0.17	0.12
	$E$ (elastic modulus)	29000 ksi	29000 ksi
	$E_T$ (initial modulus of strain hardening region)	1000 ksi	8000 ksi

Using OpenSEES, Waugh *et al.* (2009) also found that the calculated monotonic response of the specimens in the flange direction to be stiffer than the measured cyclic response, as shown in Figure 8.24. However, incorporating unloading and reloading rules into the material models used for both the steel and concrete and applying the entire load history led to good correlation between the model and the measured response of the specimens, as shown in Figure 8.25. The substantial difference between the monotonic loading envelope and the predicted cyclic behavior indicate that capturing the accumulated damage in both the steel and concrete is critical to accurately predicting the response of a specimen to demands that do not exceed those previously applied.

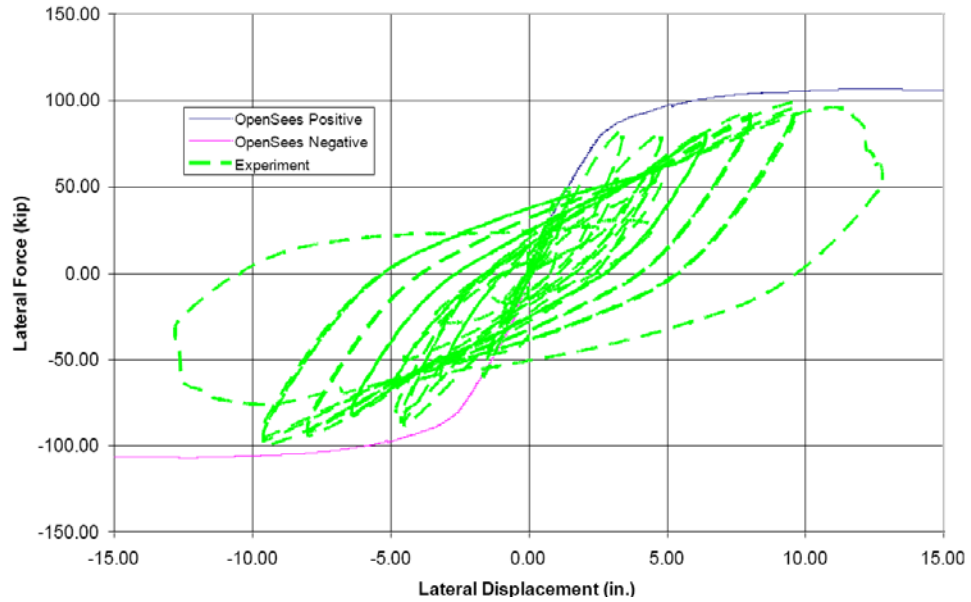


Figure 8.24. Comparison of calculated monotonic flange direction envelope of NTW1 with measured response (from Waugh *et al.* 2009).

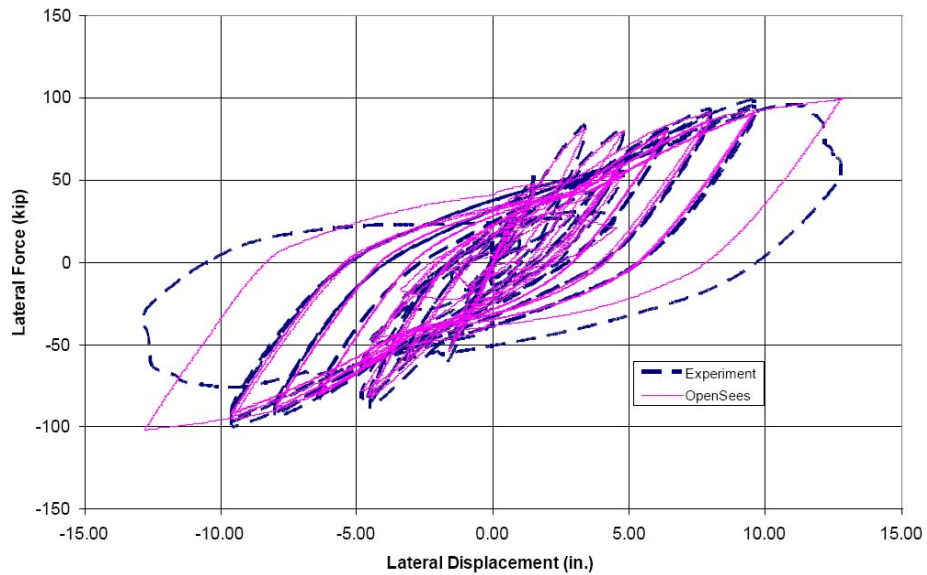


Figure 8.25. Comparison of measured and calculated flange direction cyclic response of NTW1 (from Waugh *et al.* 2009).

Waugh's model indicates that tools are available to predict the behavior of walls after previous damage. However, the F-S-SP Integration model is limited to the prediction of monotonic loading envelopes. It has very limited ability to account for

previous damage to a specimen. Removing material known to be destroyed and modifying the steel model to account for previous yielding can be done with limited computational tools, but other damage effects that can be taken into account in a more sophisticated model, such as softening of concrete, are neglected by the simplified model. At best, attempts can be made to place bounds on results. As a result, this simplified modeling procedure may not be appropriate in situations where this level of detail is desired.

### **8.2.6 Skew Direction and Multidirectional Loading**

Similar to the flange direction loading ramps discussed previously, the applied skew- and multidirectional loading patterns did not apply demands larger than the previously applied orthogonal loads. As a result, all of the issues discussed previously with flange direction loading apply to the skew- and multidirectional loading portions of the applied load histories. Figure 8.26 shows a comparison of the force-displacement responses generated with the OpenSEES tool created by Waugh *et al.* (2009) for both loading histories relative to the measured values for each of the orthogonal components (i.e., flange direction [FD] and web direction [WD] components) for the 45° skew loading ramps.

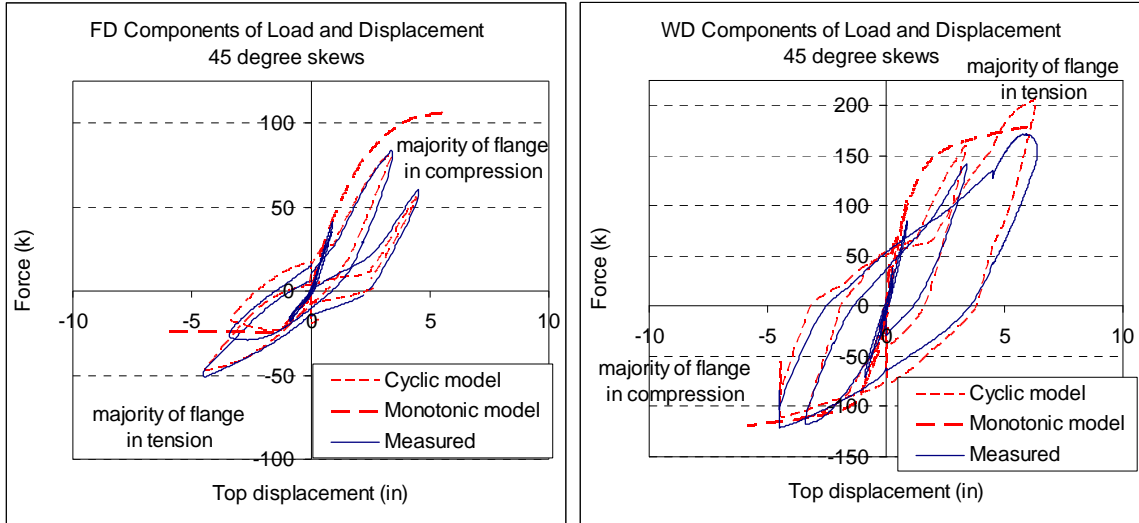


Figure 8.26. Comparison of measured and calculated 45° direction monotonic and cyclic response of NTW1 using tool from Waugh *et al.* 2009.

The differences between the responses predicted with the monotonic and cyclic loading histories are similar to those observed in the flange direction. In general, the measured response and the response predicted with the cyclic model are less stiff than the monotonic model as a result of the damage accumulating in the specimen over the course of the applied loading history. An additional difference is in the relative proportions of the components, particularly when the majority of the flange is in tension. In this loading direction, the flange direction component of the load is approximately half that predicted by the monotonic loading. Figure 8.27 shows a comparison of the orthogonal loading components calculated using each of the three models and indicates that the simplified model presented here leads to similar results as the OpenSEES model when monotonic loading is considered, although this does not represent the response of the previously damaged specimen well.

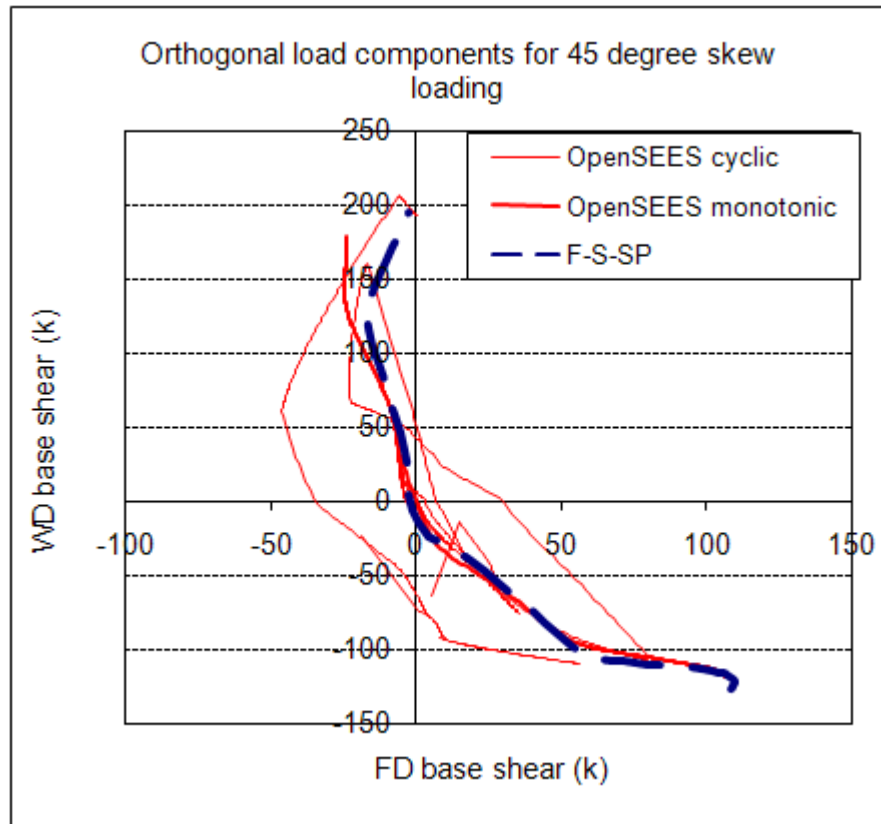


Figure 8.27. Comparison of orthogonal load components for 45° skew direction loading predicted with F-S-SP Integration model and OpenSEES model.

### 8.3 Predicting Damage States for Performance-Based Engineering

The descriptions of damage thresholds and associated local engineering demand parameters (EDPs) for reinforced concrete columns proposed by Berry *et al.* (2008) and given in Table 2.2 were adopted herein as a framework for predicting damage states for reinforced concrete structural walls. While there are some pertinent differences between structural walls and columns (i.e., the possible presence of a lightly reinforced “web” region between two boundary elements in walls), it was felt that the significant damage states and related local EDPs recommended by Berry *et al.* (2008) were appropriate for describing the damage states of walls and the associated need for repair.

Critical values for the local EDPs were then determined based on the measured crack widths and observed damage to the cover and core concrete throughout the testing of specimens NTW1 and NTW2. The recommended values for each EDP are summarized in Table 8.3. These values can be applied to design problems by comparing strains predicted using the F-S-SP Integration model or other tools to the threshold values. In this table, the first four columns represent the framework proposed by Berry *et al.* (2008), and the final column contains new threshold values of the EDPs calibrated for wall specimens. It should be noted that during the testing, observations of crack widths and concrete spalling were made only at ramp peaks and points of zero load. As a result, correlations between observed damage and each of the local EDPs can only be made at discrete points in the loading history, and critical values of the EDPs for the specimens can be given bounds but not described precisely.

Table 8.3. Recommended threshold values for EDPs

Damage Level	FEMA 356 Performance Level	Required Repair	Local EDP	Threshold Value
Negligible		None	Reinforcing steel tensile strain	$\epsilon_s < 3.5\epsilon_y$ conc. steel*
				$\epsilon_s < 7\epsilon_y$ dist. steel*
Minimum	Immediate Occupancy	Epoxy injection of cracks	Reinforcing steel tensile strain	$\epsilon_s > 3.5\epsilon_y$ conc. steel
				$\epsilon_s > 7\epsilon_y$ dist. steel
Minimal		Patching of concrete cover and epoxy injection of cracks	Cover concrete compressive strain	$\epsilon_c > 2f'_c/E_c$ or 0.003
Moderate	Life Safety	Replacement of concrete cover and epoxy injection of cracks	Core concrete compressive strain	$\epsilon_c > 4kf'_c/E_c$ **
Significant	Collapse Prevention	Replacement of section	Maximum tensile strain reduced for cyclic demand	Model indicates post-peak loss of capacity

\*Conc. steel indicates longitudinal reinforcement concentrated in boundary elements with minimal longitudinal reinforcement elsewhere. Dist. steel indicates longitudinal reinforcement uniformly distributed across wall element.

\*\* $kf'_c$  is expected compressive strength of confined core, determined using Modified Kent & Park or other appropriate model.

The damage measure associated with the need for epoxy injection of cracks is based on residual crack width (i.e., the crack width remaining after load is removed from the structure) (Berry *et al.* 2008). Because crack widths at ramp peaks were measured more frequently than residual crack widths, it was assumed that the ratio of peak to residual crack width was equal to the ratio of peak to residual longitudinal strain for a given unloading ramp. An additional increase in the data set was achieved by considering the measured strains and crack widths both near the base of the specimen and near the top of the first story, effectively doubling the number of data points.

As discussed in Section 7.5, there was a strong correlation between the spacing of longitudinal reinforcement and the distribution and width of both horizontal and diagonal

cracks. In specimens NTW1 and NTW2, the reinforcement in the boundary elements was spaced at no more than 3 ½ in. o.c., while the reinforcement outside the boundary elements was spaced at up to 12 in. o.c. except in the flange of specimen NTW2. When the reinforcement was widely spaced, diagonal (shear) cracks were consistently observed to be wider than flexural cracks. As a result of this observation, two guidelines were determined from the testing results of specimens NTW1 and NTW2 for the threshold reinforcing strain between negligible and minimum damage levels, a value of 3.5 times the yield strain (approximately 7000-7500  $\mu\epsilon$ ) of the reinforcement for cases with reinforcement concentrated in boundary elements and an increased critical value of 7 times the yield strain (approximately 14000 to 15000  $\mu\epsilon$ ) for cases with closely spaced reinforcement across the entire section. It is notable that specimens NTW1 and NTW2 were half-scale, and the clear cover dimension was reduced in the scaling. Because crack width is known to increase with cover (ACI 318-02), comparison of these critical values for the EDP to results of full-scale tests may result in a downward revision of the values.

The prediction of initial spalling of the cover concrete and spalling of the cover concrete to expose the reinforcing bars were made by correlating the concrete strains measured near the base of the wall with the observed spalling. Because spalling did not spread over a large portion of the wall height, spalling could only be correlated to strains at the base of the wall. Concrete compressive strains, measured with the embedment gauges, were used for this calibration. The observed values of compressive strain associated with initial spalling of the cover concrete were between 0.0025 and 0.0035 microstrains, so the typically-assumed maximum strain of 0.003 is an appropriate value

to predict the initial spalling of concrete cover. Because the embedded concrete strain gauges were broken as the concrete spalled and crushed and the gauges bonded to the steel accumulated tensile strains, the compressive strains associated with sufficient spalling to expose the reinforcement could not be determined directly. Instead, they were estimated by comparing the drifts associated with initial spalling and sufficient spalling to expose the reinforcement. It was assumed that the neutral axis depth remained constant between these two drift levels. As a result, for each loading direction, the ratio of compressive strains at the two points was assumed equal to the ratio of drifts.

Two approaches may be taken to predict the point beyond which replacement of the entire cross-section is necessary. These are specifying strain limits for concrete in compression (associated with significant loss of the confined core) and steel in tension (associated with fracture of reinforcement) and finding the point on the moment-curvature relationship where the moment resistance has decayed to some fraction (e.g., 90 percent) of the maximum moment resistance. The former approach has been adopted by many of the empirical expressions for plastic hinge rotation capacity (i.e., Mattock and Corley) because it can reasonably be carried out with manual calculations. The difficulty with this approach is that research has indicated that the (fictitious) concrete compressive strain at the extreme fiber associated with crushing of the concrete core varies according to the member type and dimensions. This can be seen by comparing the various empirical expressions and the research used to develop them. The latter method has the advantage of avoiding this member-dependence to some extent, although it does depend on the selected confined concrete model providing an accurate representation of the

descending branch of the material model, rather than imposing an additional cutoff on the material model. It is recommended that the latter method be used, particularly for nonrectangular walls and other members with “nonstandard” geometries.

Because a limited amount of data was used to determine the guidelines in Table 8.3 and large scatter has been observed in historical data, particularly regarding crack widths (ACI 318-02, Pagni and Lowes 2006), the given thresholds should be considered approximate and are likely to be revised as additional tests are carried out.

## **Chapter 9    Application and Validation of F-S-SP Integration Model**

### **9.1    Introduction**

This chapter provides validation of the F-S-SP Integration model and discussion of the application of the model to design problems. Section 9.2 includes the validation of the F-S-SP Integration model using the results of testing specimens NTW1 and NTW2 as well as several wall tests reported in the literature. These tests include rectangular wall tests done by Johnson (2007), T-shaped wall tests done by Thomsen and Wallace (1995), C-shaped wall tests done by Sittipunt and Wood (1995), and barbell- and hollow box-shaped bridge pier tests done by Hines (2002). Section 9.3 continues the evaluation of the F-S-SP Integration model by comparing results obtained from it to results obtained using the FEMA 356 model and the model proposed by Hines *et al.* (2004). Section 9.3.3 addresses the application of the F-S-SP Integration model in design, when actual material properties are unknown.

### **9.2    Validation of F-S-SP Integration Model**

In order to evaluate the utility of the F-S-SP Integration method, it was applied to several wall and pier specimens tested by other researchers. Each of these testing programs is described in Chapter 2. The F-S-SP Integration method was evaluated based on its ability to predict the failure mode, maximum moment capacity, and deformation capacity of the wall specimens.

### 9.2.1 Comparison of F-S-SP Integration Model to Test Results

Table 9.1 compares predictions made with the F-S-SP Integration model to measured loads and displacements at first yielding as well as the associated stiffness for both specimens NTW1 and NTW2 in the flange-in-tension and flange-in-compression loading directions, and Table 9.2 compares measured and predicted maximum load and displacement capacities in each of the orthogonal loading directions. The calculated stiffnesses are the secant stiffnesses to the point of first yielding. These predictions are made using the measured material properties for the flange-in-tension and flange-in-compression loading directions, and the measured material properties with the steel modified to account for previous yielding for flange-direction loading directions.

Table 9.1. Comparison between measured and predicted loads, displacements and stiffnesses at first yielding.

	Loading Direction	Story	Measured			Predicted			Difference		
			V (k)	$\Delta$ (in.)	V/ $\Delta$ (k/in.)	V	$\Delta$	V/ $\Delta$	V	$\Delta$	V/ $\Delta$
NTW1	Flange in Tension	2	115	0.5	250	168	0.6	294	46%	24%	18%
		4	115	0.9	130	168	1.4	122	46%	56%	-7% <del>%</del>
	Flange in Compression	2	81	0.4	188	91	0.3	303	12%	-35%	61%
		4	81	1.1	73	91	0.6	142	12%	-45%	94% <del>%</del>
NTW2	Flange in Tension	2	132	0.4	350	180	0.6	292	36%	58%	-17%
	Flange in Compression	2	84	0.3	270	98	0.4	243	17%	26%	-10%

Table 9.2. Comparison between measured and predicted wall capacities.

	Loading Direction	Maximum Shear Resistance (k) and Associated Displacement (in.)						Displacement @ Failure (90% Max. Shear) (in.)		
		Measured		Predicted		Difference		Meas.	Pred.	Diff.
		V	Δ	V	Δ	V	Δ			
NTW1	Flange Direction	100	8.7	97	7.6	-3.1%	-12.1%	10.6	8.4	-20.4%
	Flange in Tension	229	5.6	233	6.2	1.8%	12.1%	5.9	6.6	11.0%
	Flange in Compression	121	3.8	155	11.6	**	**	3.8	14.6	**
NTW2	Flange Direction	87	4.4	85	2.9	-2.8%	-34.2%	4.9	3.5	-27.6%
	Flange in Tension	240	2.0	240	2.5	0.2%	24.4%	3.3	3.1	-5.2%
	Flange in Compression	132	2.3	164	6.6	**	**	2.3	7.1	**

\*\* In the experimental study, the flange-in-compression capacity was limited by previous buckling of reinforcement in the web tip. As a result, maximum values did not correlate well with the model.

Loads and displacements at first yielding are not reported for the flange direction because the only loading cycles in the flange direction prior to yielding of the flange bars in the flange-in-tension loading direction were to 25 percent of the expected force at first yielding, and measured strains were less than 600 microstrains at this level.

In the flange-in-tension and flange-in-compression loading directions, the predicted loads at first yielding were consistently greater than the measured values. This is despite the fact that shear lag was neglected in the model, which would tend to reduce the flange-in-tension moment resistance at first yielding because the reinforcement near the center of the flange yielded prior to the reinforcement near the flange tips. A possible explanation for the observed early yielding of the reinforcement is that the strain gauges measured locally increased strains because a small portion of the reinforcing bar area was removed in order to create a flat spot for mounting the strain gauge.

Because of the differences between the measured and predicted loads at first yielding, comparing the stiffnesses at first yielding rather than the displacement provides a more informative comparison of the deformations prior to yielding. For three of the four cases considered (NTW1 and NTW2 in each of the flange-in-tension and flange-in-compression loading directions), the error in predicting the initial stiffness was less than 20 percent. For the case of NTW1 in the flange-in-compression loading direction, the predicted response was initially twice as stiff as the measured response when displacements at the top of the structure were considered. A primary contributor to this large error was the flexural response. The sectional analysis for this case indicated that cracking would be limited to the first story of the specimen at this point in the loading history, while cracks were observed in both the first and second stories. Cracks may have been present in the third or fourth stories, as well, although these stories were not inspected for cracks during the testing. Neglecting the tensile capacity of the concrete and assuming that the entire specimen is cracked at this point in the loading history improves the predicted response and reduces the magnitude of the error.

It should be noted that the applied load history found the load and displacement capacity of the specimens in the flange direction and the flange-in-tension direction, but the flange-in-compression direction capacity was not found prior to buckling of the bars in the web tip. This buckling led to their fracture at a much lower drift level than would be expected for monotonic loading in the flange-in-compression direction. As a result, direct comparison of the measured and predicted capacities listed in Table 9.2 is not meaningful for this loading direction, except to confirm that the predicted capacity

exceeds the value that was reached in the testing. For flange-in-tension and flange-direction loading, the model predicted the load capacity of the wall within 3 percent of the measured value. Because sectional analysis is known to be an accurate method of predicting moment capacities of reinforced concrete sections, the reliability of the F-S-SP Integration model for predicting the load capacity of a flexurally-controlled wall is very good.

Table 9.2 includes both the displacements associated with the maximum shear resistance and the displacements associated with a reduction to 90 percent of the maximum load measured. The error in the predicted displacement capacities is larger than the error in the predicted load capacities, with predicted displacement capacities varying from the measured values by up to one-third. It is expected that the F-S-SP Integration model would consistently predicted a reduced displacement capacity for walls of any geometry, because it neglects the effects of tension shifting on the plastic hinging of the wall. This was the case for flange-direction loading of both specimens NTW1 and NTW2.

In the flange-in-tension loading direction, the predicted displacements associated with the peak load were larger than the measured values. In specimen NTW1, the predicted displacements associated with a decrease to 90 percent of the peak load were also larger than the measured values. This was the only case considered that resulted in an “unconservative” estimate of the ultimate drift capacity (i.e., displacement associated with wall failure). It should be recalled that the observed failure in this loading direction was the result of an apparent premature failure of the confining reinforcement: the 135°

hooks on the confining hoops unwound and disengaged the hoops from the concrete core. Had the confinement not failed in this manner, the displacement capacity of the specimen may have been significantly larger than observed in the test, possibly exceeding the predicted value. In specimen NTW2, the measured descending branch from the peak moment resistance to the failure was nearly flat. The displacement at failure (i.e., reduction of load resistance to 90 percent of the maximum measured resistance) was 1.65 times greater than the displacement at the maximum load resistance. The model predicted a larger displacement at maximum moment, but it predicted a reduced post-peak displacement capacity, so that the predicted ultimate displacement capacity was less than the measured capacity.

Figure 9.1 through Figure 9.4 compare the measured and F-S-SP predicted load versus displacement responses for each of the specimens in each of the orthogonal directions at the top of the top story of each specimen (i.e., the fourth story of specimen NTW1 and the second story of specimen NTW2), and Figure 9.5 through Figure 9.8 compare the measured and F-S-SP predicted load versus displacement responses for the top of the first story of each specimen.

In addition to visualizing the information discussed above, these figures allow for qualitative comparison of the overall shape of the measured and predicted load-displacement relationships. It can be seen that the predicted response of both specimens in the flange-in-tension and flange-in-compression loading directions captured the shape of the measured response envelope reasonably well, with the exception of the tendency to underpredict the displacement capacity. The flange-direction response was not captured

as well, with a generally stiffer response predicted for all cases. This was the case even after modifying the material model for the steel to account for the yielding of the flange reinforcement in flange-in-tension loading prior to substantial flange-direction loading taking place, as described in Section 8.2.5.

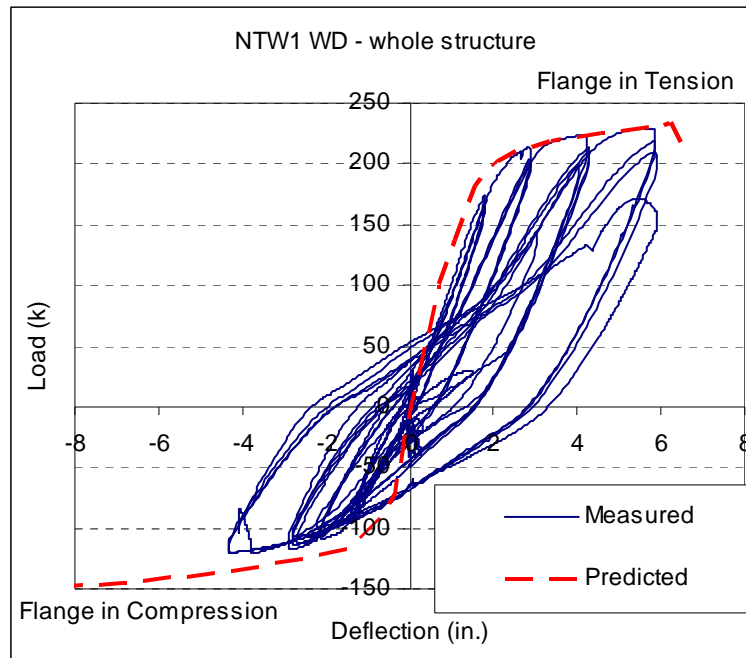


Figure 9.1. Comparison of measured and predicted responses, NTW1 web direction loading, at top of specimen.

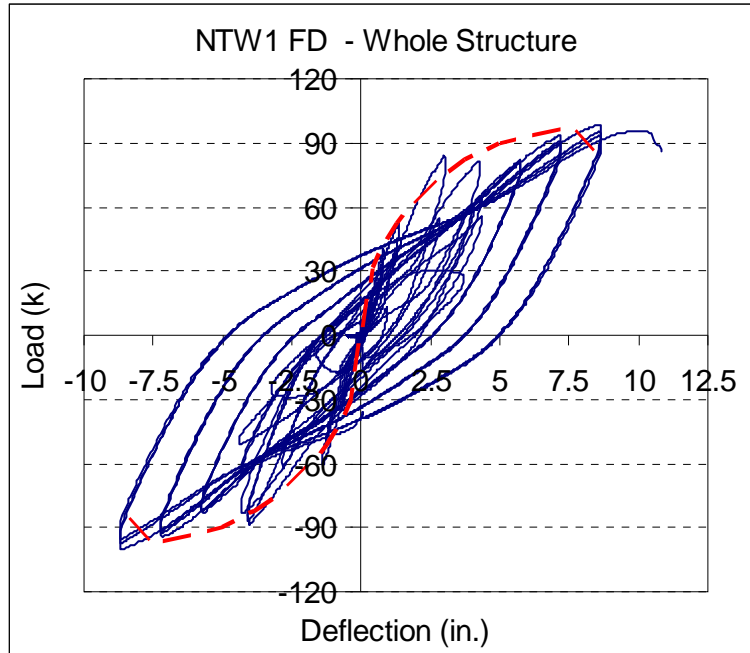


Figure 9.2. Comparison of measured and predicted responses, NTW1 flange direction loading, at top of specimen.

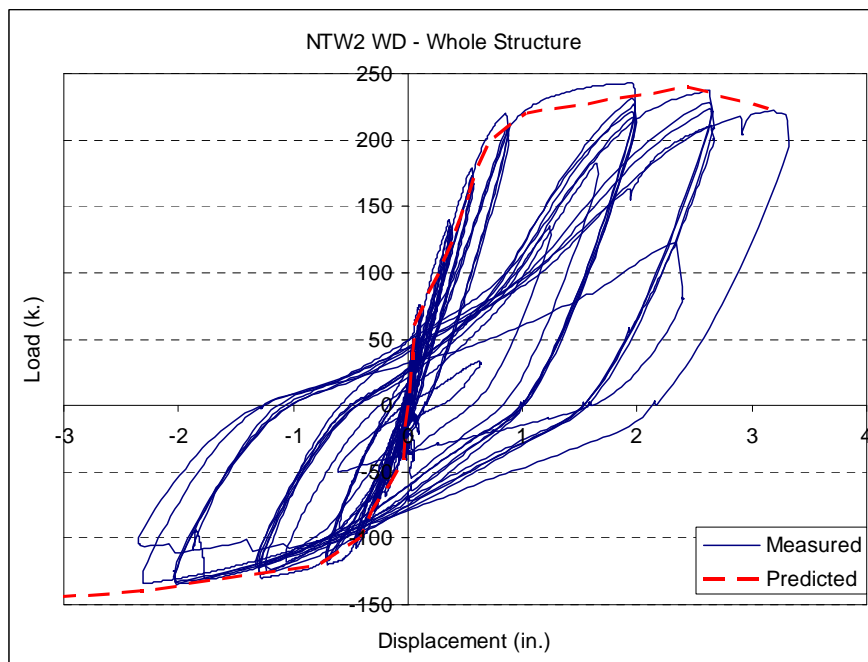


Figure 9.3. Comparison of measured and predicted responses, NTW2 web direction loading, at top of specimen.

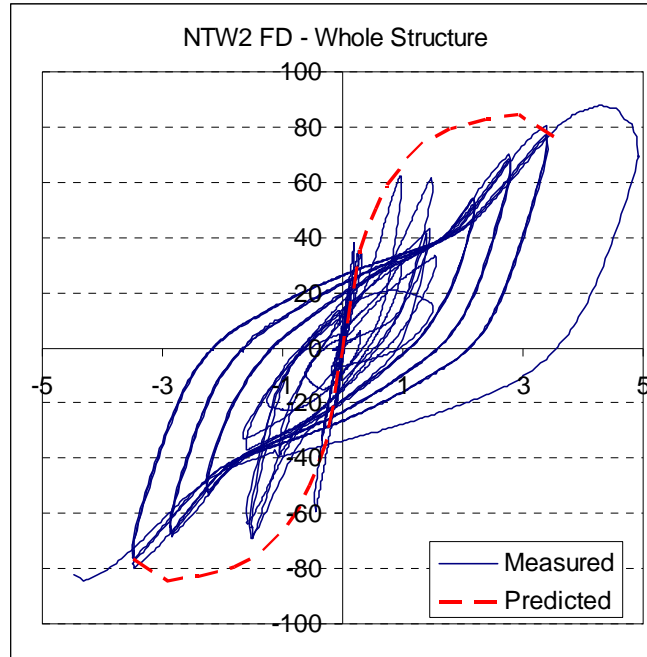


Figure 9.4. Comparison of measured and predicted responses, NTW2 flange direction loading, at top of specimen.

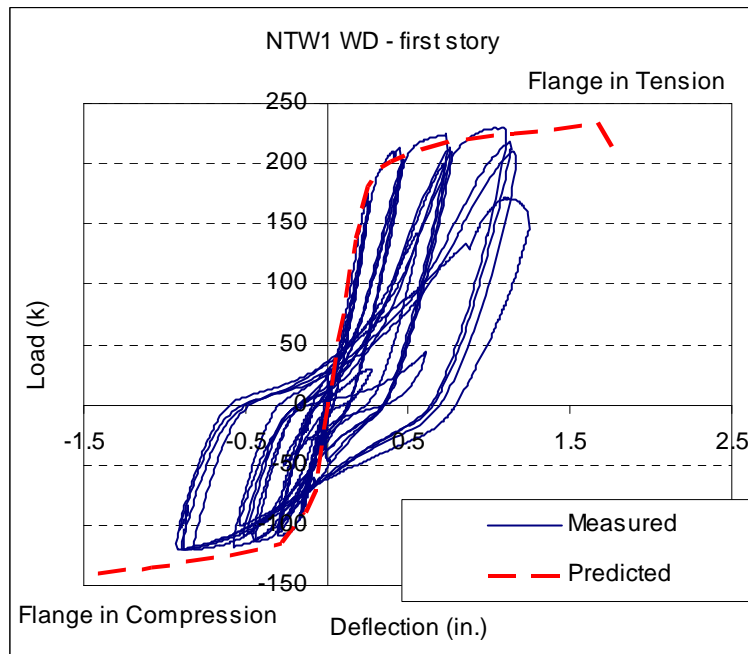


Figure 9.5. Comparison of measured and predicted responses, NTW1 web direction loading, at top of first story.

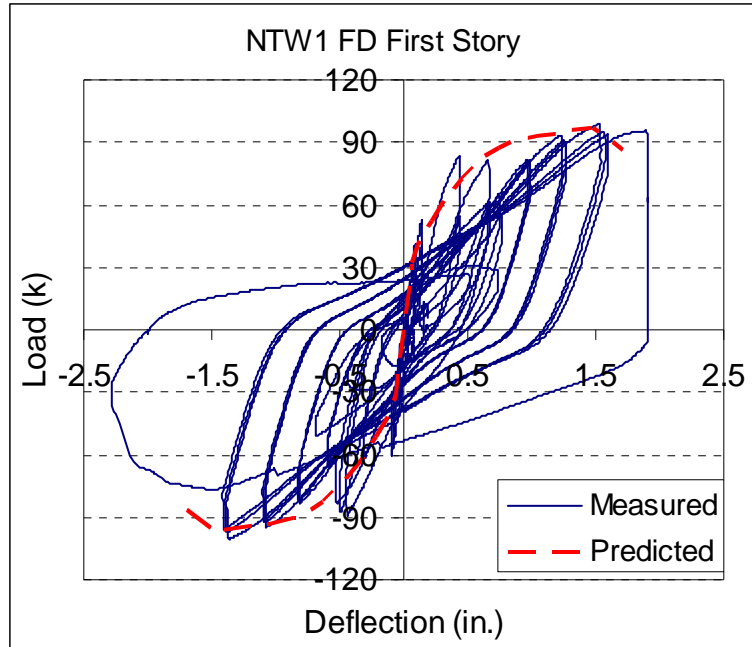


Figure 9.6. Comparison of measured and predicted responses, NTW1 flange direction loading, at top of first story.

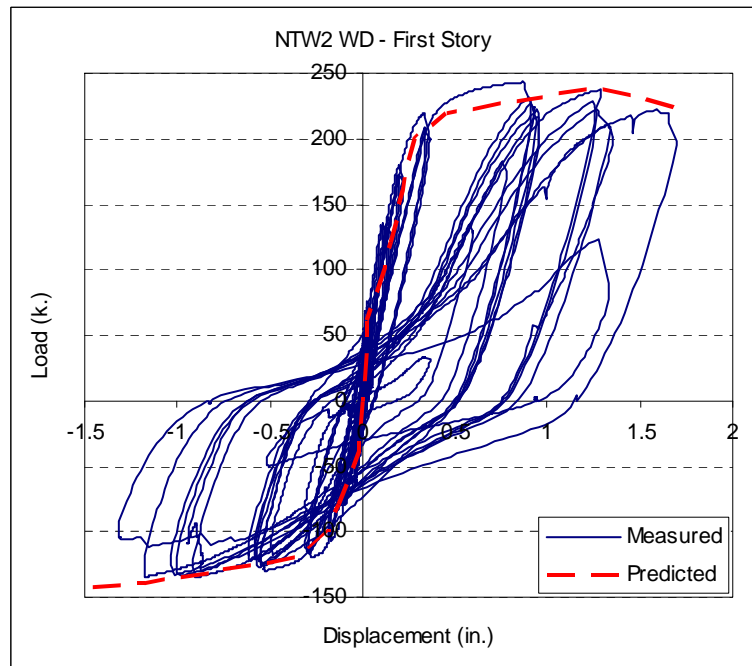


Figure 9.7. Comparison of measured and predicted responses, NTW2 web direction loading, at top of first story.

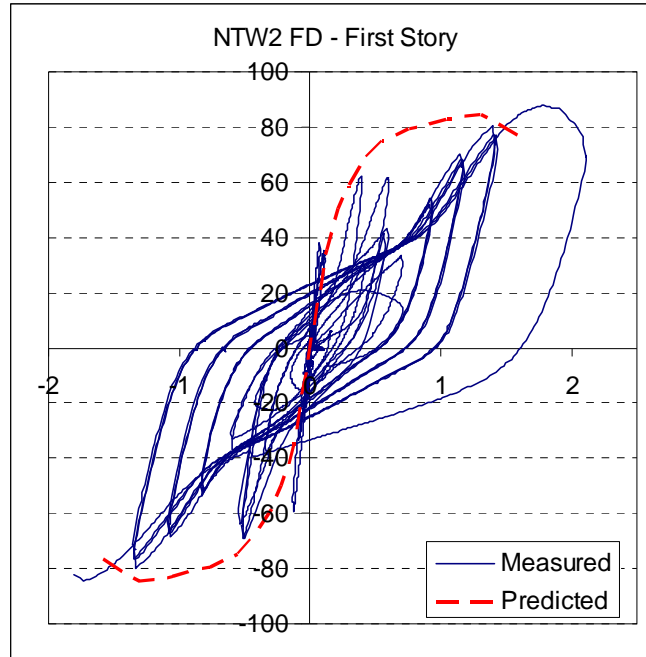


Figure 9.8. Comparison of measured and predicted responses, NTW2 flange direction loading, at top of first story.

### 9.2.2 Rectangular Walls (Johnson 2007)

Two of the three rectangular walls described in Johnson (2007) were analyzed using the F-S-SP Integration model. These were RWN, with continuous reinforcement over the height of the wall, and RWS, with lap splices located at the base of the wall, just above the foundation block. These predictions were done using the measured material properties from the specimens. Sufficient information was available to include details such as the yield plateau in the steel model.

In this specimen, failure was due to crushing of the confined concrete when the No. 9 bars were in tension. As a result, the monotonic capacity of the wall in the opposite direction, with the No. 5 and No. 6 bars in tension, was not found. Figure 9.9 compares the predicted load-deformation response of specimen RWN to the measured response, and Figure 9.10 through Figure 9.12 compare the contributions of each of the

components of deformation to the total. Deformations due to flexure and shear are considered both at the top of the first “story” of the wall (69 in. above the foundation block) and over the whole specimen (measured at the point of applied load 240 in. above the foundation block). Deformations due to strain penetration were only considered in determining the lateral displacements at the point of applied load because this portion of the deformation was due to rigid-body rotation of the wall and no additional information would be found by considering the response at other locations over the height of the wall.

In the loading direction with the No.5 and No.6 bars in tension, the prediction of each of the components had very good accuracy, with the prediction slightly underestimating the contributions of shear and strain penetration. The model predicted that had the wall been loaded monotonically to failure in this loading direction, failure would have been due to fracture of the steel in tension. In the loading direction with the No.9 bars in tension, the predicted flexural response was very accurate, and the predicted failure mode of crushing of the boundary element was correct, but errors were observed in the prediction of deformations due to shear and strain penetration, particularly in the No. 9 in tension loading direction. At very small demand levels (less than one-half of the yield load, or an average shear stress of approximately  $2\sqrt{f'_c}$  based on actual material properties) shear deformations are overestimated. At larger demand levels than this, shear deformations are underestimated. This increase in measured shear deformations was not associated with an underdesign for shear; shear reinforcement in this specimen was designed to promote a flexural failure in both loading directions. Horizontal cracks were observed in this specimen prior to testing, and sliding across these cracks was

observed during the testing. This shear sliding was likely the source of the discrepancy between the prediction and the measured behavior. It should be noted that the maximum shear stress applied to the specimens was less than  $5\sqrt{f'_c}$  and less than one-half the maximum shear stress of  $10\sqrt{f'_c}$  allowed by Section 21.7.4.5 of ACI 318-02.

The measured rotations due to strain penetration are greatly underpredicted when the No. 9 bars were in tension. Waugh *et al.* (2009) also observed this difficulty and recommended increasing the bar slip by a factor of five to better represent the observed strain penetration behavior. This group of reinforcement consisted of eight bars with standard hooks, which led to congestion in the boundary element. The embedment lengths and clear spacing between these bars met the requirements of ACI 318-02, so a pullout failure was not expected. However, the top surface of the base block was cracked and a portion of the cover concrete popped out near the edges of the wall at this end, indicating a larger amount of distress to the concrete than was observed near the group of No. 5 and No. 6 bars and the possibility of splitting cracks forming, reducing the maximum bond stress. It can be seen in Figure 9.12 that using the modification suggested by Waugh *et al.* (2009) improved the prediction of rotation due to strain penetration greatly, and in Figure 9.9 that this modification improved the overall prediction of the load-displacement relationship in the No. 9 in tension loading direction. The final model using the F-S-SP Integration method predicted the load capacity in the loading direction with No. 9 bars in tension to within 4.5 percent of the measured value, and in the opposite direction, it predicted the load associated with the maximum drift applied to within 4.5 percent of the measured value. The top displacement at failure in

the No. 9 in tension direction was underpredicted by 15 percent, primary due to the shear deformations being underpredicted. In both loading directions, the F-S-SP Integration model overestimated the stiffness at first yielding. In the No. 5 and No. 6 in tension direction, the stiffness at first yielding was overestimated by 13 percent; in the No. 9 in tension direction the stiffness was overestimated by 30 percent. In both loading directions, these differences were the result of errors in predicting the shear and strain penetration components of deflection, rather than the flexural component.

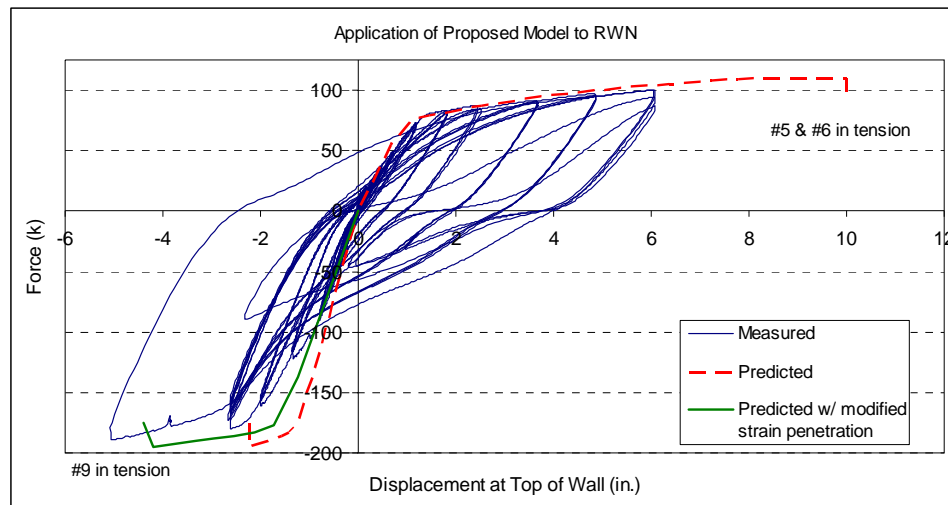


Figure 9.9. Application of F-S-SP Integration model to specimen RWN (described in Johnson 2007)

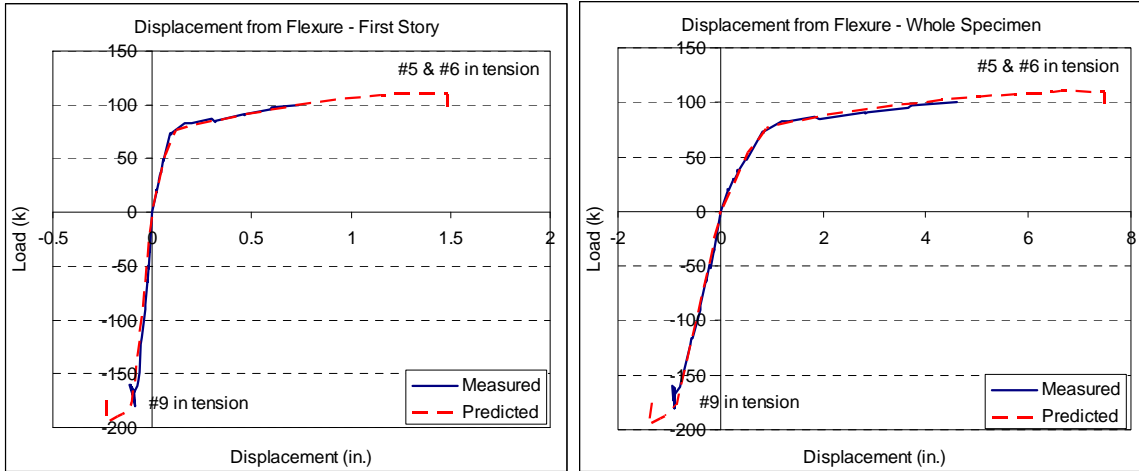


Figure 9.10. Measured and predicted flexural envelope of RWN (described in Johnson 2007)

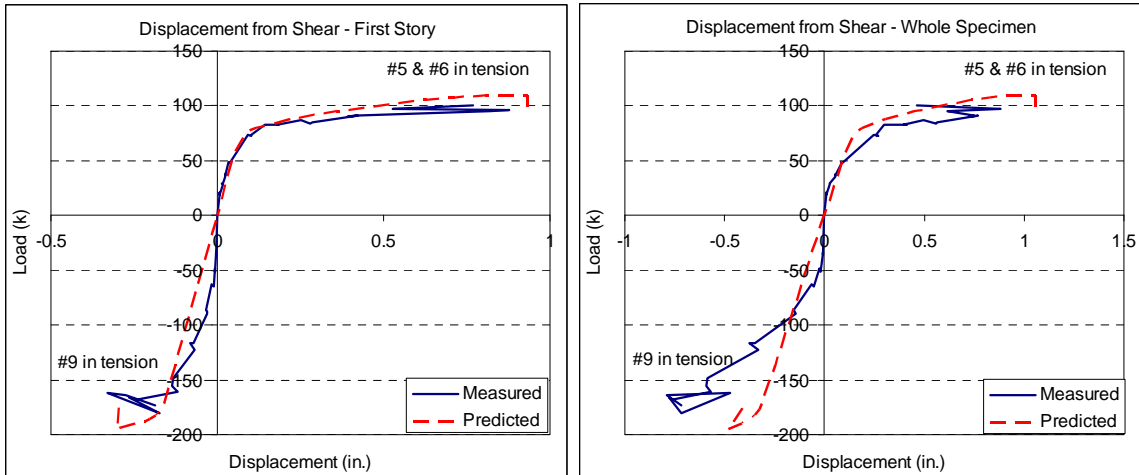


Figure 9.11. Measured and predicted shear envelope of RWN (described in Johnson 2007)

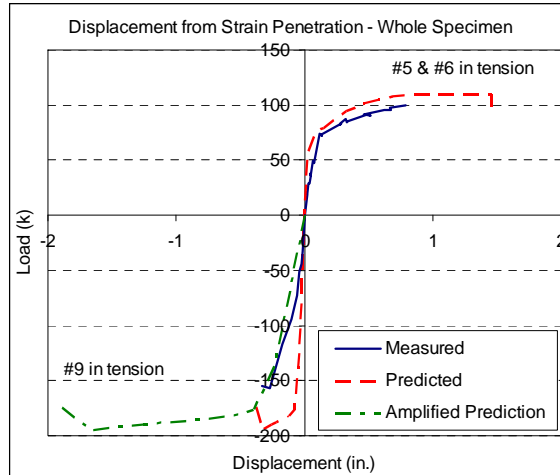


Figure 9.12. Measured and predicted strain penetration envelope of RWN (described in Johnson 2007)

Figure 9.13 shows the application of the F-S-SP Integration model to specimen RWS (Johnson 2007) with a lap splice located at the base of the wall. As in the modeling of RWN above, the strain penetration effects in the No. 9 in tension direction were amplified. This figure includes the results obtained both neglecting the splice in the model and including the splice by assuming that the splice region had doubled reinforcement. Because localized damage was observed at the base of the wall, a short region without the doubled reinforcement was included at the base of the wall. A length of 2 in. was chosen for this representation based on the region of observed concentrated damage; the use of any length up to the bar development length could be justified for this purpose. Figure 9.14 shows the curvature distribution over the height of the wall resulting from this assumption at the maximum moment in the No. 5 and No. 6 bar-in-tension loading direction.

As shown in Figure 9.13, in the No. 5 and No. 6 bar in tension loading direction, the model predicted a moment capacity 7 percent larger than the measured capacity,

which was limited by failure of the lap splices. Deformations in this loading direction were bounded by the two modeling approaches considered. This indicates that a length greater than the assumed 2 in. would be more appropriate to represent the region of concentrated damage in this wall. However, the purpose of this discussion is not to tune the model to fit a particular wall. In the No. 9 in tension loading direction, both modeling approaches failed to capture all of the deformation occurring after approximately 2/3 of the load at first yielding. The measured wall response in this loading direction was very similar to that of RWN prior to the splice failure in the No. 5 and No. 6 bar-in-tension loading direction. The differences between the measured response and the predicted response were very similar to those in RWN, with the largest portion of the discrepancy due to shear deformations being underpredicted.

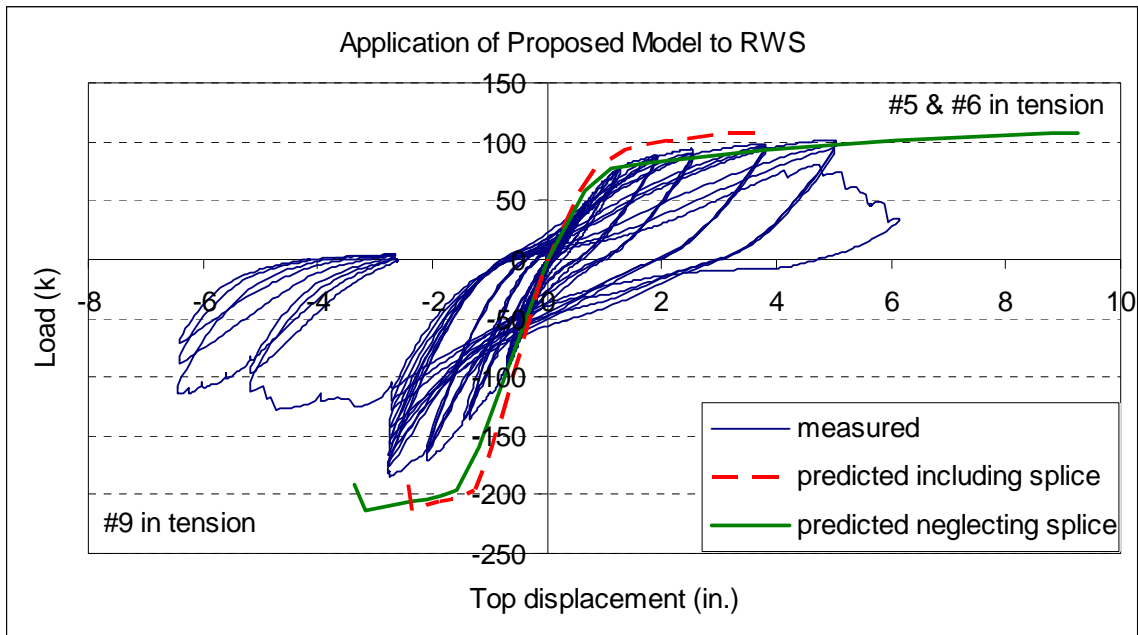


Figure 9.13. Application of F-S-SP Integration model to specimen RWS (described in Johnson 2007)

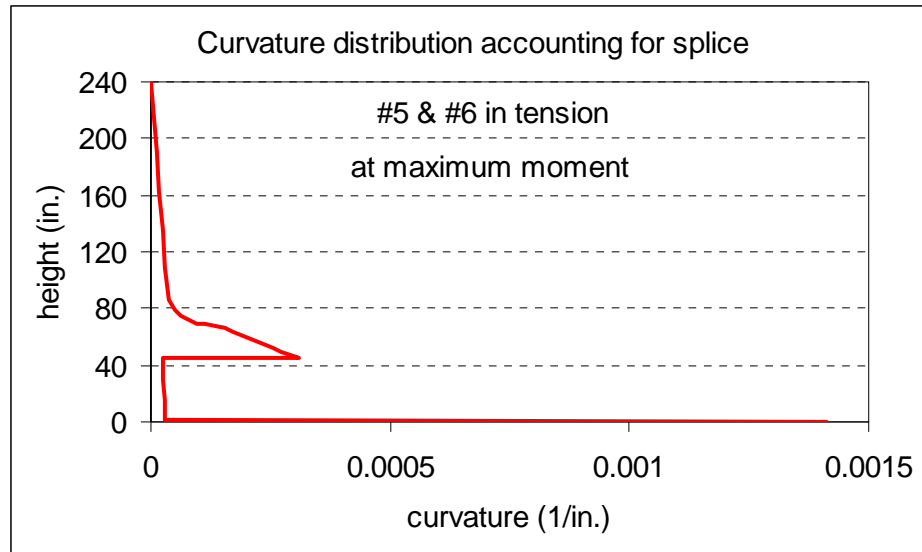


Figure 9.14. Curvature distribution accounting for splice in application of proposed model to RWS (described in Johnson 2007)

### 9.2.3 T-Shaped Wall TW2 (Thomsen and Wallace 1995)

One of the two T-shaped walls tested by Thomsen and Wallace (1995) analyzed using the F-S-SP Integration model. This wall differed from specimens NTW1 and NTW2 in having a smaller scale ( $\frac{1}{3}$  compared to  $\frac{1}{2}$ ) and in having different proportions and detailing.

Figure 9.15 compares the load-displacement relationship predicted by the F-S-SP Integration model to the measured relationship for this wall. In the flange-in-tension loading direction, the predicted stiffness at first yielding was 17 percent larger than the measured value. The predicted failure load was 3 percent greater than the measured value. Difficulty was encountered in predicting the drift capacity and failure mode. The observed failure mode was global out-of-plane buckling of the web tip at a net drift level of 2.25 percent (removing rigid body rotations resulting from rocking due to the foundation being inadequately anchored). The F-S-SP Integration model predicted

failure due to crushing of the confined concrete in the web at a drift level of only 0.6 percent drift.

The theoretical moment-curvature relationship determined by Thomsen and Wallace was used as the input for the F-S-SP Integration model after verification. A major difference between the observed wall response and the prediction was that tensile strains of approximately 0.02 were measured during the testing, while the model predicted crushing of the concrete and loss of capacity associated with tensile strains of only 0.004. The source of this discrepancy is not clear, and Thomsen and Wallace (1995) did not provide a discussion of it. It is possible, although unlikely, that there was a large difference between the concrete compressive strength measured from test cylinders and the unconfined compressive strength of the concrete in the wall. In the flange-in-compression loading direction, the correlation between the F-S-SP Integration model and the measured results was much better. The predicted stiffness at first yielding was 5 percent smaller than the measured value. The drift capacity of the wall in this loading direction was not reached prior to failure in the opposite loading direction. At the maximum drift level reached in this loading direction, the predicted load was 0.2 percent smaller than the measured load.

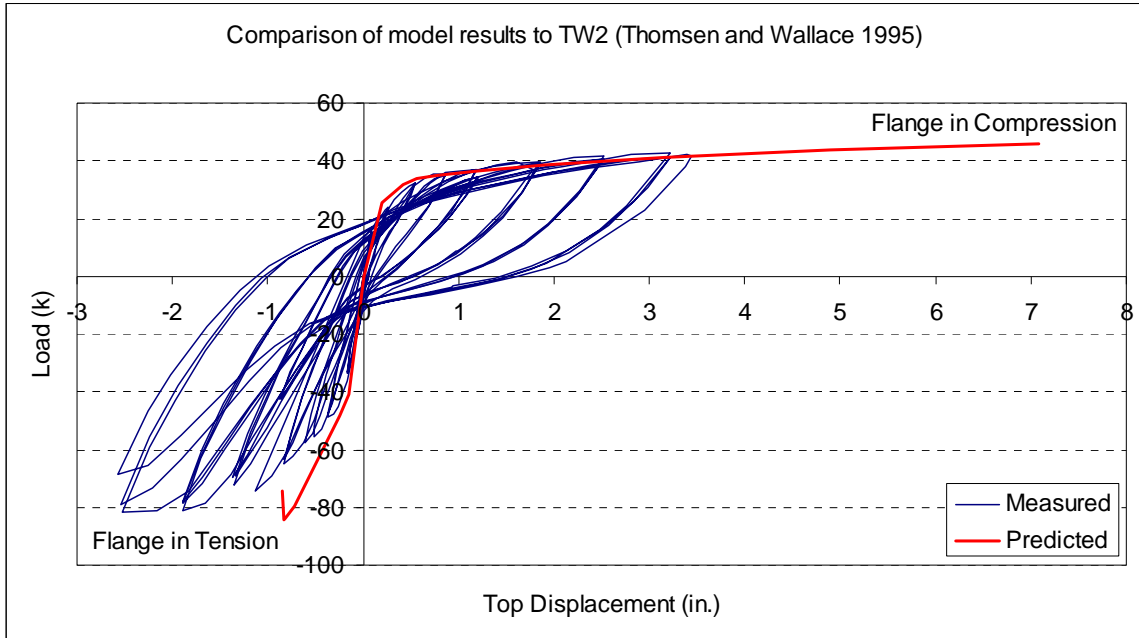


Figure 9.15. Application of F-S-SP Integration model to specimen TW2 tested by Thomsen and Wallace (1995)

#### 9.2.4 C-Shaped Wall CMS (Sittipunt and Wood 1993)

One of the two C-shaped walls tested by Sittipunt and Wood (1995) was analyzed using the F-S-SP Integration model. This wall was analyzed using the F-S-SP Integration method in order to investigate the utility of the model for a wall with non-rectangular section that was not a T-shape. Limited information was available regarding the material properties of the reinforcing steel, so a bilinear model was assumed using the given yield and ultimate stresses.

Figure 9.16 compares the load-displacement relationship predicted using the F-S-SP Integration method to the envelope measured in the test. In the flange-in-tension loading direction, the predicted stiffness at first yielding was 8 percent smaller than the measured value. The predicted failure load was 1 percent greater than the measured value, and the failure mode was correctly predicted as crushing of the confined concrete.

The model indicated that this crushing should occur at a drift of 1.2 percent, while the specimen reached a drift of 2.1 percent. Sittipunt and Wood (1995) do not report measured strains or curvatures, so determining the source of this discrepancy is difficult. In the flange in compression loading direction, the predicted stiffness at first yielding was 30 percent larger than the measured value. The drift capacity of the wall in this loading direction was not reached prior to failure in the opposite loading direction. At the maximum drift level reached in this loading direction, the predicted load was 16 percent larger than the measured load.

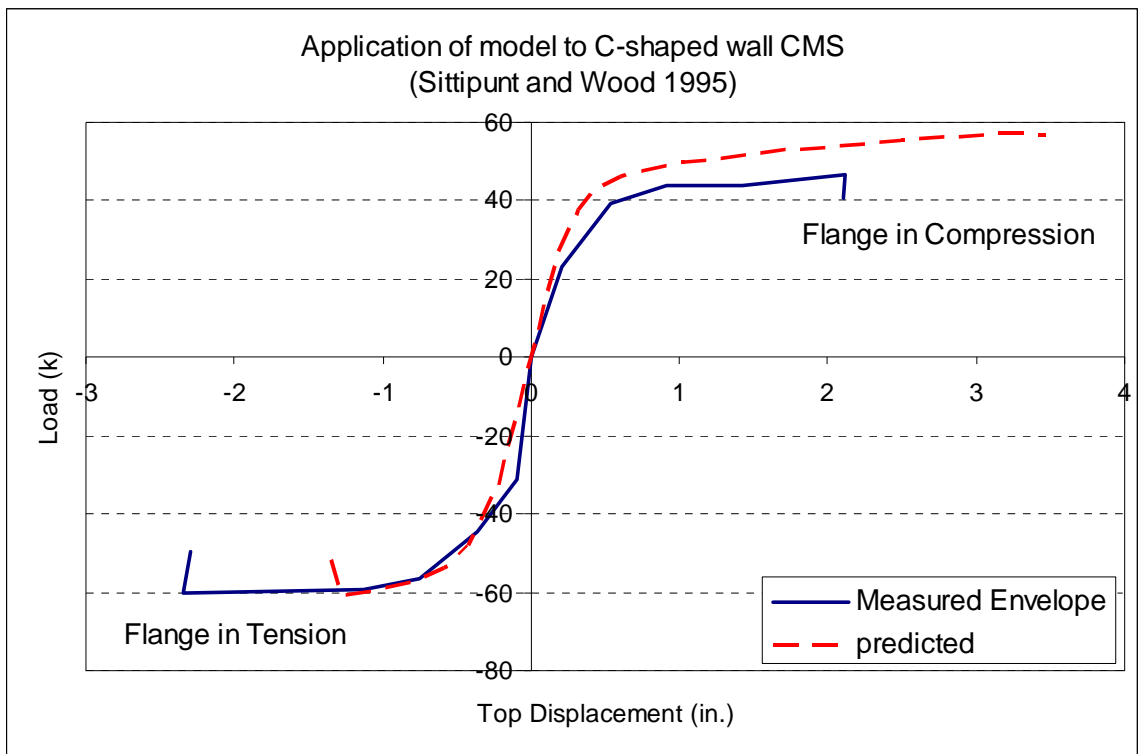


Figure 9.16. Application of F-S-SP Integration model to specimen CMS tested by Sittipunt and Wood (1995)

### 9.2.5 Barbell and Hollow Box Bridge Piers (Hines 2002)

One barbell-shaped and one hollow box-shaped bridge pier specimen tested by Hines (2002) were analyzed using the F-S-SP Integration method in order to investigate the utility of the method for specimens of additional geometries and shorter shear spans. For these specimens, the results of the F-S-SP Integration model are also compared to the predictions made by Hines (2002) using the simplified model developed based on the results of their testing program.

Figure 9.17 compares the load-displacement relationship predicted using the F-S-SP Integration method to the envelope measured in the test of barbell-shaped pier 3A and the response predicted using the model proposed by Hines *et al.* (2004). The F-S-SP Integration method predicted the stiffness at first yielding to be 60 percent larger than the measured value and the failure load to be 3 percent greater than the measured value. The F-S-SP Integration model indicated that failure due to crushing of the confined concrete would occur at a drift of 3.7 percent, while the specimen failed due to web crushing, which was not considered in the F-S-SP Integration model, at a drift of 3.5 percent. The model proposed by Hines *et al.* (2004) predicted the same failure load as the F-S-SP Integration model when web crushing failure was neglected. The most significant difference between the two models was that the model proposed by Hines *et al.* (2004) predicted that yielding would be spread over a larger portion of the pier, because it included effects of tension shifting. This caused a marked reduction in the post-yielding stiffness when compared to the measured pier response or the F-S-SP Integration method.

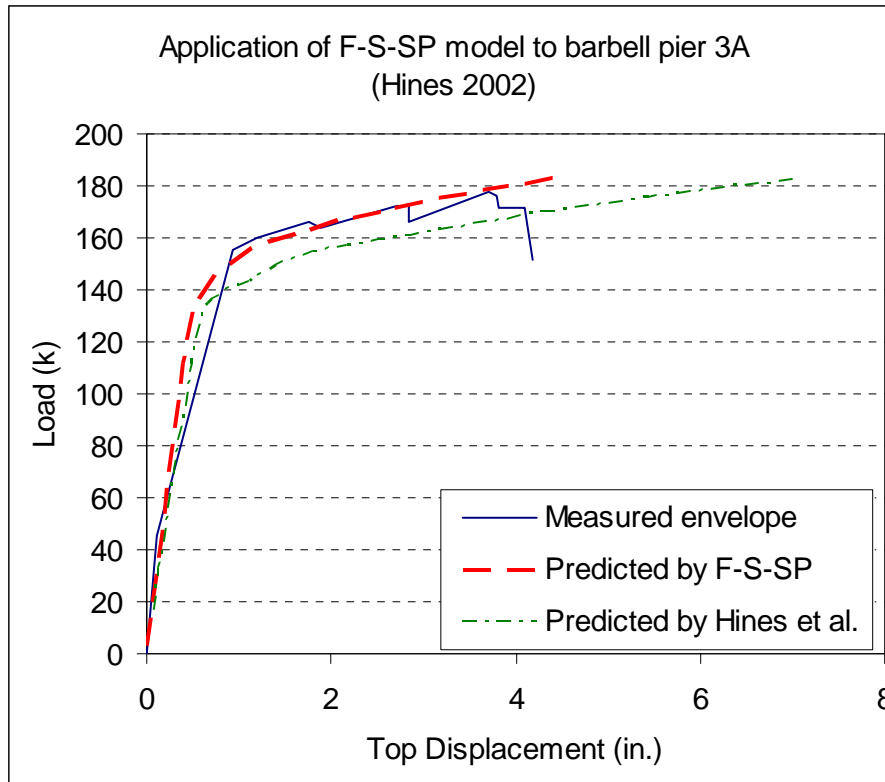


Figure 9.17. Application of F-S-SP Integration model to specimen 3A tested by Hines (2002)

Figure 9.18 compares the load-displacement relationship predicted using the F-S-SP Integration method to the envelope measured in the test of the hollow box pier LPT and the response predicted by the model proposed by Hines *et al.* (2004). The F-S-SP Integration method predicted the stiffness at first yielding to be 20 percent larger than the measured value and the failure load to be 7 percent smaller than the measured value. The F-S-SP Integration model indicated that failure due to fracture of the reinforcing steel should occur at a drift of 4.6 percent, while fracture of the steel was observed in the test at a drift of 6.0 percent. Hines (2002) reported several parameters describing the reinforcing steel properties, including yielding and ultimate stresses and the strain associated with initial strain hardening, but did not report the measured tensile strain

capacity of the reinforcing bars used in this specimen. A maximum strain of 0.10 was assumed for the moment-curvature analysis used with the F-S-SP Integration model. Increasing this maximum strain would lead to increases in the predicted displacement capacity. The model proposed by Hines *et al.* (2004) also predicted failure due to fracture of the reinforcing steel. Similar to the analyses of pier 3A, the model proposed by Hines *et al.* (2004) predicted a reduced post-yielding stiffness and very large displacement capacity when compared to either the measured results or the F-S-SP Integration method.

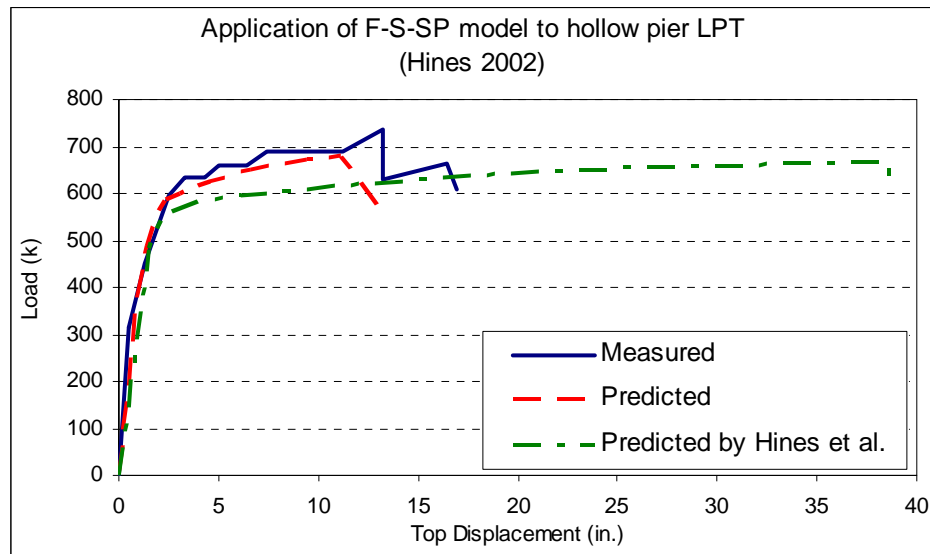


Figure 9.18. Application of F-S-SP Integration model to specimen LMS tested by Hines (2002)

### 9.3 Comparison to Other Simplified Models

This section compares the predicted responses of NTW1 and NTW2 in the flange-in-tension and flange-in-compression loading directions using the F-S-SP Integration model to the responses predicted by the simplified model recommended in FEMA 356 and the simplified model proposed by Hines *et al.* (2004). In all of these modeling efforts, measured material properties were used for both the concrete and steel. The

FEMA 356 model was applied to both NTW1 and NTW2. The Hines *et al.* model was applied only to NTW1 because the assumptions of this model precluded its use in determining displacements for any location on the height of the wall other than inflection points. Comparisons are not made for flange-direction loading because of the significant damage that was accumulated in the flanges prior to the majority of the flange-direction loading ramps. Because modification of the material properties was necessary to capture some of this damage, evaluating the relative accuracy of the models for this case is difficult.

### **9.3.1 FEMA 356 Model**

Figure 9.19 and Figure 9.20 compare the FEMA 356 model to the F-S-SP Integration model for predicting the web direction (flange-in-tension and flange-in-compression) load-displacement responses of NTW1 and NTW2, respectively. Actual, rather than nominal, material properties were used in both models. These figures include the prediction of loads and displacements associated with the immediate occupancy, life safety, and collapse prevention performance levels. Performance levels associated with the FEMA 356 model were predicted using the prescribed drift levels included in that model, and performance levels associated with the F-S-SP Integration model were predicted using the threshold strain values developed in Section 8.3.

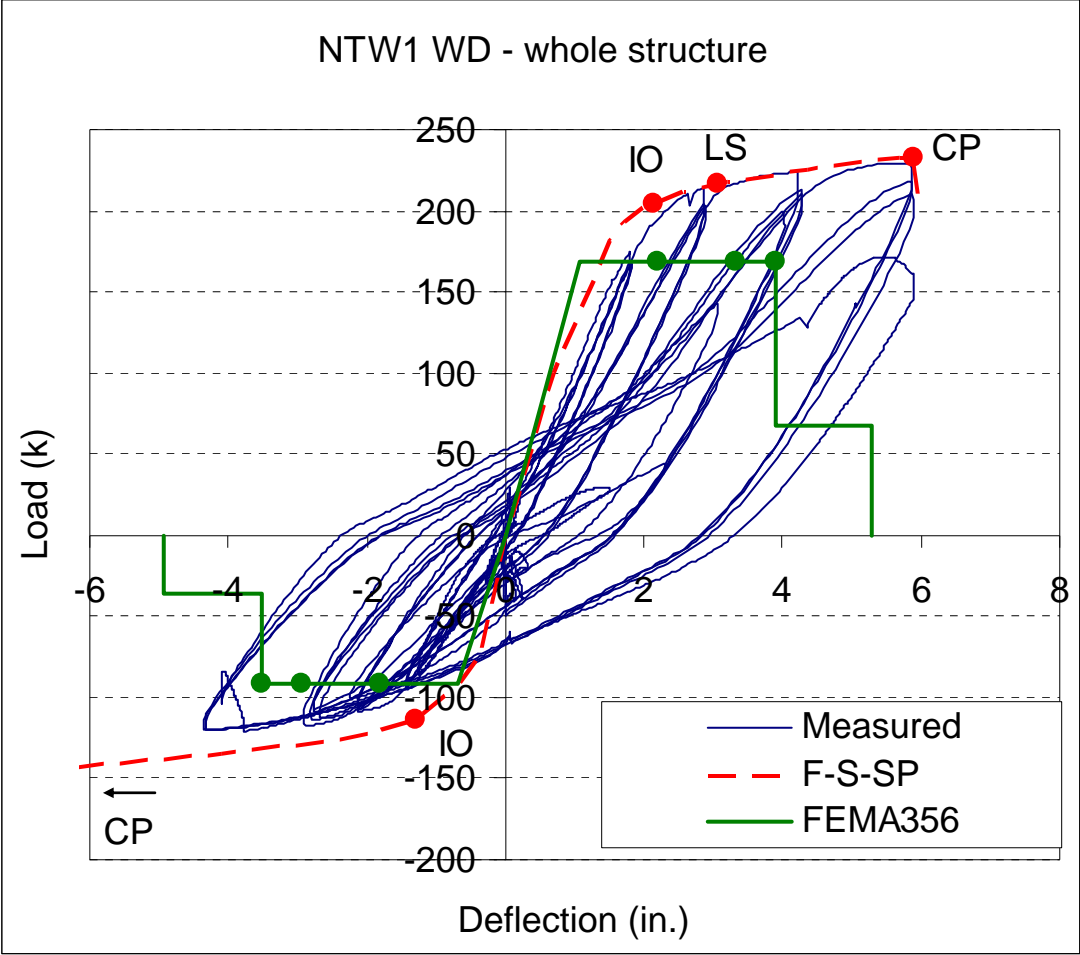


Figure 9.19. Comparison of F-S-SP Integration model and FEMA 356 simplified model: NTW1 web direction loading.

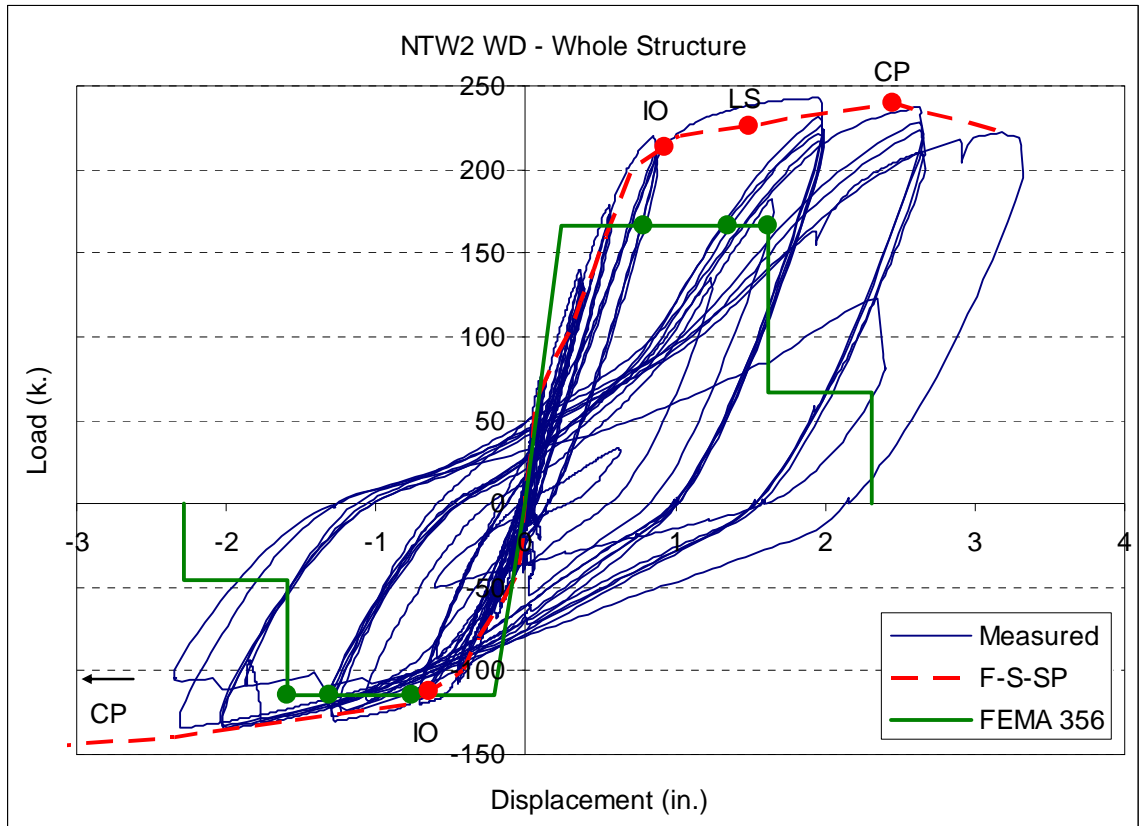


Figure 9.20. Comparison of F-S-SP Integration model and FEMA 356 simplified model: NTW2 web direction loading.

As expected, the FEMA 356 model predicted a higher stiffness at yielding than the measured values or the F-S-SP Integration model. The stiffnesses calculated using the simplifying assumptions in the FEMA 356 model were 85 percent to 125 percent greater than the measured values and 7 percent to 100 percent greater than the values calculated using the F-S-SP Integration method. This increased stiffness resulted because the FEMA 356 model includes only flexural deformations and neglects the contributions of shear and strain penetration. The stiffness calculated using the FEMA 356 model is not the same as the flexural component stiffness calculated for the F-S-SP Integration model, but is slightly less stiff, offsetting a portion of the effects of neglecting the

contributions of shear and strain penetration to the total deformation. The FEMA 356 model assumes a cracked section over the entire specimen height, while the sectional analysis underlying the F-S-SP Integration model considers the tensile strain in the concrete in determining whether or not the section is cracked at a given height.

Additionally, the FEMA 356 model assumes that the moment capacity of a wall is limited by the resistance at first yielding, so the predicted value is consistently less than the measured value or the value predicted by models that include post-yielding strength increases. For the four cases considered (NTW1 and NTW2 in each of the flange-in-tension and flange-in-compression loading directions), the measured load capacity was 25 percent to 27 percent greater than the predicted resistance at yielding.

The effect of a third simplification, assuming a constant plastic hinge rotation capacity regardless of wall geometry, is conservative in both loading directions. In the flange-in-tension loading direction, the FEMA 356 model predicted a drift capacity 37 percent less than the capacity measured or predicted using the F-S-SP Integration model. In the flange-in-compression direction, the actual drift capacity of the specimen was not found prior to buckling of the web-tip reinforcement. However, the drift capacity predicted by the FEMA 356 model was 10 percent less than the maximum value reached during the testing, and 70 percent less than the drift capacity predicted using the F-S-SP Integration method.

When the predictions of the performance levels are compared, the FEMA 356 model was very conservative with regard to predicting both the load capacity in both loading directions, primarily because it neglects increases in moment resistance after first

yielding. It was also conservative with regard to predicting many of the displacements associated with the various performance levels. In the flange-in-tension loading direction, the FEMA 356 model predicted displacements associated with immediate occupancy and life safety 10 to 15 percent smaller than the displacements determined with the F-S-SP Integration model, and it predicted displacements associated with collapse prevention up to 40 percent smaller than the those determined with the F-S-SP Integration model. In the flange-in-compression loading direction, the FEMA 356 model overestimated the drift associated with immediate occupancy by up to 30 percent. Additionally, the FEMA 356 model was unable to recognize the large ductility of the specimen in the flange-in-compression direction.

From this comparison, it is apparent that the F-S-SP Integration method addresses the difficulties of the simplified modeling procedure recommended by FEMA 356. In particular, the F-S-SP Integration model improves the prediction of the initial response through yielding, includes post-yielding increases in capacity in the model in order to avoid gross overdesign, and considers wall geometry and detailing in the prediction of significant damage levels, including the collapse-prevention drift capacity. All of these are significant for the increased adoption of performance-based engineering by designers.

### **9.3.2 Hines *et al.* (2004) model**

Figure 9.21 compares the model proposed by Hines *et al.* (2004) to the F-S-SP Integration model for predicting the load-displacement responses of NTW1. The application of this model to NTW2 is difficult because shear deformations are calculated only at inflection points. Because the same sectional analysis was used to determine the

moment-curvature response used in both models, the loads at first yielding and at failure are identical in the models. There is not a consistent relationship between the initial stiffness predicted by the Hines model and that predicted by the F-S-SP Integration model. In the flange-in-tension loading direction, the Hines model was 11 percent stiffer, while in the flange-in-compression loading direction, the Hines model was 12 percent less stiff. Three factors contributed to the differences in stiffness at first yielding: the Hines model assumes a fully cracked section for the flexural response, which consistently reduces the overall stiffness, different assumptions are made in determining the rotation due to strain penetration, and different assumptions are made in determining the deflection due to shear deformations. Details of the Hines model can be found in Section 2.3.4.

After yielding, the model proposed by Hines *et al.* (2004) predicted a decreased stiffness and an increased drift capacity. This was the result of the Hines model including the effects of tension shifting and the spread of plastic hinging over a larger region of the wall than is predicted using the F-S-SP Integration model. For the cases considered, the F-S-SP Integration model more closely matched the measured wall response. In the flange-in-tension loading direction, the F-S-SP Integration model predicted a drift capacity within 1 percent of the measured value, while the Hines model predicted a drift capacity 53 percent larger. In the flange-in-compression loading direction, the drift capacity was not reached in the testing, but the Hines model predicted a drift capacity of over 13 percent, which is three times that predicted by the F-S-SP Integration method. It

is unlikely that this drift level could be reached prior to collapse due to global instability (i.e., P- $\Delta$  effects).

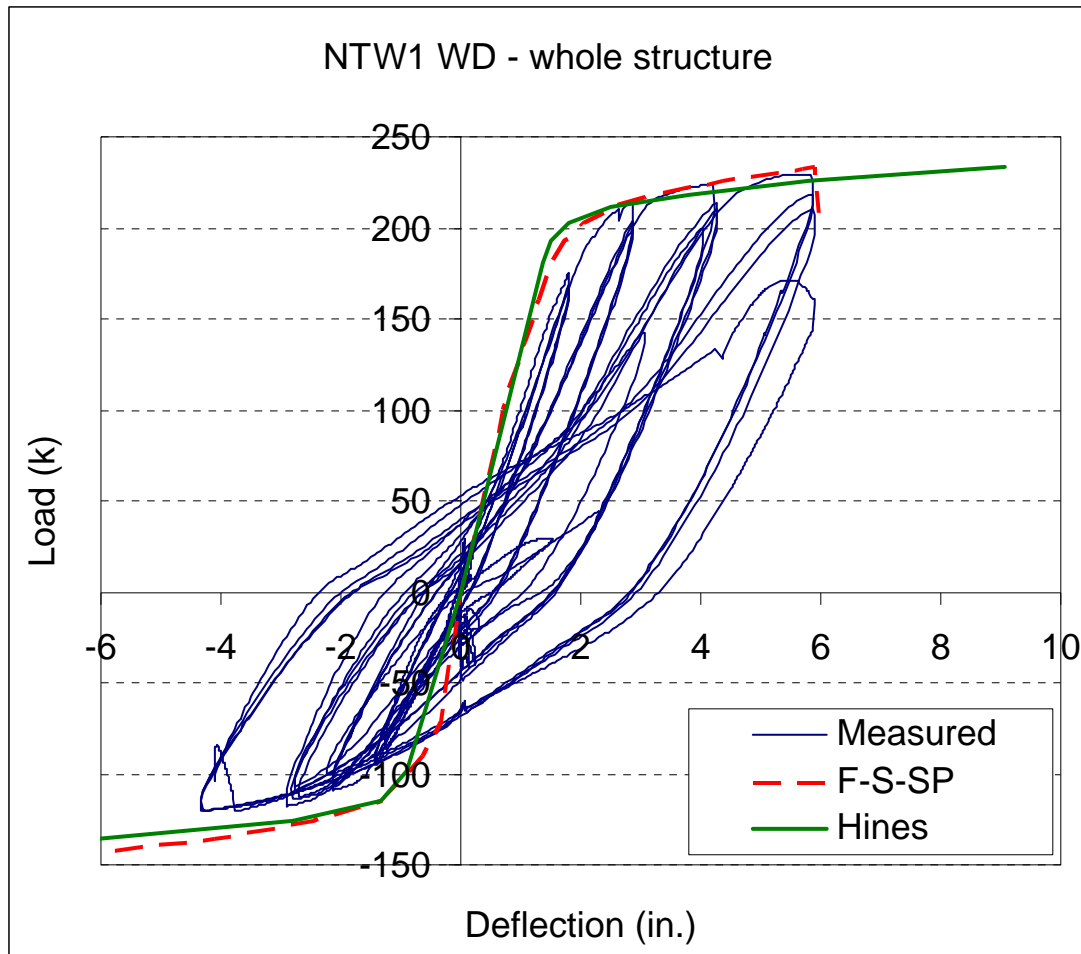


Figure 9.21. Comparison of F-S-SP model to Hines *et al.* (2004) model: NTW1

### Components of Deformation

Figure 9.22 through Figure 9.24 compare the components of deformation predicted using the F-S-SP Integration model and the Hines *et al.* (2004) model to the measured components. These figures show the sources of the differences between the models. It can be seen from these figures that the F-S-SP Integration model underpredicts the flexural deformation capacity in the flange-in-tension direction because

tension shifting is neglected, while the Hines model overpredicts the effects of tension shifting on the plastic hinge capacity. In the prediction of shear deformations, both models use an assumed diagonal crack angle of  $45^\circ$  and an empirical or semi-empirical approach. However, the Hines model predicts a much stiffer shear response than the F-S-SP Integration model, with predicted shear deformations one-third to one-half as large as the F-S-SP Integration model. The measured shear response fell between these two values.

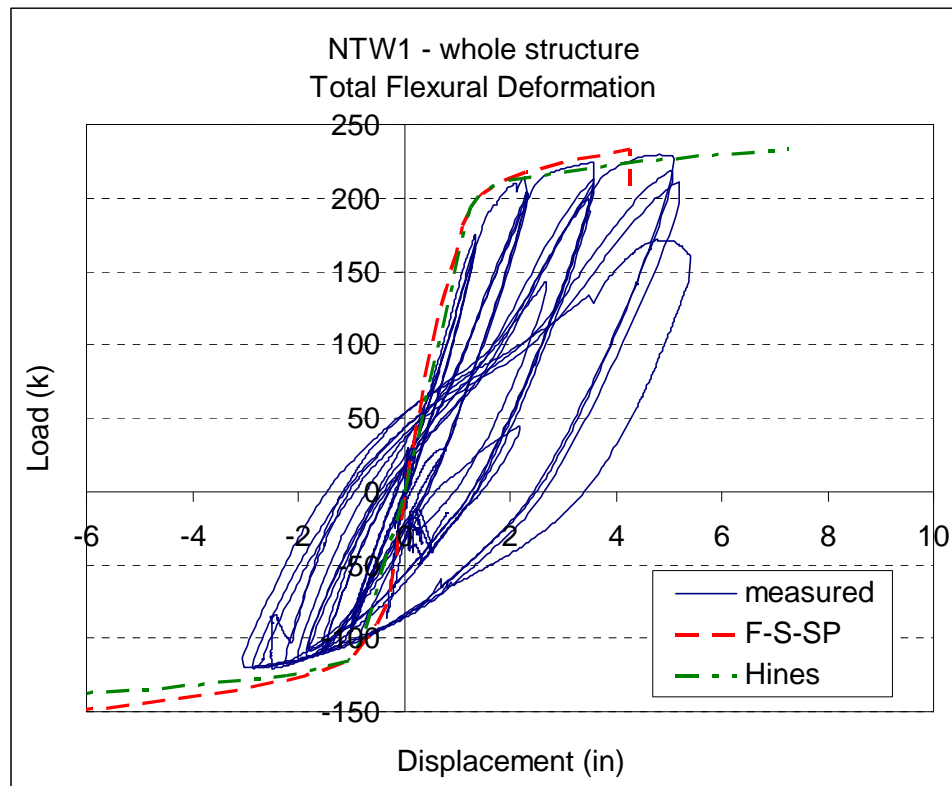


Figure 9.22. Comparison of F-S-SP model to Hines *et al.* (2004) model: NTW1 flexural deformation

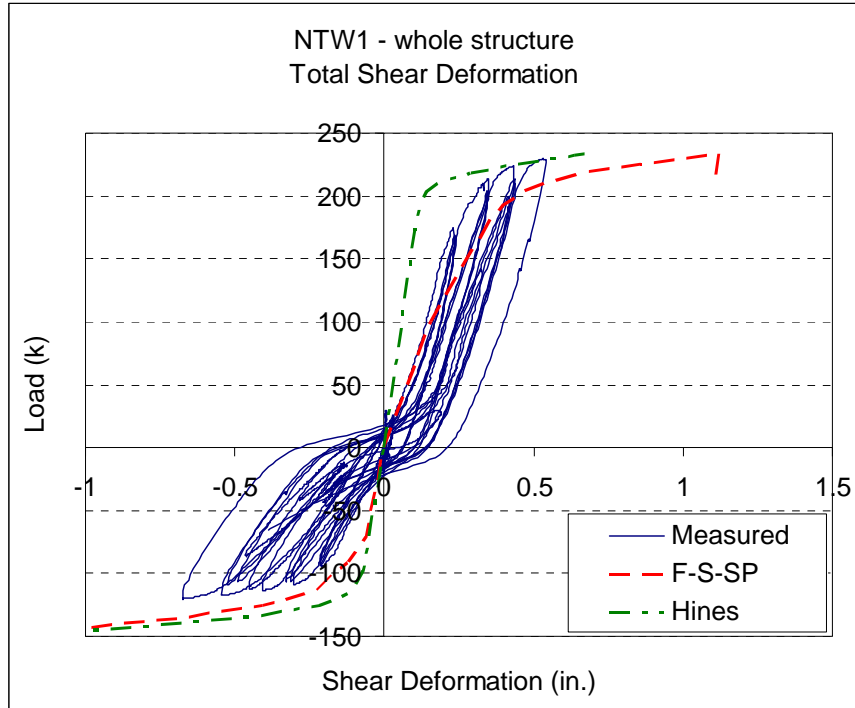


Figure 9.23. Comparison of F-S-SP model to Hines *et al.* (2004) model: NTW1 shear deformation

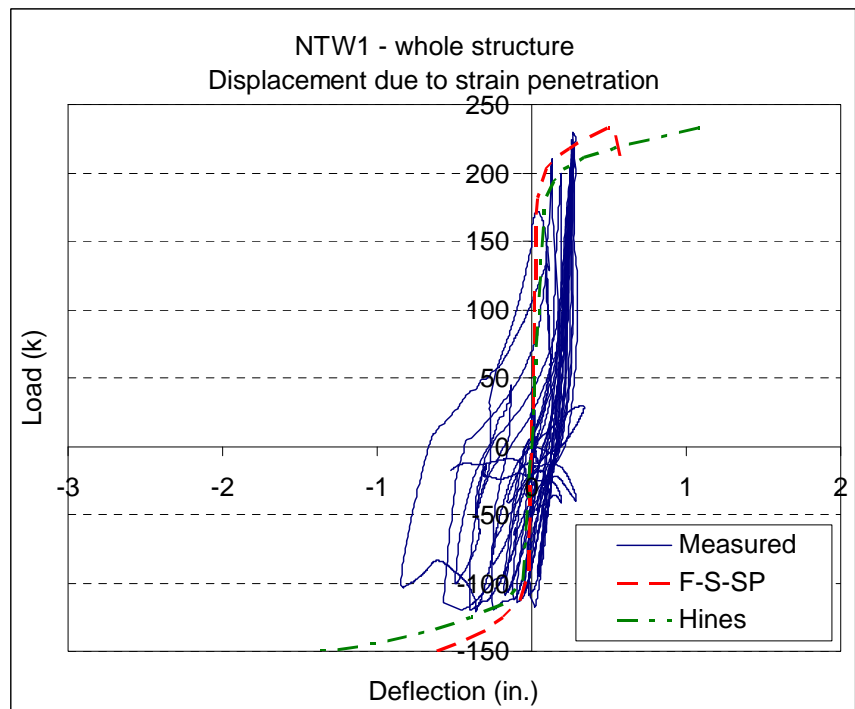


Figure 9.24. Comparison of F-S-SP model to Hines *et al.* (2004) model: NTW1 strain penetration

For the cases considered, the F-S-SP Integration model generally provided a better prediction of the measured wall response than the Hines model. However, the primary advantage of the F-S-SP Integration model over the Hines model is its ability to determine the wall response, including each component of deformation, at any location on the height of the wall. The ability to predict not only the deflection at the top of a wall but also the inter-story deformations increases the usefulness of the model for predicting the type and degree of damage that is associated with various demand levels.

### **9.3.3 Use of Nominal Material Properties and Effects of Material Property Variation on Model Results**

In the previous sections, measured material properties were used in the simplified model. However, these values are not known during the initial design of a structure. Nowak and Szerszen (2003) have used Monte Carlo analysis to establish the expected variation in the strength of reinforced concrete beams. They reported that the mean flexural strength of beams constructed with grade 60 reinforcement and normal strength concrete ( $f'_c \leq 6000$  psi) or high strength concrete ( $f'_c \geq 7000$  psi) was 1.190 or 1.160 times that calculated using nominal material properties, respectively, with coefficients of variation of 0.089 and 0.090.

To evaluate the effects of material property variations on the behavior of flexural structural walls, a rudimentary investigation of the effects of material property variations was conducted using the geometry of specimen NTW1 and the flange-in-tension/flange-in-compression loading directions. Mean values of material properties and the associated coefficients of variation were taken from Nowak and Szerszen (2003). A bilinear material model was assumed for the reinforcing steel, and the Modified Kent and Park

model was used to determine the properties of the confined concrete. A limited suite of 10 combinations of material properties was analyzed to estimate the effects of material properties on the predicted ultimate strength and curvature of the section. These combinations are summarized in Table 9.3. For the purpose of this investigation, it was assumed that the values of  $f'_c$  and  $kf'_c$  were perfectly correlated, and also that the values of  $f_y$  and  $f_u$  were perfectly correlated (Kappos, Chryssanthopoulos, and Dymiotis 1999). Additionally, only the effects of material strength were considered. Preliminary analysis indicated that the effects of material strain capacities (compressive strain associated with crushing of concrete and tensile strain associated with rupture of steel) on both moment and curvature capacity were an order of magnitude smaller than the effects of material strengths, so variations in the strain capacity of the steel and concrete were neglected for this limited study. Additionally, the effects of geometric variations in construction were neglected.

Table 9.3. Cases considered to estimate effects of material strength variations on analysis

Case	Steel Strength	Concrete Strength	$f'_c$ (psi)	$kf'_c$ (psi)	$f_y$ (ksi)	$f_u$ (ksi)
1)	Nominal	Nominal	5000	5720	60	90
2)	Mean	Mean	5750	6580	68.7	103
3)	Mean	Mean-1sd	5420	6200	68.7	103
4)	Mean	Mean+1sd	6080	6960	68.7	103
5)	Mean-1sd	Mean	5750	6580	65.3	97.9
6)	Mean+1sd	Mean	5750	6580	72.1	108.2
7)	Mean-1/ $\sqrt{2}$ sd	Mean-1/ $\sqrt{2}$ sd	5510	6310	66.3	99.4
8)	Mean+1/ $\sqrt{2}$ sd	Mean-1/ $\sqrt{2}$ sd	5510	6310	71.1	106.6
9)	Mean-1/ $\sqrt{2}$ sd	Mean+1/ $\sqrt{2}$ sd	5990	7250	66.3	99.4
10)	Mean+1/ $\sqrt{2}$ sd	Mean+1/ $\sqrt{2}$ sd	5990	7250	71.1	106.6
11)	Measured	Measured	7260	8310	62.0	92.0

sd = standard deviation

Figure 9.25 shows the moment versus curvature relationships calculated for specimen NTW1 using the measured, nominal, and mean material properties (Cases 1 and 2 in Table 9.3), as well as the envelope defined by Cases 3 through 10. This envelope was defined by the cases with the largest and smallest maximum moment capacities. Additionally, data points are included to indicate the maximum moment and the associated curvature for each of the cases, as well as the ultimate curvature capacity defined as the curvature associated with a decrease to 90 percent of the maximum moment capacity for each case. In the flange in compression direction, these points coincide because the moment capacity is predicted to immediately drop to less than 25 percent of the maximum immediately after the maximum is reached.

For this particular wall geometry and detailing, the mean strength values predicted yield and ultimate strengths between 12 and 13 percent larger than the values predicted with the nominal material properties, which is smaller than predicted by Nowak and Szerszen (2003) for beams. For all cases, failure was associated with crushing of the

concrete in compression. The curvature capacity predicted using the mean material properties varied in the range of 5 to 9 percent from that predicted using nominal material properties. Varying the material properties from the mean with Cases 3 through 10 caused the yield and ultimate strengths to vary 4 to 6 percent from the mean values. In the flange-in-compression loading direction, varying the material properties from the mean caused variations of up to 7 percent in the curvature capacity, but in the flange-in-tension loading direction, it caused much larger variations of up to 17 percent in the curvature capacity.

When the response calculated using the measured material properties is compared to the response calculated using the nominal properties, the moment capacity was 24 percent larger in the flange-in-tension loading direction and 4 percent larger in the flange-in-compression loading direction using the measured material properties. The curvature capacity was 77 percent larger in the flange-in-tension direction and 16 percent larger in the flange-in-compression loading direction.

The relatively large effect of material property variations on the curvature capacity in the flange-in-tension loading direction was the result of the wall geometry considered having a large area of steel in the flange and a relatively deep compression block when the flange was in tension. As shown in Figure 9.26, as the strength of the steel increases (or the strength of the concrete decreases), the compression block must become deeper to resist the larger tensile force. The maximum compressive strain of the confined concrete calculated using the Modified Kent and Park model remains approximately constant regardless of the variation in concrete compressive stress, so

increasing the neutral axis depth reduces the curvature at failure and the tensile strain when the concrete crushes. Conversely, as the strength of the steel decreases (or the strength of the concrete increases), the tensile strain and curvature associated with crushing of the concrete increase.

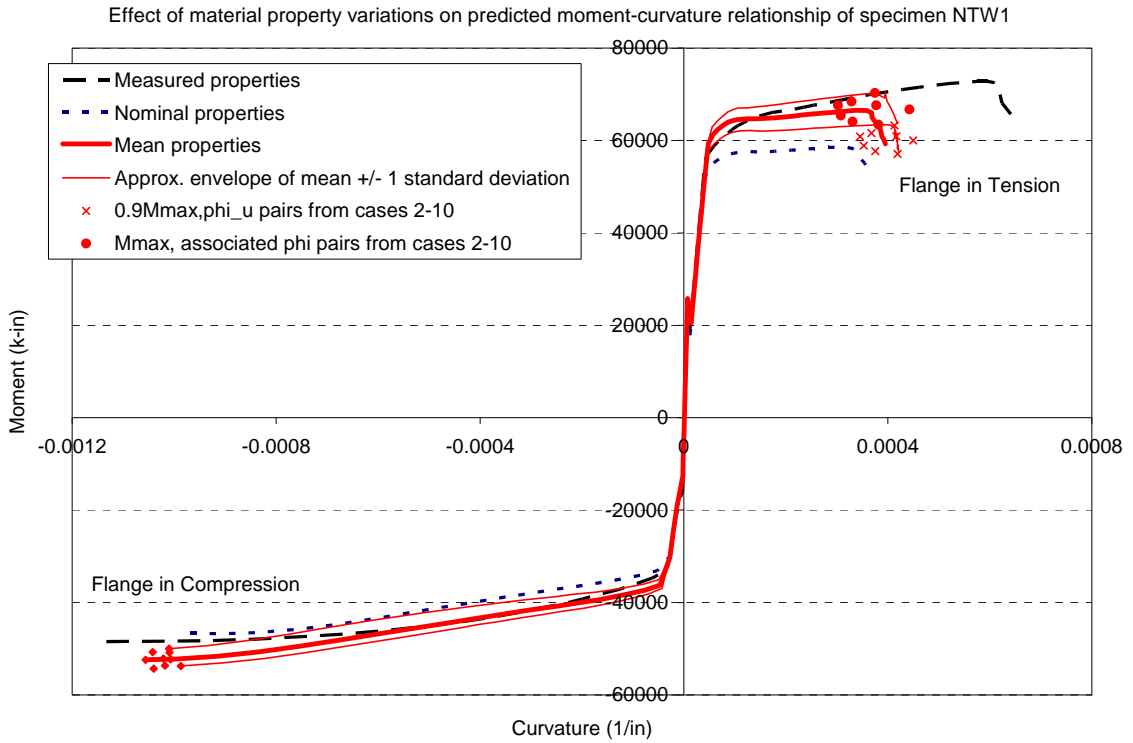


Figure 9.25. Predicted moment versus curvature relationships with varying material properties, NTW1 web direction.

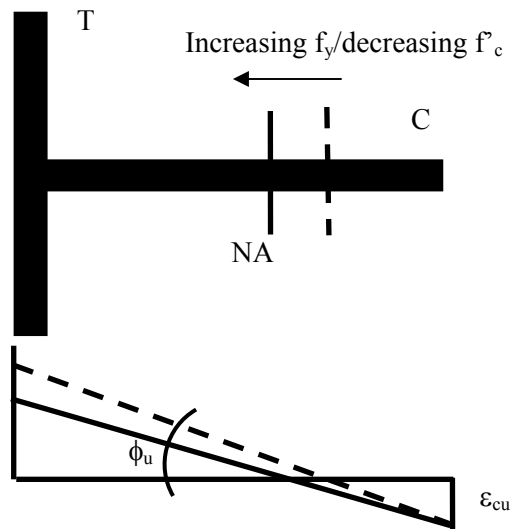


Figure 9.26. Effect of material strengths on curvature at failure.

Figure 9.27 compares the load-deflection response, including all components of deformation, of specimen NTW1 in the flange-in-tension and flange-in-compression loading directions predicted using the nominal material properties to the measured response and the response predicted using the measured material properties. As with the moment-curvature responses shown in Figure 9.25, the differences caused by the change in material properties were more substantial in the flange-in-tension loading direction than in the flange-in-compression loading direction.

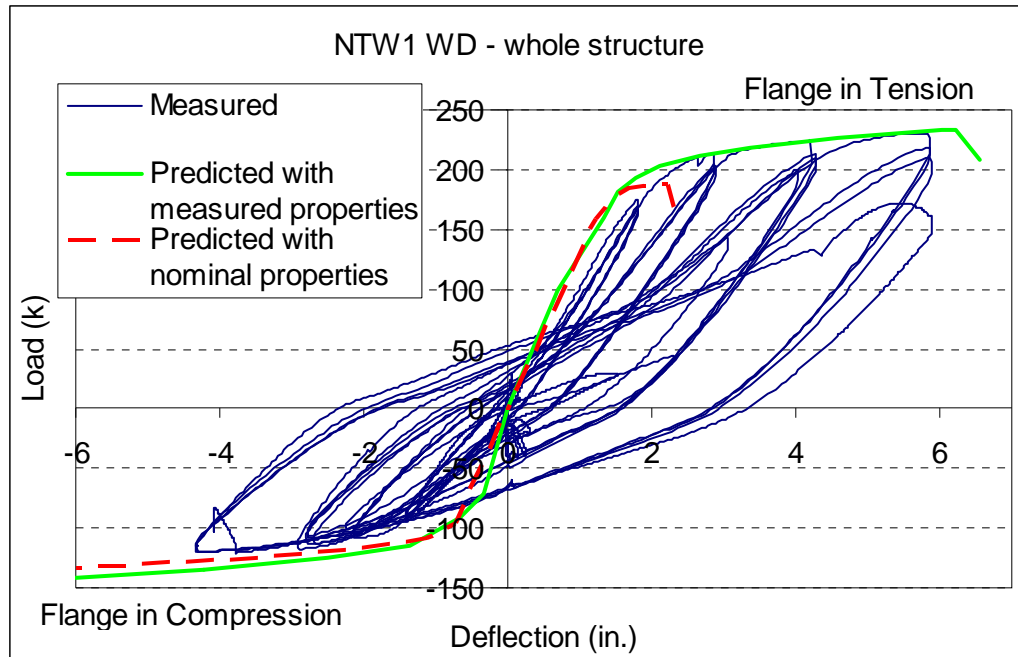


Figure 9.27. Comparison of measured web-direction response of Specimen NTW1 and response predicted using measured and nominal material properties.

## Chapter 10 Conclusions and Recommendations

### 10.1 Design and detailing of non-rectangular structural walls

#### 10.1.1 Applicability of current design provisions

In general, this research indicates that the design provisions in ACI 318-02 can be applied to nonrectangular walls as well as the rectangular walls for which they were originally developed without leading to poor performance in seismic events. Additional consideration beyond the code provisions should be given to ensuring that brittle failures are avoided, either as a result of an over-reinforced section with limited flexural ductility or insufficient shear capacity to ensure a flexural failure.

#### Confined Regions

In the testing of specimen NTW1, the failure in the flange-in-tension direction was the result of failure of the confining reinforcement, which led to crushing of the concrete core and buckling of the longitudinal reinforcing steel. The moment resisted by the section rapidly decreased as the applied displacement was increased further because the buckling of the reinforcement and crushing of the concrete rapidly progressed to involve the entire confined boundary element and then progressed into the unconfined portion of the web. The initial failure of the confining reinforcement appeared to be associated primarily with unwinding of the confining hoops near the base of the web tip, rather than fracture of the hoops. This premature failure was not expected, and similar cases have not been reported by other researchers. This effect may have been the result of scaling effects and the use of smaller bars (D5 wire) to make the confining hoops. There are two potential causes for this reduced performance: indentations, rather than

external lugs, serve as deformations in wire, potentially decreasing pullout resistance; and the ratio of flexural stiffness to axial capacity is decreased as diameter decreases because the moment of inertia ( $I$ ) is proportional to diameter to the fourth power ( $d_b^4$ ), while axial load capacity is proportional to diameter squared ( $d_b^2$ ).

Two modifications were made in the construction of specimen NTW2 in order to mitigate this failure mechanism and potentially increase the drift capacity of the specimen. First, care was taken to ensure that the open corner of the hoops (i.e., the corner with the 135° hooks) was not located around the extreme compression reinforcement, in order to reduce the demand placed on this apparently critical portion of the hoop. Second, the horizontal dimension of the confined region was extended an additional 3 ½ in. beyond the value required by the displacement-based method recommended in ACI 318-02.

In specimen NTW1, a moment resistance of at least 90 percent of the measured maximum resistance was maintained through a measured drift of 2.0 percent. The F-S-SP Integration model proposed in Chapter 8 predicted that this specimen would retain at least 90 percent of its maximum moment capacity up to a drift of 2.2 percent. This overprediction of the drift capacity was attributed to the observed premature failure of the confining hoops discussed previously. In specimen NTW2, a moment resistance of at least 90 percent of the measured maximum was maintained through a measured drift of 2.4 percent. The model proposed in Chapter 8 predicted that this specimen would retain at least 90 percent of its maximum moment capacity up to a drift of 2.3 percent. All of these drifts were measured at the top of the second story of each specimen.

The first modification, orienting the confining hoops to minimize demand on the hooks, was successful: the confining reinforcement failed by fracture rather than unwinding and disengaging from the concrete core. Taking care to orient confining hoops with the hooks located away from the extreme compression fiber is recommended as good practice, particularly for researchers constructing reduced-scale test specimens, but this single observation does not warrant an additional provision in specifications such as ACI 318. Based on the similarity of the observed drift capacities as well as the observed progression of failure into the unconfined portion of the web after the initial observation of crushing of the confined core and buckling of the extreme compression reinforcement, increasing the horizontal dimension of the confined region had little effect on the performance of the specimen. This is not unexpected, because this modification does not prevent the initiation of the failure in the extreme compression fiber of the concrete or reinforcing steel. Similar observations of the inevitability of web crushing failures following closely after crushing of the confined region have been reported by other researchers (Oesterle *et al.* 1979, Wallace and Moehle 1992, Thomsen and Wallace 2004).

It is possible that decreasing the confining hoop spacing to meet all requirements of ACI 318-02 may have increased the drift capacity of the specimen by increasing the strain capacity of the confined concrete core somewhat and by providing increased resistance to buckling of the longitudinal reinforcement. However, constructability issues associated with very closely spaced hoops introduce additional difficulties, such as increased likelihood of poor consolidation of concrete.

The design drift level of 2 percent was reached or exceeded in all orthogonal loading directions in both specimens prior to the observed failures. As a result, the tests described herein of NTW1 and NTW2 provide additional confirmation that the displacement-based recommendations introduced into ACI 318-02, which often lead to reduced confinement regions when compared with the previous stress-based requirements, are appropriate for design to reach a desired drift level. However, designers should be aware that flanged walls, particularly those with a single flange, may have a reduced displacement capacity when compared to rectangular walls or walls with symmetric flanges, and may not meet the requirements for tension-controlled sections, as observed in TW1 and TW2 tested by Thomsen and Wallace (1995). This is the result of having a relatively large area of reinforcement in the flange combined with a narrow compression region, requiring a deep neutral axis. It should be noted that when the tensile reinforcement strain at failure is limited, the inclusion of a confined region detailed according to the provisions of ACI 318-02 may not ensure that the desired drift capacity is achieved. At a minimum, designers should take care to check that walls satisfy the requirements for tension-controlled sections and consider alternate geometries if these requirements are not met.

These tests also indicate that the trapezoidal shape of the compression block resulting from skew-direction loading does not cause significantly greater maximum compression strains than orthogonal loading to the same drift level, nor does it lead to large compression strains in the unconfined portion of the wall that would lead to premature web failure. Basing the dimensions of the confined region on the desired

orthogonal-direction drift capacities is appropriate, and more involved analysis is not warranted.

Additionally, no distress was observed at the intersection between the web and flange elements, indicating that the addition of special confinement reinforcement to ensure shear flow through the joint is not necessary. Because of the large shear demand in this region, it is recommended that the requirement that shear reinforcement be sufficiently anchored, for instance by standard hooked bars engaged around longitudinal reinforcement, not be relaxed.

### Shear Reinforcement

In both of the specimens tested in this research, care was taken to ensure that the shear capacity of the wall was sufficient to avoid shear failure preceding flexural failure in order to ensure ductile behavior. This was accomplished by adopting the ACI 318-02 provisions for determining the probable moment capacity  $M_{pr}$  of beams in the design of beam-column connections, as recommended by SEAOC (1999). This special consideration is particularly important when the provided moment resistance is significantly larger than the required resistance, which is more likely to occur in flanged walls, where designers must ensure that minimum moment capacities are achieved in multiple loading directions, than in rectangular walls, where the design can be easily optimized for a single loading direction. Using this method (i.e., increasing the yield strength of the steel by 25 percent and using the Whitney stress block with a maximum concrete strain of 0.003) to determine the provided moment capacity was sufficient to avoid brittle failure.

In both of these tests, diagonal shear cracks in the web were wider than the flexural cracks in the boundary element and shear sliding was observed across horizontal cracks. Sliding was limited to the lightly-reinforced regions in the webs of both specimens and the flange of specimen NTW1 and was arrested by the confined boundary elements. Shear sliding was not observed in the flange of specimen NTW2, which had reinforcing steel uniformly distributed over its entire width.

When performance-based engineering is applied, designers should consider decreasing the spacing between longitudinal as well as horizontal bars in lightly-reinforced web regions in order to limit crack widths so that diagonal shear cracks are not wider than horizontal flexural cracks, requiring repair at lower drift levels. Based on the results of this research as well as the modeling done by Sittipunt and Wood (1995), the benefits of decreasing the spacing between the bars or increasing the area of shear reinforcement beyond that required to ensure a flexurally-controlled wall appear to be limited to serviceability and minimizing crack widths. As a result, a significant associated increase in the energy dissipation capacity of a wall is unlikely. However, this expectation is based on limited research, and may be revised as a result of additional work.

#### **10.1.2 Shear Lag Effects**

Additional research is needed to more fully understand and predict shear lag effects in flanged walls. This information becomes more critical as the industry adopts performance-based engineering and the importance of predicting the response of a wall to small- and moderate-level seismic events is of interest. This is particularly important for

predicting damage to nonstructural elements of a building, such as mechanical systems and architectural finishes, at low demand levels. This research demonstrates that even when a flange is expected to be fully effective at large displacement levels, shear lag does affect the pre-yielding stiffness of the wall and its response at small ductility levels. This is because the extreme bars in a flange may be engaged enough to yield at large drift levels, but the strains in these bars may be much less than that of the bars near the center of the flange. In the specimens tested, strains in the bars in the flange tips were measured to be approximately one-half the strains in the bars near the center of the flange. As a result, shear lag effects were pronounced at smaller drift levels, but may be mitigated or eliminated as the applied drift level increases and all of the bars yield in the plastic hinge region. Shear lag effects likely do remain in the portion of the wall outside the plastic hinge region, but their effects on the total wall deformation are limited because plastic hinging dominates the response.

While shear lag effects were measurable in both specimens at small and moderate drift levels (<1 percent drift to the top of the second story), the distribution of the longitudinal reinforcement had a significant effect on the magnitude of the shear lag effects. Prior to yielding, shear lag effects were up to 60 percent larger in specimen NTW1 with reinforcement concentrated in the flange tips than in specimen NTW2 with reinforcement uniformly distributed over the flange width. In specimen NTW1, shear lag in the flange caused a deviation of 35 percent between the measured and expected moment resistance for a given steel strain, while in specimen NTW2 this deviation was only 20 percent. Two mechanisms contributed to this: in specimen NTW1, a larger

proportion of the longitudinal reinforcement was located near the flange tips where the strain was reduced, and the reduced longitudinal reinforcement in the center of the flange led to a larger strain gradient across the flange width, further reducing the strain in the flange tips.

More sophisticated handling of shear lag effects than the current effective flange width determination in ACI 318 may be appropriate in some cases, especially where accurate understanding of response at low ductility levels is desired for the determination of nonstructural damage. This may include using dual requirements for assuming fully effective flanges depending on the drift or ductility level under consideration. In this scenario, a more restrictive limitation could be placed on the effective flange width at first yielding and low ductility levels, reducing the initial stiffness, to account for the more significant shear lag effects, and at larger drifts through the ultimate capacity, the existing ACI 318 requirements could be used for determining the effective flange width. Additionally, a refined handling of shear lag effects may include a distinction based on the amount of reinforcement in the center of the flange, with an increased effective flange width associated with uniform distribution of reinforcement in the flange relative to concentration of reinforcement in the boundary elements and minimum reinforcement in the center of the flange.

### **10.1.3 Distribution of Longitudinal Reinforcement**

In addition, to the effects on shear lag, discussed above, modifying the distribution of longitudinal reinforcement within a wall element has additional effects on the behavior of the wall. First, concentration of reinforcement in the boundary elements

leads to fewer, but wider, cracks in the lightly reinforced portion, as opposed to more, but narrower, cracks. This was discussed briefly above with regards to shear deformations and damage. As a result, the critical drift level that can be sustained before cracks must be repaired is increased when reinforcement is distributed uniformly over an entire element. By potentially reducing the downtime and repair expenses after a small or moderate level seismic event, uniformly distributing reinforcement can reduce the long-term costs incurred by a building owner.

The primary benefit of concentrating longitudinal reinforcement in the confined boundary elements is that it leads to modest increases in both the in-plane load and displacement capacities of the element, which is expected because it increases the moment arm between the resultant tensile and compressive forces in the wall element (Park and Paulay 1975). These benefits were observed in the comparison of the flange direction response of the two specimens tested. Specimen NTW1, with reinforcement concentrated in the boundary elements had a load capacity 15 percent greater and a drift capacity measured at the top of the second story 14 percent greater than specimen NTW2, with reinforcement uniformly distributed across the flange width. It should be noted that there were additional differences in the reinforcement of the two flanges besides the distribution. Specimen NTW1 had slightly more total flange reinforcement than specimen NTW2 and that the yield stress of the reinforcement in specimen NTW1 was less than that of specimen NTW2.

In the prototype building geometry considered in this study, it was found that even modestly increasing the flange direction load capacity would have a substantial

effect on the potential building response because it maximized the flange direction load resistance without increasing the web direction flexural overstrength or requiring the addition of supplementary rectangular walls. The increase in drift capacity is less significant to designers, because both specimens had a drift capacity that significantly exceeded the design drift of 2 percent. In cases such as this, where uniformly distributing the flange reinforcement has undesirable consequences, it may be beneficial to concentrate the reinforcement in the boundary elements, in order to maximize the moment capacity, and to use smaller reinforcing bars in the region between the boundary elements, with the spacing of the bars constant over the flange width. Additional study is required to confirm the effectiveness of this approach, but it is likely to minimize crack widths while also minimizing flexural overstrength in the perpendicular direction.

#### **10.1.4 Location of Lap Splices at the Base of the Second Story**

In specimen NTW2, lap splices with lap lengths meeting the requirements of ACI 318-02 were located with the lap beginning at the top of the first floor slab and laps contained within the second story of the wall. This location was chosen because it was outside the plastic hinge length predicted by existing empirical relationships and for ease of construction. The lap splice was observed to interrupt the yielding over the vertical height of the wall. In specimen NTW1, with continuous reinforcement over the entire height of the specimen, yielding extended over an area approximately twice as large as the predicted plastic hinge length. In specimen NTW2 with lap splices, yielding was interrupted by the lap splice, with yielding measured immediately above and below the lap region, but not within the lap region itself. Unlike the rectangular wall specimen

tested by Johnson (2007) with a lap splice located at the wall-to-foundation interface, there was no evidence of the lapped bars slipping or causing localized damage concentration in this specimen. Interrupting the plastic hinge did have a very small effect on the deformed shape of the specimen, but did not lead to decreased displacement or rotation capacity of the plastic hinge region or premature failure of the specimen.

Based on the results of these tests, the recommendation by SEAOC (1999) to avoid lap splices in expected plastic hinge regions is reiterated. However, using any of the existing empirical expressions to estimate the plastic hinge length (i.e., Paulay and Priestley 1992) is acceptable for the purposes of determining an acceptable location for a lap splice; increasing the plastic hinge length so that all yielding near the splice location is avoided is not necessary based on the results of testing NTW2. Based on the rectangular wall study completed by Johnson (2007), when it is necessary to locate a splice within an expected plastic hinge region, the use of mechanical couplers meeting the requirements of ACI 318-02 is recommended to avoid premature failure and reduced energy dissipation capacity.

## **10.2 Simplified Modeling of Reinforced Concrete Structural Walls**

The F-S-SP Integration model was developed in order to provide engineers with a model that is applicable to any flexurally-controlled wall section, regardless of its shape, dimensions, proportions, or detailing. It can be applied to walls with general lateral load distributions and is capable of determining displacements at any location on the height of the wall. The computational resources required for the use of the model are a sectional analysis program, such as BIAX (Wallace 1992), and a spreadsheet. The model was

validated against the results of eight wall and pier tests with a variety of geometry and detailing, and the results of the model were compared to two existing simplified modeling procedures, the procedure described in FEMA 356 (2000) and the procedure described by Hines *et al.* (2004).

The F-S-SP Integration model is based on a flexural section analysis. This analysis assumes that plane sections remain plane, neglecting deep beam action and shear lag effects, but is otherwise mechanics-based and can be reasonably expected to apply to any flexurally-controlled wall. Each of the three components of wall deformation (flexure, shear, and strain penetration) is calculated separately in the F-S-SP Integration model, although information from the flexural section analysis is used in the determination of each component. Flexural deformations are determined by numerical integration of the moment-curvature relationship over the height of the wall. Shear deformations are determined using an empirically-based method to predict shear deformations and the interaction between shear deformations and flexural damage. Deformations due to strain penetration are determined from a simplified mechanics-based model that was adapted in order to minimize computational effort.

The primary contribution of error in the flexural portion of the F-S-SP Integration model is the neglect of tension shifting effects, which is not uncommon in wall modeling procedures (i.e., Waugh *et al.* 2009). This leads to a reduced prediction of plastic hinge length and plastic hinge rotation, which leads to an underprediction of displacements post-yielding. For most purposes, this underprediction is conservative, because the initial stiffness is not affected, only the post-yielding response. One potential method for

incorporating tension shifting into the F-S-SP Integration model is the assumption of some minimum plastic hinge length and modification of the moment diagram as needed to ensure that the modeled wall has this hinge length. However, this approach will introduce significant assumptions based on empirical evidence, which may not be appropriate for all wall geometries.

The F-S-SP Integration model assumes that the shear deformation mechanism includes diagonal cracks that form at  $45^\circ$  angles, which does not fully capture the shear deformations. Additional factors to consider for refinement of the shear portion of the model include the neutral axis location and maximum or average longitudinal tensile strains and their effects on the angle of the diagonal cracks.

The strain penetration model incorporated is mechanics-based, but significant simplifying assumptions are made to decrease the modeling time and effort. This very simplified model gives reasonable results, but existing models with fewer simplifying assumptions exist and can be incorporated to refine this portion of the model if desired.

For performance-based engineering, correlations are made between the significant performance levels (i.e., immediate occupancy, life safety, and collapse prevention), types and degrees of damage, and strains in the steel and concrete. Local engineering demand parameters (EDPs) of strains, rather than global EDPs such as drift were selected because they are likely to be less sensitive to wall geometry. These threshold strain values were determined by correlating observed cracking and crushing of concrete during the testing to measured strains and provide guidance for designers in predicting the displacements associated with each performance level. It is expected that these values

will be revised as additional data is collected from tests of walls with a variety of geometries. In particular, because the threshold values are based on one-half scale models, there may be some scaling effects related to increased clear cover and bar spacing dimensions in full-scale structures.

### **10.2.1 Validation of Model**

The F-S-SP Integration model was validated using the results of test specimens NTW1 and NTW2 as well as six other wall and pier tests reported in the literature. Many of the reported tests were of asymmetric specimens, so sixteen distinct loading directions were used for this validation. All of the validations were done using the reported, actual material properties.

In general, the F-S-SP Integration model gave good predictions of the behavior of each specimen considered. With one exception, the predicted load capacity was within 7 percent of the reported measured value. The F-S-SP Integration model failed to predict the splice failure in rectangular wall RWS tested by Johnson (2007); this error was expected because the F-S-SP Integration model assumes that any lap splices are located away from plastic hinge regions and relative slip of the lapped bars is negligible. In most cases where failure was not precipitated by prior buckling of reinforcement, the displacement capacity predicted by the F-S-SP Integration model was 10 to 20 percent smaller than the reported values. This was expected because the F-S-SP Integration model neglects tension shifting effects, reducing the plastic hinge rotation capacity. Exceptions to this are NTW1 in the flange-in-tension loading direction, where a premature confinement failure was observed, and two cases (Thomsen and Wallace,

1994, and Sittipunt and Wood 1993) where the predicted displacement capacity was less than half the reported value. It is unclear why the displacement was grossly underpredicted in these cases.

One shortcoming of the F-S-SP Integration model is that it does not account for damage that may be accumulated in a multi-directional loading history. When compared to the more sophisticated fiber-based model developed by Waugh *et al.* (2009), it can be seen that the F-S-SP Integration model predicts monotonic pushover curves very well, but that it is unable to account for damage accumulated from loading in directions other than the one being considered. This limitation leads to an overprediction of specimen stiffness when the specimen has been damaged previously. This difficulty can be mitigated by modifying the reinforcing steel material properties to account for previous yielding, but it cannot be eliminated entirely.

### **10.2.2 Comparison to Other Simplified Models**

The F-S-SP Integration model was compared to two existing simplified models intended for use with walls or bridge piers and found to have advantages over both. The FEMA 356 model uses a limited number of parameters and does not account for the contributions of shear and strain penetration to the total deformations. One consequence of the great simplicity of this model is that it tends to be highly conservative, particularly with regard to load capacity. The F-S-SP Integration model is more accurate than the FEMA 356 model because it considers all components of deformation and because it makes fewer simplifying assumptions. The F-S-SP Integration model does take more time to apply than the FEMA 356 model, but the time required for using the F-S-SP

Integration model is reasonable for use in typical engineering practice and the F-S-SP Integration model provides increased accuracy in return for this effort.

The model proposed by Hines *et al.* (2004) for bridge piers is more sophisticated than the FEMA 356 model and includes terms representing all three components of deformation. The Hines *et al.* (2004) model and the F-S-SP Integration model require similar time and computational resources for application. However, the Hines *et al.* (2004) model is limited to use with walls or piers with a single point load and can describe the load-displacement response only at the top of the wall. These limitations are not restrictive when bridge piers are considered, but they cause some difficulties with walls, which are assumed to have the total lateral load distributed among several floors. The Hines *et al.* model includes the calculation of an extended plastic hinge region based on an approximation of the effects of tension shifting. However, the application of this model to wall and pier specimens indicated that it often overestimates the plastic hinge length, leading to unconservative predictions of displacement capacity. The provisions to limit the response based on web crushing address a particular failure mode and should not be relied upon to address this difficulty. As a result, the F-S-SP Integration model was found to predict the displacement capacity more accurately for the limited number of cases that were modeled with both approaches.

### **10.3 Recommendations for Further Research**

This research was limited to testing only two T-shaped wall specimens. While it addressed many issues with regard to the design and detailing of nonrectangular walls, additional research is recommended to increase the understanding of these structural

elements. Some of this research will require the testing of large scale specimens to failure, while other portions of it may be addressed through numerical studies.

In particular, testing of nonrectangular walls with different proportions is recommended. The specimens tested in this study were intentionally designed with proportions similar to those tested by Thomsen and Wallace (1995). In particular, study of walls with varying flange widths will increase the understanding of shear lag effects and allow for improved prediction of wall responses at all drift levels. Additionally, testing of nonrectangular walls of varying proportions to failure in non-orthogonal directions is needed to confirm that the capacities of walls in these directions are calculated correctly with existing tools. Finally, the consideration of additional axial loads and shear-to-moment ratios is useful in investigating the effects of building height on boundary element demands and flexure-shear interaction.

The availability of facilities such as the MAST laboratory at the University of Minnesota is especially useful for this because it allows for the consistent application of any axial load and any desired shear-to-moment ratio to a subassembly, eliminating the need to construct a very tall specimen in order to provide a large shear span. The results of all of these suggested tests, as well as additional analysis of existing wall test results, can be used to verify and refine the threshold engineering demand parameter (EDP) values proposed herein for the correlation between measured and predicted strain values to important damage levels for performance-based engineering.

## Chapter 11 References

- ACI Committee 318, 2002. *Building Code Requirements for Structural Concrete (ACI 318-02)*, American Concrete Institute, Farmington Hills, MI.
- ACI Committee 318, 2008. *Building Code Requirements for Structural Concrete (ACI 318-08)*, American Concrete Institute, Farmington Hills, MI.
- ACI Committee 408, 1992, reapproved 2005. *Bond Under Cyclic Loads (ACI 408.2R-92)*, American Concrete Institute, Farmington Hills, MI.
- ACI Committee 503, 2007. *Specification for Crack Repair by Epoxy Injection (ACI 503.7-07)*, American Concrete Institute, Farmington Hills, MI.
- Applied Technology Council, 1996. *Seismic Evaluation and Retrofit of Concrete Buildings*, ATC-40, Report No. SSC 96-01, Seismic Safety Commission, Redwood City, CA.
- Applied Technology Council, 2004. "Engineering Demand Parameters for Structural Framing Systems," *ATC-58 Project Task Report, Phase 2, Task 2.2*, Redwood City, CA.
- Belarbi, H., and Hsu, T.C.C., 1994. "Constitutive Laws of Concrete in Tension and Reinforcing Bars Stiffened by Concrete," *ACI Structural Journal* 91 (4), pp. 465-474.
- Berry, M.P., Lehman, D.E., and Lowes, L.N., 2008. "Lumped-Plasticity Models for Performance Simulation of Bridge Columns," *ACI Structural Journal* 105 (3), pp. 270-279.
- Brueggen, B.L., French, C.W., Jung, N., and Nakaki, S.D., 2006. "Non-rectangular Reinforced Concrete Shear Walls: Design Issues and Performance," *Proceedings, 100<sup>th</sup> Anniversary Earthquake Conference*, EERI, Oakland, CA.
- Chang, G.A., and Mander, J.B., 1994. "Seismic Energy Based Fatigue Damage Analysis of Bridge Columns: Part 1 – Evaluation of Seismic Capacity," NCEER Technical Report No. NCCR-94-0006, State University of New York, Buffalo, NY.
- Collins, M.P., and Mitchell, D., 1991. *Prestressed Concrete Structures*, Prentice Hall, Englewood Cliffs, NJ.
- Eligehausen, R., Popov, E.P., and Bertero, V.V., 1983. *Local Bond Stress-Slip Relationships of Deformed Bars under Generalized Excitations*, Report. No. UCB/EERC-83/23 EERC, Univ. of California, Berkeley, CA, 162 pp.
- Federal Emergency Management Agency, 2000. *Prestandard and Commentary for the Seismic Rehabilitation of Buildings (FEMA 356)*, Federal Emergency Management Agency, Washington, DC.
- Federal Emergency Management Agency, 1997. *NEHRP Guidelines for the Seismic Rehabilitation of Buildings (FEMA 273)*, Federal Emergency Management Agency, Washington, DC.
- Federal Emergency Management Agency, 1997. *NEHRP Commentary on the Guidelines for the Seismic Rehabilitation of Buildings (FEMA 274)*, Federal Emergency Management Agency, Washington, DC.
- Federal Emergency Management Agency, 2003. *NEHRP Recommended Provisions for*

- Seismic Regulations for New Buildings and Other Structures (FEMA 450)*, Federal Emergency Management Agency, Washington, DC.
- Field, E.H., *et al.*, 2005. "Loss Estimates for a Puente Hills Blind-Thrust Earthquake in Los Angeles, California," *Earthquake Spectra* 21 (2), pp. 329-338.
- Hassan, M., and El-Tawil, S., 2003. "Tension Flange Effective Width in Reinforced Concrete Structural walls," *ACI Structural Journal* 100 (3), pp. 349-356.
- Hewlett, P.C., ed., 1998. *Lea's Chemistry of Cement and Concrete*, John Wiley and Sons, New York.
- Hines, E.M., 2002. "Seismic Performance of Hollow Rectangular Concrete Bridge Piers with Confined Corner Elements," Ph.D. Thesis, University of California, San Diego, CA, 312 pp.
- Hines, E.M., Restrepo, J.I., and Seible, F., 2004. "Force-Displacement Characterization of Well-Confined Bridge Piers," *ACI Structural Journal* 101 (4), pp. 537-548.
- International Code Council, 2002. *2003 International Building Code*, Country Club Hills, IL.
- International Conference of Building Officials, 1994. *Uniform Building Code (UBC 1994)*, Whittier, CA.
- Johnson, B.M., 2007. *Longitudinal Reinforcement Anchorage Detailing Effects on RC Structural wall Behavior*, M.S. Thesis, University of Minnesota, 391 pp.
- Jung, N., 2007. *Preliminary Design of Structural wall Specimens Tested with MAST*, M.S. Thesis, University of Minnesota, 257 pp.
- Kappos, A.J., Chryssanthopoulos, M.K., and Dymiotis, C., 1999. "Uncertainty Analysis of Strength and Ductility of Confined Reinforced Concrete Members," *Engineering Structures*, 21 (3), pp. 195-208.
- Lowes, L., and Altoontash, A., 2003. "Modeling Reinforced Concrete Beam-Column Joints Subjected to Cyclic Loading," *Journal of Structural Engineering*, 129 (12), pp. 1686-1697.
- Mander, J.B., M.J.N. Priestley, and R. Park, 1988a. "Observed Stress-Strain Behavior of Confined Concrete," *Journal of Structural Engineering* 114 (8), 1827-1849.
- Mander, J.B., M.J.N. Priestley, and R. Park, 1988b. "Theoretical Stress-Strain Model for Confined Concrete," *Journal of Structural Engineering* 114 (8), 1804-1826.
- Massone, L.M., Orakcal, K., and Wallace, J.W., 2006. "Shear-Flexure Interaction for Structural Walls," *Deformation Capacity and Shear Strength of Reinforced Concrete Members under Cyclic Loading*, ACI Special Publication 236, pp. 127-150.
- Mazzoni, S., McKenna, F., Scott, M.H., and Fenves, G.L., 2004. "Open System for Earthquake Engineering Simulation," *Pacific Earthquake Engineering Research Center*, University of California, Berkeley, CA, Ver. 1.6.0.
- Naeim, F., ed., 2001. *The Seismic Design Handbook*, Kluwer, Boston.
- Nowak, A.S., and Szerszen, M.M., 2003. "Calibration of Design Code for Buildings (ACI 318): Part 1 – Statistical Models for Resistance," *ACI Structural Journal*, 100 (3), pp 377-382.
- Oosterle, R.G., Aristizabal-Ochoa, J.D., Fiorato, A.E., Russell, H.G., and Corley, W.G., 1979. *Earthquake Resistant Structural Walls – Tests of Isolated Walls – Phase II*,

- Report to National Science Foundation, Portland Cement Association, 334 pp.
- Pagni, C.A., and Lowes, L.N., 2006. "Fragility Functions for Older Reinforced Concrete Beam-Column Joints," *Earthquake Spectra* 22 (1), pp. 215-238.
- Palermo, D., and Vecchio, F.J., 2002. "Behavior of Three-Dimensional Reinforced Concrete Structural walls," *ACI Structural Journal* 99 (1), pp. 81-89.
- Pantazopoulou, S.J., and French, C.W., 2001. "Slab Participation in Practical Earthquake Design of Reinforced Concrete Frames," *ACI Structural Journal*, 98 (7), pp. 479-489.
- Pantazopoulou, S.J., and Moehle, J.P., 1990. "Identification of Effect of Slabs on Flexural Behavior of Beams," *Journal of Structural Engineering*, 116 (1), pp. 91-104.
- Park, R., and Paulay, T., 1975. *Reinforced Concrete Structures*, John Wiley and Sons, New York.
- Paulay, T., and Priestley, M.J.N., 1992. *Seismic Design of Reinforced Concrete and Masonry Buildings*, John Wiley and Sons, New York.
- Richart, F.E., A. Brandzaeg, and R.I. Brown, 1928. "A Study of the Failure of Concrete Under Combined Compressive Stresses," *University of Illinois Bulletin* 26 (12), 104 pp.
- Saatcioglu, M. and S.R. Razvi, 1992. "Strength and Ductility of Confined Concrete," *Journal of Structural Engineering* 118 (6), 1590-1607.
- Sasani, M., and Der Kiureghian, A., 2001. "Seismic Fragility of RC Structural Walls: Displacement Approach," *Journal of Structural Engineering*, 127 (2), pp. 219-226.
- Schiff, A.J., ed., 1999. *Hygoken-Nanbu (Kobe) Earthquake of January 17, 1995*, ASCE, Reston, VA.
- Seismology Committee, Structural Engineers Association of California, 1999. *Recommended Lateral Force Requirements and Commentary*, Structural Engineers Association of California, Sacramento, CA.
- Sheikh, S.A., 1982. "A Comparative Study of Confinement Models," *ACI Journal* 79 (4), 296-306.
- Sittipunt, C., and Wood, S.L., 1995. "Influence of Web Reinforcement on the Cyclic Response of Structural Walls," *ACI Structural Journal*, 92 (6), pp. 1-12.
- Sritharan, S., Ingham, J.M., Priestley, M.J.N., and Seible, F., 1998. "Bond Slip of Bridge Column Reinforcement Anchored in Cap Beams," *Bond and Development of Reinforcement – A Tribute to Dr. Peter Gergely*, ACI Special Publication 180, pp. 319-345.
- Sritharan, S., Priestley, M.J.N., and Seible, F., 1996. *Seismic Response of Column/Cap Beam Tee Connections with Cap Beam Prestressing*. Structural Systems Research Report No. SSRP-96/09, Division of Structural Engineering, University of California, San Diego.
- Stanford University Structural Engineering and Geomechanics Program, 2008. *Performance-based engineering*. <http://www.stanford.edu/group/strgeo/pbe.html>
- Thomsen, J. H., IV, and Wallace, J. W., 1995. *Displacement-Based Design of RC Structural Walls: Experimental Studies of Walls with Rectangular and T-shaped*

- Cross Sections*, Report No. CU/CEE-95/96, Department of Civil and Environmental Engineering, Clarkson University, 353 pp.
- Thomsen, J.H., IV, and J.W. Wallace, 2004. "Displacement-Based Design of Slender Reinforced Concrete Structural Walls – Experimental Verification," *Journal of Structural Engineering* 130 (4), pp. 618-630.
- U.S. Geological Survey, 1996. *USGS Response to an Urban Earthquake Northridge 94*. Open-File Report 96-263. Available <http://pubs.usgs.gov/of/1996/ofr-96-0263/>
- Vecchio, F.J., and Collins, M.P., 1993. "Compression Response of Cracked Reinforced Concrete," *Journal of Structural Engineering*, 119 (12), pp. 3590-3610.
- Viwathanatepa, S., Popov, E.P., and Bertero, V.V., 1979. *Effects of Generalized Loadings on Bond of Reinforcing Bars Embedded in Confined Concrete Blocks*, Report. No. UCB/EERC-79/22 EERC, Univ. of California, Berkeley, CA, 304 pp.
- Wallace, J.W., 1992. "BIAX: Revision 1 – Computer Program for the Analysis of Reinforced Concrete and Reinforced Masonry Sections," *Report CU/CEE-92/4*, Structural Engineering, Mechanics, and Materials, Clarkson University, Potsdam, NY.
- Wallace, J.W., 1996. "Evaluation of UBC-94 Provisions for Seismic Design of RC Structural Walls," *Earthquake Spectra* 12 (2), pp. 327-348.
- Wallace, J. W., and Moehle, J. P., 1992. "Ductility and Detailing Requirements of Bearing Wall Buildings," *Journal of Structural Engineering*, 118 (6), pp. 1625-1644.
- Wallace, J.W., and Orakcal, K., 2002. "ACI 318-99 Provisions for Seismic Design of Structural Walls," *ACI Structural Journal*, 99 (4), pp. 499-508.
- Waugh, J., Aaleti, S., Sritharan, S., and Zhao, J., 2009. "Nonlinear Analysis of Rectangular and T-shaped Concrete Walls," *ISU-ERI-Ames Report ERI-09327*, Iowa State University, Ames, IA.
- Wood, S.L., 1989. "Minimum Tensile Reinforcement Requirements in Walls," *ACI Structural Journal*, 86 (4), pp. 582-591.
- Zhao, J., and Sritharan, S., 2007. "Modeling of Strain Penetration Effects in Fiber-Based Analysis of Reinforced Concrete Structures," *ACI Structural Journal*, 104 (2), pp. 133-141.

## **Appendix A**

### **Specimen As-Built Dimensions and Foundation/Top Block Design**

Appendix A contains information about the as-built specimens. Figures A.1 to A.4 show the as-built bar locations and clear cover in specimen NTW1 at the base block and at each of the slabs. A larger cover value occurred in the flange just above the first slab (i.e., in the lower portion of the second story) as a result of a form-tie failure during casting of the second story. As-built bar locations for specimen NTW2 cannot be located at this time. Figures A.5 through A.12 show scanned copies of the hand-calculations used for strut-and tie analysis of the base block. Figures A.13 through A.25 show the reinforcement of each base block and top block.

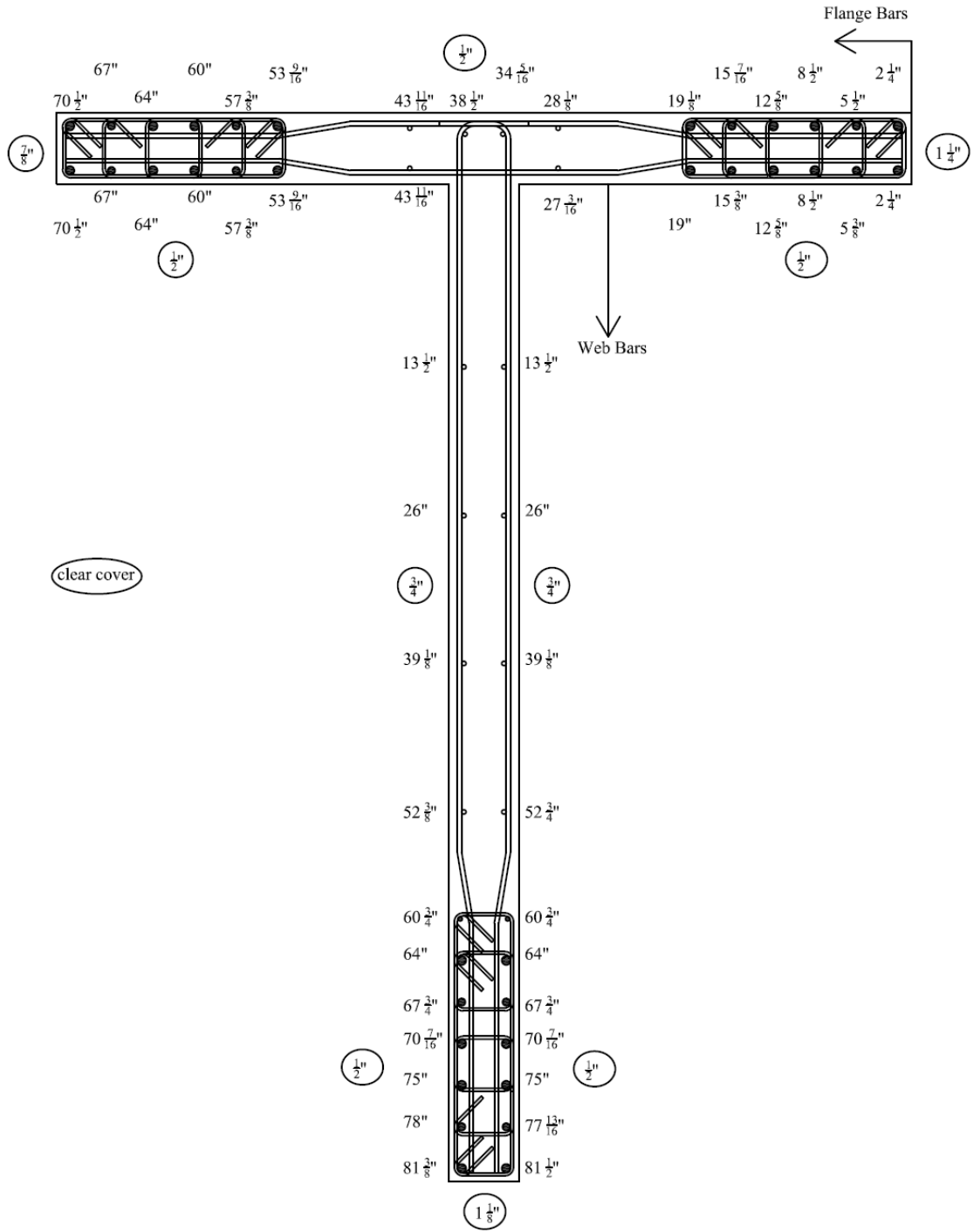


Figure A.1. Bar locations in specimen NTW1 at base of first story

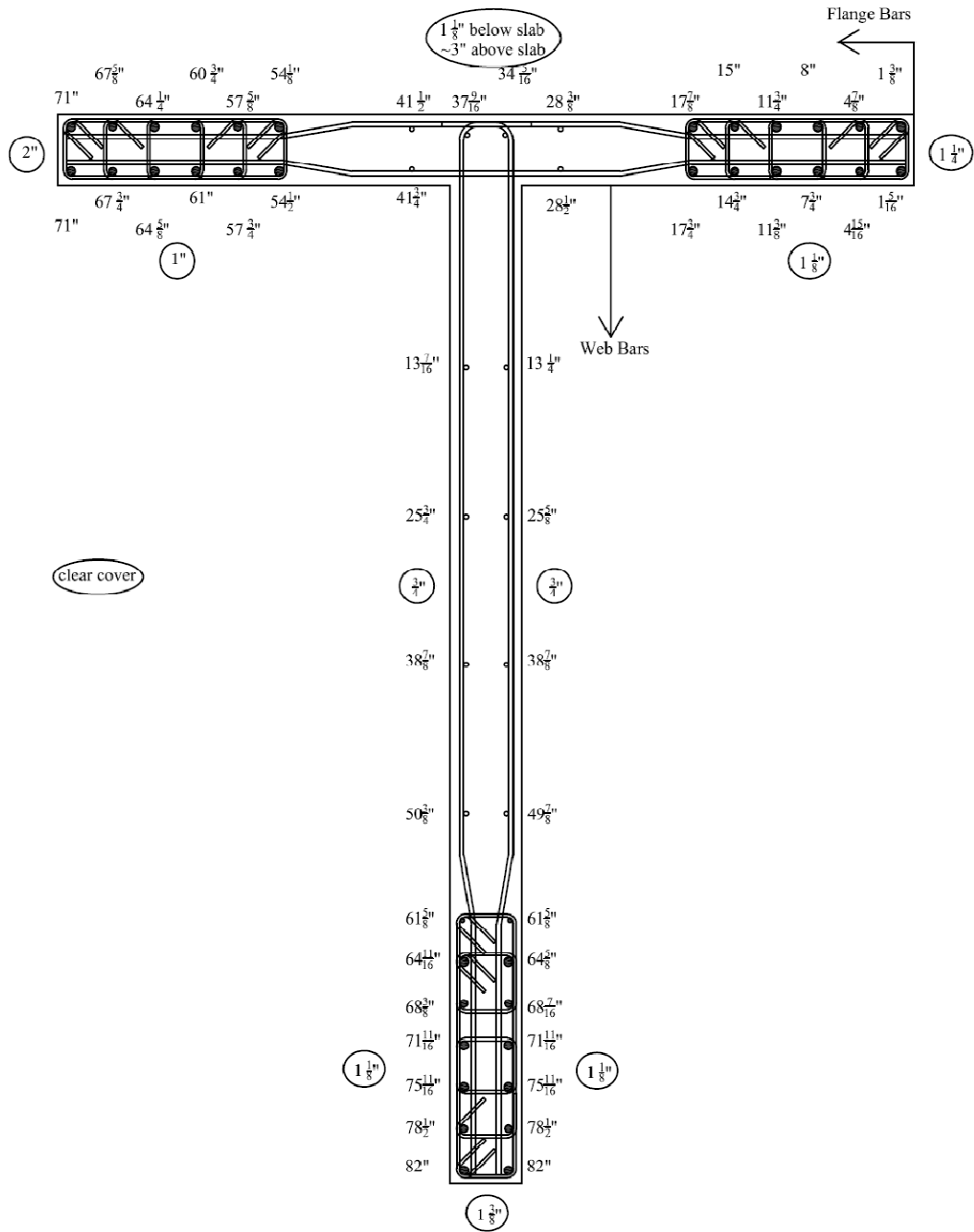
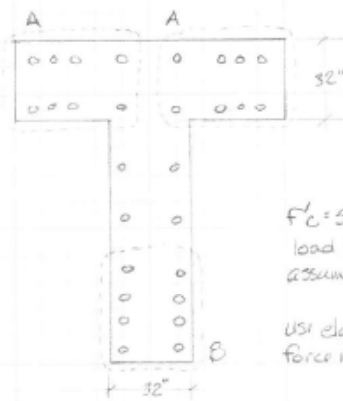


Figure A.2. Bar locations in specimen NTW1 at base of second story







total depth (into page) = 21"  
 $d = 21 - 1.5$  (cover)  $\frac{1}{2}$  (stirrups,  $\frac{1}{2}$  bars, etc.) = 19"

$F_c = 5000$  psi     $F_y = 60$  ksi     $f_u = 90$   
 load factor = 2     $\phi = 0.75$   
 assume struts are square in cross-section

use elastic finite element analysis to determine force resisted by each anchor rod

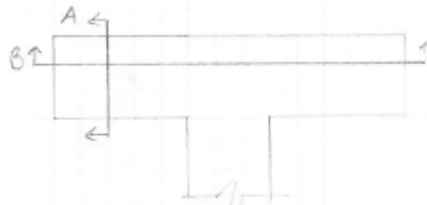
Section A - flange

rod reactions from FEM	1	2	3
	⊕ 38.6k	⊕ 151.2k	⊕ 157.6k
	⊕ 158.6k	⊕ 151.2k	⊕ 152.6k

see next page for resolution into components  
 Anchor used to determine geometry  
 (anchors are same by symmetry)

↑ thus 2 anchor rods not included in analysis, but should not increase any other forces

check  $10\sqrt{F_c} b_w d$  requirement in 2 directions (since this is a 3D block)



Section A: width = 32"     $10\sqrt{F_c} b_w d = 430k > 2 \times 151.2k = 302.4k$  ✓ ok

Section B: width = 36" (span between anchors in either half - this is a conservative length)  
 $10\sqrt{F_c} b_w d = 484k > 158.6k + 151.2k + 32k = 428.4k$  shear load ✓ ok

Note: this is not satisfied if reduced by  $\phi = 0.75$   
 increasing width to 42" will satisfy the requirement  
 this is probably reasonable, given that the struts do have finite width and some force is carried by joining sections

Figure A.5. Strut-and-tie model calculations for base block, 1 of 8

1-26-05

BCB

2/8

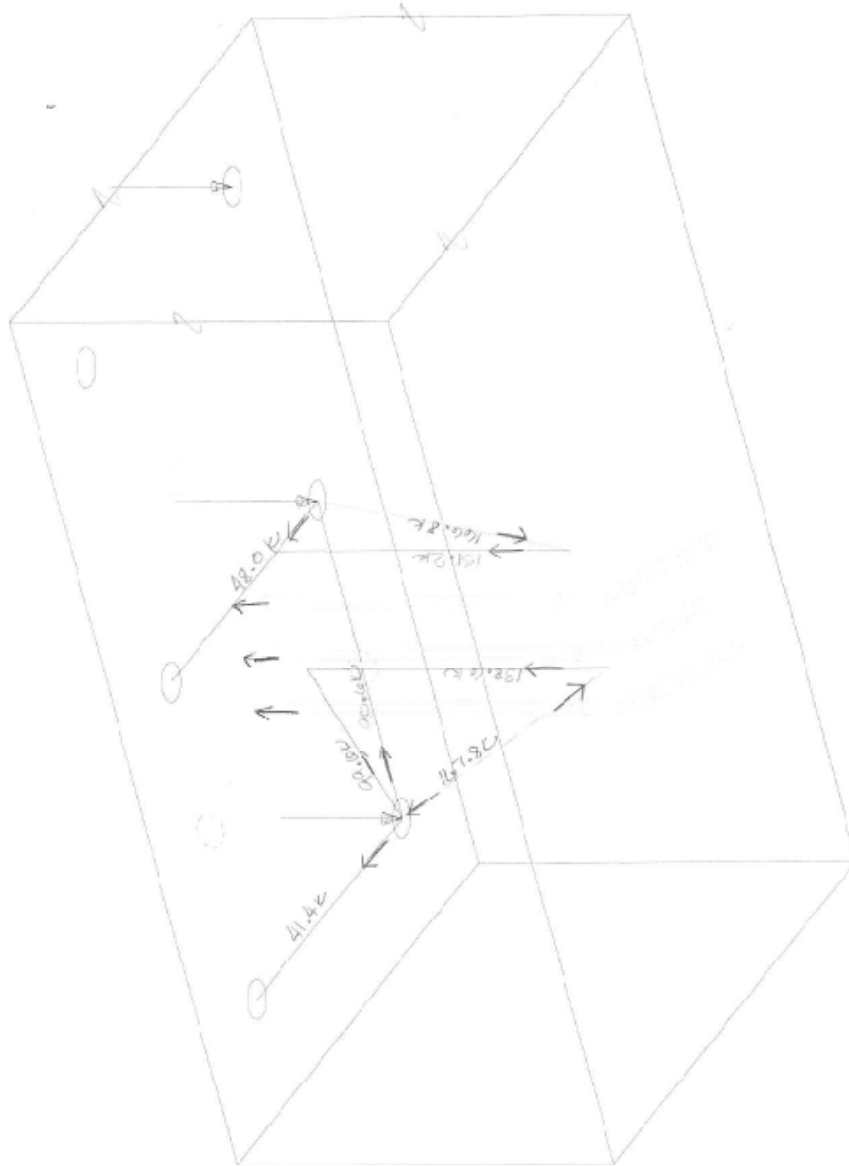


Figure A.6. Strut-and-tie model calculations for base block, 2 of 8

1-26-05

BLB

3/8

Inclined Struts:  $f_s = 0.75$  (bottle strut)  $\phi = 0.25 f_s f_c = 2.39 \text{ ksi}$

"end" struts (marked 1 & 3 on plan)

$$C = 167.8 \text{ k} \quad A_{min} = 70.2 \text{ in}^2 = (8.37 \text{ in})^2$$

"middle" struts (marked 2)

$$C = 166.8 \text{ k} \quad A_{min} = 69.8 \text{ in}^2 = (8.35 \text{ in})^2$$

Vertical Struts (around anchor rods)  $A_{min} \text{ \& precompression} = \frac{123.4 \text{ k}}{2.39 \text{ ksi}} = 51.6 \text{ in}^2 = (7.2 \text{ in})^2$

Effect of precompression:  $\Delta C = (\text{precompression}) \cdot (\text{tension change due to load}) \cdot (\text{vertical comp. of load})$

$$= T_i + \Delta T - P$$

from Salmon & Johnson  $\frac{\Delta T}{E A} = \frac{P - \Delta T}{E_c A_c}$  assume  $\frac{E_s}{E_c} = 8$   $A_s = 1.41 \text{ in}^2$   $A_c = 8.5 \text{ in}^2 = 1.41 \cdot 70.8 \text{ in}^2$   
 ↳ this is arbitrary

$$\Rightarrow \Delta T = 0.14 P \quad T_i = 123.4 \text{ k}$$

at ends (1 & 3)  $\Delta T = 0.14 \cdot 138.6 \text{ k} = 19.1 \text{ k}$

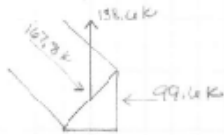
$$C = 123.4 + 19.1 - 138.6 = 3.9 \text{ k} \quad \text{required area} = \text{small}$$

at middle (2)  $\Delta T = 0.14 \cdot 151.2 \text{ k} = 21.2 \text{ k} \quad C = 123.4 + 21.2 - 151.2 = -6.6 \text{ k}$

→ This tension should let to an issue since it is physically impossible to reach this level of load (loads are increased only to minimize found crushing & cracking)

Nodes at bottom - CCT  $f_n = 0.8$   $\phi f_n = 2.55 \text{ ksi}$   
 note: strut dimension will control inclined face

ends (1 & 3) dimension into page = 8.37" (same as strut)

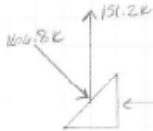


$$\text{bottom: } \frac{138.6 \text{ k}}{2.55 \text{ ksi}} = \frac{1}{8.37 \text{ in}} = 6.49 \text{ in}$$

$$\text{side: } \frac{99.6 \text{ k}}{2.55 \text{ ksi}} = \frac{1}{8.37 \text{ in}} = 4.27 \text{ in} \rightarrow \text{the node depth seems "reasonable"}$$

(section at an angle parallel to net tension direction)

middle (2) dimension into page = 8.35 in



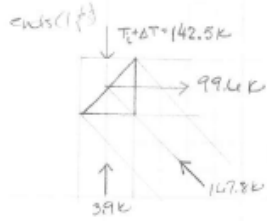
$$\text{bottom: } \frac{151.2 \text{ k}}{2.55 \text{ ksi}} = \frac{1}{8.35 \text{ in}} = 7.0 \text{ in}$$

$$\text{side: } \frac{48.0 \text{ k}}{2.55 \text{ ksi}} = \frac{1}{8.35 \text{ in}} = 2.25 \text{ in}$$

Notes are required down here

Figure A.7. Strut-and-tie model calculations for base block, 3 of 8

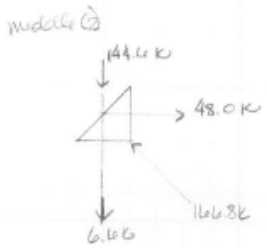
Nodes at top: CCT  $f_n = 0.8$   $f_c = 2.55 \text{ ksi}$



dimension into page =  $8.57 \text{ in}$

Required bearing area:  $\frac{142.5 \text{ k}}{2.55 \text{ ksi}} = 55.9 \text{ in}^2 = (7.56 \text{ in})^2 = 1.41 \text{ m}^2$  for rod

node depth:  $\frac{99.6 \text{ k}}{2.55 \text{ ksi}} \cdot \frac{1}{8.57 \text{ in}} = 4.67 \text{ in}$



Bearing  $\frac{144.6}{2.55} = 56.7 \text{ in}^2 = (7.62 \text{ in})^2 = 1.41 \text{ m}^2$

node depth:  $\frac{48 \text{ k}}{2.55 \text{ ksi}} \cdot \frac{1}{8.57 \text{ in}} = 2.25 \text{ in}$

bearing plates: use larger than required to minimize crushing  
 theoretically have spec for 9" square plates  
 use slightly smaller to avoid installation difficulties  
 → 8 3/4" square plates

\* required thickness:  $t_{\text{min}} = 1.7 \frac{2P_{\text{tie}}}{\phi F_y E_n} = \frac{(8.75)}{2} \sqrt{\frac{2 \cdot 166.8 \text{ k}}{0.75 \cdot 60 \cdot 29.5 \cdot 0.75}} = 1.27 \text{ in}$  use  $1 \frac{1}{2} \text{ in}$

Steel ties: divide into orthogonal components (shown on p. 2)

longitudinal:  $90.6 \text{ k}$   $A_s = \frac{90.6 \text{ k}}{0.75 \cdot 60 \text{ ksi}} = 2.01 \text{ m}^2$

2-#9 4-#7 5-#6 7-#5  
 ↳ hard to develop

transverse: use same for all cases to simplify construction

$\frac{48.0 \text{ k}}{0.75 \cdot 60 \text{ ksi}} = 1.07 \text{ m}^2$  2-#7 3-#6 4-#5

\* another option, which will reduce demand on ties (analysis to determine how much will be rather complex) is to use a single, long, plate across a group of anchor rods, i.e.

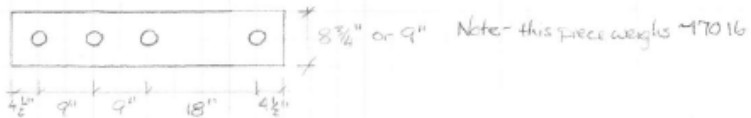


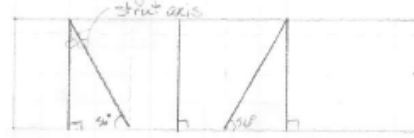
Figure A.8. Strut-and-tie model calculations for base block, 4 of 8

Required skin reinforcement

$$\sum \frac{A_s}{b_s s} \sin \theta_i \geq 0.003$$

to deal with 3rd struts, satisfy this for projection onto both transverse and longitudinal sections

Plane parallel to longitudinal direction:



to dimension into page: 30 in  
32 in for clearance between vertical bars & skin steel

required horizontal steel across vertical struts:

bar	$A_s$	#2 layers =
#2	0.049	0.098
#3	0.11	0.22

$$\frac{A_s}{b_s s} \geq 0.003 \Rightarrow S \leq \frac{A_s}{0.003}$$

- 3.108 in for #2
- 2.44 in for #3
- 4.44 in #4

using 4 layers

2.16 in

4.88 in reasonable to build, but still likely bars to minimize crack size

use 4 layers of #3 bars @ 4 1/2" spacing (1 1/2" clear above top row & below bottom) horizontal

additional vertical steel across inclined struts:

$$\text{horizontal contribution} = \frac{0.44 \text{ in}^2}{(30 \text{ in} \times 4.5 \text{ in})} \sin 56^\circ = 0.0027$$

required vertical (some can be provided by vertical legs of closed stirrups made from transverse ties - making closed stirrups helps ensure anchorage)

$$\frac{A_s}{b_s s} \sin 34^\circ \geq 0.003 \Rightarrow S = \frac{A_s}{0.003}$$

0.5542  
2 legs  
S =

- #2 6.125"
- #3 13.75"

2-#7 (stirrups) @ 8" → these @ 18" are more than adequate, but adding a single #2 or #3 stirrups @ thirds between seems reasonable, esp. given Ch. 11 requirement 5S12" (putting them at thirds avoids interference when anchor rods are used @ 9")

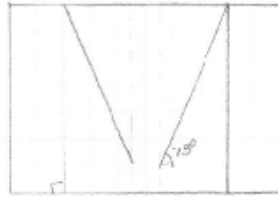
Figure A.9. Strut-and-tie model calculations for base block, 5 of 8

1-26-05

BIB

6/8

Planes parallel to transverse direction



Since stirrups @ 6" for other direction, works w/ 6" deep "slices" - b = 6"

horizontal steel required across vertical struts: "one layer in each slice"

$$\frac{A_s}{b \cdot s} \geq 0.003 \Rightarrow s \leq \frac{A_s}{0.003 \cdot b}$$

#2  $s \leq 2.72"$

#3  $s \leq 4.11"$  → tying steel will be easy if 4 1/2" spacing from longitudinal steel is watched

→ can use existing stirrup legs for top & bottom

is additional vertical steel required?

$$\frac{A_{tie}}{b \cdot s} = \frac{2 \cdot 0.049 \text{ m}^2}{(6 \text{ in} \cdot 4.5 \text{ in})} \cdot \sin 75^\circ + (6 \text{ in}) \cdot (27 \text{ in}) \cdot \cos 75^\circ = 0.00370 + 0.00018 = 0.00408 \approx 0.003 \checkmark$$

length of existing stirrups

Tie anchorage:

transverse ties are top leg of closed stirrups - not a problem

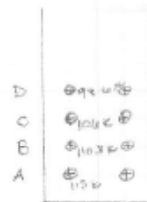
longitudinal ties - #7s

$$l_d = \frac{F_y \cdot A_s}{25 \cdot \sqrt{f_c}} \cdot d_b = \frac{60,000 \text{ psi} \cdot (1.2) \cdot (1.2) \cdot (1.0)}{25 \cdot \sqrt{3000} \text{ psi}} \cdot 0.875 \text{ in} = 44.1 \cdot 0.625 = 38.6 \text{ in, w/o hook}$$

$$\text{w/ hook } l_d = \frac{0.02 \cdot A_s \cdot \sqrt{f_c}}{25 \cdot \sqrt{f_c}} \cdot d_b = \frac{0.02 \cdot 0.06 \cdot 60,000 \text{ psi}}{25 \cdot \sqrt{3000} \text{ psi}} \cdot 0.875 = 4.8 \text{ w/o hook } \rightarrow \text{two hooks}$$

a)  $0.7 \cdot 10.4 \text{ in} \cdot 2 \cdot 2 \text{ in}$  clear beyond end of hook is included

Section B - Web



Forces reacted by each rod (from elastic analysis)

Figure A.10. Strut-and-tie model calculations for base block, 6 of 8

1-26-05

BC13

7/8

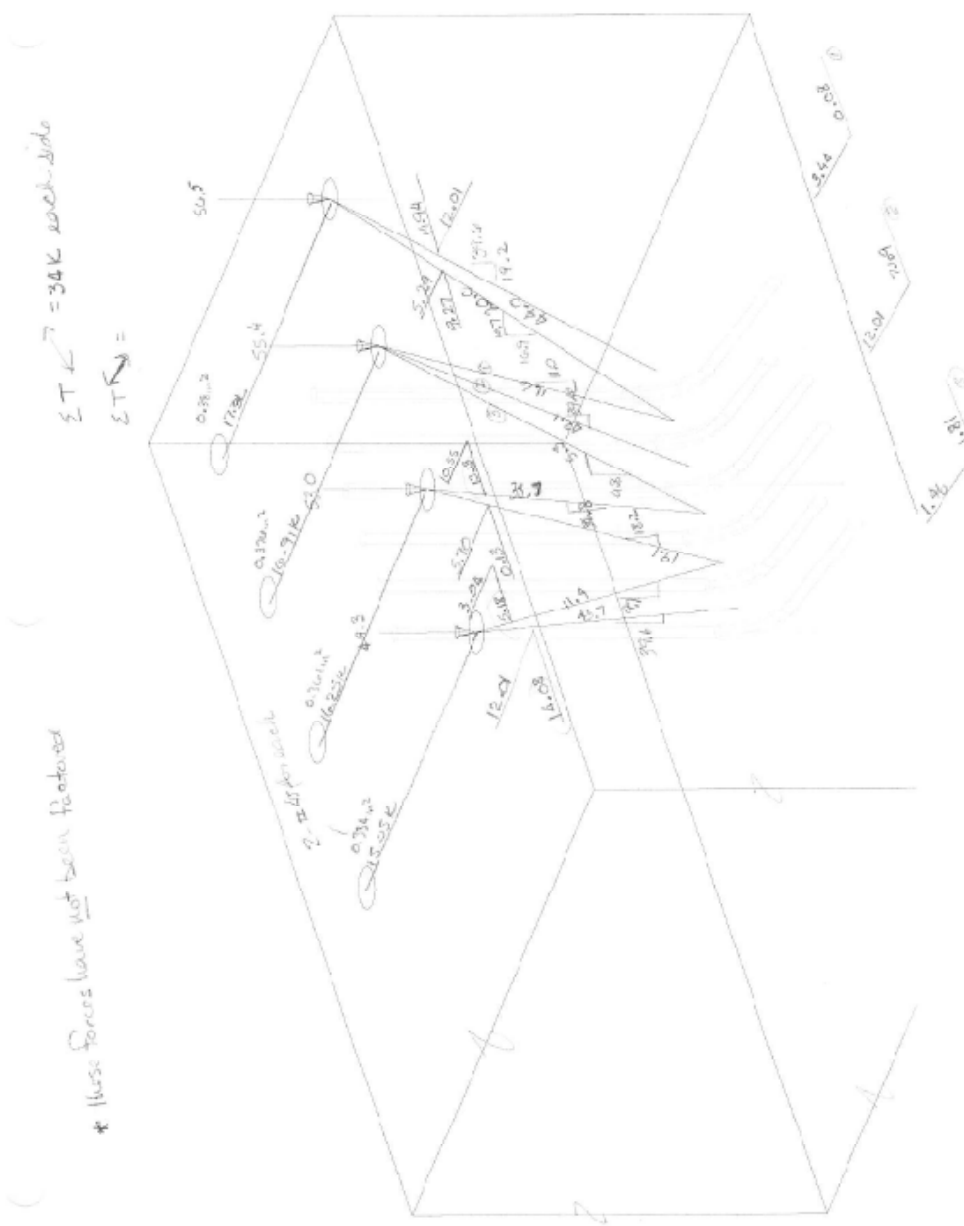


Figure A.11. Strut-and-tie model calculations for base block, 7 of 8

1-26-05

BIB

8/B

ties in this section:

longitudinal:  $\frac{68k}{0.75 \times 60k} = 1.51m^2$

2-#8's 3-#7's 4-#6's

use only 2 bars to avoid interference at the intersection of the web & flange

transverse: longest  $d_{req} = 346k \frac{34.6}{87.5 \times 2} = 0.77m^2$

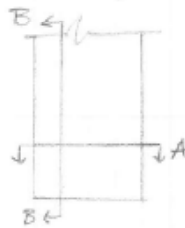
2-#6's - use 2-#7's to watch flange

development of #8 bars:  $d_d = 11.0'$  w/ hooks

$\times 0.7 = 11.9'$  w/ 2 1/2' clear cover

$\times 0.8 = 9.5'$  w/ confinement (provided by bending stem reinforcement around)

check  $10\sqrt{f_c}'$  requirement:



Section A:  $b_w = 32"$   $V_{u,max} = 226k < 430k \sqrt{f_c}$

Section B:  $b_w = 27"$  min  $10\sqrt{f_c}' b_w d = 313k < V_u = 408.4k$

\*  $b_w$  must be at least 32" - still probably reasonable

Figure A.12. Strut-and-tie model calculations for base block, 8 of 8

# Foundation Block Reinforcement

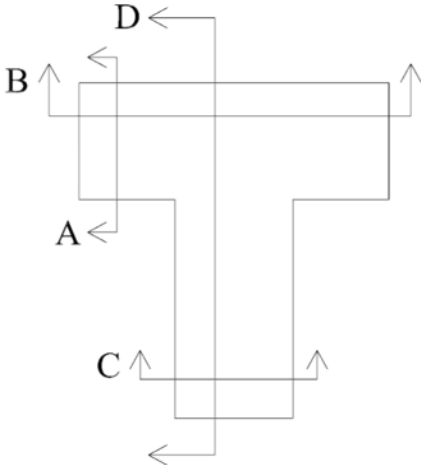
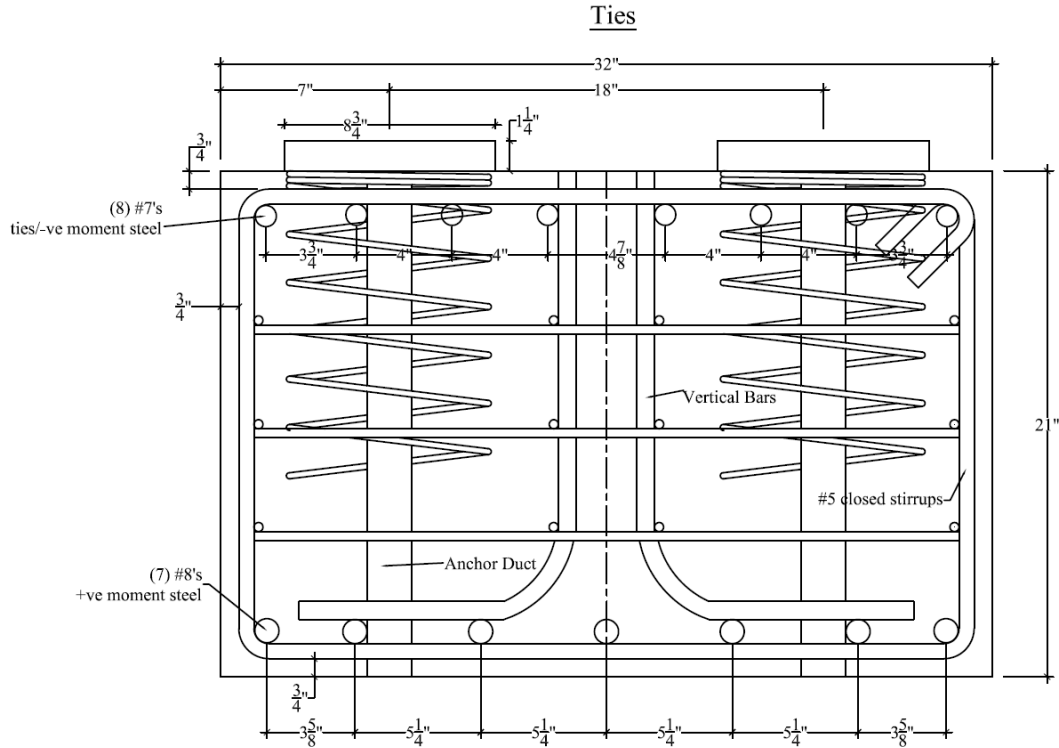


Figure A.13. Plan view showing section cuts used in Figures A.14 through A.25



Skin Reinforcement

Note #3 bars transverse (hairpins) & longitudinal may be switched in flange (A) for clearance in joint

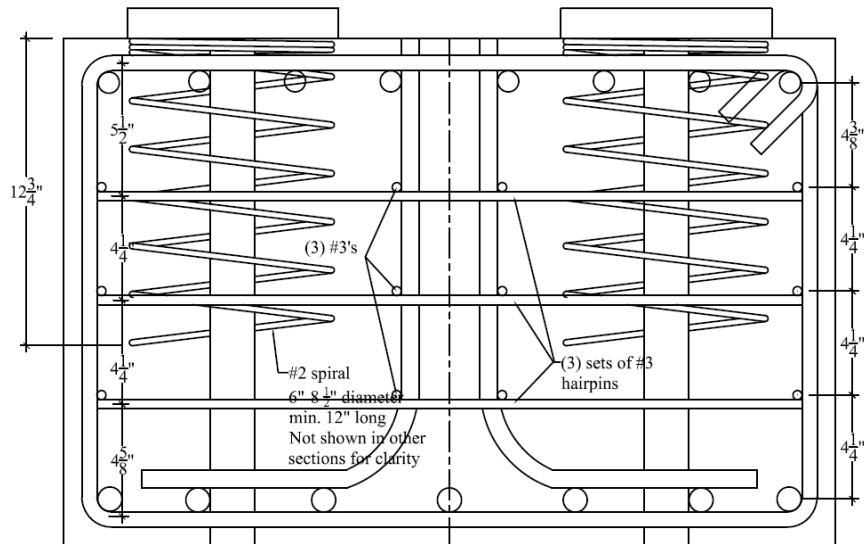


Figure A.14. Transverse sections A & C, NTW1 and NTW2 base blocks

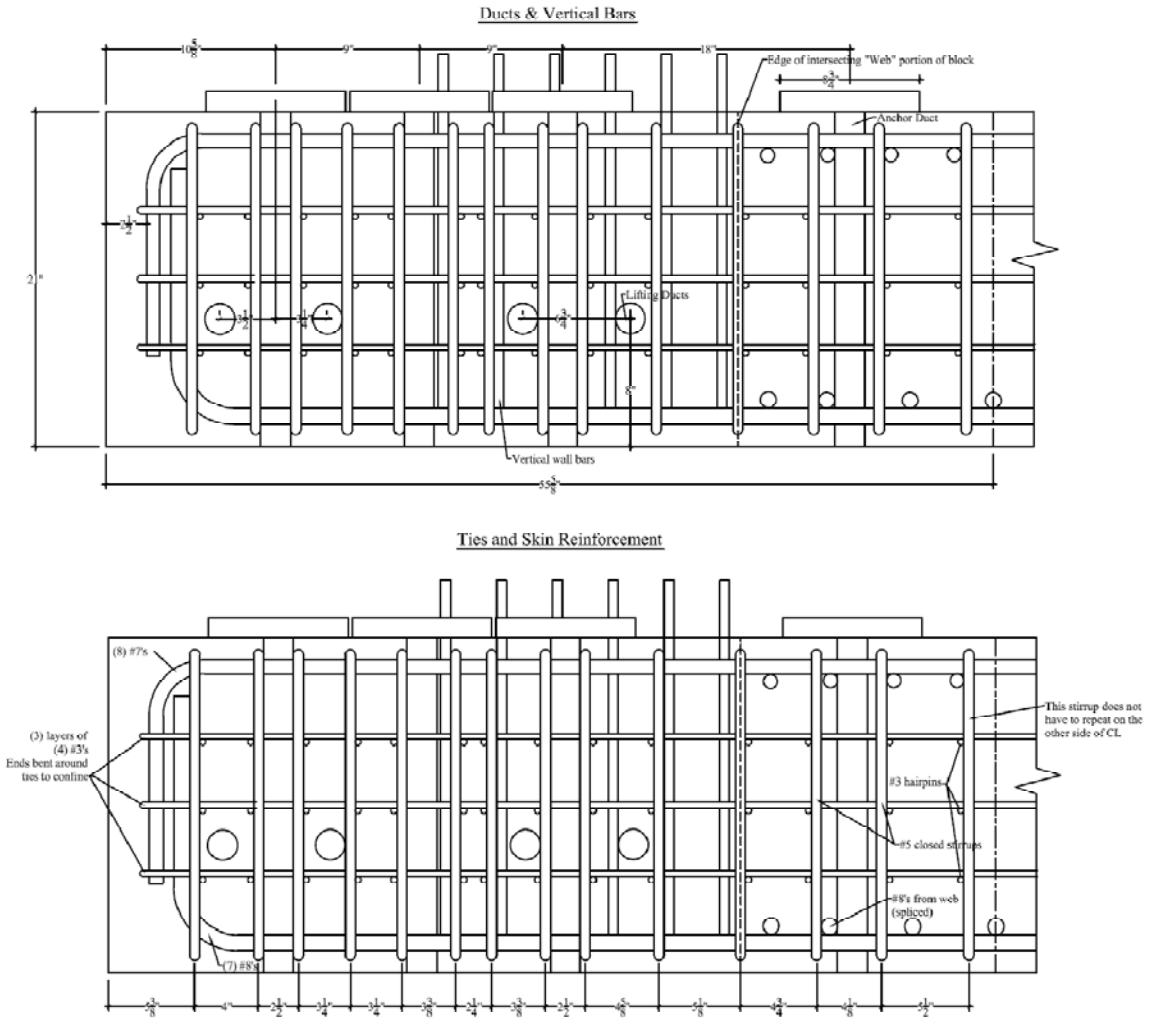


Figure A.15. Longitudinal sections B, NTW1 and NTW2 base blocks

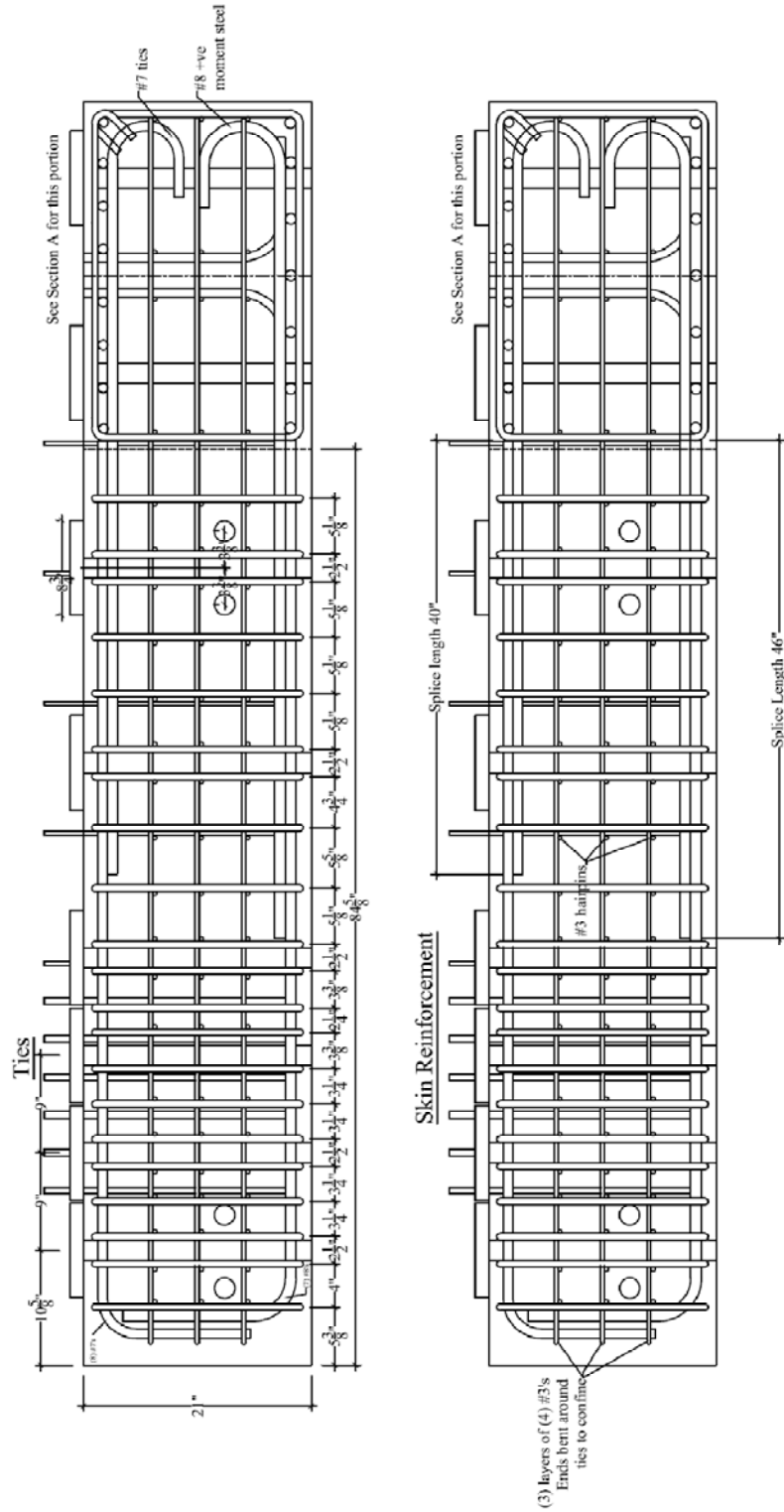


Figure A.16. Longitudinal sections D, NTW1 and NTW2 base blocks

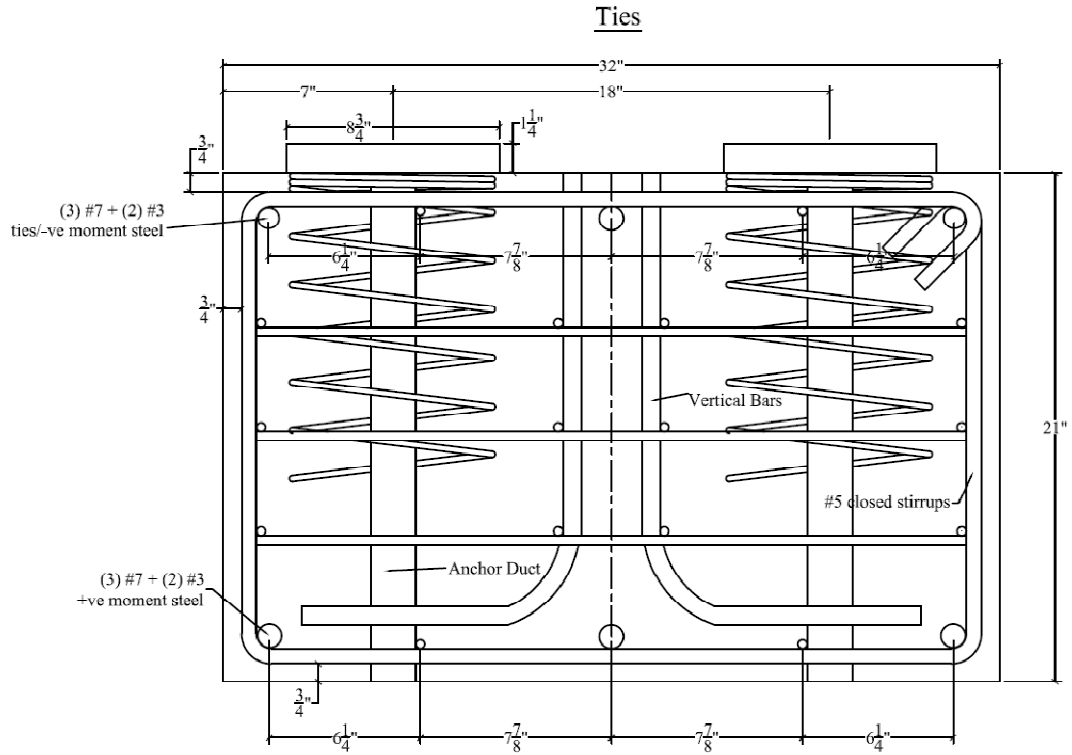


Figure A.17. Transverse sections A & C, NTW1 top block (reinforcement not called out same as base block)

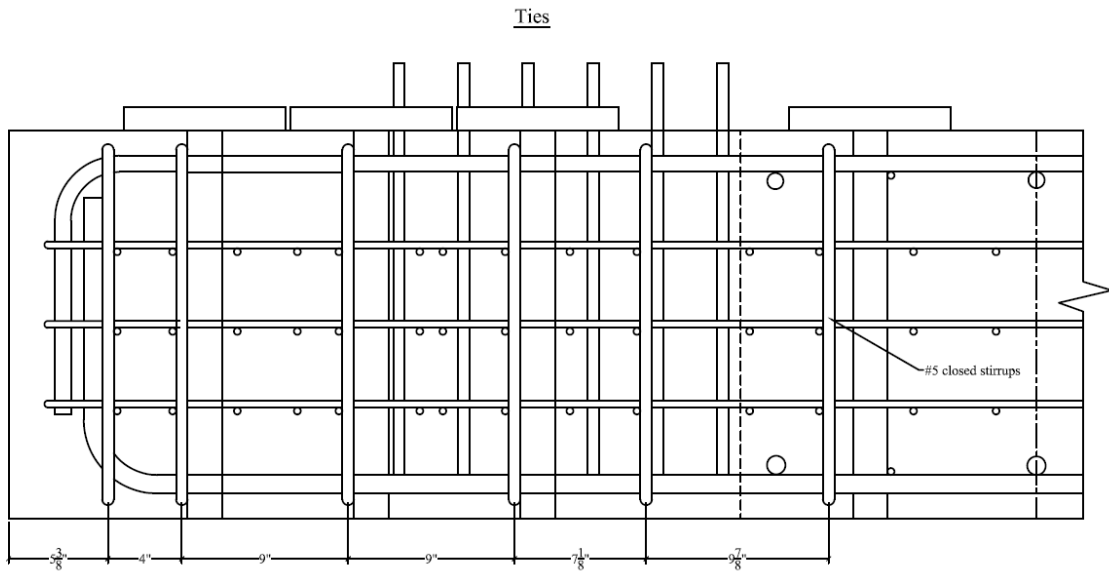


Figure A.18. Longitudinal section B, NTW1 top block (reinforcement not called out same as base block)

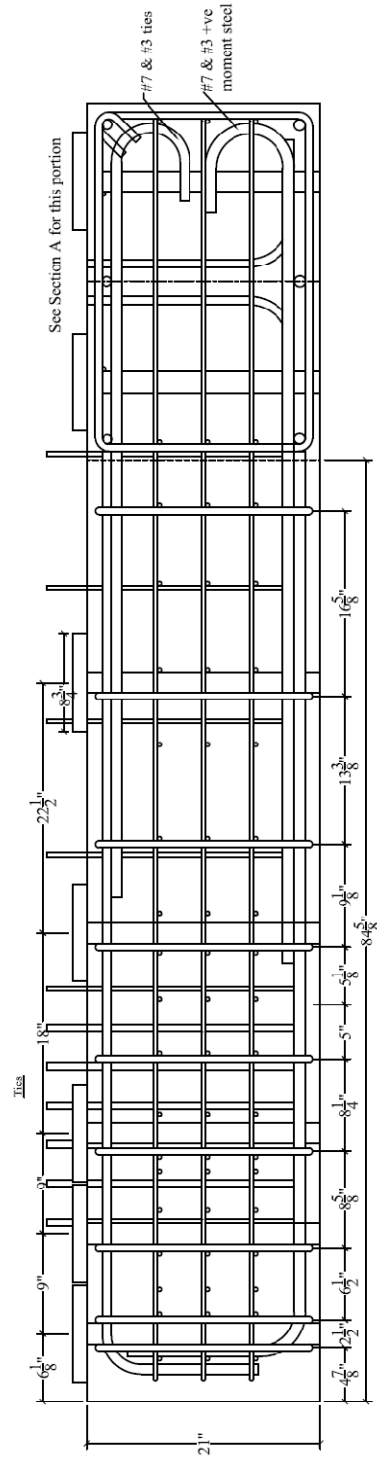


Figure A.19. Longitudinal section D, NTW1 top block (reinforcement not called out same as base block)

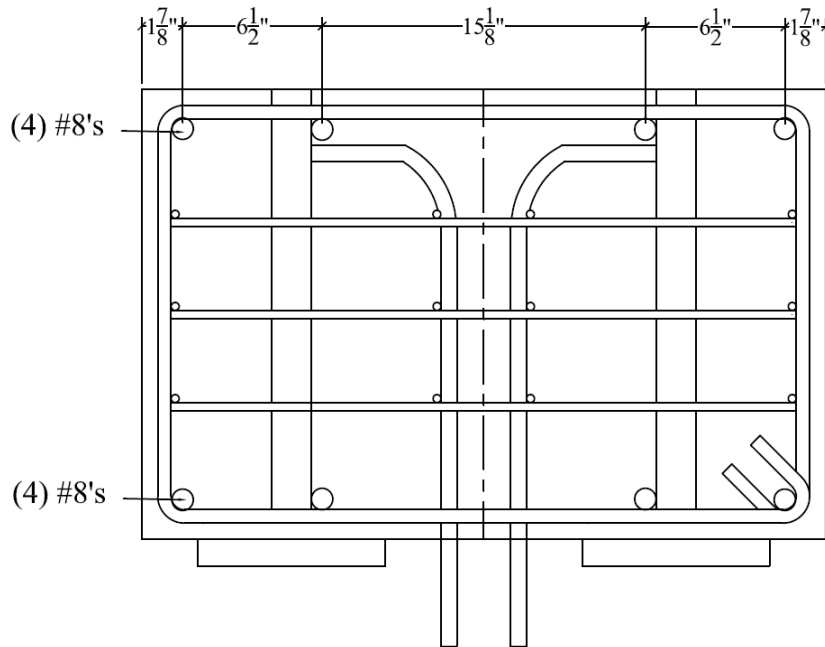


Figure A.20. Transverse sections A & C, NTW2 top block (reinforcement not called out same as base block)

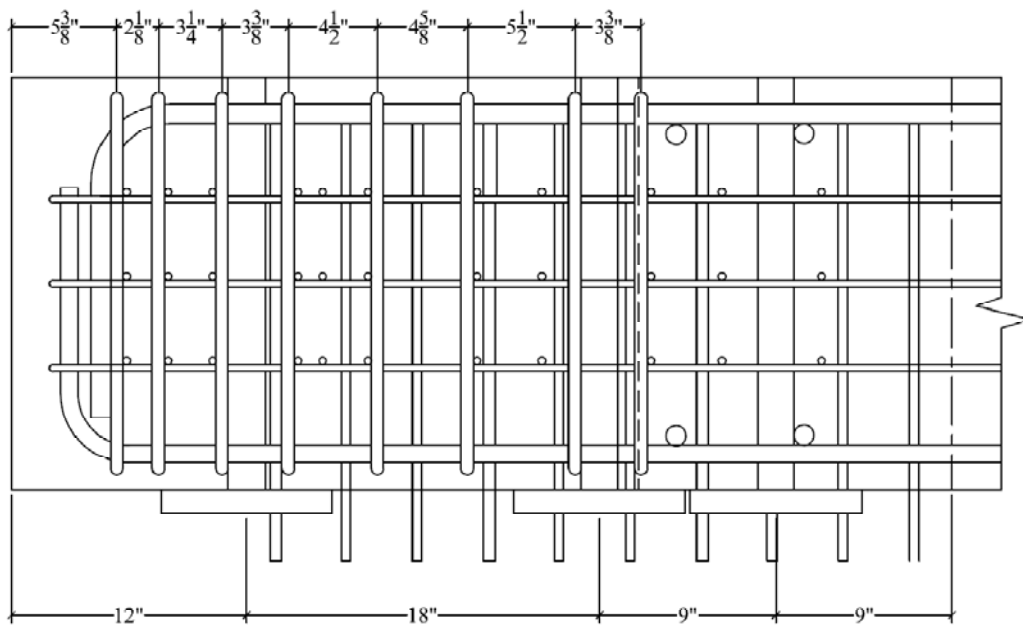


Figure A.21. Longitudinal section B, NTW2 top block (reinforcement not called out same as base block)

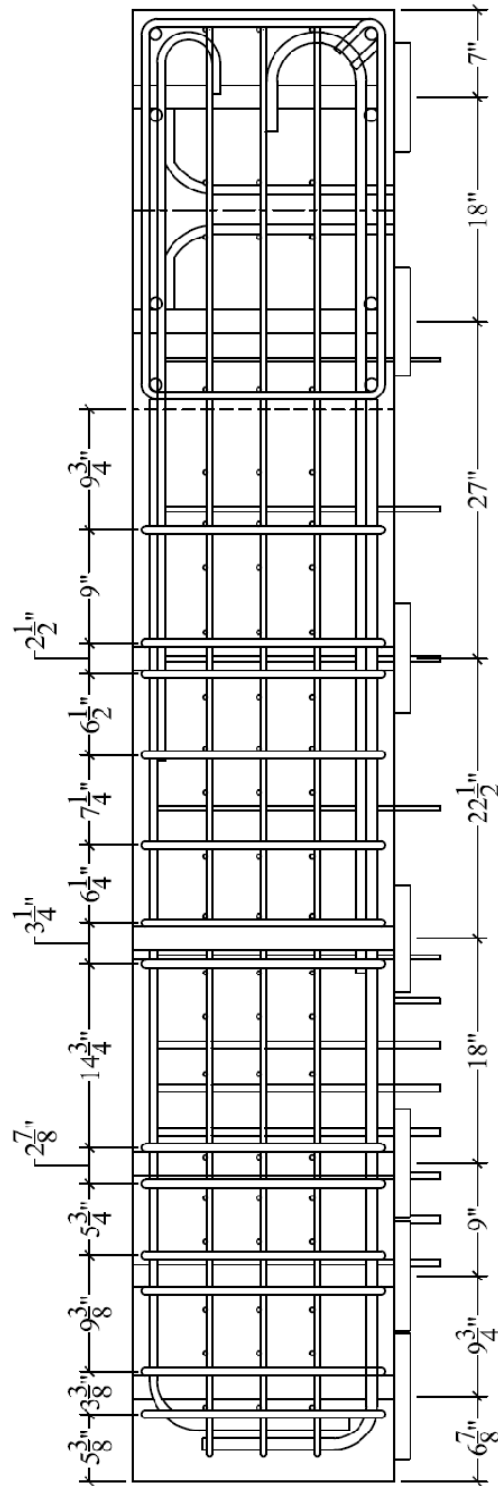


Figure A.22. Longitudinal section D, NTW2 top block (reinforcement not called out same as base block)

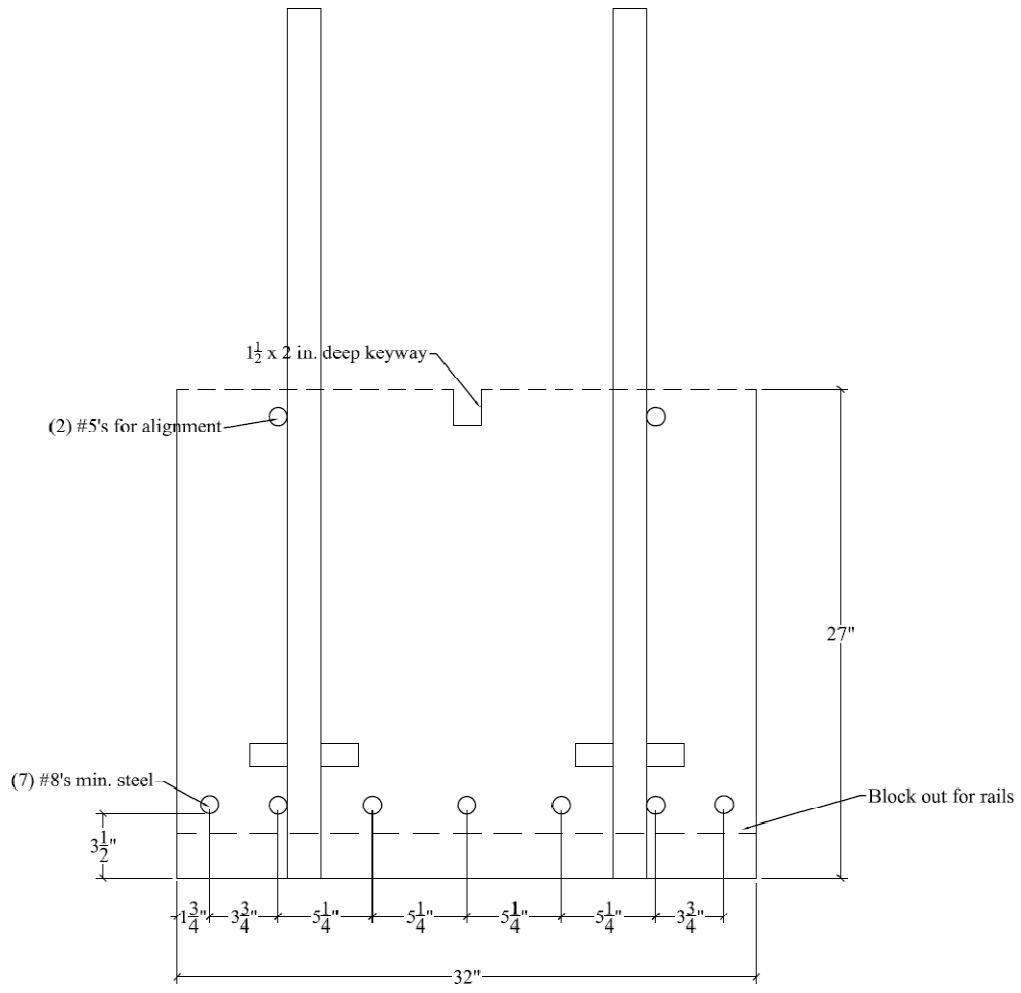


Figure A.23. Transverse sections A & C, NTW2 spacer block

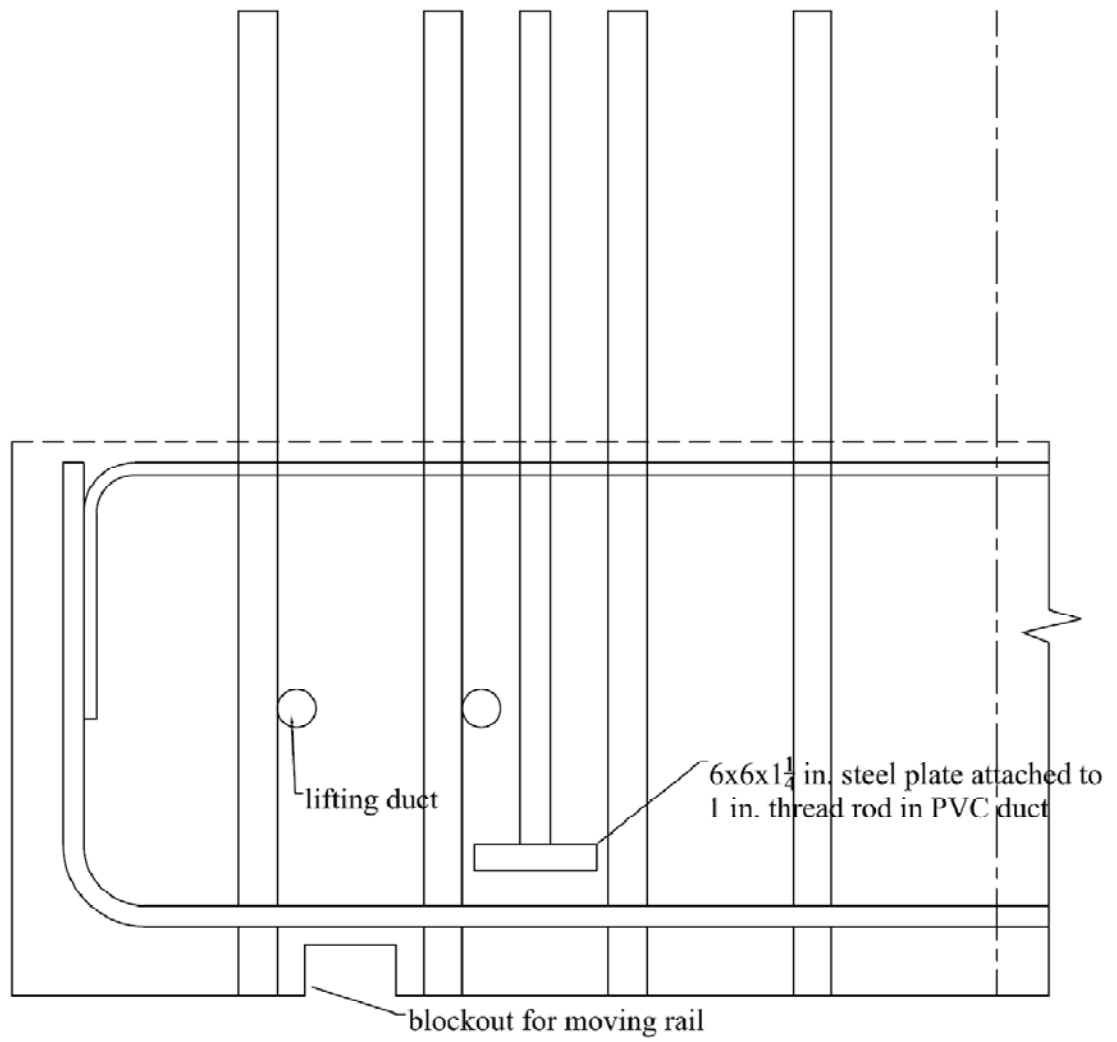


Figure A.24. Longitudinal section B, NTW2 spacer block

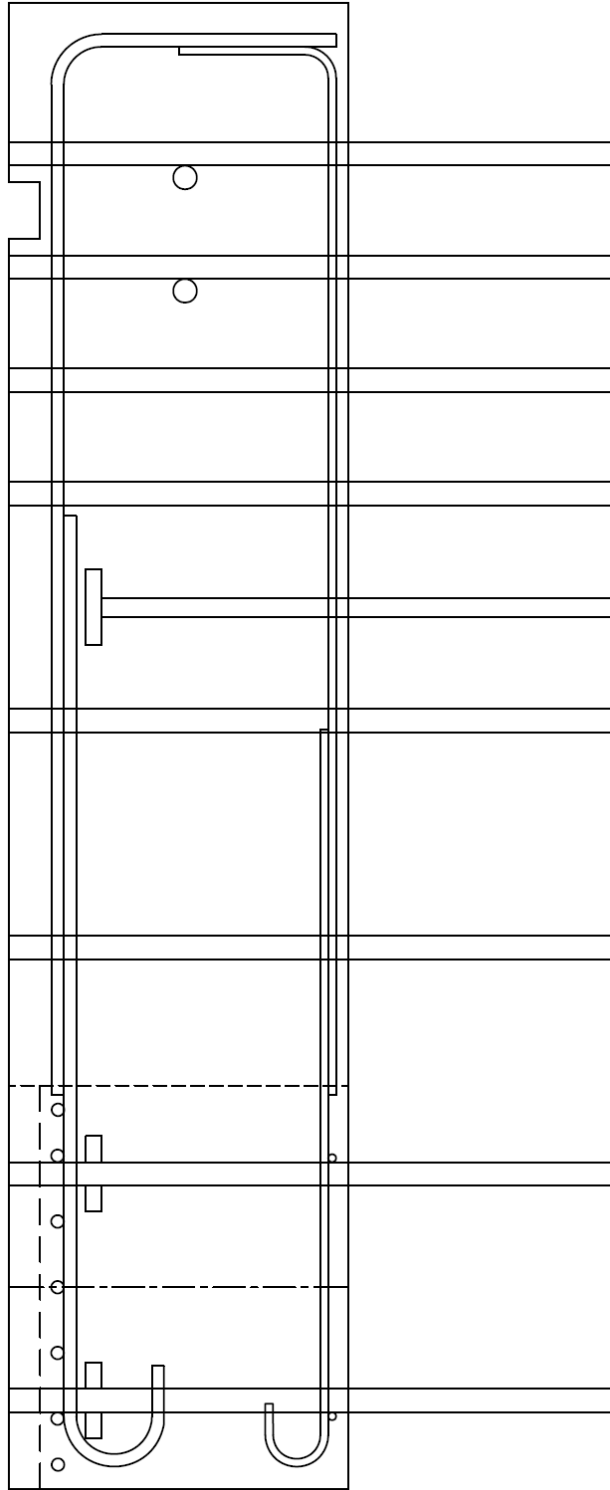


Figure A.25. Longitudinal section D, NTW2 spacer block

**Appendix B**  
**Instrumentation**

Appendix B contains information about the naming schemes used to identify instruments on each of the specimens and the as-built locations of each instrument. It should be noted that the naming scheme used with specimen NTW2 was modified slightly from the scheme used with specimen NTW1. Figures B.1 through B.13 show instrument locations for specimen NTW1 and Figures B.14 through B.25 show instrument locations for specimen NTW2.

### NTW1 Longitudinal Bar Numbering Scheme

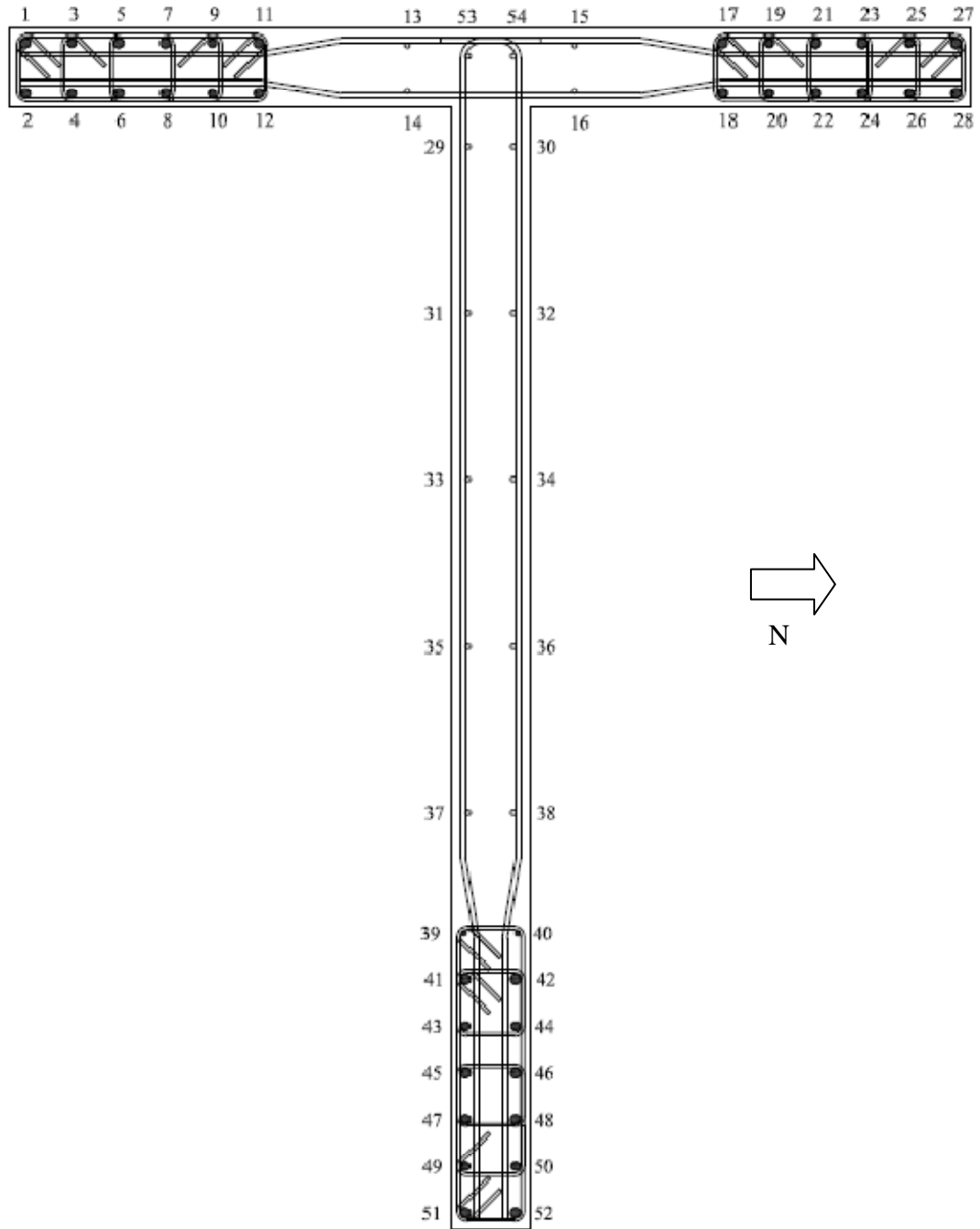


Figure B.1. NTW1 longitudinal bar numbering scheme

## NTW1 Instrumentation Naming Scheme

### Strain Gages:

- *SGmLn*: strain gage on longitudinal bar “m” at a nominal distance of “n” inches from the wall and base block interface. “n” is negative for gages inside the base block.
- *SGmHn*: strain gage on the hoop reinforcement near longitudinal bar “m”. The hoop is located at “n” inches from the wall and base block interface.
- *SGmTn*: strain gage on the transverse shear reinforcement near longitudinal bar “m”. The transverse bar is located at “n” inches from the wall and base block interface.
- *SGmCnV/H*: concrete strain gage near longitudinal bar “m”. The middle of the gage is “n” inches from the wall and base block interface. “V” denotes gages oriented vertically, and “H” denotes gages oriented horizontally.
- Most bonded strain gauges were TML type FLA-6-11 installed with CN adhesive. “PY” is appended to the names of post-yield gauges, which were TML type YFLA-5 installed with CNY adhesive. Embedded concrete gauges were TML type PML-60.

### String Pots:

- Global displacement: SP(N, S, E, W, or SW)(X or Y)*n* - Global deformation of the wall measured to the reference frame at the top of each story level. N, S, E, W or SW indicates the location on the section (flange tip [N or S], web tip [W], or middle of flange [E] or web [SW]) being measured, X & Y are used to indicate the direction of string pots measuring in the X & Y coordinates of the MAST system for the north and south flange tips or the non-orthogonal orientation used to indicate the directions of the string pots measuring the web tip and middle of web (which are not aligned with the MAST coordinate system). “n” indicates the nominal height above the base block.
- Vertical deformations: SP(L or M or R)*n*(B or T) – L, M, and R distinguish string pots at the left edge, middle, or right edge of the wall element determined looking at the wall. “n” is the story number, with 1 at the bottom of the wall and 4 at the top. B and T are used to distinguish the sub-panels of panel 1.
- Horizontal deformations: SP(L or R)H*m* – L and R distinguish the left and right halves near the bottom of the wall. “m” is the approximate vertical location of the string pot in inches, measured from the wall and base block interface.
- Diagonal deformations, bottom panel: SP(L or R)(T or B)*angle* – L, R, T, & B are used to distinguish the four sub-panels (left-top, right-top, left-bottom, right-bottom). The angle is the approximate angle of the string in degrees, where 0° corresponds to horizontal, and counter-clockwise rotations are positive.

## LVDTs:

- L(F or W) $n$ (L or S): F and W indicate attachment to Flange and Web. “ $n$ ” is the nominal horizontal distance from the south edge of the wall to the LVDT attachment. L denotes long ( $\pm 1$ ” stroke) LVDTs, and S denotes short ( $\pm 1/2$ ” stroke) LVDTs.
- L1(S or W)(L or M or R): S and W indicate attachment to South and West faces of the web and flange, respectively, and L, M, and R indicate Left, Middle, and Right edges of the panel. These LVDTs measured the vertical displacements of the lowest studs relative to the base block.
- LB $n$ : “ $n$ ” is the number of the bar the LVDT was attached to. These LVDTs measured slip of the bar out of the base block.
- L(N, S, E)Up measured any uplift of base block North, South, and East tips from floor.
- L(F or W)(F or C)Slip measured any relative slip between Flange or Web of base block relative to Floor or top block relative to Crosshead.

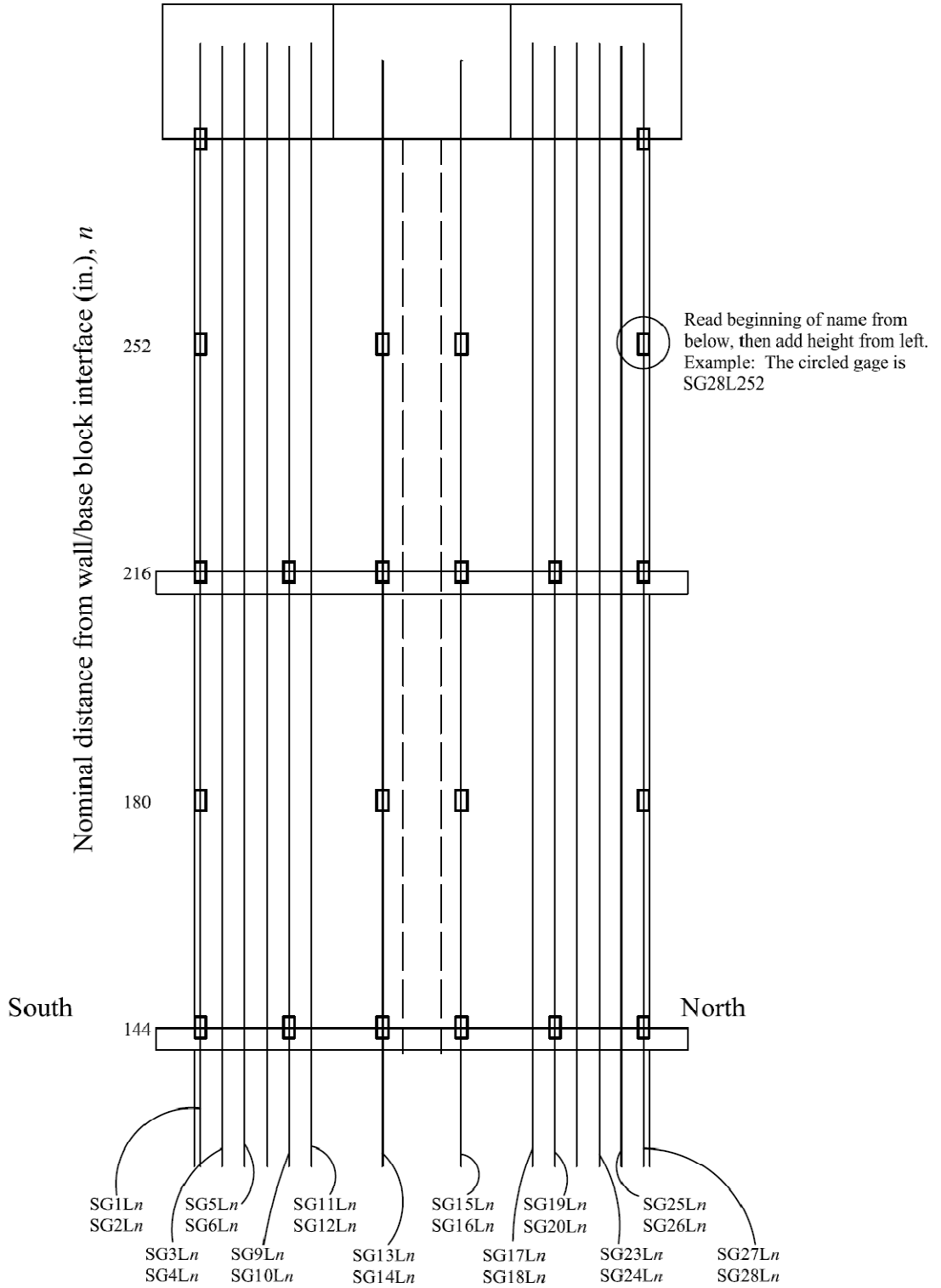
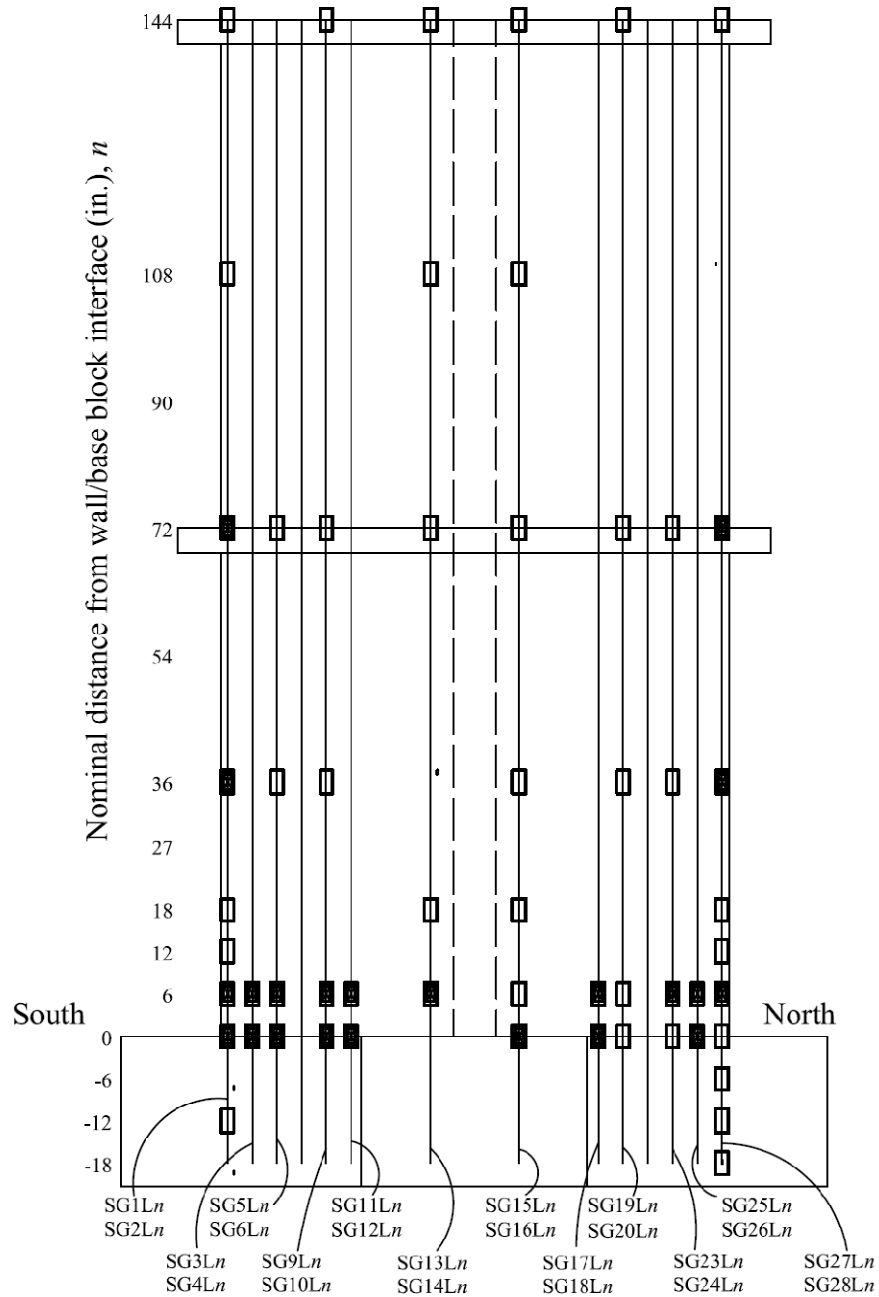


Figure B.2. Strain gauge naming scheme: NTW1 flange longitudinal bars, 3rd and 4th stories



☒ Gauge on both bars at this location

□ Gauge on one bar at this location

Figure B.3. Strain gauge naming scheme: NTW1 flange longitudinal bars, 1st and 2nd stories

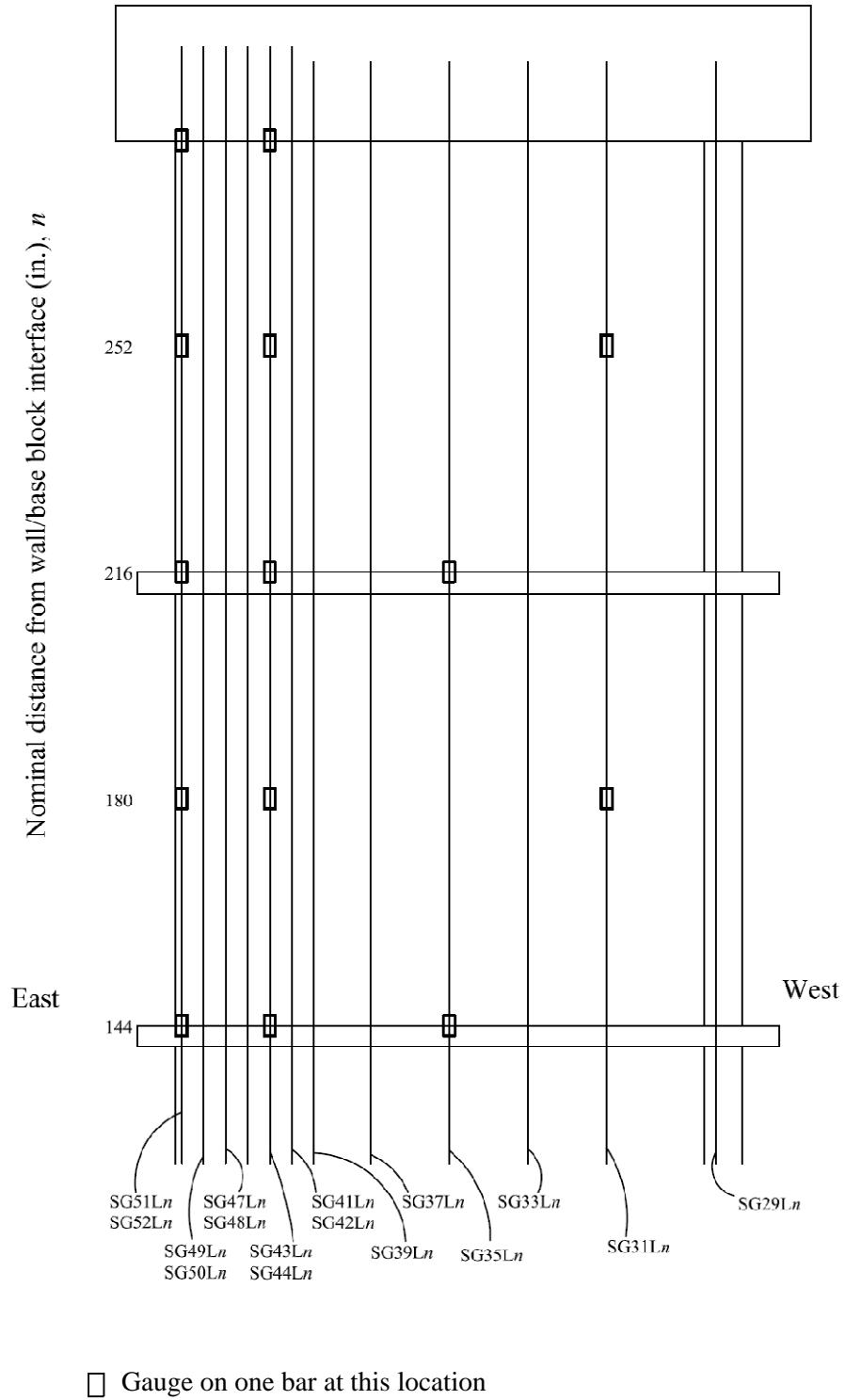
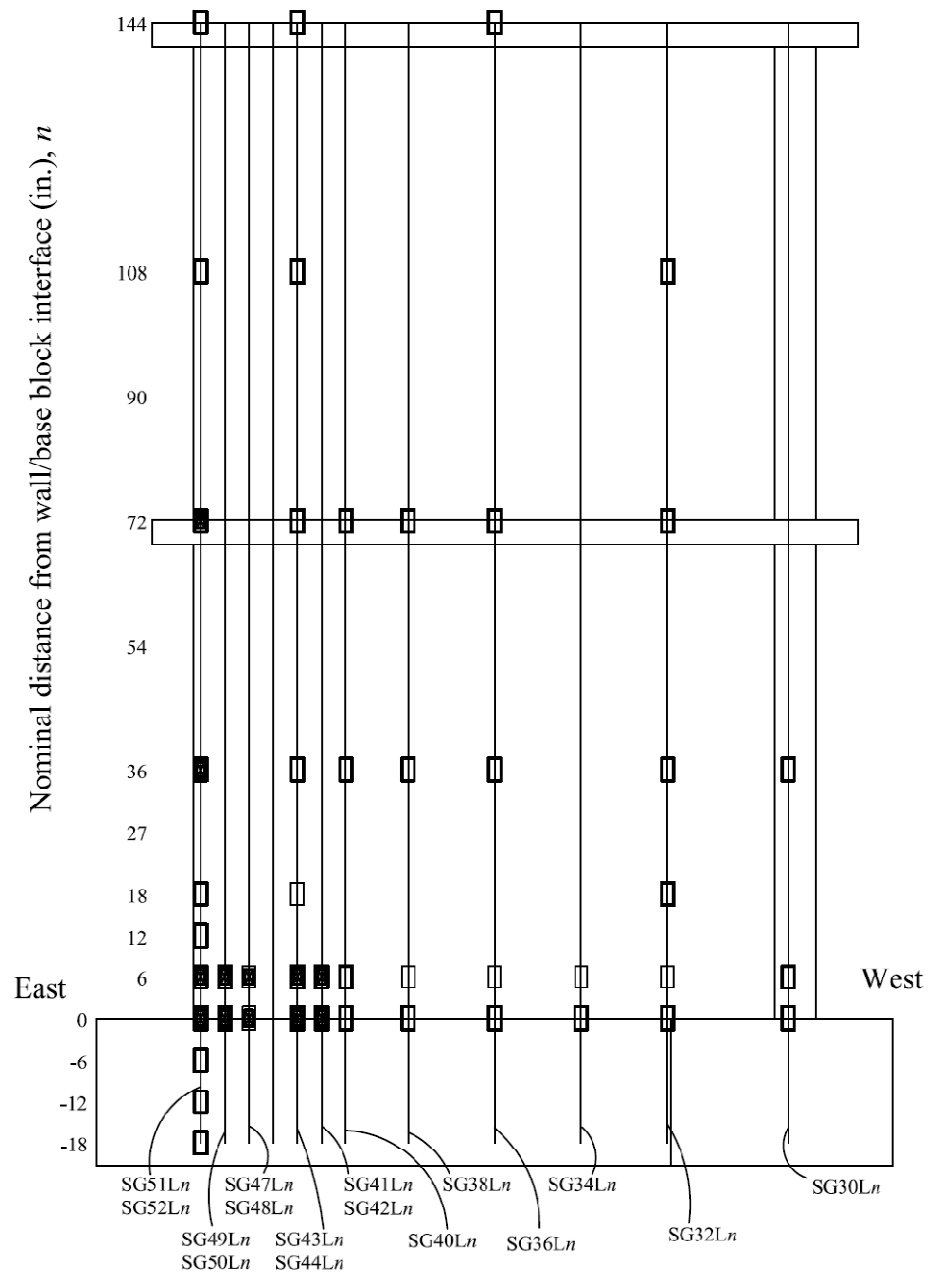


Figure B.4. Strain gauge naming scheme: NTW1 web longitudinal bars, 3rd and 4th stories



☒ Gauge on both bars at this location

□ Gauge on one bar at this location

Figure B.5. Strain gauge naming scheme: NTW1 web longitudinal bars, 1st and 2nd stories

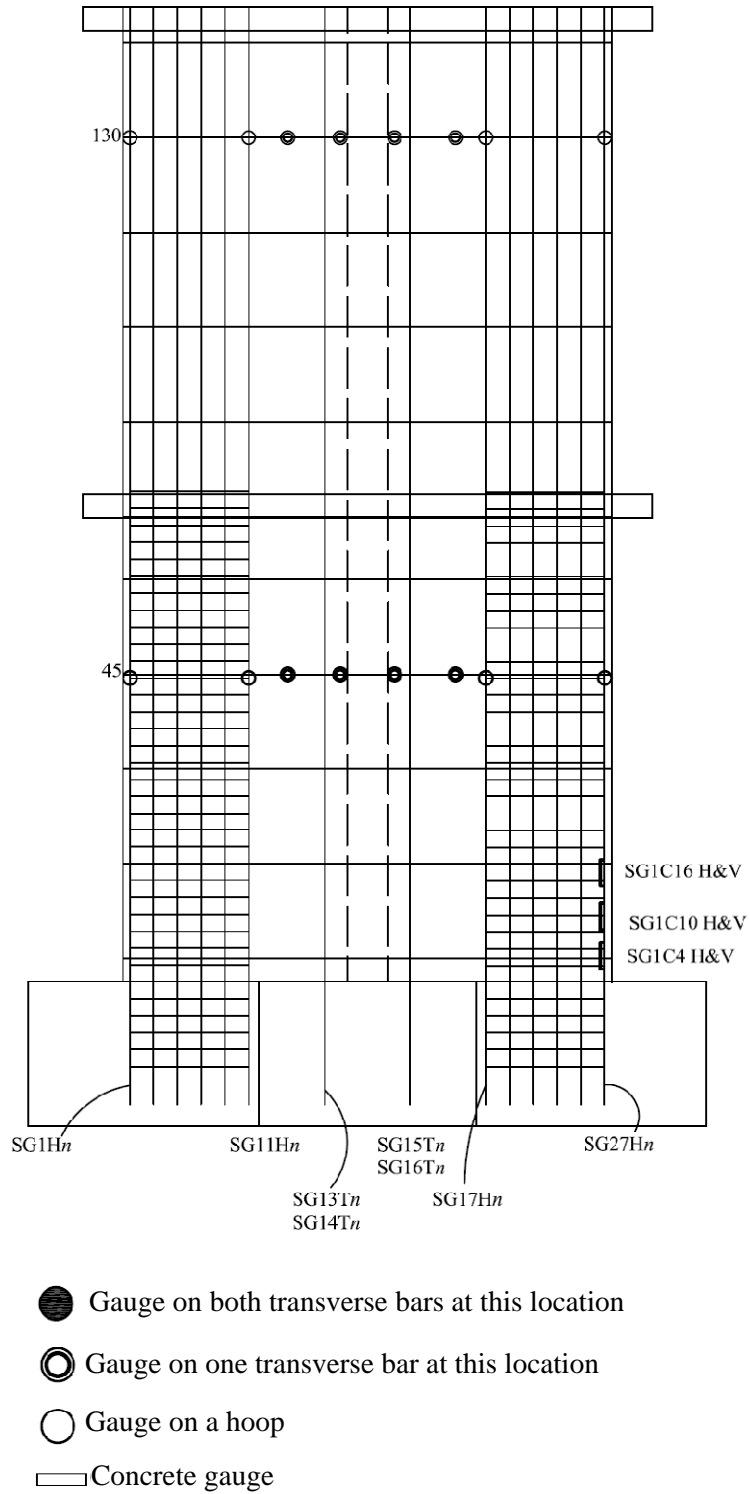
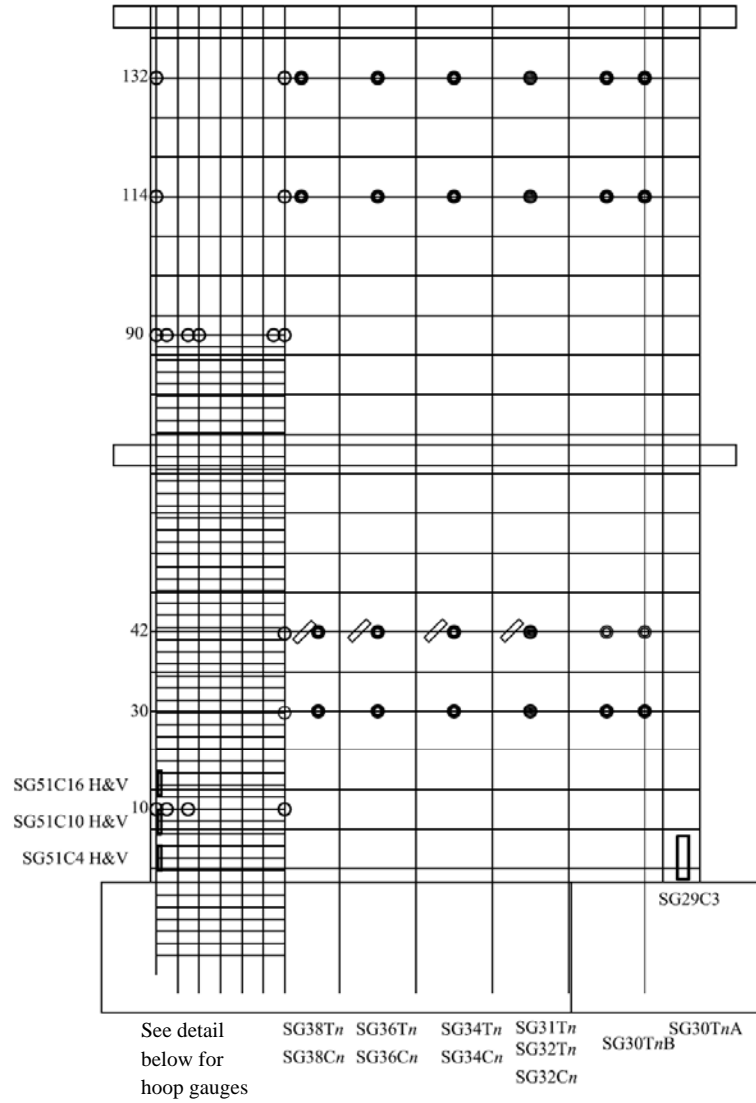


Figure B.6. Strain gauge naming scheme: NTW1 flange transverse, hoop, and concrete, 1st and 2nd stories



- Gauge on both transverse bars at this location
- ⊙ Gauge on one transverse bar at this location
- Gauge on a hoop
- ▭ Concrete gauge

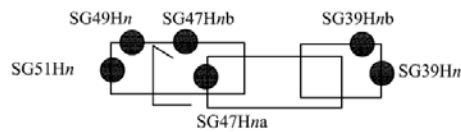


Figure B.7. Strain gauge naming scheme: NTW1 web transverse, hoop, and concrete, 1st and 2nd stories

Table B.1. NTW1 longitudinal strain gauge as-built locations

Bar ( <i>m</i> )	Distance above base block (in.)													
Nom. <i>n</i>	-12	-6	0	6	12	18	36	72	108	144	180	216	252	282
1	-13 ½	-7 ½		4 ½	11 ¾	16 ½	34 ¾	70 ½	105 ½			213 ½		282
2				3 ½			33 ¾							
3			-2 ¾				33	69 ½						
4			-2 ½	3 ½								213 ½		
5				3 ½				69 ½		141 ½				
6			-1 ¾											
9			-1 ½	4 ½				70 ½						
10			-3 ¾	2 ¼										
11			-1 ½	4 ½										
12				4 ¼										
13				3 ½		18 ½	34	70 ½	103 ½	141 ½		213 ½		
15			-3				33		105 ½					
16			-¾	5 ¼										
17			-2	4										
18			-2 ¾	3 ¼										
19				4 ¼			34 ½	70				213 ¼		
20				4 ¾										
23			-1 ½	4 ½				70 ½						
24				4 ¾										
25				4										
26			-4	2										
27				4	12	16 ½	34 ¼	70 ½		142 ¼		213 ¼	249	282
28			-1 ¾				34	70						
32				0	6		36	71 ¾						
36					6 ½		36 ¼	72 ¾		143 ¾				
38					6		36 ¾							
40				0	6									
41					6									
42				¼	6 ¼									
43				-1	5									
44			-1 ½	4 ½		18	34 ¾	70 ½	106 ¾	143				282 ¼
48				0	6									
50				-1										
51				-1 ¼			35 ¼	71						
52		-6 ¼	-¾	5 ¼	12	17 ½	35 ½	71 ¾		143 ¼	178 ½	215	249 ½	282

Table B.2. NTW1 horizontal bar strain gauge as-built locations

Face	Bar location above base (in.)	Distance from north flange tip to gauge (in.)								
		nominal (n)	measured	m=13	14	15	16			
Flange	West	45	45 ¼	22	31	39	47 ½			
		130	124 ¼	24 ¼	32 ¾	39 ¾	49			
				Distance from web tip to gauge (in.)						
Web		nominal (n)	measured	m=38	36	34	32	31	30	
	North	30	26 ¾	27 ½	38 ¼	51	62 ½	75 ¼	82 ¼	
	South	30	27				61 ½			
	North	42	39 ½	28 ½	38 ¼	51	62 ¾	76 ¾	82 ½	
	South	42	39				62			
	North	114	106 ½	28	40	52	64	77	84	
	South	114	106 ½				62			
	North	132	134 ¼	28	39	51	64	77	84	
	South	132	134 ¼				62			

Table B.3. NTW1 confinement steel strain gauge as-built locations

Hoop	Gauge Height from Base Block (in.)				
<i>m</i>	39a	39b	47	49	51
	Web Tip				
<i>n</i> =10	11 ⅜	11 ½	11 ½	10 ⅛	10 ¼
<i>n</i> =30	28	n/a	n/a	n/a	n/a
<i>n</i> =42	39	n/a	n/a	n/a	n/a
<i>m</i>	1 & 11	n/a	n/a	n/a	11 & 17
North Flange Tip <i>n</i> =45	44 ¾	n/a	n/a	n/a	44 ¾
South Flange Tip <i>n</i> =45	46	n/a	n/a	n/a	46

Table B.4. NTW1 embedded concrete gauge as-built locations

Orientation	Location	Vertical Distance above Base Block (in.)			
		3	4	10	16
Vertical	Nominal <i>n</i>				
	North Flange Tip ( <i>m</i> =1)		4 ¼	10	16 ¼
	Center of Flange ( <i>m</i> =29)	7 ¾			
	Web Tip ( <i>m</i> =51)		5 ½	11 ½	17
Horizontal	Web Tip ( <i>m</i> =51)		5 ¼	11 ½	17
		Horizontal Distance from Web Tip (in.)			
Diagonal	<i>m</i>	38	36	34	32
	Nominal <i>n</i> =42, as-built 40 in. above base block	31 ¼	40 ½	55 ¾	67 ¾



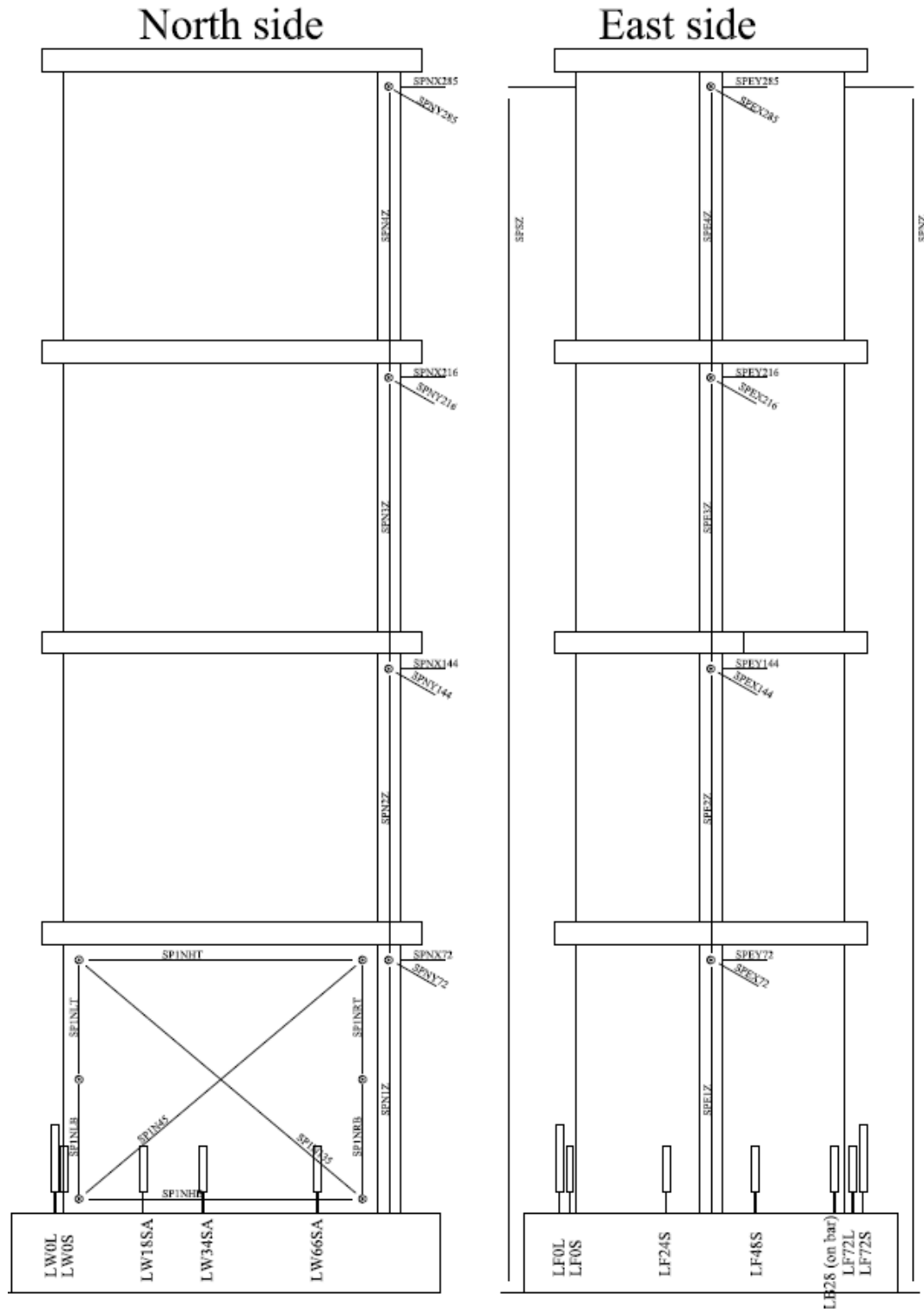


Figure B.9. NTW1 string pot and LVDT arrangement: north face of web and east face of flange

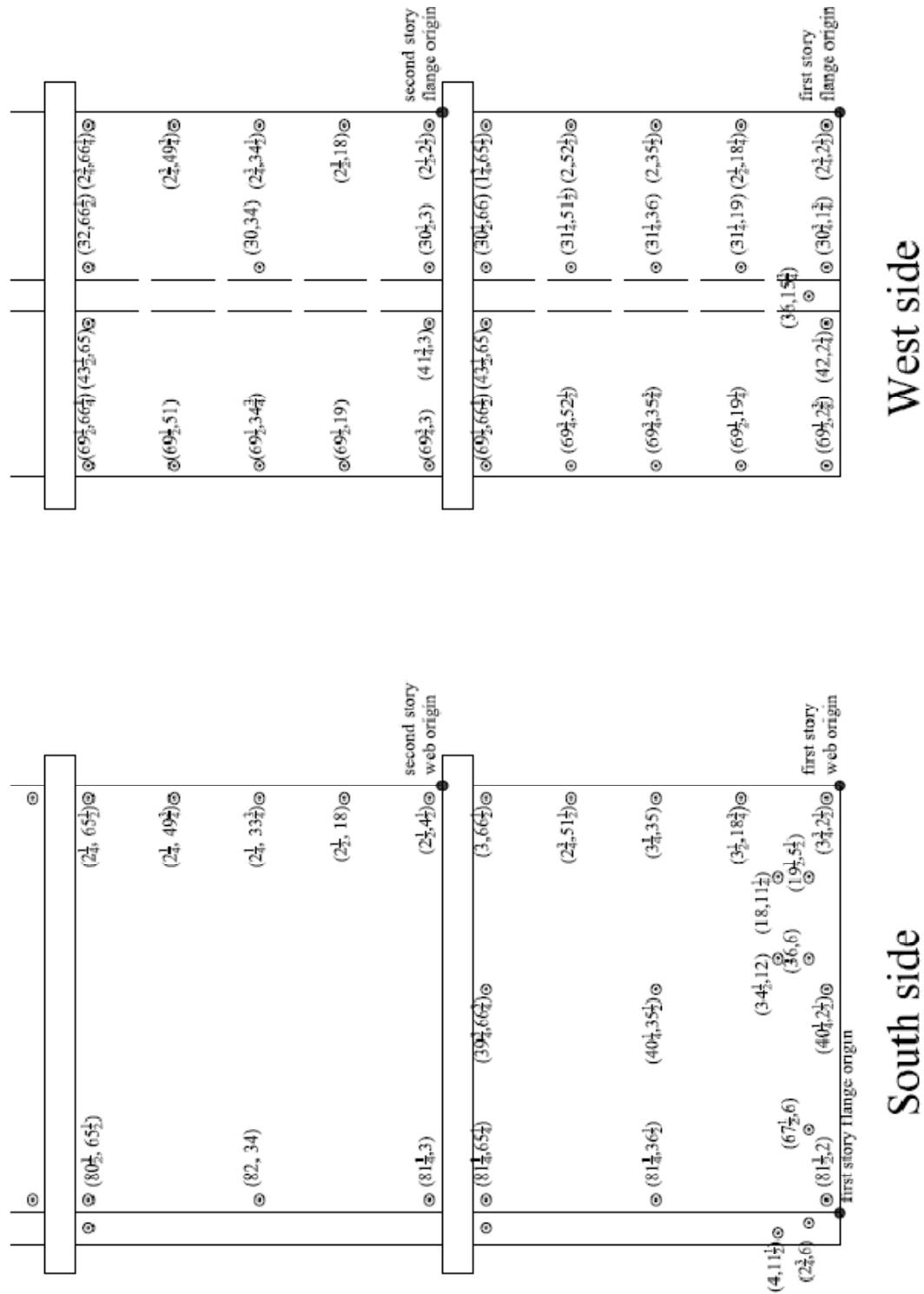


Figure B.10. NTW1 as-built string pot and LVDT mounting locations, Stories 1 & 2 south and west faces. Studs on each face are measured relative to indicated origins.

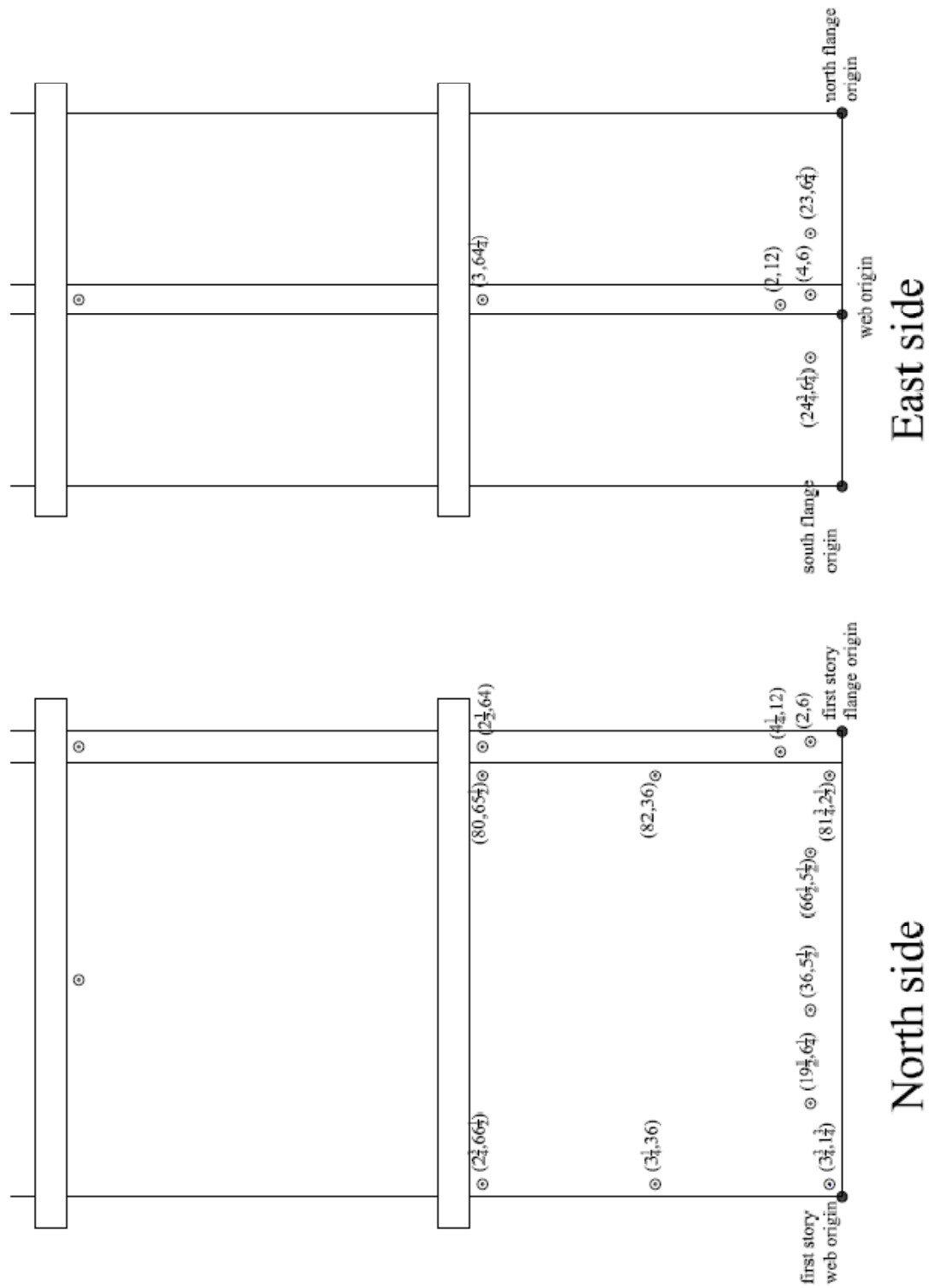


Figure B.11. NTW1 as-built string pot and LVDT mounting locations, Stories 1 & 2, north and east faces. Studs on each face are measured relative to indicated origins.

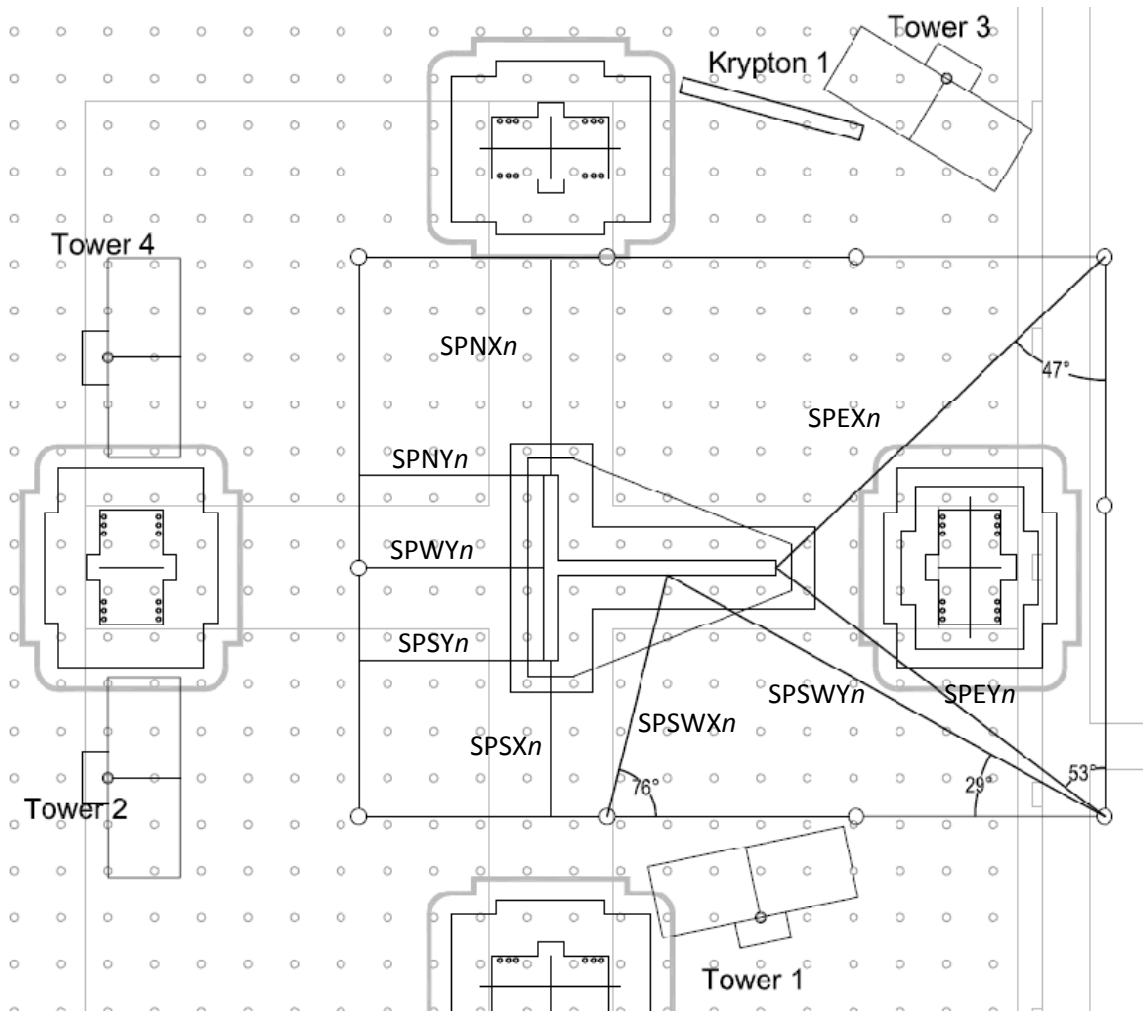
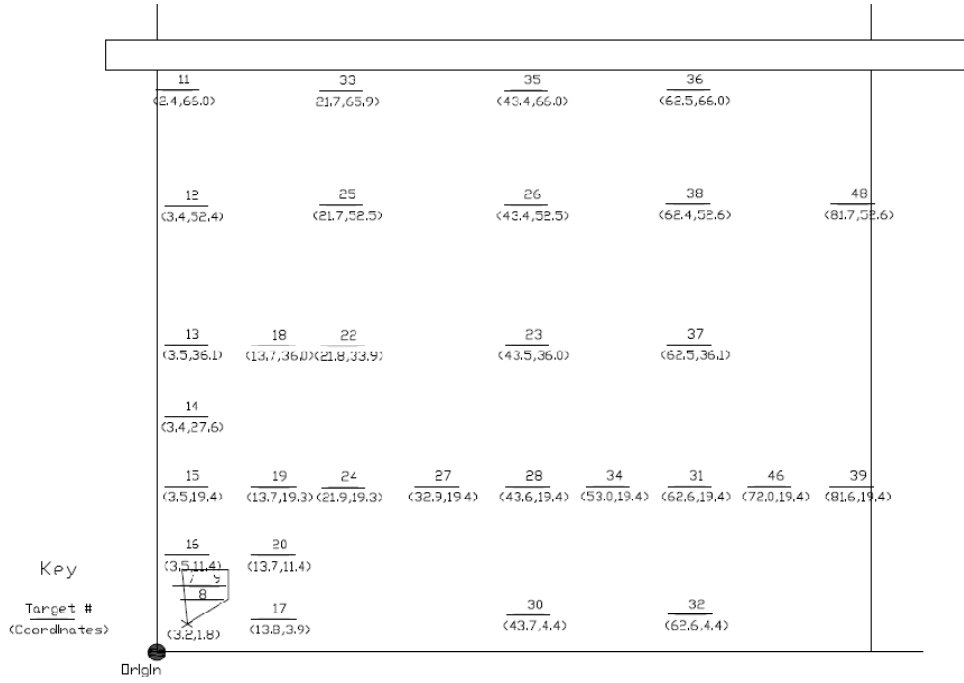


Figure B.12. NTW1 plan view showing locations of external instruments.

### Web



### Flange

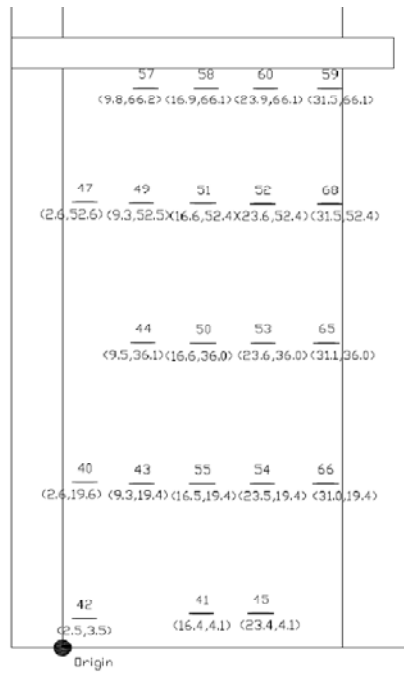


Figure B.13. NTW1 Krypton as-built target locations. LEDs on each face are measured relative to indicated origins

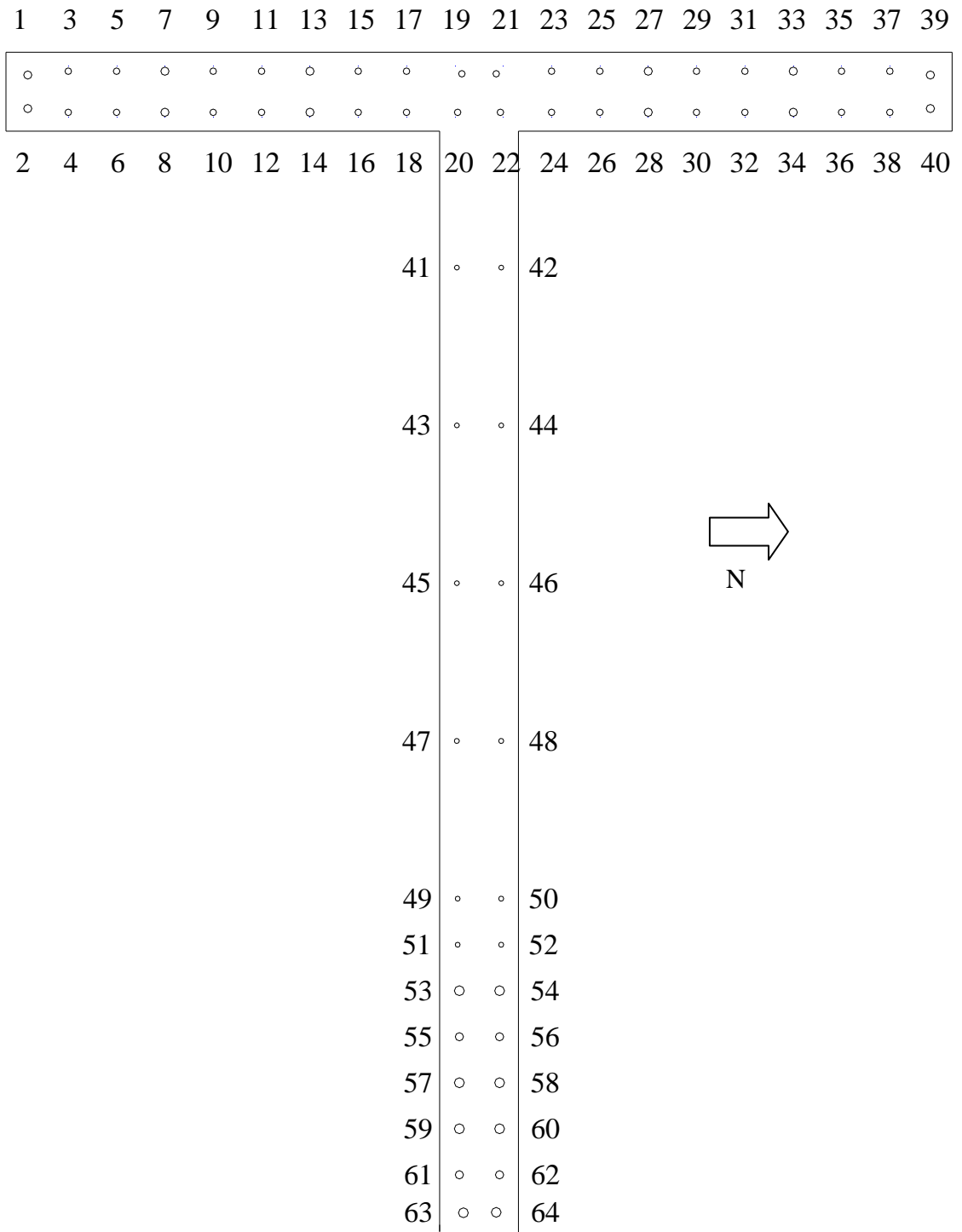


Figure B.14. NTW2 longitudinal bar numbering scheme

## NTW2 Instrumentation Naming Scheme

### Strain Gages:

- *SGmLn*: strain gage above the base block on longitudinal bar “m” at a nominal distance of “n” inches from the wall and base block interface.
- *SGmMn*: strain gage inside the base block on longitudinal bar “m” at a nominal distance of “n” inches from the wall and base block interface.
- *SGmHn*: strain gage on the hoop reinforcement near longitudinal bar “m”. The hoop is located at “n” inches from the wall and base block interface.
- *SGmTn*: strain gage on the transverse shear reinforcement near longitudinal bar “m”. The transverse bar is located at “n” inches from the wall and base block interface.
- *SGmCnV/H*: concrete strain gage near longitudinal bar “m”. The middle of the gage is “n” inches from the wall and base block interface. “V” denotes gages oriented vertically, and “H” denotes gages oriented horizontally.
- Most bonded strain gauges are TML type FLA-6-11 installed with CN adhesive. “PY” is appended to the names of post-yield gauges, TML type YFLA-5 installed with CNY adhesive. Embedded concrete gauges are TML type PML-60.

### String Pots:

- Global displacement: SP(1 or 2)(N, S, or E)(X, Y, U, or V) - Global deformation of the wall measured to the reference frame at the top of each story level. 1 or 2 indicates the story level, N, S, or E indicates the flange tip or web tip being measured, X & Y were used to indicate the direction of string pots measuring in the X & Y coordinates of the MAST system for the north and south flange tips (positive X direction is south, positive Y direction is east), U & V are used to indicate the directions of the string pots measuring the web tip (which were not aligned with the MAST coordinate system; positive U direction was southeast, positive V direction was northeast).
- Vertical deformations: SP(1 or 2)(N, S, E, W, NM, SM, or WM)*q* – 1 or 2 indicate the story level of the wall that the instrument was on. The direction (N, S, E, W, NM, SM, or WM) indicates the location of the instrument on the wall: North flange tip, South flange tip, East web tip, West end of web, North Middle of flange, South Middle of flange, or Web Middle. “*q*” is the quarter of the story level measured by the instrument, with 1 st the bottom and 4 at the top of each story.
- Horizontal deformations: SP(1 or 2)(N, S, E, or W)*Hm* – 1 or 2 indicate the story level of the wall that the instrument was on. The direction (N, S, E, W) indicates the location of the instrument on the wall: North half of flange, South half of

flange, East half of web, West half of web. “m” is the approximate vertical location of the string pot in inches on the story, measured from the wall and base block interface for the first story, and the top of the slab for the second story.

- Diagonal deformations, bottom panel: SP(1 or 2)(N, S, E, or W) *angle*(T or B) – 1 or 2 indicate the story level of the wall that the instrument was on. The direction (N, S, E, W) indicates the location of the instrument on the wall: North half of flange, South half of flange, East half of web, West half of web (or entire Web for story 2). The angle is the approximate angle of the string in degrees, where 0° corresponds to horizontal, and counter-clockwise rotations are positive. T or B indicate whether the instrument is on the Top or Bottom half of the wall.

### LVDTs:

- L(F or W)*n*(L or S): F is the flange, W is the Web, “n” is the nominal horizontal distance from the south end of the flange or the east end of the web to the LVDT attachment. L denotes long ( $\pm 1$ ” stroke) LVDTs attached 12” above the base block, and S denotes short ( $\pm 1/2$ ” stroke) LVDTs attached 6” above the base block
- Vertical deformations: L(1 or 2)(N, S, E, W, NM, SM, or WM)*q* – 1 or 2 indicate the story level of the wall that the instrument was on. The direction (N, S, E, W, NM, SM, or WM) indicates the location of the instrument on the wall: North flange tip, South flange tip, East web tip, West end of web, North Middle of flange, South Middle of flange, or Web Middle. “q” is the quarter of the story level measured by the instrument, with 1 st the bottom and 4 at the top of each story.
- LBaseUN, LBaseUS, LBaseUE, LTopUN, LTopUS, LTopUE, LTopSF, and LTopSW measure any uplift (U) or slipping (S) between the specimen and the strong floor (Base) or the top block (Top) at the given location (North flange tip, South flange tip, East web tip, slip of Flange or Web)
- LSlip*n*: These LVDTs measure slip of the bar out of the base block at bar *n*.
- LSplice*n*(B or T)(a or b): These LVDTs measured relative movement of the bars at the splice between the attachment point on the bar and the top of the slab. *n* is the number of the bar, B or T indicates which half of the splice it is: the bottom (anchored in the base block and terminating somewhere in the 2<sup>nd</sup> story level) or the top (beginning at the top of the slab and anchored in the top block), a indicates that the instrument is attached just above the slab, b indicates that the instrument is attached just below the point where the bar anchored in the base block is cut off.

### Krypton:

- Two Krypton cameras were used in this test. One was viewing the first story level of the web from the north, and the other was viewing the first story level and a very small portion of the second story level of the flange from the west.

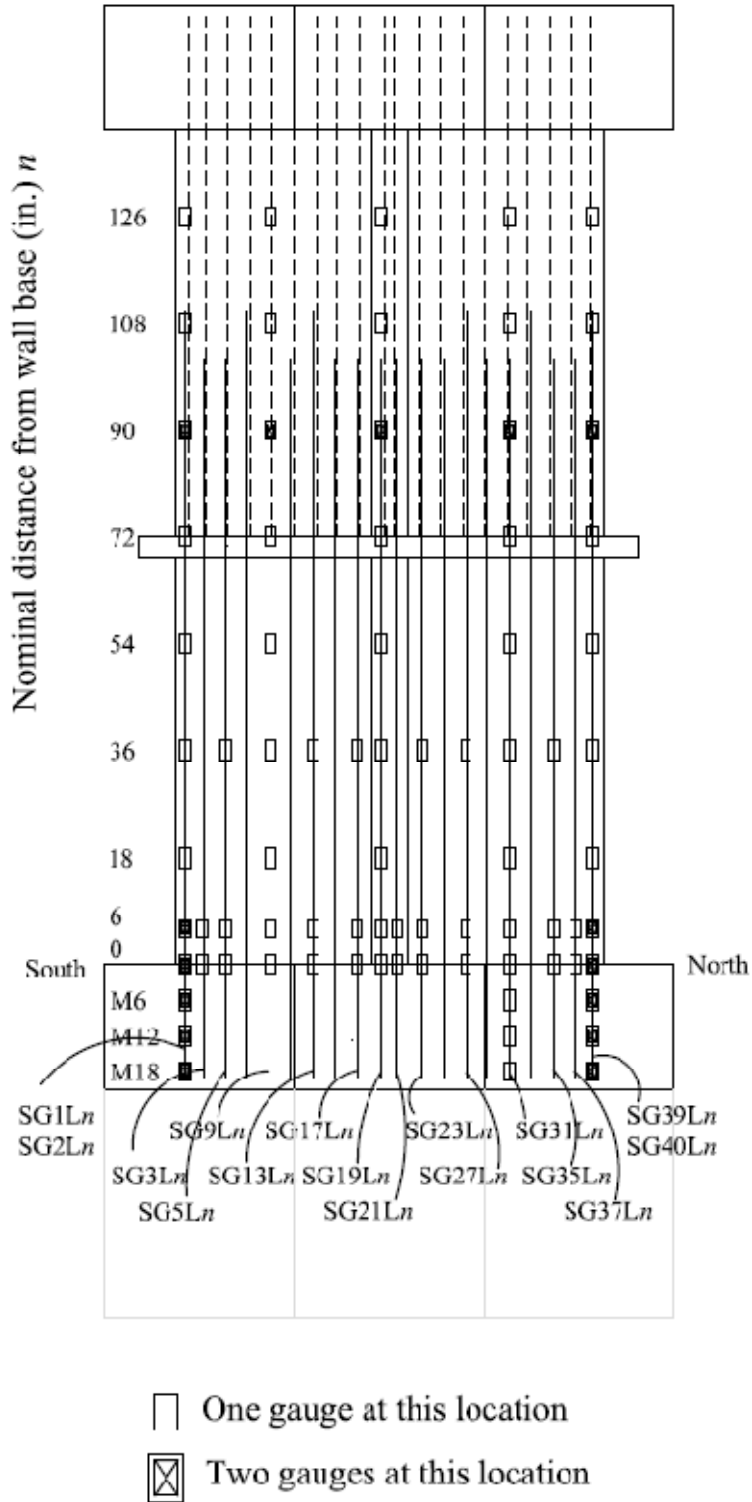


Figure B.15. Strain gauge naming scheme: NTW2 flange longitudinal bars

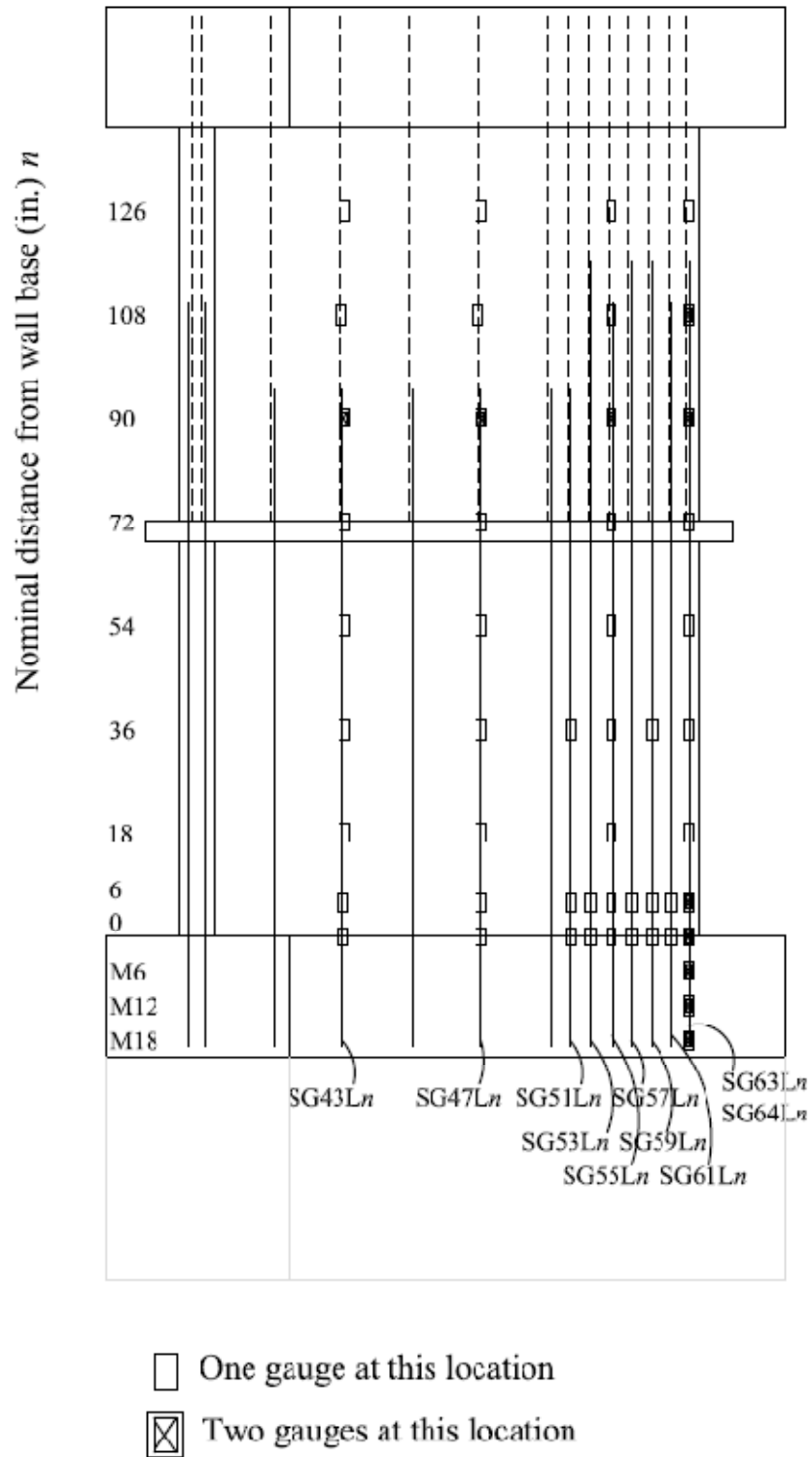
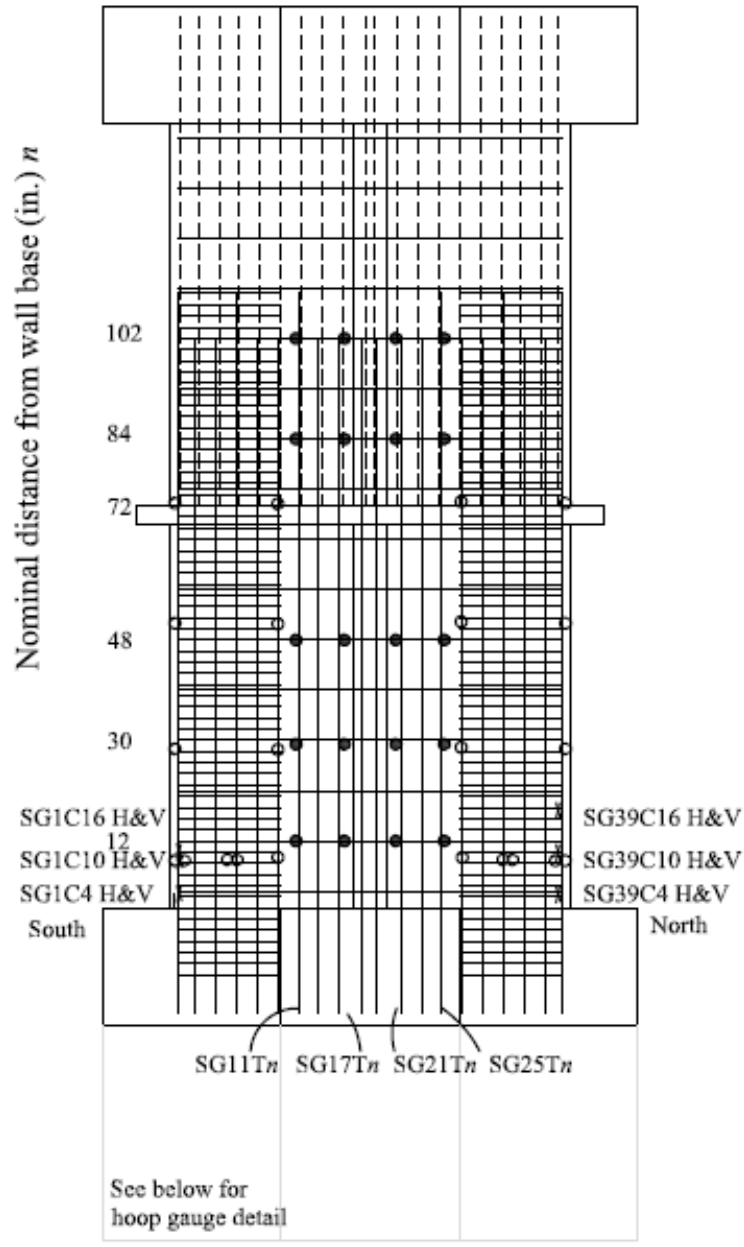


Figure B.16. Strain gauge naming scheme: NTW2 web longitudinal bars



● Gauge on horizontal steel    ○ Gauge on hoop  
 × Concrete gauge

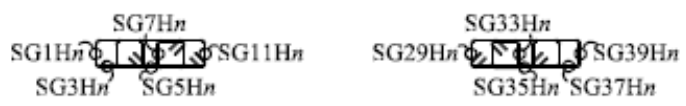


Figure B.17. Strain gauge naming scheme: NTW2 flange transverse, hoop, and concrete gauges

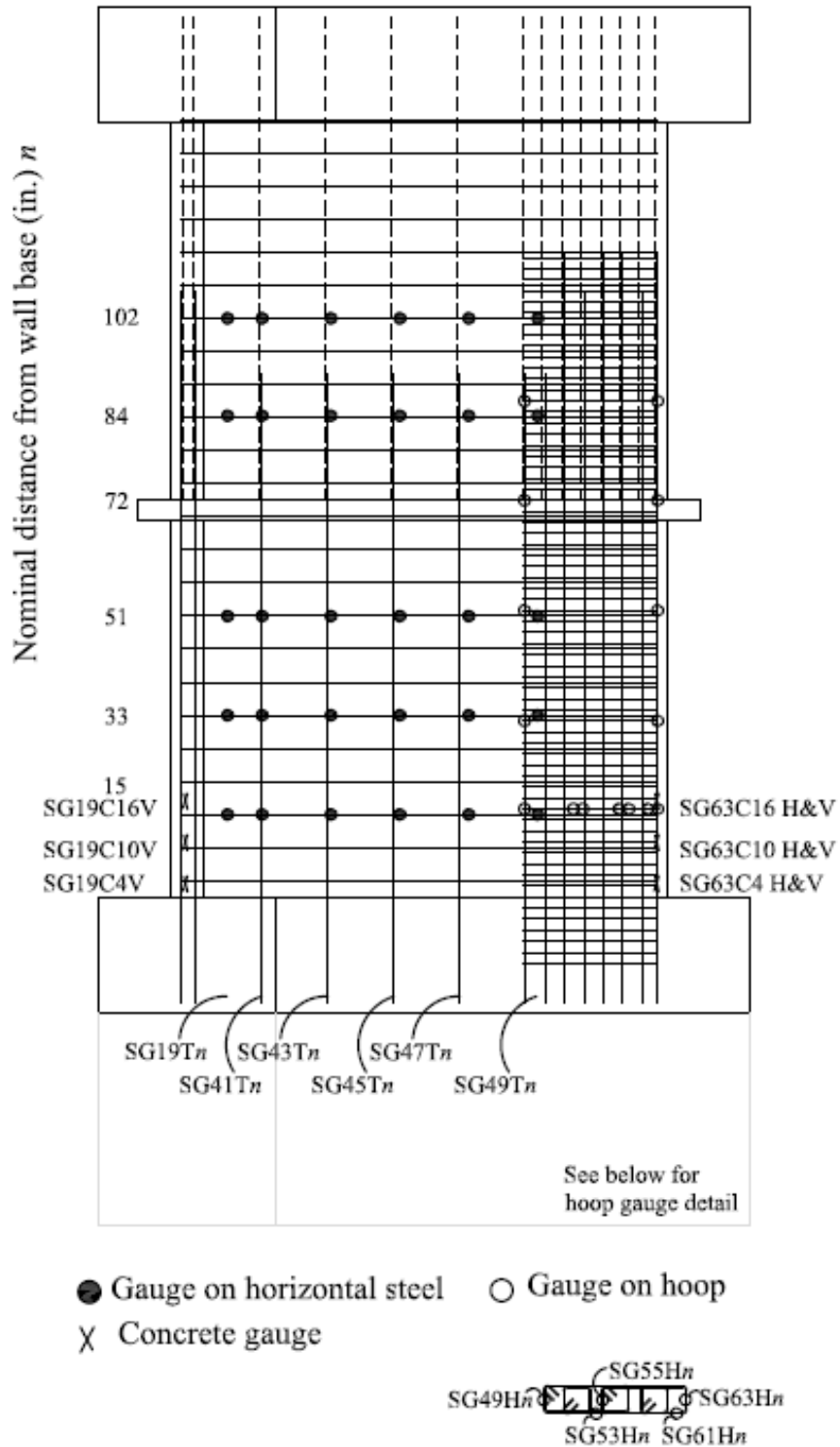


Figure B.18. Strain gauge naming scheme: NTW2 web transverse, hoop, and concrete gauges

Table B.5. NTW2 longitudinal strain gauge as-built locations

Bar <i>m</i>	Distance above base block (in.)									
	<i>n</i>	0	6	18	36	54	72	90	108	126
1b*	-1	5	15 ½	33 ½	52	69 ½	88			
1t**							90	108	126	
2b	-1 ½	4 ½								
3b	-2	4								
5b	-2	4		34						
9b	-2	4	16	34	52	70	88			
9t							90	108	128	
13b	-4	4		34						
17b	-2	4		34						
19b	-2	4	15	33	51	70	88			
19t							90	108	126	
21b	-2	4								
23b	-2	4		33						
27b	-2	4		34						
31b	-2	4	15	32	52	68	87			
31t							89	108	126	
35b	-2	4		34						
37b	-2	4								
39b	-2	4	15	33	52	68	87			
39t							90	108	126	
40b	-2	4								
43b	-2	4	15	33	51	69	87			
43t							90	108	126	
47b	-2	4	15	33	51	69	87			
47t							90	108	126	
51b	-1	5		32						
53b	-1	5								
55b	-2	4	16	34	52	69	87			
55t							88	107	125	
57b	-2	4								
59b	-2	4		35						
61b	-2	4								
63b	-2	4	16	34	53	70	87	104		
63t							89	107	125	
64b	-1	5								

\*b = bottom bar segment (anchored in foundation block)

\*\*t=top bar segment

Table B.6. NTW2 horizontal bar strain gauge as-built locations

	Face	Bar location above base (in.)		Distance from north flange tip to gauge (in.)					
		nominal ( <i>n</i> )	measured	<i>m</i> =11	17	21	25		
Flange	West	12	14	49 ½	40 ½	31 ½	22 ½		
		30	32	49 ½	41	31 ½	22 ½		
		48	48	49	40 ½	31 ½	22 ½		
		84	87	49	40 ½	31 ½	23		
		102	105	49	40 ½	31 ½	23		
				Distance from web tip to gauge (in.)					
Web	South	15	15	23 ½	36	48 ½	61	73 ½	79 ½
		33	32 ½	24	36 ½	48 ½	61	74	80
		51	51	23 ½	36	48 ½	61	73 ½	79 ½
		84	86	23 ½	36	48 ½	61	73 ½	80
		102	105 ½	24	36 ½	49	61 ½	74	80

Table B.7. NTW2 confinement steel strain gauge as-built locations

Hoop	Gauge Height from Base Block (in.)				
<i>m</i>	63	61	55	53	49
	Web Tip				
<i>n</i> =15	15	15	15 ½	15	16
<i>n</i> =33	33	n/a	n/a	n/a	33
<i>n</i> =51	50 ½	n/a	n/a	n/a	51 ½
<i>n</i> =72	74	n/a	n/a	n/a	74
<i>n</i> =84	91	n/a	n/a	n/a	91
<i>m</i>	1 & 39	3 & 37	5 & 35	7 & 33	11 & 29
	North Flange Tip				
<i>n</i> =12	15 ½	15 ½	15	16	15
<i>n</i> =30	33	n/a	n/a	n/a	34
<i>n</i> =48	49	n/a	n/a	n/a	50
<i>n</i> =72	74	n/a	n/a	n/a	74
	South Flange Tip				
<i>n</i> =12	14	14	13 ½	13 ½	13
<i>n</i> =30	34	n/a	n/a	n/a	33
<i>n</i> =48	50	n/a	n/a	n/a	50
<i>n</i> =72	74	n/a	n/a	n/a	74

Table B.8. NTW2 embedded concrete gauge as-built locations

Orientation	Location	Vertical Distance above Base Block (in.)		
		4	10	16
	Nominal $n$	4	10	16
Vertical	North Flange Tip ( $m=1$ )	7	12	18
	Center of Flange ( $m=19$ )	6	11	17
	South Flange Tip ( $m=39$ )	7	12 ½	18 ½
	Web Tip ( $m=63$ )	6	11 ½	17
Horizontal	North Flange Tip ( $m=1$ )	4	9 ½	15 ½
	South Flange Tip ( $m=39$ )	5	10	14 ½
	Web Tip ( $m=63$ )	3 ½	9	15

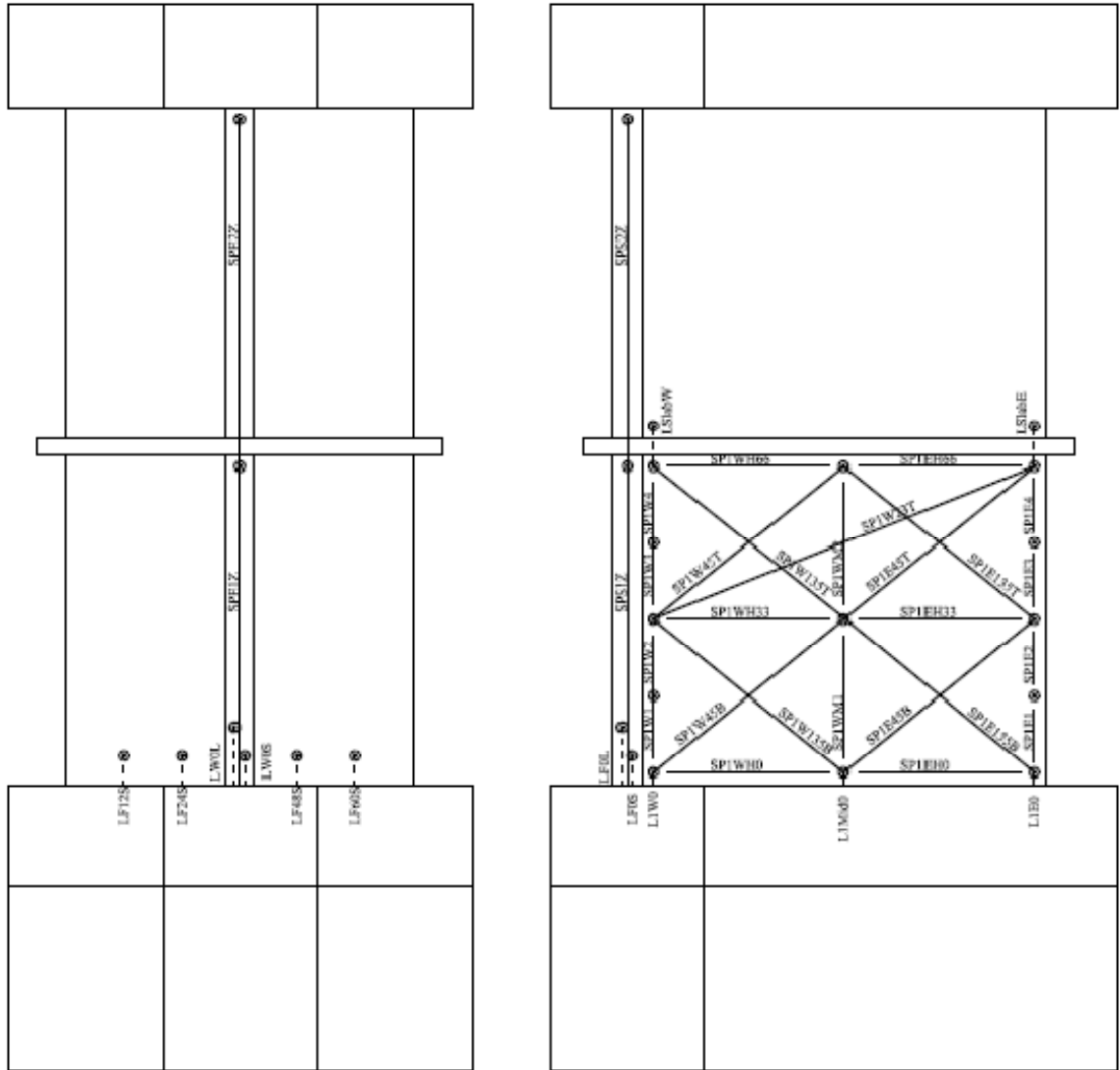


Figure B.19. NTW2 string pot and LVDT arrangement: south face of web and west face of flange

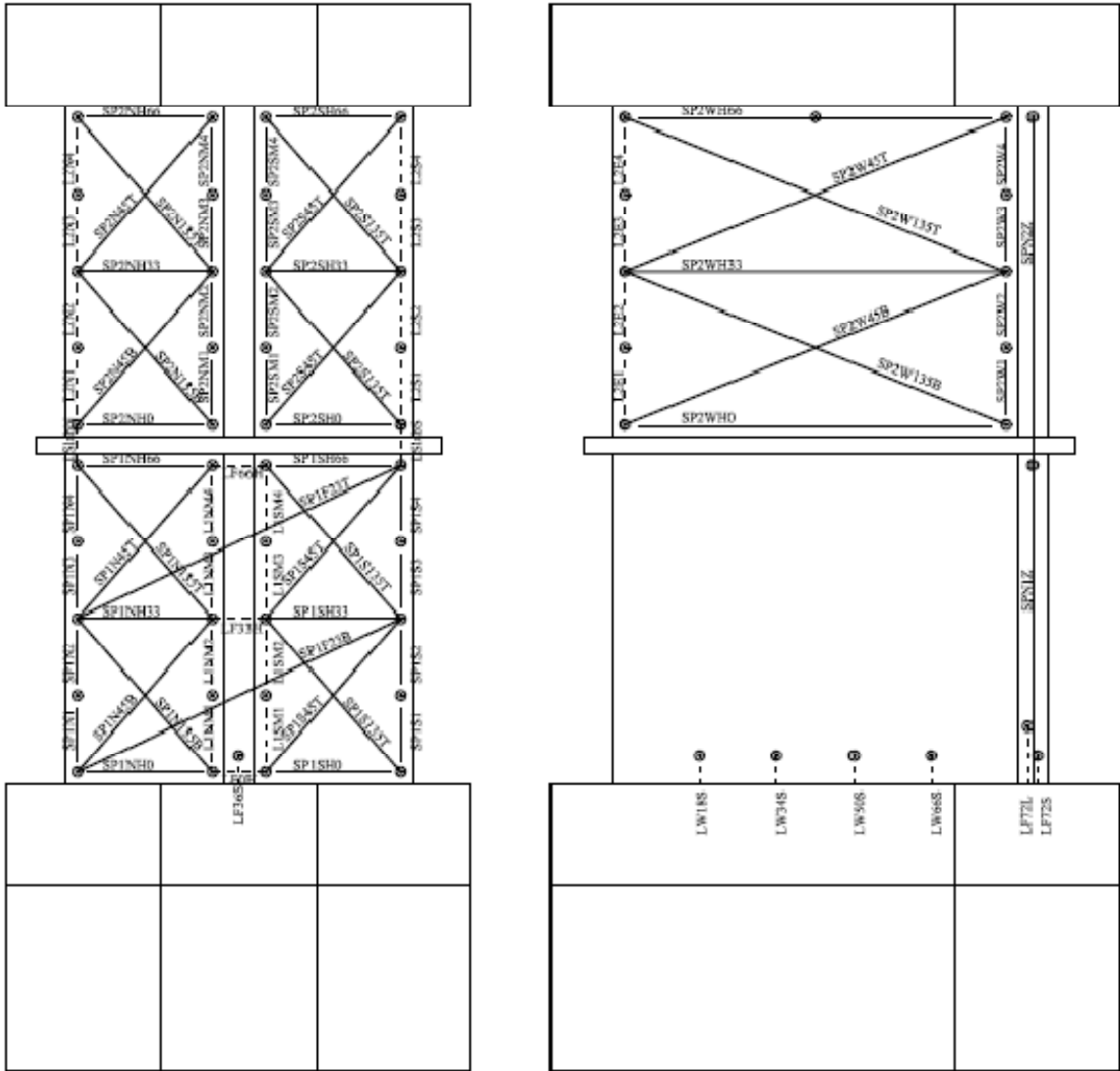


Figure B.20. NTW2 string pot and LVDT arrangement: north face of web and east face of flange

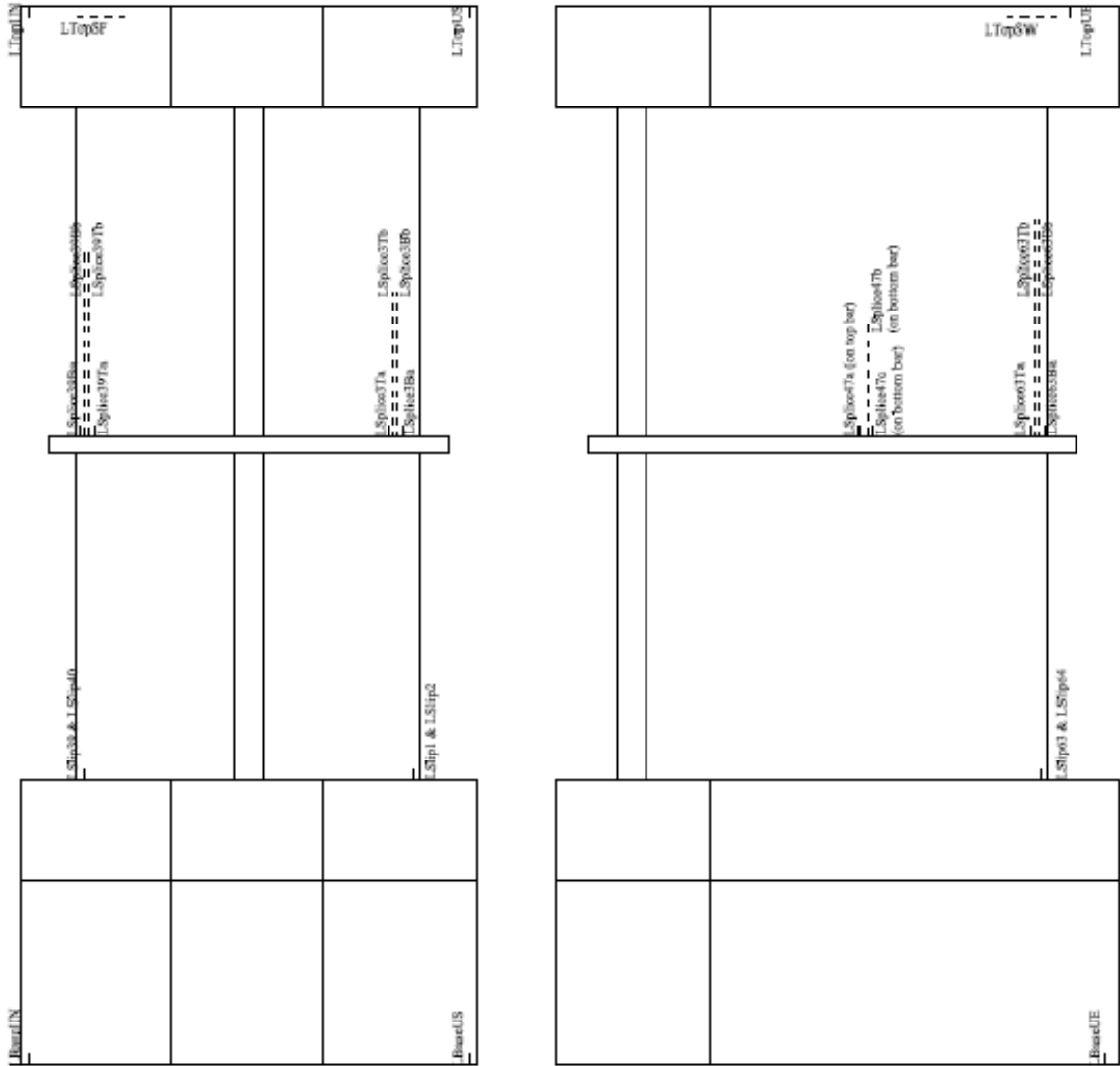


Figure B.21. NTW2 strain penetration and slip instruments: south face of web and west face of flange

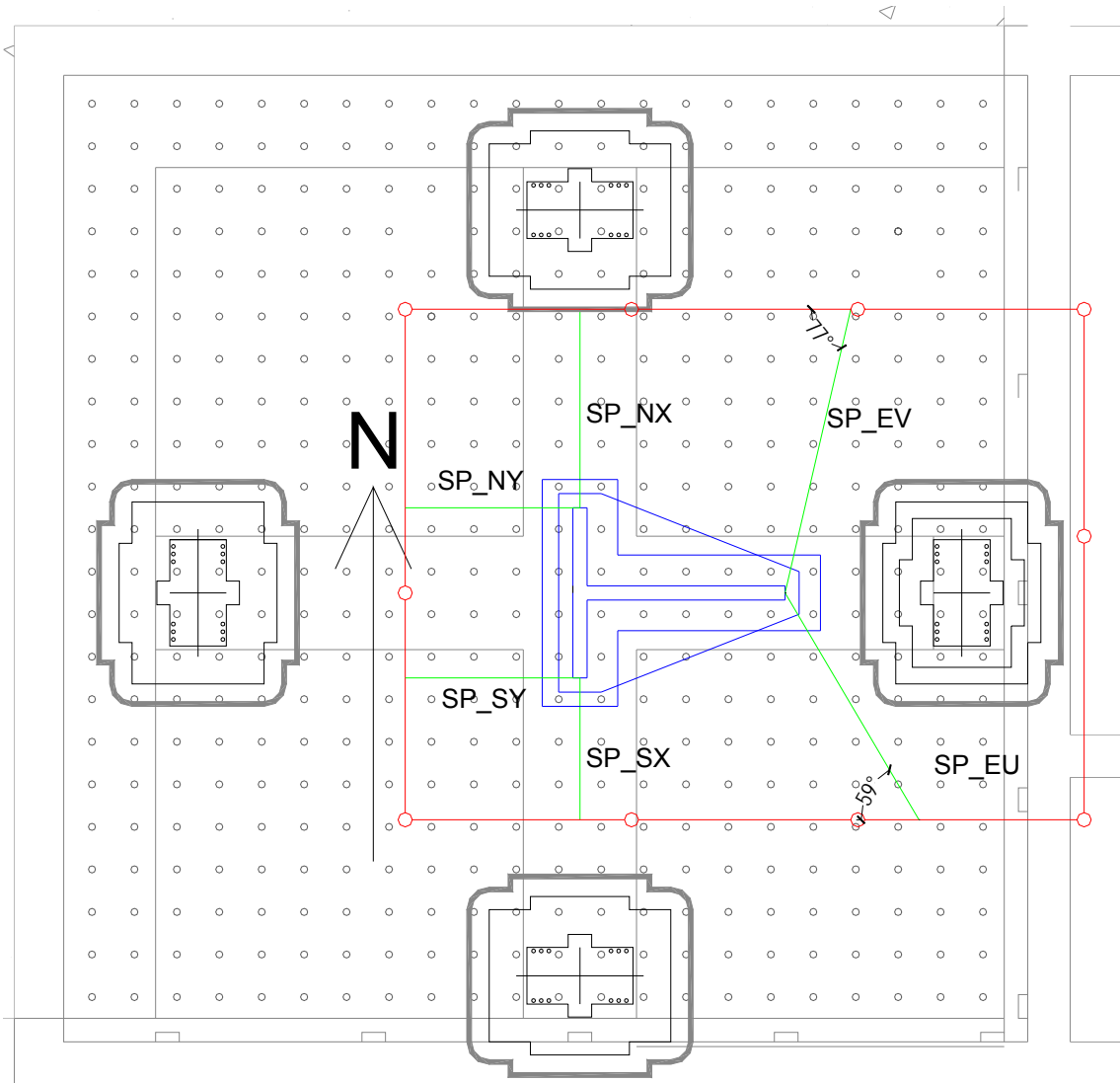


Figure B.22. NTW2 plan view showing locations of external instruments

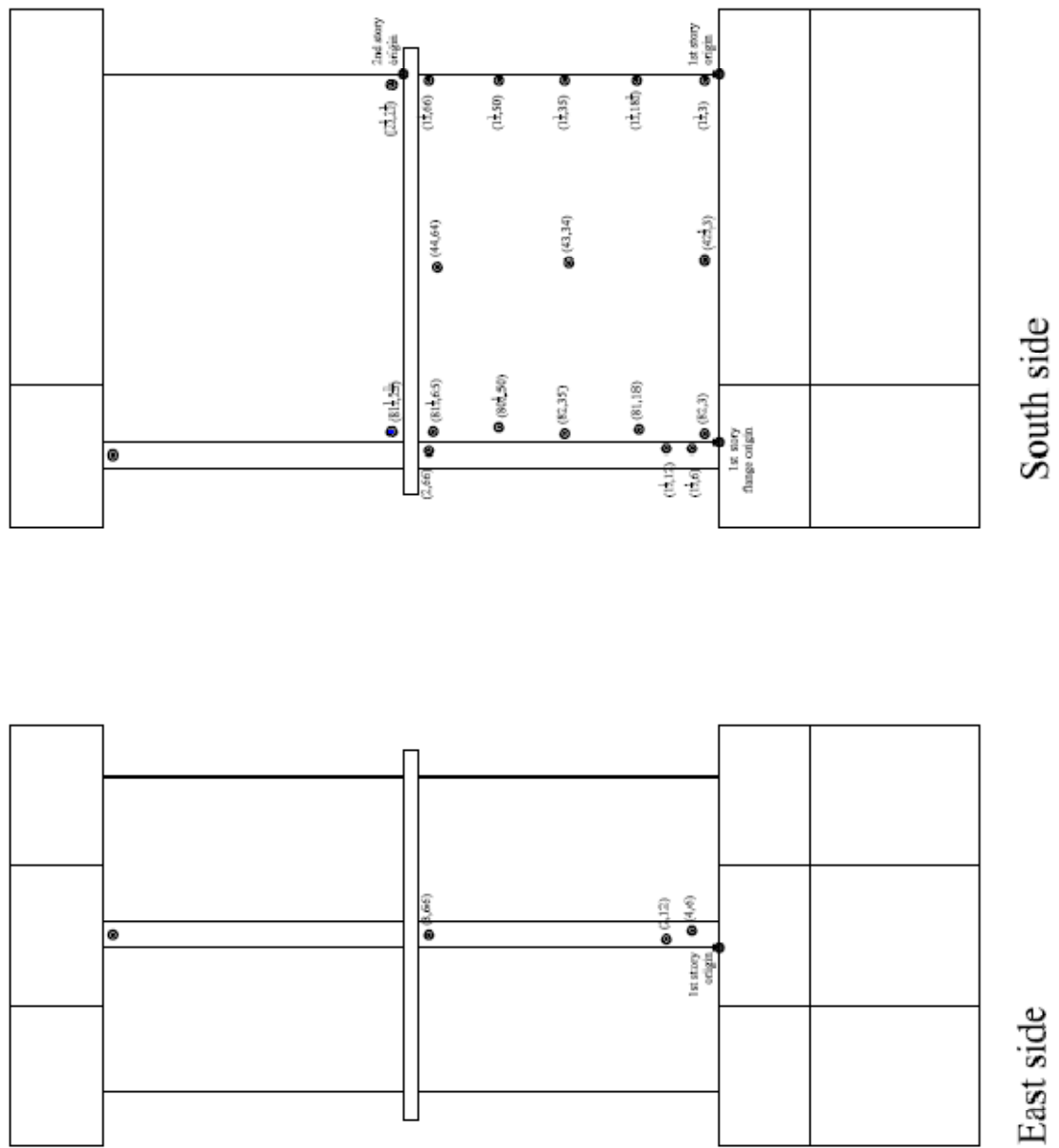


Figure B.23. NTW2 as-built string pot and LVDT mounting locations, south and east faces. Studs on each face are measured relative to indicated origins.

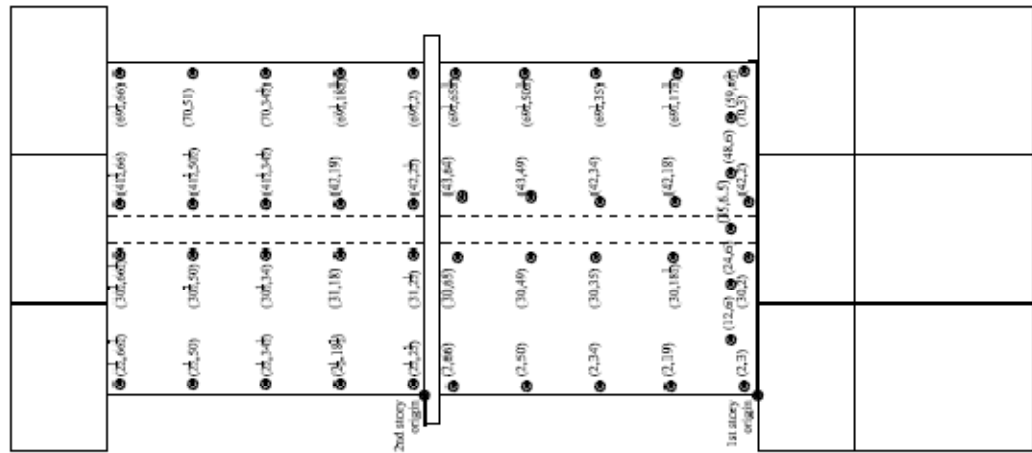
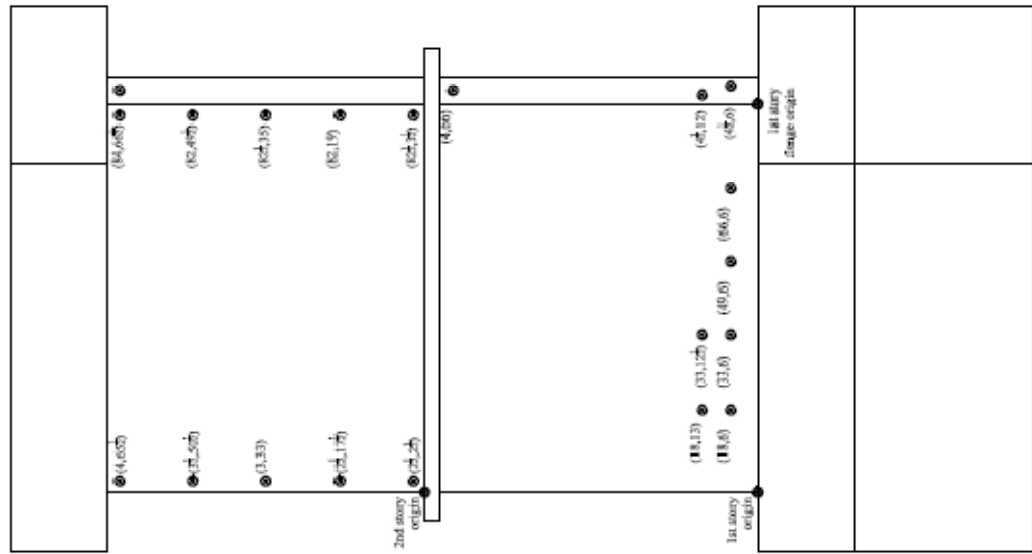
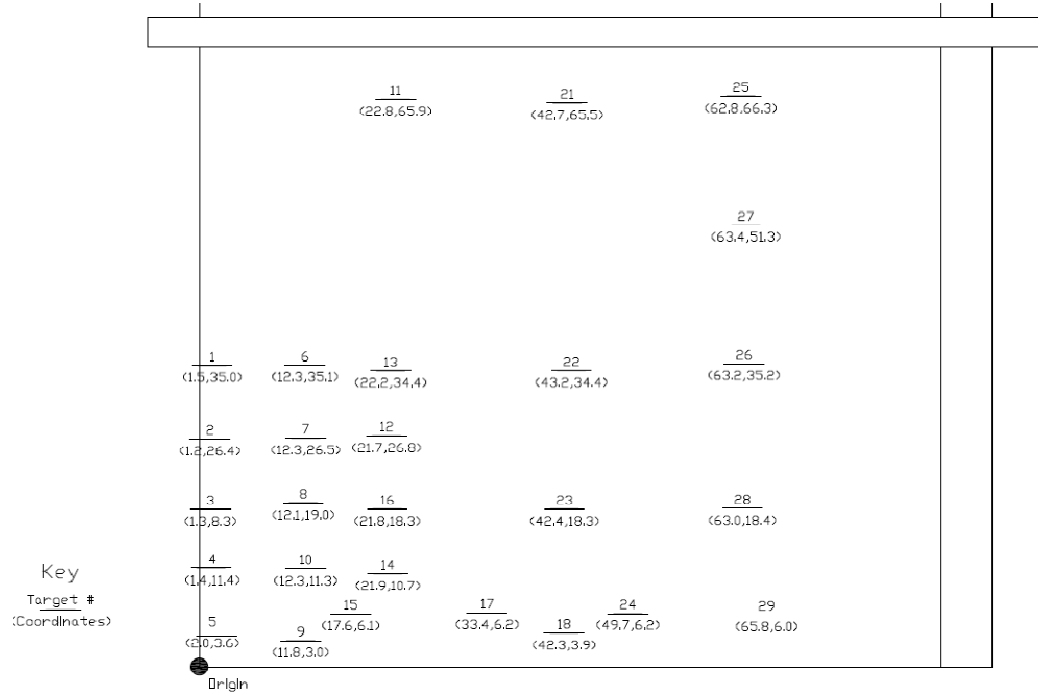


Figure B.24. NTW2 as-built string pot and LVDT mounting locations, north and west faces. Studs on each face are measured relative to indicated origins.

### Web (north face)



### Flange (west face)

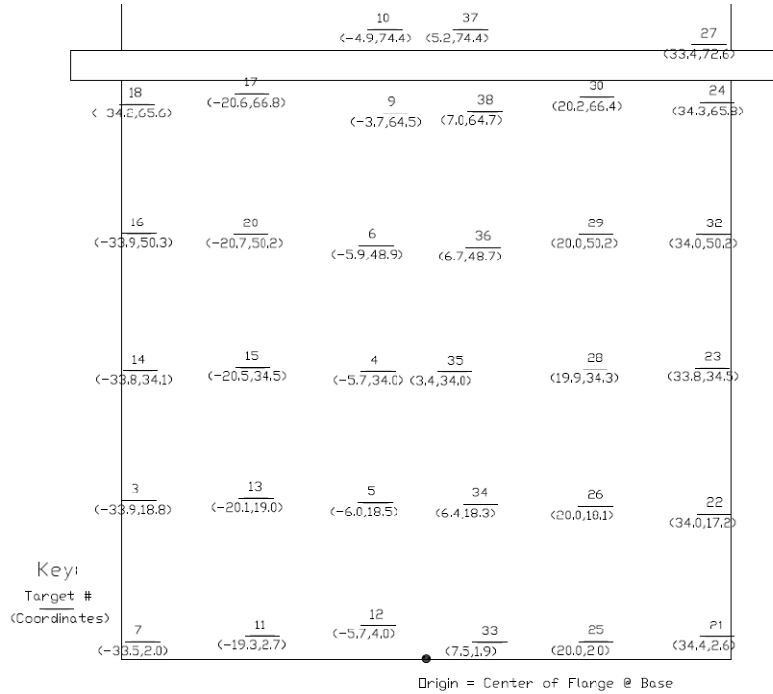
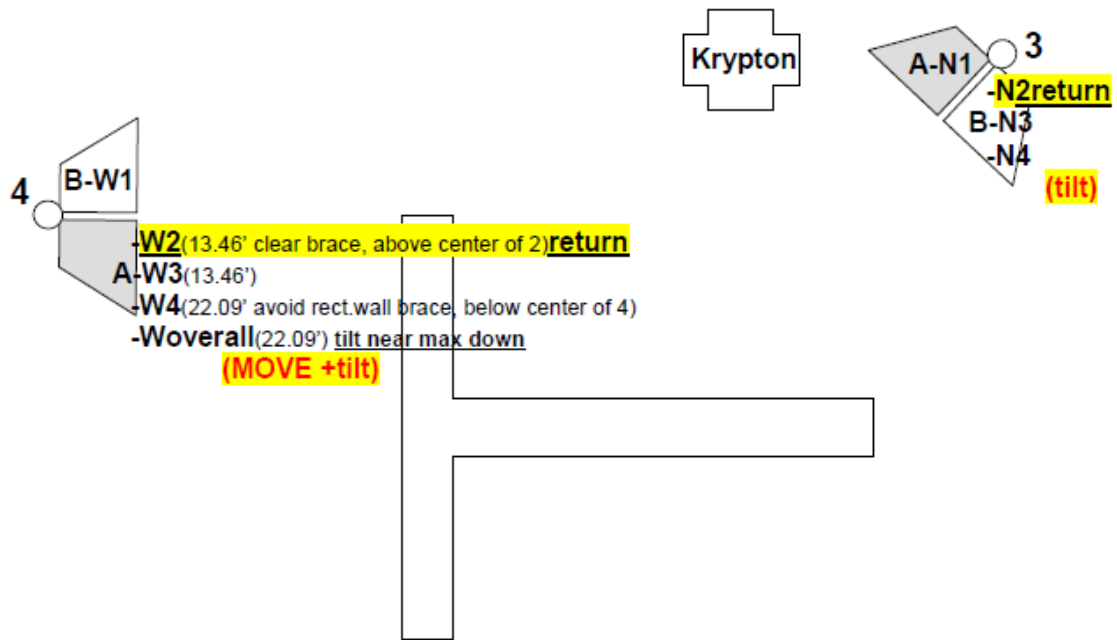


Figure B.25. NTW2 Krypton target as-built locations. LEDs on each face are measured relative to indicated origins.

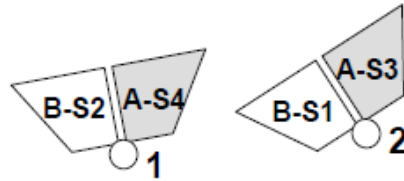
**Appendix C**  
**Telepresence System Information**

Appendix C contains information about the use of the robotic camera system at the MAST lab, which was used to capture still images and video of the testing. Figure C.1 shows the final plan used to capture still images of specimen NTW1 during testing. In addition to showing schematic camera tower locations, this diagram includes instructions regarding lighting, shelf heights, and camera tilt, which were controlled robotically. Figure C.2 shows similar information for the capture of video of specimen NTW1. Figure C.3 shows both still image and video plans for specimen NTW2. Camera shelves and tilts were static during this test, so information about moving shelves to capture multiple areas of the specimen with a single camera is not included.

## Plan for Telpresence Photos (Still Images)



Lights on all levels of S side and upper levels (3,4) ONLY on N and W sides stay on throughout test—verify w/Krypton  
 Other lights go on ONLY when shooting extensive photos.



### Plan for photos:

Take photos on stationary platforms (1A/B, 2A/B, 3A/B, 4A/B) at all pauses and occasionally (as requested) as the structure passes through zero. This will give record of levels 1,2 on all sides of structure and levels 3&4 on south side of structure throughout test.

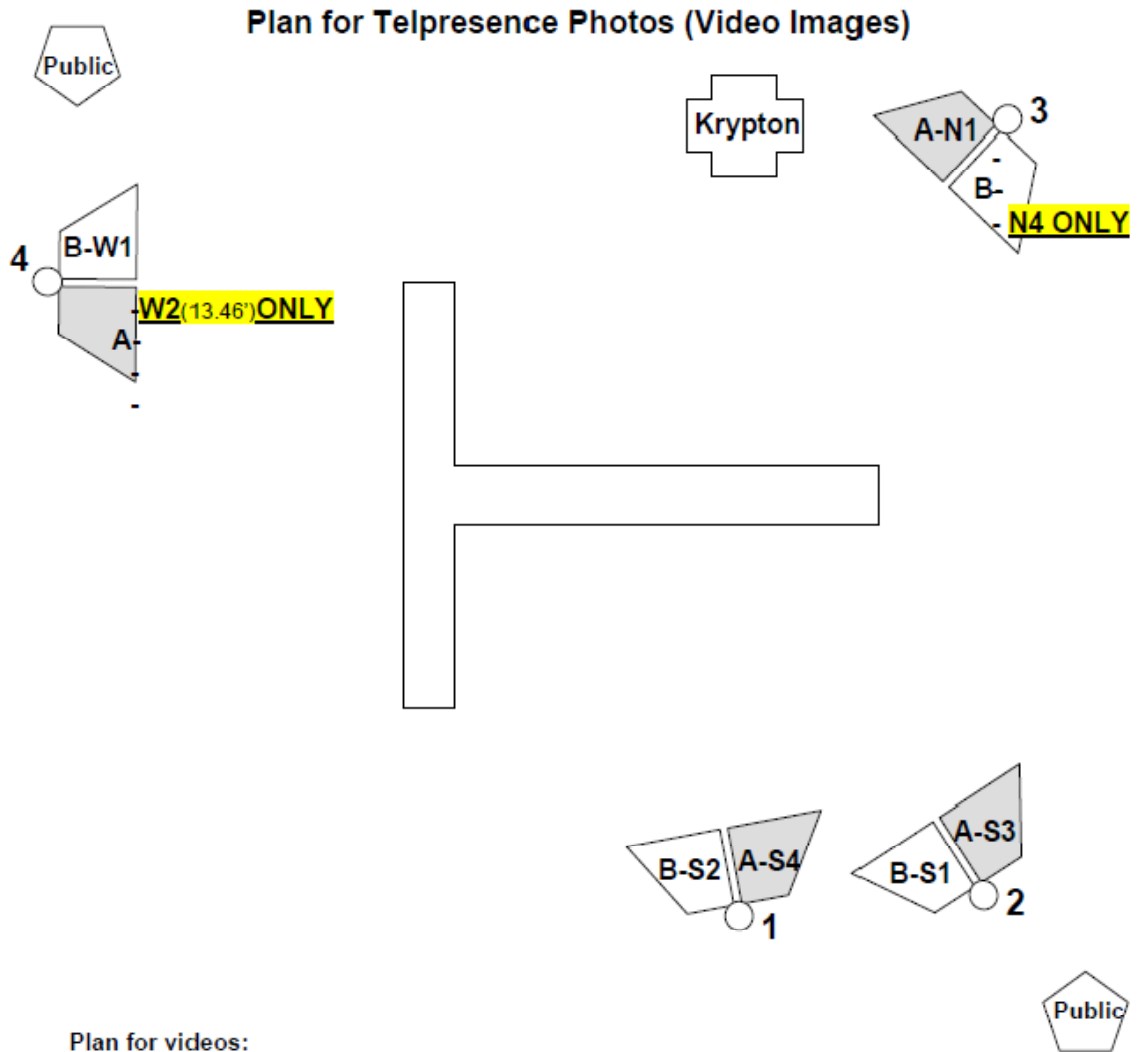
\*\*\*Important after extensive photo shoots to:

tilt camera 3B to flr. 2 and

MOVE platform 4A (~13.46') AND tilt 4A to flr. 2.

Full photo shoots should be conducted at all peaks in the first and third cycles of a group of three cycles, and at all peaks that are only done once. Full photo shoots may also be done at other discrete points of interest (as requested).

Figure C.1. Still image plan used with NTW1.



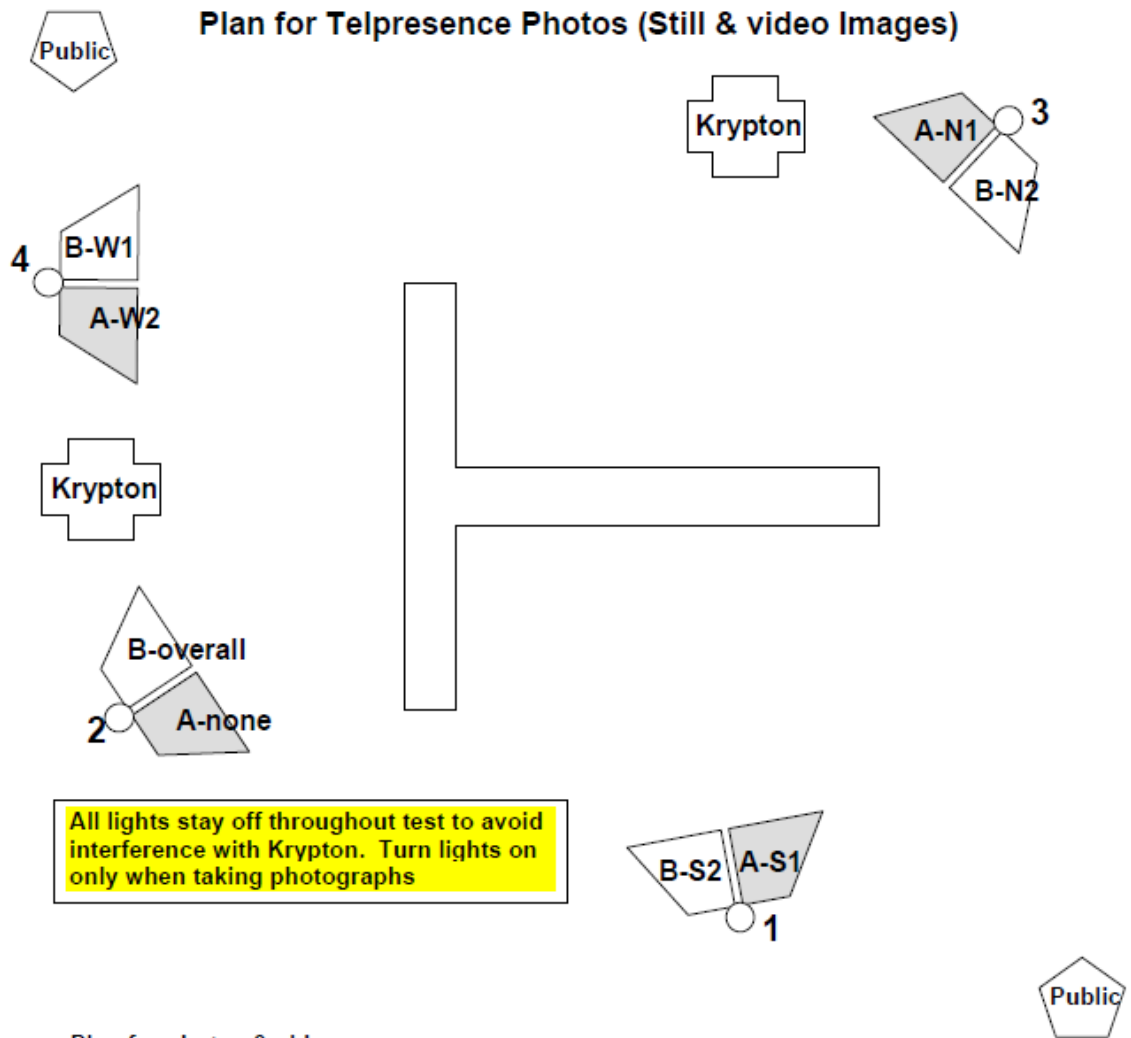
**Plan for videos:**

Take videos on stationary platforms (1A/B, 2A/B, 3A/B, 4A/B) and public telepresence throughout test. This will give record of:  
 Levels 1-4 on S side Towers 2B,1B,2A,1A  
 Level 1&4(crosshead) N side Tower 3A/B  
 Level 1&2 west side Tower 4B/A

Overall views S&N from public telepresence

\*\*\*Important to MOVE platform 4A (~13.46') to proper position after extensive photo shoots.

Figure C.2. Video plan used with NTW1.



**Plan for photos & video:**  
 Take photos at all pauses and occasionally (as requested) as the structure passes through zero.  
 Record video from all towers and public telepresence cameras throughout test.

Figure C.3. Still image and video plan used with NTW2.

**Appendix D**  
**Post-Testing Condition of Specimens**

Appendix D contains photographs taken during an “autopsy” of the first story of each specimen after testing was completed. During this examination, a small jackhammer was used to selectively remove concrete and expose the reinforcing steel so that its condition could be assessed. Figures D.1 through D.19 show specimen NTW1, and Figures D.20 through D.40 show specimen NTW2.

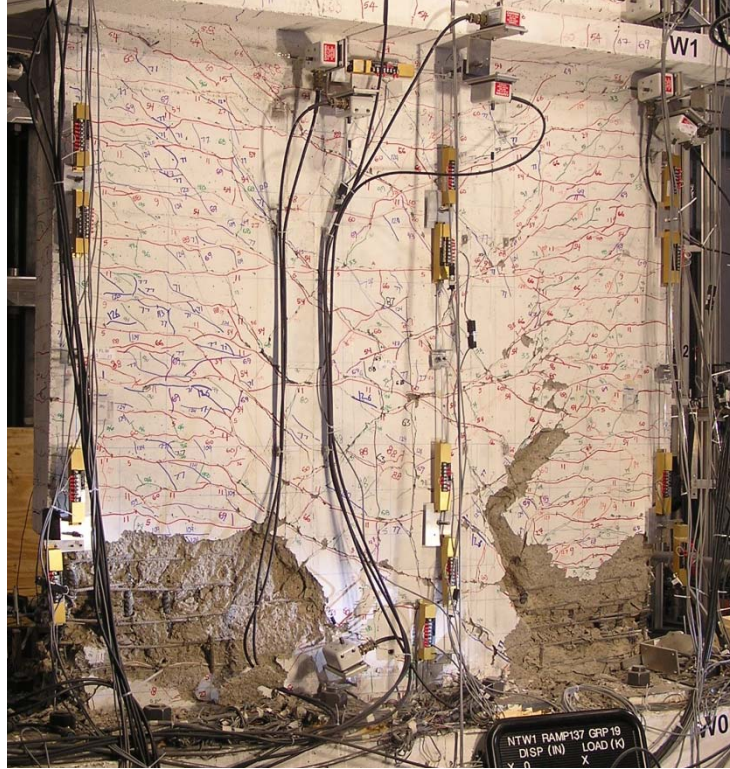
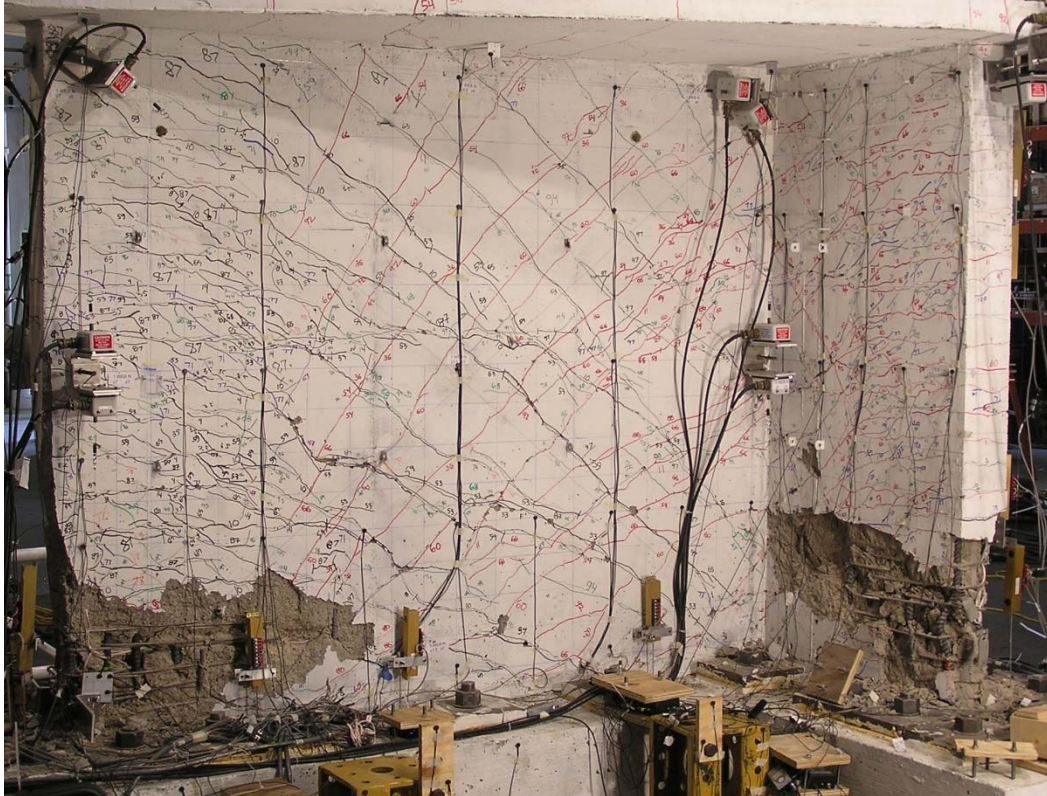


Figure D.1. First story flange of NTW1 immediately after testing



Figure

D.2. First story web of NTW1 immediately after testing

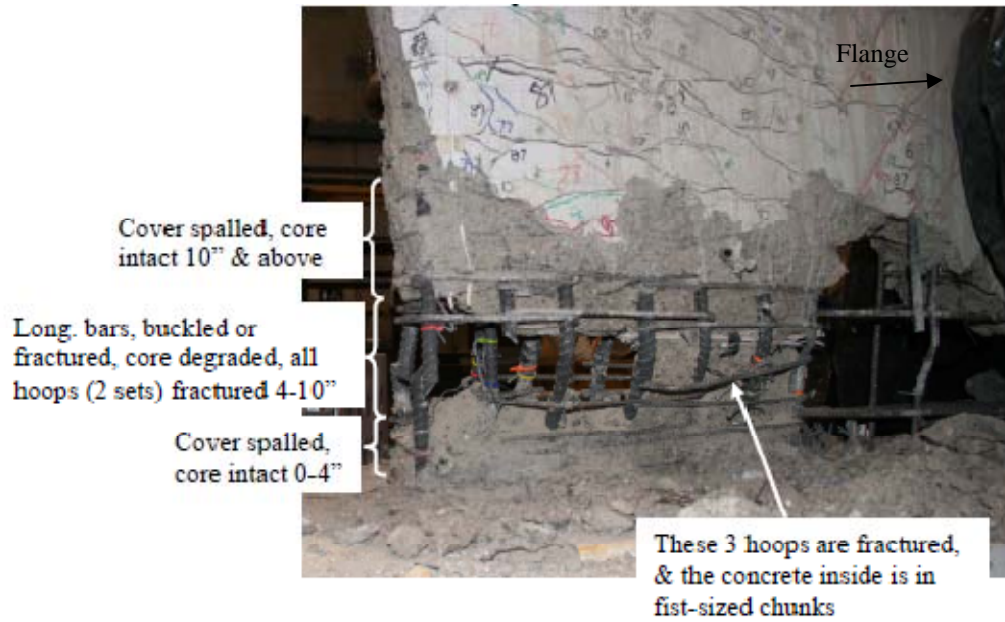


Figure D.3. NTW1 web tip near base block after removing concrete from lower 12 inches



Figure D.4. NTW1 north flange tip near base block after removing concrete from lower 12 inches

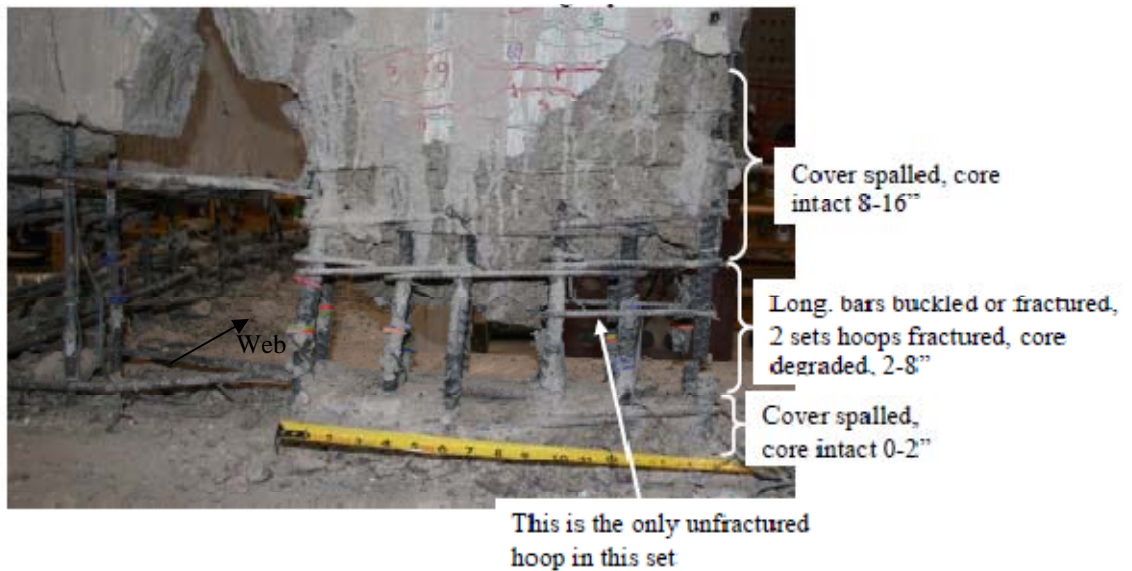


Figure D.5. NTW1 south flange tip near base block after removing concrete from lower 12 inches

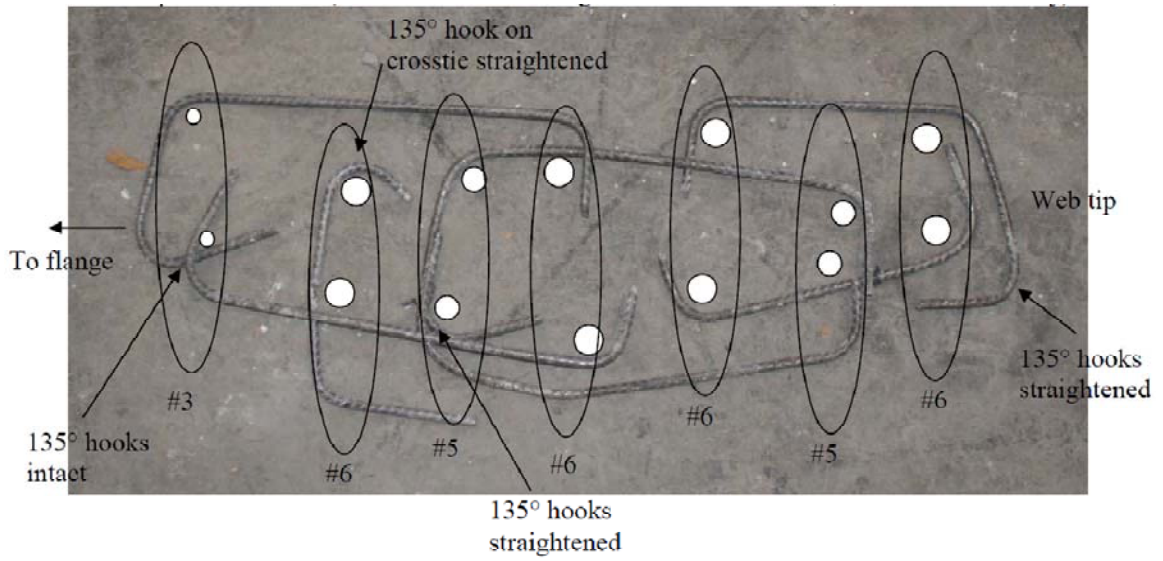


Figure D.6. NTW1 hoops and cross-ties removed from web tip. Steel is reassembled in correct order, but offset for clarity.

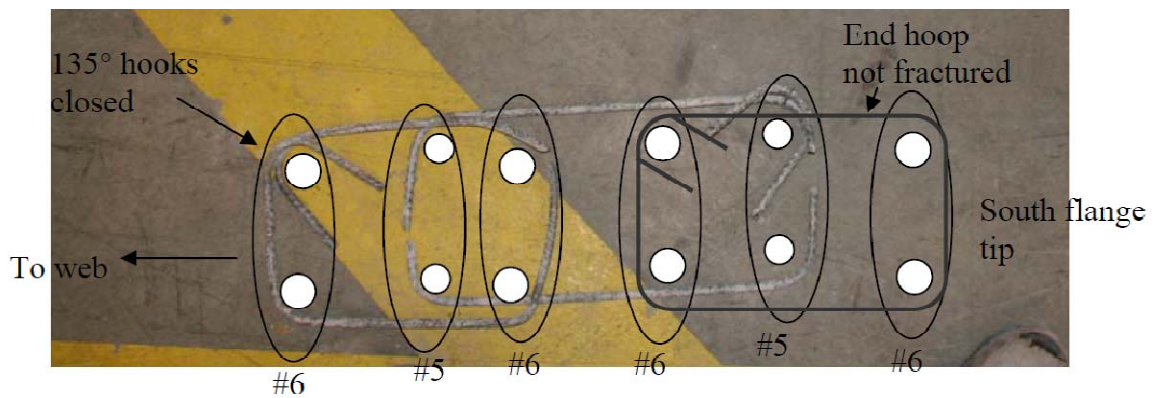


Figure D.7. NTW1 hoops and cross-ties removed from south flange tip. Steel is reassembled in correct order, but offset for clarity.

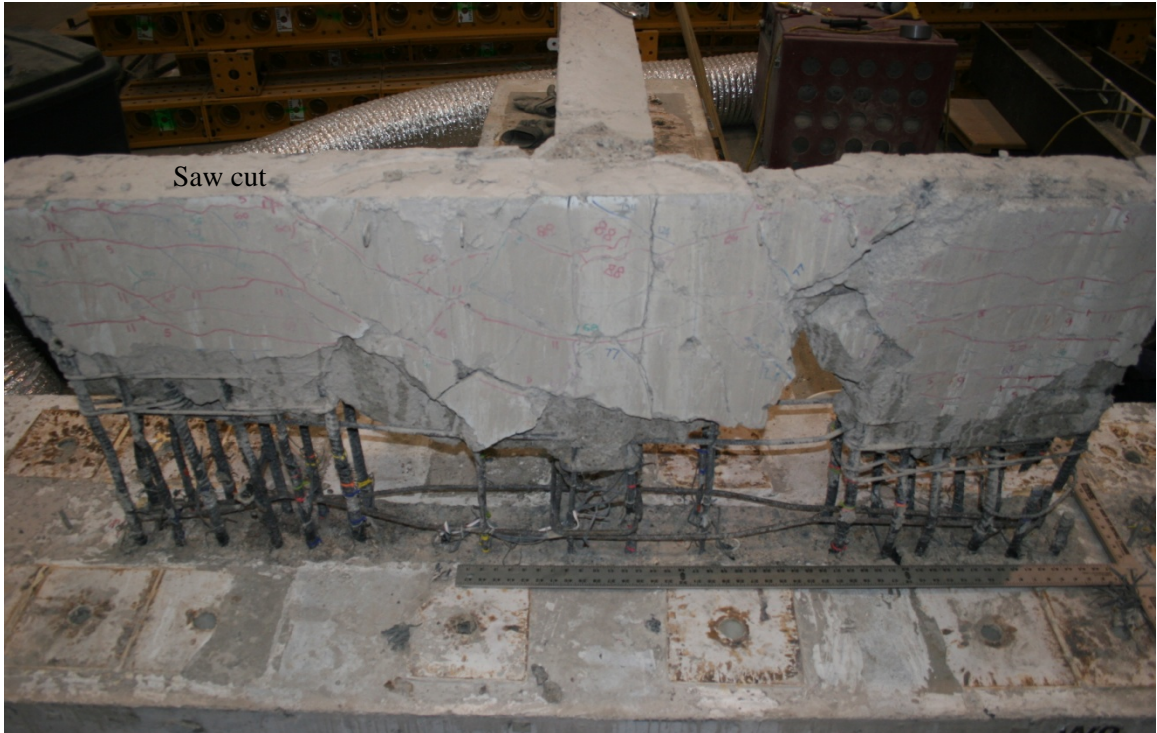


Figure D.8. NTW1 lower 30 inches of flange after removal of all concrete and confining hoops near base block.



Figure D.9. NTW1 lower 30 inches of web after removal of all concrete and confining hoops near base block.

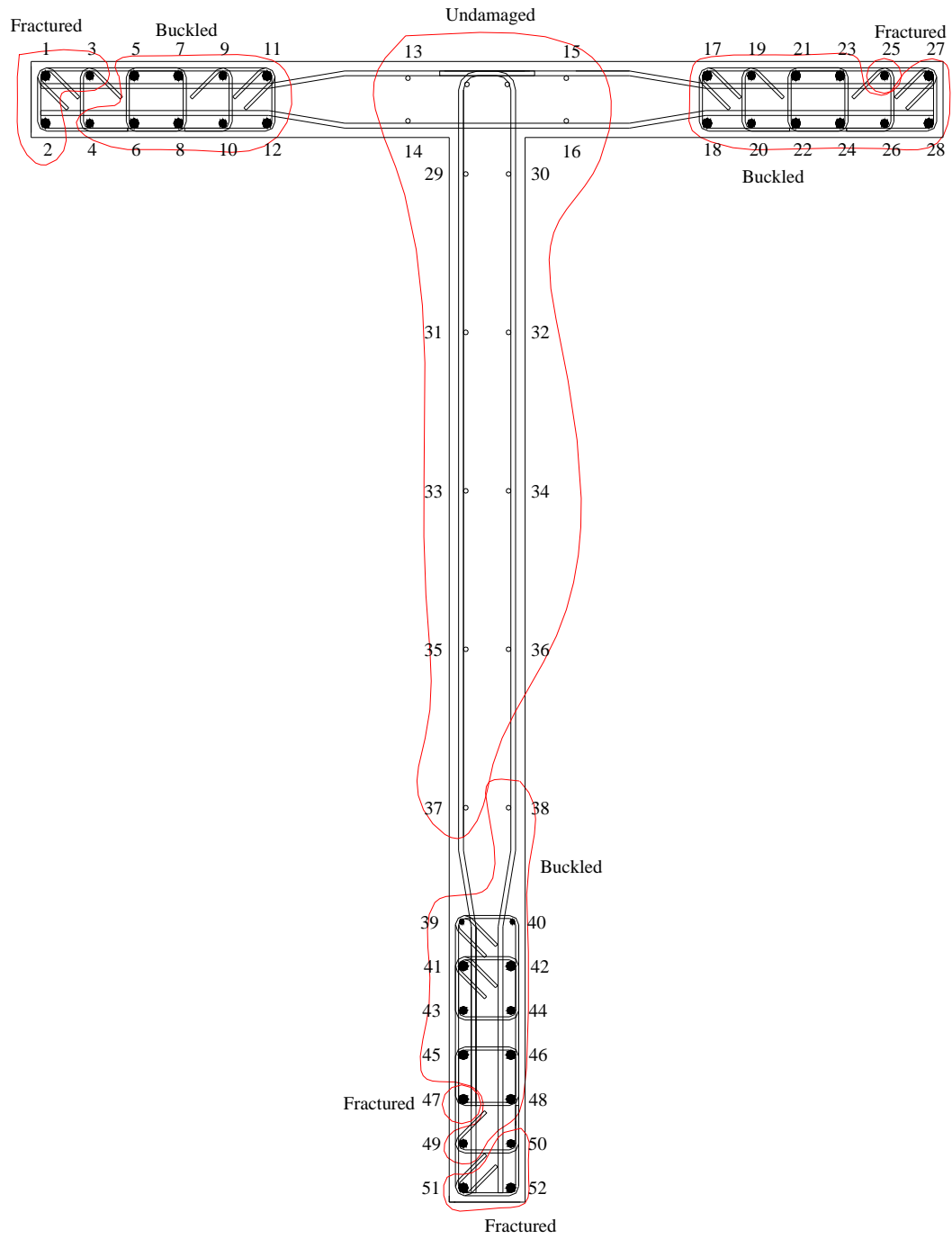


Figure D.10. NTW1 longitudinal bar condition near base block.



Figure D.11. NTW1 detailed view of web tip bars.



Figure D.12. NTW1 view of web tip from end.



Figure D.13. NTW1 detailed view of web tip bars.



Figure D.14. NTW1 detailed view of web tip bars.



Figure D.15. NTW1 north flange tip bars.



Figure D.16. NTW1 end view of north flange tip bars.



Figure D.17. NTW1 north flange tip bars.



Figure D.18. NTW1 end view of south flange tip bars.



Figure D.19. NTW1 south flange tip bars.

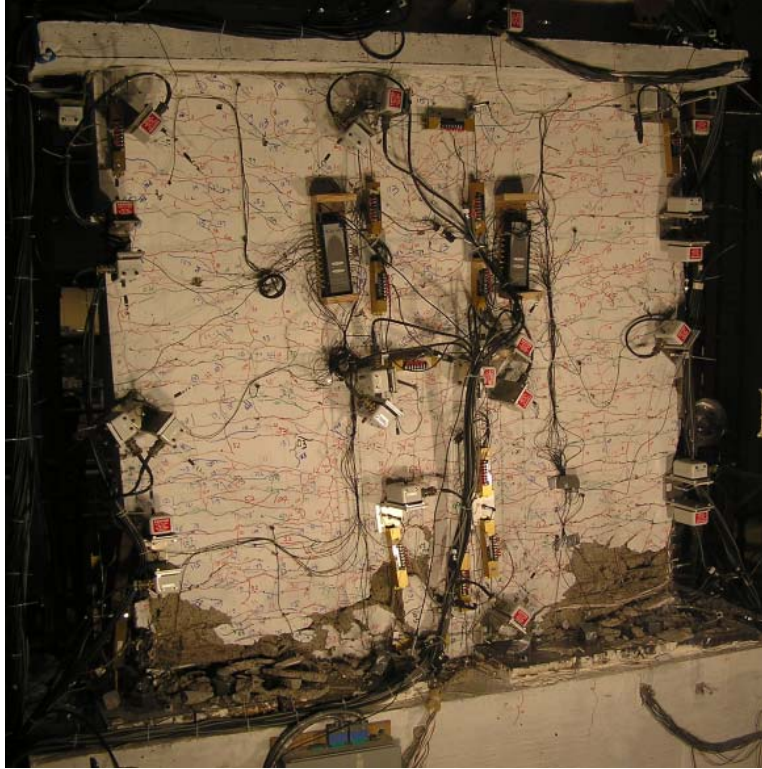


Figure D.20. NTW2 first story of flange after completion of testing.

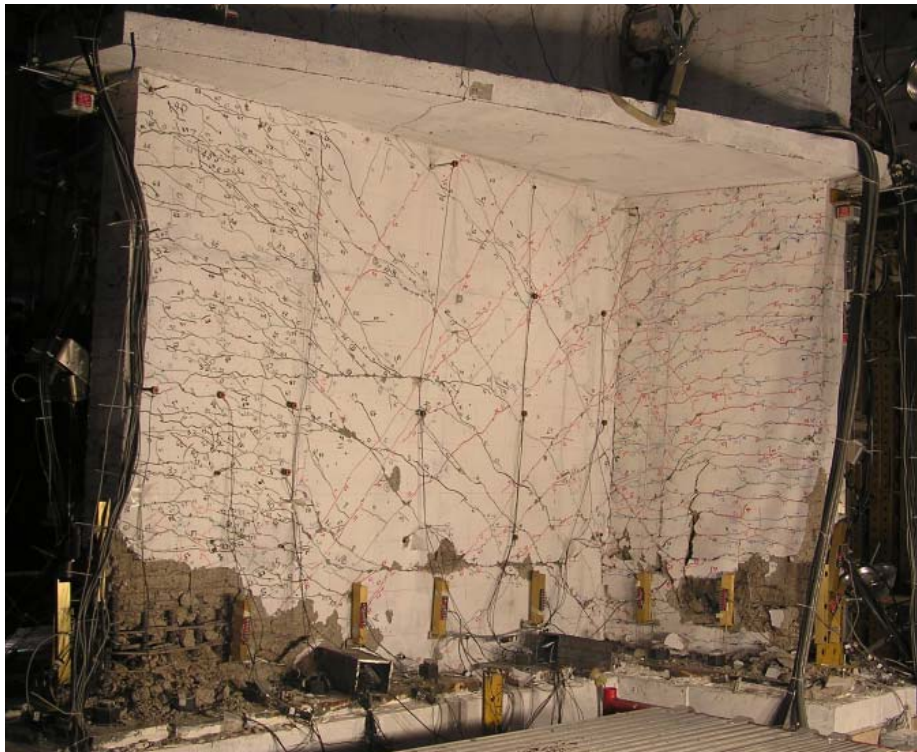


Figure D.21. NTW2 first story of flange after completion of testing.



Figure D.22. NTW2 overall view after sawcutting to remove lower 30 inches of specimen and removal of loose concrete.

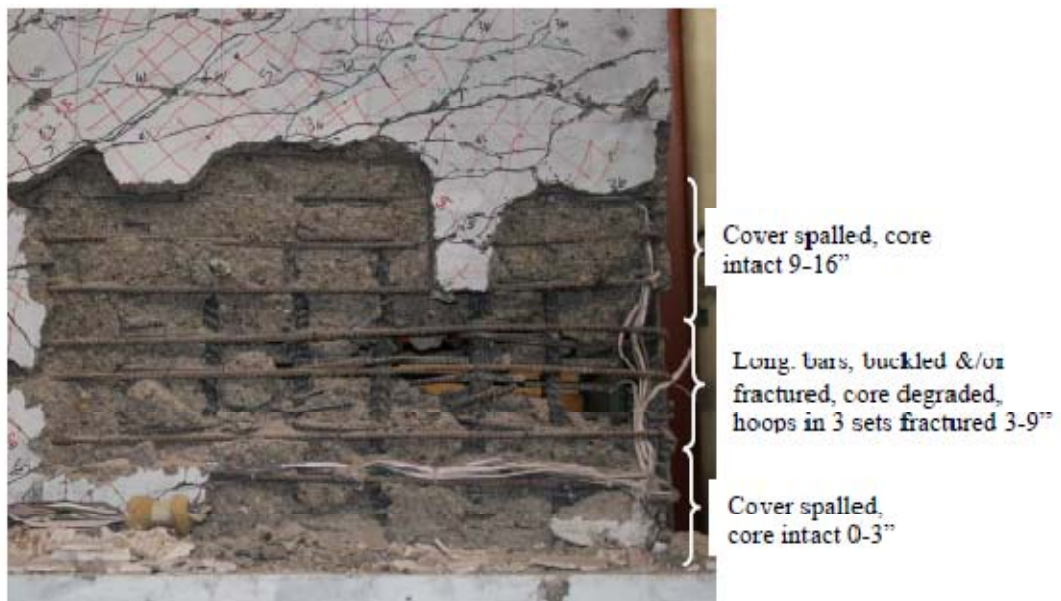


Figure D.23. NTW2 detail of web tip after removal of loose concrete.

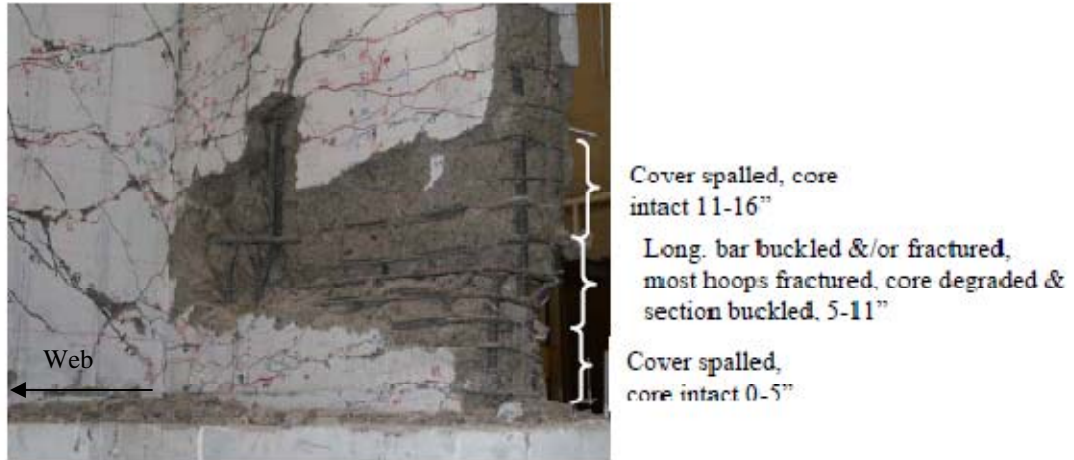


Figure D.24. NTW2 detail of north flange tip after removal of loose concrete.

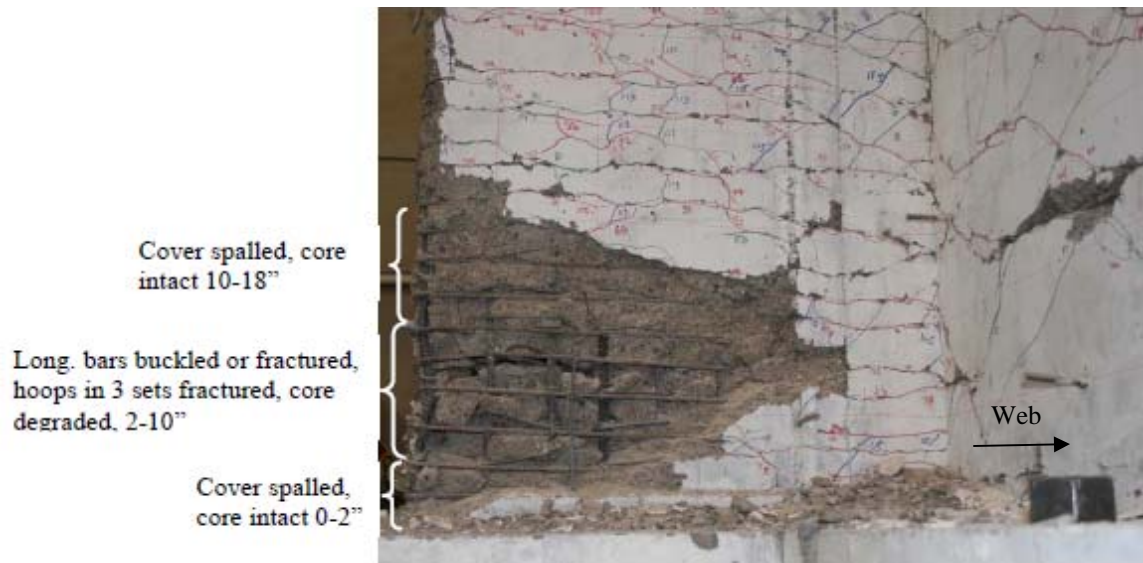


Figure D.25. NTW2 detail of south flange tip after removal of loose concrete.

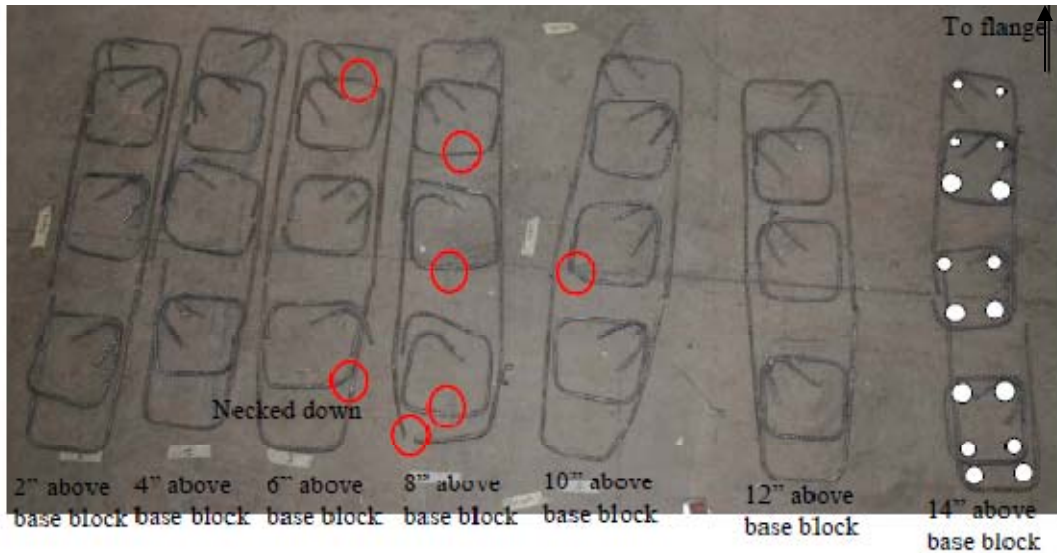


Figure D.26. NTW2 confining steel removed from web tip and reassembled in proper orientation.

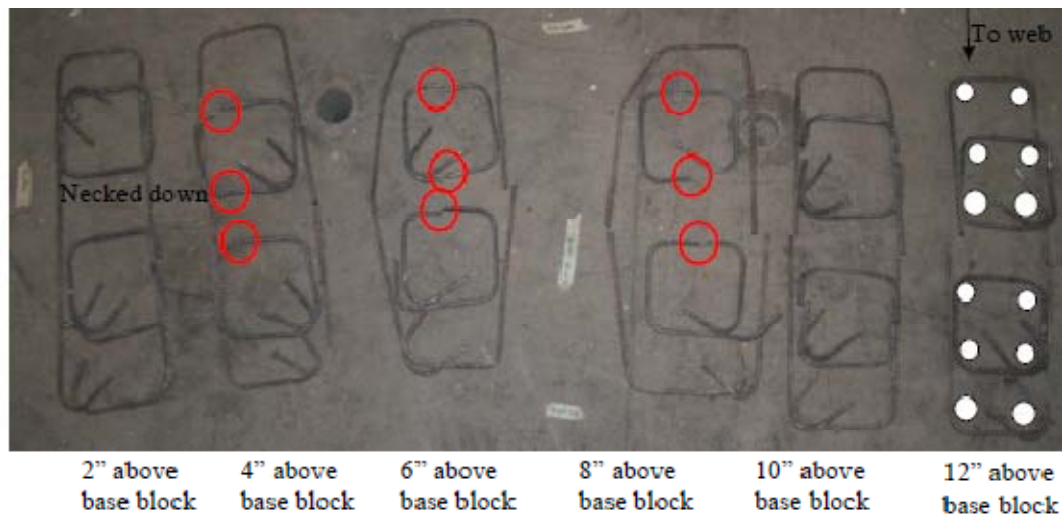


Figure D.26. NTW2 confining steel removed from north flange tip and reassembled in proper orientation.

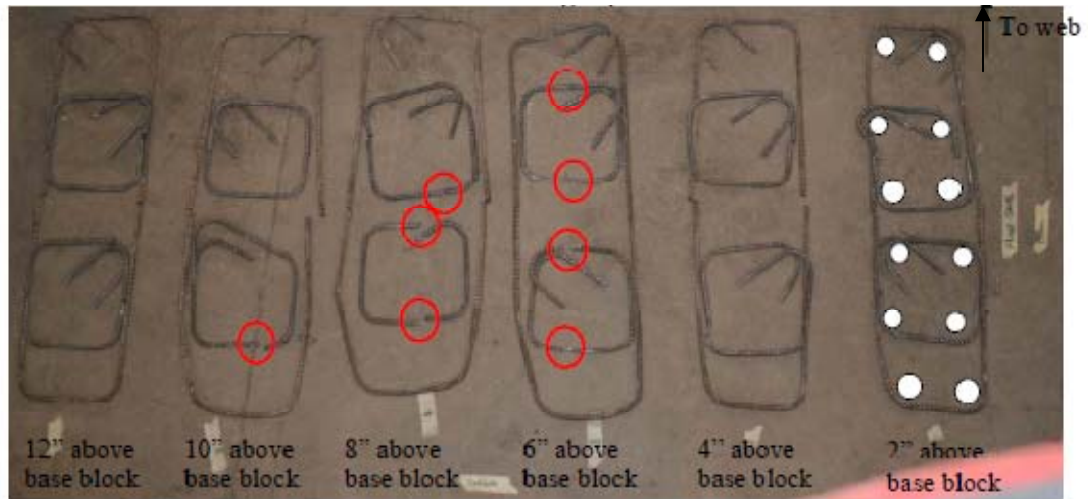


Figure D.28. NTW2 confining steel removed from south flange tip and reassembled in proper orientation.



Figure D.29. NTW2 overall view of flange after removing concrete and confining steel near base block.



Figure D.30. NTW2 overall view of web after removing concrete and confining steel near base block.

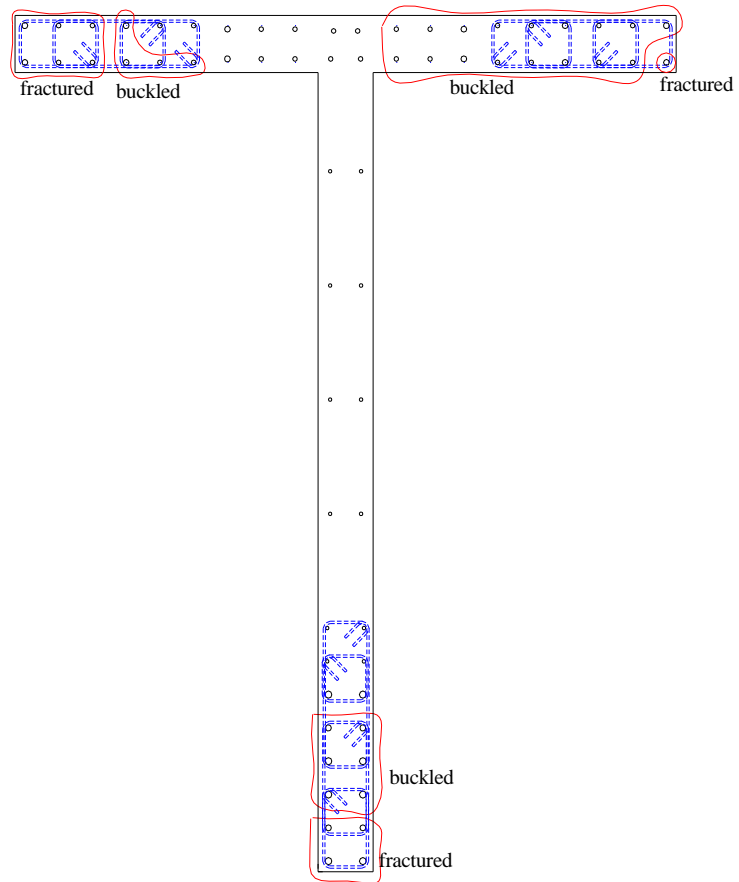


Figure D.31. NTW2 general longitudinal bar condition near base block.



Figure D.32. NTW2 detail of web tip after removal of concrete and confining steel.



Figure D.33. NTW2 end view of web tip after removal of concrete and confining steel.



Figure D.34. NTW2 detail of web tip after removal of concrete and confining steel.



Figure D.35. NTW2 detail of north flange tip after removal of concrete and confining steel.



Figure D.36. NTW2 end view of north flange tip after removal of concrete and confining steel.



Figure D.37. NTW2 north flange tip after removal of concrete and confining steel.



Figure D.38. NTW2 detail of south flange tip after removal of concrete and confining steel.



Figure D.39. NTW2 end view of south flange tip after removal of concrete and confining steel.



Figure D.40. NTW2 detail of south flange tip after removal of concrete and confining steel.

## **Appendix E**

### **Sample Calculations for F-S-SP Integration Model**



Appendix E contains sample calculations for determining the deflection associated with an arbitrarily chosen applied load to specimen NTW1 in the flange-in-tension loading direction using the F-S-SP Integration model. This Appendix begins with Table E.1 (a reproduction of Table 8.1), showing the material properties used in the modeling of specimen NTW1 and a copy of the input file used for flexural section analysis using the program BIAX. Additional information about the use of BIAX can be found in the BIAX user manual or in the help file attached to the program. This Appendix then shows the moment-curvature relationship determined using BIAX and the calculation of the various constants used in the F-S-SP model for this geometry and loading direction. These constants apply to all levels of load in this loading direction. It ends with a demonstration of the calculation of each component of deformation associated with a base moment of 70450 k-in. Deformations are calculated at two heights: 144 inches, corresponding to the top of the second story, and 288 inches, corresponding to the top of the fourth story. These values of base moment and height were chosen arbitrarily for demonstration. In order to develop a pushover curve, the process used to determine displacements under this base moment is repeated for a range of base moments. In order to determine displacements at other heights on the specimen, the upper limits of the numerical integrations are modified to represent the desired height on the specimen.

Table E.1. Material property parameters used to represent measured properties of specimen  
NTW1

Material	Parameter	Value
Unconfined Concrete	$f'_c$ (peak compressive stress)	7.26 ksi
	$\epsilon_{c0}$ (strain at $f'_c$ )	0.0025
	$\epsilon_{50u}$ (strain at 50% stress decrease)	0.0035
	$f_t$ (peak tensile stress)	0.90 ksi
Confined Concrete <sup>1</sup>	$kf'_c$ (peak compressive stress)	8.31 ksi
	$\epsilon_{c0}$ (strain at $f'_c$ )	0.0029
	$\epsilon_{50u} + \epsilon_{50h}$ (strain at 50% stress decrease)	0.019
	$f_t$ (peak tensile stress)	0.90 ksi
	$f_m$ (compressive stress at high strain)	1.66 ksi
Steel	$f_y$ (yield stress)	62.0 ksi
	$f_u$ (maximum stress)	92.0 ksi
	$f_f$ (stress at failure)	85.0 ksi
	$\epsilon_1$ (strain at onset of strain hardening)	0.002137
	$\epsilon_2$ (strain at $f_u$ )	0.08
	$\epsilon_3$ (strain at $f_f$ )	0.17
	$E$ (elastic modulus)	29000 ksi
	$E_T$ (initial modulus of strain hardening region)	1000 ksi

<sup>1</sup>Using Modified Kent and Park model

## BIAX Input File

NTW1 flange tension loading: -----

:

SYSTEM:

D=0,0,0 P=1 C=0 E=0 M=0 TOL=0.0001 :

:

SECTION:

1 HI=72 HJ=6 N1=72 N2=6 X=-36 Y=0 A=0,0,0 : flange

2 HI=6 HJ=84 N1=6 N2=84 X=-3 Y=6 A=0,0,0 : web

:

CONFINED:

1 F=74, 18, 4, 1, 72: left flange tip

2 F=125, 18, 4, 1, 72: right flange tip

3 F=806, 4, 21, 1, 6: web tip

:

STEEL:

1 X=-34.875 Y=1.25 A=0.44 T=1 R=0,0,0:

2 X=-31.375 Y=1.25 A=0.31 T=1:

3 X=-27.875 Y=1.25 A=0.44 T=1:

4 X=-24.375 Y=1.25 A=0.44 T=1:

5 X=-20.875 Y=1.25 A=0.31 T=1:

6 X=-17.375 Y=1.25 A=0.44 T=1:

7 X=-6.25 Y=1.25 A=0.11 T=1:

8 X=-2 Y=1.25 A=0.11 T=1:

9 X=34.875 Y=1.25 A=0.44 T=1:

10 X=31.375 Y=1.25 A=0.31 T=1:

11 X=27.875 Y=1.25 A=0.44 T=1:

12 X=24.375 Y=1.25 A=0.44 T=1:

13 X=20.875 Y=1.25 A=0.31 T=1:

14 X=17.375 Y=1.25 A=0.44 T=1:

15 X=6.25 Y=1.25 A=0.11 T=1:

16 X=2 Y=1.25 A=0.11 T=1:

17 X=-34.875 Y=4.75 A=0.44 T=1 R=0,0,0:

18 X=-31.375 Y=4.75 A=0.31 T=1:

19 X=-27.875 Y=4.75 A=0.44 T=1:

20 X=-24.375 Y=4.75 A=0.44 T=1:

21 X=-20.875 Y=4.75 A=0.31 T=1:

22 X=-17.375 Y=4.75 A=0.44 T=1:

23 X=-6.25 Y=4.75 A=0.11 T=1:

24 X=34.875 Y=4.75 A=0.44 T=1:

25 X=31.375 Y=4.75 A=0.31 T=1:

26 X=27.875 Y=4.75 A=0.44 T=1:

27 X=24.375 Y=4.75 A=0.44 T=1:

28 X=20.875 Y=4.75 A=0.31 T=1:

29 X=17.375 Y=4.75 A=0.44 T=1:

30 X=6.25 Y=4.75 A=0.11 T=1:

31 X=-1.75 Y=8.875 A=0.11 T=1:

32 X=-1.75 Y=21.375 A=0.11 T=1:

33 X=-1.75 Y=33.875 A=0.11 T=1:

34 X=-1.75 Y=46.375 A=0.11 T=1:

35 X=-1.75 Y=58.875 A=0.11 T=1:

36 X=-1.75 Y=67.875 A=0.11 T=1:

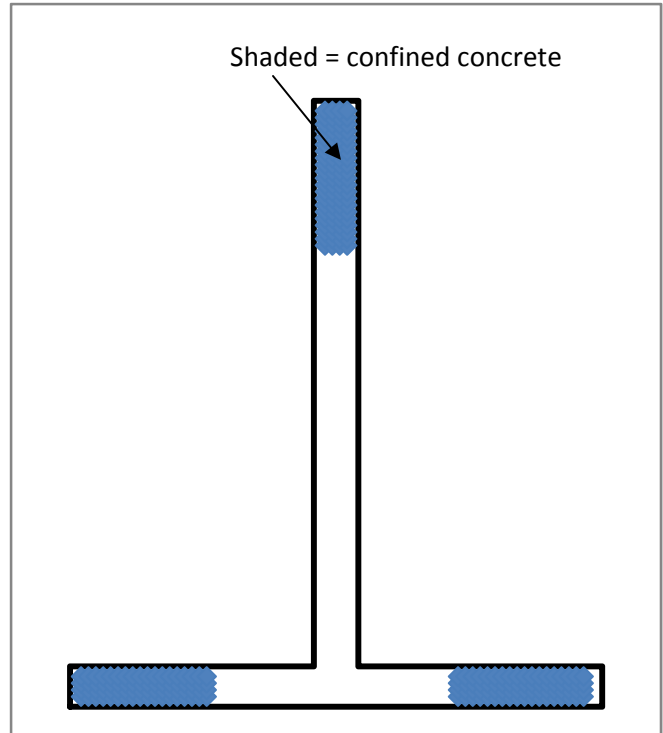
37 X=-1.75 Y=71.375 A=0.44 T=1:

38 X=-1.75 Y=74.875 A=0.31 T=1:

39 X=-1.75 Y=78.375 A=0.44 T=1:

40 X=-1.75 Y=81.875 A=0.44 T=1:

41 X=-1.75 Y=85.375 A=0.31 T=1:



42 X=-1.75 Y=88.875 A=0.44 T=1:  
 43 X=1.75 Y=8.875 A=0.11 T=1:  
 44 X=1.75 Y=21.375 A=0.11 T=1:  
 45 X=1.75 Y=33.875 A=0.11 T=1:  
 46 X=1.75 Y=46.375 A=0.11 T=1:  
 47 X=1.75 Y=58.875 A=0.11 T=1:  
 48 X=1.75 Y=67.875 A=0.11 T=1:  
 49 X=1.75 Y=71.375 A=0.44 T=1:  
 50 X=1.75 Y=74.875 A=0.31 T=1:  
 51 X=1.75 Y=78.375 A=0.44 T=1:  
 52 X=1.75 Y=81.875 A=0.44 T=1:  
 53 X=1.75 Y=85.375 A=0.31 T=1:  
 54 X=1.75 Y=88.875 A=0.44 T=1:  
 :  
 PROPERTY:  
 FC=7.26 E1= 0.002503 E2= 0.003543 FR=0.9:  
 FC=8.31 E1= 0.002866 E2= 0.0350 FR=0.9 FM=1.66 :  
 FY=62 FU= 92 FF= 85 E1=0.002138 E2=0.08 E3=0.17 E=29000 ET=1000:  
 :  
 DATA:  
 EC=0.0001 A=0 P=186.5  
 EC=0.0002 A=0 P=186.5  
 EC=0.0003 A=0 P=186.5  
 EC=0.0004 A=0 P=186.5  
 EC=0.0005 A=0 P=186.5  
 EC=0.0006 A=0 P=186.5  
 EC=0.0007 A=0 P=186.5  
 EC=0.0008 A=0 P=186.5  
 EC=0.0009 A=0 P=186.5  
 EC=0.0010 A=0 P=186.5  
 EC=0.0012 A=0 P=186.5  
 EC=0.0014 A=0 P=186.5  
 EC=0.0016 A=0 P=186.5  
 EC=0.0018 A=0 P=186.5  
 EC=0.0020 A=0 P=186.5  
 EC=0.0022 A=0 P=186.5  
 EC=0.0024 A=0 P=186.5  
 EC=0.0026 A=0 P=186.5  
 EC=0.0028 A=0 P=186.5  
 EC=0.0030 A=0 P=186.5  
 EC=0.0035 A=0 P=186.5  
 EC=0.0040 A=0 P=186.5  
 EC=0.0045 A=0 P=186.5  
 EC=0.0050 A=0 P=186.5  
 EC=0.0060 A=0 P=186.5  
 EC=0.0070 A=0 P=186.5  
 EC=0.0080 A=0 P=186.5  
 EC=0.0090 A=0 P=186.5  
 EC=0.01 A=0 P=186.5  
 EC=0.012 A=0 P=186.5  
 EC=0.014 A=0 P=186.5  
 EC=0.016 A=0 P=186.5  
 EC=0.018 A=0 P=186.5  
 EC=0.020 A=0 P=186.5  
 EC=0.025 A=0 P=186.5  
 :  
 END

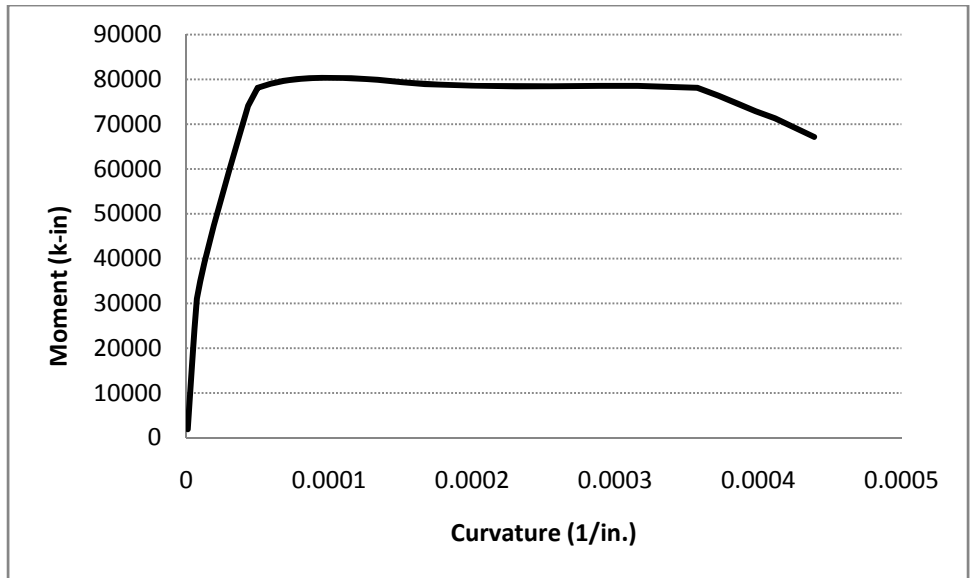


Figure E.1. Moment-curvature relationship determined using BIAX input above.

## Calculation of Sample Point on Load-Displacement Curve using Section Analysis Results

Constants applying to all loading of this section in this direction:

$$M_{yield}/\phi_{yield}=50050 \text{ k-in.}/3.67\text{E-}5 \text{ (1/in.)}=1.36\text{E+}9 \text{ k-in}^2$$

Cracked shear stiffness assuming 45° cracks  $K_{v,45} = 71432 \text{ k/rad}$  (Eq. 8.4)

Shear span  $z = 312 \text{ in.}$

Shear constant  $C = 1.36\text{E+}9 \text{ k-in}^2/(71432 \text{ k/rad} * 312 \text{ in.}) = 61.2 \text{ in.}$  (Eq. 8.5)

Development length for strain penetration  $l_a = (3/8)f_y/f'_c = 3.23 \text{ in.}$  (Eq. 8.7)

Depth to extreme tension bar = 89 in.

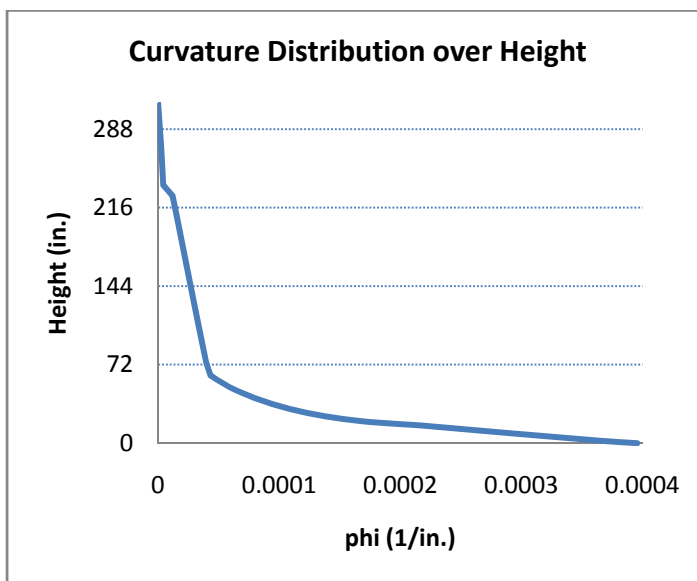
Calculation of displacements at a particular base moment:

Selected Moment = 70450 k-in

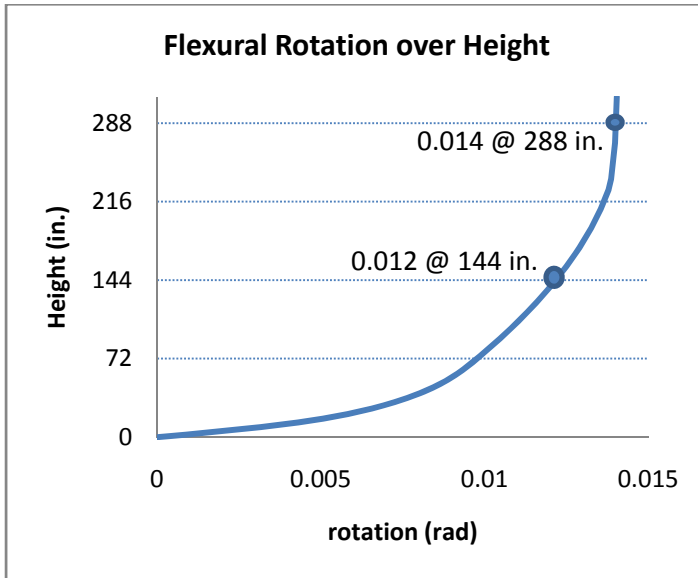
Base Shear = 70450 k-in/312 in = 225.8 k

At M=70450: phi=0.000396 1/in; neutral axis = 25.3 in; steel strain = 0.025 in/in (all from section analysis results)

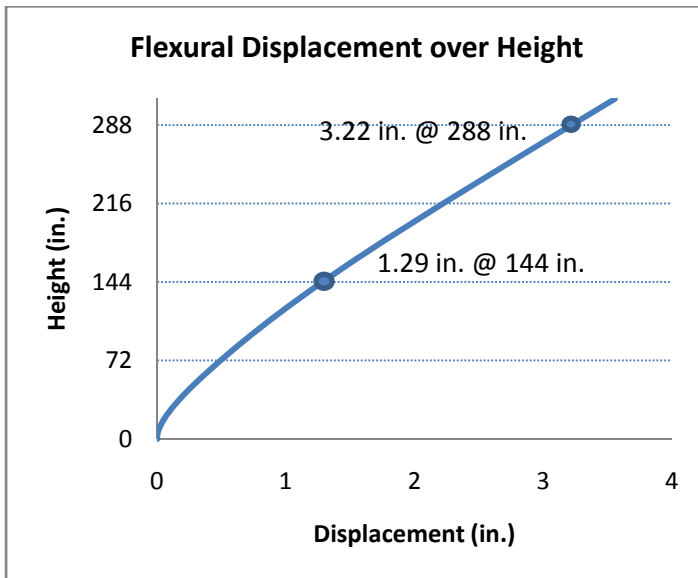
Curvature distribution over wall height based on sectional analysis is plotted in following figure



Numerical integration of curvature over height using trapezoid rule gives rotation over wall height as



Numerical integration of rotation over height using trapezoid rule gives flexural displacement over wall height as



$$\Delta_f @ 144 \text{ in.} = 1.29 \text{ in.}$$

$$\Delta_f @ 288 \text{ in.} = 3.22 \text{ in.}$$

Displacement due to shear is calculated as flexural rotation\*C:

$$\Delta_v @ 144 \text{ in.} = 0.012 * 61.2 \text{ in.} = 0.73 \text{ in.}$$

$$\Delta_v @ 288 \text{ in.} = 0.014 * 61.2 \text{ in.} = 0.86 \text{ in.}$$

Rigid body rotation due to strain penetration is calculated as

(steel strain @ base)\* $l_d$ /[(depth to extreme tensile bar) - neutral axis depth]

$$= 0.025 * 3.23 \text{ in.} / (89 \text{ in.} - 25.3 \text{ in.}) = 0.0013 \text{ rad}$$

Displacement due to rigid body rotation = rotation \* height

$$\Delta_{sp} @ 144 \text{ in.} = 0.0013 * 144 \text{ in.} = 0.18 \text{ in.}$$

$$\Delta_{sp} @ 288 \text{ in.} = 0.0013 * 288 \text{ in.} = 0.37 \text{ in.}$$

Total displacement  $\Delta_T = \Delta_f + \Delta_v + \Delta_{sp}$

$$\Delta_T @ 144 \text{ in.} = 1.29 \text{ in.} + 0.73 \text{ in.} + 0.18 \text{ in.}$$

$$\Delta_T @ 288 \text{ in.} = 3.22 \text{ in.} + 0.86 \text{ in.} + 0.37 \text{ in.}$$